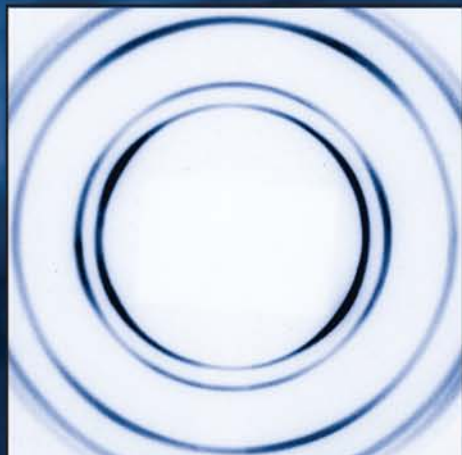
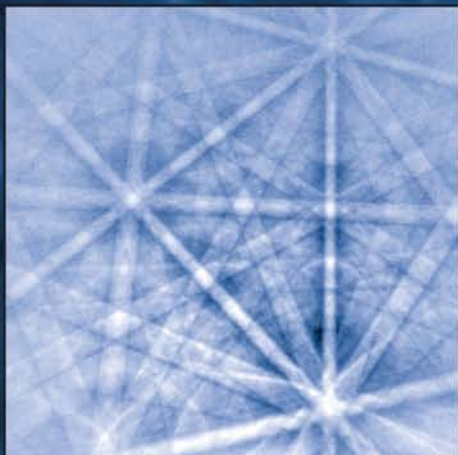


SECOND EDITION

Introduction to TEXTURE ANALYSIS

Macrotecture, Microtexture,
and Orientation Mapping



OLAF ENGLER
VALERIE RANDLE



CRC Press
Taylor & Francis Group

SECOND EDITION

Introduction to
TEXTURE
ANALYSIS

Macrotexture, Microtexture,
and Orientation Mapping

SECOND EDITION

Introduction to

TEXTURE ANALYSIS

Macrotecture, Microtexture,
and Orientation Mapping

OLAF ENGLER
VALERIE RANDLE



CRC Press

Taylor & Francis Group

Boca Raton London New York

CRC Press is an imprint of the
Taylor & Francis Group, an **informa** business

CRC Press
Taylor & Francis Group
6000 Broken Sound Parkway NW, Suite 300
Boca Raton, FL 33487-2742

© 2010 by Taylor and Francis Group, LLC
CRC Press is an imprint of Taylor & Francis Group, an Informa business

No claim to original U.S. Government works

Printed in the United States of America on acid-free paper
10 9 8 7 6 5 4 3 2 1

International Standard Book Number: 978-1-4200-6365-3 (Paperback)

This book contains information obtained from authentic and highly regarded sources. Reasonable efforts have been made to publish reliable data and information, but the author and publisher cannot assume responsibility for the validity of all materials or the consequences of their use. The authors and publishers have attempted to trace the copyright holders of all material reproduced in this publication and apologize to copyright holders if permission to publish in this form has not been obtained. If any copyright material has not been acknowledged please write and let us know so we may rectify in any future reprint.

Except as permitted under U.S. Copyright Law, no part of this book may be reprinted, reproduced, transmitted, or utilized in any form by any electronic, mechanical, or other means, now known or hereafter invented, including photocopying, microfilming, and recording, or in any information storage or retrieval system, without written permission from the publishers.

For permission to photocopy or use material electronically from this work, please access www.copyright.com (<http://www.copyright.com/>) or contact the Copyright Clearance Center, Inc. (CCC), 222 Rosewood Drive, Danvers, MA 01923, 978-750-8400. CCC is a not-for-profit organization that provides licenses and registration for a variety of users. For organizations that have been granted a photocopy license by the CCC, a separate system of payment has been arranged.

Trademark Notice: Product or corporate names may be trademarks or registered trademarks, and are used only for identification and explanation without intent to infringe.

Library of Congress Cataloging-in-Publication Data

Engler, Olaf.

Introduction to texture analysis : macrotecture, microtexture, and orientation mapping / Olaf Engler and Valerie Randle. -- 2nd ed.

p. cm.

Randle's name appears first on the earlier edition.

Includes bibliographical references and index.

ISBN 978-1-4200-6365-3 (alk. paper)

1. Materials--Texture. 2. Materials--Analysis. I. Randle, V. (Valerie) II. Title.

TA418.5.R36 2010

620.1'1292--dc22

2009013699

Visit the Taylor & Francis Web site at
<http://www.taylorandfrancis.com>

and the CRC Press Web site at
<http://www.crcpress.com>

Contents

Preface.....	xiii
Authors	xv

Part I Fundamental Issues

1. Introduction	3
1.1 The Classical Approach to Texture.....	3
1.2 The Modern Approach to Texture: Microtexture.....	7
1.2.1 Applications of Microtexture.....	8
1.2.2 Electron Backscatter Diffraction	11
1.2.3 Orientation Microscopy and Orientation Mapping	12
1.3 A Guide to the Book	13
2. Descriptors of Orientation.....	15
2.1 Introduction	15
2.2 Crystal Structures and Crystal Symmetries	16
2.3 Transformation between Coordinate Systems:	
The Rotation Matrix	20
2.3.1 Coordinate Systems	20
2.3.2 The Rotation (Orientation) Matrix.....	24
2.3.3 Crystallographically Related Solutions	25
2.4 The “Ideal Orientation” (Miller or Miller–Bravais Indices) Notation.....	27
2.5 The Reference Sphere, Pole Figure, and Inverse Pole Figure.....	30
2.5.1 The Pole Figure	30
2.5.2 The Inverse Pole Figure.....	33
2.6 The Euler Angles and Euler Space	33
2.6.1 The Euler Angles.....	34
2.6.2 The Euler Space	36
2.7 The Angle/Axis of Rotation and Cylindrical Angle/Axis Space	39
2.7.1 Angle/Axis of Rotation	40
2.7.2 Angle/Axis Description of Misorientation	42
2.7.3 The Cylindrical Angle/Axis Space.....	43

2.8	The Rodrigues Vector and Rodrigues Space	46
2.8.1	The Rodrigues Vector	46
2.8.2	The Fundamental Zone	47
2.8.3	Properties of Rodrigues Space	49
2.9	Summation	50
3.	Application of Diffraction to Texture Analysis	51
3.1	Introduction	51
3.2	Diffraction of Radiation and Bragg's Law	52
3.3	Structure Factor	59
3.4	Laue and Debye-Scherrer Methods	61
3.5	Absorption and Depth of Penetration	64
3.6	Characteristics of Radiations Used for Texture Analysis	66
3.6.1	X-Rays.....	66
3.6.2	Neutrons	68
3.6.3	Electrons	69
3.7	Summation	71

Part II Macrotexture Analysis

4.	Macrotexture Measurements	75
4.1	Introduction	75
4.2	Principle of Pole Figure Measurement.....	75
4.3	X-Ray Diffraction Methods.....	79
4.3.1	Generation of X-Rays	80
4.3.2	Pole Figure Diffractometry in the Texture Goniometer.....	86
4.3.3	Principles of Pole Figure Scanning.....	90
4.3.4	X-Ray Detectors	92
4.3.5	Energy-Dispersive Diffractometry	98
4.3.6	Correction and Normalization of Pole Figure Data.....	101
4.3.7	Inverse Pole Figures.....	105
4.4	Neutron Diffraction Methods	107
4.4.1	Pole Figure Measurement by Neutron Diffraction.....	107
4.4.2	Time-of-Flight Measurements.....	109
4.5	Texture Measurements in Low-Symmetry and Multiphase Materials.....	112
4.5.1	Peak Separation	113
4.5.2	Multiphase Materials.....	115
4.6	Sample Preparation.....	117
4.7	Summation	121

5. Evaluation and Representation of Macrotexture Data	123
5.1 Introduction	123
5.2 Pole Figure and Inverse Pole Figure.....	124
5.2.1 Normalization and Contouring of Pole Figures.....	124
5.2.2 Representation of Orientations in the Inverse Pole Figure	126
5.3 Determination of the Orientation Distribution Function from Pole Figure Data	126
5.3.1 The Orientation Distribution Function.....	126
5.3.2 The Series Expansion Method.....	129
5.3.3 Direct Methods.....	137
5.3.4 Comparison of Series Expansion and Direct Methods.....	140
5.4 Representation and Display of Texture in Euler Space	141
5.4.1 Properties of Euler Space.....	142
5.4.2 Representation and Display of Textures.....	143
5.5 Examples of Typical Textures in Metals	147
5.5.1 Deformation Textures of fcc Metals.....	147
5.5.2 Deformation Textures of bcc Metals	153
5.5.3 Deformation Textures of Hexagonal Metals	157
5.5.4 Recrystallization Textures of fcc Metals	161
5.5.5 Recrystallization Textures of bcc Metals	166
5.5.6 Recrystallization Textures of Hexagonal Metals	170
5.6 Summation.....	171

Part III Microtexture Analysis

6. The Kikuchi Diffraction Pattern.....	175
6.1 Introduction	175
6.2 The Kikuchi Diffraction Pattern	176
6.2.1 Formation of Kikuchi Patterns.....	176
6.2.2 Comparison between Kikuchi Patterns Arising from Different Techniques.....	180
6.2.3 Projection of the Kikuchi Pattern	181
6.2.4 Qualitative Evaluation of the Kikuchi Pattern	182
6.3 Quantitative Evaluation of the Kikuchi Pattern.....	183
6.3.1 Principles of Orientation Determination.....	185
6.3.2 Automation of Pattern Indexing and Orientation Determination by Electron Backscatter Diffraction.....	188
6.3.3 Automated Evaluation of Electron Backscatter Diffraction Patterns	191

6.3.4	Automated Evaluation of Transmission Electron Microscopy Kikuchi Patterns.....	195
6.3.4.1	Dynamic Range.....	196
6.3.4.2	Bright and Dark Kikuchi Lines.....	197
6.3.4.3	Unambiguous Indexing	197
6.3.5	Automated Evaluation of Selected Area Channeling Patterns.....	198
6.4	Pattern Quality	198
6.5	Summation.....	201
7.	Scanning Electron Microscopy-Based Techniques.....	203
7.1	Introduction.....	203
7.2	Micro-Kossel Technique.....	203
7.3	Electron Channeling Diffraction and Selected-Area Channeling	205
7.4	Evolution of Electron Backscatter Diffraction	208
7.5	EBS� Specimen Preparation.....	213
7.6	Experimental Considerations for EBSD	217
7.6.1	Hardware.....	217
7.6.2	Data Collection Efficiency	220
7.6.3	Experiment Design Philosophy.....	221
7.6.4	Phase Identification.....	223
7.6.5	Resolution and Operational Parameters	224
7.6.5.1	Microscope Parameters.....	225
7.6.5.2	Material.....	225
7.6.5.3	Specimen/Microscope Geometry	225
7.6.5.4	Accelerating Voltage.....	226
7.6.5.5	Probe Current.....	227
7.6.5.6	Pattern Clarity.....	228
7.6.6	Diffraction Pattern Enhancement	229
7.7	Calibration of an EBSD System.....	231
7.7.1	Calibration Principles.....	231
7.7.2	Calibration Procedures	233
7.7.2.1	Shadow Casting	233
7.7.2.2	Known Crystal Orientation.....	234
7.7.2.3	Pattern Magnification.....	236
7.7.2.4	Iterative Pattern Fitting	237
7.8	Operation of an EBSD System and Primary Data Output.....	238
7.9	Summation	240
8.	Transmission Electron Microscopy-Based Techniques	241
8.1	Introduction	241
8.2	High-Resolution Electron Microscopy.....	242

8.3	Selected Area Diffraction.....	243
8.3.1	Selected Area Diffraction Patterns	243
8.3.2	Selected Area Diffraction Pole Figures.....	247
8.3.3	Small Convergence Beam Electron Diffraction	250
8.4	Kikuchi Patterns, Microdiffraction, and Convergent Beam Electron Diffraction	251
8.5	Summation.....	256
9.	Evaluation and Representation of Microtexture Data	257
9.1	Introduction	257
9.1.1	Statistical Distribution of Orientation and Misorientation Data.....	258
9.1.2	Orientation and Misorientation Data Related to the Microstructure	259
9.2	Representation of Orientations in a Pole Figure or Inverse Pole Figure.....	260
9.2.1	Individual Orientations.....	262
9.2.2	Density Distributions	262
9.3	Representation of Orientations in Euler Space	265
9.3.1	Individual Orientations.....	266
9.3.2	Continuous Distributions	266
9.3.3	Statistical Relevance of Single-Grain Orientation Measurements.....	270
9.4	Representation of Orientations in Rodrigues Space	275
9.5	General Representation of Misorientation Data	280
9.5.1	Representations Based on the Angle/Axis Descriptor	281
9.5.2	Intragrain Misorientations.....	285
9.6	Representation of Misorientations in Three-Dimensional Spaces.....	286
9.6.1	Representation of Misorientations in Euler Space.....	286
9.6.2	Representation of Misorientations in the Cylindrical Angle/Axis Space	289
9.6.3	Representation of Misorientations in Rodrigues Space	290
9.7	Normalization and Evaluation of the Misorientation Distribution Function.....	292
9.8	Extraction of Quantified Data	298
9.9	Summation	300
10.	Orientation Microscopy and Orientation Mapping.....	303
10.1	Introduction	303
10.2	Historical Evolution	304
10.3	Orientation Microscopy	305

10.3.1	Mechanisms to Locate Sampling Points	305
10.3.2	Sampling Schedule.....	306
10.3.3	Data Storage and Output.....	307
10.4	Orientation Mapping and Its Applications	308
10.4.1	Spatial Distribution of Microtexture Components	309
10.4.2	Misorientations and Interfaces	313
10.4.3	True Grain Size/Shape Distributions	314
10.4.4	Pattern Quality Maps.....	315
10.4.5	Phase Maps.....	317
10.5	Orientation Microscopy in the TEM.....	318
10.6	Summation	321
11.	Crystallographic Analysis of Interfaces, Surfaces, and Connectivity	323
11.1	Introduction.....	323
11.2	Crystallographic Analysis of Grain Boundaries.....	324
11.2.1	The Coincidence Site Lattice	324
11.2.2	The Interface–Plane Scheme	326
11.2.2.1	Tilt Boundaries	327
11.2.2.2	Twist Boundaries	328
11.3	Crystallographic Analysis of Surfaces	328
11.3.1	Sectioning Technique Principles	329
11.3.1.1	Two-Surface Sectioning	331
11.3.1.2	Calibrated Serial Sectioning	331
11.3.1.3	Thin Sections: TEM Methods	332
11.3.2	Photogrammetric Techniques.....	333
11.3.3	“Five-Parameter” Analysis and Stereological Techniques.....	334
11.3.4	Three-Dimensional EBSD.....	340
11.4	Orientation Connectivity and Spatial Distribution.....	344
11.5	Orientation Relationships between Phases	347
11.6	Summation	350
12.	Synchrotron Radiation, Nondiffraction Techniques, and Comparisons between Methods	351
12.1	Introduction	351
12.2	Texture Analysis by Synchrotron Radiation.....	352
12.2.1	Individual Orientations from Laue Patterns	353

12.2.2	Local Textures from Debye–Scherrer Patterns in Polycrystalline Regions.....	356
12.3	Texture Analysis by Nondiffraction Techniques	361
12.3.1	Ultrasonic Velocity	362
12.3.2	Optical Methods.....	363
12.4	Summation: Comparison and Assessment of the Experimental Methods for Texture Analysis	368
Appendices		375
Glossary		403
References		411
General Bibliography		431
Index		435

Preface

Most solid-state materials, including metals, ceramics, and minerals, have a polycrystalline structure in that they are composed of a multitude of individual crystallites or “grains.” This book is concerned with a specific aspect of such materials—the crystallographic orientation of its components or the crystallographic texture, or simply *texture*, of the polycrystalline compound. The significance of texture lies in the anisotropy of many material properties; that is, the value of this property depends on the crystallographic direction in which it is measured. In most cases grain orientations in polycrystals, whether naturally occurring or technologically fabricated, are not randomly distributed and the preference of certain orientations may indeed affect material properties by as much as 20%–50% of the property value. Therefore, the determination and interpretation of texture are of fundamental importance in materials technology. Furthermore, analysis of the texture changes during the thermomechanical treatment of materials yields valuable information about the underlying mechanisms, including deformation, recrystallization, or phase transformations. In geology, texture analysis can provide insight into the geological processes that led to rock formations millions of years ago.

Nowadays there is a selection of techniques available to analyze the texture of materials. The well-established methods of x-ray or neutron diffraction, known as macrotexture techniques, are now supplemented by methods whereby individual orientations are measured in transmission or scanning electron microscopes and directly related to the microstructure, which has given rise to the term *microtexture*. Microtexture practice has grown principally through the application of electron backscatter diffraction, and it is now possible to measure orientations automatically from predetermined coordinates in the microstructure, which is known generically as *orientation mapping*. From the full range of texture techniques now available, insights can be gained into material processing, corrosion, cracking, fatigue, grain boundary properties, and other phenomena with a crystallographic component.

Over the past 70 years, a large number of publications on texture analysis have appeared in the literature. However, there are only a few monographs on the subject, many of which are highly specialized with a strong focus on the mathematical aspects of texture. We have written the second edition of *Introduction to Texture Analysis* to provide comprehensive coverage of the range of concepts, practices, and applications of the techniques for determining and representing texture. The mathematics of the subject has been kept to the minimum necessary to understand the scientific principles. For a more complete treatment, a comprehensive bibliography directs the reader to more specialized texts. The text is inclined toward microtexture

analysis, reflecting both the growing emphasis on this modern approach to texture analysis and the greater requirement for detailed explanation of the philosophy, practice, and analysis associated with microtexture. The book is intended for materials scientists, physicists, and geologists—both nonspecialists, including students, and those with more experience—who wish to learn about the approaches to orientation measurement and interpretation, or to understand the fundamental principles on which measurements are based to gain a working understanding of the practice and applications of texture.

The sequence of the book is as follows. Part I, Fundamental Issues, addresses the descriptors and terminology associated with orientations and texture and their representation in general. This part concludes with an introduction to the diffraction of radiation, since this phenomenon forms the basis of almost all texture analysis. Part II, Macrotexture Analysis, covers both data acquisition and representation. Part III, Microtexture Analysis, provides experimental details of the transmission or scanning electron microscope-based techniques for microtexture analysis, followed by a description of how microtexture data are evaluated and represented. The innovative topics of orientation microscopy and orientation mapping are introduced, and more advanced issues concerning crystallographic aspects of interfaces and connectivity are treated.

We are indebted to a large number of colleagues from whom we have learned, with whom we have discussed and interacted, or who have provided thoughtful comments on parts of this book. In particular, we would like to acknowledge Michael Dahms, Austin Day, Günter Gottstein, Jürgen Hirsch, Martin Hölscher, Dorte Juul Jensen, Jerzy Jura, Fred Kocks, Ingo Lischewski, Kurt Lücke, Jan Pospiech, Dierk Raabe, Robert Schwarzer, Steve Vale, Hasso Weiland, Rudy Wenk, and Stefan Zaefferer.

**Olaf Engler
Valerie Randle**

Authors

Olaf Engler is senior scientist of metallurgy at the Research and Development Center of Hydro Aluminium in Bonn, Germany. Prior to that, he was at the University of Technology in Aachen, Germany, and the Materials Science and Technology Division of Los Alamos National Laboratory in the United States. Since 2004, he has also been an adjunct professor for texture and crystal plasticity at the NTNU Trondheim, Norway, and a member of the international committee of the International Conference on Texture of Materials (ICOTOM).

Engler has more than 20 years of experience in analysis, interpretation, and modeling of the development of microstructure and texture during the thermomechanical processing of metallic materials and control of the resulting materials properties.

Valerie Randle has been eminent in the field of electron backscatter diffraction for more than 20 years. Her other main research interest is grain boundary engineering in metals and alloys. She has written more than 300 scientific publications on these research topics, including five textbooks.

Randle is a past Welsh Woman of the Year and recipient of the Institute of Materials' Rosenhain Medal. Currently, she heads the Materials Research Centre at Swansea University in Wales, United Kingdom.

Part I

Fundamental Issues

1

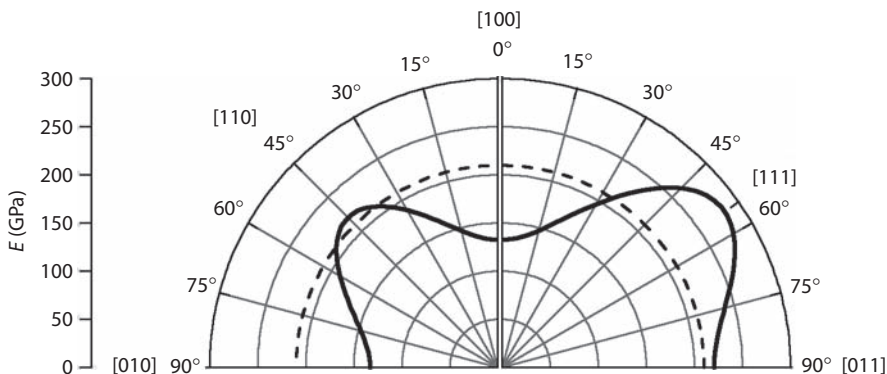
Introduction

1.1 The Classical Approach to Texture

This book is concerned with a specific aspect of the structure of natural and technological materials—the crystallographic orientation of its component units. The *crystallographic orientation*, or in this context simply *orientation*, refers to how the atomic planes in a volume of crystal are positioned relative to a fixed reference. This characteristic applies to all solids whose structure is crystalline, including minerals, ceramics, semiconductors, superconductors, and metals. Almost all of these materials are polycrystalline (rather than mono- or bicrystalline), and their component units are referred to as crystals or “grains.”

Grain orientations in polycrystals, whether naturally occurring or fabricated, are rarely randomly distributed. One of the few examples where grain orientations are randomly distributed is a polycrystalline aggregate that has been made by compression of a powder. However, in most materials, there is a pattern in the orientations that are present and a propensity for the occurrence of certain orientations caused first during crystallization from a melt or amorphous solid state and subsequently by further thermomechanical processes. This tendency is known as *preferred orientation* or, more concisely, *texture*. The importance of texture to materials lies in the fact that *many material properties are texture specific*. Indeed, it has been found that the influence of texture on material properties is, in many cases, 20%–50% of the property values (Bunge, 1987). As an example, Figure 1.1 shows the elastic modulus of iron single crystals as a function of crystal direction. Clearly, the elastic properties strongly differ from the well-known bulk modulus of 210 GPa (dotted line), which is only obtained in an isotropic, that is, texture-free material. Some examples of properties that depend on the average texture of a material are as follows:

- Young’s modulus
- Poisson’s ratio
- Strength
- Ductility

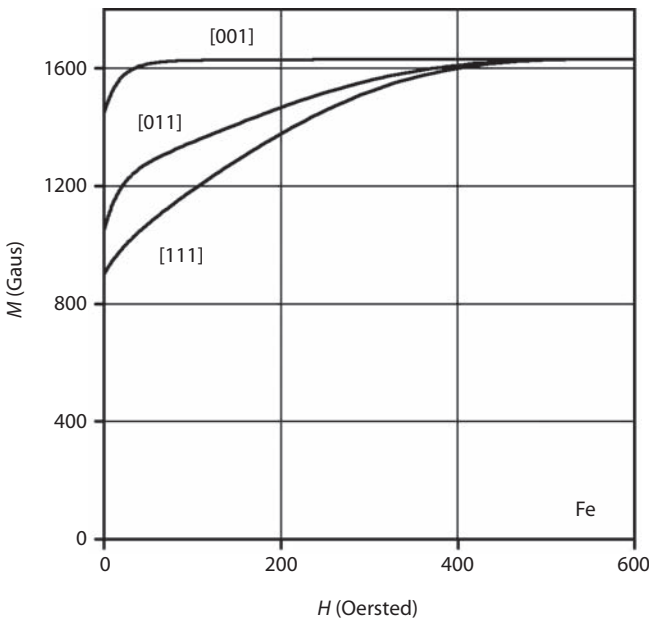
**FIGURE 1.1**

Elastic (Young's) modulus E of single-crystalline iron as a function of crystal direction. Clearly, the values strongly differ from the well-known bulk modulus of 210 GPa (dotted line), which is only obtained in isotropic, that is, texture-free material.

- Toughness
- Magnetic permeability
- Electrical conductivity
- Thermal expansion (in noncubic materials)

The effect of texture on properties is exploited in materials technology to produce materials with specific characteristics or behavior. In general, the exact mechanisms by which particular textures evolve are incompletely understood, although the empirical validation is sufficient for many processes to become established commercial practice. Three examples of texture/property links follow: The first two examples are well-established practices, whereas the third is an example of an application of texture control that is still evolving.

Grain-Oriented Silicon Iron. It is well known that the optimal crystallographic direction of magnetization in Fe–3%Si steels for power transformers is $\langle 001 \rangle$. Figure 1.2 displays the magnetization curves of transformer steels for $\langle 001 \rangle$, $\langle 011 \rangle$, and $\langle 111 \rangle$, showing that the $\langle 001 \rangle$ direction is magnetically the softest; that is, it experiences minimum magnetization losses upon remagnetization. Hence, processing of these steels is directed toward making a product with a high proportion of very large grains having the so-called Goss orientation that has $\langle 001 \rangle$ coinciding with the direction in which the product

**FIGURE 1.2**

Anisotropy of magnetization in different crystal directions of iron. The [001] crystal direction is magnetically the softest, so that sheets with a pronounced [001] texture—typically a Goss texture (110)[001]—sustain minimum magnetization losses in transformer steels.

has been rolled to sheet. Even though technologically this is a vitally important process, the exact mechanisms that control the texture formation are still not completely understood (Dorner et al., 2007).

Strip Metal Products. Very large tonnages of steel and aluminum alloys for deep-drawing applications, such as car bodies or beverage (drinks) cans, are produced every year. For steels, the deep-drawing process is greatly facilitated by maximizing the number of {111} planes that lie nearly parallel to the sheet surface before the drawing operation. For aluminum alloys, the required textures are rather more complex, and industrial processes concentrate on efficient use of material by balancing the texture effects so that a homogeneously shaped drawn product results (Knorr et al., 1994; Lins et al., 2007; Engler and Hirsch, 2007). To illustrate the deleterious effect of pronounced texture on formability, Figure 1.3 shows a cylindrical cup that is deep-drawn from a circular blank of a heavily textured aluminum sheet, displaying the well-known *earing* behavior (Section 5.5).

**FIGURE 1.3**

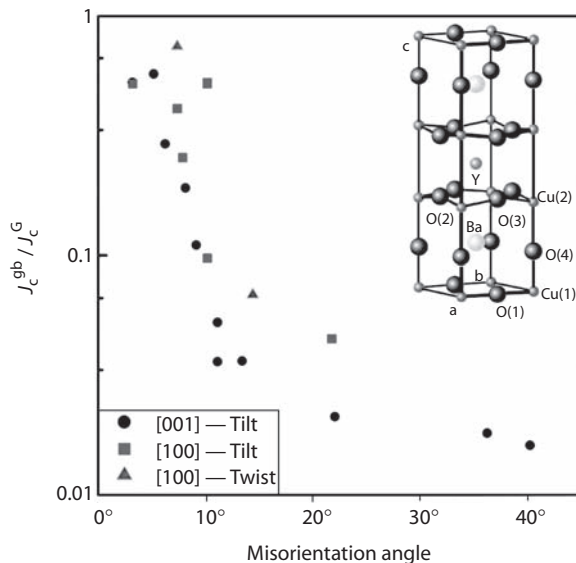
Typical appearance of a deep-drawn cup with ears under 0° and 90° to the rolling direction (marked) from a heavily textured aluminum sheet (AA 1200-O, i.e., commercial purity aluminum, cold rolled, and soft annealed).

Superconductors. The practical application of bulk polycrystalline superconductors such as $\text{YBa}_2\text{Cu}_3\text{O}_{7-x}$ depends on obtaining a high value of transport critical current density J_c . As illustrated in Figure 1.4, J_c has been found to depend critically on the degree of texturing in the material and, more precisely, on the type of grain boundaries that certain textures produce (Zhu et al., 1991). Manufacture of superconductors is tailored to produce textured materials (Obst et al., 2003; Koblischka-Veneva et al., 2008).

A natural or technological material will often exhibit a completely new texture after such processes as deformation, recrystallization, and phase transformations. Characterization of such changes can be used as an experimental probe to investigate the history of the material, especially where the changes involved are well defined. This widely used application of texture as a diagnostic tool constitutes the second reason why knowledge of texture is valuable. Hence, texture research has proceeded on two broad (and related) fronts:

- Technological control of material processing
- Further understanding of fundamental materials science and geological sciences

The most established method for measuring textures is x-ray diffraction using a texture goniometer (Section 4.3), which gives a measure of the volume fraction of a particular family of planes, for example, {111}, {0001}, which are orientated for diffraction. Hence the texture that is obtained is an *average* value for the whole sampled volume, typically comprising thousands of grains. The x-ray technique for texture evaluation was first used several decades ago, and much

**FIGURE 1.4**

(See color insert following page 240.) Current transmission, that is, the ratio of intergrain (gb) and intragrain (G) critical current densities J_c across grain boundaries in YBCO superconductors as a function of misorientation angle (at 5 K). High superconducting current transmission requires maximum fraction of low-angle grain boundaries, that is, a very sharp texture. (Courtesy of B. Obst.)

effort has gone during the intervening years into refining it to produce a standard system to provide quantitative texture data in conventionally accepted formats, that is, *pole figures* (Sections 2.5, 4.3.2, and 5.2) or *orientation distribution functions* (ODFs) (Sections 5.3 and 5.4).

This section has established that the importance of texture lies first in its direct relationship with material properties and second as a method of fingerprinting the history of a material. The dominant approach to texture research and practice before the early 1980s was the use of x-rays to probe the average texture of a specimen, and indeed this approach is still valid if knowledge of the average texture is all that is required.

1.2 The Modern Approach to Texture: Microtexture

The hallmark of the x-ray approach is that it provides efficiently an overview of the texture. In turn, this texture is compiled from numerous individual grains, each of which possesses a discrete orientation. The x-ray texture tells us what volume fraction of the specimen (obtained from the intensity

of diffraction by particular planes) has a particular orientation. However, it does not tell us how these grains are distributed throughout the material. An approach that deals with the orientation statistics of a population of individual grains, and usually encompasses the *spatial location* of these grains, that is, the *orientation topography*, has been termed *microtexture*—the conjoining of microstructure and texture (Randle, 1992, 2003). To avoid ambiguity with the traditional view of texture, a texture that reflects an average value obtained from many different grains is often termed “*macrotexture*” rather than just “*texture*.”

In the study of fabricated and natural materials, it is important to have knowledge of both microstructure and crystallography. The traditional approach has been to make parallel, but separate, investigations: Optical microscopy, scanning electron microscopy (SEM) (plus chemical analysis), and image analysis to analyze microstructure; and x-ray texture determination or diffraction in the transmission electron microscope (TEM) for crystallographic analysis, with some contribution from Kossel diffraction and selected area channeling (SAC) in the scanning electron microscope (SEM). A typical profile of a material might therefore include the grain size distribution plus the texture as determined by x-rays.

The principal disadvantage of the traditional approach has been the lack of a direct connection between the study of microstructure and crystallography. This has meant that although the overall average orientation distribution could be measured, the orientation of individual crystals could only be extracted from this database on a small scale and by tedious means, mostly involving TEM. Hence a wealth of information concerning the spatial component of grain orientations, including the interface regions where grains join, was inaccessible. Furthermore, where phases having identical or similar chemistry, but different crystallography, coexist in the microstructure, they could not be distinguished by any simple method. However, with the advent, since the early 1980s, of innovative techniques in both SEM and TEM, it is now possible to obtain microtexture measurements in a routine manner. Several recent conferences, or parts of conferences, have been dedicated specifically to microtexture (see General Bibliography).

1.2.1 Applications of Microtexture

If the spatial location plus the orientation of individual grains in a sample population is known, access to a whole new stratum of knowledge is heralded, since the crystallographic and morphological aspects of structure evolution become fused. The following phenomena, which are all directly linked to microtexture (i.e., individual grain orientation), can be explored:

- Local property effects
- Interfacial parameters and properties

- Morphological/geometrical grain parameters, that is, size, shape, and location
- Orientation variations within individual grains
- Phase relationships
- Direct ODF measurement

The importance of the way in which grain orientations are distributed can be illustrated by the idealized sketch of a microstructure in Figure 1.5. Here a simplified case is considered where some grains have a strong *preferred orientation X* (with a spread of, say, 15°) and the remaining grains have “random” (i.e., no discernable preferred orientation) textures. Two limiting spatial conditions are considered: In Figure 1.5a, all the X grains are located in a contiguous patch, and in Figure 1.5b, the same number of X grains are spread singly throughout the microstructure.

Local property effects. The effect of property variations with orientation will be magnified where grains occur in clusters rather than singly. For example, slip transmission may be facilitated between grains of favorable orientations, such as the contiguous X grains in Figure 1.5a. Another example is that compressed plates of tantalum take up an “hourglass” shape due to the occurrence of two different

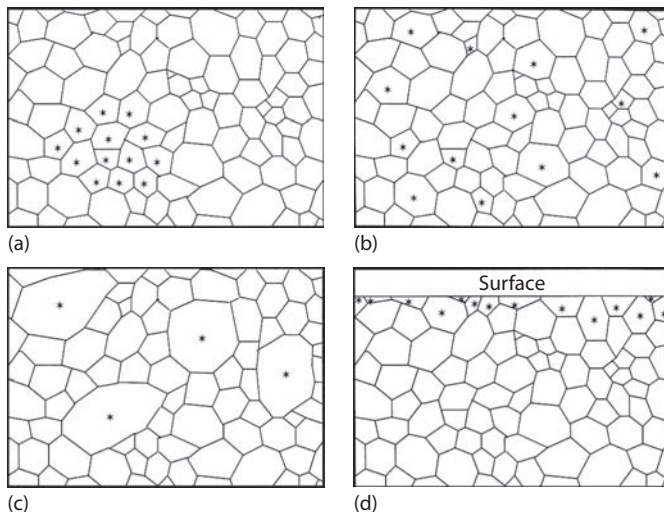


FIGURE 1.5

Idealized portrayal of microtexture or orientation topography. Grains having orientation X are (a) contiguous in the microstructure; (b) located singly in the microstructure; (c) in a different size class to the rest of the microtexture; (d) located in a special way with respect to the specimen, for example, near the surface.

microtextures, which in turn have different deformation characteristics, at the specimen surface and the center (Wright et al., 1994a).

Interfacial parameters and properties. If individual orientations are known, it is possible to calculate the orientation difference or *misorientation* between neighboring grains and hence provide information about the distribution of grain boundary geometry, which is sometimes called *mesotexture*, that is, the texture between grains (Chapter 11). This is a very powerful aspect of microtexture since it allows access to grain boundary structure/property links, which is unavailable via a macrotexture approach. In recent years, it has been realized that the properties of grain boundaries vary markedly with their structure, and moreover the structure of boundaries can be manipulated to produce boundaries that perform better.

With regard to the simple example in Figure 1.5, the misorientations between grains having orientations X will be low angle since the orientations are similar, and misorientations between X and other grains and also between non-X grains will be mainly high angle. Hence the low-angle boundaries—which have physical properties different from the boundaries that are high angle—are spatially connected. This grouping will have a major effect on intergranular transport properties in the material, since some pathways in the grain boundary network will effectively be blocked (Randle et al., 2006).

Morphological/geometrical grain parameters. The morphological/geometrical characteristics of grains—grain size, shape, and macroscopic location—cannot be accessed by macrotexture measurements. A microtexture approach, however, allows concurrent access to both geometrical and orientational parameters, which in turn permits correlations to be made between the two. Referring again to Figure 1.5, the X grains may belong, for example, to a particular size class or be located in a specific way with respect to the specimen geometry, such as adjacent to the specimen surface, as shown in Figures 1.5c and 1.5d, respectively.

A grain or crystal is formally defined as a unit having a single orientation (but see the following text). A direct consequence of this definition is that the grains themselves can be depicted by knowing where in the microstructure orientation changes take place. This leads to “mapping” of microtexture (Section 1.2.3 and Chapter 10).

Orientation variations within individual grains. By classical definition, a grain has a single, distinct orientation. However, in practice the orientation within a grain may vary in a continuous or discontinuous manner, which can be termed *orientation perturbation*. In particular, there may be perturbations close to interfaces and in deformed structures reflecting the distribution of strain. A microtexture technique

is able to characterize these distributions on a local level, which is not a capability of a macrotexture technique.

Phase relationships. So far, we have considered that the hypothetical grains in Figure 1.5 are all the same phase. In exactly the same manner, multiphase materials can also be studied to produce concurrently the texture of each phase, the distribution of its orientations, and orientation relationships between individual crystals of each phase.

Direct ODF measurement. The traditional route for ODF measurement relies on calculation from several pole figures that have been determined by macrotexture methods (Chapter 5). These procedures admit inherent inaccuracies that are obviated when a microtexture technique is used to obtain the orientation distribution. For this case, full grain orientations are obtained *directly* rather than calculated from crystal plane distributions as in the x-ray case. Hence ODFs obtained by microtexture measurements give the *true* orientation distribution of the sampled grains.

Although the schematic illustration in Figure 1.5 might seem rather hypothetical, in practice such microstructures have been observed—for example, where clusters of similarly oriented grains aggregate into “supergrains” (Mason and Adams, 1994; Huh et al., 2005), in a superplastically deformed aluminum alloy (Randle, 1995a), and in various sheet metals and ceramics (Fionova et al., 1993)—and are a focus of research interest. More generally, microtextures may consist of several preferred orientations rather than only one as depicted in Figure 1.5. However, the preferred orientations tend to be spatially distributed nonrandomly, which gives rise to anisotropic distributions of grain boundary and grain properties as described earlier, and demonstrates the cruciality of obtaining microtexture information to address these complexities.

In summary, this section has introduced the concept of microtexture, which is a recent approach to orientation-related analyses. Microtexture focuses texture analysis onto a local basis and allows it to be correlated with the microstructure. This, in turn, allows whole facets of the microstructure to be explored, which were inaccessible by macrotexture methods, and has indeed enlarged the view of microstructure to synthesize both the morphological and crystallographic aspects.

1.2.2 Electron Backscatter Diffraction

The ability to obtain microstructure-level information implies that the probe size formed by the exploring radiation (i.e., x-rays, neutrons, or electrons; Section 3.6 and Table 3.1) must be smaller than the size of the microstructural

units themselves. This rules out x-ray diffraction as an experimental tool for microtexture measurement. Electrons are ideal for combined microstructural/crystallographic studies, and indeed until the 1980s, TEM was the major technique used for such work (Chapter 8), with some input from Kossel diffraction (Section 7.2) and SAC (Section 7.3) in an SEM. Since that time a more convenient SEM-based technique for microtexture has been developed, known as electron backscatter diffraction (EBSD) (Sections 7.4 through 7.8). EBSD is now the backbone of most microtexture research. EBSD or, as it is equivalently known, backscatter Kikuchi diffraction (BKD), or electron backscatter patterns (EBSP), is an add-on package to an SEM. The most attractive feature of EBSD is its unique capability to perform concurrently rapid, automatic diffraction analysis to give crystallographic data and imaging with a spatial resolution in the nanometer range, combined with the regular capabilities of an SEM such as capacity for large specimens, concurrent chemical analysis, and the ability to image rough surfaces (Venables and Harland, 1973; Dingley, 1984; Randle, 2003).

EBSD is, without doubt, the most suitable and widely used experimental technique for the determination of microtexture. For this reason, and moreover because EBSD with all its latest ramifications is still a relatively new technique compared to x-ray methods, it is described in detail in Chapter 7. Briefly, the technique relies on positioning the specimen within the SEM sample chamber such that a small angle, typically 20°, is made between the incident electron beam and the specimen surface. This simple expedient enhances the proportion of backscattered electrons able to undergo diffraction and escape from the specimen surface. The resulting diffraction pattern is captured and interrogated in real time, and computer algorithms allow the orientation of each diffraction pattern to be obtained and stored. From this raw data a microtexture is constructed serially. At the time of writing, a state-of-the-art EBSD system could automatically position a stationary probe on a suitable specimen, capture a diffraction pattern, index it, and store the result at the rate of approximately 400 patterns per second on suitable materials. Future-generation EBSD systems will achieve even faster data collection rates (Schwarzer, 2008; Søfferud et al., 2008).

It is no exaggeration to say that, since its inception, EBSD has revolutionized texture investigations in both research and industry. The technique has passed through various stages of development, and in its most refined form provides a totally synthesized approach to orientation and microstructure.

1.2.3 Orientation Microscopy and Orientation Mapping

Automated EBSD is exploited to select a grid of sampling points whose spacing is much finer than the grain size. If a representation of the orientation at each grid point is plotted, a crystallographic map of the microstructure is obtained. This is known variously as crystal orientation mapping (COMTM)

or orientation imaging microscopy (OIM™) (Adams et al., 1993). The terms “automated crystal orientation mapping” (ACOM), “orientation scanning microscopy,” and “crystal orientation imaging” are other versions that have been adopted. In this book, the term *orientation microscopy* is used to describe the procedures involved in getting the data and *orientation mapping* is used to describe the output of data (Chapter 10).

Orientation microscopy/mapping is a landmark innovation in the field of EBSD and microtexture because it links orientation *directly* to the microstructure. In other words, the crystal orientation map portrays faithfully the orientational components, that is, those concerned with crystallography, of the microstructure in an analogous manner to the mapping of chemical elements in the microstructure via energy dispersive spectroscopy in an SEM. As the potential and capabilities of orientation mapping are considered in greater depth, it emerges that there are many subtle ramifications to its application, which introduce a degree of *quantification* into the definition of microstructure that was hitherto not possible. An orientation map can highlight different aspects of the microstructure, depending on the distribution/step size of the sampling schedule plus the scale and requirements of the inquiry, as specified by the user.

1.3 A Guide to the Book

This book is intended for the reader who is familiar with crystalline materials and wishes to gain a working understanding of the practice and applications of texture. The following prior knowledge, at an introductory level, is assumed:

- Basic crystallography (crystal planes and directions)
- Principles of electron microscopy (TEM and SEM)
- Familiarity with vectors and matrix algebra

Several standard textbooks cover different aspects of this information (see General Bibliography). In this book, the mathematics of the subject area has been kept to that required to understand the scientific principles. Many of the examples relate to metallic materials because this group is the largest to be affected by texture-associated phenomena. It is, however, recognized that semiconductors, superconductors, and geological materials are growing areas of interest, particularly where microtexture is concerned.

The sequence of the book is as follows. We begin in Chapter 2 by addressing the fundamental descriptors and terminology associated with orientations and their representation in general. Chapter 3 is an introduction to diffraction of

radiation, since this phenomenon forms the basis of almost all texture analysis. This completes Part I, which is on Fundamental Issues.

Part II (Chapters 4 and 5) describes Macrotexture Analysis, both data acquisition (Chapter 4) and data representation (Chapter 5). This part is shorter than Part III on Microtexture Analysis, reflecting both the growing emphasis on the modern microtexture approach to texture analysis and the greater requirement for detailed explanation of the philosophy, practice, and analysis associated with microtexture. These are all dealt with in Part III. Methods for evaluation of the basic “raw data” of microtexture, the Kikuchi diffraction pattern, need to be covered in some detail, and this is accomplished in Chapter 6. Chapters 7 and 8 describe experimental details of SEM- and TEM-based techniques, respectively, followed in Chapter 9 by how the statistics of microtexture data are analyzed and represented. Orientation microscopy and mapping is an innovative topic, and Chapter 10 is devoted to a treatise on this new subset of microtexture. Chapter 11 is another spin-off of the microtexture approach, and describes more advanced crystallographic issues concerning interfaces and connectivity. Finally, Chapter 12 covers minority techniques for microtexture evaluation and comparisons between all the techniques for texture measurement.

2

Descriptors of Orientation

2.1 Introduction

In this chapter, after a short review of crystal structures and symmetries (Section 2.2), the main mathematical parameters that are used to describe an orientation are defined and explained. These are as follows:

- Orientation matrix (Section 2.3)
- “Ideal orientation,” that is, Miller or Miller–Bravais indices (Section 2.4)
- Euler angles (Section 2.6)
- Angle/axis of rotation (Section 2.7)
- Rodrigues vector (Section 2.8)

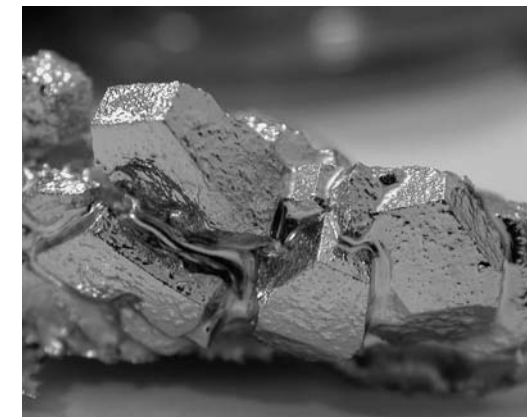
All these descriptors are employed to process and represent different aspects of macrotexture and microtexture measurements. This chapter will elucidate the theoretical aspects of these parameters and their interrelationships. For graphical representation, it is usual to plot orientations, represented as projected poles, Euler angles, angle/axis, or the Rodrigues vector, in an appropriate “space.” These spaces—the pole figure or inverse pole figure “projected space,” Euler space, cylindrical angle/axis space, and Rodrigues space—are explained in Sections 2.5 through 2.8. These explanations encompass only the basic theoretical aspects; in practice, their utilization is customized according to whether they are employed to display and analyze macrotexture or to display and analyze microtexture data. Therefore, these two divisions are discussed separately, in Chapters 5 and 9.

The term *crystallographic orientation* can refer either to a crystal (grain), which is three-dimensional (3-D) and therefore comprises three independent variables, or to a crystallographic plane, which comprises two independent variables. Where the term *orientation* is used throughout this book, it refers to the orientation of the full crystal, rather than of a plane, unless it is made clear otherwise.

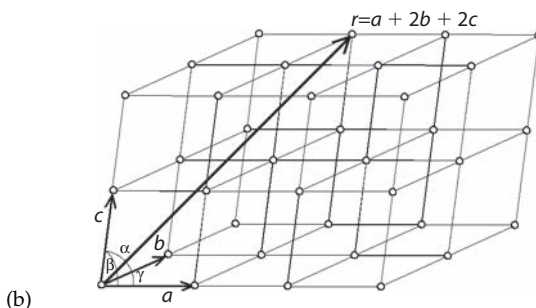
2.2 Crystal Structures and Crystal Symmetries

Materials are called crystalline if the constituent atoms, molecules, or ions are packed in a regularly ordered, repeating pattern extending in all three spatial dimensions. Figure 2.1a shows an example of several centimeter-sized gallium crystals, a poor metal with orthorhombic crystal structure. Gallium melts just above room temperature and, when allowed to crystallize undisturbed, can grow into large orthorhombic crystals. The crystal structure can be idealized into having discrete translation symmetry at the atomic level. That is to say, the arrangement of the atoms is repeated periodically on a *lattice* in three dimensions. As shown in Figure 2.1b, the lattice can be generated by three noncoplanar unit vectors, a , b , and c and a set of integers l , m , and n such that each lattice point, identified by a vector r , can be obtained from

$$r = l \cdot a + m \cdot b + n \cdot c \quad (2.1)$$



(a)



(b)

FIGURE 2.1

- (a) Centimeter-sized crystals of pure gallium. (From Wikipedia, The Free Encyclopedia, "Gallium," http://en.wikipedia.org/wiki/Image:Gallium1_640x480.jpg. With permission.);
- (b) Construction of a 3-D crystal lattice based on a set of three unit vectors a , b , and c .

Thus, a lattice is an infinite set of points generated by a set of discrete translation operations. A crystal is made up of one or more atoms that are repeated at each lattice point. The crystal then looks the same when viewed from any of these lattice points. In most of the common metals, the lattice points are occupied by single atoms. In more complex structures, the lattice points contain identical groups of atoms, called a *motif* (or *basis*) of atoms. That is to say, the crystal structure consists of the same atoms, or motifs, positioned around each and every lattice point. This group of atoms, therefore, repeats indefinitely in three dimensions according to the arrangement of the *crystal lattices*. In total, there are 14 lattices that fill the 3-D space, which are the well-known 14 *Bravais lattices* presented in Figure 2.2. The characteristic rotation and mirror symmetries of the atoms or motifs are described by the crystallographic *point groups*, of which there are 32, and *space groups*, of which there are 230 (Hahn, 2005).

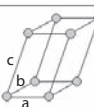
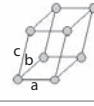
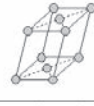
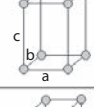
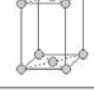
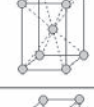
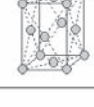
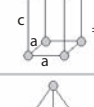
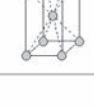
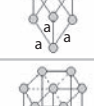
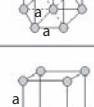
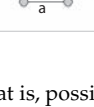
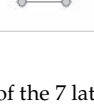
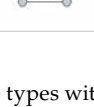
Name	Conditions	Primitive	Base centered	Body centered	Face centered
Triclinic	$a \neq b \neq c$ $\alpha \neq \beta \neq \gamma$				
Monoclinic	$a \neq b \neq c$ $\alpha = \gamma = 90^\circ \neq \beta$				
Orthorhombic	$a \neq b \neq c$ $\alpha = \beta = \gamma = 90^\circ$				
Tetragonal	$a = b \neq c$ $\alpha = \beta = \gamma = 90^\circ$				
Rhombohedral (trigonal)	$a = b = c$ $\alpha = \beta = \gamma \neq 90^\circ$				
Hexagonal	$a = b \neq c$ $\alpha = \beta = 90^\circ, \gamma = 120^\circ$				
Cubic	$a = b = c$ $\alpha = \beta = \gamma = 90^\circ$				

FIGURE 2.2

Unit cells of the 14 Bravais lattices, that is, possible combination of the 7 lattice types with one of the lattice centerings.

The defining property of a crystal is its inherent symmetry, which means that certain operations result in an atomic configuration identical to the original configuration. For example, rotating the crystal by 90° or 180° about a certain axis may leave the crystal unchanged. The crystal is then said to have, respectively, a fourfold or twofold rotational symmetry about this axis. In addition to rotational symmetries like this, a crystal may have symmetries in the form of mirror planes and translational symmetries, and also the so-called compound symmetries that are a combination of translation and rotation/mirror symmetries. A full classification of a crystal is achieved when all of these inherent symmetries of the crystal are identified.

A crystal lattice is conveniently described by its unit cell, a tiny box containing one or more atoms, which is characterized by its lattice parameters a , b , and c as well as the angles α , β , and γ between them. There may be additional lattice points at the center of certain faces or at the center of volume within the unit cell. The positions of the atoms inside the unit cell are described by the set of atomic positions (x_i, y_i, z_i) measured from the origin, a lattice point at the corner of the unit cell. There are only seven possible crystal systems that atoms can pack together to produce an infinite 3-D space lattice in such a way that each lattice point has an identical environment to that around every other lattice point. The crystal systems are a grouping of crystal structures according to the axial system used to describe their lattice. Each crystal system consists of a set of three axes in a particular geometrical arrangement:

- *Triclinic*. No symmetry other than translational symmetry
- *Monoclinic*. One twofold rotation axis or one mirror plane
- *Orthorhombic*. Three twofold rotation axes or one twofold rotation axis and two mirror planes
- *Tetragonal*. One fourfold rotation axis
- *Rhombohedral (also called trigonal)*. One threefold rotation axis
- *Hexagonal*. One sixfold rotation axis
- *Cubic (also called isometric)*. Four threefold rotation axes

The vast majority of metals crystallize in either cubic or hexagonal crystal structure. Examples for metals with tetragonal crystal structure include tin and indium, whereas gallium, uranium, and neptunium are orthorhombic. Plutonium has, among several others, a monoclinic allotrope, whereas (solid) mercury as well as several metalloids like antimony, bismuth, and arsenic are rhombohedral.

Combination of the seven crystal systems with the various lattice centerings yields the well-known 14 *Bravais lattices* (or *space lattices*) shown in Figure 2.2. They describe the geometric arrangement of the lattice points,

and thereby the translational symmetry of the crystal. The possible lattice centerings are as follows:

- *Primitive (P)*. Lattice points on the cell corners only, that is, at the coordinates $(x,y,z) = (0,0,0)$
- *Body centered (I)*. One additional lattice point at the center of the cell so that for each atom at $(0,0,0)$ there is another one at $(1/2,1/2,1/2)$
- *Face centered (F)*. One additional lattice point at the center of each of the faces of the cell, that is, there are also atoms at $(1/2,1/2,0)$, $(1/2,0,1/2)$, and $(0,1/2,1/2)$
- *Base centered (C)*. One additional lattice point at the center of the base of the cell (the so-called C-plane containing a and b), that is, at $(1/2,1/2,0)$

It is seen that not all combinations of the crystal systems and lattice centerings are needed to describe the possible space lattices. There are in total $7 \times 6 = 42$ combinations, but it can be shown that several of these are in fact equivalent to each other, reducing the number of combinations to the 14 Bravais lattices shown in Figure 2.2. With a view to texture analysis, the expansion of the seven crystal systems into the 14 Bravais lattices is of importance since the latter affect diffraction measurements (Sections 3.2 and 3.3) and evolution of textures through activation of slip systems (Section 5.5).

The existence of the translation lattice limits the number of symmetry elements that can be present. There are 32 possible combinations of rotations, mirror planes, and an inversion center, collectively called the 32 point groups or crystal classes. When these point groups are combined with the translation symmetries, we arrive at the 230 possible space groups, containing all symmetry elements that transform every crystal lattice into itself. However, since the space groups are generally not of interest in texture analysis, they will not be discussed here any further.

For texture analysis by diffraction techniques, it is more important whether or not the crystals are centrosymmetric, that is, contain an inversion center so that for every point (x,y,z) in the unit cell there is an indistinguishable point $(-x,-y,-z)$ (Weiss and Wenk, 1985; Matthies et al., 1987; Kocks, 1998). A diffraction (Laue) experiment produces a projection of the lattice planes (Chapter 3). Hence, the resulting reflection diagram must comprise the symmetry of the crystal structure. However, a diffraction diagram will always be centrosymmetric, even if the crystal is not. This is caused by the fact that the intensities reflected at two opposite planes (hkl) and $(\bar{h}\bar{k}\bar{l})$ are equal (Friedel's law; Friedel, 1913). Hence, diffraction experiments are only able to distinguish between the various centrosymmetric crystal classes. These 11 so-called *Laue classes* or *Laue groups* containing an inversion center are listed in Table 2.1, whereas Figure 2.3 shows their symmetry elements. As a matter

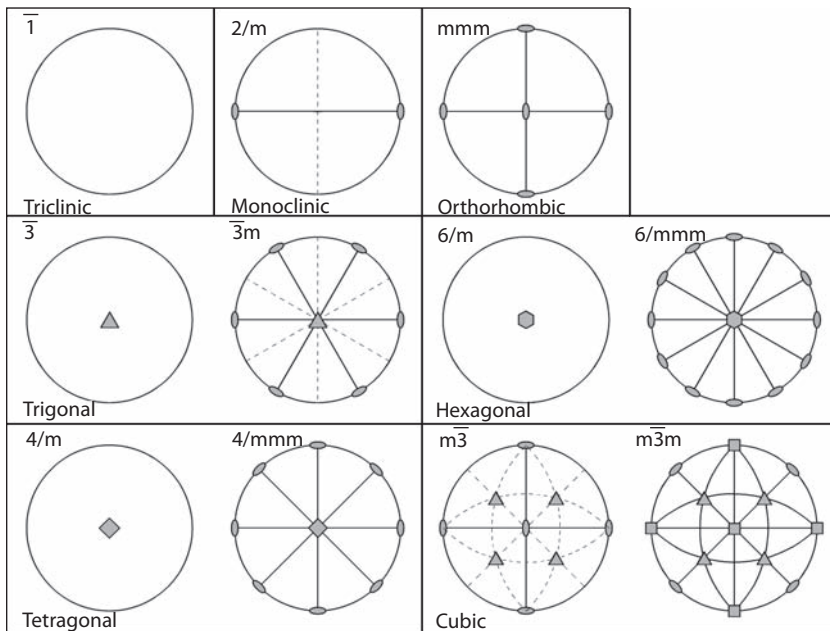


FIGURE 2.3
Symmetry elements in the 11 Laue groups.

of fact, all crystal lattices and the majority of crystals are centrosymmetric, that is, they do contain an inversion center. Crystal structures with a multi-atom motif generally have a lower symmetry than that of the lattice, some of them lacking an inversion center. Anyhow, the diffraction patterns of these 21 noncentrosymmetric classes become centrosymmetric through addition of an inversion center to the corresponding crystal class, such that the apparent symmetry of the crystal is then one of the 11 Laue classes (Table 2.1). In texture analysis, symmetry of the Laue groups feeds through to the size and symmetry of orientation space necessary to represent texture information of the corresponding crystal structure (Section 2.6.2).

2.3 Transformation between Coordinate Systems: The Rotation Matrix

2.3.1 Coordinate Systems

To specify an orientation, it is necessary to set up terms of reference, each of which is known as a *coordinate system* (Bollmann, 1970; McKie and McKie, 1974; Hansen et al., 1978; Bunge, 1985a; Kocks, 1998). Two systems are required: one relating to the

TABLE 2.1

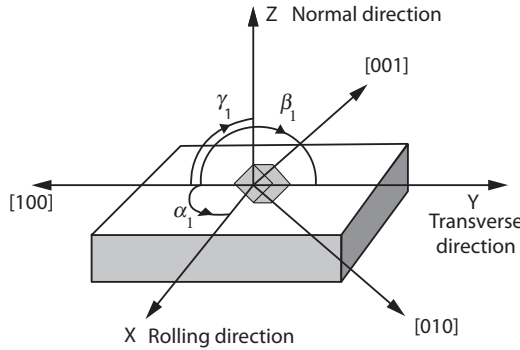
The 11 Laue Groups and Their Noncentrosymmetric Subgroups
in Hermann–Mauguin Notation

Crystal System	Space Group G_C (Schönflies Notation)	Laue Class	Noncentro-symmetric Classes	Number of Symmetry Elements
Triclinic	C_1	$\bar{1}$	1	1
Monoclinic	C_2	$2/m$	$2, m$	2
Orthorhombic	D_2	mmm	$222, mm2$	4
Trigonal	C_3	$\bar{3}$	3	3
	D_3	$\bar{3}m$	$3m, 32$	6
Tetragonal	C_4	$4/m$	$4, \bar{4}$	4
	D_4	$4/mm$	$4\ mm, \bar{4}m2, 422$	8
Hexagonal	C_6	$6/m$	$6, \bar{6}$	6
	D_6	$6/mmm$	$6mm, \bar{6}\ m2, 622$	12
Cubic	T	$m\bar{3}$	23	12
	O	$m\bar{3}m$	$\bar{4}3m, 432$	24

Source: Data from Kleber, W., Bautsch, H.J. and Bohm, J., in *Einführung in die Kristallographie*, Oldenbourg Wissenschaftsverlag, München, 2002.

whole specimen and the other relating to the crystal. Both systems are Cartesian (i.e., having axes at right angles) and preferably right handed. The axes of the *sample* or *specimen coordinate system* $S = \{s_1 s_2 s_3\}$ are chosen according to important surfaces or directions associated with the external form or shape of the specimen. For example, for a fabricated material there are obvious choices defined by the processing geometry. One of the most common of these relates to a rolled product, and hence the directions associated with the external shape are the rolling direction (RD); the through-thickness direction, that is, the direction normal to the rolling plane (ND); and the transverse direction (TD). These directions are illustrated in Figure 2.4. Other specimens, such as a tensile test piece, a rod, or a wire, have only uniaxial symmetry; hence it is only necessary to specify one axis in the specimen coordinate system and the other two axes can be chosen arbitrarily. In natural rocks, the plane of foliation and a line of lineation within that plane often make a natural choice for specimen axes. Sometimes there are no clearly defined directions associated with the specimen. For these cases, the specimen coordinate system can be chosen arbitrarily and it is conventional in experimental work for the normal to the “principal” specimen surface, from which diffraction information is collected, to be labeled Z as shown in Figure 2.4. The X and Y axes are both perpendicular to Z and should form a right-handed set.

The second coordinate system, the *crystal coordinate system* $C = \{c_1 c_2 c_3\}$ is specified by directions in the crystal. The choice of directions is in principle arbitrary, although it is convenient to adapt it to the crystal symmetry. Hence, for example, for

**FIGURE 2.4**

Relationship between the specimen coordinate system XYZ (or RD , TD , ND for a rolled product) and the crystal coordinate system $100,010,001$ where the (cubic) unit cell of one crystal in the specimen is depicted. The cosines of the angles α_1 , β_1 , γ_1 give the first row of the orientation matrix (see text). (Courtesy of K. Dicks.)

crystals of the orthogonal branch (cubic, tetragonal, orthorhombic), the axes $[100]$, $[010]$, $[001]$ already form an orthogonal frame—that is, they are mutually perpendicular—and are adopted as the crystal coordinate system (Figure 2.5a). For hexagonal and trigonal symmetry, an orthogonal frame needs to be associated with the crystal axes. As indicated in Figures 2.5b and I.1b, the two obvious choices are

$$X_1 = [10\bar{1}0], Y_1 = [\bar{1}2\bar{1}0], Z = [0001] \quad (2.2a)$$

or

$$X_2 = [2\bar{1}\bar{1}0], Y_2 = [01\bar{1}0], Z = [0001] \quad (2.2b)$$

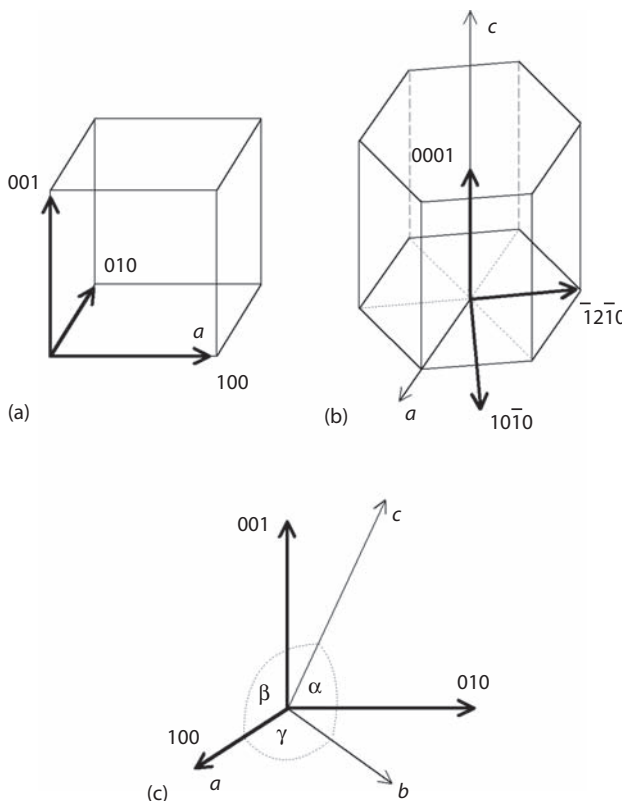
Subsequently the crystal axes are made orthonormal, that is, normalized to be all the same length, which is shown in Figures 2.5b and 2.5c. This procedure is carried out, in the general case, by premultiplying a zone axis, referenced to the crystal coordinate system, by a matrix L having the following elements (Young and Lytton, 1972):

$$\begin{aligned} l_{11} &= a \\ l_{12} &= b \cos \gamma \\ l_{13} &= c \cos \beta \\ l_{21} &= 0 \\ l_{22} &= b \sin \gamma \\ l_{23} &= \frac{c(\cos \alpha - \cos \beta \cos \gamma)}{\sin \gamma} \end{aligned} \quad (2.3a)$$

$$l_{31} = 0$$

$$l_{32} = 0$$

$$l_{33} = \frac{c(1 + 2 \cos \alpha \cos \beta \cos \gamma - \cos^2 \alpha - \cos^2 \beta - \cos^2 \gamma)^{1/2}}{\sin \gamma}$$

**FIGURE 2.5**

Orthonormalized crystal coordinate systems for (a) cubic, (b) hexagonal, and (c) general (triclinic) symmetries.

where a, b, c are the lattice parameters and α, β, γ are the interzonal angles. In this way all crystal systems have the same form of crystal coordinate system, that is, orthonormal. The general matrix given in Equation 2.3a can be simplified in all, but the triclinic case. For example, for orthorhombic crystals where all angles are 90° , the transformation matrix L simplifies to

$$L = \begin{pmatrix} a & 0 & 0 \\ 0 & b & 0 \\ 0 & 0 & c \end{pmatrix} \quad (2.3b)$$

For hexagonal crystals, the transformation matrix L becomes

$$L = \begin{pmatrix} a & -a/2 & 0 \\ 0 & a\sqrt{3}/2 & 0 \\ 0 & 0 & c \end{pmatrix} \quad (2.3c)$$

Conversely, to transform from orthonormal coordinates back to the crystal reference system, it is necessary to premultiply by the inverse crystal matrix L^{-1} . Directions and planes in hexagonal or trigonal crystals can be described using either Miller or Miller–Bravais indices (Appendix I).

2.3.2 The Rotation (Orientation) Matrix

Having specified the specimen and crystal coordinate systems, an orientation is then defined as “the position of the crystal coordinate system with respect to the specimen coordinate system,” that is,

$$C_C = g \cdot C_S \quad (2.4)$$

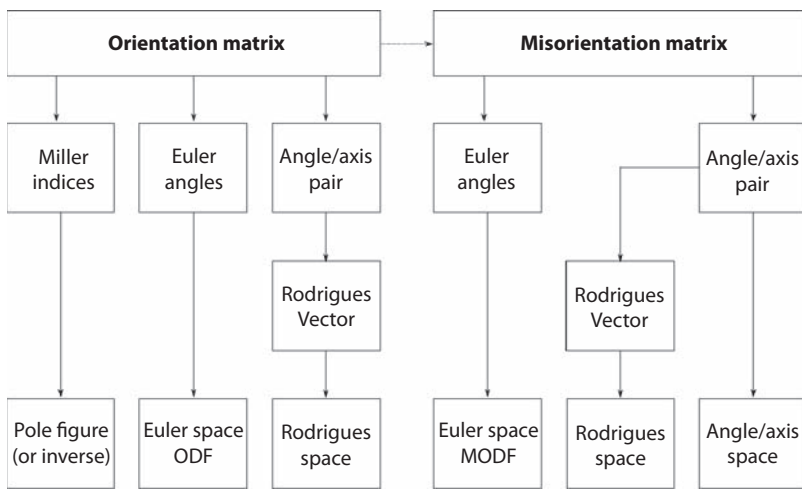
where C_C and C_S are the crystal and specimen coordinate systems, respectively, and g is the orientation. g can be expressed in several different ways, and these are listed in Section 2.1. The fundamental means for expressing g is the *rotation* or *orientation matrix*, which embodies the rotation of the specimen coordinates onto the crystal coordinates.

The orientation matrix is a square matrix of nine numbers and is obtained as follows. The first row of the matrix is given by the cosines of the angles between the first crystal axis, [100], and each of the three specimen axes, X, Y, Z , in turn. These three angles, $\alpha_1, \beta_1, \gamma_1$, are labeled in Figure 2.4. The second row of the orientation matrix is given by the cosines of the angles $\alpha_2, \beta_2, \gamma_2$ between [010] and X, Y, Z in turn. Similarly, the third row of the matrix comprises the cosines of the angles $\alpha_3, \beta_3, \gamma_3$ between [001] and X, Y, Z . Hence the complete matrix is

$$g = \begin{pmatrix} \cos \alpha_1 & \cos \beta_1 & \cos \gamma_1 \\ \cos \alpha_2 & \cos \beta_2 & \cos \gamma_2 \\ \cos \alpha_3 & \cos \beta_3 & \cos \gamma_3 \end{pmatrix} = \begin{pmatrix} g_{11} & g_{12} & g_{13} \\ g_{21} & g_{22} & g_{23} \\ g_{31} & g_{32} & g_{33} \end{pmatrix} = \begin{pmatrix} 0.768 & -0.582 & 0.267 \\ 0.384 & 0.753 & 0.535 \\ -0.512 & -0.308 & 0.802 \end{pmatrix} \quad (2.5)$$

The orientation matrix allows a crystal direction to be expressed in terms of the specimen direction to which it is parallel, and vice versa. Equation 2.5 shows the orientation matrix in terms of the direction cosines, elements, and a numerical example.

Both the rows and columns of the matrix are unit vectors, that is, the matrix is orthonormal and the inverse of the matrix is equal to its transpose. Since a crystal orientation needs only three independent variables to specify it (Section 2.1), it is clear that the matrix, having nine numbers, contains non-independent elements. In fact the cross product of any two rows (or columns) gives the third and for any row or column the sum of the squares of the three elements is equal to unity. These properties can be checked using the example in Equation 2.5. The pertinence of the orientation matrix is that it is the mathematical tool for calculation of all the other descriptors of orientation, as shown in Figure 2.6.

**FIGURE 2.6**

Relationship between the orientation matrix and the most commonly used orientation descriptors.

2.3.3 Crystallographically Related Solutions

We have stated that the crystal coordinate system and specimen coordinate system are related by the orientation (rotation) matrix. However, specification of both these coordinate systems is not usually unique, and a number of solutions can exist depending on the symmetry of both the crystal and the specimen. To consider the crystal symmetry, there are 24 different ways in which a crystal with cubic symmetry can be arranged. Consequently, there are 24 solutions for an orientation matrix of a material having cubic symmetry. The 24 *crystallographically related solutions* for the example matrix given in Equation 2.5 are listed in Table 2.2, and it can be seen that the rows of the matrix, and the signs of the elements, interchange. The full set of solutions are obtained by premultiplying the orientation matrix by each of 24 “symmetry matrices,” which are listed in Appendix II, in turn. These matrices describe the symmetry operations—two rotations of 120° about each of the four ⟨111⟩, three rotations of 90° about each of the three ⟨100⟩, and one rotation of 180° about each of the six ⟨110⟩, plus the identity matrix. Crystal systems other than cubic have fewer crystallographically related solutions (Schmidt and Olesen, 1989); for example, the 12 and 4 solutions for hexagonal and orthorhombic crystals are also listed in Appendix II.

It is important to stress that each of the matrices in Table 2.2 describes the *same* orientation and so in general any one can be chosen to represent the orientation. However, depending on what method is chosen to represent an orientation (i.e., Miller indices, angle/axis pair, Rodrigues vector, Euler angles, as described in the remainder of this chapter) or misorientation, the selection of a particular crystallographically related solution may both

TABLE 2.2Twenty-Four Equivalent Descriptions for $(123)[6\bar{3}\bar{4}]$

Ideal Orientation	Orientation Matrix	Angle/Axis Pair ($\theta/u \ v \ w$)	Rodrigues Vector ($R_1 \ R_2 \ R_3$)	Euler Angles ($\phi_1 \ \Phi \ \phi_2$)
$(123)[6\bar{3}\bar{4}]$	0.768 -0.582 0.267 0.384 0.753 0.535 -0.512 -0.308 0.802	48.6°/0.562 -0.520 -0.644	0.254 -0.235 -0.291	307.0° 36.7° 26.6°
$(32\bar{1})[\bar{4}3\bar{6}]$	-0.512 -0.308 0.802 0.384 0.753 0.535 -0.768 0.582 -0.267	120.9°/-0.028 -0.915 -0.403	-0.048 -1.613 -0.711	232.9° 105.5° 56.3°
$(\bar{1}2\bar{3})[\bar{6}34]$	-0.768 0.582 -0.267 0.384 0.753 0.535 0.512 0.308 -0.802	155.3°/0.271 0.933 0.237	1.239 4.263 1.081	121.0° 143.3° 333.4°
$(\bar{3}21)[436]$	0.512 0.308 -0.802 0.384 0.753 0.535 0.768 -0.582 0.267	74.6°/0.579 0.814 -0.039	0.441 0.620 -0.030	52.9° 74.5° 303.7°
$(13\bar{2})[6\bar{4}\bar{3}]$	0.768 -0.582 0.267 -0.512 -0.308 0.802 -0.384 -0.753 -0.535	122.5°/0.922 -0.386 -0.041	1.679 -0.704 -0.075	333.0° 122.3° 18.4°
$(1\bar{2}\bar{3})[\bar{6}3\bar{4}]$	0.768 -0.582 0.267 -0.384 -0.753 -0.535 0.512 0.308 -0.802	153.3°/-0.937 0.272 -0.220	-3.944 1.146 -0.925	121.0° 143.3° 153.4°
$(1\bar{3}2)[643]$	0.768 -0.582 0.267 0.512 0.308 -0.802 0.384 0.753 0.535	72.2°/-0.816 0.061 -0.574	-0.595 0.045 -0.419	153.0° 57.7° 161.6°
$(2\bar{1}3)[3\bar{6}4]$	0.384 0.753 0.535 -0.768 0.582 -0.267 -0.512 -0.308 0.802	67.4°/0.022 -0.567 0.824	0.015 -0.378 0.550	301.0° 36.7° 116.6°
$(\bar{1}2\bar{3})[\bar{6}\bar{3}\bar{4}]$	-0.768 0.582 -0.267 -0.384 -0.753 -0.535 -0.512 -0.308 0.802	149.3°/-0.222 -0.240 0.945	-0.807 -0.872 3.440	301.0° 36.7° 206.6°
$(\bar{2}13)[\bar{3}6\bar{4}]$	-0.384 -0.753 -0.535 0.768 -0.582 0.267 -0.512 -0.308 0.802	125.6°/0.354 0.014 -0.935	0.688 0.027 -1.820	301.0° 36.7° 296.6°
$(231)[3\bar{4}6]$	0.384 0.753 0.535 -0.512 -0.308 0.802 0.768 -0.582 0.267	109.2°/0.732 0.124 0.670	1.030 0.174 0.942	52.9° 74.5° 33.7°
$(312)[\bar{4}63]$	-0.512 -0.308 0.802 0.768 -0.582 0.267 0.384 0.753 0.535	141.2°/-0.388 -0.334 -0.859	-1.102 -0.948 -2.442	153.0° 57.7° 71.6°
$(\bar{2}3\bar{1})[\bar{3}\bar{4}6]$	-0.384 -0.753 -0.535 -0.512 -0.308 0.802 -0.768 0.582 -0.267	168.4°/0.548 -0.582 -0.600	5.413 -5.748 -5.920	239.2° 105.5° 326.3°
$(\bar{3}12)[4\bar{6}3]$	0.512 0.308 -0.802 -0.768 0.582 -0.267 0.384 0.757 0.535	71.7°/-0.537 0.625 0.567	-0.388 0.451 0.409	153.0° 57.7° 251.6°

Continued

TABLE 2.2 *Continued*

Ideal Orientation	Orientation Matrix	Angle/Axis Pair ($\theta/u\ v\ w$)	Rodrigues Vector ($R_1\ R_2\ R_3$)	Euler Angles ($\phi_1\ \Phi\ \phi_2$)
($\bar{3}1\bar{2}$)[$46\bar{3}$]	0.512 0.308 -0.802 0.768 -0.582 0.267 -0.384 -0.753 -0.535	143.3°/0.854 0.350 -0.385	2.577 1.055 -1.163	333.0° 122.3° 288.4°
($2\bar{3}\bar{1}$)[$34\bar{6}$]	0.384 0.753 0.535 0.512 0.308 -0.802 -0.768 0.582 -0.267	106.7°/-0.722 -0.680 0.126	-0.971 -0.914 0.169	232.9° 105.5° 146.3°
($\bar{2}\bar{3}1$)[$\bar{3}46$]	-0.384 -0.753 -0.535 0.512 0.308 -0.802 0.768 -0.582 0.267	113.9°/-0.120 0.712 -0.692	-0.185 1.094 -1.062	52.9° 74.5° 213.7°
($3\bar{1}\bar{2}$)[$\bar{4}6\bar{3}$]	-0.512 -0.308 0.802 -0.768 0.582 -0.267 -0.384 -0.753 -0.535	137.1°/0.357 -0.871 0.338	0.907 -2.216 0.860	333.0° 122.3° 108.4°
($21\bar{3}$)[364]	0.384 0.753 0.535 0.768 -0.582 0.267 0.512 0.308 -0.802	178.6°/-0.832 -0.457 -0.315	-67.983 -37.363 -25.710	121.0° 143.3° 63.4°
($\bar{1}32$)[$\bar{6}43$]	-0.768 0.582 -0.267 -0.512 -0.308 0.802 0.384 0.753 0.535	140.4°/0.038 0.511 0.859	0.107 1.421 2.387	153.0° 57.7° 341.6°
($3\bar{2}1$)[$\bar{4}36$]	-0.512 -0.308 0.802 -0.384 -0.753 -0.535 0.768 -0.582 0.267	177.3°/0.493 -0.351 0.796	20.621 -14.661 33.260	52.9° 74.5° 123.7°
($\bar{2}1\bar{3}$)[$\bar{3}64$]	-0.384 -0.753 -0.535 -0.768 0.582 -0.267 0.512 0.308 -0.802	143.3°/-0.482 0.876 0.013	-1.453 2.644 0.039	121.0° 143.3° 243.4°
($\bar{1}\bar{3}\bar{2}$)[$\bar{6}4\bar{3}$]	-0.768 0.582 -0.267 0.512 0.308 -0.802 -0.384 -0.753 -0.535	175.9°/-0.339 -0.808 0.481	-9.362 -22.343 13.305	333.0° 122.3° 198.4°
($\bar{3}\bar{2}1$)[$4\bar{3}\bar{6}$]	0.512 0.308 -0.802 -0.384 -0.753 -0.535 -0.768 0.582 -0.267	138.9°/-0.850 0.026 0.527	-2.269 0.068 1.407	232.9° 105.5° 236.3°

facilitate representation and allow insight into the physical meaning of the data. These points are expanded in Sections 2.7 and 9.6.

2.4 The “Ideal Orientation” (Miller or Miller–Bravais Indices) Notation

A practical way to denote an orientation is via the Miller indices. Formally, the direction cosines in both the first column (the specimen X direction expressed in crystal coordinates) and the last column (the specimen Z

direction expressed in crystal coordinates) of the orientation matrix are multiplied by a suitable factor to bring them to whole numbers, then divided by their lowest common denominator and conventionally written as $(hkl)[uvw]$ or $\{hkl\}\langle uvw \rangle$ if nonspecific indices are quoted, for example, $(112)[1\bar{1}\bar{1}]$ and $\{112\}\langle 111 \rangle$. These are the Miller indices, and for the example in Equation 2.5, the ideal orientation is $(123)[63\bar{4}]$. Thus, rotation matrix g and Miller indices $(hkl)[uvw]$ are related through

$$g = \begin{pmatrix} u / N_1 & q / N_2 & h / N_3 \\ v / N_1 & r / N_2 & k / N_3 \\ w / N_1 & s / N_2 & l / N_3 \end{pmatrix} \quad (2.6)$$

The center column $[qrs]$ corresponds to the specimen Y direction expressed in crystal coordinates (with $[qrs] = (hkl) \times [uvw]$). The constants N_i are required to normalize the three columns of the matrix to unity. It should be remembered that it is generally only for cubic materials that the indices for a plane and a direction are identical and hence it is less straightforward for non-cubic symmetries to extract the ideal orientation from the rotation matrix (Partridge, 1969).

In practice, the direction cosines from the orientation matrix are “idealized” to the nearest low-index Miller indices. For example, the following orientation is expressed in both direction cosines and the nearest family of Miller indices and is 2° and 6° away from (hkl) and $[uvw]$, respectively:

$$(0.662 \ 0.684 \ 0.306)[0.095 \ -0.482 \ -0.871] \rightarrow (221)[0\bar{1}\bar{2}] \quad (2.7)$$

This shorthand method of representation is very popular in metallurgy. Most usually single digit Miller indices are used to formulate the ideal orientation, although the components of the direction cosines could also simply be multiplied by 100 or 1000. An ideal orientation is also commonly formulated for hexagonal metals, for example, $(1\bar{2}10)[10\bar{1}0]$.

The crystallographically related solutions for an orientation feed through to the ideal orientation notation, as shown in the 24 equivalent solutions for $(123)[63\bar{4}]$ listed in Table 2.2. However, there are also orientations that, when denoted in the ideal orientation notation, can appear confusingly similar. For example, the orientation $(123)[\bar{6}3\bar{4}]$ is *not* a crystallographically related solution of $(123)[63\bar{4}]$, and it does not therefore appear in the list in Table 2.2. Another way to express this is that the matrix associated with $(123)[\bar{6}3\bar{4}]$ is

$$g = \begin{pmatrix} -0.768 & 0.582 & 0.267 \\ -0.384 & -0.753 & 0.535 \\ 0.512 & 0.308 & 0.802 \end{pmatrix} \quad (2.8)$$

which cannot be transformed into the matrices in Table 2.2 by column swapping, that is, multiplying by the symmetry matrices in Appendix II. For the most general case, there are four different orientations that have the same Miller indices families, $\{hkl\}\langle uvw \rangle$. These are

$$\begin{aligned} & (hkl)[uv\bar{w}] \\ & (hkl)[\bar{u}\bar{v}w] \\ & (khl)[vu\bar{w}] \\ & (khl)[\bar{v}\bar{u}w] \end{aligned} \quad (2.9)$$

Appendix III lists all 24 crystallographically related solutions for each of these, using $(123)[6\bar{3}\bar{4}]$ as an example, illustrating that there is no duplication among the 24×4 solutions (Davies and Randle, 1996). These four different sets of solutions are related through symmetries of the specimen coordinate system (Sections 2.7, 5.4.2, and 9.4).

The main advantage of the ideal orientation notation is that it highlights important planes and directions that are parallel to principal directions in the specimen. These are often of great practical importance in texture analysis (Hatherly and Hutchinson, 1979). Furthermore, for cubic materials it is usually possible to extract the ideal orientation "by eye" from the orientation matrix and it is easy to visualize the particular orientation. For example, Figure 2.7 shows a schematic diagram of the $(110)[001]$ orientation that is called the Goss orientation and is very important for power transformer technology (Section 1.1). Here (110) lies in the plane of the sheet, that is, the direction normal to this plane is parallel to the specimen ND, or Z axis; $[001]$ is parallel to the specimen RD, or X axis. For hexagonal materials, the relationship between the ideal orientation expressed as

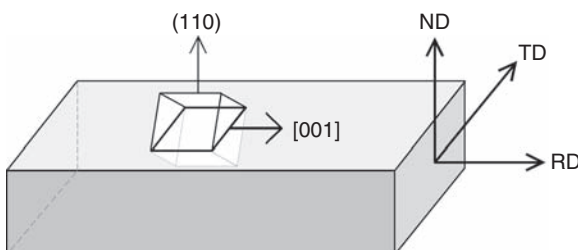


FIGURE 2.7

Schematic illustration of the relationship between the crystal and specimen axes for the $(110)[001]$ Goss orientation, that is, the normal to (110) is parallel to the specimen ND, or Z axis and $[001]$ is parallel to the specimen RD, or X axis.

Miller–Bravais indices and the orientation matrix is more complex (Section 2.3). For example,

$$(\bar{5}\bar{7}\bar{2}\bar{9})[\bar{2}\bar{4}\bar{2}\bar{5}] \rightarrow \begin{pmatrix} -0.429 & 0.855 & -0.291 \\ -0.826 & -0.291 & 0.510 \\ 0.366 & 0.459 & 0.810 \end{pmatrix} \quad (2.10)$$

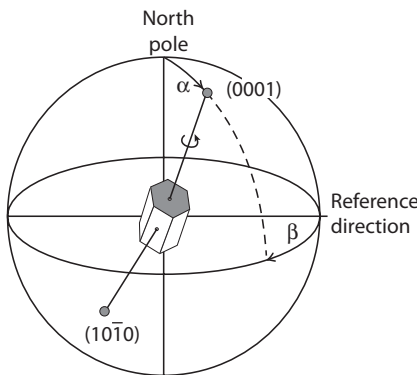
2.5 The Reference Sphere, Pole Figure, and Inverse Pole Figure

The direction of any 3-D vector in a crystal—a crystallographic direction or the normal to a crystal plane—can be described as a point on the *unit reference sphere*, that is, a sphere with radius 1 notionally residing around the crystal (Appendix IV). As an example, Figure 2.8 shows the (0001) plane in a hexagonal crystal. The point of intersection of the normal to this plane with the reference sphere, that is, its *pole*, is a measure for the arrangement of this plane in the crystal. Provided that the reference unit sphere is attached to an external frame, the position of the pole on the sphere also provides information on the crystallographic orientation of the crystal with respect to this frame, although the crystal has still one degree of freedom by rotating around this particular axis.

Representation of the 3-D orientation information on the unit sphere in a two-dimensional (2-D) plane requires a projection of the sphere onto that plane. This problem is well known from the presentation of geographic features on the surface of the earth in a 2-D map in earth science. In crystallography and metallurgy, most commonly the *stereographic projection* is used, the principle of which is shown in Figure 2.9 and explained in more detail in Appendix IV. In geology, the *equal area* (or *Lambert*) *projection*, which is also explained in Appendix IV, tends to be more popular. Derivatives of the stereographic or equal area projection (pole figures and inverse pole figures; see Sections 2.5.1 and 2.5.2) are discussed further with respect to macrotexture and microtexture in Sections 5.2 and 9.2, respectively.

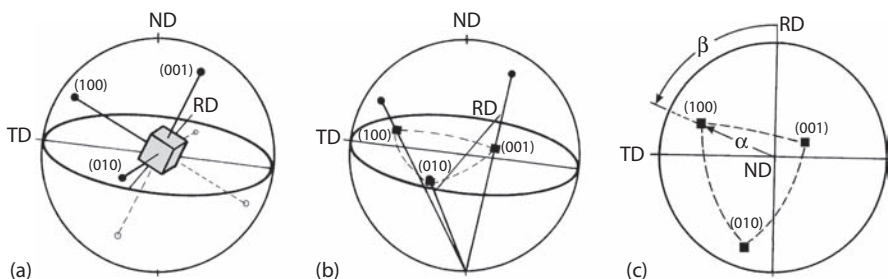
2.5.1 The Pole Figure

Poles are projected from the reference sphere onto a *pole figure* as follows. The position of a given pole on the sphere is commonly characterized in terms of two angles (Hansen et al., 1978): The angle α describes the azimuth of the pole, where $\alpha = 0^\circ$ is the north pole of the unit sphere, and the angle β characterizes the rotation of the pole around the polar axis,

**FIGURE 2.8**

Orientation of the basal plane (0001) in a hexagonal crystal. The position of the (0001) pole on the unit sphere with regard to an external reference frame is described by the two angles α and β . However, since the crystal can still rotate about the (0001) pole, for an unequivocal definition of the orientation of the crystal more information, here the position of the (1010) pole, is required.

starting from a specified reference direction (Figure 2.8). To characterize the crystallographic orientation of the crystal under investigation, the spatial arrangement of the corresponding poles in terms of the angles α and β has to be determined with respect to an external reference frame, that is, the sample or specimen coordinate system S (Section 2.3.1). For instance, for rolling symmetry, the sheet normal direction ND is typically chosen to be in the north pole of the sphere, so that $\alpha = 0^\circ$ for ND, and the rotation angle β is 0° for the rolling direction RD or, less frequently, the transverse direction TD. For other deformation modes or specimen geometries an appropriate 3-D, preferably right-handed, coordinate system has to be established (Section 2.3.1).

**FIGURE 2.9**

Presentation of the {100} poles of a cubic crystal in the stereographic projection. (a) Crystal in the unit sphere; (b) projection of the {100} poles onto the equator plane; (c) {100} pole figure and definition of the pole figure angles α and β for the (100) pole.

Thus, the reference system of the pole figure is the specimen coordinate system S given by the specimen axes $\{s_1 s_2 s_3\}$, and the crystal orientation given by the axes of the crystal coordinate system $C = \{c_1 c_2 c_3\}$ is projected into this frame. If R is a vector parallel to the pole of interest ($X Y Z$), then it can be expressed in the two frames S and C according to

$$R = s_1 \sin \alpha \cos \beta + s_2 \sin \alpha \sin \beta + s_3 \cos \alpha \quad (2.11a)$$

and

$$R = \frac{1}{N} (c_1 X + c_2 Y + c_3 Z) \quad (2.11b)$$

($X Y Z$) are the coordinates of the pole in the crystal frame, for example, (111), and N is a constant with $N = \sqrt{X^2 + Y^2 + Z^2}$ to normalize R to unity. Scalar multiplication of Equations 2.11a and 2.11b in succession by the three vectors s_i under consideration of the definition of an orientation (Equation 2.4) finally yields

$$\begin{pmatrix} \sin \alpha \cos \beta \\ \sin \alpha \sin \beta \\ \cos \alpha \end{pmatrix} = \frac{1}{N} \begin{pmatrix} g_{11} & g_{21} & g_{31} \\ g_{12} & g_{22} & g_{32} \\ g_{13} & g_{23} & g_{33} \end{pmatrix} \cdot \begin{pmatrix} X \\ Y \\ Z \end{pmatrix} \quad (2.12)$$

(note that $g^T = g^{-1}$ appears here). Equation 2.12 yields nine equivalent expressions to derive the pole figure angles α and β for a given pole ($X Y Z$) from the orientation matrix g (Hansen et al., 1978). The opposite way, that is, the indexing of the poles and determination of the orientation g from a given pole figure, is described in Appendix V.

So far, only individual poles have been considered. However, as already mentioned, one pole does not yield the entire orientation information, since the crystal can still rotate about this particular pole (Figure 2.8). For this reason, the distribution of the c axes in a hexagonal material, that is, its (0001) pole figure, does not provide an unambiguous representation of the texture of the sample; other poles have to be considered to represent unambiguously an orientation. In this example, the additional information about the position of, say, the (10̄10) pole would determine the orientation in an unequivocal manner (Figure 2.8). Although in this example the orientation is fully characterized by two poles, in general—depending on the symmetry of the crystal or the poles—three poles are necessary to derive completely the orientation matrix g in Equation 2.12. Usually, the additional information is provided by other poles of the same family of planes (Appendix I), that is, different poles (hkl) of the family $\{hkl\}$. For instance, the hexagonal crystal has three equivalent {1120} planes, (1120), (12̄10), and (2̄110), so that each orientation in the corresponding {1120} pole figure is exactly characterized by the corresponding three poles. In pole figures like {1121} and {1101}, any orientation is defined

by six equivalent poles. In cubic crystals, a given orientation is described by (not counting the same poles with negative signs) three $\{100\}$, four $\{111\}$, six $\{110\}$, twelve $\{012\}$, $\{112\}$, $\{113\}$, etc., and—in the most general case—twenty-four $\{hkl\}$ poles, which means that all pole figures of cubic crystals comprise enough poles to describe unambiguously an orientation.

2.5.2 The Inverse Pole Figure

Rather than representing the orientation of the crystal coordinate system in the specimen coordinate system, that is, in a pole figure, vice versa the orientation of the specimen coordinate system can be projected into the crystal coordinate system. This representation is called the *inverse pole figure*. Thus, the reference system of the inverse pole figure is the crystal coordinate system C , and the “orientation” is defined by the axes of the specimen coordinate system S , for example, RD, TD, and ND. In an analogy to Equation 2.11a, where the pole figure angles α and β of a unit vector parallel to the crystallographic axis (XYZ) have been considered in the frame S , now the angles γ and δ of a vector parallel to a specimen axis s_i in the coordinate system C must be introduced:

$$s_i = c_1 \sin \gamma_i \cos \delta_i + c_2 \sin \gamma_i \sin \delta_i + c_3 \cos \delta_i \quad (2.13)$$

Scalar multiplication now leads to (see Equation 2.12)

$$\begin{pmatrix} \sin \gamma \cos \delta \\ \sin \gamma \sin \delta \\ \cos \delta \end{pmatrix} = \begin{pmatrix} g_{11} & g_{12} & g_{13} \\ g_{21} & g_{22} & g_{23} \\ g_{31} & g_{32} & g_{33} \end{pmatrix} \cdot \begin{pmatrix} X_s \\ Y_s \\ Z_s \end{pmatrix} \quad (2.14)$$

These expressions describe the elements of the orientation matrix g in terms of the position of the specimen axes. Inverse pole figures are often used for axial symmetric specimens, where only one of the axes is prescribed. For instance, for compression or tensile specimens the orientation changes of the compression or tensile axis are plotted in the crystal coordinate system. According to the crystal symmetry it is not necessary to show the entire pole figure, but one unit triangle (Appendix IV) will suffice. In the case of cubic crystal symmetry, the well-known unit triangle $\langle 100 \rangle$, $\langle 110 \rangle$, and $\langle 111 \rangle$ is used.

2.6 The Euler Angles and Euler Space

Both the orientation matrix and the ideal orientation notation overdetermine the orientation, since only three variables are needed to specify an orientation. The most well-established method of expressing these three

numbers is as the three *Euler angles*, which reside in a coordinate system known as *Euler space*.

2.6.1 The Euler Angles

The Euler angles refer to three rotations that, when performed in the correct sequence, transform the specimen coordinate system onto the crystal coordinate system—in other words, specify the orientation g . There are several different conventions for expressing the Euler angles. The most commonly used are those formulated by Bunge, as shown in Figure 2.10 (Bunge, 1965, 1982). The rotations are as follows:

1. φ_1 about the normal direction ND, transforming the transverse direction TD into TD' and the rolling direction RD into RD'
2. Φ about the axis RD' (in its new orientation)
3. φ_2 about ND'' (in its new orientation)

where φ_1 , Φ , φ_2 are the Euler angles (Bunge definition). The effect of the operation sequence of these three rotations can be seen in Figure 2.10.

Analytically, the three rotations are expressed as

$$g_{\varphi_1} = \begin{pmatrix} \cos \varphi_1 & \sin \varphi_1 & 0 \\ -\sin \varphi_1 & \cos \varphi_1 & 0 \\ 0 & 0 & 1 \end{pmatrix} \quad (2.15a)$$

$$g_{\Phi} = \begin{pmatrix} 1 & 0 & 0 \\ 0 & \cos \Phi & \sin \Phi \\ 0 & -\sin \Phi & \cos \Phi \end{pmatrix} \quad (2.15b)$$

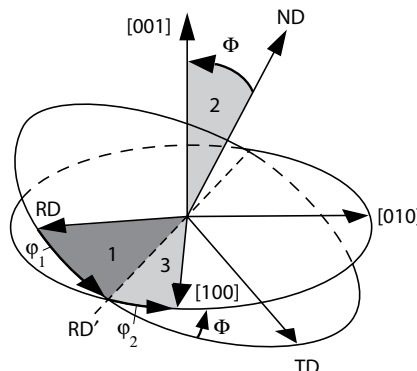


FIGURE 2.10

Diagram showing how rotation through the Euler angles φ_1 , Φ , φ_2 , in order 1, 2, 3 as shown describes the rotation between the specimen and crystal axes.

$$g_{\varphi_2} = \begin{pmatrix} \cos \varphi_2 & \sin \varphi_2 & 0 \\ -\sin \varphi_2 & \cos \varphi_2 & 0 \\ 0 & 0 & 1 \end{pmatrix} \quad (2.15c)$$

By multiplication of these three matrices in order, an expression is obtained, which links the rotation matrix g to the three Euler angles:

$$g = g_{\varphi_2} \cdot g_\Phi \cdot g_{\varphi_1} \quad (2.16a)$$

The elements of the matrix in terms of the Euler angles are, therefore, given by

$$\begin{aligned} g_{11} &= \cos \varphi_1 \cos \varphi_2 - \sin \varphi_1 \sin \varphi_2 \cos \Phi \\ g_{12} &= \sin \varphi_1 \cos \varphi_2 + \cos \varphi_1 \sin \varphi_2 \cos \Phi \\ g_{13} &= \sin \varphi_2 \sin \Phi \\ g_{21} &= -\cos \varphi_1 \sin \varphi_2 - \sin \varphi_1 \cos \varphi_2 \cos \Phi \\ g_{22} &= -\sin \varphi_1 \sin \varphi_2 + \cos \varphi_1 \cos \varphi_2 \cos \Phi \\ g_{23} &= \cos \varphi_2 \sin \Phi \\ g_{31} &= \sin \varphi_1 \sin \Phi \\ g_{32} &= -\cos \varphi_1 \sin \Phi \\ g_{33} &= \cos \Phi \end{aligned} \quad (2.16b)$$

The ideal orientation (123)[63̄], which is used as an example throughout this chapter, can equivalently be expressed as Euler angles $\varphi_1 = 59.0^\circ$, $\Phi = 36.7^\circ$, $\varphi_2 = 51.2^\circ$. Table 2.2 shows the effect of the symmetry-related solutions on these Euler angles.

From the definition of the Euler angles, it follows that they are periodic with period 2π . Thus, it holds:

$$g\{\varphi_1 + 2\pi, \Phi + 2\pi, \varphi_2 + 2\pi\} = g\{\varphi_1, \Phi, \varphi_2\} \quad (2.17)$$

Moreover, there is the identity

$$g\{\varphi_1 + \pi, 2\pi - \Phi, \varphi_2 + \pi\} = g\{\varphi_1, \Phi, \varphi_2\} \quad (2.18)$$

representing a reflection in the plane $\Phi = \pi$ with a simultaneous displacement through π in both φ_1 and φ_2 . This means that there is a glide plane in the Euler angle space. Thus, in the most general case, the Euler angles are defined in the range $0^\circ \leq \varphi_1, \varphi_2 \leq 360^\circ$, and $0^\circ \leq \Phi \leq 180^\circ$. It is noted, however, that the sine and cosine functions in Equation 2.16b are only defined in the range $-90^\circ \leq \varphi_1, \Phi, \varphi_2 \leq 90^\circ$. Therefore, determination of the Euler angles from

the rotation matrix (Equation 2.16b) is not straightforward, since the range of the angles has to be considered too. For example, let $\Phi = 35^\circ$ and $g_{31} = 0.439$. In that case, $\varphi_1 = \arcsin(g_{31}/\sin\Phi)$ can be both 50° and 130° . The correct value has to be decided by taking the information in other matrix elements into account, for example, g_{32} .

Besides the convention of Euler angles according to Bunge, two other definitions are in use. Independently of Bunge, Roe (1965) proposed a set of Euler angles Ψ, Θ, Φ that differs from Bunge's definition by the second rotation being performed about the transverse direction rather than the rolling direction (note that the same definition is used by Matthies et al. [1987], but the angles are labeled α, β, γ). More recently, Kocks (1988) introduced a set of so-called symmetric Euler angles Ψ, Θ, ϕ . Although the rotations of Ψ and Θ are identical to those introduced by Roe, ϕ was defined as to be $\pi - \Phi_{\text{Roe}}$. In this set, the orientation matrix g becomes its transpose upon an interchange of Ψ and ϕ , which gives a symmetry between the "reference" and the "rotated" frame, which is not present in any of the other conventions.

The equivalence between these two sets and the Bunge angles is as follows:

Bunge–Roe:

$$\varphi_1 = \Psi + \pi/2 \quad \Phi = \Theta \quad \varphi_2 = \Phi - \pi/2 \quad (2.19a)$$

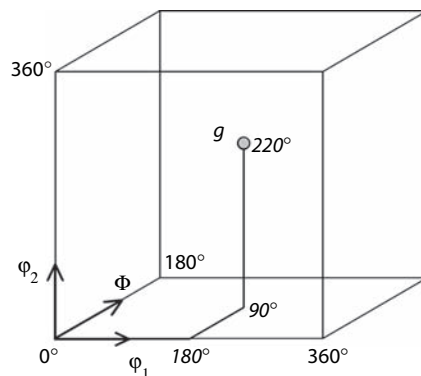
Bunge–Kocks:

$$\varphi_1 = \Psi + \pi/2 \quad \Phi = \Theta \quad \varphi_2 = \pi/2 - \phi \quad (2.19b)$$

The Euler angles formed the backbone of texture research and practice for many years and have been particularly associated with x-ray analysis of textures. Details of their use in practice are given in Sections 5.4, 5.5, 9.3, and 9.6.1. Although the Euler angles are less intuitive than the ideal orientation nomenclature, they do present a fully quantitative description of the texture that is suitable for graphical representation.

2.6.2 The Euler Space

Any orientation expressed in terms of its Euler angles can be represented unequivocally as a point in a 3-D coordinate system whose axes are spanned by the three Euler angles (Figure 2.11). The resulting space is referred to as *Euler space* (which is one example of an *orientation space* or *g-space*). Although the common Cartesian Euler space suffers from several disadvantages (see the following text), it is by far the most common orientation space in which to represent macrotexture data and hence we will encounter it throughout this book. In particular, the quantitative analysis of x-ray macrotextures is mainly based on the representation of textures in Euler space, and this issue will be discussed in detail in Sections 5.4 and 5.5. Accordingly, Euler space is also used to represent individual orientations and orientation distributions

**FIGURE 2.11**

Representation of orientations in a three-dimensional orientation space defined by the Euler angles. Each orientation g corresponds to a point in the Euler space whose coordinates are given by the three Euler angles φ_1 , Φ , φ_2 describing the orientation (Bunge's convention).

that are determined by techniques for single-grain orientation measurements (Section 9.3). For the representation of misorientations, other spaces are more advantageous; but nonetheless, misorientation distributions can be represented in Euler space, which warrants a short discussion (Section 9.6.1).

As shown in the preceding section, in the most general case of triclinic crystal symmetry and no sample symmetry, the Euler angles are defined in the range $0^\circ \leq \varphi_1, \varphi_2 \leq 360^\circ$, and $0^\circ \leq \Phi \leq 180^\circ$, which in turn defines the maximum size of the Euler angle space, the so-called asymmetric unit. However, as already discussed (Sections 2.3 and 2.4), symmetries of the crystal or the specimen frame result in a number of different, but equivalent, descriptions of a given orientation. Such symmetries lead to a reduction in the size of the Euler space that is required to represent unequivocally all possible crystallographic orientations and, consequently, leads also to a number of symmetrically equivalent subspaces (Table 2.3). The necessary transformation laws for the various symmetry operations can be found in Hansen et al. (1978), Pospiech (1982), Bunge (1982), and Kocks (1998).

Different *sample symmetries* affect the range of the angle φ_1 . In the most general case, which is no sample symmetry (sometimes called triclinic symmetry), the full range $0^\circ \leq \varphi_1 \leq 360^\circ$ is required to represent all possible orientations, whereas any symmetry in the specimen coordinate system reduces the size of the Euler space. In specimens deformed by rolling—or more generally under a plane strain deformation state—it is usually assumed that two mirror planes exist, one in the rolling direction and the other in the transverse direction. In this case of *orthonormal sample symmetry*, the range of the Euler angle φ_1 is reduced to one quarter, that is, to $0^\circ \leq \varphi_1 \leq 90^\circ$. When only one symmetry plane is present, the Euler space is halved to $0^\circ \leq \varphi_1 \leq 180^\circ$. This *monoclinic sample symmetry* is given for specimens deformed by shear, for example, in torsion experiments, which comprise a twofold symmetry

TABLE 2.3

Size of the Euler Space Necessary to Represent Unequivocally Orientations for Different Sample and Crystal Symmetries

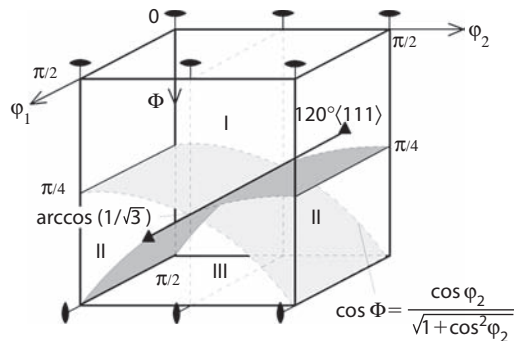
Crystal System	Laue Class	Crystal Symmetry	Sample Symmetry		
			Orthonormal	Monoclinic	None (Triclinic)
			Φ	φ_2	φ_1
Triclinic	$\bar{1}$		180°	360°	
Monoclinic	2/m		180°	180°	
Orthorhombic	mmm		90°	180°	
Trigonal	$\bar{3}$		180°	120°	
	$\bar{3}m$		90°	120°	90°
Tetragonal	4/m		180°	90°	180°
	4/mmm		90°	90°	360°
Hexagonal	6/m		180°	60°	
	6/mmm		90°	60°	
Cubic	$m\bar{3}$		90° ^a	180°	
	$m\bar{3}m$		90° ^a	90°	

^aThreefold symmetry due to 120°⟨111⟩ symmetry.

axis (diad) in the shear plane perpendicular to the cylinder axis. This symmetry also applies for the surface layers of a rolled sheet. In contrast to the plane strain state at the sheet center, in the surface layers the deformation is no longer symmetrical with regard to the transverse direction, but only with regard to the rolling direction (Section 5.4.2).

Crystal symmetry further reduces the size of the Euler space by affecting the range of the angles Φ and φ_2 . In general, an n -fold symmetry axis reduces the Euler space by a factor of n . This means that the Euler angles $(\varphi_1, \Phi, \varphi_2)$ and $(\varphi_1, \Phi, \varphi_2 \pm 360^\circ/n)$ are equivalent. Thus, the threefold axis in trigonal crystal symmetry reduces the range by a factor of 3, which means that a range of $0^\circ < \varphi_2 < 120^\circ$ is sufficient to represent all possible orientations. Accordingly, for tetragonal (fourfold axis) and hexagonal crystals (sixfold axis), φ_2 can be reduced to 90° and 60°, respectively. An additional twofold symmetry or mirror planes affects Φ by reducing the range from 180° to 90°, which is given in all but triclinic crystal symmetry (Table 2.3).

For cubic crystal symmetry it has already been discussed in Section 2.3.3 that there are 24 possibilities to describe one and the same orientation of a cube in any reference frame, so that the Euler space can be subdivided into 24 equivalent subspaces. In accordance with these considerations, the three

**FIGURE 2.12**

Symmetry elements in the Euler space for cubic crystal symmetry and orthonormal sample symmetry.

fourfold axes (i.e., $90^\circ/\langle 100 \rangle$ rotations) and the six twofold axes (i.e., $180^\circ/\langle 110 \rangle$ rotations) reduce the necessary Euler angle space to the range $0^\circ \leq \varphi_1 \leq 360^\circ$, $0^\circ \leq \Phi, \varphi_2 \leq 90^\circ$, which means that there are only eight equivalent subspaces (i.e., equivalent to tetragonal symmetry). However, this reduction does not consider the four threefold axes, that is, the $120^\circ/\langle 111 \rangle$ rotations. Since a further reduction in the threefold symmetry would lead to a complex-shaped subspace, this operation is not usually carried out and, therefore, for cubic crystals each orientation appears three times in the reduced Euler angle space. Figure 2.12 shows the symmetry elements in the Euler space for cubic crystal symmetry and orthonormal sample symmetry (Hansen et al., 1978).

If we now consider *misorientations* between two crystals, as opposed to the orientation of a crystal with respect to an external reference frame, the Euler space is further reduced by applying the crystal symmetry of the second crystal rather than sample symmetry (Section 2.7.2). Furthermore, the Euler space is reduced by an additional factor of 2 due to the equivalence of the misorientation and the inverse misorientation, because with respect to the misorientation the two crystallites are indistinguishable. Thus, for cubic crystal symmetry one has $24 \times 24 \times 2$ equally valid descriptions of a given misorientation, which contain 24 generally different rotation angles θ . Section 9.6.1 discusses one of the resulting 1152 equivalent subspaces of the Euler space.

2.7 The Angle/Axis of Rotation and Cylindrical Angle/Axis Space

In Section 2.3 we showed how an orientation can be described by the concept of three rotations that transform the coordinate system of the crystal onto the

reference, that is, a specimen, coordinate system. The same final transformation can be achieved if the crystal coordinate system is rotated through a *single* angle, provided that the rotation is performed about a *specific* axis. This angle and axis are known as the *angle of rotation* and *axis of rotation*, or more briefly the *angle/axis pair*.

2.7.1 Angle/Axis of Rotation

Figure 2.13a illustrates the angle/axis of rotation between two cubic coordinate systems. The left-hand cube (axes $X_1Y_1Z_1$) is chosen as the fixed, reference position and the right-hand cube (axes $X_2Y_2Z_2$) would need to be rotated through 50° about an axis that is vertical in the diagram and parallel to the common [001] to achieve the reference orientation. It is important to notice that the rotation axis [001] is *the same direction in both cubes*. Similarly, Figure 2.13b shows angle/axis of rotation between two hexagons.

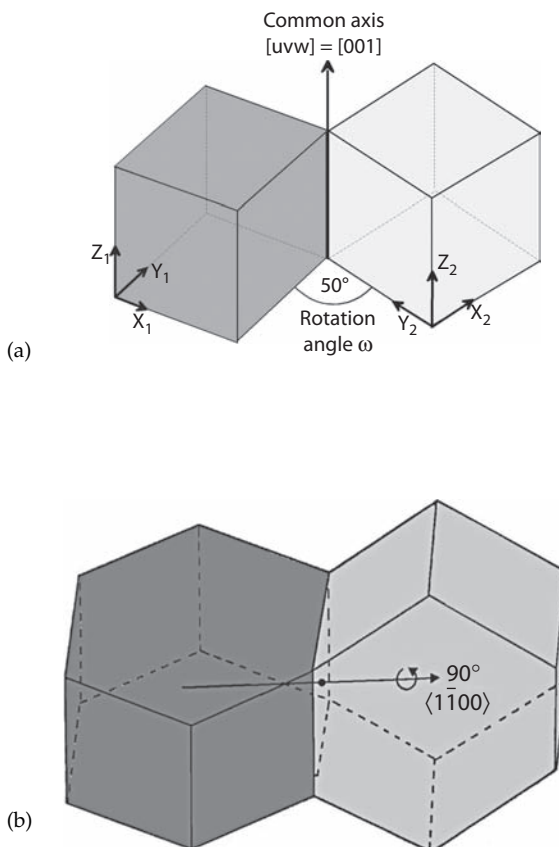


FIGURE 2.13

Diagram showing the angle/axis of rotation between (a) two cubes and (b) two hexagons.

If we now consider the orientation of crystal lattices, $X_1Y_1Z_1$ is replaced by the specimen coordinate system as a reference, for example, RD, TD, ND, and $X_2Y_2Z_2$ is replaced by the crystal axes 100,010,001. The three independent variables that embody an orientation comprise one variable for the rotation angle θ and two variables for the rotation axis r , since r is normalized such that $r_1^2 + r_2^2 + r_3^2 = 1$, and so the third index is redundant. The transformation from the angle/axis pair θ/r to the orientation matrix g is given by

$$\begin{aligned} g_{11} &= (1 - r_1^2) \cdot \cos\theta + r_1^2 \\ g_{12} &= r_1 r_2 \cdot (1 - \cos\theta) + r_3 \cdot \sin\theta \\ g_{13} &= r_1 r_3 \cdot (1 - \cos\theta) - r_2 \cdot \sin\theta \\ g_{21} &= r_1 r_2 \cdot (1 - \cos\theta) - r_3 \cdot \sin\theta \\ g_{22} &= (1 - r_2^2) \cdot \cos\theta + r_2^2 \\ g_{23} &= r_2 r_3 \cdot (1 - \cos\theta) + r_1 \cdot \sin\theta \\ g_{31} &= r_1 r_3 \cdot (1 - \cos\theta) + r_2 \cdot \sin\theta \\ g_{32} &= r_2 r_3 \cdot (1 - \cos\theta) - r_1 \cdot \sin\theta \\ g_{33} &= (1 - r_3^2) \cdot \cos\theta + r_3^2 \end{aligned} \quad (2.20)$$

Vice versa, the angle/axis of rotation is extracted from the orientation matrix as follows:

$$\begin{aligned} \cos\theta &= \frac{(g_{11} + g_{22} + g_{33} - 1)}{2} \\ r_1 &= \frac{(g_{23} - g_{32})}{(2 \sin\theta)} \\ r_2 &= \frac{(g_{31} - g_{13})}{(2 \sin\theta)} \\ r_3 &= \frac{(g_{12} - g_{21})}{(2 \sin\theta)} \end{aligned} \quad (2.21a)$$

If $\theta = 0^\circ$ or 180° , $\sin\theta$ becomes 0. In that case, r can be derived from

$$\begin{aligned} r_1 &= \left(\frac{(g_{11} + 1)}{2} \right)^{1/2} \\ r_2 &= \left(\frac{(g_{22} + 1)}{2} \right)^{1/2} \\ r_3 &= \left(\frac{(g_{33} + 1)}{2} \right)^{1/2} \end{aligned} \quad (2.21b)$$

For example, the orientation matrix given in Equation 2.5 yields an angle/axis pair of $48.6^\circ/(0.562 -0.520 -0.644)$. The reference orientation, chosen to

coincide with the specimen axes, is described by the identity matrix. It is not usually necessary to ascribe a handedness to the rotation, since conventionally the rotation is described as a right-handed screw operation and hence θ is always a positive angle (Mykura, 1980). A negative angle is equivalent to changing the sign of r . An example of where it is necessary to know the sense of a rotation is when measuring the orientation of adjacent subgrains (Sections 9.5.2 and 10.4.1). If the rotations are all in the same sense, then the total rotation is cumulative; otherwise, adjacent rotations of the same magnitude cancel each other out (Hansen and Juul Jensen, 1994; Randle et al., 1996).

Section 2.3.3 describes the crystallographically related solutions of a single orientation. It follows then that these solutions will give rise to the same number of axis/angle pairs, each of which is calculated from the crystallographically related solution of the matrix (Appendix II). Table 2.2 includes the 24 angle/axis pairs that accompany the ideal orientation $(123)[6\bar{3}\bar{4}]$. Inspection of Table 2.2 shows that, even though each of these angle/axis pairs describes exactly the same orientation, this could not have been known from the format of the angle/axis pairs themselves—numerically they appear to be quite unrelated. The relationship only becomes clear from concurrent inspection of the matrix or ideal orientation.

2.7.2 Angle/Axis Description of Misorientation

There is a second choice for designation of a reference orientation. Instead of choosing the specimen axes for the reference orientation, it could be the axes (orientation) of another grain in the specimen, usually the neighboring grain. The orientation of grain 2—a grain having crystal axes parallel to $X_2Y_2Z_2$ —is then expressed relative to the orientation of grain 1, which is similarly a grain having crystal axes parallel to $X_1Y_1Z_1$. For the examples in Figures 2.13a and 2.13b, the angle/axis of misorientation is $50^\circ/\langle 001 \rangle$ and $90^\circ/\langle 1100 \rangle$, respectively, where the latter axis is given in Miller–Bravais indices. The purpose of such a descriptor of orientation is to characterize the orientation relationship (between different phases) or the misorientation (between two grains of the same phase) (Lange, 1967; Santoro and Mighell, 1973). For the latter case, specification of the misorientation gives access to the grain boundary crystallography, which is a very important subset of microtexture (Randle, 1993). Chapter 11 describes extraction and analysis of grain boundary parameters from the misorientation.

A misorientation is calculated from the orientations of grains 1 and 2 by

$$M_{12} = g_1^{-1}g_2 \quad (2.22)$$

where M_{12} is the matrix that embodies the misorientation between g_2 and g_1 , where g_1 is arbitrarily chosen to be the reference orientation. The angle/axis of rotation (usually called the *angle/axis of misorientation* to distinguish it as

a grain or phase boundary parameter) is calculated by using Equation 2.21 and substituting the elements of the misorientation matrix M_{12} for those of the orientation matrix g .

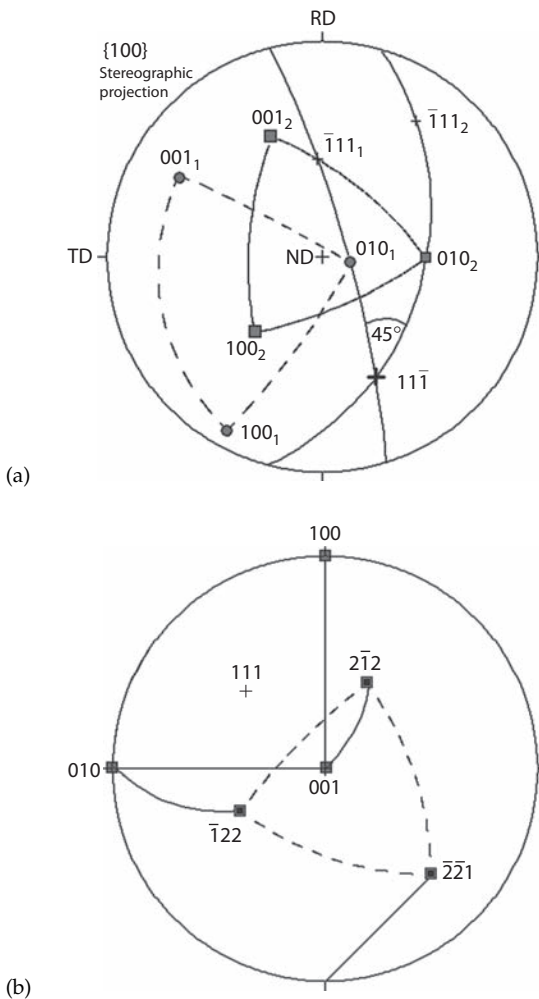
In summary, the essential difference between an angle/axis pair description of the orientation of a single grain and an angle/axis pair description of the misorientation between the crystal lattices of two grains is simply the choice of reference axes. This is illustrated graphically in the stereogram shown in Figure 2.14 (the stereographic projection is explained in Appendix IV). In Figure 2.14a, the {100} crystal axes of two grains 1 and 2 are represented relative to the specimen axes RD, TD, and ND; hence, the reference axes are the specimen axes. The location of r , common to both orientations, is plotted on the stereogram along with the angle θ through which $[100]_2$, $[010]_2$, $[001]_2$ must be rotated to make them parallel with the crystal axes $[100]_1$, $[010]_1$, $[001]_1$ of grain 1. The misorientation axis r can be constructed from the intersection of two great circles that bisect pairs of the same crystal axes in both grains, whereas the angle between the poles of two of these great circles gives the misorientation angle θ .

In Figure 2.14b, the reference axes are the crystal axes of grain 1. Accordingly, the crystal axes of grain 2 are expressed in the frame of grain 1, that is, $[2\bar{2}1]_2$, $[\bar{1}22]_2$, $[2\bar{1}2]_2$. The misorientation axis (cross) and angle (arcs of small circles) between grains 2 and 1 are also expressed relative to the crystal axes of grain 1. In summary, Figure 2.14a depicts the orientation, sometimes called the *absolute orientation*, of grains 1 and 2 and Figure 2.14b depicts the misorientation between grains 1 and 2, both expressed as an angle/axis pair. Figure 2.6 includes the most common parameters that are derived from the misorientation matrix.

As it stands, the angle/axis pair is not a very useful representation of an orientation since it does not convey easily understood physical information about the relationship between the orientation and important axes in the specimen. However, the angle/axis pair is an extremely effective means for representation of a misorientation, since the description actually relates physically to the grain or phase boundary misorientation angle and axis, which in turn is used for categorization and subsequent analysis (Section 11.2). Frequently, the angle and axis of misorientation are represented separately, which is discussed in Section 9.5.1. Finally, it should be noted that the value of the angle/axis description of orientation is as a starting point for the Rodrigues vector, or R -vector formulation, which leads to a superior way of representing orientations and misorientations (Section 2.8).

2.7.3 The Cylindrical Angle/Axis Space

Orientations and misorientations can also be represented in a 3-D space formed by the parameters of the angle/axis pair description. As the angle/axis representation is easy to visualize and convenient for analysis

**FIGURE 2.14**

Stereographic representation of (a) an orientation and (b) a misorientation. In (a) the crystal axes of two grains 1 and 2 are represented relative to the specimen axes RD, TD, ND. The misorientation axis is given by the intersection of great circles that bisect pairs of the same crystal axes in both grains. The angle between the poles of two of these great circles gives the misorientation angle (Appendix IV). In (b) the misorientation axis (cross) and angle (arcs of small circles) are expressed relative to the crystal axes of one grain. This particular example is a twin. (Adapted from Randle, V. and Ralph, B., *Proc. R. Soc. Lond.*, 415A, 239, 1988.)

and interpretation of orientation correlations, the angle/axis space will mostly be used for the representation of misorientations, but the basic principles discussed in the following text also hold for the presentation of orientations.

As described in Section 2.7.1, both orientations and misorientations can be expressed in terms of rotational parameters, that is, the rotation axis r and the rotation angle θ . To represent the orientations or misorientations in a suitable angle/axis space, the rotation axis $r = (r_x, r_y, r_z)$ is expressed in terms of two angles ϑ and ψ :

$$r_x = \cos \psi \sin \vartheta, r_y = \sin \psi \sin \vartheta, r_z = \cos \vartheta \quad (2.23)$$

Thus, the angle/axis rotational parameters are now given by the three angles θ , ϑ , and ψ . The necessary analytical descriptions connected with this way of representing orientations and misorientations are given by Pospiech (1972) and Pospiech et al. (1986). In calculations, the relations between Euler angles $(\varphi_1, \Phi, \varphi_2)$ and the rotational parameters $(\theta, \vartheta, \psi)$ might be useful:

$$\sin \frac{\theta}{2} \cdot \sin \vartheta = \sin \frac{\Phi}{2}, \quad \cos \frac{\theta}{2} = \cos \frac{\Phi}{2} \cdot \cos \frac{\varphi_1 + \varphi_2}{2}, \quad \psi = \frac{1}{2}(\varphi_1 - \varphi_2) \quad (2.24)$$

All possible orientations can be presented in the interval ($0^\circ \leq \theta \leq 360^\circ$, $0^\circ \leq \vartheta \leq 90^\circ$, $0^\circ \leq \psi \leq 360^\circ$) into a space with the simple shape of a cylinder, that is, *cylindrical angle/axis space* (Figure 2.15). When the cylinder axis is chosen parallel to the θ axis, the base plane of the cylinder corresponds to a stereographic projection of the rotation axis r . Thus for each misorientation angle θ , the corresponding rotation axis r can readily be derived from its position in the stereographic triangle, which is a very familiar way to evaluate misorientation data (Section 9.5.1). Examples of *misorientation distribution functions* (MODFs) in the cylindrical angle/axis space are shown in Sections 9.6.2 and 9.7.

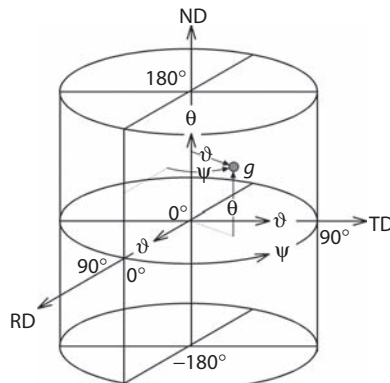


FIGURE 2.15

Representation of an orientation g given by the angle/axis description parameters r and θ in a cylindrical orientation space defined by the rotational parameters ϑ , ψ , and θ .

2.8 The Rodrigues Vector and Rodrigues Space

In the previous section, we have seen that the angle/axis formulation is not very useful for representing macrotexture data since it does not convey easily understood physical information about the relationship between the crystal orientations and specimen axes. However, the angle/axis pair provides useful microtexture information, in that the description actually relates physically to the misorientation angles and axes, which in turn is used for categorization and subsequent analysis of grain or phase boundaries (Section 11.2). The values of the angle/axis description of orientation is also a starting point for the Rodrigues vector, or R -vector formulation, which is used with great effect to convey and represent both orientations and, most notably, misorientations. In summary, the formulation of the angle/axis of misorientation is an end in itself and also used further to calculate R vectors, whereas the angle/axis of rotation for orientations is not a particularly effective parameter except to illustrate the principles of the R vector.

2.8.1 The Rodrigues Vector

An orientation can be expressed as a 3-D vector, since such a vector requires three variables to specify its position in space and similarly an orientation requires three variables for its specification. Such an “orientation vector” is most easily described and visualized from the angle/axis descriptor: The rotation axis gives the *direction* of the vector and the rotation angle its *magnitude*. The *Rodrigues vector R* combines the angle and axis of rotation into one mathematical entity; thus,

$$R = \tan\left(\frac{\theta}{2}\right) \cdot r \quad (2.25)$$

For example, the first angle/axis pair entry in Table 2.2 gives a Rodrigues vector with elements $R_1 R_2 R_3$ given by

$$\begin{aligned} R_1 &= \tan\left(\frac{\theta}{2}\right) \cdot r_1 = 0.254 \\ R_2 &= \tan\left(\frac{\theta}{2}\right) \cdot r_2 = -0.235 \\ R_3 &= \tan\left(\frac{\theta}{2}\right) \cdot r_3 = -0.291 \end{aligned} \quad (2.26)$$

The attraction of this parameterization is that the three components of the R vector define a vector that lies in a Cartesian coordinate system whose axes can be chosen to correspond to either the specimen or the

crystal axes. Hence, a population of R vectors, each of which represents an orientation or misorientation, can be represented in a 3-D space known as *Rodrigues–Frank (RF) space* or *Rodrigues space*. Since the R vector is derived directly from the angle/axis pair, it can be described by a number of different crystallographically related solutions, with the precise number of solutions depending on the crystal system and symmetry (Section 2.3.3). The R vector is a function of θ , and so it follows that the smallest value of the vector is calculated from the smallest θ . Such R vectors will lie closest to the origin of RF space, and therefore the crystallographically related solution of an orientation or misorientation having the smallest angle (e.g., the first row in Table 2.2) is the most convenient one to select for representation in Rodrigues space.

Use of Rodrigues space is a relatively new field compared with the long-established Euler space approach for representation of rotations (Frank, 1988). The explanation for the late introduction of Rodrigues space is that its application is intimately connected with microtexture, that is, discrete orientation measurements, whereas representation of texture in Euler space relates to the representation of continuous orientation distributions as calculated from pole figures (Sections 2.6 and 5.3). Microtexture data can be, and frequently are, represented in either Euler space or Rodrigues space (Chapter 9), whereas macrotexture data tend to be represented only in Euler space because commercial systems are configured for this approach (Chapter 5).

The geometrical features of Rodrigues space offer considerable benefits for microtexture analysis. Here we will describe the essential features of Rodrigues space, and the methodology of its use in Sections 9.4 and 9.6.3. Mathematical formalisms are kept to a minimum since these are not essential to the understanding and use of Rodrigues space, and moreover details can be found elsewhere (Becker and Pancharadeeswaran, 1989; Neumann, 1991a,b; Randle and Day, 1993; Field, 1995).

2.8.2 The Fundamental Zone

The entirety of Rodrigues space encompasses each one of the crystallographically related solutions of a rotation (Section 2.3.3). Since it is simpler for each orientation from a sample population to be represented only once, it is convenient to formulate the R vector from only one crystallographically related solution. That solution with the lowest rotation angle is chosen because it feeds through to give the smallest R vector. By use of the lowest-angle description, all orientations—represented by the endpoints of their R vectors—can be made to reside in a polyhedron known as the *fundamental zone of Rodrigues space*, which contains the origin of the space. Hence any orientations that lie outside the fundamental zone can be reexpressed by equivalent points lying within it by rechoosing the crystallographically related solution to be the lowest angle one. Exceptionally, an orientation may lie on the

surface of the fundamental zone and will be matched by an equivalent point on the opposite face.

The shape of the fundamental zone is governed by the crystal symmetry of the material, and the geometry of these polygons has been derived for each crystal system (Morawiec and Field, 1996) and for combinations of lattices (Heinz and Neumann, 1991). For cubic symmetry, the shape of the zone is a cube with truncated corners such that the bounding surfaces are six octahedra and eight equilateral triangles as shown in Figure 2.16. The axes XYZ of the fundamental zone are also marked. For the representation of orientations, the XYZ axes are aligned with the specimen axes. Alternatively XYZ can be aligned with the crystal axes, which is convenient for the representation of misorientations.

The distance of the point where the reference axes intercept the zone surface is represented, in terms of crystal coordinates, by the angle/axis pair $45^\circ/\langle 100 \rangle$ that gives $R = (0.4142, 0, 0)$. The R vectors of the centers of the equilateral triangles that form the truncated corners of the zone are given by the angle/axis pair $60^\circ/\langle 111 \rangle$ and a corresponding R vector $(0.333, 0.333, 0.333)$. Another point that defines the shape of the fundamental zone for cubic crystals is an apex of the equilateral triangle, given by $62.8^\circ/\langle 11(\sqrt{2}-1) \rangle$, which represents the greatest possible misorientation between two cubes, and yields an R vector of $(0.4124, 0.4124, 0.1716)$. The shapes of fundamental zones for all crystal systems are described in Table 2.4. It can be seen that the shape of the zone is equivalent to the crystal symmetry. For monoclinic and triclinic symmetries, the fundamental zone corresponds to the entire Rodrigues space, and for this case the space has no boundaries, which is a disadvantage to the representation of orientations having this symmetry. However, most materials of interest from a texture point of view fall into other symmetry categories and can be represented readily in Rodrigues space, for example, trigonal Al_2O_3 (Morawiec and Field, 1996).

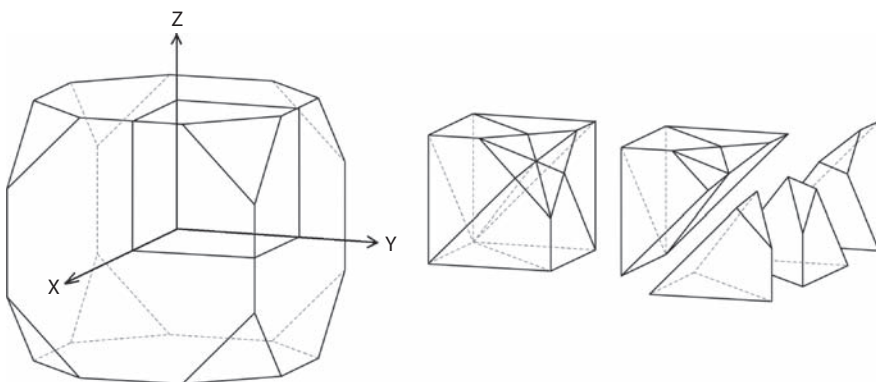


FIGURE 2.16

The fundamental zone of Rodrigues space for cubic symmetry, showing also the decomposition of the space into 48 subvolumes. (Adapted from Day, A., PhD Thesis, University of Bristol, U.K., 1994.)

TABLE 2.4

Parameters of Rodrigues Space According to Crystal System

Crystal System	Distance of the Main Face from the Origin	Description	Subvolume Fraction
Cubic	$\tan \pi/8$	Six octagonal faces normal to the fourfold axes; eight triangular faces normal to the threefold axes	1/48
Hexagonal	$\tan \pi/4$	Two dodecagonal faces normal to the sixfold axis; 12 square faces normal to the diad axes	1/12
Trigonal	$\tan \pi/4$	Two hexagonal faces normal to the threefold axis; six square faces normal to the diad axes	1/6
Tetragonal	$\tan \pi/6$	Eight triangular faces perpendicular to the threefold axes (i.e., a regular octahedron)	1/24
Orthorhombic	$\tan \pi/4$	Six faces normal to the diads (i.e., a square)	1/8
Icosahedral	$\tan \pi/10$	Twelve pentagonal faces normal to the fivefold symmetry axes (i.e., a regular dodecahedron)	1/120

Source: Data from Morawiec, A. and Field, D.P., *Philos. Mag.*, 73A, 1113, 1996.

2.8.3 Properties of Rodrigues Space

The most powerful aspect of Rodrigues parameterization for the representation of orientations and misorientations is that *only rectilinear*, that is, *straight-line geometry* is involved, which renders the space easy to handle and visualize. The rectilinear geometry of Rodrigues space is manifest by the following:

- The axis of rotation gives the direction of the R vector. Hence rotations about the same axis of rotation lie on a straight line that passes through the origin.
- The angle of rotation gives the length of the R vector. Hence small-angle boundaries cluster close to the origin. These first two

points are especially relevant to the analysis of misorientations (Section 9.6.3).

- Orientations that include a common direction, for example, a fiber texture, lie on a straight line that in general does not pass through the origin.
- The edges of zones in Rodrigues space are straight lines, and the faces of zones are planar.

In summary, every straight line in Rodrigues space represents rotations about a certain, fixed axis. These are called *geodesic lines* and remain straight even if the origin of the space is shifted (Frank, 1988; Neumann, 1991a,b). Another advantageous aspect of Rodrigues space is that it is nearly *homochoric*, that is, a distribution of untextured orientations will be distributed almost uniformly throughout the space. The invariant orientation volume is actually within a factor of 2 (Neumann, 1991a,b), which is generally considered low enough for orientation distributions in the space to be evaluated in a straightforward manner.

The fundamental zone can be further divided into identical subvolumes, as shown in Figure 2.16 (Randle, 1990). There are 48 of these for the cubic system, and the subvolume fraction for other crystal systems is shown in Table 2.4. Subvolumes are used for the display of misorientation data.

2.9 Summation

This chapter has established the terminology associated with analysis, representation, and display of orientation and misorientation data. All the descriptors of orientation and their associated spaces that are commonly encountered in the field of texture—the orientation matrix, “ideal orientation”/Miller indices, Euler angles, angle/axis of rotation, and Rodrigues vector plus the misorientation counterparts, where appropriate—have been explained. There is some variation in the popularity and patterns of usage for each descriptor. Briefly, the orientation matrix is the mathematical calculation instrument, and the ideal orientation notation and Euler angles have been traditional descriptors of texture and associated with x-ray diffraction, whereas the angle/axis of rotation and Rodrigues vector have come to the fore much more recently and are used more for misorientations. However, a modern approach to texture can draw upon any of the texture descriptors, and so an introductory knowledge of each is desirable to choose the most convenient descriptor for a particular task.

3

Application of Diffraction to Texture Analysis

3.1 Introduction

The vast majority of techniques for texture analysis are founded on the diffraction of radiation by a crystal lattice, and so it is vital to understand this phenomenon to appreciate the principles on which the various techniques for experimental texture measurement are based. Radiation, which is diffracted by crystallographic lattice planes, is able to provide information on their arrangement and, consequently, on the orientation of the sampled volume of material with respect to some fixed reference axes (Section 2.3). To instigate diffraction of radiation at lattice planes, the wavelength of the incident radiation must be smaller than the lattice spacing, which for materials of interest is typically 10ths of a nanometer. Table 3.1 shows the wavelengths, in addition to other characteristics, of various radiations that are commonly used for texture measurements. Data for light are included only for comparison, since x-rays, neutrons, and electrons are diffracted by lattice planes, whereas light is not.

The various kinds of radiation interact with matter in different ways. This manifests itself by substantial differences in the absorption of radiation by matter and, with regard to texture analysis, by the depth of penetration of radiation into the sample material. To illustrate this, the scale of penetration depths for the various radiations is also given in Table 3.1. Thus, the particular characteristics of radiation have strong impact on the application. This chapter addresses the fundamental aspects of diffraction, the characteristics of various radiations, and the way these relate to the experimental setups for texture measurement. It is pertinent to have some knowledge of subjects such as structure factor (Section 3.3) and characteristics of radiation (Section 3.6) to understand subsequently the principles of texture determination. (For further details, see Bacon, 1975; Cullity, 1978; Thomas and Goringe, 1979; Barrett and Massalski, 1980; Goodhew et al., 2001.)

TABLE 3.1

Average Diffraction Properties of Radiation Used for Texture Measurement by Diffraction

	Light	Neutrons	X-Rays	Electrons
Wavelength (nm)	400–700	0.05–0.3	0.05–0.3	0.001–0.01
Energy (eV)	1	10^{-2}	10^4	10^5
Charge (C)	0	0	0	-1.602×10^{-19}
Rest mass (g)	0	1.67×10^{-24}	0	9.11×10^{-28}
Penetration depth, absorption length (mm)	–	10–100	0.01–0.1	10^{-3}

Note: Light is included for comparison.

3.2 Diffraction of Radiation and Bragg's Law

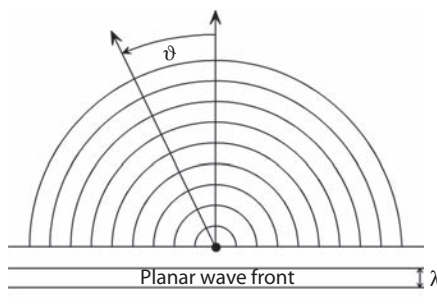
Electromagnetic radiation, like light and x- or γ -rays, is diffracted by elastic scattering of the incident waves at the atoms of the sample material. Particle beams, like electrons and neutrons, can also be considered as waves of radiation, with their wavelength given by the de Broglie relation:

$$\lambda = \frac{h}{mv} \text{ or } \lambda = \frac{h}{\sqrt{2mE_{\text{kin}}}} \quad (3.1)$$

where λ = wavelength, h = Planck's constant, and m , v , and E_{kin} = mass, velocity, and kinetic energy of the particles, respectively.

When a plane wave of radiation hits an atom, this acts as a source for a spherical wave of the same wavelength (Figure 3.1). The efficiency of an atom in scattering radiation is usually described in terms of the atomic scattering amplitude (or scattering length) f . Since the intensity of a wave is the square of its amplitude, f^2 is a measure for the intensity of the scattered wave in dependence on the sort of the atoms, the scattering angle ϑ , the wavelength λ of the incident beam, and the kind of radiation (Doyle and Turner, 1968; Bacon, 1975; Cullity, 1978; Prince, 2004).

X-rays are scattered by the shell electrons of the atoms through an interaction between the charged electrons and the electromagnetic field of the x-rays. Since the size of the atoms is of the same order as typical x-ray wavelengths, different waves that are scattered at the various electrons of the atom interfere, which gives rise to a strong dependency of the scattering amplitude f_x on the atomic radius R and the scattering angle ϑ . Whereas near the incident beam, that is, for small angles ϑ , the individual scattered waves will all nearly be in phase and reinforce each other, for large angles

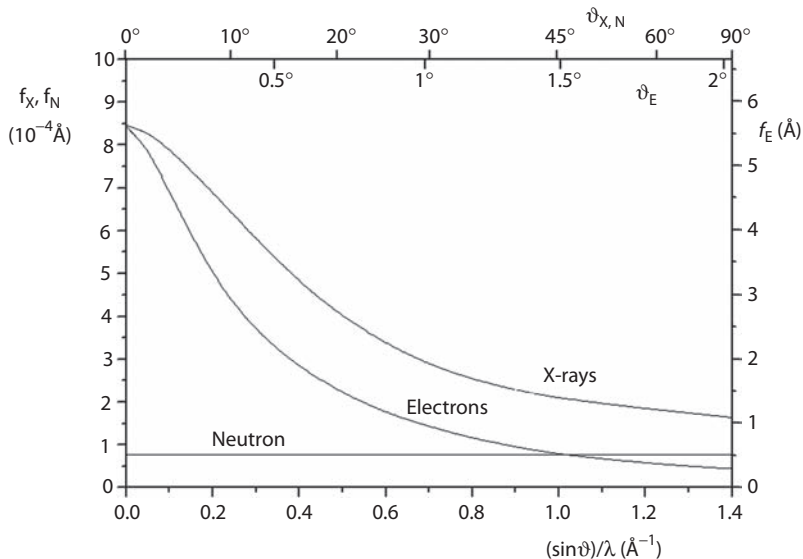
**FIGURE 3.1**

Scattering of a planar wave front at a point source giving rise to the formation of a Huygens spherical wave.

ϑ , they are out of phase and hence reinforce each other much less. Accordingly, f_X strongly decreases with increasing scattering angle ϑ or, more precisely, with an increasing value of $\sin\vartheta/\lambda$, as shown in Figure 3.2. *Electrons* interact with both the shell electrons and the nucleus of the scattering atoms (Section 3.6.3). Their scattering amplitude f_E decreases with $\sin\vartheta/\lambda$ similarly as f_X does, though more rapidly, but the value of f_E is approximately four orders of magnitude greater than f_X (Figure 3.2). Thus, electrons scatter much more intensely than x-rays, and this is the reason why electrons can be used with such a high resolution in electron microscopy. *Neutrons*, in contrast, mainly interact with the nucleus of the atom (except for magnetic materials where magnetic scatter with the shell electrons takes place; Section 3.6.2). As the size of the atomic nucleus is negligible compared to the typical wavelengths in neutron diffraction experiments, the scattering amplitudes for neutrons f_N are virtually independent of the reflection angle ϑ (Figure 3.2).

When radiation interacts with matter, rather than with individual atoms, the individually scattered waves interfere to form a secondary wave (Huygens–Fresnel principle), as shown schematically in Figure 3.3. In most cases, the different waves will be out of phase, which leads to an annihilation of the reflected intensity to zero. Only at specific angles will the wave fronts be in phase, which means that at those angles diffraction of the incoming radiation can be observed. For this to occur, three conditions must be fulfilled:

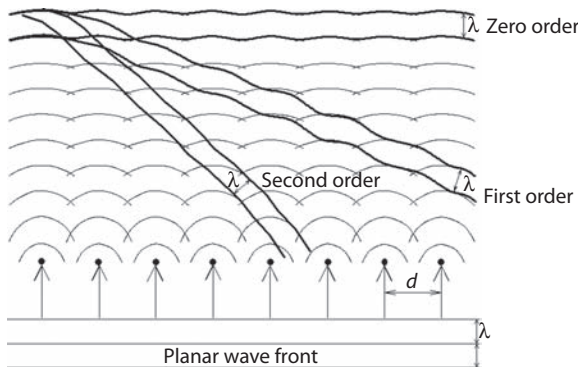
- The atomic arrangement must be ordered, that is, crystalline.
- The radiation must be monochromatic, that is, consist only of one wavelength λ .
- This wavelength must be of the same size order or smaller than the diffracting features.

**FIGURE 3.2**

Angular variation of the atomic scattering amplitude f of copper for x-rays, electrons, and neutrons (note different scales for electrons). The reflection angles of the upper axis were calculated with $\lambda = 0.07107 \text{ nm}$ for x-rays and neutrons, and with $\lambda = 0.00251 \text{ nm}$ for electrons (see Table 3.1). (Data for x-rays and electrons taken from Doyle, P.A. and Turner, P.S., *Acta Crystallogr.*, A24, 390, 1968; data for neutrons taken from Bacon, G.E., *Neutron Diffraction*, Clarendon Press, Oxford, 1975.)

Under these circumstances, independent of the kind of radiation, specific diffraction maxima are observed.

From Figure 3.3 it appears that the angles θ at which diffraction occurs depend on both the wavelength λ and the spacing of the scattering atoms d . To derive this dependency, *diffraction* of radiation at the individual atoms in a crystal can be considered to be *reflection* of radiation at a set of semi-transparent "mirrors," at a distance d . Bragg (1913) showed that these mirrors are formed by atomic planes, that is, the lattice planes $\{hkl\}$, which are considered to be geometrically smooth. Figure 3.4 shows a section through a lattice with three atom layers A, B, and C. Rays are incident on these planes in the direction LM at the angle θ . A small portion of the incident radiation is reflected at the angle 2θ at plane A, whereas the rest continues traveling into the lattice until it is reflected at layers further below. The line L-L₂ is drawn perpendicular to the incident beam to indicate one of the crests of the approaching in-phase waves. To get a reinforced, reflected beam in the direction MN, the waves must again be in phase along the line N_{2A}-N_{2C}. To achieve this, the lengths of path for beams reflected at different, successive layers in the crystal must be equal to an integral number of wavelengths. In the example shown in Figure 3.4 this means that for instance the path difference between the two

**FIGURE 3.3**

Reinforcement of scattered waves producing diffracted beams in the different orders. (Adapted from Barrett, C.S. and Massalski, T.B., *Structure of Metals: Crystallographic Methods, Principles and Data*, McGraw-Hill, New York, 1980.)

reflected beams $L-M-N$ and $L_1-M_1-N_{1B}$ —that is, the distance $P-M_1-Q$ —is either one wavelength λ or a multiple of it— $n\lambda$. It can be seen that

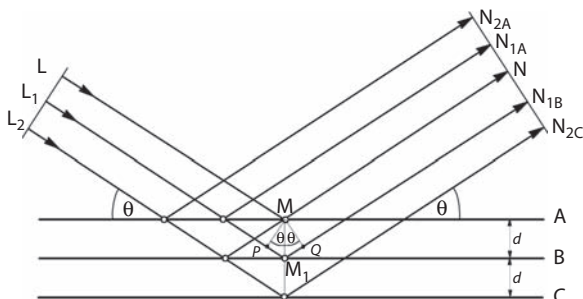
$$PM_1 = M_1Q = d \sin\theta \quad (3.2)$$

It is clear from Figure 3.4 that the other reflected beams bear the same geometrical relationships and, therefore, the condition for reinforcement of all reflected beams can be written as

$$n\lambda = 2d \sin\theta \quad (3.3)$$

where n is the order of reflection and d is the interplanar spacing. This is *Bragg's law* and is usually written as

$$\lambda = 2d \sin\theta_B \quad (3.4)$$

**FIGURE 3.4**

Diffraction from lattice planes, indicating the geometry that leads to the derivation of Bragg's law.

since often only first-order diffraction ($n = 1$) is considered. Accordingly, the specific angles at which reflection is observed are termed *Bragg angles* θ_B . (Laue et al. [1912/1913] derived a similar relation from consideration of scattering at individual atoms.)

Bragg's law is fundamental to texture work since, for radiation of known wavelength, lattice planes can be identified from measurement of the Bragg angles through which the waves are diffracted. Although the phenomenon that occurs is diffraction and not reflection, diffracted beams are frequently referred to as "reflected beams" and the lattice planes as "reflecting planes" or "reflectors." Note that it is convenient to distinguish between the reflecting planes $\{hkl\}$, written with braces, and the corresponding reflected beam hkl , written without braces. Because each set of lattice planes $\{hkl\}$ has a different lattice spacing d , reflections from various sets of lattice planes can be distinguished by setting the detector to the corresponding angle 2θ with respect to the incident radiation. For cubic structures, the lattice spacing d of lattice planes $\{hkl\}$ is related to the material's lattice constant a through

$$d = \frac{a}{\sqrt{h^2 + k^2 + l^2}} \quad (3.5)$$

For noncubic structures, the relations are more complex. For orthorhombic structures, the relationship is

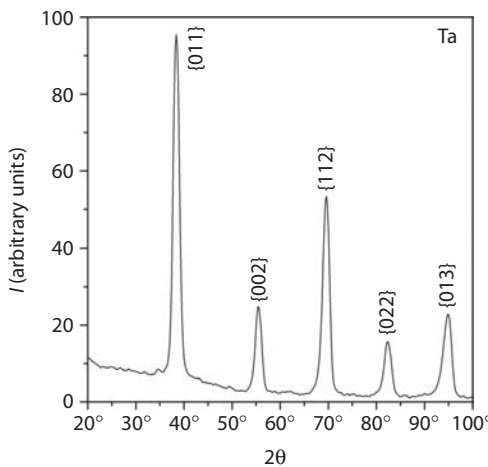
$$\frac{1}{d^2} = \frac{h^2}{a^2} + \frac{k^2}{b^2} + \frac{l^2}{c^2} \quad (3.6)$$

which contains Equation 3.5 as a special case. Finally, for hexagonal close-packed (hcp) crystals, the relationship is

$$\frac{1}{d^2} = \frac{4}{3} \left(\frac{h^2 + hk + k^2}{a^2} \right) + \frac{l^2}{c^2} \quad (3.7)$$

Figure 3.5 shows the diffraction spectrum of a tantalum powder sample with body-centered cubic crystal structure. Such spectra, which are well known from powder diffractometry, can be obtained by recording the reflected intensities as a function of the diffraction angle for gradually increasing angles θ and 2θ . Provided the lattice constant is known, the individual peaks can be indexed with the help of Bragg's law. This can readily be accomplished, for instance, by setting up a table containing all possible reflectors, as in Table 3.2.

However, comparison of the possible reflections in Table 3.2 with the actual diffraction spectrum in Figure 3.5 shows that reflection through the respective Bragg angle is not observed for *all* possible sets of lattice planes. To illustrate this, we consider the reflection at the $\{100\}$ planes in

**FIGURE 3.5**

$\theta/2\theta$ diffraction spectrum of a bcc tantalum powder sample (x-ray CuK α radiation).

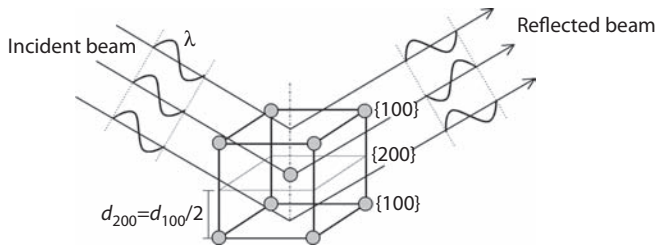
a body-centered crystal, as schematically shown in Figure 3.6. To obtain 100-reflection, the Bragg angle must be set so that the {100} planes are in reflection position, that is, for lattice spacing d_{100} . However, the {200} planes with spacing $d_{200} = d_{100}/2$ are situated exactly halfway between the {100} planes (in Figure 3.4, this would mean we consider reflection at the planes A and C with the plane B in-between). For these intermediate planes, it turns out that the path difference P–M₁–Q in Figure 3.4 is

TABLE 3.2

Bragg Angles θ for Diffraction of Radiation at Different Reflectors hkl in Tantalum

hkl	$h^2 + k^2 + l^2$	2θ
100	1	26.9
110	2	38.5
111	3	47.6
200	4	55.5
210	5	62.8
211	6	69.6
220	8	82.4
221/300	9	88.6
310	10	94.9
311	11	101.1
222	12	107.6

Note: Body-centered cubic: $a = 0.331$ nm, $\lambda = 0.15418$ nm.

**FIGURE 3.6**

Extinction of the 100-reflection by antiphase reflection at the intermediate {200} plane in a body-centered crystal.

exactly $\lambda/2$ (Equations 3.3 and 3.4), rather than an integer multiple of λ as required to reinforce the reflected beam. Hence, reflection at the {100} planes is rendered extinct by the antiphase reflection at the {200} planes in-between. This cancellation will not occur if the crystal is irradiated at the Bragg angle for second-order reflection (i.e., $n = 2$), as then the scattering from both the {100} and {200} planes will be in phase. In general, extinction occurs when there is an equivalent plane halfway between the planes that are in the Bragg position for reflection. For body-centered crystal structures, this is always given when the sum over all Miller indices $h + k + l$ is odd. Vice versa, reflection is obtained from the planes {110}, {200}, {211}, {310}, etc. (Figure 3.5 and Table 3.3).

For face-centered structures, reflection is observed when the individual Miller indices h , k , and l of the reflecting planes are either all odd or all even, that is, {111}, {200}, {220}, {311}, etc. (Table 3.3). For the sake of completeness, the results for base-centered crystals are also included in Table 3.3. In general, the relative intensity of a given reflector and, consequently, the rules of extinction can be deduced from calculation of the *structure factor*, which is shown in Section 3.3.

TABLE 3.3

Geometrical Rules for the Structure Factor F

Crystal Structure	Observed Reflection	Structure Factor F
Primitive	All h, k, l	f (1 atom per unit cell)
Body centered	$(h + k + l)$ even	$2f$ (2 atoms per unit cell)
Base centered	$(h + k)$ even	$2f$ (2 atoms per unit cell)
Face centered	h, k, l all odd or even	$4f$ (4 atoms per unit cell)
Hexagonal close packed	$h + 2k = 3n, l$ even; $h + 2k = 3n \pm 1, l$ odd; $h + 2k = 3n \pm 1, l$ even	$2f$ (e.g., {0002}, {1120}, ...); $\sqrt{3}f$ (e.g., {1011}, {1013}, ...); f (e.g., {1010}, {1012}, ...)

3.3 Structure Factor

Diffraction of radiation at the various atoms in a crystalline structure is governed by the structure factor F , which is the unit cell equivalent of the atomic scattering amplitude f . Each atom j within a given unit cell scatters radiation with an amplitude proportional to f_j for that atom and with a phase difference with regard to the incident beam that is determined by the position (x_j, y_j, z_j) of that atom in the unit cell. The summation over the waves scattered by each of the atoms in the unit cell gives the amplitude of the wave being reflected at the plane $\{hkl\}$, which is called structure factor F :

$$F = \sum_j f_j \exp[2\pi i(hx_j + ky_j + lz_j)] \quad (3.8)$$

(i is the imaginary constant, i.e. $i = \sqrt{-1}$). Since the intensity of a wave is proportional to the square of its amplitude, the intensity of the reflected radiation is proportional to F^2 and, hence, reflection only occurs if the reflected waves are all in phase, that is, if $F \neq 0$.

The differences between the various radiations used for texture analysis, that is, x-rays, neutrons, and electrons, are represented by the atomic scattering amplitude f (Section 3.2), but the geometrical considerations associated with structure factor F hold for all kinds of radiation. In the following text, we will calculate the structure factors for several simple crystal structures and, therewith, derive the rules of extinction introduced in the preceding section. The results are summarized in Table 3.3.

If there is only one atom at the position $(x, y, z) = (0, 0, 0)$ in the unit cell, the structure factor F is independent of $\{hkl\}$ since for all combinations of h , k , and l , $F = f$ holds. Thus, in a crystal with primitive structure, all lattice planes would reflect radiation. For body-centered crystals, we have two atoms, one at $(x_1, y_1, z_1) = (0, 0, 0)$ and the other at $(x_2, y_2, z_2) = (\frac{1}{2}, \frac{1}{2}, \frac{1}{2})$. Substituting these values for (x, y, z) in Equation 3.8, the structure factor F becomes

$$F = f \cdot \left[1 + \exp\left(2\pi i\left(\frac{h}{2} + \frac{k}{2} + \frac{l}{2}\right)\right) \right] \quad (3.9)$$

To derive the rules of extinction, the following relations with complex numbers are helpful:

$$\exp(\pi i) = \exp(3\pi i) = \exp((2n+1)\pi i) = -1$$

$$\exp(2\pi i) = \exp(4\pi i) = \exp(2n\pi i) = +1$$

It is seen that if $(h + k + l)$ is odd, the exponential term in Equation 3.9 becomes -1 , so that $F = 0$. However, if $(h + k + l)$ is even, then $F = 2f$, which

means that in accordance to the qualitative considerations in Section 3.2, reflection in body-centered crystals only occurs at planes for which $(h + k + l)$ is even (Table 3.3 and Figure 3.5).

For face-centered crystals, four atoms have to be considered, with positions $(0,0,0)$, $(\frac{1}{2},\frac{1}{2},0)$, $(\frac{1}{2},0,\frac{1}{2})$, and $(0,\frac{1}{2},\frac{1}{2})$. In this instance, the structure factor F is

$$F = f \cdot [1 + \exp(\pi i(h+k)) + \exp(\pi i(h+l)) + \exp(\pi i(k+l))] \quad (3.10)$$

Considering the possible combinations of h , k , and l , it turns out that if all three are either odd or even, then all of the exponential terms are $\exp(2n\pi i) = 1$. In those cases, the structure factor F equals $4f$ and reflection occurs. In the other possible cases, however, two of the three phase factors will be odd multiples of π , giving two terms of -1 in Equation 3.10 and, therewith, $F=0$ (Table 3.3). Note that these considerations are valid regardless of what structure the body- or face-centered crystal belongs to.

The hcp cell contains two atoms with the coordinates $(0,0,0)$ and $(1/3,2/3,1/2)$. Inserting these values in Equation 3.8, we get:

$$F = f \cdot \left[1 + \exp\left(2\pi i\left(\frac{h}{3} + \frac{2k}{3} + \frac{l}{2}\right)\right) \right] \quad (3.11)$$

Table 3.3 lists the results for F for the possible combinations of h , k , l . It turns out that extinction occurs if $h + 2k$ (or $h - k$) is a multiple of 3 and l is odd. Thus, $\{0002\}$ and $\{1120\}$ reflections occur, whereas $\{0001\}$ and $\{1121\}$ are absent. $\{101l\}$ reflections are obtained for all values of l , although with different structure factors and, in consequence, intensities. As an example, Figure 3.7 shows the diffraction spectrum of the hexagonal metal titanium.

So far, only reflection of radiation in pure metals has been considered, which means that the unit cell only contains atoms of one sort. For unit cells consisting of different species of atoms—intermetallic phases and ordered structures—the scattering factors f_i of the atoms differ, so that the various phase factors do not necessarily cancel out. Thus, there will be only a weakening but no complete extinction of the reflection. For example, in pure nickel the 100-reflection is absent, but it appears, though weak, in the ordered intermetallic compound Ni_3Al (Figure 3.8). The Ni_3Al unit cells have the Al atom on the $(0,0,0)$ sites and the three Ni atoms on the centers of the faces ($\text{L}1_2$ -structure). Hence, the structure factor is given by

$$F = f_{\text{Al}} + f_{\text{Ni}} \cdot [\exp(\pi i(h+k)) + \exp(\pi i(h+l)) + \exp(\pi i(k+l))] \quad (3.12)$$

In analogy to the face-centered lattice, reflection occurs with $F = (f_{\text{Al}} + 3f_{\text{Ni}})$ if h , k , l are all either odd or even. However, for mixed h , k , l , the structure factor is not zero but $F = (f_{\text{Al}} - f_{\text{Ni}})$, so that the missing peaks occur as well, though with weaker intensity (the so-called superlattice peaks; Figure 3.8).

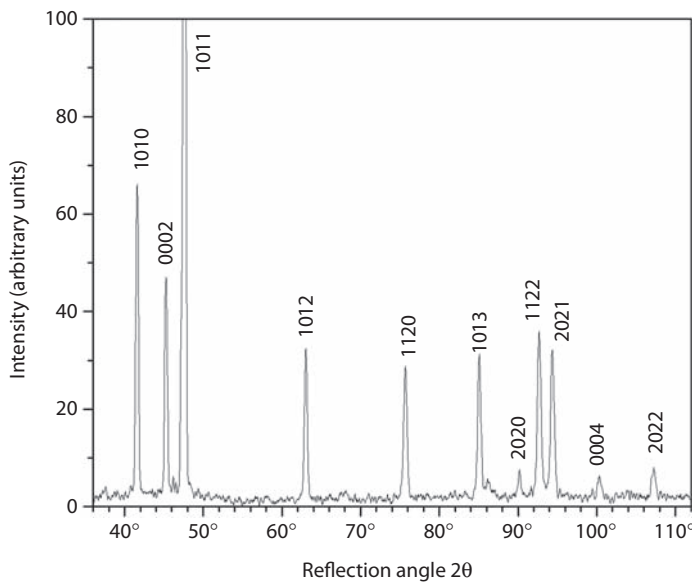


FIGURE 3.7
0/2θ diffraction spectrum of a hexagonal titanium powder sample (x-ray CoK α radiation).

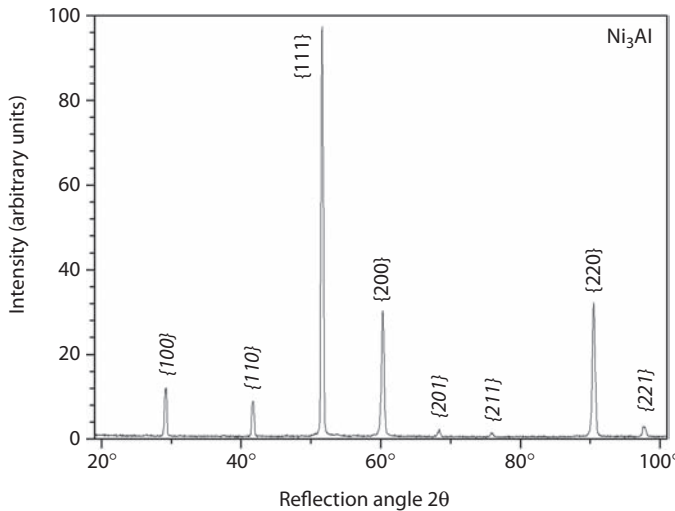


FIGURE 3.8
0/2θ diffraction spectrum of ordered Ni₃Al (L1₂ structure) showing superstructure peaks (x-ray CoK α radiation).

3.4 Laue and Debye–Scherrer Methods

According to Bragg's equation (Equation 3.4), reflection of radiation at a given set of lattice planes {hkl} is observed under a certain angle θ for a given

wavelength λ . In principle, crystallographic orientations can be studied by means of two different approaches:

- At constant θ , the wavelength λ is varied (Laue method).
- At constant λ (i.e., monochromatic radiation), θ is varied; either by rotation of a single crystal (rotating crystal method) or by analyzing a multitude of grains with random texture (powder method).

These two methods go back, respectively, to Laue et al. (1912/1913) and to Debye and Scherrer (1916, 1917), shortly after Röntgen (1896) discovered x-radiation. Accordingly, they are strongly linked to this kind of radiation, though their principles hold for other radiations as well. In fact, in Section 8.3.2 we will introduce an application of the Debye–Scherrer method in electron diffraction, namely, the determination of pole figures from small volumes in the TEM.

Until 1912, both the periodic lattice structure of crystals and the electromagnetic character of the x-radiation were only hypotheses, when Laue et al. (1912/1913) proved both presuppositions in one single experiment. They irradiated crystals of zinc blende and copper sulfate with a finely collimated, polychromatic (i.e., “white”) x-ray beam and recorded the transmitted intensities on a film. Rather than finding homogeneously scattered intensities, they observed a large number of spots that were symmetrically arranged in a characteristic pattern (Figure 3.9), which looked as if the crystal contained an arrangement of “mirrors” at different angles. A few months later, Bragg (1913) showed that these mirrors are formed by the various lattice planes in the crystal, which led to the formulation of Bragg’s law, described in Section 3.2.

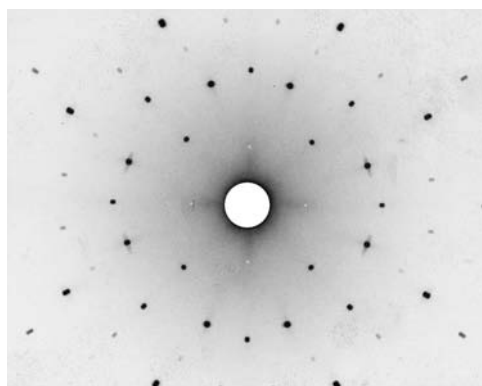
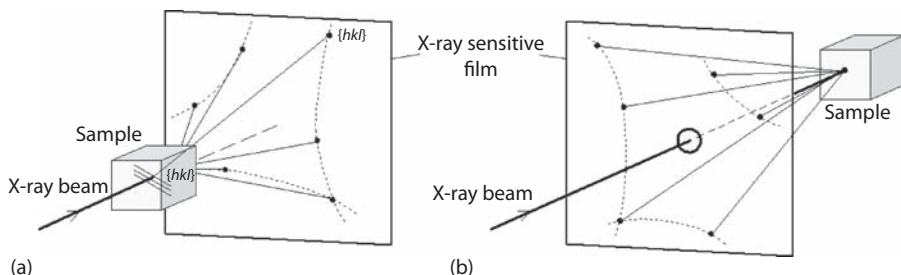


FIGURE 3.9

Laue diagram of a silicon single crystal (reflection technique).

**FIGURE 3.10**

Measurement of individual orientations according to the Laue technique. (a) Transmission technique, (b) reflection technique.

To utilize the Laue method for orientation determination, a finely collimated x-ray beam is focused on the single crystal or the grain of interest in a polycrystalline sample. Because white, that is, polychromatic, x-radiation is used in this method, for each set of lattice planes $\{hkl\}$, there are x-rays that fulfill Bragg's condition for diffraction (Figure 3.10). The diffracted beams result in a point for each set of lattice planes in the Laue diagram (Figure 3.9). Provided the crystal structure is known, the spatial orientation of the corresponding planes and, thus, the crystallographic orientation can be evaluated from the position of the diffraction spots.

Probably the most momentous contribution to modern texture analysis was made by Debye and Scherrer (1917), who observed interference of x-rays in fine-grained polycrystalline powders that were irradiated with monochromatic x-radiation, that is, at constant wavelength λ . In a powder sample typically all possible orientations are present, so that always some crystals will have lattice planes that are oriented at the corresponding Bragg angle with respect to the incident beam (whereas in the Laue method, the lattice planes "select" the proper wavelength out of the white x-radiation). The diffracted intensities lie on a cone with half apex angle 2θ about the direction of the incident beam. To produce a Debye–Scherrer pattern, the sample is placed in the center of a cylindrical camera and the diffraction cones are recorded on an x-ray sensitive film situated at the inner wall of the camera (Figure 3.11), where the cones form segments of circles with the radius 2θ that through Bragg's law is related to the lattice spacing d .

Powder samples having a random orientation distribution produce patterns with homogeneous Debye–Scherrer rings, as the number of reflecting planes is equal in all spatial directions. By contrast, in samples with a preferred orientation distribution, the number of reflecting planes varies in different directions. Hence, the intensity distribution along the Debye–Scherrer rings becomes inhomogeneous, and in heavily textured samples, some parts of the rings may even be completely missing (examples of

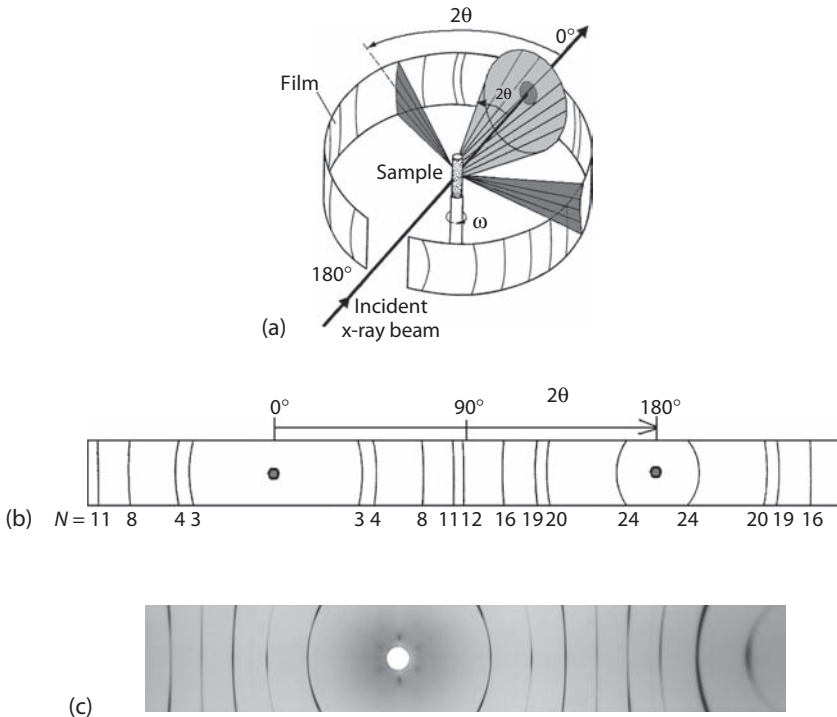


FIGURE 3.11

(a) Debye-Scherrer technique to determine the crystal structure and texture of a polycrystalline sample. Diffraction cones from two lattice planes are shown intersecting the film. (b) Schematic diffraction pattern of an fcc crystal on an unrolled film. (c) An example of a Debye-Scherrer diagram of bcc tungsten. (Courtesy of J. Ihringer.)

such Debye-Scherrer diffraction patterns are shown in Figures 4.16b and 12.2b and, for electron diffraction, in Figures 8.4b and 8.4c). Wever (1924) utilized this fact to generate the first pole figures of heavily cold-rolled aluminum, before pole figure goniometers and Geiger counters were introduced in the 1940s to enable quantitative texture analysis. This is discussed in Chapter 4.

3.5 Absorption and Depth of Penetration

In Section 3.2 we saw that the various kinds of radiation—x-rays, neutrons, and electrons—interact with atoms in different ways. With regard to texture analysis of large crystalline arrangements, these interactions manifest themselves as substantial differences in the absorption of radiation by matter

(Table 3.1). On transmission of radiation through a sample with thickness t , the incident intensity I_0 is attenuated according to

$$I = I_0 \exp(-\mu t) \quad (3.13)$$

Here, μ is the linear absorption coefficient (commonly given in cm^{-1}) that depends on the radiation and the investigated material as well as the wavelength of the radiation. Often, the absorption coefficient is related to the specific weight ρ , which yields the mass absorption coefficient μ/ρ ($\text{cm}^2 \text{ g}^{-1}$). Table 3.4 gives data of μ/ρ for x-rays with different wavelengths as well as for neutrons in various pure metals. For alloys, μ/ρ can be calculated by a summation over the absorption coefficients $(\mu/\rho)_i$ of the individual components i with the weight fractions w_i :

$$\frac{\mu}{\rho} = \sum_i w_i \cdot \left(\frac{\mu}{\rho} \right)_i \quad (3.14)$$

TABLE 3.4

Mass Absorption Coefficients (μ/ρ) for X-Rays and Neutrons for Different Wavelengths

Material (Atomic Number, Z)	X-Ray			Neutrons
	$\lambda = 0.07107 \text{ nm}$ (MoK α)	$\lambda = 0.15418 \text{ nm}$ (CuK α)	$\lambda = 0.17902 \text{ nm}$ (CoK α)	$\lambda = 0.108 \text{ nm}$
Be (4)	0.3	1.5	2.3	0.0003
Mg (12)	4.1	38.6	59.5	0.001
Al (13)	5.16	48.6	74.8	0.003
Ti (22)	24.2	208	308	0.044
Mn (25)	34.7	285	414	0.083
Fe (26)	38.5	308	52.8	0.015
Co (27)	42.5	313	61.1	0.21
Ni (28)	46.6	45.7	70.5	0.028
Cu (29)	50.9	52.9	81.6	0.021
Zn (30)	55.4	60.3	93.0	0.0055
Mo (42)	18.4	162	243	0.009
Ag (47)	25.8	218	321	0.2
Cd (48)	27.5	231	338	14
W (74)	99.1	172	253	0.035
Au (79)	115	208	302	0.17
Pb (82)	120	232	334	0.0003

Note: Examples of absorption edges are italic. (Section 3.6.1).

Source: X-rays—Data for x-rays taken from Barrett, C.S. and Massalski, T.B., *Structure of Metals: Crystallographic Methods, Principles and Data*, McGraw-Hill, New York, NY, 1980; data for neutrons taken from Bacon, G.E., in *Neutron Diffraction* (3rd edition), Clarendon Press, Oxford, 1975.

The mass absorption coefficients for x-rays are typically of the order of $100 \text{ cm}^2 \text{ g}^{-1}$ (Table 3.4), so that it readily follows from Equation 3.13 that x-rays are heavily absorbed by matter. For example, the intensity of x-radiation with wavelength 0.17902 nm (CoK α) that passes through a 10 μm thick zinc foil ($\rho = 7.13 \text{ g cm}^{-3}$) is reduced to approximately 50% of its initial intensity, whereas a 100 μm sheet would almost completely absorb the x-rays ($I/I_0 < 1\%$). Thus, the depth of penetration of x-ray in matter is limited to layers of 10–100 μm , which has a strong impact on the design of techniques for texture determination by means of x-rays (Chapter 4). Neutrons are much less absorbed by matter, and with a few exceptions, the mass absorption coefficients are of the order of $0.01 \text{ cm}^2 \text{ g}^{-1}$ (Table 3.4). Thus, to attenuate neutron radiation to 50% of its initial intensity as in the earlier example, a zinc sample with a thickness of 17 cm is necessary, which means that the penetration depth of neutrons is larger by approximately four orders of magnitude than that of x-rays. Electrons, however, are much more strongly absorbed than x-rays. Here, mass absorption coefficients of $10^4 \text{ cm}^2 \text{ g}^{-1}$ are obtained, so that the penetration of electrons is limited to values as low as 1 μm (Table 3.1).

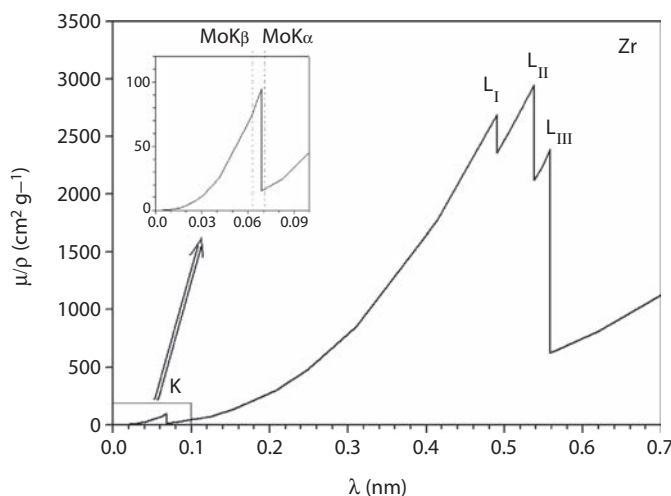
3.6 Characteristics of Radiations Used for Texture Analysis

3.6.1 X-Rays

X-ray diffraction is the most established technique for texture measurement, and reveals the integral macrotexture of a volume of material from a flat specimen by measuring the intensities of diffraction maxima. X-radiation suited for diffraction experiments is commonly produced with x-ray tubes (Section 4.3.1) or, for special applications, obtained from a synchrotron source (Section 12.2). As discussed in detail in Sections 4.2 and 4.3, application of x-ray diffraction to measure macrotextures in a material of known lattice parameter involves the use of a monochromatic beam of radiation of a given wavelength with the Bragg angle fixed for a chosen set of lattice planes $\{hkl\}$. If a polycrystal of this material is rotated in space, then when grains in the sampled volume become oriented such that their $\{hkl\}$ planes coincide with the Bragg condition for their interplanar spacing, a diffracted intensity is measured. The direct output from an x-ray texture goniometer is a chart showing the diffracted intensity with respect to the rotation angles of the specimen, which can be represented in a pole figure (Sections 4.2 and 5.2) or used for calculation of the 3-D ODF (Section 5.3).

In Section 3.5, we noted that the high absorption of x-rays in matter is a very important aspect of texture analysis using x-ray radiation, as it limits the penetration depth to approximately 100 μm and, as discussed in Chapter 4, it also influences the choice of an appropriate x-ray tube.

The mass absorption coefficients of most metals are in the range 10–350 $\text{cm}^2 \text{g}^{-1}$ (Table 3.4). Beryllium has a notably lower absorption of approximately 1 $\text{cm}^2 \text{g}^{-1}$, and is therefore used as window in x-ray tubes and detectors. It is seen in Table 3.4 that the absorption in general increases with increasing atomic number Z of the analyzed sample material and the wavelength λ of the used radiation. For a given wavelength, however, there are steep drops in absorption by up to one order of magnitude between certain elements; some examples are italicized in Table 3.4. These *absorption edges* are caused by the efficiency of the x-rays in emitting photoelectrons from the electron shells of the sample material. For a given material, if the wavelength of the radiation is too long (i.e., the energy is too low) to eject photoelectrons, the radiation will pass through the material accompanied by quite low absorption. Waves with shorter wavelengths may have sufficient energy to eject an electron from one of the shells of the absorbing atom, however. The absorbed energy released by the recombination of the electron hole is emitted as *fluorescence*, which leads to a much higher absorption of such radiation. Accordingly, ejection of an electron from the K-shell results in K-excitation, and the discontinuity in absorption is called the K-absorption edge. As an example, the K- and L-absorption edges in zirconium are shown in Figure 3.12. This effect is utilized to produce (quasi) monochromatic radiation by eliminating $\text{K}\beta$ -radiation from the x-ray spectrum by appropriate filters (Section 4.3.1). For texture analysis high absorption is undesirable, however, and hence the corresponding combinations of x-radiation and sample material should be avoided.

**FIGURE 3.12**

Variation of the mass absorption coefficient μ/ρ with wavelength λ in zirconium, showing the K- and L-absorption edges. The inlay shows the K_{Zr} absorption edge used to produce (quasi) monochromatic $\text{MoK}\alpha$ radiation for x-ray diffraction experiments (see Section 4.3.1).

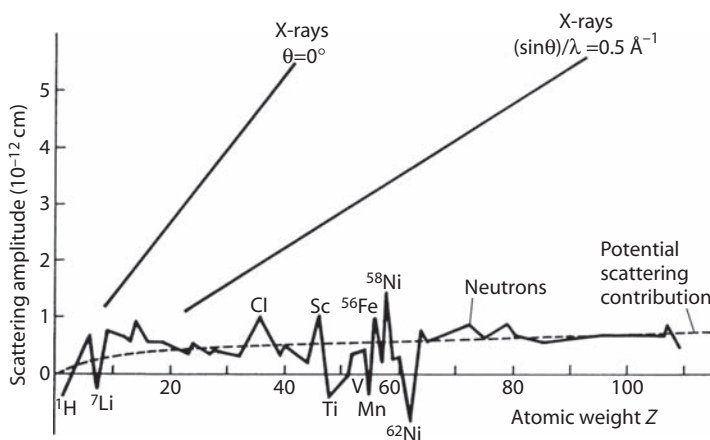
3.6.2 Neutrons

Neutron diffraction is used to obtain an average macrotexture in a manner very similar to that for x-rays (Section 4.4). However, the low availability of the specialized facility required (mostly a beam line on a nuclear reactor) means that neutrons are only used for texture work where they can offer specific advantages over x-rays. Such situations are as follows:

- Where the greater depth of penetration is an advantage, for example, irregularly shaped or large-grained specimens and small volume fractions of second phases or porous materials
- Where the speed of measurement related to the greater volume is an advantage, for example, for dynamic studies of texture development
- Where low crystal symmetry or multiphase systems is present
- Where the sample must not be prepared for x-ray texture analysis, that is, nondestructive texture analysis

The elastic scattering of thermal neutrons by crystalline matter consists of two contributions, nuclear and magnetic scattering. *Nuclear scattering* is caused by the interaction between the neutrons and the atomic nuclei. These interactions lead to diffraction effects akin to the diffraction of x-rays and are utilized for analysis of the crystallographic texture. However, there are some characteristic differences between x-ray and neutron diffraction, which warrant mentioning at this stage. Since neutrons are mainly scattered at the atomic nucleus, interaction is much weaker than the interaction of x-rays at the shell electrons, leading to a much lower absorption and much higher penetration depth (Section 3.5). Furthermore, for x-rays the scattering amplitude f_x increases proportionally with the atomic number Z (Figure 3.13). However for neutrons, no such simple dependency exists, but the nuclear scattering consists of the potential scattering (scattering of a planar wave at a rigid sphere), which increases with $Z^{1/3}$, and the resonance scattering, which yields an irregular dependence on Z (Figure 3.13). Because of the resonance scattering, different isotopes of the same elements may have different scattering amplitudes and can consequently be separated with neutron diffraction. Moreover, signals from light elements are similar in magnitude to those from heavy ones, so that they can also be detected by neutron diffraction.

The scattering amplitude of x-rays strongly depends on the diffraction angle θ , whereas that of neutrons is virtually independent of θ (Figure 3.2), though the overall intensity still decreases somewhat with θ because of thermal vibration and other effects. Therefore, peaks at higher diffraction angles can be evaluated better by neutron diffraction. Furthermore, most neutron diffraction instruments provide better spectral resolution than x-rays, which is advantageous for deconvoluting complex diffraction patterns

**FIGURE 3.13**

Variation of the neutron scattering amplitude with atomic number Z due to the superposition of resonance scattering and potential scattering. The regular increase in x-rays is shown for comparison. (Data taken from Bacon, G.E., *Neutron Diffraction*, Clarendon Press, Oxford, 1975.)

with overlapping peaks, such as in multiphase systems or low-symmetry materials (Section 4.5).

Magnetic scattering results from the classical dipole–dipole interaction of the magnetic momentum of the neutrons with the electrons of the atomic shell when these have a resulting magnetic momentum (Bacon, 1975; Szpunar, 1984; Bunge, 1989b). In general, the intensity of the magnetic scattering is much weaker than that of the nuclear scattering and can be neglected for texture analysis. However, in some magnetic materials—Fe and Mn—magnetic scattering can give rise to peaks in the diffraction pattern, which can be exploited to derive magnetic pole figures, that is, the distribution of the magnetic dipoles in the sample. However, the magnetic contribution to diffracted neutrons is always superimposed by the contribution of the nuclear scattering, that is, the crystallographic texture, which means that the magnetic pole figures have to be separated from the crystallographic pole figures (Mücklich et al., 1984; Zink et al., 1994; Birsan et al., 1996).

3.6.3 Electrons

Electron diffraction is employed in a fundamentally different way to x-rays or neutrons for studying texture. This is a consequence of first the fact that electrons are the only radiation listed in Table 3.1 to carry a charge, and second their penetration depth and interaction volume is small enough to allow diffraction from *individual* grains rather than volumes containing many grains as for x-ray/neutron diffraction. The charge on electrons allows them to be deflected by magnetic lenses and scanned in a raster, and therefore to be used to produce highly magnified images in TEM and SEM, respectively.

This means that diffraction information from discrete sample volumes that are submicron in size can be obtained concurrently with images of the same region. Hence, electron diffraction is used to obtain the orientations of individual grains, that is, microtexture, rather than the macrotextures as obtained by x-ray/neutron diffraction experiments.

The wavelength λ of the electron radiation is controlled by the accelerating voltage U of the electron microscope; it can be computed from the de Broglie relation (Equation 3.1) considering the relativistic mass increase of the electrons:

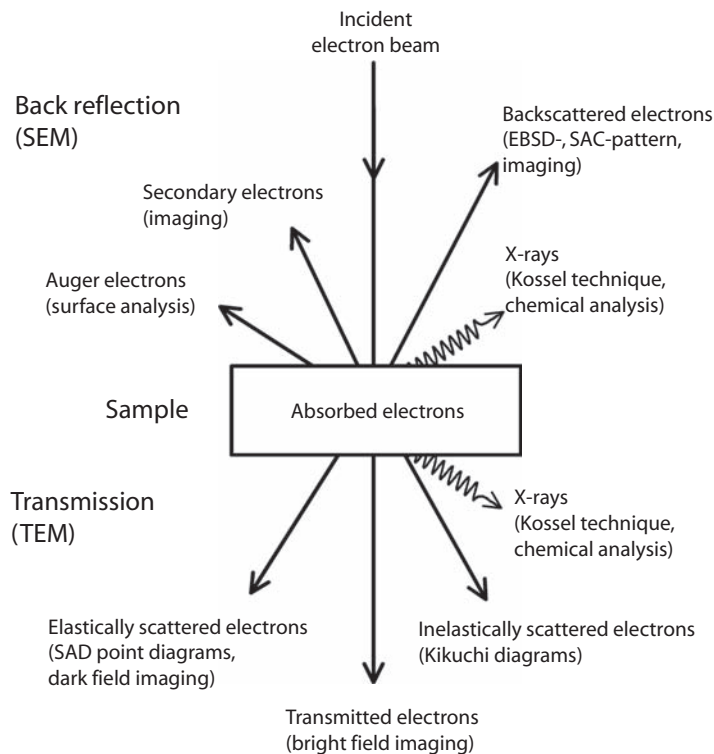
$$\lambda = \frac{h}{\sqrt{2meU}} = \frac{h}{\sqrt{2m_0eU(1 + eU/(2m_0c^2))}} \quad (3.15)$$

where h = Planck's constant, e = charge on an electron, m = electron mass, m_0 = electron rest mass, and c = velocity of light.

For typical accelerating voltages of $U = 20$ kV in an SEM and $U = 200$ kV in a TEM, the wavelengths are $\lambda = 0.00859$ nm and $\lambda = 0.00251$ nm, respectively (Table 3.1). Because of these small wavelengths—and the strong dependence of the diffracted intensity on the scattering angle (Section 3.2; Figure 3.2)—the Bragg angles θ_B for reflection of electrons (Equation 3.4) are typically very small. Even in the case of high-index planes, the angles reach only approximately 2° . This means that the reflecting lattice planes are always situated approximately parallel to the primary electron beam.

When the electron beam in an electron microscope is directed onto a metallic sample, different scattering events and interactions with the sample material give rise to a variety of different electron and x-ray signals (Figure 3.14). These signals are used to produce the images in electron microscopes; they also provide information on the chemical composition and, with regard to the subject of this book, on the crystallography and crystallographic orientation of the sampled volume. Part of the primary electron signal is scattered elastically without losing energy. Elastically backscattered electrons are used for imaging purposes, as their intensity yields information on the atomic number Z (Z -contrast) of the sample material and thus on the chemical composition of the sampled region, for example, of particles. In transmission, coherent elastic scatter of electrons at crystalline objects gives rise to selected area diffraction (SAD) patterns that can be used for orientation determination (Section 8.3).

Electrons that are inelastically scattered at the atomic shell are subject to energy loss and absorption or they induce emission of secondary electrons, Auger electrons, or x-rays. Secondary electrons with an energy less than 50 eV come from a depth of only a few nanometers and are consequently very well suited for imaging of the sample topography in an SEM with high spatial resolution. Auger electrons with energies up to 2 keV are formed in the furthest

**FIGURE 3.14**

Summary of the various signals obtained by interaction of electrons with matter in an electron microscope.

surface layers ($\sim 1 \text{ nm}$). As their energy depends on the emitting element, they can be used for surface analysis. X-rays are typically used for chemical analysis, but they also yield information on the crystallographic orientation since they can be diffracted at the crystal lattice to give Kossel diffraction (Section 7.2). Multiple scatter of electrons in somewhat thicker sample regions gives rise to Kikuchi diagrams, which are very well suited for orientation determination in the TEM, as discussed in Section 8.4. In the SEM, similar diagrams can be produced by SAC (Section 7.3) and EBSD (Sections 7.4 through 7.8).

3.7 Summation

Most techniques for texture analysis rely on diffraction and Bragg's law. Since the angle between the incident and diffracted beam cannot exceed 90° , it essentially follows from Bragg's law that the wavelength λ of the incident

radiation must be of the same or smaller size order as the lattice spacing d or, more precisely, $\lambda \leq 2d$ (Equation 3.4). Comparing the wavelengths of different radiations given in Table 3.1, it is clear that x-rays, neutrons, and electrons are diffracted by lattice planes, whereas light is not.

Besides categorization of the techniques for texture determination with respect to the type of radiation used as a probe—x-rays, neutrons, or electrons—the techniques can also be classified on the basis of whether it is a macrotexture (averaged orientation data from many grains; Section 1.1) or a microtexture (single orientations; Section 1.2) method. Figure 3.15 shows all the mainstream techniques for texture measurement by diffraction. A few peripheral techniques such as acoustic, ultrasonic, magnetic, or optical methods also exist, some of which are described in Chapter 12. With regard to the usage of the techniques featured in Figure 3.15, x-ray goniometry and EBSD are by far the most popular choices for macrotexture and microtexture analysis, respectively. All the techniques in Figure 3.15 are discussed in this book, with the extent of the coverage depending on the relevance to modern texture analysis. The choice of method(s) used to obtain orientation information will depend ultimately on factors such as the scale and resolution of the inquiry, the nature of the information sought, and the equipment available.

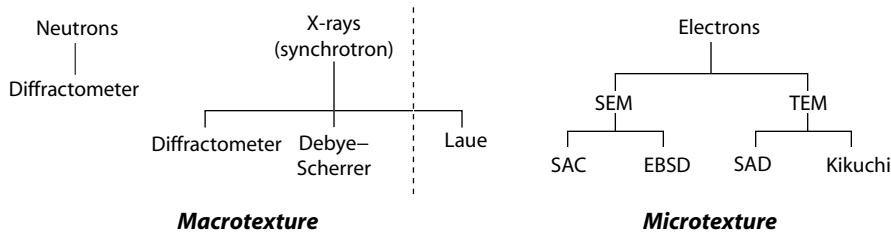


FIGURE 3.15

Categorization of the mainstream techniques for texture determination according to the radiation used as a probe. Macrotexture and microtexture methods are on the left- and right-hand parts of the diagram, respectively.

Part II

Macrotecture Analysis

4

Macrotexture Measurements

4.1 Introduction

This chapter introduces the common techniques to derive the distribution of crystallographic orientations present in a crystalline sample (its *macrotexture*) by means of x-ray and neutron diffraction. As mentioned in Section 3.4, x-ray diffraction was first employed in 1924 by Wever to investigate preferred orientations in metals by evaluating the inhomogeneous intensity distribution along the Debye–Scherrer rings. With the introduction of texture goniometer and the use of Geiger counters by Decker et al. (1948) and Norton (1948), pole figures could directly be recorded, and in particular the fundamental work by Schulz (1949a,b) initiated modern quantitative x-ray texture analysis. The principles of pole figure analysis by diffraction methods and the techniques and procedures to obtain quantitative texture data by means of x-ray diffraction are described in Sections 4.2 and 4.3. Since the 1960s, neutron diffraction has also been employed regularly to determine crystallographic textures, and the corresponding methods are discussed in Section 4.4.

The principles of texture analysis by x-ray or neutron diffraction apply for all materials, independent of their crystal structure. However, when investigating materials with low crystal symmetry or multiphase systems, some specific additional problems arise, which are addressed in Section 4.5.

4.2 Principle of Pole Figure Measurement

The principle of pole figure measurement by means of diffraction techniques is based on Bragg's law for reflection of radiation, x-rays, or neutrons, at the crystal lattice planes (Equation 3.4). Chapter 3 discusses the diffraction of monochromatic radiation at the lattice planes in a nontextured polycrystalline material. Now we will focus on the use of diffraction to determine the orientation of an individual crystal. To derive the crystallographic orientation

of a given crystallite, the arrangement, with respect to an external reference frame, of a set of lattice planes (hkl) has to be determined. As each set of lattice planes has a different lattice spacing d , reflections from various sets of lattice planes can be distinguished by setting the detector to the corresponding angle 2θ with respect to the incident radiation (Section 3.2). First, we consider reflection at a single crystallite as schematically shown in Figure 4.1. The crystal is irradiated with monochromatic radiation at the proper Bragg angle for reflection at the lattice planes (hkl), and the detector is set at the angle 2θ with respect to the primary beam. Of course, a reflected intensity is only measured if the corresponding lattice planes are arranged such that they lie parallel to the sample surface, that is, their normal is the bisector of the angle between the incident and reflected beams, as shown in Figure 4.1a, which means that in most cases *no* reflection is obtained (Figure 4.1b). To ensure reflection, the sample has to be rotated or tilted until the lattice planes are in reflection condition, that is, parallel to the sample surface (Figure 4.1c). The necessary rotation and tilt angles are a measure for the arrangement of the lattice planes within the crystal, which means they are characteristic of the orientation of the crystal with respect to the external sample frame. For example, when we irradiate a Goss-oriented crystal— $\{110\}<001>$ (“cube-on-edge”; see Figure 2.7)—at the Bragg angle for reflection from the (200) planes, reflected intensities will be obtained for a sample tilt of 35° plus an additional rotation by either 90° or 270° (Figure 4.1d). A third peak would be expected at a sample tilt of 90° , but in that case the incident beam is parallel to the sample surface so that no reflection can occur (Section 4.3.2).

To determine an unknown crystal orientation in practical applications, the sample is systematically rotated in a texture goniometer about well-defined angles in such a way that all possible lattice planes are successively brought into the reflection condition and the reflected intensities are recorded as a function of these rotation angles. As we will see later, the rotation angles are directly related to the pole figure angles α (radial) and β (azimuthal), so that the reflected intensities can readily be represented in a pole figure (Section 2.5.1).

For polycrystalline samples, which are composed of an array of single crystallites, the intensity recorded at a certain sample orientation is directly proportional to the number of crystallites—more precisely, to the volume fraction of crystallites—which currently is in a reflection condition (this statement is qualified later in this section). Thus, the pole figure of a polycrystalline sample reflects the distribution of orientations in that sample, that is, its crystallographic texture. As an example, Figure 4.2 shows the $\{111\}$ pole figure of aluminum, after rolling to 97% thickness reduction, plotted in the stereographic projection together with the definition of the pole figure angles α and β (Section 2.5.1).

Two different geometrical setups of texture goniometers are conceivable: transmission and reflection geometry. Determination of texture can be performed on thin samples that are penetrated by the neutrons or x-rays; this

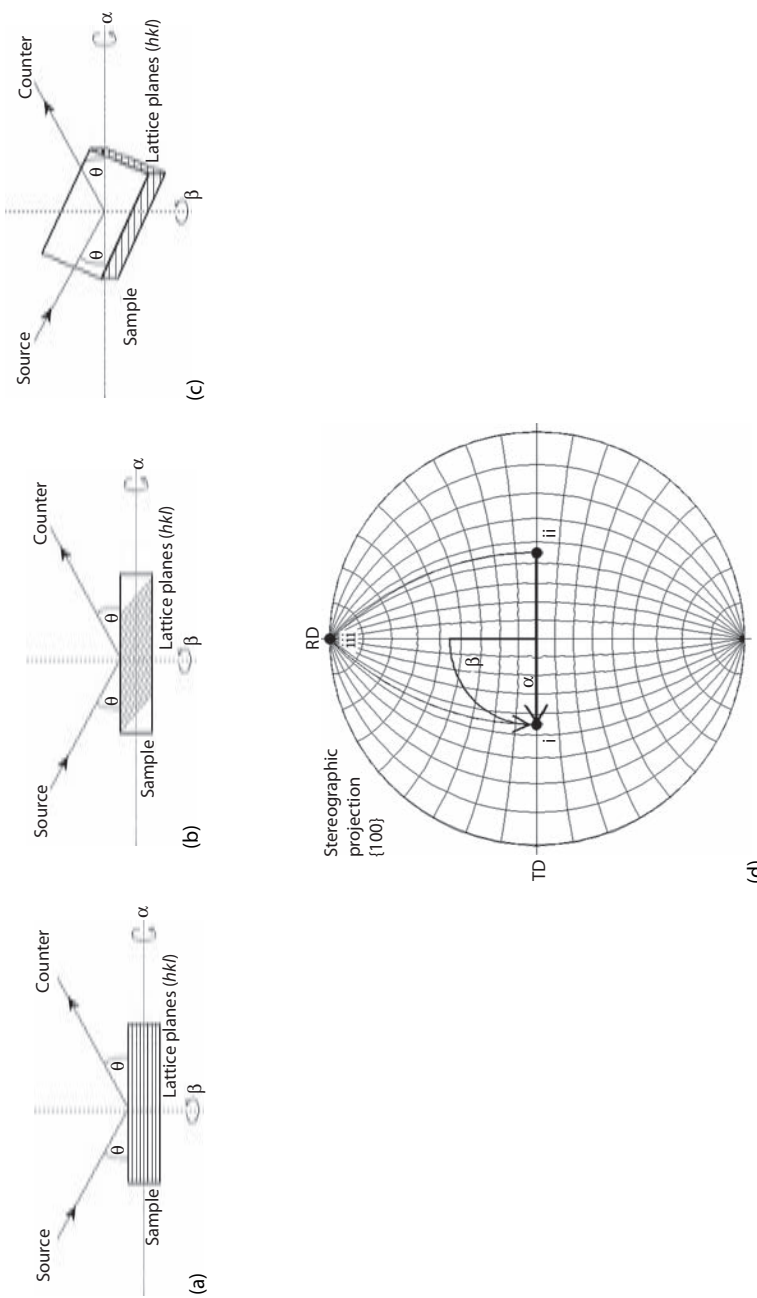
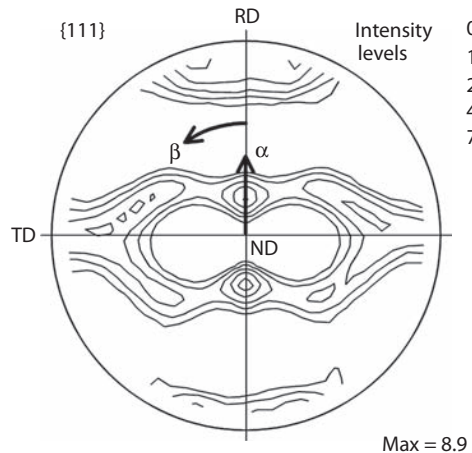
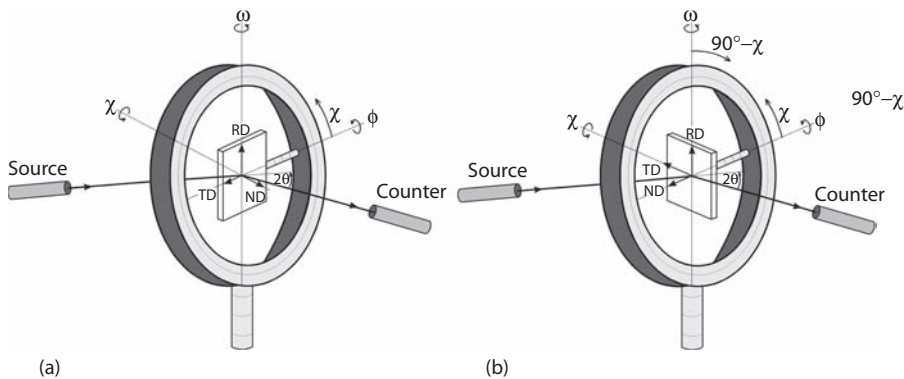


FIGURE 4.1
Sketch to illustrate the effect of sample rotation on the arrangement of the lattice planes and the resulting reflection conditions in a texture goniometer.

**FIGURE 4.2**

{111} Pole figure of 97% cold-rolled aluminum with the definition of the pole figure angles α and β . The orientation densities are given by iso-intensity lines in multiples of a random orientation distribution.

transmission geometry is shown in Figure 4.3a (Decker et al., 1948; Schulz, 1949b). Note that in Figure 4.3 we use a nomenclature for the rotation axes that is different from that in Figures 4.1 and 4.2. The nomenclature with the axes θ , ϕ , χ , and ω is standard in single-crystal diffractometry and marked on most diffractometers. Section 4.3.2 describes how these angles are related to the pole figure angles α and β . As discussed in Section 3.5, neutrons are readily able to transmit samples of several centimeters' thickness, and therefore texture analysis by neutron diffraction is generally performed in transmission geometry. X-rays, in contrast, are strongly absorbed by matter, and

**FIGURE 4.3**

Diffraction in four-circle texture goniometers with definition of the instrument angles. (a) Transmission geometry; (b) reflection geometry.

so the transmission method is generally restricted to materials with low absorption (e.g., magnesium or aluminum) and to extremely thin samples with thicknesses below approximately 100 μm . However, with a sufficiently strong x-ray source, which has been utilized for online texture control of steel sheets in industrial applications (Kopinek, 1994), sheets with thicknesses up to several millimeters can be penetrated by x-rays. Besides such exceptions, however, x-ray texture analysis is mostly performed on thick bulk samples with a plane surface in *reflection geometry*, as shown in Figures 4.1 and 4.3b (Schulz, 1949a).

In the preceding discussion of the principle of pole figure measurements, it was stated that the intensity recorded at a certain sample position is proportional to the volume fraction of crystallites in a reflection condition. This statement is oversimplified, however, and needs three supplements:

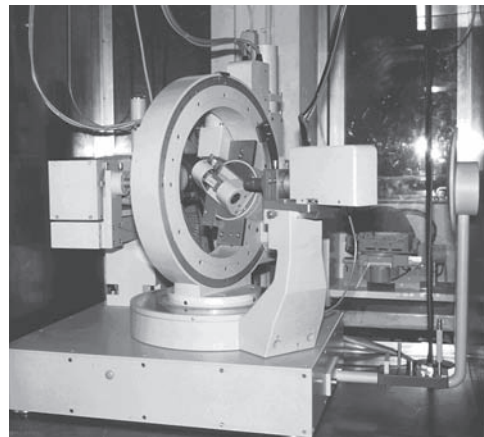
- The pole figure data need several corrections, which are described in Section 4.3.6.
- The positions of at least two poles are required (Section 2.5.1) to characterize unambiguously a given orientation in a pole figure. In turn, this means that a pole figure does not provide the complete *orientation* distribution but only the distribution of the *poles*.
- The reflections hkl and $\bar{h} \bar{k} \bar{l}$ from the opposite sides of a given lattice plane have equal intensities. This is caused by the fact that the diffraction averages over the volume, and it is irrelevant whether the beam impinges a lattice plane from the front or the back side, which is known as Friedel's law (Friedel, 1913). Therefore, pole figures measured with diffraction techniques are always centrosymmetric, that is, the symmetry contains an inversion center, even if the crystals are noncentric (Section 2.2). As we will see later, this also causes the "ghost error" during computation of the ODFs from pole figure data (Section 5.3.2).

4.3 X-Ray Diffraction Methods

A complete x-ray texture goniometer system is composed of the following main units:

- X-ray generator and x-ray tube
- Goniometer with a sample stage
- Detection system

Electronics and computer controls to control the rotations and read the recorded intensities are also required. Figure 4.4 shows a photograph of the setup that has been developed at the Institut für Metallkunde und Metallphysik,

**FIGURE 4.4**

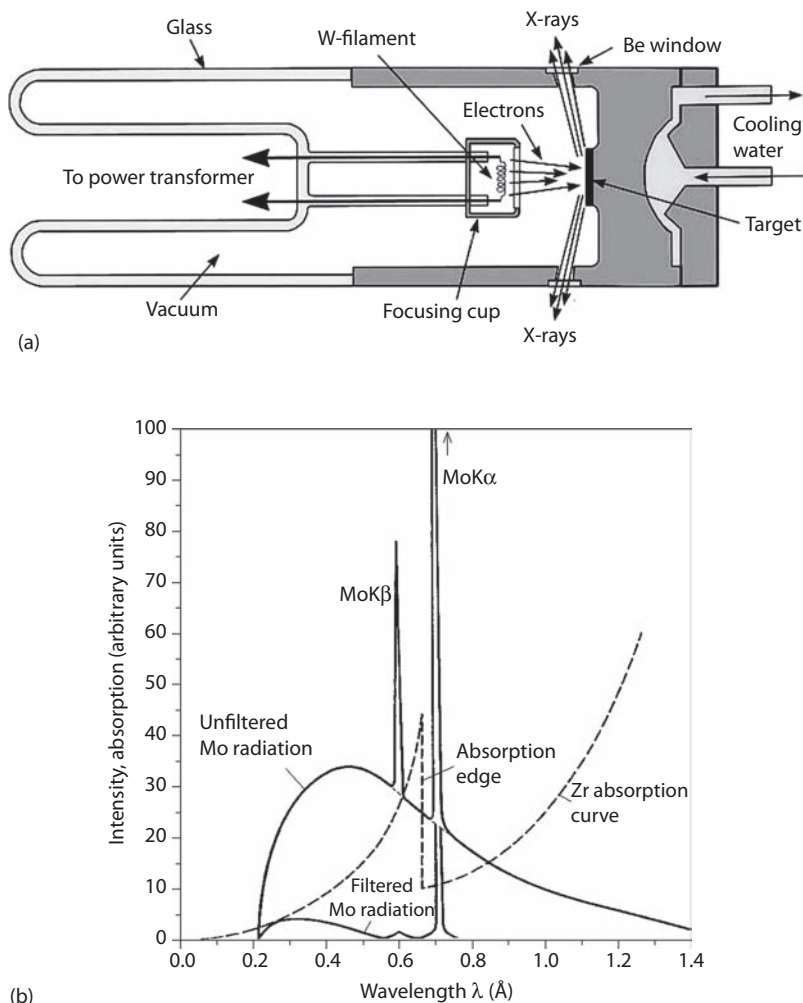
Texture goniometer at the Institut für Metallkunde und Metallphysik, RWTH Aachen.

RWTH Aachen (Hirsch et al., 1986). Nowadays, fully functional texture systems are commercially available from several vendors. Sections 4.3.1 through 4.3.7 address the various units. As already mentioned, x-ray pole figure measurements are mostly performed in reflection geometry today. Accordingly, we will mainly focus on reflection geometry, and transmission geometry is only occasionally addressed for completeness.

4.3.1 Generation of X-Rays

In most texture applications, conventional sealed x-ray tubes with a particular target metal are used as an x-ray source. A high-voltage power source is connected across the cathode and anode of the tube, leading to the emission of electrons from the cathode (Figure 4.5a). When these electrons hit the anode, they are slowed down, producing x-rays. However, x-ray production is very inefficient—99% of the incident energy is lost in the form of heat—such that the dissipation of heat at the focal spot is one of the main limitations on the power that can be applied. By rotating the anode past the focal spot, the heat load can be spread over a larger area, enabling five to ten times higher intensities than in ordinary vacuum tubes. However, such rotating anode tubes are much more expensive and require considerable maintenance. Hence, they are not often used for diffraction experiments.

X-ray tubes produce a continuous wavelength spectrum (also called white radiation or *Bremsstrahlung*) that, at sufficiently high accelerating voltages of several tens of kilovolts, is superimposed by several sharp intensity maxima. As an example, Figure 4.5b shows the spectrum of a Mo-tube operating at 55 kV. Since these peaks are extremely narrow and since their wavelengths

**FIGURE 4.5**

(a) Scheme of an x-ray tube for diffraction experiments and (b) emission spectrum of a molybdenum x-ray tube operating at 55 kV and absorption spectrum of a zirconium filter (see Figure 3.12).

are characteristic of the particular anode material, but do *not* depend on the accelerating voltage, they are called *characteristic lines*. Characteristic radiation appears when the bombarding electrons have sufficient energy to knock out electrons of an inner shell of the target material. Then electrons from higher states drop down to fill the vacancy, emitting x-ray photons with precise energies determined by the electron energy levels of the actual target material.

TABLE 4.1

Characteristics of Various X-Ray Tubes and Appropriate Filters

Anode Material	Wavelength (nm)			Kβ Filter		
	Kα	Kβ	Material	Edge Wavelength (nm)	Thickness for Kβ/Kα = 1/500 (μm)	Loss in Kα (%)
Cr	0.22909	0.20848	V	0.22690	17	51
Fe	0.19373	0.17565	Mn	0.18964	18	53
Co	0.17902	0.16208	Fe	0.17433	19	54
Cu	0.15418	0.13922	Ni	0.14880	23	60
Mo	0.07107	0.06323	Zr	0.06888	120	71
Ag	0.05609	0.04970	Rh	0.05338	92	73
			Pd	0.05092	90	74

Source: Data taken from Hahn, T. (Ed.), in *International Tables for Crystallography Vol. A*, Springer-Verlag, Dordrecht, the Netherlands, 2005.

For x-ray diffraction, the most important characteristic lines are K α 1, K α 2, and K β . Since the K α 1 and K α 2 doublet lines have very close wavelengths, they are often referred to as a single K α line. Table 4.1 lists the wavelengths of the characteristic K α and K β radiations of some typical anode materials. It is seen in Figure 4.5b that the K α peak has an intensity that is about 100 times higher than the wavelengths of the adjacent continuous spectrum and about five to ten times higher than the K β peak, and this obviously favors the characteristic K α radiation for x-ray diffraction experiments.

For most techniques of texture analysis, monochromatic radiation is required; but, besides the strong K α peak, the x-ray spectrum also contains the K β peak as well as the continuous spectrum. The K β peak can substantially be reduced by applying a filter in front of the detector, which is made of a material whose K-absorption edge (Section 3.6.1; Figure 3.12) lies just between the K α and the K β peaks of the tube material. For a molybdenum tube, zirconium is the right filter material. The absorption edge of zirconium as well as the resulting filtered x-ray spectrum are shown in Figure 4.5b. Suitable filter materials for other tubes are given in Table 4.1. As an example, following the discussion in Section 3.5, for the commonly used copper tube, the intensity of the K β radiation is reduced to less than 1% if radiation passes through a 20 μm nickel foil ($\mu/\rho = 283 \text{ cm}^2 \text{ g}^{-1}$) whereas K α is only attenuated to 44%. Considering further that the intensity of K β has only 10%–20% of the intensity of the K α peak in the first place, it means that an appropriate K β filter reduces the ratio of K β to K α to approximately 1:500, which gives sufficiently “monochromatic” radiation for most texture applications. Thicker filters would further improve the ratio of K β to K α , but of course they would also attenuate the intensity of the desired K α radiation.

Continuous contributions to the x-ray spectrum remain at wavelengths larger than K α and at very short wavelengths (Figure 4.5b). Although these

intensities are relatively small compared to the $K\alpha$ intensity, they may become significant in the case of very sharp textures, for example, for diffraction from single crystals or from thin films that are superposed on those from a substrate crystal. This is illustrated in Figure 4.6 for a 400 nm thin film of the high-temperature superconductor yttrium–barium–cuprate ($YBaCuO$) that had been deposited on a lanthanum-aluminate ($LaAlO_3$) substrate crystal (Wenk, 1992). The pole figure measured with truly monochromatic $CuK\alpha$ radiation (Figure 4.6b) contains much less peaks than the pole figure of the same sample measured with nickel-filtered $CuK\alpha$ radiation (Figure 4.6a). The additional poles arise from diffraction by the substrate with some wavelengths of the continuous spectrum, and thus they are artifacts. Figure 4.7 shows the $\{200\}$ pole figure of aluminum foil for high-capacity condenser applications. This material is produced to develop a very sharp cube texture $(001)[100]$ so as to yield maximum capacitance (Section 5.5.4). It is seen that the nonmonochromatic parts of a $K\beta$ -filtered x-ray spectrum are sufficiently strong to produce weak yet noticeable pole figure intensities for reflection at the $\{111\}$, $\{220\}$, and $\{311\}$ planes.

Truly monochromatic radiation can be obtained by using single-crystal monochromators, which yield radiation of a certain wavelength in accordance with Bragg's law (Equation 3.4). The crystal type in a monochromator is selected based on the performance required in terms of intensity and resolution. Crystals such as Si, Ge, and quartz have small rocking angles, resulting in high resolution but low intensities. Graphite and LiF crystals, in contrast, produce high intensity but lower resolution due to larger mosaic spreads. With a mosaic graphite monochromator, intensities of the effective beam are only slightly lower than those for $K\beta$ -filtered x-rays. As the monochromator also reduces the background intensity, the signal-to-background

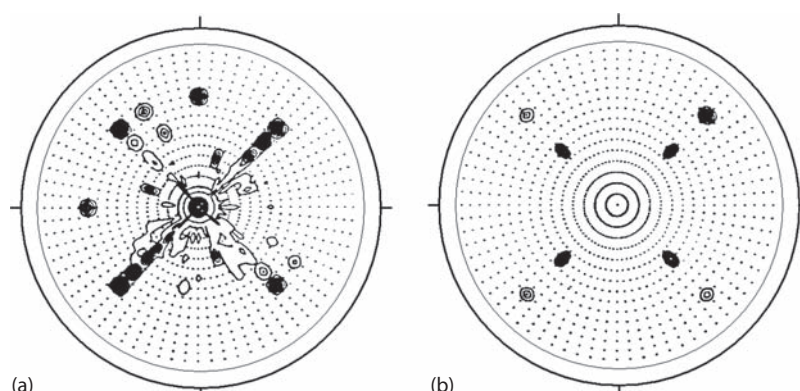
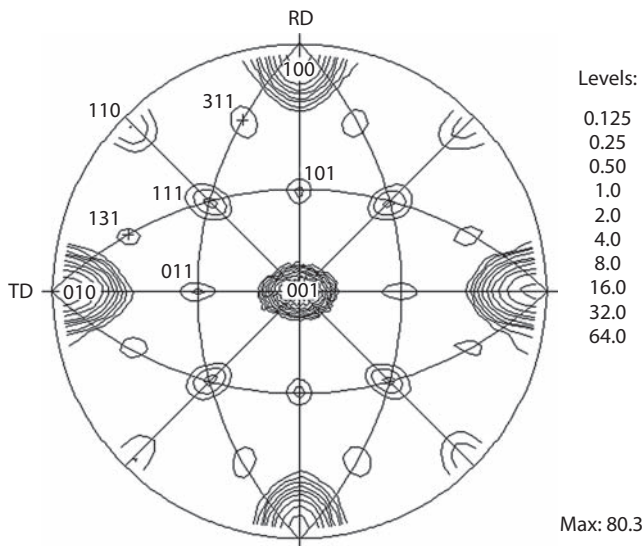
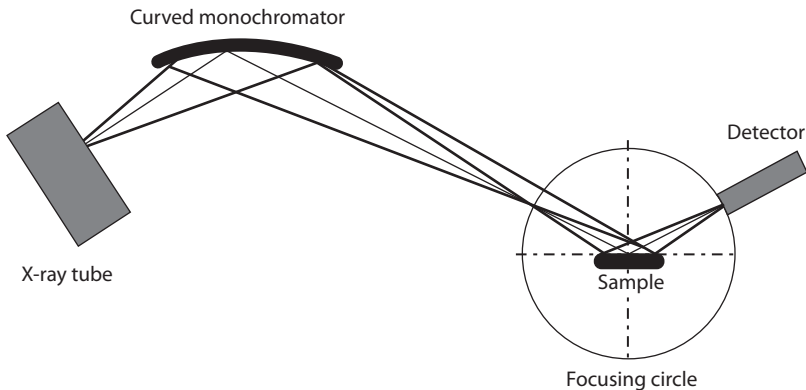


FIGURE 4.6

{102} Pole figure of a 400 nm $YBaCuO$ film on a $LaAlO_3$ substrate measured with (a) $K\beta$ -filtered $CuK\alpha$ radiation and (b) truly monochromatic $CuK\alpha$ radiation. Note additional peaks in (a) that are due to diffraction with different wavelengths on the substrate. (Courtesy of H.R. Wenk.)

**FIGURE 4.7**

[200] Pole figure of highly textured aluminum foil, showing additional weak reflection peaks of nonmonochromatic radiation at different lattice planes.

**FIGURE 4.8**

Principle of a curved monochromator in the primary beam path to produce monochromatic radiation.

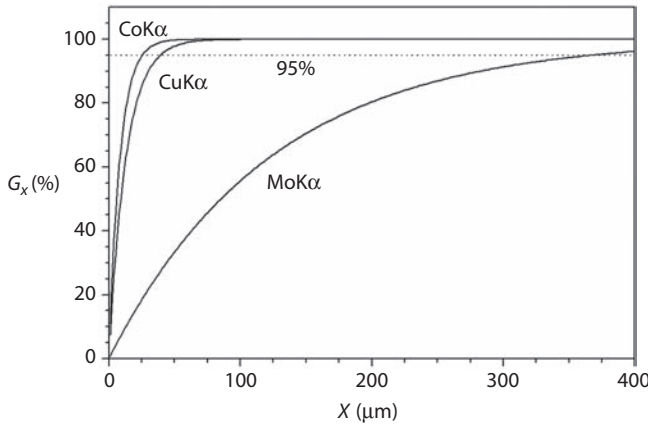
ratio is even better than that for filtered radiation. A flat monochromator crystal produces a parallel x-ray beam, whereas curved monochromators may be used to focus x-rays (Figure 4.8). The monochromator is best inserted into the primary beam between the x-ray tube and the collimator, since such a geometry causes no problems with defocusing during pole figure measurements. If the monochromator is inserted into the reflected beam, that is, between the sample and the detector, the x-ray path must be controlled by Soller slits that reduce the intensity.

As already addressed in Section 3.5, x-ray texture analysis is strongly influenced by the high absorption of x-rays in matter because this accounts for the penetration depth of x-rays in the sample and also influences the choice of an appropriate anode material of the x-ray tube. In general, absorption increases with rising atomic number Z of the analyzed sample material (Table 3.4). Furthermore, it increases with the wavelength of the x-ray tube used, which means that x-rays with short wavelengths (silver, molybdenum, or copper anode) are typically less absorbed than those with large wavelengths (cobalt, iron, or chromium anode). However, there are some combinations of sample and target materials that yield anomalously high absorption because in these instances the x-ray photons have a sufficiently high energy to yield fluorescence (Section 3.6.1). Since high absorption is generally undesirable for texture analysis, such unfavorable combinations of x-ray tubes and sample material should be avoided. For example, steel or materials containing cobalt and manganese should not be analyzed with $\text{CuK}\alpha$ radiation (Table 3.4).

Another important aspect of absorption is the depth of x-ray penetration. The mass absorption coefficients for x-rays are typically of the order of $100 \text{ cm}^2 \text{ g}^{-1}$ (Table 3.4), and for transmission geometry it has already been discussed in Section 3.5 how the intensity of x-rays passing through a material with a given absorption coefficient can be derived (Equation 3.13). In reflection geometry, the situation is more complicated. Here the question is, from what depth of the specimen does the diffracted information come? For normal incidence, that is, a nontilted sample ($\alpha = 0^\circ$), the fraction G_x of the total diffracted intensity that is contributed by the surface layer of depth x can be estimated from (Cullity, 1978)

$$G_x = 1 - \exp\left(\frac{-2\mu x}{\sin \theta}\right) \quad (4.1)$$

(The factor 2 considers that the radiation has to pass through the layer twice, namely, before and after the reflection.) If we now arbitrarily define that a contribution from the surface layer of 95% (or 99%) of the total diffracted intensity is sufficient, then x is the depth of penetration. It is seen that the penetration depth increases with Bragg angle θ , and it would also decrease with increasing sample tilt α . Figure 4.9 shows the evolution of G_x with depth x in aluminum for three different x-ray tubes—three different absorption coefficients (Table 3.4)—for a Bragg angle $\theta = 20^\circ$ and a nontilted sample ($\alpha = 0^\circ$). If we consider $\text{CoK}\alpha$ or $\text{CuK}\alpha$ radiation, it turns out that 95% of the reflected intensity comes from a layer with a thickness of 25 or 39 μm , respectively, which typically in recrystallized samples would mean that only one or two grain layers are recorded. Furthermore, this information is again heavily weighted; when 95% of the recorded information stems from a depth of 39 μm , then 50% of that information originates in the first 8.4 μm . Some further examples of sample thicknesses calculated for G values of 95% are listed in Table 4.2. Note that fluorescence leads to very low G values of only 2 μm if iron is analyzed with $\text{CuK}\alpha$ radiation.

**FIGURE 4.9**

Evolution of G_x with depth x in aluminum for three different x-ray tubes (reflection angle $\theta = 20^\circ$, normal incidence).

TABLE 4.2

Depth x (in μm) That Leads to G_x Values of 95% for Different X-Ray Tubes and Materials Analyzed in Reflection Geometry at a Bragg Angle $\theta = 20^\circ$

	CoK α	CuK α	MoK α
Al	25.4	39.1	368.0
Fe	12.3	2.1	16.9
Cu	7.0	10.8	11.2

4.3.2 Pole Figure Diffractometry in the Texture Goniometer

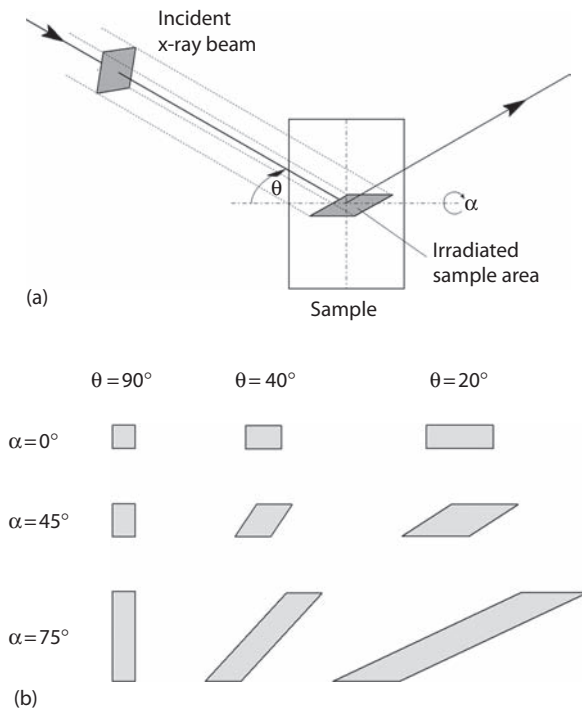
A pole figure goniometer essentially consists of a four-axis single-crystal diffractometer. The goniometer positions the detector with respect to the incident x-ray beam at the proper Bragg angle 2θ . In the widely used *Eulerian cradle* (Figures 4.3 and 4.4), the sample is positioned relative to the x-ray beam by rotations about the three perpendicular axes φ , χ , and ω ; the ω axis coincides with θ (Figure 4.3). Stepper motors, controlled by a personal computer, allow positioning of the goniometer to any arbitrary angular position of the four axes 2θ , ω , χ , and φ (within a certain range to avoid mechanical collisions).

In *reflection geometry*, a sample with a flat surface is mounted on the sample holder with its normal direction parallel to the axis of the φ -rotation (Figure 4.3b). Then, it is rotated in its plane about the φ axis, so that the angle φ corresponds to the azimuth β of a pole in the pole figure. After one full rotation, the sample is tilted about the χ axis, but as χ and the pole figure radial angle α are defined in the opposite direction, the relation is $\alpha = 90^\circ - \chi$.

For most applications ω is kept constant at 0° , so that the χ circle is symmetrical between incoming and diffracted beams, that is, it is positioned at the Bragg angle θ . This arrangement is referred to as the Bragg–Brentano focusing condition for reflection geometry. ω -Scans (rocking curves) can be used to assess the quality of crystals and derive exact peak shapes (Heidelbach et al., 1992; Tizliouine et al., 1996; Sous et al., 1997; Borbély et al., 2008). For special applications, such as texture measurements in thin films, it may be advantageous to use a low incident beam angle to increase the path length of the x-rays in the specimen (grazing beam technique; e.g., Bowen and Wormington, 1992; Szpunar et al., 1993; Van Acker et al., 1994; Tizliouine et al., 1996; Groves et al., 2001). In that case, the χ circle is no longer symmetrical and ω is the deviation from the bisecting position.

Although the limiting value for α in the Bragg–Brentano focusing condition is obtained when both the incident and the reflected beams are parallel to the sample surface, so that $\alpha_{\max} \leq 90^\circ$, there are two aspects that usually limit α_{\max} to values of 60° – 85° . Even when we analyze a sample with a perfectly uniform “random” texture, the intensity of the reflected peak strongly decreases with α . With increasing tilting angle α , the intersection of the incident x-ray beam with the sample—the projection of the beam onto the sample surface—becomes increasingly elongated; furthermore, different incident angles θ add an additional distortion of the projected beam (Figure 4.10a). Figure 4.10b shows the area irradiated by an originally square-shaped x-ray beam on the sample surface for different angles α and θ . Owing to the penetration depth of the x-rays into the sample, the true geometry of the reflecting volume is even more complicated. The projected area on the sample surface, and therewith the region from where x-rays are reflected, increases with increasing sample tilt α . It also increases with an increasing deviation of the Bragg angle θ from the $\theta = 90^\circ$ position, and therefore pole figures should not be measured at $\theta < 10^\circ$. To achieve optimum angular resolution, diffractometers are constructed such that reflection of the—originally divergent—incident x-ray beam at the plane surface of an *untilted* sample ($\alpha = 0^\circ$) brings the diffracted beam back into a focal point that coincides with the receiving slits of the detector. Tilting of the sample to angles $\alpha > 0^\circ$ has the effect that half of the sample is behind and half of it is in front of its original plane. For those sample regions, however, the focusing condition is no longer exactly fulfilled, which leads to a decrease in intensity simultaneously with a broadening of the reflected peaks. Accordingly, this effect is called the *defocusing error*.

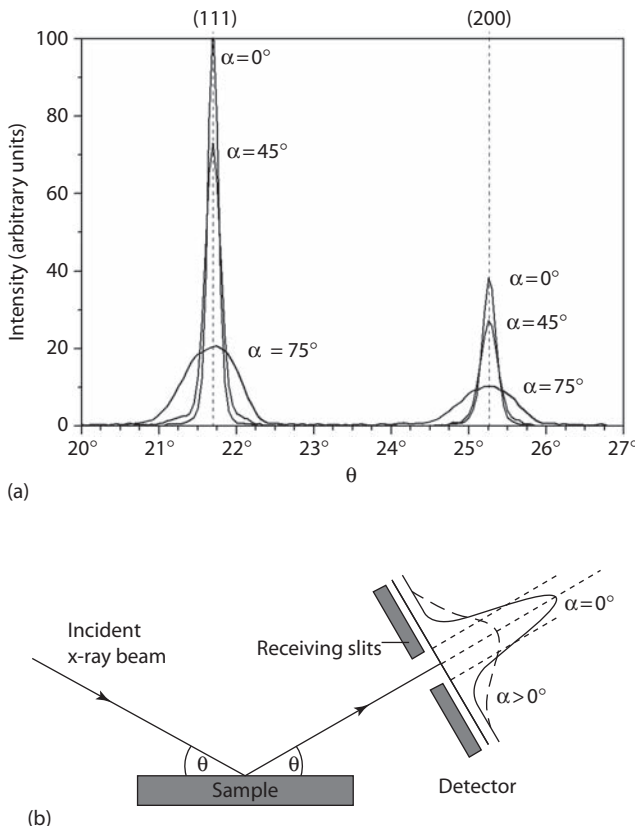
Figure 4.11a shows the peak broadening for two diffraction peaks (111 and 200) of a randomly oriented copper powder sample for three different tilting angles α . Although the *integral* intensity of the peak remains constant, the detector, which is equipped with a system of receiving slits, records only the intensities diffracted from a small, constant area of the sample surface, so that the recorded intensity decreases with increasing sample tilt (Figure 4.11b). Measures to correct for the intensity drop due to defocusing are given in Section 4.3.6. Besides the defocusing error, absorption of the

**FIGURE 4.10**

(a) Sketch to visualize the distortion of the irradiated spot on the sample surface. (b) Shape of the irradiated spot in dependence on tilting angle α and Bragg angle θ for a square-shaped incident beam.

x-rays within the sample also has to be considered; with increasing sample tilting, the path length of the x-rays in the sample increases, which means that the reflected intensity decreases due to absorption. However, for thick samples this increase in absorption is exactly balanced by the increase in irradiated volume that contributes to the diffracted intensity (Schulz, 1949a). Note that “thick” samples mean that the sample is thicker than the x-ray penetration depth, which, as we have seen earlier, is usually only of the order of 100 μm . However, this does not hold for very thin samples; for example, for thin films, and in such cases, absorption has to be corrected for as well (Section 4.3.6).

In *transmission geometry*, the sample holder is turned 90° such that the sample, a thin sheet, is mounted normal to the χ axis (Figure 4.3a). Here, the angle φ is kept constant at 0° and the sample is tilted about the ω axis, which corresponds to the complement of the pole distance ($90^\circ - \alpha$) in the pole figure. The azimuthal angle β in the pole figure is obtained from a rotation of the sample about the χ axis. In transmission geometry, the outer parts of the pole figure with $\alpha_{\min} \leq \alpha \leq 90^\circ$ are covered. As described for reflection geometry, the recorded intensity strongly decreases with

**FIGURE 4.11**

- (a) Peak broadening with increasing tilting angle α (copper powder sample, CuK α radiation).
 (b) Sketch to visualize the defocusing error.

sample tilt ω , so that the practical minimum of α is reached before the theoretical limit, which is given when the incident or reflected beam is parallel to the sample surface, so that $\omega < 90^\circ - \theta$ or $\alpha_{\min} = \theta$. In transmission geometry, the increase in absorption with sample tilt is not compensated for by the increase in the reflecting volume (Decker et al., 1948; Schulz, 1949b), so that an absorption correction is always necessary (Section 4.3.6).

We have seen that for pole figures measured in reflection geometry, the errors strongly increase with α , so that the inner circles of a pole figure (e.g., $\alpha < 45^\circ$) can practically be obtained without corrections, whereas the outer parts need strong corrections ($\alpha > 45^\circ$) or are even not accessible at all ($\alpha \approx 90^\circ$). In transmission geometry vice versa, the outer parts of a pole figure can readily be determined and the inner circles are missing. Accordingly, *complete pole figures* can be obtained by combination of

two pole figures, one of which is measured in reflection and the other in transmission geometry. Subsequently, the pole figure data are overlapped, which often requires some intensity adaptations to bring the two measurements to the same intensity scale. However, because of the laborious preparation of samples for transmission texture measurements, nowadays in most cases only incomplete pole figures are measured in reflection with tilting angles up to typically 60° – 85° . If necessary, complete pole figures are derived by recalculation from the 3-D orientation distribution functions (Section 5.3.2).

Besides the rotations to scan the pole figure described so far, the sample can be subjected to an additional translation in its plane to increase the sampling area (Bunge and Puch, 1984; Section 4.6).

4.3.3 Principles of Pole Figure Scanning

Older texture goniometers were driven by only one motor, and the pole figures were scanned by changing both angles α and β simultaneously on a spiral (Figure 4.12a). In modern stepper motor–driven goniometers, the pole figures are mostly scanned on equidistant concentric circles of constant α in steps of typically 5° in both α and β (Figure 4.12b). For a complete pole figure, this results in $(\alpha \times \beta) = 19 \times 72 = 1368$ points. At counting times of typically 1 s per point, this yields a total measuring time of less than 30 min per pole figure. For very sharp textures, the standard $5^\circ \times 5^\circ$ grid may be too coarse and finer grids, for example, $2.5^\circ \times 2.5^\circ$, are required. Also, for calculating ODFs according to the series expansion method (Section 5.3.2) with high series expansion coefficients l_{\max} , finer grids may be necessary to derive a sufficient number of data points.

For each point (α, β) , the reflected intensity is measured by an electrical counter (Section 4.3.4) that “sees” a certain angular range of the pole figure.

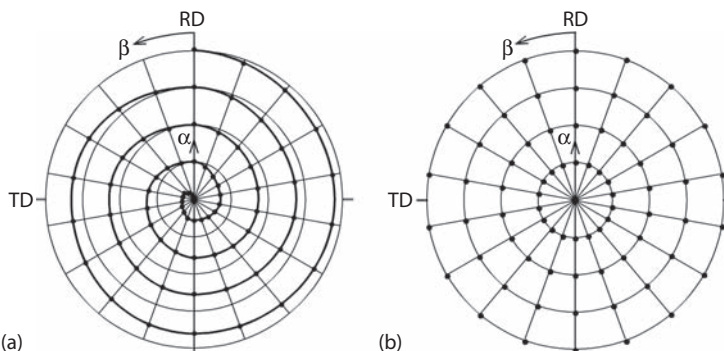
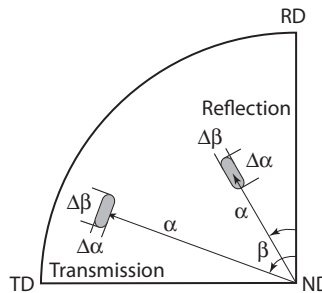


FIGURE 4.12

(a) Spiral and (b) circular, equal-angle scanning grids for pole figure measurements (note that for clarity both scanning schemes are shown in steps of 20°).

**FIGURE 4.13**

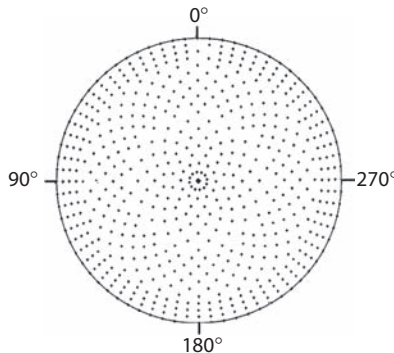
Shape of the pole figure window for reflection and transmission geometry.

This *pole figure window* not only is defined by the aperture systems of x-ray tube and counter, and especially by the receiving slits of the latter, but also depends on the geometry of the setup, that is, the reflection or transmission geometry, and on the settings of the Bragg angle θ and sample tilt α . Usually, the pole figure window has an elongated shape, as shown schematically in Figure 4.13.

With regard to pole figure scanning, two different modes are possible: step scanning and continuous scanning (Bunge and Puch, 1984). In the step mode, the sample is rotated by a certain angle $\Delta\beta$, typically 5° , either on a spiral or on concentric circles, and then at this position the reflected intensity is determined by counting for a given time, for example, 1 s. In the continuous mode, the intensities are recorded continuously, thus integrating over an angular interval $\Delta\beta$, and subsequently the measured intensity is attributed to the center point β of that interval. In modern texture goniometers, the rotations are performed by stepper motors, which can be moved in small steps of say 0.01° so that with a suitable computer control both scanning modes can readily be realized.

It should be noted that in the step mode, intensities are missed and sharp peaks may even be skipped entirely, as the step width is typically larger than the pole figure window $\Delta\beta$ (Figure 4.13). Continuous scanning, however, records all intensities in a certain range of $\Delta\beta$. As the length $\Delta\alpha$ of the pole figure window concurrently integrates over a range $\Delta\alpha$, continuous scanning ensures a rather comprehensive coverage of the entire pole figure. However, continuous scans are restricted to homogeneous scanning grids like spirals or concentric circles, whereas more complex scanning grids, such as equal area scans (see the following text), require step scanning.

In the standard *equal angle* ($\alpha \times \beta$) $5^\circ \times 5^\circ$ grid, the density of measuring points per area is very inhomogeneous, as the pole figure center is covered with a much higher density in β than the outer circles (Figure 4.12b). To cover the pole figure more uniformly, an *equal area* scan can be applied, and

**FIGURE 4.14**

Equal area scanning grid for pole figure measurements. (Adapted from Brokmeier, H.-G., *Textures Microstruct.*, 10, 325, 1989.)

various schemes to achieve equal area coverage have been proposed in the literature (Welch, 1986; Will et al., 1989; Morris and Hook, 1992; Matthies and Wenk, 1992; Helming, 1996). All these schemes have the following in common: They are close to a true equal area coverage (Appendix IV) and reduce the number of measurement points by about one-half (Figure 4.14). Thus, for a given angular resolution, the recording time can be halved, which is particularly interesting if measuring time is of concern (e.g., in neutron diffraction; Section 4.4), or, by allowing the same total measuring time, the angular resolution can be doubled. If necessary, the data for the conventional $5^\circ \times 5^\circ$ grid, or for any other grid, are subsequently obtained by interpolation.

4.3.4 X-Ray Detectors

In modern computer-controlled texture goniometers, the reflected x-ray intensities are recorded by means of an appropriate electrical counter. There are four different types of counters that are suitable for x-ray diffraction experiments:

- Geiger counters
- Scintillation counters
- Proportional counters
- Semiconductor counters

All these counters depend on the power of the x-rays to ionize atoms, either of a gas (Geiger and proportional counters) or of a solid (scintillation and semiconductor counters). Appendix VI describes the working principles and characteristics of these four types of x-ray counters.

Geiger counters were the first electrical counters used to detect radiation, but these are now virtually obsolete in diffractometry. In all counters that are commonly used today—scintillation, proportional, and semiconductor—the output voltage is proportional to the energy of the triggering x-ray quanta. Therefore, electrical units that distinguish between pulses of different sizes, *pulse-height analyzers*, can distinguish between x-rays of different energies. As discussed in more detail in Appendix VI, with the use of pulse-height analyzers, background and fluorescent radiation with different wavelengths can efficiently be reduced, so that the peak-to-background ratio can markedly be improved.

When we analyze the diffraction spectra of materials with high crystal symmetry, cubic or hexagonal, the diffraction lines are usually widely spaced (Figures 3.5 and 3.7). Thus, even when considering some peak broadening at large tilting angles (defocusing error; Sections 4.3.2 and 4.3.6), the reflected peaks can generally be separated easily (Figure 4.11a). In some cases, finer receiving slits may be necessary to improve angular resolution (e.g., to separate the 0002 and 1011 reflections in Figure 3.7). However, this is not necessarily true in samples with line-rich diffraction patterns—materials with low crystal symmetry or multiphase alloys, where peaks may partially, or even completely, overlap (Section 4.5.1). In such cases, the peaks can no longer be separated, and peak profile analysis becomes necessary to attribute unambiguously the recorded intensities to the individual hkl reflections. To register the peak profiles with conventional counters, the $\theta/2\theta$ spectrum must be scanned successively with a small receiving slit for each pole figure point (α, β) to achieve sufficiently high angular resolution. The resulting peaks are then separated by an appropriate deconvolution procedure, for example, by fitting the diffraction spectra with Gauss, Lorenz, or other functions, which finally yields the exact integral intensity of the various peaks for each pole figure point. This is an extremely time-consuming procedure, however, which can be accomplished much more easily with the help of a location-sensitive counter that records the entire peak profile simultaneously (Heizmann and Laruelle, 1986; Wcislaw et al., 1993; Tarkowski et al., 2005).

A typical 1-D *position-sensitive detector* (PSD) suitable for texture analysis consists of a location-sensitive proportional counter with a resistance wire anode (Figure 4.15a). An incoming x-ray quantum generates an electrical charge Q at the point x of the anode. This electrical charge Q has the possibility to flow off in both directions to the left and right preamplifiers. However, due to the resistivity of the wire, the partial charges Q_l and Q_r flowing to either side generate voltage pulses U_l and U_r with the ratio $U_l/U_r = x/L-x$, where L is the active length of the resistance wire. Thus, the location x of the incoming x-ray quantum can be detected electronically and the electrical pulse is accumulated in the corresponding channel of a multi-channel analyzer (MCA). So, eventually, the contents of the various channels of the MCA reflect the intensity distribution of the diffraction peak at different locations of the PSD. Alternatively, a linear silicon strip detector has been

developed that consists of 128 Si strips, each 100 μm wide, so that the total width is 12.8 mm (Dabrowski et al., 2003).

In most applications, short linear detectors are used, which are mounted tangential to the 2θ -goniometer circle (a setup where the PSD records

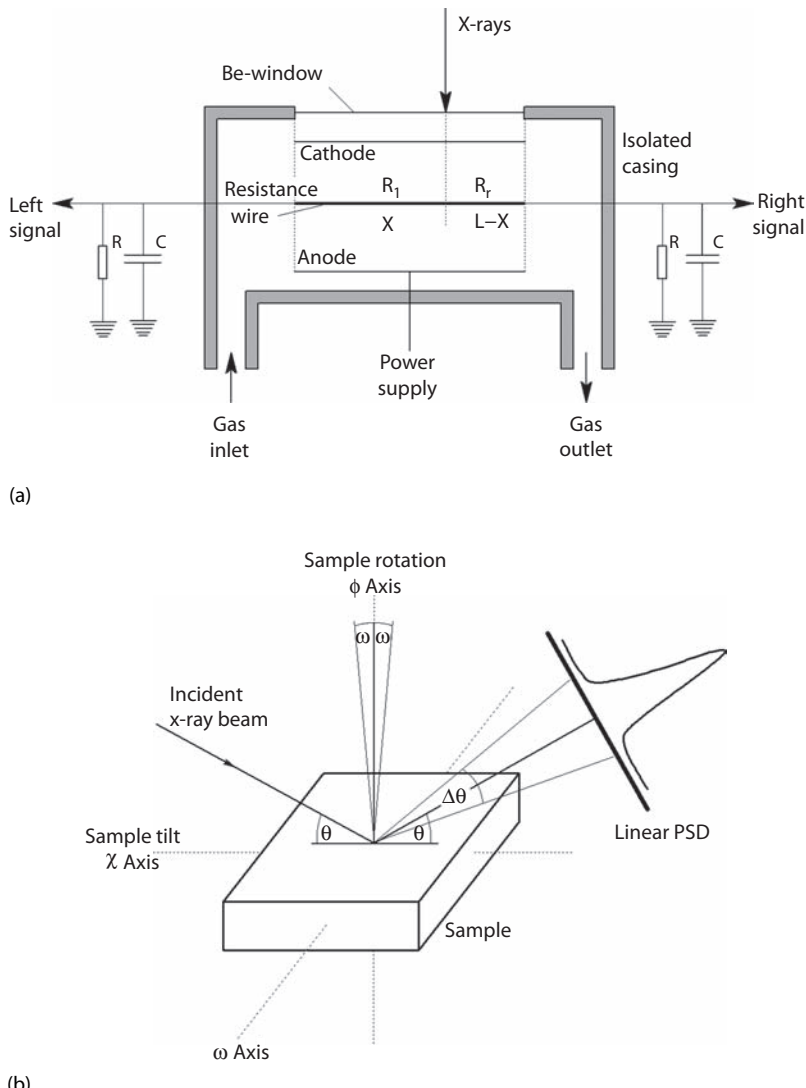


FIGURE 4.15

(a) Principle of a one-dimensional location-sensitive proportional overflow, overpressure gas ionization counter. (b) Pole figure measurements with a position-sensitive detector (PSD). (c) Deviation from the Bragg-Brentano focusing condition for a linear PSD. (Adapted from Wcislaw, L. and Bunge, H.-J., in *Texture Analysis with a Position Sensitive Detector*, Cuvillier Verlag, Göttingen, Germany, 1996.)

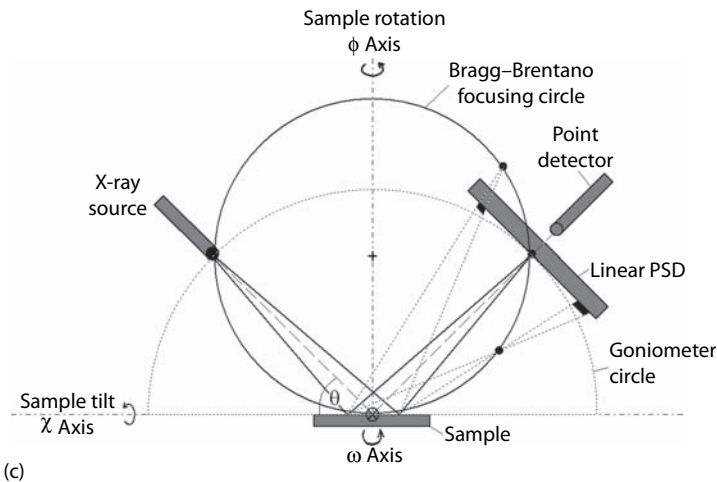


FIGURE 4.15 (Continued)

intensities along the α circle is described in Section 4.4.1). Such PSDs typically provide a viewing angle of 5° – 10° with an angular resolution of the order of 0.01° , which is sufficient to record individual peaks, inclusive of peak broadening at high tilting angles, and this also permits the separation of overlapping peaks. Long, curved detectors with viewing angles of up to 120° are also in use (Wölfel, 1983; Bessières et al., 1991). However, these are mainly used to record diffraction spectra for phase analysis rather than for texture measurements, since with increasing deviation from the Bragg–Brentano diffraction condition two problems arise, which are described in the following.

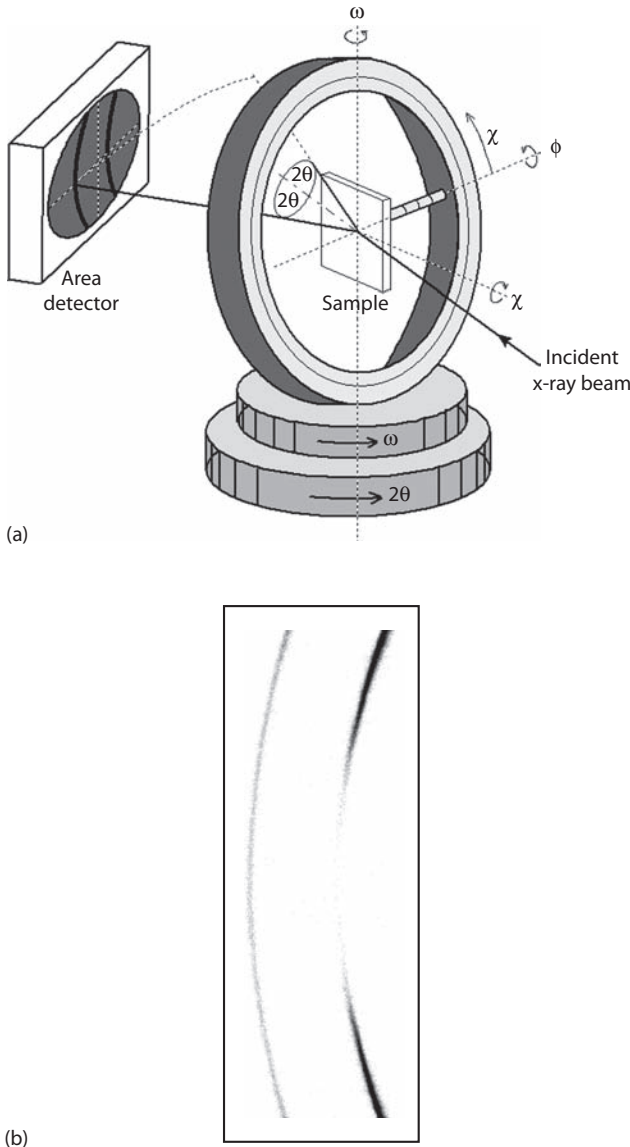
In the Bragg–Brentano diffraction condition, the Eulerian cradle is set in such a way that the χ circle coincides with the bisector of the angle between the incident and diffracted beams, and any direction on the pole figure can be brought parallel to this direction by two rotations, 90° – χ and ϕ , corresponding to the pole figure coordinates α and β (see the preceding text). With a PSD this is true only for one position that is usually the middle of the detector, whereas for all other positions the χ circle is inclined by ω to the bisector (Figure 4.15b) (in the PSD geometry, ω is equal to $\Delta\theta$, the deviation of the χ circle from the bisecting position). As illustrated in Figure 4.15c, this means that the focusing condition is violated, leading to some peak broadening, and this effect increases with increasing distance from the exact Bragg–Brentano reflection condition (Heizmann and Laruelle, 1986; Wcislak and Bunge, 1991). Furthermore, when several pole figures are measured simultaneously, a given setting (ω, χ, ϕ) of the texture goniometer corresponds to different pole figure angles (α, β) . Thus, the (ω, χ, ϕ) coordinates need to be transformed into the pole figure angles (α, β) , and the corresponding transformation laws have been derived for transmission geometry (Bunge et al., 1982; Heizmann and Laruelle, 1986) and reflection geometry

(Wcislak and Bunge, 1991). However, poles with $\alpha < \omega$ cannot be brought into coincidence with the bisector, which results in a nonmeasured “blind” area in the center of the pole figure. With increasing deviation from the exact Bragg–Brentano condition (with increasing ω), the size of this blind area increases, which means that the pole figures become less meaningful. Thus, for these two reasons—the violation of the focusing condition and the blind area—too large deviations from the exact Bragg–Brentano condition should be avoided.

A 1-D PSD records the intensities linearly, mostly along a circle in the equator plane, whereas a 2-D (area) detector would simultaneously register a certain part of the sphere. Accordingly, a conventional single detector can be considered as a zero-dimensional point counter. As area detectors yield a high angular resolution in two dimensions, they enable measuring sharp textures with high accuracy. If materials with peak-rich diffraction spectra are investigated, peak profile analysis can be performed and, under certain circumstances, the high angular resolution even allows determination of the orientations of individual crystals in a polycrystalline aggregate (Bunge and Klein, 1996; Rodriguez-Navarro, 2006).

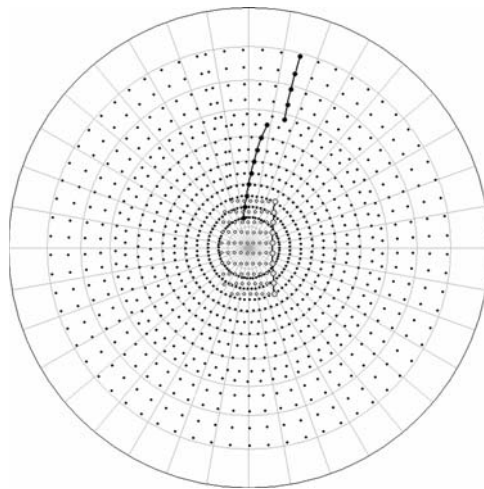
In principle, a *photographic film* positioned so as to record part of the diffraction sphere is a 2-D area detector (Wassermann and Grewen, 1962). More recently, *image plates* have been used for texture analysis (Brokmeier and Ermrich, 1994; Ermrich et al., 1997), which are far superior to films in terms of dynamic range, sensibility, and efficiency. However, they also require separate registration and readout periods of several minutes, which prevent an interactive, online analysis of the results. To overcome this shortcoming, charged-coupled device (CCD)–based detector systems have been developed for recording diffraction patterns generated by synchrotron radiation (Bourgeois et al., 1994; Garbe et al., 1996; Section 12.2). For real-time texture analysis in conventional x-ray texture goniometers, Siemens developed a 2-D *multiwire proportional counter* filled with a high-pressure xenon gas mixture (Smith and Ortega, 1993; He, 2003). The detector is equipped with a concave beryllium window with a diameter of 11.5 cm. The reflected intensity data are received as a 1024×1024 pixel frame that can be transferred into a computer for storage and evaluation. Such a system is now available as general area detector diffraction system (GADDS) from Bruker AXS. Figure 4.16a shows a schematic of a standard x-ray diffractometer equipped with a 2-D area detector, which simultaneously records parts of two Debye–Scherrer rings, whereas Figure 4.16b gives an example of the {111} and {200} rings of a heavily textured aluminum sample.

For an area detector all diffraction vectors belonging to one Debye sector form an arc (bisector) on the pole sphere, with its center being given by the direction of the primary beam (Bunge and Klein, 1996; Klein et al., 1996; Helming and Prechwindel, 2005; Rodriguez-Navarro, 2007). Thus, for a fixed position of the pole figure angles ω and α , a large portion of the pole figure

**FIGURE 4.16**

(a) Pole figure measurement with an area detector; (b) {111} and {200} Debye–Scherrer rings of a strongly textured aluminum sample. (Courtesy of I. Lischewski.)

can be scanned with one β scan, that is, sample rotation. The exact coverage of the pole sphere naturally depends on many geometrical details of the entire setup, including the preset diffraction angle 2θ and, most notably, the distance between the sample and the detector. In general, a shorter sample–detector distance leads to a greater field of view, but at the expenses

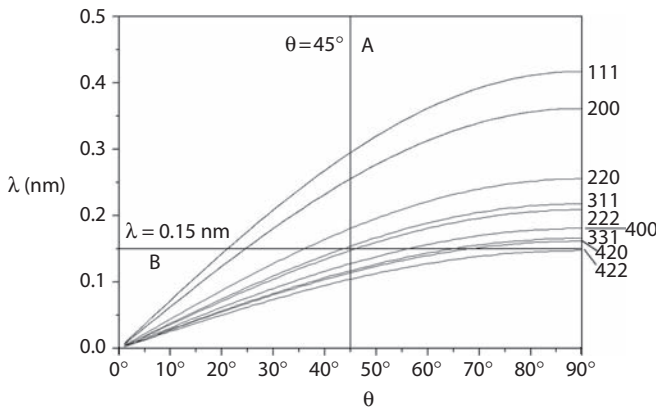
**FIGURE 4.17**

Pole figure coverage with two β scans (rotations) for $\alpha = 40^\circ$ and 80° (black symbols) and one ω scan at $\alpha = \beta = 0^\circ$ (gray symbols). In this example, the diffraction angle was $2\theta = 45^\circ$, enabling simultaneous analysis of {111} and {200} pole figures in an aluminum sample.

of angular resolution. Figure 4.17 shows an example of the pole figure coverage ({111} and {200} pole figures simultaneously), which may be achieved with two β scans for α angles 40° and 80° , respectively (black symbols). This may be combined with an ω scan performed at constant α and β (gray symbols). However, the maximum angle ω and hence the covered pole figure area is restricted by the Bragg angle θ , since $0^\circ < \omega < \theta$. Thus, in the present example, three scans with the area detector give approximately the same information as 38 scans with a conventional point detector. Similarly as discussed for the 1-D PSD, the results obtained by an area detector have finally to be transformed into the standard $\alpha \times \beta$ pole figure grid for further evaluation and ODF computation.

4.3.5 Energy-Dispersive Diffractometry

In all applications mentioned so far, the counters were used in an *angular-dispersive* way—the diffracted intensities for monochromatic radiation were recorded in dependence on different angular settings of the sample, and energy discrimination is only used to reduce background and fluorescence by setting a narrow window of the pulse-height analyzer (Appendix VI). Figure 4.18 is a representation of Bragg's law $\theta = f(\lambda)$ for reflection at the various lattice planes (hkl) in copper. To determine the reflection spectrum in conventional angular-dispersive experiments with x-rays of a given wavelength, $\theta/2\theta$ scans are performed with x-rays of a given wavelength, for example, $\lambda = 0.15$ nm (line B in Figure 4.18), and diffraction peaks are detected at

**FIGURE 4.18**

Representation of Bragg's law for reflection at the various lattice planes (hkl) in copper. The vertical line A represents the energy-dispersive and the horizontal line B the angular-dispersive diffraction experiments.

each intersection of line B with the Bragg curves for the lattice planes (hkl). Alternatively, the energy or wavelength of the reflected radiation can be exploited as well (*energy-dispersive diffractometry*; Giessen and Gordon, 1968; Buras et al., 1975). If we introduce the energy of the radiation into Equation 3.4, we can write Bragg's law in a different way:

$$E = hv = h \frac{c}{\lambda} = \frac{hc}{2 \sin \theta} \cdot \frac{1}{d_{hkl}} \quad (4.2)$$

It is seen that at a constant setting with Bragg angle θ , the energy of the diffracted radiation E is a measure for the lattice spacing d_{hkl} of the reflecting crystal planes (hkl). Thus, for polychromatic radiation covering a whole range of wavelengths, a detector at a fixed scattering angle, for example, $\theta = 45^\circ$ (line A in Figure 4.18), would again record the various hkl diffractions that now are distinguished by different wavelengths. To perform energy-dispersive diffractometry, the diffracted intensities of polychromatic radiation are recorded by an energy-dispersive detector and then analyzed by an MCA that transforms the pulse-height spectrum into a wavelength (or energy) spectrum. To achieve maximum energy resolution, use of a semiconductor counter is recommended, but nonetheless, the resolution of neighboring diffraction lines is inferior to that of conventional angular-dispersive techniques. The diffraction spectrum is obtained by plotting the contents of the various channels of the MCA and, as an example, Figure 4.19 shows a diffraction spectrum obtained from a polycrystalline steel sheet measured with a chromium tube at a constant Bragg angle $\theta = 15^\circ$. The fluorescence lines at the low-energy side of the spectrum are

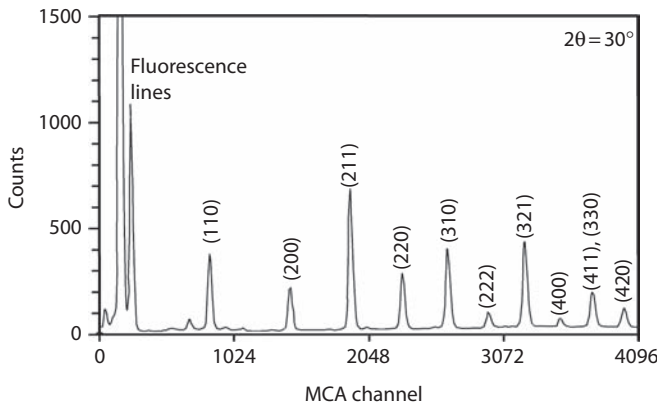


FIGURE 4.19

Diffraction spectrum of a steel sheet with random texture, obtained by energy-dispersive diffractometry. During the measurement, the sample was rotated about its normal direction; the time necessary to acquire the diffraction spectrum was 200 s ($2\theta = 30^\circ$, CrK α radiation, liquid nitrogen-cooled Ge-semiconductor counter). (Adapted from Shimizu, M., Katayama, M., and Kitagawa, H., in *Experimental Techniques of Texture Analysis*, DGM Inf. Ges., Oberursel, Germany, 1986.)

characteristic of the sample material, whereas the diffraction lines disclose its crystallographic structure.

To utilize the results obtained by energy-dispersive diffractometry for deriving the texture of the sampled volume, the wavelength spectrum must be convoluted into the contributions from the different reflector planes. By rotating the sample in a goniometer as in conventional angular-dispersive applications, a whole range of lattice planes can be registered simultaneously (Szpunar and Gerward, 1980). This means that the measuring time is virtually independent of the number of pole figures recorded, which makes this method particularly attractive for low-symmetry materials with peak-rich diffraction spectra. Furthermore, as mentioned for the PSDs, overlapping peaks can be separated by peak profile analysis.

Alternatively, the diffraction spectra can be exploited for a given, fixed sample position, which means that the sample does not have to be moved during texture analysis. The resulting texture information corresponds to an inverse pole figure of the sample surface (Szpunar et al., 1974; Shimizu et al., 1986; Section 4.3.7). Texture data from four inverse pole figures have been used to calculate a 3-D ODF with a reasonable accuracy (Szpunar, 1990). Texture analysis at a fixed sample position is also of great interest for *in situ* experiments (Gerward et al., 1976) as well as for online quality control in production plants. In the arrangement described by Kopinek (1994) and Klinkenberg et al. (1999), a system for online texture analysis with energy-dispersive detectors has been installed at the exit of a continuous annealing line of steel sheets. Four detectors, each recording the reflected intensities of five lattice planes, provide enough information to compute the low-order

C coefficients that can be used to calculate average physical properties of the final sheet product, including r value, Young's modulus, and magnetic properties (Bunge, 1993).

4.3.6 Correction and Normalization of Pole Figure Data

Before the pole figures can be evaluated, or used for subsequent ODF calculation, several corrections have to be applied (Humbert, 1986). This section discusses measures to correct for background errors and errors introduced by defocusing and absorption, and also addresses the influence of counting statistics. Finally, the texture data that are given as counts per pole figure point need to be normalized to standard units—multiples of a random orientation distribution (mrd)—that are independent of any experimental parameters.

The first error that has to be corrected for is the *background error* (Figure 4.20). Background intensities are caused by incoherent scattering and fluorescence in the sample. Minor contributions may also result from interaction of the x-ray beam with any material in the path of the x-rays—collimator, beam stop, and air—as well as from electronic noise. Especially when the experiments are performed with “monochromatic” x-radiation produced by a $K\beta$ -absorption filter, reflection of x-rays with other wavelengths of the continuous spectrum strongly contributes to the overall background intensity. Several measures to improve the peak-to-background ratio have been addressed in earlier sections: To prevent fluorescent radiation an appropriate x-ray tube with wavelength larger than the K-absorption edge of the sample material should be used (Section 4.3.1), but the short-wave components of the continuous spectrum may still excite fluorescence. A monochromator (Section 4.3.1) or an energy-dispersive detector (Section 4.3.5) substantially

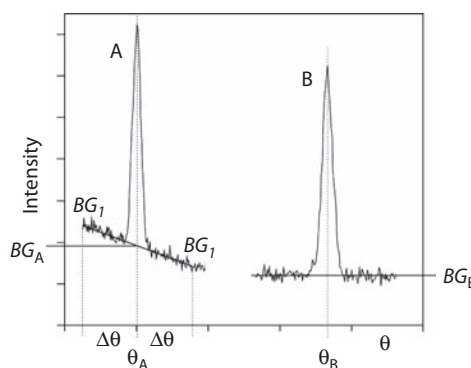


FIGURE 4.20

Determination of the background intensity BG in a $\theta/2\theta$ -diffraction spectrum. Case A illustrates a strong dependence of the reflected intensity on θ , whereas in case B the background is almost independent of θ .

reduces background intensities with different wavelengths. With conventional counters, the background can be reduced by choosing a small window of the pulse-height analyzer (Appendix VI). Background is also diminished by using smaller receiving slits, but this would enhance the “defocusing error,” that is, the drop in peak intensity with increasing tilting angle α (see the following text).

Although background intensities can—and of course should—be reduced by such measures, they cannot completely be eliminated in practice, and therefore the diffraction data have to be corrected by subtracting the background from the measured intensity (Figure 4.20). For correcting pole figure data, the background intensity BG is determined and subtracted from the measured pole figure intensity I_{meas} :

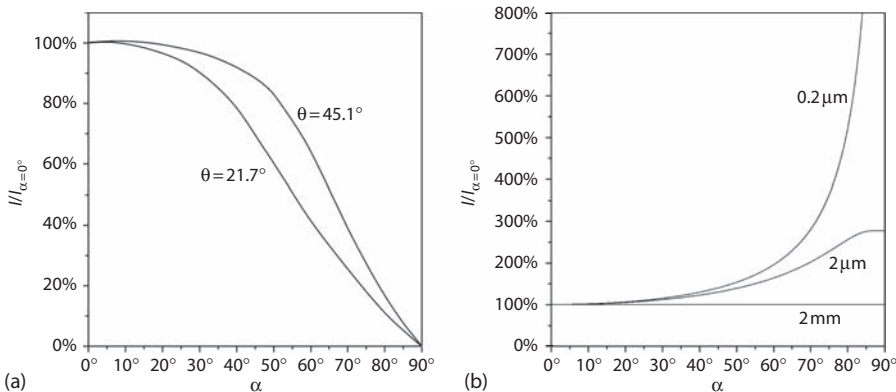
$$I_{\text{corr}} = I_{\text{meas}}(\alpha, \beta) - BG(\alpha) \quad (4.3)$$

Within a given pole figure, the background changes with increasing tilting angle α , but—for sufficiently large samples—does not depend on the sample rotation β . Thus, a background correction curve $BG(\alpha)$ can be obtained by measuring a complete pole figure away from the diffraction peak θ and integrating over the pole circles, that is, over β . At small angles θ the background typically strongly decreases with θ , and hence it is necessary to measure the background at either side of the Bragg peak and subsequently interpolate the results (case A in Figure 4.20). Measuring at one side may suffice if the background intensities remain more or less constant with θ (case B in Figure 4.20). Of course, in both cases it must be ensured that the distance from the Bragg peak is large enough to allow for peak broadening at large sample tilts α but that it does not interfere with neighboring peaks. The decrease in the background intensity with α is fairly independent of θ . Therefore, it is sufficient to measure the background intensity only at one angle α , typically $\alpha = 0^\circ$, and then derive the background values for other α from a predetermined correction curve.

Not only the background intensity but also the reflected peak intensity strongly decreases with α . Increasing sample tilt leads to a broadening of the reflected peaks (Figure 4.11a). The detector, however, is equipped with a system of receiving slits and hence “sees” only a small, constant area of the sample surface, so that peak broadening results in a marked decrease in recorded intensity (Figure 4.11b). A typical intensity drop obtained for copper with increasing α , normalized to 100% for $\alpha = 0^\circ$, is shown in Figure 4.21a for two different Bragg angles θ , that is, two different pole figures.

To correct for this *defocusing error*, a correction function $U(\alpha)$ must be applied, which for any value of α normalizes the intensity of a random sample to the values at $\alpha = 0^\circ$:

$$I_{\text{corr}} = \frac{I_{\text{meas}}(\alpha, \beta) - BG(\alpha)}{U(\alpha)} \quad (4.4)$$

**FIGURE 4.21**

(a) Intensity drop with increasing sample tilt α , normalized to 100% for $\alpha = 0^\circ$. Data were obtained experimentally by recording the {111} ($\theta = 21.7^\circ$) and {311} ($\theta = 45.1^\circ$) pole figures of a copper powder sample with CuK α radiation. (b) Evolution of I with α for three different sample thicknesses, computed according to Equation 4.6 and normalized to 100% for $\alpha = 0^\circ$. For the 2 mm thick sample the increase in absorption is exactly balanced by the increase in diffracting volume, whereas for the thinner samples an absorption correction is necessary ({200} pole figure).

As described in Section 4.3.2, the defocusing error is mainly determined by the sample position in terms of the two angles α and θ . Therefore, it appears reasonable to obtain the correction curve from geometrical considerations (Gale and Griffiths, 1960; Tenckhoff, 1970). However, the intensity drop also depends on the alignment of sample and goniometer as well as the size of the collimator and the receiving slit. The smaller the collimator size and the larger the receiving slit, the smaller is the defocusing error, though large receiving slits decrease the angular resolution. Thus, empirical correction curves $U(\alpha)$, as derived from measurements of a random sample with the particular experimental setup, usually give better results. For that purpose, pole figures of a sample with a random texture are measured at the Bragg peak, integrated over the rotation angle β , and normalized to unity, that is, $U(0^\circ) = 1$ (Figure 4.21a). It should be mentioned here that the preparation of a standard sample with a completely random texture is not trivial. In most cases, powder compacts are used, which may be slightly compacted or embedded, as in epoxy. Isostatically pressed powders can reveal too pronounced textures when the stress was not purely hydrostatic, whereas in too loosely bonded powder compacts, the reflected intensity may deviate from the curves obtained for 100% dense bulk samples. However, it is not necessary to have powder samples for all materials measured. As the defocusing correction $U(\alpha)$ only slightly depends on the Bragg angle θ , correction curves of other materials with similar Bragg angles can be used if no powder sample is available. Thus, textures obtained in different steel or aluminum alloys

can generally be corrected with the correction curves derived from a powder sample from pure iron and aluminum, respectively.

Another error that has to be considered is caused by *absorption*. When a sample analyzed in transmission geometry is tilted, the path length of the x-rays within the sample increases much more than the increase in the diffracting volume, resulting in a strong decrease in diffracted intensity. According to Schulz (1949b) and Cullity (1978), the intensity of the reflected x-ray, in dependence on the Bragg angle θ and the tilting angle ω ($\alpha = 90^\circ - \omega$), can be derived from

$$\frac{I_\omega}{I_{\omega=0^\circ}} = \frac{\cos \theta}{\mu t} \cdot \frac{\exp\{-\mu t / \cos(\theta - \omega)\} - \exp\{-\mu t / \cos(\theta + \omega)\}}{\exp\{-\mu t / \cos \theta\} \cdot \{\cos(\theta - \omega) / \cos(\theta + \omega) - 1\}} \quad (4.5)$$

where μ is the linear absorption coefficient (Section 3.5). In the case of reflection of x-rays at an “infinitely” thick sample, the increase in absorption is exactly balanced by the increase in diffracting volume, such that the reflected integrated intensity remains constant and a special correction is not necessary. In the case of very thin samples (thin films), however, the volume increase is dominating and an absorption correction becomes necessary. The ratio between the reflected intensities from a sample of thickness t and an infinite thick sample is given by (Schulz, 1949a)

$$\frac{I(t)}{I_\infty} = 1 - \exp\left(-\frac{2\mu t}{\sin \theta \cos \alpha}\right) \quad (4.6)$$

In Figure 4.21b, the evolution of $I(t)/I_\infty$ with α is shown for copper sheet with three different thicknesses, again normalized to 100% for $\alpha = 0^\circ$ (Figure 4.21a). For the 2 mm “thick” sample (or a material with a very high absorption coefficient) the correction factor stays constant at 1. With decreasing sample thickness, and especially for the 0.1 μm thin film, the intensity increases greatly with sample tilt, however. Generally speaking, when the sample thickness is below the penetration depth of the x-radiation, a correction of the absorption/volume effect (Equation 4.6) is necessary (Chateigner et al., 1994).

Finally, it should be mentioned that any pole figure measurement is influenced by *counting statistics* that imposes an uncertainty on each measurement with a standard error of the net intensity (Cullity, 1978; Humbert, 1986). The number of counts N derived per time unit at a given sample position is subject to statistical scatter that, for sufficiently large N , follows a Gauss law with the average value N_0 and a standard deviation $\sigma = \sqrt{N_0}$. In the presence of a background, the situation is slightly more complicated (Figure 4.20). If N_p and N_{BG} are the number of counts obtained in the peak and the background, respectively, then the relative standard deviation σ is

$$\sigma = \frac{(N_p + N_{BG})^{1/2}}{N_p - N_{BG}} \quad (4.7)$$

For instance, for $N_p = 1000$ and $N_{BG} = 100$, Equation 4.7 yields a relative standard deviation σ of 3.7%. Note that the error only depends on the *number* of pulses counted, and not on the *rate*. Thus, the accuracy of the measurements can be improved by prolonging the counting times. In the preceding example, doubling the measuring time would yield $N_p = 2000$ and $N_{BG} = 200$, and this would reduce the relative error to 2.6%.

After pole figure measurement and subsequent correction of the data with respect to background intensity, defocusing error, and, if necessary, absorption, the pole figure data are available as number of counts, or counts per second, per pole figure point (α, β) . For representation of the pole figures and for a subsequent evaluation, however, it is necessary to normalize the intensities to standard units that are not dependent on the experimental parameters. The commonly used convention is to express the data in mrd. For that purpose, a normalization factor N is derived by integrating over the measured and corrected intensities $I_{corr}(\alpha, \beta)$ over the full pole figure and weighting the intensities with regard to their areal contribution in the pole figure:

$$I_{norm}(\alpha, \beta) = \frac{1}{N} \cdot I_{corr}(\alpha, \beta) \quad (4.8)$$

where $N = \int_i I_{corr}(\alpha, \beta) \sin \alpha_i / \int_i \sin \alpha_i$. Therewith, the integral over the full pole figure range becomes 1, which means that the pole figure of a randomly oriented standard sample would be 1 at all points. Pole figure regions with densities larger than 1 indicate that more lattice planes are aligned in those directions than in a random sample, and vice versa.

For incomplete pole figures a true normalization is not possible, but a pseudonormalization factor N' can be derived by summation over the measured pole figure range:

$$N' = \frac{\sum_{\alpha_{min}}^{\alpha_{max}} \sum_{\beta=0}^{360} I_{corr}(\alpha, \beta) \cdot (\cos(\alpha - \Delta\alpha/2) - \cos(\alpha + \Delta\alpha/2)) \cdot \Delta\beta}{2\pi \cdot (\cos(\alpha_{min} - \Delta\alpha/2) - \cos(\alpha_{max} + \Delta\alpha/2))} \quad (4.9)$$

A more accurate normalization factor can be derived during a subsequent ODF analysis.

4.3.7 Inverse Pole Figures

In most cases, inverse pole figures—the presentation of the sample axes with respect to the crystal axes (Section 2.5.2)—are recalculated from the 3-D ODF that has been derived from conventional pole figure data of the corresponding

sample (Section 5.3.2). However, inverse pole figures (not to be confused with “pole figure inversion,” Section 5.3.1) can also directly be measured by means of diffraction methods (Harris, 1952; Morris, 1959; Bunge and Roberts, 1969). The sample is mounted in reflection geometry with its normal parallel to the direction of interest—usually RD, TD, or ND—and the reflected intensities are measured in a $\theta/2\theta$ scan. The resulting peak intensities are normalized to the intensities of a standard sample with random texture and then the inverse pole figure can be constructed.

Thus, inverse pole figures can be derived with fixed sample geometry; no rotations in χ or ϕ are necessary, so that a standard powder diffractometer without Eulerian cradle can be used. In particular, use of a PSD (Section 4.3.4) or energy-dispersive detector (Section 4.3.5) allows rapid acquisition of the necessary data without any moving parts.

However, this technique only yields the intensities of reflections hkl that are in the accessible θ range, that is, θ is smaller than 90° , and for which no extinction rules apply. Furthermore, most experimental points lie on symmetry lines so that this method is much inferior to the conventional pole figures with a continuous coverage of the pole sphere. As an example, Figure 4.22 shows the inverse pole figure of a rolled steel sheet that consists of only eight reflections. The results are superimposed on the inverse pole figure that has been recalculated from the ODF of the same sample, indicating fairly good agreement between both methods. It is seen that although for high-symmetry materials only a couple of diffraction peaks can be considered, the coverage is better for materials of low crystal symmetry with line-rich

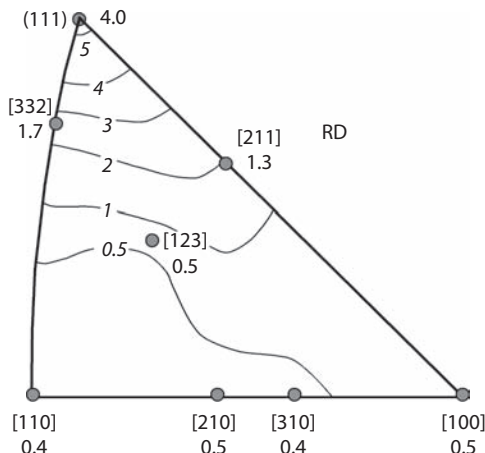


FIGURE 4.22

Inverse pole figure of the sheet normal direction ND obtained from a commercially produced stabilized steel sheet in the temper-rolled condition. Measured points—inverse pole figure measured as described in the text; intensity lines—inverse pole figure recalculated from the three-dimensional ODF. (Adapted from Bunge, H.-J. and Roberts, W.T., *J. Appl. Crystallogr.*, 2, 116, 1969.)

diffraction patterns. Application of an energy-dispersive detector is advantageous, as this allows one to consider high-index planes that correspond to the short-wavelength components of the x-ray spectrum (Szpunar et al., 1974; Okamoto et al., 1985). However, the decreasing intensity of high-index reflections and problems with peak separation still limit the application of this method for texture analysis.

Finally, it should be mentioned that from several inverse pole figures—obtained for different sample directions—the ODFs can be calculated in a similar way as that used for pole figures (Section 5.3.2).

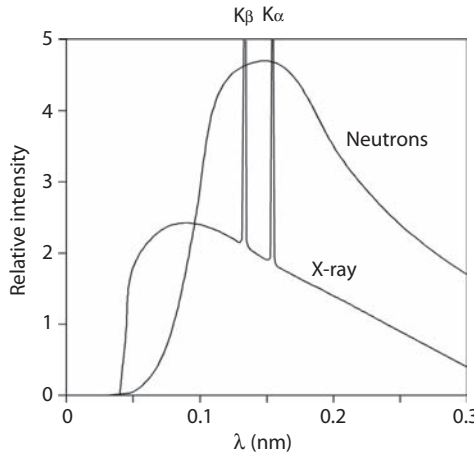
4.4 Neutron Diffraction Methods

The first texture measurements by means of neutron diffraction were performed in 1953 by Brockhouse at Chalk River National Laboratory in an attempt to determine magnetic structures in steel (Brockhouse, 1953). In the 1960s, this technique was further developed by Tobisch and coworkers (Kleinstück and Tobisch, 1968; Tobisch et al., 1969; Kleinstück et al., 1976) and the advantages of neutron diffraction for texture analysis have been established (Section 3.6.2). Nowadays, the application of neutron diffraction for texture analysis is well established; see the reviews by Szpunar (1984), Welch (1986), Bunge (1989a), Wenk (1991, 2006), and Brokmeier (1997, 2006). In principle, pole figure analysis by neutrons is equivalent to x-ray pole figure measurements (Section 4.4.1). However, more sophisticated methods like time-of-flight (TOF) measurements (Section 4.4.2) offer additional advantages over x-ray diffraction techniques.

4.4.1 Pole Figure Measurement by Neutron Diffraction

Texture investigations by means of neutron diffraction are mostly performed in research reactors where nuclear fission provides a supply of fast neutron. The neutrons are slowed down by interaction with appropriate moderators, until they approach an approximate Maxwell velocity distribution with a maximum wavelength in the desired range from 0.05 to 0.3 nm, which is suitable for diffraction experiments (Figure 4.23). However, no pronounced maxima analogous to the characteristic x-ray peaks form, so that application of a monochromator is required to receive monochromatic radiation. Often copper (111) or graphite (0002) monochromator crystals are used.

The advantages of TOF measurements (Section 4.4.2) have encouraged interest in pulsed neutron sources, and this has drawn attention to using linear accelerators for generating neutron beams. When pulses of electrons accelerated to energies of 100 MeV fall on a target of a heavy element, through the intermediary of γ rays, pulses of neutrons are generated that can be used

**FIGURE 4.23**

Wavelength spectrum of a thermal neutron source, compared with the spectrum of a copper x-ray tube with characteristic lines.

for diffraction experiments (Bacon, 1975). A more efficient way is to use high-energy proton beams that produce neutrons by a process called *spallation* (Bauer, 1989; Lisowski et al., 1990). When high-energy protons with energies of several 100 MeV hit the atomic nuclei of a given target material, neutrons and a variety of other spallation products are produced. The spallation products may react with other target nuclei, producing a cascade of particles with approximately 10–50 times more neutrons emitted than incident protons. To utilize these processes for generating a neutron beam, a high-energy (approximately 1 GeV) proton beam is generated in a particle accelerator and focused on a heavy metal target, for example, lead or tungsten. The energy of the resulting neutrons is too high (i.e., the wavelength is too small) for diffraction experiments, however, which means that moderation to thermal Maxwell distribution is necessary.

The principles of pole figure analysis by neutron diffraction are equivalent to x-ray pole figure measurements. The neutron detector is set to the corresponding Bragg angle 2θ for the selected lattice planes $\{hkl\}$. The pole densities of that lattice plane in different sample directions are scanned with a goniometer by rotating the sample around two axes, φ and χ , corresponding to the pole figure angles β and α , to cover the entire orientation range (Section 4.3.2). The main difference between neutron and x-ray diffraction is the much lower, almost negligible, absorption of neutrons by matter (Table 3.4). Therefore, large samples, usually several centimeters in size, can be analyzed in transmission geometry. As shown by Tobisch and Bunge (1972), roughly spherical samples are completely sufficient for neutron experiments. In contrast to x-ray experiments, where the x-ray beam must not leave the sample surface, the sample must not leave the neutron

beam for neutron diffraction experiments. Then, no intensity corrections are necessary and complete pole figures (up to $\alpha = 90^\circ$) can be obtained in one scan. The number of grains encountered is much larger, usually, by four to five orders of magnitude, which means that grain statistics is much better. Because of the low absorption, environmental stages can be used for *in situ* investigations during heating, cooling, and straining of the samples (Hansen et al., 1981; Elf et al., 1990).

One drawback of neutron diffraction is that even in high flux reactors, the intensity is much lower compared to x-ray experiments, so that counting statistics (Equation 4.7) become an important consideration. A conventional pole figure scan takes between 6 and 48 h, compared to approximately 30 min in x-ray diffraction (Section 4.3.3). Since further access to neutron beam time is generally limited, techniques to accelerate the pole figure measurement are of great interest.

To speed up neutron diffraction experiments, the faster equal area scanning grids are frequently used (Section 4.3.3). Furthermore, measuring time can be cut down very efficiently by using PSDs that record the diffracted intensities of several pole figures simultaneously. In most applications, a curved 1-D PSD is mounted to record a certain range of the 2θ spectrum (Bunge et al., 1982; Will et al., 1989), as discussed in Section 4.3.4 for x-ray texture analysis. Unlike in x-ray diffractometry, however, the samples analyzed by neutrons are typically small compared to the goniometer dimensions, and therefore the focusing condition is still fulfilled for larger deviations from the exact Bragg–Brentano condition. This allows determination of continuous diffraction profiles from which integrated intensities can be extracted and used for pole figure determination, peak separation, etc.

An alternative arrangement with a vertical detector fixed at the position $2\theta = 90^\circ$ was realized at the neutron source DR3 at Risø National Laboratory, Denmark (Juul Jensen and Kjems, 1983) before the reactor was shut down in 2000. This unique arrangement simultaneously recorded the diffracted intensities corresponding to a range of positions within a given pole figure, rather than one point of several pole figures, so that fast texture analysis was possible. With recording times of about 15 min per pole figure, this system could be used for *in situ* investigations, for example, in recrystallization kinetics or phase transformations (Juul Jensen and Leffers, 1989). To measure different pole figures, the wavelength of the incident neutrons had to be varied, which was realized by a special setup that allowed continuous rotation of the entire detection unit—the monochromator, the beam path between monochromator and sample, and the Eulerian cradle—about the center of the monochromator.

4.4.2 Time-of-Flight Measurements

In analogy to the energy-dispersive x-ray diffractometry described in Section 4.3.5, an alternative method to measure large numbers of pole

figures simultaneously utilizes the *polychromatic* nature of the neutron source. However, as no energy-sensitive detectors for neutrons are available, another way had to be found. The method is to determine the flight time of the neutrons, which in a given experimental setup is a measure for their energy or wavelength, giving rise to the term *time-of-flight* (TOF; Szpunar, 1984; Feldmann, 1989; Wenk, 1994). It follows from the de Broglie relation (Equation 3.1) that energy and wavelength of the neutrons are related to their velocity through

$$E = \frac{1}{2} m_N v_N^2 = \frac{h^2}{2\lambda^2 m_N} \text{ or } v_N = \frac{h}{\lambda m_N} \quad (4.10)$$

where m_N is the mass and v_N the velocity of the neutrons. Thus, for neutrons with an energy spectrum between 10^{-3} and 10 eV (corresponding to wavelengths between $\lambda = 0.5$ and 0.01 nm), the velocities would range from $v_N = 10^3 \text{ m s}^{-1}$ to $4 \times 10^4 \text{ m s}^{-1}$. In a given experimental arrangement, such velocities can be determined in terms of the flight times of the neutrons. Figure 4.24 shows a schematic arrangement to perform TOF measurements. The total flight time T of the neutrons is given by their velocity v_N and the distance they travel, which is the length L_1 between source and sample plus the length L_2 between sample and detector. Thus, the relation between TOF, t_{TOF} and the energy E —or wavelength λ —is given by

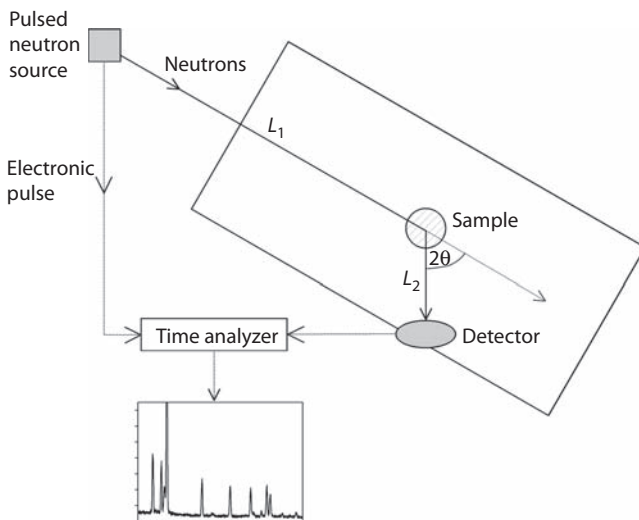


FIGURE 4.24

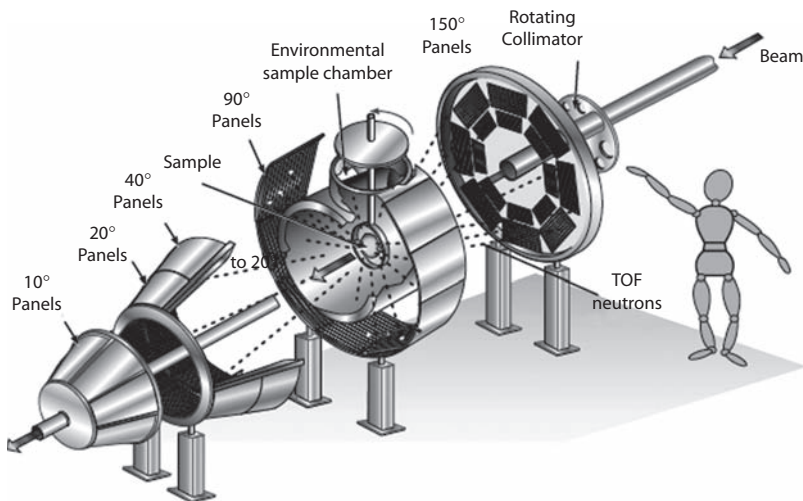
Schematic arrangement to perform TOF measurements. The total flight time T of the neutrons is determined by their velocity and the length L_1 between source and sample and L_2 between sample and detector.

$$t_{\text{TOF}} = \frac{(L_1 + L_2)}{v_N} = \frac{(L_1 + L_2)}{(2E / m_N)^{1/2}} = \frac{(L_1 + L_2) \cdot h}{\lambda m_N} \quad (4.11)$$

This means that in a typical setup with flight lengths $L_1 + L_2$ of approximately 10–50 m, time differences of the order of milliseconds have to be resolved. To apply TOF in practice for determination of diffraction spectra, a pulsed neutron source is required, that is, TOF experiments have to be conducted either at a pulsed reactor (Feldmann et al., 1980; Walther et al., 1995) or at a spallation source (Wenk et al., 1988b; Helming et al., 1992; Jansen et al., 1998). The detector signal is stored in a multichannel time analyzer that is started synchronously with each neutron pulse. The recorded spectrum is successively built up in dependence on the neutron flight time, which means that the first signals that correspond to the fastest (i.e., high energy/low wavelength) neutrons are stored in the first channels and so on.

Considering the possibilities of PSDs and TOF, it appears that a combination of both would substantially speed up pole figure measurements, and this has indeed been realized at the Intense Pulsed Neutron Source (IPNS) at Argonne National Laboratory and at the Los Alamos Neutron Science Center (LANSCE) (Wenk et al., 1991). With the installed setups, coverage of the entire hemisphere of reciprocal space—that is, complete pole figures for a number of different reflections hkl plus background data—requires about 27 different sample settings as opposed to the 1368 points for *one* pole figure measured in conventional angular-dispersive diffractometry (Section 4.3.3).

In 1998–2002, a further refined neutron TOF diffractometer called HIPPO (high-pressure preferred orientation) was designed and installed at LANSCE (Wenk et al., 2003; Vogel et al., 2004). HIPPO achieves very high neutron count rates by virtue of a short (9 m) initial flight path and a novel 3-D arrangement of detector banks with 1360 ^3He tubes situated on five conical rings with scattering angles ranging from $2\theta = 10^\circ$ to 150° around the incident beam direction (Figure 4.25). The large detector coverage of 4.8 m^2 allows texture measurements with a very small number of changes of sample orientation, typically between four and eight. Furthermore, rotation around a single axis is sufficient, compared to the standard two-circle goniometers employed on conventional neutron and x-ray texture instruments. This provides the unique capability of rapid texture measurements under various sample conditions, such as temperature and uniaxial stress. The exceptionally high data rates of HIPPO also make it useful for time-resolved studies. In addition to the standard ancillary equipment (100-specimen sample changer, closed-cycle He refrigerator, furnace), HIPPO has unique high-pressure anvil cells capable of achieving pressures of 30 GPa at ambient and high (2000 K) temperatures with samples up to 100 mm^3 in volume. A low-temperature gas cell allows studies in the pressure range up to 5 kbar and temperatures between 10 K and ambient temperature. The uniaxial stress-rig CRATES, built by the Technical University Hamburg-Harburg, Germany, allows the study of crystal lattice strains and texture changes *in situ* during deformation (Hartig et al., 2006).

**FIGURE 4.25**

Schematic view of the neutron time-of-flight diffractometer HIPPO with five banks of detector panels arranged on rings of constant diffraction angle. The sample is located in a sample chamber. For scale a sketch of a fairly large person is added; the distance from the 150° panels to the 10° panels is 3 m. (Courtesy of S. Vogel)

4.5 Texture Measurements in Low-Symmetry and Multiphase Materials

Of course, the principles of texture analysis by x-ray or neutron diffraction and subsequent ODF calculation described so far apply for all materials, independent of their crystal structure. However, in the case of multiphase materials or structures with low crystal symmetry, there are some specific additional problems that have to be considered (Bunge, 1985b; Brokmeier, 1989):

- Problems with peak separation caused by peak-rich diffraction spectra in both multiphase and low-symmetry materials (Section 4.5.1)
- Volume fraction of the various phases in multiphase materials (Section 4.5.2)
- Anisotropic absorption of the reflected x-rays in multiphase materials (Section 4.5.2)

In general, neutron diffraction offers some advantages over x-rays in analyzing both low-symmetry and multiphase materials. It should be emphasized here that the problems mentioned do not occur when the samples are studied by means of single-grain orientation methods (e.g., EBSD), where the textures of all phases can be derived separately (Section 10.4.5).

4.5.1 Peak Separation

Both multiphase materials and low-symmetry materials are characterized by line-rich diffraction spectra; Figures 4.26a and 4.26b show examples for two-phase α/β brass with 20 vol% β phase and for calcite with trigonal crystal structure, respectively. In such line-rich diffraction spectra, the various diffraction peaks may be situated very close together, which can cause the problem of a proper separation of the contributions of the corresponding reflections/phases. Figure 4.26a shows that the $\{111\}$ peak of the α brass is situated very close (0.5°) to the $\{011\}$ - β -peak. In particular, with peak broadening at high sample tilting during pole figure analysis, this can lead to a substantial overlapping of such closely spaced diffraction peaks, which makes texture analysis in complex crystal structures—e.g., high-temperature superconductors—a very challenging task (Wenk et al., 1996).

In contrast to the *partial coincidence* of reflection peaks in the examples in Figure 4.26, diffraction peaks can also *completely overlap*. For instance, in cubic metals the two sets of lattice planes $\{330\}$ and $\{411\}$ have the same lattice spacing d , namely, $d_{330} = d_{411} = a / \sqrt{18}$ (a : lattice constant). Consequently, the Bragg angles are identical too, which means that these two diffraction peaks completely coincide (Figure 4.19). Although this is not really a problem in the cubic structures—the example was chosen only as a simple illustration of the effect—there are more severe cases where all diffraction peaks of a given phase are systematically overlapped by another phase that is usually related by a phase transformation. Examples include ferrite and martensite in dual-phase steels (Schwarzer and Weiland, 1988) and the primary α phase and the martensitic α'' phase in two-phase titanium alloys (Dunst and Mecking, 1996). Enantiomorphic materials, that is, materials consisting of left-handed

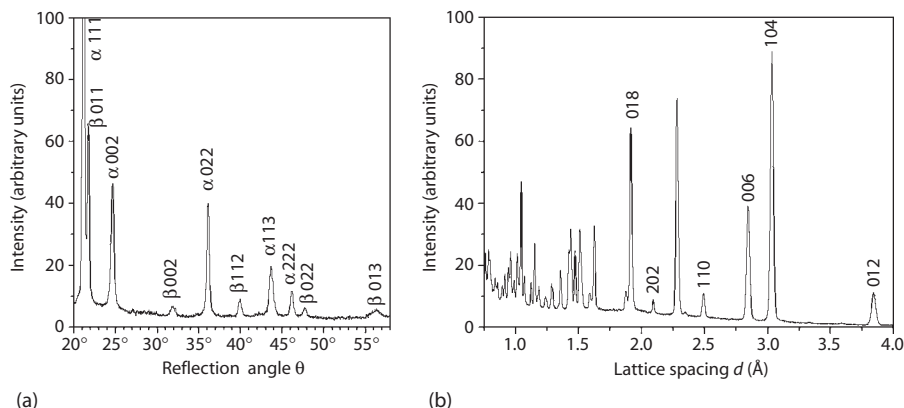


FIGURE 4.26

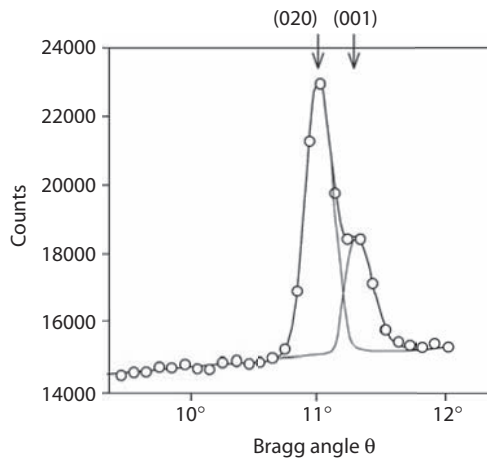
Examples of line-rich diffraction spectra. (a) Two-phase brass (Cu–40%Zn, x-ray $\theta/2\theta$ spectrum). (From Engler, O. and Juul Jensen, D., *Scr. Mater.*, 30, 25, 1994. With permission.) (b) Calcite (neutron TOF spectrum.) (Data from Lutterotti, L., Matthies, S., Wenk, H.-R., Schultz, A.J., and Richardson, Jr. J.W., *J. Appl. Phys.*, 81, 594, 1997.)

and right-handed crystals, can be considered as special cases of two-phase materials with complete coincidence of *all* peaks so that the textures of the two phases cannot be determined from macrotexture pole figures (Bunge, 1985b). In such cases of complete peak coincidence, texture analysis has to be performed by electron diffraction (microdiffraction) techniques that determine the textures of the various phases independently.

In the case of a *partial coincidence*, peak separation can slightly be improved by using a smaller receiving slit of the detector (Section 4.3.4). Use of an x-ray tube producing x-rays of a longer wavelength (Table 4.1) would shift the reflections toward larger Bragg angles θ and, in particular, would increase the distance $\Delta\theta$ between neighboring peaks. However, this can eventually result in the loss of diffraction peaks at too high reflection angles ($\theta \geq 90^\circ$) and, furthermore, the problem of fluorescence must be considered (Section 4.3.1). Likewise, second-order peaks at larger θ are more widely spaced, but they suffer from poor signal-to-noise ratio (Figure 4.26a). Neutron diffraction is superior to x-ray diffraction as neutron diffractometers in general offer a higher spectral resolution, especially at large Bragg angles (Section 3.6.2). However, in many cases only a few peaks are affected; for example, in α/γ -duplex steels only the {111} peak of the face-centered cubic (fcc) γ austenite and the {011} peak of the body-centered cubic (bcc) α ferrite overlap (similar to that in Figure 4.26a). In such cases usually enough nonoverlapping pole figures are available to compute the ODF; if necessary, the overlapping pole figures can eventually be recalculated (Section 5.3.2).

A very efficient way to separate partially overlapping peaks is to record the entire diffraction profile of the overlapping peaks by means of a PSD or area detector (Section 4.3.4) or an energy-dispersive detector (Section 4.3.5). The peaks are fitted with appropriate functions that allow derivation of the integral intensities of the corresponding pole figures (Jansen et al., 1988; Wenk and Pannetier, 1990; Antoniadis et al., 1990; Rodriguez-Navarro, 2006). Figure 4.27 shows an example of separation of the (020) and (001) peaks in feldspar, which are less than 0.5° apart.

Dahms and Bunge (1989) developed an analytical deconvolution scheme that achieves peak separation by an iterative procedure of ODF calculation and recalculation of the corresponding pole figures until a proper peak separation is obtained. This method even allows determination of the textures of two phases in cases where some peaks *completely* overlap, and where all other methods described so far would necessarily fail. Examples of successful peak separation have been given for low-symmetry materials (natural quartz; Dahms, 1992), for multiphase systems (α/γ -titanium aluminides [Dahms et al., 1994] and two-phase titanium alloys [Dunst and Mecking, 1996]), as well as for a combination of both low-symmetry and multiphase materials, namely, paragneiss, a natural mineral consisting of quartz, feldspar, and mica (Heinicke et al., 1991). A similar scheme to separate overlapping peaks based on the direct WIMV method (Section 5.3.3) has been developed by Kallend et al. (1991b).

**FIGURE 4.27**

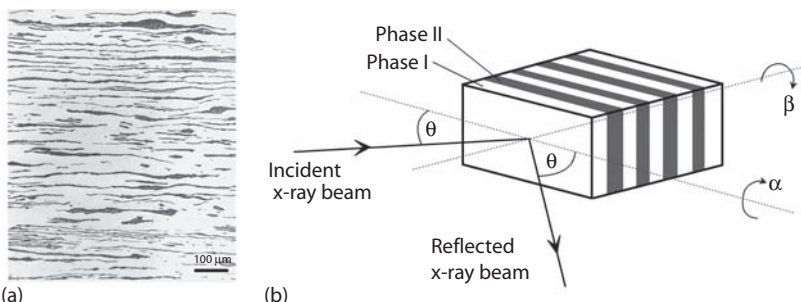
Separation of two partially overlapping feldspar diffraction peaks recorded by a linear PSD. (Adapted from Brokmeier, H.-G., *Textures Microstruct.*, 10, 325, 1989.)

Rather than extracting information from single diffraction peaks, it would be more efficient to use the whole diffraction spectrum and extract texture information in a way similar to that by which crystallographers extract structural information from a powder pattern with the Rietveld technique (Rietveld, 1969). A method proposed by Wenk et al. (1994) relies on an iterative combination of crystallographic Rietveld profile analysis and quantitative ODF calculation (Rietveld texture analysis [RITA]). Meanwhile, this method has been applied to several synthetic test cases (Matthies et al., 1997; Wang et al., 1997) as well as to geological materials (Lutterotti et al., 1997; Von Dreele, 1997; Wenk et al., 2001) and complex oxide ceramics (Jones et al., 2004; Guilneau et al., 2005). In all cases resolution was very good, even for the highly overlapped regions of the diffraction spectrum. Thus, the RITA method can be expected to improve quantitative texture analysis of low-symmetry compounds and multiphase materials with overlapping peaks, to enable efficient data collection by requiring only a small part of the pole figure, and to make maximal use of data obtained by means of energy-dispersive methods that record complete spectra with many diffraction peaks, especially at neutron TOF facilities (Section 4.4.2).

4.5.2 Multiphase Materials

Besides the problem of overlapping peaks treated in the preceding section, two further problems have to be considered in the case of multiphase materials:

1. The reflected intensity is proportional to the volume fraction of the considered phase and hence it becomes difficult to determine properly pole figures of phases with small volume fractions (Bunge, 1985b). In Figure 4.26a, it is obvious that in the case of 20% β brass, the diffraction peaks of the minor component are much smaller than those of the α phase—resulting in a rather poor signal-to-background ratio for the former—though in this case the textures of both phases could properly be determined (Engler and Juul Jensen, 1994). In general, 5 vol% can be estimated to be the lower limit for texture analysis by x-ray diffraction techniques. Because of the much higher penetration depth of neutrons, a much larger volume contributes to the reflected intensities in neutron diffraction, yielding sufficient counting statistics also for phases with small volume fractions. Brokmeier and Bunge (1988) obtained reliable texture data in aluminum with only 1% copper and even the diffraction peaks of as little as 0.05% copper in aluminum could be recorded (Brokmeier, 1989).
2. A given phase may be strongly elongated. In particular, in deformed materials the various phases are typically highly aligned along the deformation direction (Figure 4.28a). Differences in the absorption of x-rays in the different phases can cause errors in x-ray texture measurements (Bunge, 1985b). Depending on the sample setting—Bragg angle θ and pole figure angles α and β —the intensity reflected in a given phase has to pass through different lengths of the other phase, and hence it is differently attenuated by absorption (Figure 4.28b). In the case of large differences in absorption coefficients in the different phases, this can cause large errors in the intensity distribution in the pole figures obtained. For neutron diffraction, absorption is much lower (Section 3.6.2) and—dependent of the sample setting—the

**FIGURE 4.28**

(a) Microstructure of cold-rolled two-phase Cu-40%Zn illustrating the alignment of the phases with deformation. (b) Schematic representation of the reflection of x-rays during pole figure measurements, illustrating the occurrence of anisotropic absorption in layered two-phase structures.

neutrons are scattered from the total sampled volume so that neutron absorption is virtually not affected by a possible alignment of the various phases (Bunge, 1985b; Brokmeier, 1989; Engler and Juul Jensen, 1994).

In conclusion, for texture measurements in multiphase materials, neutron diffraction is advantageous compared to x-ray diffraction because of the much higher penetration depth in matter of the former (Bolmaro and Brokmeier, 1999). Smallest volume fractions can be determined with sufficient counting statistics and the anisotropic absorption as described for x-rays can be neglected in the case of neutron diffraction.

4.6 Sample Preparation

One of the advantages of neutron diffraction experiments is the flexibility in the sample geometry suitable for neutron texture analysis, so that in most cases only a minimum of sample preparation is required. Because of the large penetration depth of neutrons, bulk samples of centimeter size can readily be investigated in transmission geometry (Section 4.4.1). Neutron texture analysis was greatly advanced by the spherical sample method (Figure 4.29) since in this geometry no absorption correction is necessary, yielding highest accuracy of the texture (Tobisch and Bunge, 1972). The deviations from the exact sphere may be quite large, however, so that cylindrical or even cubic samples, maybe with rounded edges, are usually sufficient (Welch, 1986; Brokmeier and Ostwaldt, 1996). Thus, roughly spherical bulk samples can generally be analyzed without special sample preparation, which makes neutron diffraction attractive for geological studies. For analysis of too thin specimens, such as sheet material, a cylindrical composite sample may be produced by stacking several disks cut from the sheet and tied together with screws or a wire (preferably of a material with different diffraction peaks), as shown in Figure 4.29e. Gluing is less suitable since the hydrogen in the glue produces a significant amount of neutron scattering. One may wish to

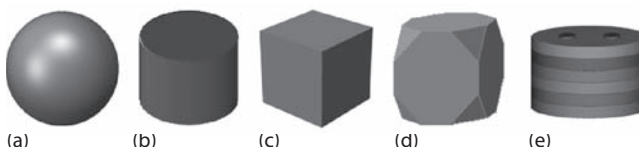


FIGURE 4.29

Samples for texture analysis through neutron diffraction. (a) Spherical sample; (b) cylindrical sample; (c) cubic sample; (d) cubic sample with rounded edges; (e) cylindrical composite sample produced by stacking several disks cut from a thin sheet.

first electropolish or etch the sheets so as to reduce the influence of a possible surface texture (Juul Jensen and Kjems, 1983).

In contrast, the low penetration depth of x-rays in most materials usually entails a certain amount of sample preparation. Texture measurements in transmission geometry require very thin parallel samples with thickness typically below 100 μm , so that this method is restricted to foils or thin wires that can be penetrated by the x-rays. Thicker samples may be thinned by grinding and etching. Today, a vast majority of texture measurements are performed in reflection geometry, and in the following text, we will address some ways for an appropriate preparation of the samples for x-ray texture analysis in reflection geometry.

To obtain the textures of wires, a bundle of parallel wires is mounted on a flat holder (Wenk, 1998). In most cases, production of the wires results in very heterogeneous textures with the mantle of the wire being different from the core. Provided the penetration depth of the x-rays used is not too large, the surface texture can be measured from the wires as they are, that is, without any preparation. Subsequently, the surface can be removed by chemical etching and the texture of the core determined (Montesin and Heizmann, 1992). When only the average texture is of interest, texture measurements can be conducted on the cross section of a bundle of wires. However, for analysis of axial-symmetric textures in general, an arrangement with the symmetry axis being parallel to the sample surface, rather than perpendicular to it, is advantageous with a view to separation of crystallographic texture and artifacts caused by geometrical corrections (Wenk and Phillips, 1992).

Preparation of bulk samples, including sheet materials, for x-ray pole figure measurements in reflection geometry is usually easy and can be performed with standard metallographic techniques. Samples can be round or rectangular shaped, with their size typically ranging from 10 to 30 mm and a thickness of 0.5 mm up to several millimeters. The sample surface must be flat, and the samples should carefully be ground down to 1000 grit. Finer grinding or additional polishing is generally not necessary. However, the sample surface must not show any deformation as this would alter the texture of the affected layers and, therewith, the results obtained. Therefore, chemical etching or, if appropriate, short electropolishing of the surface is essential. For most metals, standard etching reagents that homogeneously attack the surface yield satisfactory results, for example,

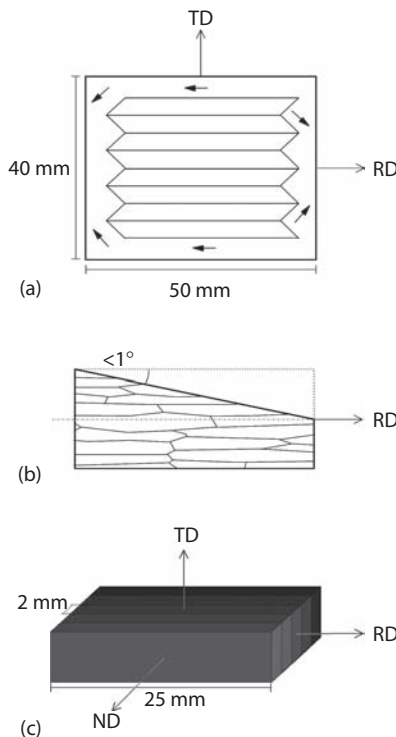
- For *aluminum* and many *aluminum alloys*, best results are obtained by etching for 10–20 min in approximately 50% NaOH. Heating of the solution to $\sim 60^\circ\text{C}$ ensures a more homogeneous etching, but should be avoided for deformed samples to prevent recovery. After the etch, many aluminum alloys (in particular, copper-containing ones) have a gray or black layer that can readily be removed in $\sim 10\%$ HNO₃.
- *Copper* can be etched in diluted HNO₃. For copper alloys too high concentrations (e.g., exceeding 50%) should be avoided as they might selectively etch different phases.

- *Ferritic steels*, including low-carbon steel and iron–silicon transformer steel, can be etched for 1–2 min in a solution of 100 mL H_2O_2 and 5–15 mL HF. In alloys with high chromium contents, 10 mL HNO_3 and 15 mL HCl can be added.
- Etchants suitable for some other bcc metals are 100 mL HCl, 90 mL HF, 100 mL HNO_3 , 30 mL H_2O_2 (*tungsten*); 100 mL H_2SO_4 , 40 mL HNO_3 , 40 mL HF (*tantalum*); 100 mL HNO_3 , 35 mL HF, 1–5 mL H_2SO_4 (*niobium*); and 100 mL HNO_3 , 8 mL HF or 100 mL HCl, 30 mL H_2O_2 (*molybdenum*). Etching time of 20–30 min removes 5 μm (Raabe, 1992).
- Kelly et al. (1996) developed an etching technique for *tantalum* and *tantalum alloys*, which can be used for preparation of samples for x-ray analysis. After standard mechanical grinding and polishing, the specimens are swab etched with a solution consisting of lactic acid, HNO_3 , and HF. It turned out that this technique is suitable for a surprising variety of materials, including other bcc metals and alloys as well as *titanium* and *titanium alloys*.

For ceramics and geological materials, sawing and mechanical grinding are generally adequate. The bulk samples are usually cut with a diamond saw and then further ground with silicon carbide, alumina, or diamond abrasive powders down to a grit size of 10 μm .

Owing to the small penetration depth of x-rays, grain statistics often is a problem for x-ray texture analysis. If we assume a penetration depth of 0.1 mm and an area of $10 \times 10 \text{ mm}^2$ being irradiated by the x-ray beam, the recorded volume is of the order of 10 mm^3 . Then, for a material with a grain size of 25 μm , more than 10^6 grains contribute to the reflected intensity that definitely yields good statistical evaluation. For a grain size of 250 μm , in contrast, only slightly more than 1000 grains are recorded, which is anticipated to be the lower limit for sufficient grain statistics (Section 9.3.3). The number of grains that contribute to the reflected intensity can be enlarged by a translation movement of, for example, 10 mm in the plane of measurement (Bunge and Puch, 1984), provided the sample is sufficiently large. For samples with elongated grains (deformed materials), it is advantageous to perform this translation perpendicular to the direction of the grain elongation (i.e., parallel TD for rolled sheets) as this enlarges the number of encountered bands.

To enlarge further the sampling area, it has been proposed to perform a meander-shaped scan of the sample surface (Hirsch et al., 1986). By this, a sampling area of as much as $50 \times 40 \text{ mm}^2$ can be completely scanned (Figure 4.30a), so that textures of coarse-grained materials can be determined. However, this method requires a rather complicated control of the goniometer head with the possibility for an x/y-sample positioning. Rather, it is much easier to measure pole figures of several standard-sized samples and then average the resulting pole figure data (Engler et al., 1996b). This procedure is easy to perform and the sampling size is (theoretically) unlimited. It must be emphasized

**FIGURE 4.30**

Measures to increase the sampling area during x-ray texture analysis. (a) Meander scan: The sample is translated in x and y direction, and at the end of each x-stroke of 42 mm, a lateral movement of 4 mm is carried out. After eight of these lateral shifts, the direction is reversed. (b) Sample with slightly slanted surface averaging over several through-thickness layers (not drawn to scale). (c) "Sandwich" sample stacked from several rotated pieces.

that to enlarge the sampling area these methods require a homogeneous texture; in other words no pronounced texture gradients should exist throughout the positions from which the different scans are taken.

For rolled sheets with strongly elongated but very thin deformed bands, the measuring statistics can also markedly be improved by preparing the sample with a slightly slanted surface (Figure 4.30b). If we allow for a maximum angle of 1°, which is tolerable in most cases, at a sheet sample of length 25 mm, a depth profile of 450 µm would be sampled, which for most materials is significantly more than the average penetration depth of x-rays (Table 4.2). The "extreme case" of a sample with a slanted surface would be a sample that is prepared perpendicular to the reference direction—rotated by 90° about one of the reference directions. For example, in the case of hot-rolled bands, preparation of a sandwich sample from five pieces stacked together

gives very satisfactory results (Figure 4.30c). Note that in these cases, the resulting textures integrate over the sample thickness; that is, they reveal an average over the different layers of the sheet.

In any case, some preliminary knowledge on the microstructure and, if possible, on the texture of the material investigated is valuable to select the best way of sample preparation and, therewith, to achieve optimum experimental results.

4.7 Summation

Measurements of pole figures by means of x-ray diffraction started in the 1940s by introducing texture goniometers to scan the pole figures and electrical counters to record the reflected intensities. Since the 1960s, pole figures are also regularly determined by neutron diffraction. Today, automated computer-controlled systems are available and the corresponding measuring techniques and the necessary correction methods that have been introduced in this chapter are very well established, so that diffraction experiments can routinely be performed to yield reliable, quantitative results for macrotecture.

Because of the much easier access to x-ray goniometers than to neutron sources, a vast majority of pole figure measurements are performed by means of x-ray diffraction. Neutron diffraction offers some advantages, however, which are mainly attributed to the much lower absorption of neutrons by matter. The much greater penetration depth of neutrons in the sample material allows investigation of spherical samples of centimeter size in transmission geometry, which yields the opportunity to perform nondestructive texture measurements or *in situ* experiments. Complete pole figures can be obtained without intensity corrections. The grain statistics are better, which is of particular interest in coarse-grained samples or for detection of low volume fractions of a second phase.

Texture analysis can be greatly advanced by the use of PSDs or energy-dispersive detectors (in neutron diffraction: TOF experiments). In contrast to the conventional point detectors, these detectors record a part of the diffraction spectrum, so that the intensities of several pole figures, or large parts of one pole figure, can be measured simultaneously. This can be used for fast texture analysis—in online applications or *in situ* experiments. Furthermore, PSDs and energy-dispersive detectors greatly facilitate texture analysis in low-symmetry and multiphase materials with line-rich diffraction patterns, where overlapping peaks can be separated by peak profile analysis.

5

Evaluation and Representation of Macrotexture Data

5.1 Introduction

Chapter 4 introduced the common techniques used to determine macrotextures experimentally by means of x-ray and neutron diffraction. The direct output of such texture measurements is the reflected intensity in the form of two pole figure angles α and β , that is, the distribution of the poles in the traditional *pole figure*. Hence the pole figure is the obvious choice for a critical assessment of experimental texture results. This method is discussed in some detail in Section 5.2.

The projection of the 3-D orientation distribution onto a 2-D pole figure causes a loss of information, so it is not possible to determine the orientation density of crystallites in a polycrystalline sample, that is, its *texture*, from the experimental pole figures without a certain ambiguity. Thus, for quantitative analysis of macrotexture a 3-D description—in terms of the 3-D ODF—is required. However, unlike pole figures, ODFs cannot be directly measured by means of diffraction techniques; they need to be calculated from the pole figure data, typically from a set of several pole figures obtained from a given sample. Section 5.3 introduces the most common approaches to accomplishing this *pole figure inversion* and addresses their main advantages and disadvantages.

To display the 3-D ODF, a representation in an appropriate 3-D frame is required. Chapter 2 introduced several suitable orientation spaces, namely, Euler space (Section 2.6), cylindrical angle/axis space (Section 2.7), and Rodrigues space (Section 2.8). Among them, the Euler space is most often used to represent macrotexture data. Section 5.4 addresses the properties of Euler space and describes suitable techniques for displaying textures in Euler space. A “statistical” MODF can be derived from the ODF and displayed in Euler space. However, since the topic of misorientation distributions is more relevant to microtexture, the statistical MODF is discussed in Section 9.7 rather than in this chapter. The cylindrical angle/axis space and Rodrigues space are mostly used to represent microtexture data (Chapter 9),

but have not found wide applications in conventional macrotexture analysis so far.

Section 5.5 presents a number of examples of the most typical rolling and recrystallization textures of fcc, bcc, and hexagonal metals. It provides a guide to the characteristic texture types that are frequently encountered in metallic materials.

5.2 Pole Figure and Inverse Pole Figure

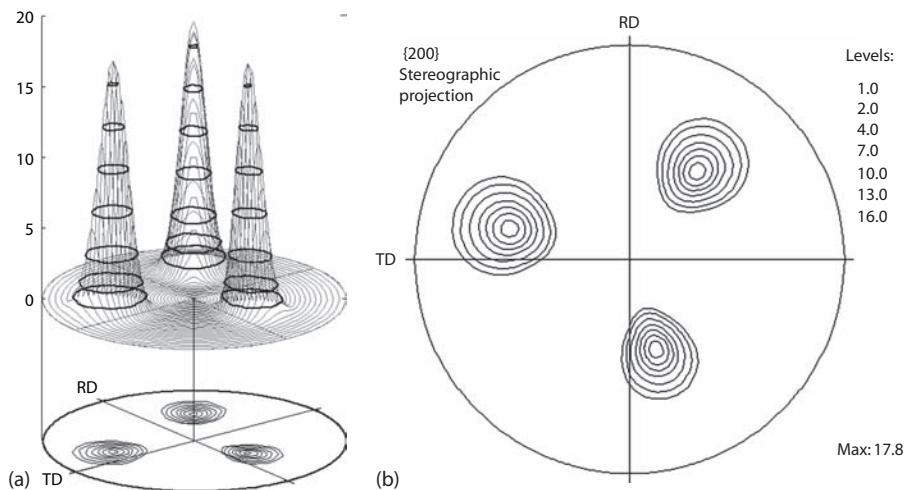
This section introduces the principles of representing textures in pole figures (Section 2.5.1) and inverse pole figures (Section 2.5.2), which form the backbone of macrotexture analysis. We will address means of normalizing and contouring the orientation densities in a pole figure, and illustrate use of the inverse pole figure, which finds applications in the case of axial symmetric textures (e.g., in tensile tests).

5.2.1 Normalization and Contouring of Pole Figures

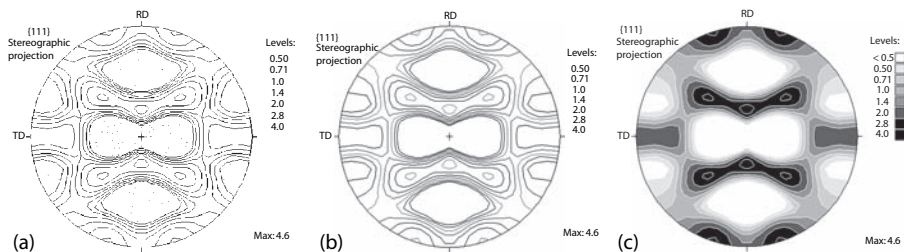
For a comparison of pole figures of different samples, it is necessary to normalize the orientation densities to standard units that are not dependent on the experimental setup. The commonly used convention is to express the data in m.r.d. of orientations, which means that the pole figure of a random standard sample would be “ $\times 1$ ” at all points (Section 4.3.6). Pole figure regions with intensities higher than this indicate that more lattice planes are aligned in those directions than in a sample with random texture, and vice versa.

The most commonly used way of contouring the orientation density in a pole figure is to draw lines of equal pole density, or equal intensity, as known from topographic or weather maps (Figure 5.1). Iso-intensity lines, also called contour lines or isopleths, are curves that connect contiguous points of the same pole density. As an example, every point along a line marked “ $\times 2$ ” indicates a pole density of two times random. Note that iso-intensity lines must not touch or cross, nor do they branch or fork.

The values of the various contour lines do not need to be linearly spaced. Often, it is more instructive to use logarithmic progression to reveal texture details (Figure 5.2a). For an easy visual comparison of different pole figures, it is of considerable help to use standard distances, preferably starting at the same minimum level. In other words, levels in a given percentage, say 10%, 30%, 50%, and 75%, of the maximum intensity should be avoided. In some cases, in particular for weak textures, contour lines may be ambiguous, which means that intensity variations may not unmistakably be resolved. In such cases the individual contour lines need to be labeled with their values

**FIGURE 5.1**

(See color insert following page 240 for Figure 5.1a.) Contouring of a 3-D pole density distribution to derive the standard 2-D pole figure presentation ([200] pole figure, stereographic projection).

**FIGURE 5.2**

(See color insert following page 240 for Figure 5.2b.) {111} Pole figure plotted with contour lines (logarithmic progression; regions with intensity lower than 0.5 are dotted); (b) same pole figure as in (a) plotted with colored contour lines; (c) same pole figure as in (a) plotted in gray shades (aluminum alloy AA 5005-H22, partially recrystallized).

(Figure 5.3) or clearly marked by different (minimum 3) line styles or colors (Figure 5.2b). In many cases, those ambiguities can be avoided by simply marking pole figure regions below the minimum or above the maximum level by shadings or by dots (Figures 5.2a and 5.3). Alternatives to the contour lines are different gray shadings or colors in accordance with the intensity of the corresponding pole figure regions (Figure 5.2c). Such pole figures are more complicated to reproduce, however.

**FIGURE 5.3**

Inverse pole figure of titanium deformed by extrusion to a von Mises equivalent strain of 1.75 (inverse pole figure of the extrusion axis). (Adapted from Rollett, A.D. and Wright, S.I., *Texture and Anisotropy, Preferred Orientations in Polycrystals and Their Effect on Materials Properties*, Cambridge University Press, 1998.)

5.2.2 Representation of Orientations in the Inverse Pole Figure

Figure 5.3 shows the inverse pole figure of the extrusion axis of titanium, which was plotted with iso-intensity lines in the hexagonal standard triangle formed by the axes (0001) , $(11\bar{2}0)$, and $(10\bar{1}0)$. The texture displays a concentration of the extrusion axis in the vicinity of $(10\bar{1}0)$. This means that the basal plane normals are perpendicular to the extrusion axis, which is the common texture of hexagonal materials deformed by extrusion (Rollett and Wright, 1998). Although it is generally anticipated that in uniaxially deformed samples a fiber texture is present, this information cannot be derived from Figure 5.3 since the inverse pole figure only shows the orientation of one reference axis—here the extrusion axis—whereas rotations about this axis are not considered. Thus, for a complete representation of the 3-D orientation distribution, the orientations of *two* reference axes would be required. Although for analysis of the macrotexture of fiber textures this may not be necessary, for the evaluation of misorientations the full orientation information must be available. Section 9.6 addresses the implications of this in more detail. In conclusion, for the representation of macrotexture data, inverse pole figures are usually inferior to the pole figures.

5.3 Determination of the Orientation Distribution Function from Pole Figure Data

5.3.1 The Orientation Distribution Function

The projection of the 3-D orientation distribution onto a 2-D projection plane results in a loss in information, so that in turn the 3-D orientation

distribution (the texture) cannot be derived from a given pole figure without some uncertainty. Only in the case of very simple textures consisting of a small number of orientations—textures of single crystals or the cube texture in recrystallized aluminum or copper—may the pole figures be sufficient to yield unambiguously the entire texture information in a quantitative manner. In general, however, the intensities of the individual poles that form a given orientation cannot clearly be assigned to that orientation, in particular when the poles of different orientations overlap, which renders a clear separation of the volumes associated with the individual orientations complicated or even impossible. Furthermore, most experimentally obtained pole figures are *incomplete pole figures*, which means that not the entire pole figure range has been recorded (Section 4.3.2). This further reduces the texture information available in such pole figures.

To overcome these ambiguities and thus to permit a quantitative evaluation of the textures, it is necessary to describe the orientation density of grains in a polycrystal in an appropriate 3-D representation, that is, in terms of its ODF. The ODF is defined as a probability density function of orientations g , expressed, for example, in the form of the Euler angles φ_1 , Φ , and φ_2 . Let us assume a microstructure consisting of different grains i of volume V_i with different orientations (Figure 5.4). Grains of similar orientations g within an orientation range dg are color coded with the same gray value. The ODF $f(g)$ is defined by the following relationship:

$$\frac{dV}{V} = f(g)dg, \text{ with } dg = \frac{1}{8\pi^2} \sin \Phi d\varphi_1 d\Phi d\varphi_2 \text{ and } \oint f(g)dg = 1 \quad (5.1)$$

where V is the sample volume and dV is the volume of all crystallites i with the orientation g in the angular element dg .

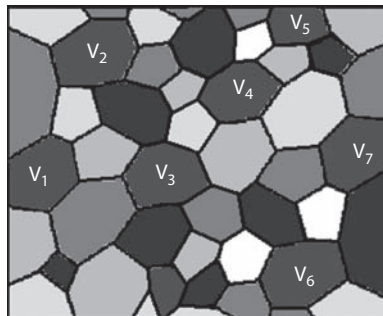


FIGURE 5.4

Schematic representation of a microstructure consisting of different grains i of volume V_i with different orientations. Similar orientations g within an orientation range dg are color coded with the same gray value.

Note that the volume element dg is heavily distorted in orientation space, which is related to the definition of the Euler angles (Section 2.6.1; see also Section 5.4.1).

Experimental input for ODF computation is usually provided by macro-texture pole figure measurements (Section 4.3). Mathematically, the pole figure is defined by the volume fraction dV/V of crystals having their crystal direction h parallel to the sample direction y —typically given by the two pole figure angles α and β (see Section 2.5.1):

$$\frac{dV}{V} = \frac{1}{4\pi} P_h(y) dy \quad (5.2)$$

where $y = \{\alpha, \beta\}$ and $dy = \sin \alpha d\alpha d\beta$.

Note that this pole figure definition is based on directions $h = [h_1, h_2, h_3]$ in the *direct* crystal lattice. Experimental pole figures, however, are commonly expressed in terms of the reflecting lattice plane normals, whose Miller (or Miller–Bravais) indices—e.g., {111} or {1120}—correspond to the coordinates of the crystal direction h in the *reciprocal* lattice. This distinction is not important for cubic structures (Appendix I), but it must be taken into account for the noncubic crystal classes.

As discussed in the preceding section, pole figures are usually normalized such that the pole densities are given in m.r.d. For that purpose, the pole figure data expressed in arbitrary units (in counts per seconds) are normalized such that

$$\frac{1}{4\pi} \cdot \oint P_h(y) dy = 1 \quad (5.3)$$

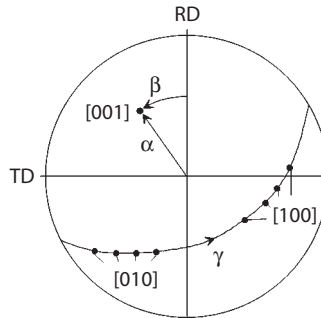
This expression can be used to normalize the pole figure, as described in Section 4.3.6.

As shown schematically in Figure 5.5, a pole that is defined by the direction y in a given 2-D pole figure $P_h(y)$ corresponds to a region in the 3-D ODF $f(g)$ that contains all possible rotations with angle γ about this direction y in the pole figure. Written in a mathematical manner, this means

$$P_h(y) = \frac{1}{2\pi} \cdot \int_{\gamma=0}^{2\pi} f(g) d\gamma \quad (5.4)$$

where $y = \{\alpha, \beta\}$ and $g = \{\varphi_1, \Phi, \varphi_2\}$.

The factor $1/2\pi$ is necessary because of the two normalization conditions of ODF (Equation 5.1) and pole figure (Equation 5.3). The integral Equation 5.4 represents the *fundamental equation of ODF computation*, which has to be solved to calculate the ODF. This is called *pole figure inversion*. In general, the ODF is not completely determined by one pole figure, and the missing information must be provided by additional pole figures. An analytical solution to the problem of pole figure inversion is not possible, however. In the literature, several mathematical approaches to solving Equation 5.4 have been proposed. In the following

**FIGURE 5.5**

Representation of the fundamental equation of pole figure inversion in a {100} pole figure.

sections, we will briefly introduce some of the most common methods for pole figure inversion. These sections are by no means intended to provide a rigorous mathematical description of the various approaches, but they try to outline their underlying ideas and compare their main advantages and disadvantages.

5.3.2 The Series Expansion Method

The basic premise of the *series expansion method* is the assumption that both the measured pole figures $P_h(y)$ and the ensuing ODF $f(g)$ can be fitted by a series expansion with suitable mathematical functions. Appropriate functions to use in a spherical coordinate system are the “spherical harmonic functions,” and therefore this method has also been called the *harmonic method*. A complete scheme for texture analysis by series expansion has been developed independently by Bunge (1965) and Roe (1965). The following text outlines the series expansion method, based on the description by Bunge and Esling (1985) (for more details, see Jura and Pospiech, 1978; Bunge, 1982; Bunge and Esling, 1982; Kallend, 1998).

The series expansion method is based on the fact that an analytical solution to Equation 5.4 can be given for certain specific distribution functions—the generalized harmonic functions. For these functions, $k_l^n(y)$ and $T_l^{mn}(g)$, Equation 5.4 becomes

$$\frac{1}{2\pi} \cdot \int_0^{2\pi} T_l^{mn}(g) d\gamma = \frac{2}{2l+1} \cdot k_l^{*m}(h) \cdot k_l^n(y) \quad (5.5)$$

where the asterisk indicates the complex-conjugate quantity and $k_l^{*m}(h)$ and $k_l^n(y)$ are the surface spherical harmonic functions defined on a sphere fixed to the crystal frame and the sample frame, respectively.

The distribution described by the latter is the special pole figure belonging to the special ODF $T_l^{mn}(g)$. Thus, the pole figure $P_h(y)$ and the ODF $f(g)$ can be described by functions for which the solution is known.

In the series expansion method, the ODF is expanded in a series of (symmetrized) generalized spherical harmonic functions $T_l^{mn}(g)$:

$$f(g) = \sum_{l=0}^{\infty} \sum_{m=-l}^l \sum_{n=-l}^l C_l^{mn} \cdot T_l^{mn}(g) \quad (5.6)$$

There is one such function $T_l^{mn}(g)$ for every possible combination of the indices l , m , and n . Any ODF $f(g)$ can be composed by adding functions $T_l^{mn}(g)$ in appropriate amounts, that is, each function $T_l^{mn}(g)$ is multiplied by an appropriate factor C_l^{mn} . Thus, the ODF is completely described by the series expansion coefficients C_l^{mn} . This is the general principle of a series expansion, which is well known in the form of Fourier analysis, where the special functions are sine or cosine functions. The harmonic functions $T_l^{mn}(g)$ are more complex 3-D functions, but the principle is the same. Numerical values of the harmonic functions $T_l^{mn}(g)$, $k_l^{*m}(h)$, and $k_l^n(y)$, which are independent of the experimental data, are usually precalculated and stored in numerical libraries (Pospiech and Jura, 1975; Wagner et al., 1982; Bunge, 1982).

The pole figures can also be expanded in a series expansion. As the pole figure is characterized by the two angles α and β , an expansion in (symmetrized) spherical harmonic functions $k_l^n(y)$ is sufficient:

$$P_h(y) = \sum_{l=0}^{\infty} \sum_{n=-l}^l F_l^n(h) \cdot k_l^n(y) \quad (5.7)$$

Substitution of Equations 5.6 and 5.7 into Equation 5.4 under consideration of Equation 5.5 yields an expression relating the 2-D series expansion coefficients $F_l^n(h)$ to the C_l^{mn} coefficients:

$$F_l^n(h) = \frac{4\pi}{2l+1} \cdot \sum_{m=-l}^l C_l^{mn} \cdot k_l^{*m}(h) \quad (5.8)$$

If the coefficients $F_l^n(h)$ and C_l^{mn} fulfill Equation 5.8, then the functions $f(g)$ and $P_h(y)$ fulfill the fundamental Equation 5.4. Therefore, the solution of Equation 5.8 yields the solution of Equation 5.4.

Equation 5.8 forms a system of linear equations that can be solved to derive the unknown C_l^{mn} coefficients. There is one such system for every combination of the indices l and n , containing $2l+1$ unknowns, which

correspond to the values of index m , with $-l \leq m \leq +l$. The number of equations in this system is given by the number of different values of h , that is, by the number of different pole figures $P_h(y)$. Thus, the C_l^{mn} coefficients can be determined unambiguously up to $l = L$ if the coefficients $F_l^n(h)$ are known for $2L + 1$ pole figures. The indices m in the functions $T_l^{mn}(g)$ correspond to the different crystal symmetries. For triclinic crystals, all values of $-l \leq m \leq +l$ are required in the series expansion, whereas for higher crystal symmetries, only a subset of m values is needed. From Figure 5.6, it appears that this considerably reduces the number of unknowns in Equation 5.8 and, accordingly, the number of pole figures necessary to compute an ODF.

To solve Equation 5.8, the coefficients $F_l^n(h)$ of the series expansion of the pole figure $P_h(y)$ must be known, which can be obtained by multiplying Equation 5.7 by $k_l^{*n'}(y)$ and integration over y :

$$\int P_h(y) \cdot k_l^{*n'}(y) dy = \sum_{l=0}^{\infty} \sum_{n=-l}^{+l} F_l^n(h) \int k_l^n(y) \cdot k_l^{*n'}(y) dy \quad (5.9)$$

This yields

$$F_l^n(h) = \int P_h(y) k_l^n(y) dy \quad (5.10)$$

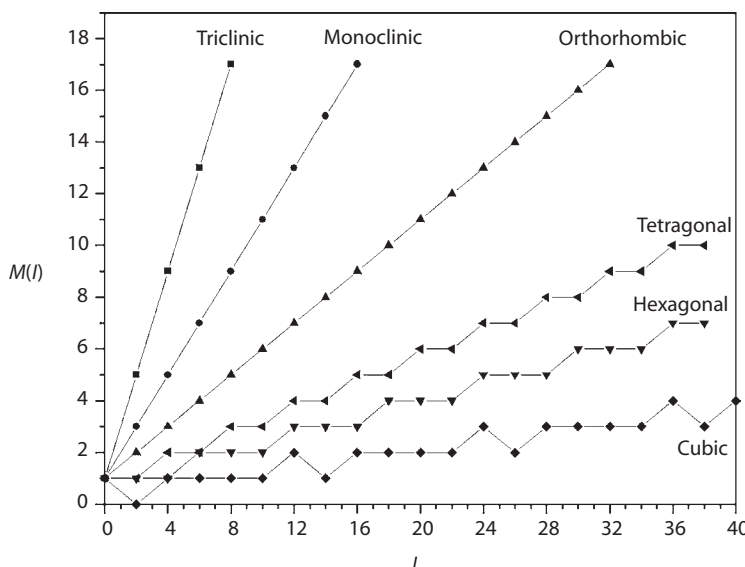


FIGURE 5.6

Number of linearly independent harmonic functions $M(l)$ as a function of the degree of series expansion l for different crystal symmetries (only for even-order l). (Data taken from Bunge, H.-J., *Texture Analysis in Materials Science: Mathematical Methods*, Butterworths, London, 1982.)

In short, the solution to the fundamental Equation 5.4 is achieved by solving Equations 5.10, 5.8, and 5.6, in turn. Equation 5.10 is used to develop the experimental pole figure $P_h(y)$ into a series with the coefficients $F_l^n(h)$. Then, Equation 5.8 is solved for the unknown C_l^{mn} coefficients. Finally, with Equation 5.6 the ODF $f(g)$ can be generated for any orientation g .

Whenever possible, a larger number of pole figures are used to calculate an ODF than is mathematically necessary. For instance, for cubic and hexagonal materials, respectively, three to four and five to six pole figures are usually determined. The experimental data are then averaged by a least-square scheme that reduces the impact of measuring errors and, in particular, allows the use of incomplete pole figures for the ODF calculation (Pospiech and Jura, 1974; Van Houtte, 1980, 1984; Humbert and Bergmann, 1980; Dahms and Bunge, 1986). For I incomplete pole figures available in a range Z , the C_l^{mn} coefficients are determined from the condition that the deviation between the experimental pole figures $P_h(y)_{\text{exp}}$ and the pole figures recalculated from the C_l^{mn} coefficients $P_h(y)_{\text{calc}}$ is minimized:

$$\Delta = \sum_{i=1}^I w_i \int_Z [P_{hi}(y)_{\text{exp}} - P_{hi}(y)_{\text{calc}}]^2 dy \stackrel{!}{=} \min \quad (5.11)$$

where w_i is the weighting factor of pole figure i , often simply chosen to unity.

The recalculated pole figures $P_h(y)_{\text{calc}}$ are derived from the C_l^{mn} coefficients using Equations 5.7 and 5.8. Note that it is also possible to recalculate pole figures that cannot be measured, either because of the extinction rules in the specific material (Section 3.3) or because of overlapping diffraction peaks in line-rich materials (Section 4.5.1).

Instead of the pole figure $P_h(y)$, a general axis distribution function $A(h,y)$ is often used (Bunge, 1982). If the sample direction y is varied for a constant crystal direction h (e.g., {111} or {200} poles), the general axis distribution function $A(h,y)$ reduces to the pole figure $P_h(y)$. However, the general axis distribution function $A(h,y)$ can also be specified in the opposite way, that is, the sample direction y is kept constant while the crystal direction h is varied. Then, the general axis distribution function $A(h,y)$ becomes the inverse pole figure $R_y(h)$. Thus, inverse pole figures can likewise be used to compute an ODF and, vice versa, from an ODF, inverse pole figures can be recalculated.

An ODF computed as described earlier contains several errors, even under the assumption of ideal pole figure data. One error is caused by the necessity to truncate the series expansion of pole figure and ODF expansion. This *truncation error* leads to broadening of the texture peaks as well as to minor artifact intensities in the vicinity of strong texture components. The summations in Equations 5.6 and 5.7 are controlled by the index l , which means that the truncation error is determined by the maximum value of l_{\max} . In any series expansion, the higher the degree l_{\max} of the expansion the sharper the function, whereas a smooth function only requires a low number of series

terms. The value of l_{\max} at which truncation errors can be neglected depends on the orientation resolution $\Delta\omega$ (Matthies, 1982):

$$l_{\max} = \frac{360^\circ}{2\Delta\omega} \quad (5.12)$$

To illustrate the impact of the truncation error, Figures 5.7a through 5.7c show ODFs composed of two orientations—the Bs orientation $\{011\}\langle211\rangle$ at $(\varphi_1, \Phi, \varphi_2) = (35^\circ, 45^\circ, 0^\circ)$ and the S orientation $\{123\}\langle634\rangle$ at $(60^\circ, 35^\circ, 65^\circ)$ —computed with $l_{\max} = 12, 22$, and 34 , respectively. All three ODFs qualitatively display the same orientation distributions, with approximately similar intensity ratios among the two main components. The texture sharpness strongly increases with l_{\max} , however, by more than doubling between $l_{\max} = 12$ and 34 . Simultaneously, the orientation peaks become narrower (Figure 5.7d). This reflects the better resolution of sharp peaks, which is achieved with

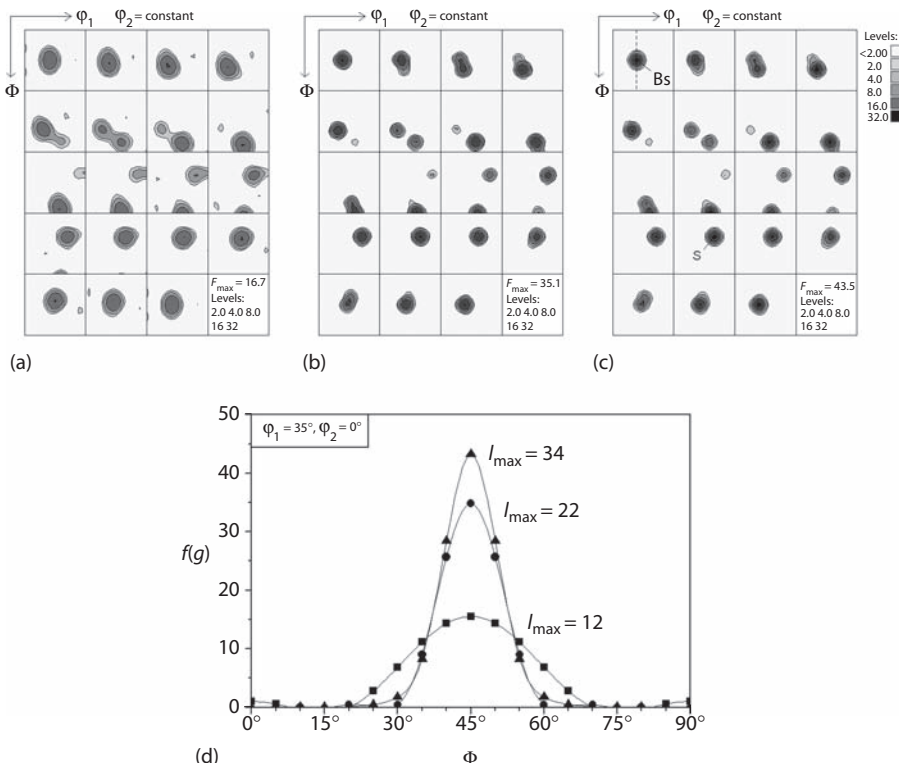


FIGURE 5.7

ODFs composed of two orientations—the Bs orientation $\{011\}\langle211\rangle$ at $(\varphi_1, \Phi, \varphi_2) = (35^\circ, 45^\circ, 0^\circ)$ and the S orientation $\{123\}\langle634\rangle$ at $(60^\circ, 35^\circ, 65^\circ)$ —computed with different degrees of series expansion l_{\max} : (a) $l_{\max} = 12$; (b) $l_{\max} = 22$; (c) $l_{\max} = 34$. (d) Orientation density profile through the Bs peak (dashed line in [c]).

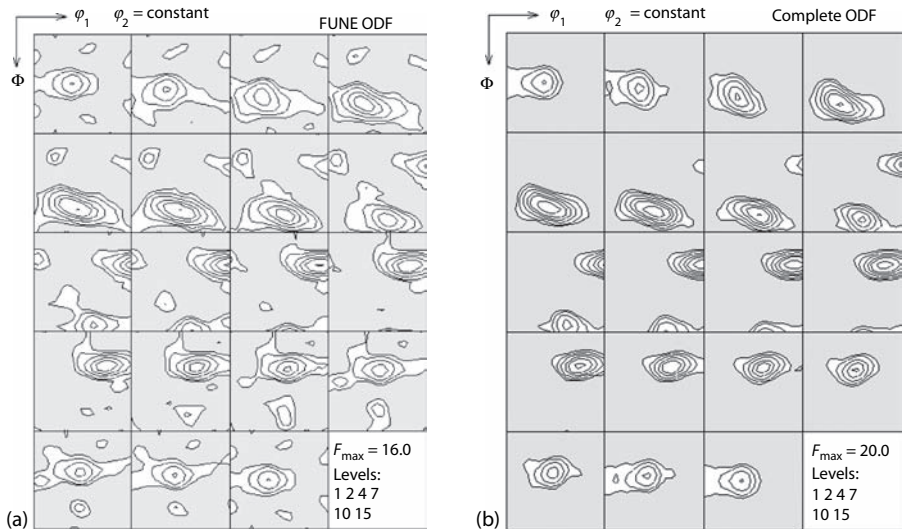
higher degrees of l_{\max} . It is also seen that largest differences arise between $l_{\max} = 12$ and 22, whereas the differences between 22 and 34 are much less pronounced, mainly concerning the maximum intensity. Accordingly, for cubic materials the order of the series expansion is usually limited to $l_{\max} = 22$ or, for sharper texture, to $l_{\max} = 34$, which yields sufficiently accurate results with an acceptable computation effort.

Another, more severe, problem of ODF calculation is the so-called *ghost error*. In the 1970s, Lücke et al. (1981) observed that intensities of the ODF may be missing (negative ghosts), or wrong intensities may appear (positive ghosts). Matthies (1979) proved that these ghosts are caused by the lack of the odd-order series expansion coefficients C_l^{mn} . The definition of the pole figure in Equation 5.2 is based on an individual crystal direction $[h_1, h_2, h_3]$, for example, $\langle\bar{1}\bar{1}1\rangle$, as opposed to a family of crystallographically equivalent directions $\langle h_1, h_2, h_3 \rangle$, for example, $\langle 111 \rangle$. Although this distinction is irrelevant for directions related to each other by rotational symmetry elements, it is important for inversion centers in that a pole figure $h = [h_1, h_2, h_3]$ needs to be distinguished from its counterpart $-h = [\bar{h}_1, h_2, \bar{h}_3]$. Thus, because of the centrosymmetry of the experimental pole figures derived by diffraction experiments (Section 2.2), they contain less information than necessary to reproduce unambiguously an ODF. Written in a formal manner, the complete ODF $f(g)$ is composed of two parts (Matthies, 1979):

$$f(g) = \tilde{f}(g) + \tilde{\tilde{f}}(g) \quad (5.13)$$

The first part, $\tilde{f}(g)$, which is defined by the even-order C coefficients, can be derived from diffraction pole figures, whereas the second part, $\tilde{\tilde{f}}(g)$, which is given by the odd-order C coefficients, cannot. Because of the missing odd part $\tilde{\tilde{f}}(g)$, it may seem that as much as one-half of the information is missing. However, since the odd-order C coefficients are zero for low l and quite small for large l , the impact of the odd-order C coefficients is limited in practice and the errors are typically approximately 20%. To visualize the impact of the ghost error on the ODFs, Figure 5.8a shows the rolling texture of an AlFeSi alloy as obtained from the experimental pole figures, that is, the even part $\tilde{f}(g)$, plotted in sections through the 3-D Euler space (Section 5.4). Then, the odd-order C coefficients are obtained according to the method proposed by Dahms and Bunge (see the following text). The complete—ghost-corrected—ODF $f(g)$ is shown in Figure 5.8b. Although the general texture features are similar, it is obvious that the overall sharpness of the ghost-free ODF is higher by approximately 20% and that some small intensities of the experimental ODF (Figure 5.8a) are missing, which means that these are ghosts.

Thus, to derive complete, ghost-corrected textures by means of the series expansion method, the part $\tilde{\tilde{f}}(g)$ given by the odd-order C coefficients must be determined under certain assumptions. Most procedures to derive the odd-order C coefficients make use of the condition that the ODF must be nonnegative for all orientations, that is, $f(g) > 0$.

**FIGURE 5.8**

Rolling texture of an Al-Fe-Si alloy. (a) Reduced ODF $\tilde{f}(g)$ as obtained from the experimental pole figures; (b) complete ODF $f(g)$, that is, ODF from (a) plus subsequent ghost correction according to the method by Dahms and Bunge (1988, 1989).

In the *zero-range* method proposed by Bunge and Esling (1979) and Esling et al. (1981), ranges in the pole figures with zero intensity yield an approximation to the indeterminable part $\tilde{f}(g)$ of the ODF. From the pole figure zero ranges, the corresponding zero ranges in the orientation space can be derived by geometrical considerations. For these ranges, it readily follows:

$$\tilde{\tilde{f}}(g) = -\tilde{f}(g) \quad (5.14)$$

Thus, in the zero ranges of the orientation space, the function $\tilde{\tilde{f}}(g)$ is known and can be expressed in terms of the series expansion. The corresponding C coefficients are now considered as an approximate solution of $\tilde{\tilde{f}}(g)$ in the *entire* orientation space. It is obvious that this method can only yield satisfactory results for pole figures with well-defined zero ranges—in the case of sharp textures.

In the *quadratic method* (Van Houtte, 1983), the ODF $f(g)$ is expressed in a quadratic form $h^2(g)$, or alternatively in an exponential form (Van Houtte, 1991), which cannot be negative. The function $h(g)$, which produces a satisfactory description of the true ODF $f(g)$, is then found in an iterative procedure. This method disadvantageously alters the (known) even-order C coefficients, which introduces some residual errors. As in the case of the zero-range method, the quadratic method is only applicable if well-defined zero ranges exist, that is, for sharp textures.

The *positivity method* by Dahms and Bunge (1988, 1989) is a generalization of the zero-range method. At the n th step of this iterative procedure, the ODF $f(g)$ is given by

$$f_n(g) = f_{n-1}(g) + \tilde{f}'_n(g) \quad (5.15)$$

where the (complete) correction function $f'(g)$ approximates the negative parts of the $(n - 1)$ th function $f_{n-1}(g)$ (Figure 5.9):

$$f' = \begin{cases} -f_{n-1}(g), & \text{if } f_{n-1}(g) < 0 \\ 0, & \text{if } f_{n-1}(g) \geq 0 \end{cases} \quad (5.16)$$

The initial solution ($n = 0$) is the experimental ODF, that is, the ODF directly calculated from the pole figure data. Note that only the odd part of the correction function is added to the previous solution in Equation 5.15, so that the (known) even part of the ODF $\tilde{f}(g)$ is never modified. This procedure is repeated until the entire ODF is positive or until the remaining negative regions are sufficiently small. This method was improved by introducing a small positive offset r in Equation 5.16 (Dahms and Bunge, 1989; Wagner et al., 1990). By choosing different values of r , the width of the range of possible solutions can be estimated, and the solution with maximum r corresponds

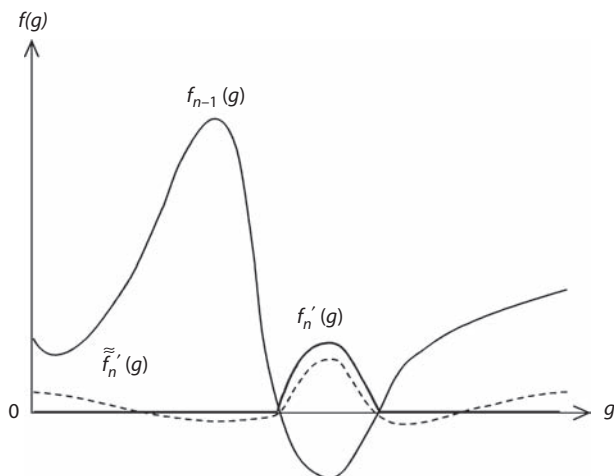


FIGURE 5.9

Ghost correction according to the method by Dahms and Bunge (1988, 1989) at the n th iteration step in a 1-D representation. $f_{n-1}(g)$: ODF at the preceding iteration step; $f'_n(g)$: (complete) correction function to approximate the negative ranges of $f_{n-1}(g)$; $\tilde{f}'_n(g)$: odd part of the correction function $f'_n(g)$. (Adapted from Wagner, F. and Dahms, M. in *Advances and Applications of Quantitative Texture Analysis* (Eds. H. J. Bunge and C. Esling), DGM, Oberursel, Germany, 1991, 101.)

to the solution with maximum isotropic background, or “phon” (Matthies, 1984; Dahms, 1992). This generalized positivity method offers a fast, efficient way to obtain the complete ODF and thus to correct for the ghost error. It was used for the example shown in Figure 5.8b.

In a similar context, the concept of *maximum entropy* has been developed (Wang et al., 1988, 1992; Schaeben, 1988, 1991). Out of the possible range of complete ODFs, the solution with maximum “entropy” has the smoothest distribution with minimum additional information to avoid artifacts, for example, ghosts, for which there is no evidence in the pole figures (the term “entropy” is not meant in a thermodynamic sense here). This method has the advantage of providing ghost correction also in cases where no negative ODF ranges occur.

Lücke et al. (1981, 1986) proposed to deconvolute the experimental ODF into a set of several—typically five to ten—individual orientations. From this set of orientations, a model ODF is calculated by associating with each orientation a Gauss-type scatter in Euler space. This method, which is discussed in more detail in Section 9.3.2, yields a complete ODF; both odd- and even-order C coefficients are obtained. By subtracting the even-order part of the model ODF from the experimental ODF, a difference ODF is obtained that can then be used to improve the fit between the model ODF and the experimental ODF by shifting the position of the model components or by adding new ones. The complete ODF is finally derived by combining the even-order C coefficients of the experimental and the odd-order C coefficients of the model ODF. By this method, the entire experimental information is retained but still a substantial reduction of the ghost error is achieved, even if the model fit is poor. As a rule of thumb, a fit of the difference ODF to 20% (which in most cases is easy to achieve) or, better, to 10% would, respectively, reduce the ghost error to 4% or even as little as 2%. It should be emphasized that although the assumption of Gauss-type orientations—in case of weak textures or pronounced fiber textures—is not necessarily justified, this method yields very satisfactory results with regard to a reduction of the ghost error. This method has successfully been applied to a huge amount of experimental data by the Aachen texture group. Furthermore, the information of the volume fractions and scatter widths of the main Gauss components can be used for a very condensed, quantitative description of the ODFs (Engler et al., 1994b). The major disadvantage of this method is that the iterative derivation of the model ODF has not been automated so far; thus the method is rather time consuming to apply.

5.3.3 Direct Methods

Besides calculating the ODF by means of the harmonic method in a Fourier-space, other algorithms have been developed to derive the ODF values $f(g)$ directly from the pole figure data. These methods are summarized under the head *direct methods*. Such methods consider the pole figures $P_h(y)$ at a finite number of individual points y_i and, accordingly, the ODF $f(g)$ at a finite number of individual orientations g_j . Typically, both the pole figures and the

orientation space are subdivided into a regular grid with a spacing of 2.5° or 5° . The relation between the individual pole figure points and the corresponding cells of the orientation space is established under consideration of the crystal geometry. Then the integral in the fundamental Equation 5.4 can be replaced by a finite summation for each pole figure cell i :

$$P_i = \sum_{j=1}^J \sigma_{ij} f_j \quad (5.17)$$

Equation 5.17 defines a set of linear equations that, under appropriate conditions, can be solved to yield the ODF $f(g)$. After an initial estimate of the ODF, the fit between the ODF values and the value of the associated pole figure points is improved by means of an iterative procedure. In all direct methods, the positivity condition is directly taken into account.

In the following text, the principles of the so-called *WIMV method* is outlined, which is implemented in the Los Alamos texture software package popLA (Kallend et al., 1991a) as well as the Berkeley texture package BEARTEX (Wenk et al., 1998). The method goes back to Williams (1968) and Imhof (1977) and has since been improved by Matthies and Vinel (1982), which led to the acronym WIMV. For a more comprehensive review, the reader is referred to Matthies and Wenk (1985), Kallend (1998), and Matthies (2002).

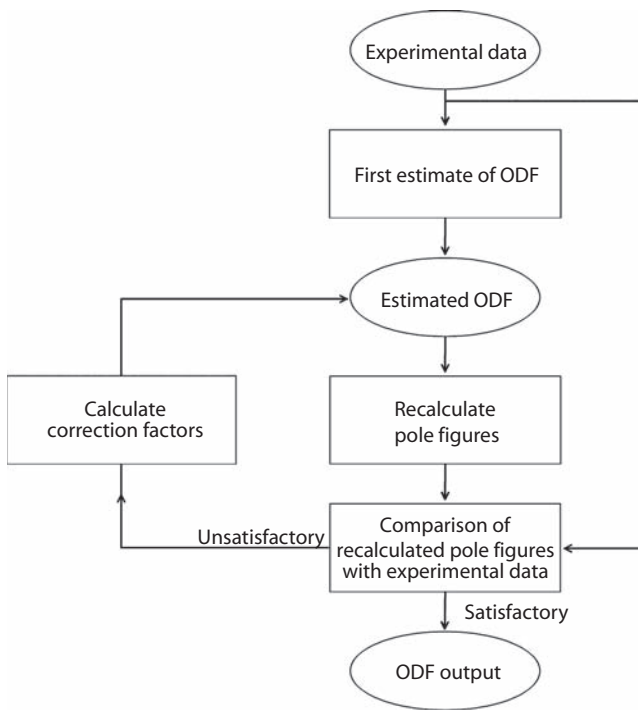
The initial $f(g)$ values of each ODF cell (e.g., in a $5^\circ \times 5^\circ \times 5^\circ$ grid) are estimated by the geometric mean of the values in the associated cells in the experimental pole figures, $P_{h_i}^{\text{exp}}$:

$$f_0(g) = N_0 \cdot \prod_{i=1}^I \prod_{m_i=1}^{M_i} \left[P_{h_i}^{\text{exp}}(y_{m_i}) \right]^{1/I \cdot M_i} \quad (5.18)$$

where I = number of measured pole figures, M_i = multiplicity of pole i , and N = normalization.

Thus, as required, zero values in the pole figure automatically lead to zero values in the orientation space. The ODF is then refined by a series of the so-called inner iterations (Figure 5.10). If $P_{h_i}^n$ denotes the recalculated pole figure after the n th iteration step, for each cell of the ODF a correction factor is derived as the ratio of the geometric mean of the corresponding cells in the experimental pole figure to the one in the recalculated pole figure $P_{h_i}^n$. The next estimate is then derived by multiplying the value of each ODF cell with this correction factor:

$$f_{n+1}(g) = N_n \cdot f_n(g) \cdot \frac{f_0(g)}{\prod_{i=1}^I \prod_{m_i=1}^{M_i} \left[P_{h_i}^n(y_{m_i}) \right]^{1/I \cdot M_i}} \quad (5.19)$$

**FIGURE 5.10**

Flow chart of ODF calculation according to the WIMV algorithm. (Adapted from Kallend, J.S., *Texture and Anisotropy, Preferred Orientations in Polycrystals and their Effect on Materials Properties*, Cambridge University Press, 1998.)

If, for example, the ODF value in a given cell is too large, then the corresponding recalculated pole figure values would also be too large. Consequently, the correction factor would be less than 1 so that the corresponding ODF value is reduced in the next step.

Additionally, an outer iteration can be applied to limit the minimum value of the ODF to $f(g) \geq f(g)_{\min}$, which means that the phon is raised. By this any potential negative ghost will be filled, which in turn reduces the corresponding positive ghosts as well. In practice, the algorithm converges rapidly, and typically a satisfactory solution is obtained after approximately 10 iterations.

Besides the WIMV method, there are several further direct methods for ODF computation that are listed here for completeness:

- Based on the WIMV method, Pawlik developed the *arbitrary defined cells* (ADC) method (Pawlik, 1986, 1994; Pawlik et al., 1991). Although most direct methods consider projection lines in relating the pole figures to the ODF cells, ADC uses projection *tubes*. The cross section of these tubes is determined by the shape of the corresponding pole figure cells.

Computation of the intersections of the tubes with the ODF cells allows to derive the volume fraction of an ODF cell that contributes to the pole figure and leads to a better smoothing in the final result. This method is implemented in the commercial texture software package *LaboTex*.

- In the *vector method*, both the pole figures and the orientation space are subdivided into small subregions, which are considered as components of vectors of high dimensions (Ruer and Baro, 1977; Ruer and Vadon, 1982; Schaeben et al., 1985; Vadon and Heizmann, 1991). The two vectors are coupled by a huge, though sparse, matrix that contains the geometrical relations between the pole figures and the orientation space. The texture vector representing the final ODF is derived from the pole figure vectors through an iterative fitting procedure. The method is straightforward and easy to apply, but handling of the large matrices causes problems with computation efficiency, which reduces the resolution of this method.
- In the *component method* put forward by Helming and colleagues (Helming and Eschner, 1990; Helming et al., 1994; Helming, 1998), the ODF is described by a set of a finite number (mostly less than 30) of generalized Gauss components. The orientations and some parameters to describe these generalized Gauss components are directly derived from the pole figures by an iterative nonlinear optimization procedure. Though this method is rather tedious to apply, it provides a very condensed description of textures with physically meaningful quantities. Furthermore, this method is well suited to derive ODFs from incomplete pole figures with uncommon nonmeasured areas, such as SAD pole figures (Helming and Schwarzer, 1994; see Section 8.3.2).

5.3.4 Comparison of Series Expansion and Direct Methods

Comparing the series expansion method, along with its different approaches to derive the odd part of the ODF, with the various direct methods reveals some characteristic advantages of each, which are summarized in the following text.

The series expansion method is a fast, reliable method that is rather insusceptible to experimental scatter in the pole figures. Its main output (the C coefficients) represents a condensed manner with which to characterize the texture, which is superior to storing the entire ODF data. The C coefficients also disclose valuable additional information on texture-related properties—elastic modulus and elastic and plastic anisotropy. Furthermore, changes in the reference coordinate system can be accommodated by manipulation of the C coefficients, so that texture changes during phase transformations (Davies et al., 1976; Kallend et al., 1976; Park and Bunge, 1994; Brückner and Pospiech, 1996) or recrystallization (Pospiech and Lücke, 1979; Lücke and Engler, 1990; Engler, 1997) can readily be analyzed. Rotations in the sample frame are also possible (Inoue and Takasugi,

2001). Finally, normalization of the experimental pole figures (Section 4.3.6) is easier.

In the direct methods, the condition of nonnegativity and the handling of the ghost problem are usually implicitly fulfilled, and no truncation error arises. Analysis of incomplete pole figures as well as different sample or crystal symmetries is easier to accomplish than in the harmonic method. In general, direct methods require fewer pole figures to obtain satisfactory solutions, which is of particular interest when low-symmetry materials are analyzed.

All current approaches to compute ODFs from pole figure data have now been developed to a state that, provided good experimental data are available, they are able to yield routinely reliable and reproducible quantitative texture results (Wenk et al., 1988a; Matthies et al., 1988; Bacroix et al., 1994). Nonetheless, because of the systematic differences between different methods, it is highly recommended not to change the method within a series of experiments, and especially not to switch between series expansion and direct methods.

5.4 Representation and Display of Texture in Euler Space

The quantitative description of a given texture in terms of its ODF, that is, the orientation density in terms of the three Euler angles, necessitates an appropriate 3-D orientation space for its representation. The first orientation space was introduced by Perlwitz et al. (1969) by defining three angles ρ_1 , ρ_2 , and ρ_3 to represent the orientation distributions of rolled copper and brass, which were determined by electron diffraction in a TEM (Pitsch et al., 1964). This space was chosen so that the most important rolling texture components all came to lie in a 2-D section with $\rho_3 = 0^\circ$ through the 3-D space, which strongly facilitated the visualization and evaluation of textures in this space.

In Section 5.4.1, we focus on the orientation space—the Euler angle space—that is most frequently used today. This orientation space is formed by the three Euler angles such that an orientation given by a triple of Euler angles corresponds to a distinct point in Euler space whose coordinates are defined by these three angles (Figure 2.11).

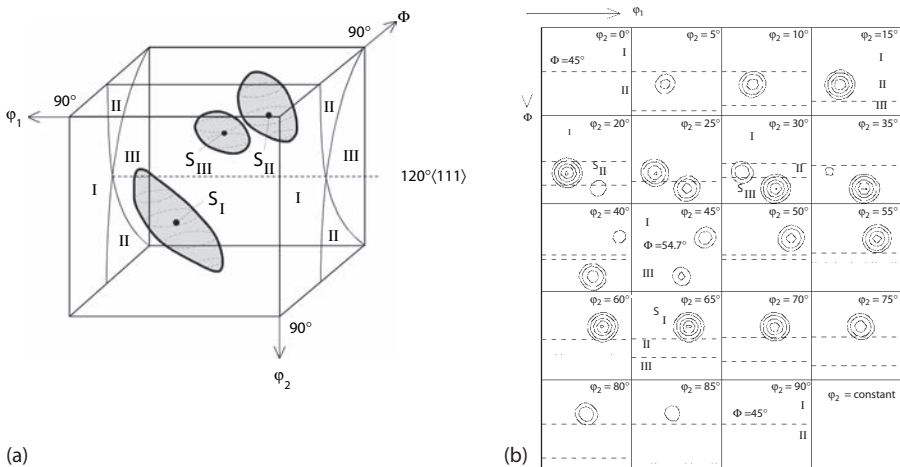
Because of the necessity to represent the orientation data in a 3-D orientation space, texture analysis is often considered a complicated problem that requires a large ability to visualize things. This task can greatly be facilitated by suitable ways to display and, if possible, condense the texture information. In Section 5.4.2, we address the common methods used to represent textures in the Euler space as well as appropriate means to condense textures and thus to facilitate texture analysis.

5.4.1 Properties of Euler Space

The Euler space is a 3-D orientation space whose axes are formed by the three Euler angles. In most cases, the three Euler angles are chosen to form an orthogonal coordinate system resulting in a Cartesian Euler angle space (Morris and Heckler, 1968; Van Houtte, 1987). With regard to the axes of this space, Section 2.6.1 introduced three different sets of the Euler angles, namely, the angles $\varphi_1, \Phi, \varphi_2$ (Bunge); Ψ, Θ, Φ (Roe); or Ψ, Θ, ϕ (Kocks). Although all these conventions likewise define an orientation space, in the remainder of this section the discussion is confined to Bunge's angles $\varphi_1, \Phi, \varphi_2$, as these are by far most commonly used in the literature. The principal considerations hold for all conventions, however.

As already pointed out in Section 2.6.2, an orientation given by a triple of Euler angles corresponds to a distinct point in Euler space whose coordinates are unequivocally given by these three angles (Figure 2.11). We have also seen how sample and crystal symmetry influence the size of the Euler angle space necessary to represent all possible orientations in an unequivocal manner (Table 2.3), and it turns out that the widely used method of representing textures in a cubic Euler space with $0^\circ \leq (\varphi_1, \Phi, \varphi_2) \leq 90^\circ$ inevitably assumes orthonormal sample symmetry. It should be emphasized that even in cases where orthonormal sample symmetry applies in principle—in samples deformed in plane strain—this reduction can lead to loss in information and can even cause errors. It is clear that asymmetries in the textures that point to deviations from the idealized plane strain state cannot be resolved in such reduced ODFs (Sections 5.4.2). More severely, in all cases where the initial texture of a sample did not depict orthonormal symmetry before deformation, reduction of the Euler angles under the assumption of orthonormal sample symmetry is misleading, although orthonormal sample symmetry does apply. For instance, single crystals in most cases have no orthonormal symmetry (with the exception of crystals with highly symmetrical orientations like cube $\{001\}\langle100\rangle$ and Goss $\{011\}\langle100\rangle$) so that important texture features such as direction and amount of rotations cannot properly be resolved.

In accordance with the definition of the Euler angles (Section 2.6.1), for $\Phi = 0^\circ$ (and $\Phi = 180^\circ$), the two remaining angles φ_1 and φ_2 describe rotations about the same axis, namely, the normal direction, which gives rise to strong distortions in the Euler angle space. Figure 5.11a shows the position of the three equivalent variants of the orientation $(123)[634]$ in the reduced Euler angle space. For each central orientation (marked by a dot), an isotropic scatter of $\sim 10^\circ$ is marked. It is obvious that the resulting spheres in the Euler angle space are far from being isotropic, but rather show strong distortions that become most pronounced for small angles Φ . An orientation with $\Phi = 0^\circ$ even deteriorates to a line with the condition $\varphi_1 + \varphi_2 = \text{constant}$. These distortions become most evident by representing the texture in the (unusual) Φ sections; an example is shown in Section 9.6.1. With regard to the cube-recrystallization texture, the distortions of Euler space result in the fact that RD rotations of the cube orientation $\{001\}\langle100\rangle$ can be found in the $\varphi_2 = 0^\circ$

**FIGURE 5.11**

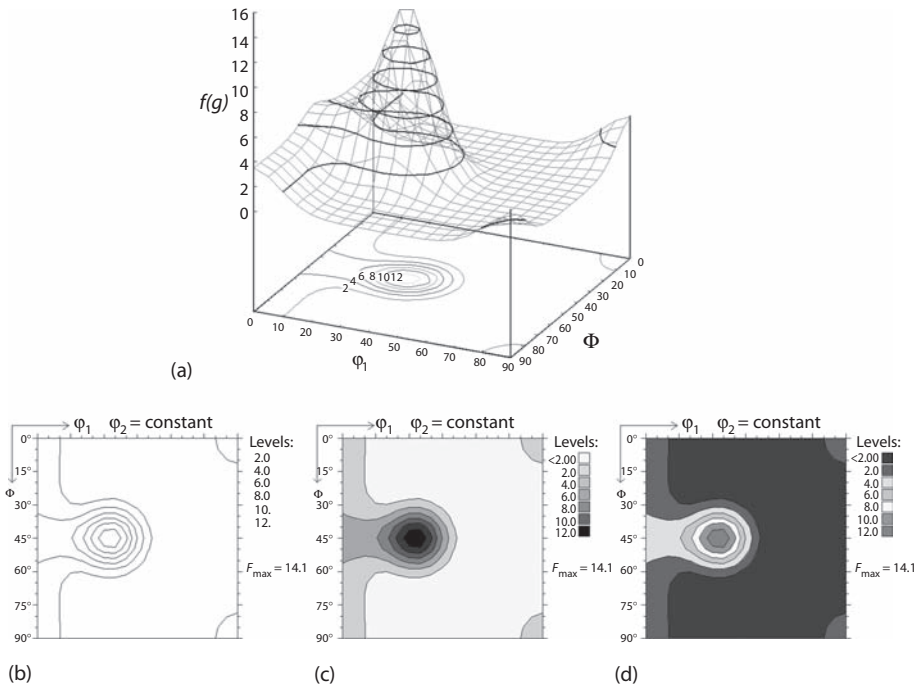
Spatial arrangement of the three components of the orientation $(123)[63\bar{4}]$ with isotropic scatter of 10° in the reduced Euler angle space showing strong distortions at small angles Φ . (b) Same texture as in (a) plotted with iso-intensity lines in φ_2 sections ($\Delta\varphi_2 = 5^\circ$) through the Euler space.

section by following the angle Φ at $\varphi_1 = 0^\circ$, whereas TD rotations are visible in the same section along Φ at $\varphi_1 = 90^\circ$. In Section 5.4.2, we will see that these distortions can be reduced by representing the textures in polar rather than Cartesian coordinates.

5.4.2 Representation and Display of Textures

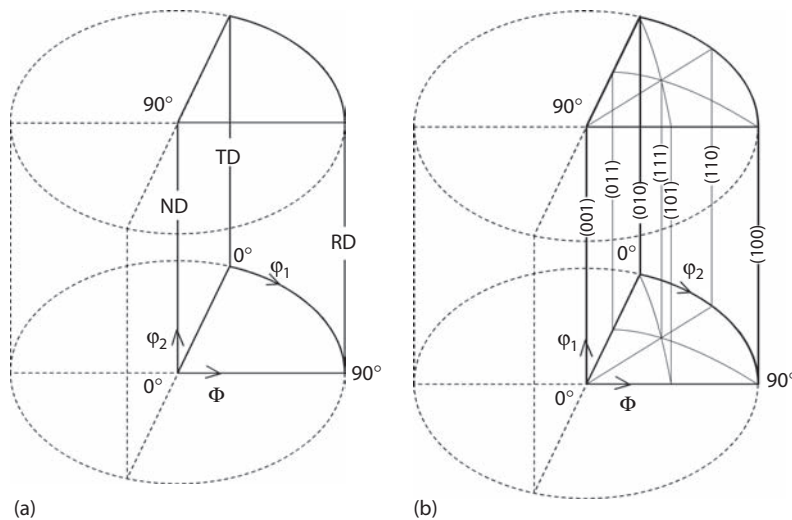
A representation of an ODF in a 3-D space as in Figure 5.11a is generally not suitable for publication on the printed page. Therefore, it is common practice to represent ODFs in the form of sections through the orientation space (Figure 5.11b). As already discussed for the pole figures, the intensity distribution in the individual sections can be displayed by different colors, different gray values, or, most commonly, by iso-intensity lines (Figure 5.12). Usually, equal-distance sections along one of the angles in 5° steps (sometimes 10° steps) are used. In principle, sections of all three Euler angles can be produced and evaluated alike, though surveying the literature shows that ODFs of fcc materials are usually presented in φ_2 sections, whereas the textures of bcc materials are traditionally shown in φ_1 sections, though φ_2 sections offer some advantages (see the following text). For hexagonal materials both φ_1 and φ_2 sections are found. Φ Sections are hardly ever used, in contrast.

As mentioned in Section 5.4.1, the distortions in the Cartesian Euler space at small angles Φ can be greatly reduced by representing texture data in polar rather than the usual Cartesian coordinates (Williams, 1968; Hansen et al., 1978; Wenk and Kocks, 1987). For that purpose, the angles φ_1 and Φ are plotted in

**FIGURE 5.12**

(See color insert following page 240.) (a) Contouring of a 3-D orientation distribution to derive the standard 2-D presentation of ODF sections; (b) orientation distribution of (a), plotted with iso-intensity lines; (c) orientation distribution of (a), plotted with gray shades; (d) orientation distribution of (a), plotted with colors (ODF $\varphi_2 = 0^\circ$ section).

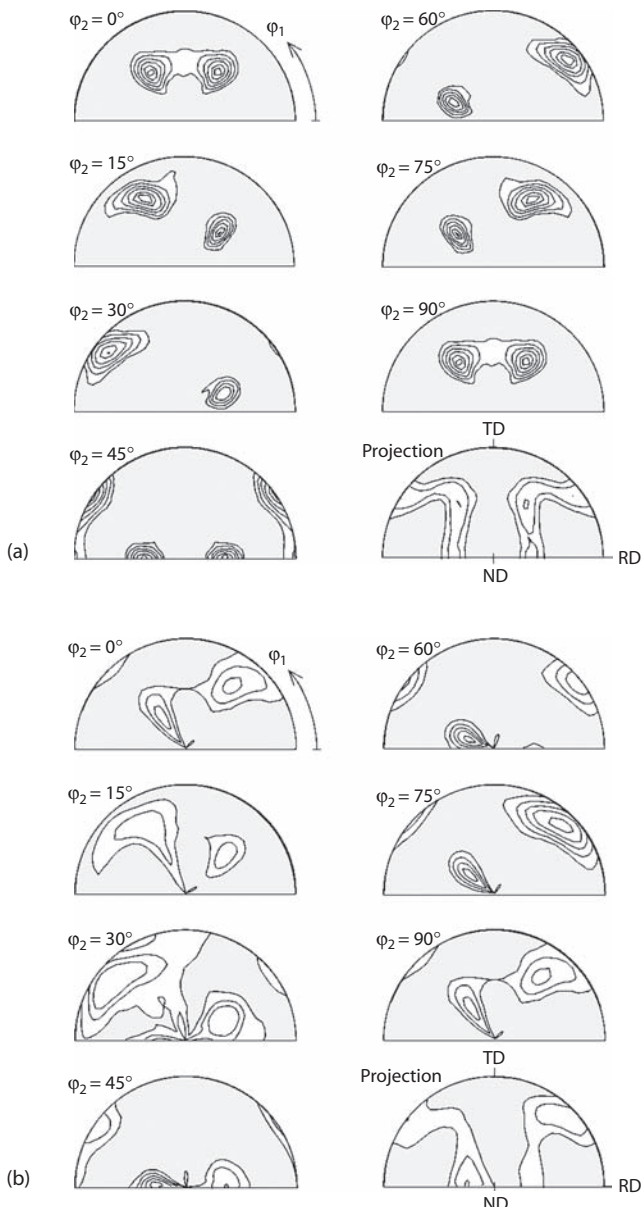
polar coordinates—just as in a pole figure—and φ_2 is represented as the axis of a cylinder perpendicular to the polar plot, as shown in Figure 5.13a. Analogous to the φ_2 sections through the Cartesian Euler space (Figure 5.11b), a set of sections through the resulting cylindrical space at constant values of φ_2 is adequate to represent texture in a 2-D image (Figure 5.14). Following the definition of the Euler angles (Section 2.6.1), for fixed values of φ_1 and Φ , the angle φ_2 defines a rotation about a distinct [001] axis. Thus, the projection of the ODF in the plane with $\varphi_2 = 0^\circ$ corresponds to a {100} pole figure (Figures 5.13a and 5.14). φ_2 Sections have been labeled *crystal orientation distribution* (COD) to indicate that in this representation the crystal orientations are expressed in a sample coordinate system (Wenk and Kocks, 1987). Alternatively, one may wish to represent the angles φ_2 and Φ in polar coordinates with φ_1 as cylinder axis (Figure 5.13b). As for fixed angles φ_2 and Φ , φ_1 indicates a rotation about the sample normal direction ND, a projection of the ODF in the plane with $\varphi_1 = 0^\circ$ corresponds to an inverse pole figure of the ND. For that reason, φ_1 sections may be referred to as *sample orientation distribution* (SOD) (Wenk and Kocks, 1987).

**FIGURE 5.13**

Representation of the orientation space in a cylindrical Euler space. (a) Cylinder axis parallel to φ_2 ; the projection of texture on the base ($\varphi_2 = 0^\circ$) corresponds to a pole figure (COD). (b) Cylinder axis parallel to φ_1 ; the projection of texture on the base ($\varphi_1 = 0^\circ$) corresponds to an inverse pole figure (SOD).

The texture presentation in a cylindrical space in sections $\varphi_2 = \text{constant}$ is particularly suitable for demonstration of the influence of sample symmetry on the necessary range of orientation space. As outlined in Section 2.6.2, sample symmetry affects the range of φ_1 . Thus, for orthonormal, monoclinic, and triclinic sample symmetry, respectively, a quarter circle ($\varphi_1^{\max} = 90^\circ$), a semicircle ($\varphi_1^{\max} = 180^\circ$), and a full circle ($\varphi_1^{\max} = 360^\circ$) are necessary to present the texture. As an example, Figures 5.14a and 5.14b show the texture of a hot band of an aluminum alloy at the band center and at the surface, respectively. In both cases, the textures are represented in the cylindrical Euler space in φ_2 sections (i.e., CODs). At the center layers of the sheet, the assumption of orthonormal sample symmetry is very well fulfilled, which results in symmetric semicircles representing the different φ_2 sections as well as in a symmetric projection, that is, pole figure (Figure 5.14a). At the band surface, in contrast, the different semicircles evidently are not symmetric (Figure 5.14b), representing the deviation of the strain state from orthonormal sample symmetry.

It is seen in Figure 5.14 that the representation of ODFs in polar coordinates still reveals some problems at small Φ angles—at the center of the circular sections—which may particularly affect representation of the cube orientation. These distortions can further be refined by introducing *oblique σ sections* (with $\sigma = (\varphi_1 + \varphi_2)/2$; Bunge, 1988; Matthies et al., 1990), which, however, is not discussed here. The main disadvantage of the representation of textures in the cylindrical Euler space is that determination of the orientations is more complicated than in an orthogonal space.

**FIGURE 5.14**

Texture of hot-rolled aluminum AA 6016 represented in the cylindrical Euler space (φ_2 sections, COD). (a) Rolling texture at the center layer of the sheet, depicting orthonormal sample symmetry. The sections $\varphi_2 = 0^\circ$, 45° , and 90° as well as the (projected) pole figure are symmetrical with respect to TD. Also, note symmetries between sections $\varphi_2 = 15^\circ$ and 75° and $\varphi_2 = 30^\circ$ and 60° . (b) Shear texture at the sheet surface, depicting monoclinic sample symmetry. The various semicircles show no symmetry with respect to TD, representing the deviation of the strain state from orthonormal sample symmetry.

In many studies, a series of comparable textures is analyzed, for example, rolling textures at different levels of deformation or recrystallization textures obtained after annealing at different temperatures. To compare the—usually rather similar—textures in such cases, it may be useful to confine the representation to the sections of the ODF that display the characteristic texture changes, which typically affect only one or two sections rather than the entire Euler angle space. For instance, most texture aspects of bcc materials can be found in the ODF section with $\varphi_2 = 45^\circ$. Therefore, despite the fact that bcc textures are traditionally represented in φ_1 sections (see the preceding text), analysis of the section $\varphi_2 = 45^\circ$ offers a very condensed way of analyzing bcc rolling and recrystallization textures, examples of which are given in Sections 5.5.2 and 5.5.5. Many interesting features of recrystallization textures in fcc materials are visible in the $\varphi_2 = 0^\circ$ section (Engler et al., 1995a).

Alternatively, instead of displaying the entire ODFs, many textures can be represented in a very condensed way by plotting the orientation intensity along certain characteristic paths or distinct crystallographic *fibers* through the orientation space versus an angle that defines the position along this path or fiber (Bunge and Tobisch, 1968; Lücke et al., 1985). For instance, the characteristic texture evolution during rolling can readily be visualized by plotting the orientation density along the corresponding rolling texture fibers, examples of which are given in Section 5.5. Provided that the texture information not covered by these fibers is of minor importance, such diagrams evidently represent a very convenient way of displaying characteristic textural features compared to the ODF plots.

5.5 Examples of Typical Textures in Metals

A number of examples of the characteristic deformation and annealing textures of fcc, bcc, and hexagonal metals are described in this section. Given the large body of publications on textures, it is not practicable to address all possible textures or present an exhaustive survey of the existing literature. Rather, the intention is to provide the reader with a guide to the most typical texture types that are frequently encountered in metallic materials and address the underlying formation mechanisms during deformation and recrystallization.

5.5.1 Deformation Textures of fcc Metals

In the earlier days of texture analysis by pole figure measurements, most effort was made to analyze the rolling textures of fcc metals and alloys, most notably, of copper and Cu alloys. In those days, rolling textures were

subdivided into two categories, namely, textures of *pure metals*—copper, nickel, and aluminum, and *alloy-type* textures—typically observed in brass and austenitic steel. In many fcc metals and alloys, there is a characteristic dependence of the rolling texture on the materials' *stacking fault energy* (SFE). The SFE depends on the sample material and is usually strongly affected by alloying elements. For example, pure metals such as nickel and aluminum have very high SFEs in excess of 200 mJ m^{-2} , whereas copper and gold have an intermediate value of $50\text{--}60 \text{ mJ m}^{-2}$ (Gallagher, 1970). Most alloy elements appreciably reduce the SFE to very low values of below 20 mJ m^{-2} , for example, in Cu alloys such as brass or bronze or in austenitic steel. Interestingly, pure silver has a very low SFE as well and, in consequence, reveals typical "alloy"-type rolling textures (Schmidt and Lücke, 1979; Liu et al., 1998). The influence of SFE on the rolling texture can be understood in terms of its impact on the deformation mechanisms, most notably, deformation twinning. In metals with medium to high SFE deformation, twinning is not observed; hence, deformation is solely attained through dislocation slip. Low SFE enables deformation twinning and, subsequently, massive shear band formation, which results in the altered deformation texture evolution (Hutchinson et al., 1979; Hirsch et al., 1988; Leffers and Bilde-Sørensen, 1990). As an example, Figure 5.15 shows the {111} pole figures of cold-rolled pure copper and brass (Cu–37%Zn), whereas the corresponding ODFs are given in Figure 5.16.

The texture shown in Figures 5.15a and 5.16a is a typical example of the characteristic "pure-metal" (or *copper-type*) rolling texture. This texture is commonly described in terms of three main texture components, the copper (or Cu) orientation $\{112\}\langle111\rangle$, the S orientation $\{123\}\langle634\rangle$, and the brass (or Bs) orientation $\{011\}\langle211\rangle$ (Table 5.1). However, a more detailed analysis of the pole figure (Figure 5.15a) and, especially, the ODF (Figure 5.16a) reveals that

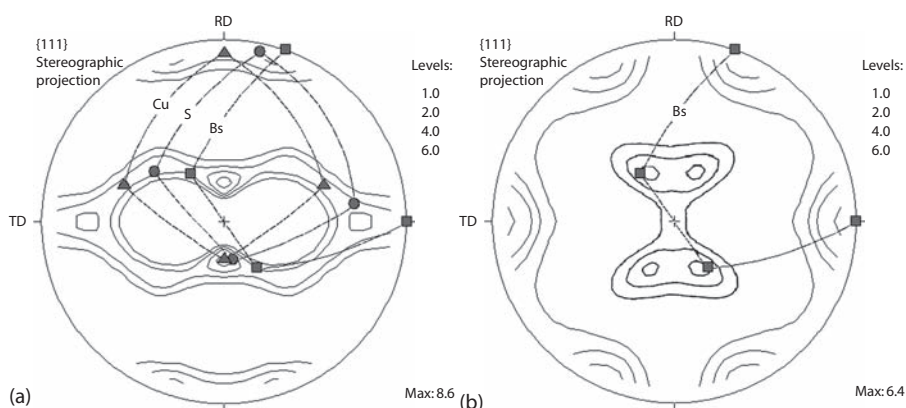
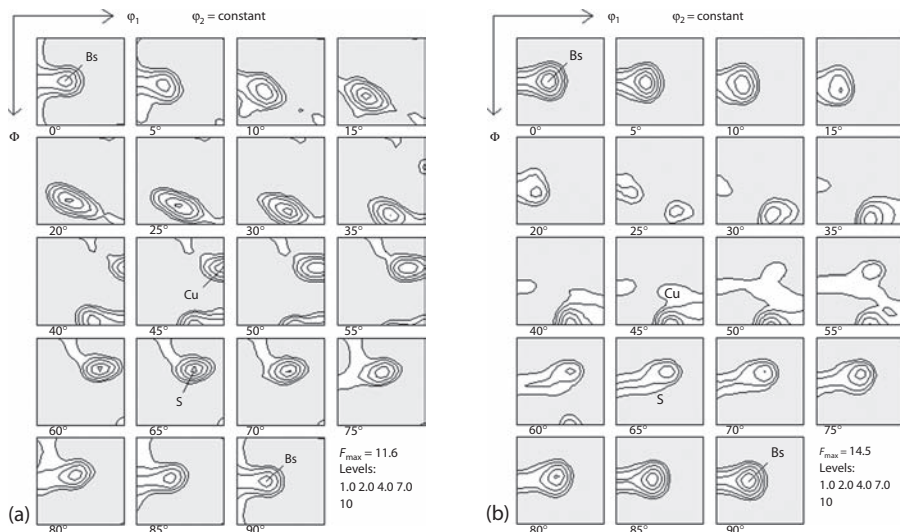


FIGURE 5.15

Rolling texture ({111} pole figure) of (a) pure copper and (b) brass (Cu–37%Zn).

**FIGURE 5.16**

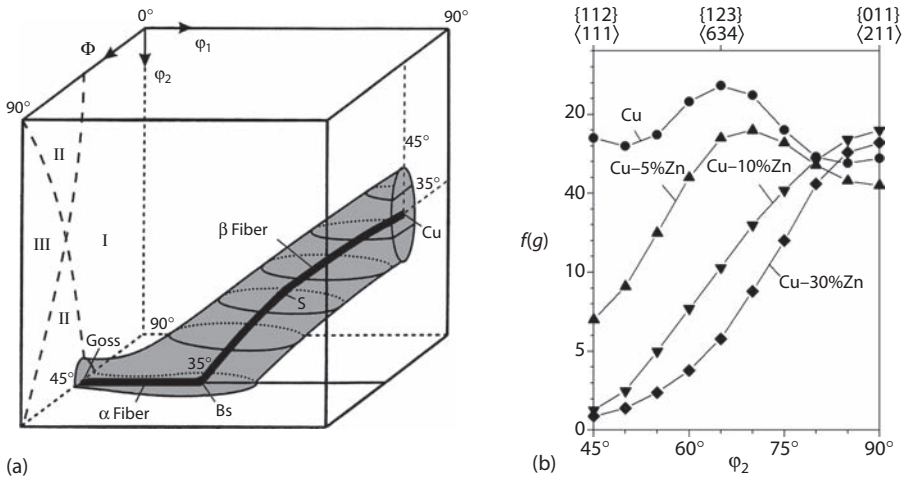
Rolling texture (ODF) of (a) pure copper and (b) brass (Cu-37%Zn).

TABLE 5.1

Miller Indices and Euler Angles of the Most Important Orientations of Al and Al alloys after Rolling and after Recrystallization (Approximated)

Designation	Miller Indices $\{hkl\}\langleuvw\rangle$	Euler Angles $\varphi_1 \Phi \varphi_2$
Copper (Cu)	$\{112\}\langle111\rangle$	$90^\circ 30^\circ 45^\circ$
S	$\{123\}\langle634\rangle$	$59^\circ 34^\circ 65^\circ$
Brass (Bs)	$\{011\}\langle211\rangle$	$35^\circ 45^\circ 0^\circ/90^\circ$
Goss	$\{011\}\langle100\rangle$	$0^\circ 45^\circ 0^\circ/90^\circ$

a description with ideal components is inadequate. Rather, the textures can be described as a spread of the orientations from the Cu orientation through the S orientation to the Bs orientation. That is to say, the typical copper-type rolling texture is best described by a continuous *orientation tube* running through orientation space. Figure 5.17a shows a schematic representation of this orientation tube in Euler space (for clarity only one of the symmetrically equivalent branches in the range $45^\circ \leq \Phi \leq 90^\circ$ is shown). The orientation tube is usually described in terms of its central fiber. In fcc metals, the most important orientation fibers are the α and the β fibers: At low deformation degrees the α fiber with $\{011\}/\text{RD}$ is observed, which runs from the Goss

**FIGURE 5.17**

(a) Sketch of the position of α and β fibers in Euler space (for clarity, only one of the symmetrical variants is shown); (b) β fibers of pure copper and three different copper–zinc alloys, showing the influence of stacking fault energy on the rolling textures (95% rolling reduction). (Adapted from Hirsch, J. and Lücke, K., *Acta Metall.*, 36, 2863, 1988.)

TABLE 5.2

Characteristic Fibers in fcc Metals and Alloys

Fiber	Fiber Axis	Euler Angles ^a
α	$\langle 011 \rangle // ND$	$0^\circ, 45^\circ, 0^\circ — 90^\circ, 45^\circ, 0^\circ$
γ	$\langle 111 \rangle // ND$	$60^\circ, 54.7^\circ, 45^\circ — 90^\circ, 54.7^\circ, 45^\circ$
τ	$\langle 011 \rangle // TD$	$90^\circ, 0^\circ, 45^\circ — 90^\circ, 90^\circ, 45^\circ$
β	^b	$90^\circ, 35^\circ, 45^\circ — 35^\circ, 45^\circ, 90^\circ$

^a Typical values without symmetry considerations.

^b Defined by the maximum intensity rather than by exact crystallographic position.

orientation $\{011\}\langle 100 \rangle$ to the Bs orientation $\{011\}\langle 211 \rangle$. At higher deformation degrees the β fiber prevails, which runs from the Cu orientation $\{112\}\langle 111 \rangle$ through the S orientation $\{123\}\langle 634 \rangle$ to the Bs orientation $\{011\}\langle 211 \rangle$ where it meets the α fiber. Table 5.2 summarizes the characteristics of these two fibers together with several other fibers that are less frequently observed in the textures of fcc materials.

Thus, specific differences in the rolling textures of different fcc materials can conveniently be displayed by plotting the intensity distribution along the α and β fibers. Figure 5.17b shows the β fibers of rolled pure copper and copper with different amounts of zinc after 95% rolling reduction. Note that—unlike most other texture fibers—the path of the β fiber is not fixed in Euler space;

the β fiber rather connects the relative intensity maxima in the corresponding ODF sections along the fiber, giving rise to the alternative term *skeleton line*. Therefore, besides analyzing the intensity distribution along the β fiber, subtle details in the position of the β fiber in Euler space can be evaluated, which may yield valuable information with regard to the underlying deformation mechanisms (Hirsch and Lücke, 1988; Engler et al., 1989).

The alloy, or brass, type texture displayed in Figures 5.15b and 5.16b is dominated by a quite pronounced Bs orientation $\{011\}\langle 211 \rangle$. Figure 5.17b shows that there is a systematic decrease in the intensities close to the Cu and S orientations to the advantage of the Bs orientation with increasing zinc content, that is, with decreasing SFE. This reflects the characteristic rolling texture transition from the copper or pure metal type to the brass or alloy type (Wassermann and Grewen, 1962; Hirsch and Lücke, 1988).

Rather than changing the SFE, alloy additions may precipitate in the form of second-phase particles, and different precipitation states affect the deformation behavior by interaction of the slip dislocations with the particles in dependence on particle size and volume. Figure 5.18 shows the rolling textures obtained in an aluminum–copper alloy after different pre-aging treatments, where it turned out that the resulting different precipitation states significantly influenced the intensity distribution along the β fiber (Engler et al., 1989; Lücke and Engler, 1990). Other parameters including initial grain size (Engler, 1995), deformation temperature (Maurice and Driver, 1997), and initial texture (Leffers and Juul Jensen, 1986; Mao et al., 1988; Engler et al., 2005a) have also been shown to affect the intensity

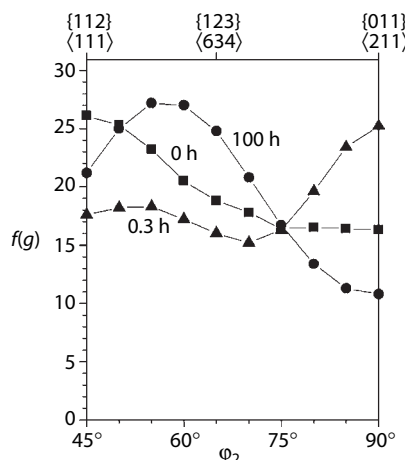


FIGURE 5.18

β fibers of Al-1.8%Cu cold rolled after different aging treatments, showing the influence of precipitates on rolling textures (95% rolling reduction). (Data taken from Engler, O., Hirsch, J., and Lücke, K., *Acta Metall.*, 37, 2743, 1989.)

distribution along the various fibers, though generally less dramatically than alloy composition.

With a view to the latter point—impact of initial texture—Figure 5.19a shows an example of the rolling texture obtained in Al beverage can stock (alloy AA 3104, AlMn1Mg1). This example is of great importance for the aluminum industry because of the correlation of texture and mechanical anisotropy, especially, the *earing* behavior. When a cylindrical cup is deep drawn from a circular blank of a textured sheet, the rim of this cup will not be level but will depict a number of distinct high points—usually called ears—and an equal number of low points, called troughs, as shown in Figures 5.19b and 5.19c. This earing is very undesirable, as it causes inhomogeneous wall thickness reduction and may interfere with automated deep-drawing operations.

For Al beverage cans, highly cold-rolled states (H19) are used to meet the strength requirements. Thus, the sheets comprise a strong β -fiber rolling texture, which is inevitably accompanied by the formation of ears at the four positions $\pm 45^\circ$ to the rolling direction, RD. Upon the production of Al can stock, it is aimed at offsetting these 45° ears by a proportion of $\langle 001 \rangle \langle 100 \rangle$ cube texture that is retained from the recrystallized hot strip (Section 5.5.4). Due to the slow rotation rate of the cube orientation, the resultant $0^\circ/90^\circ$ ears

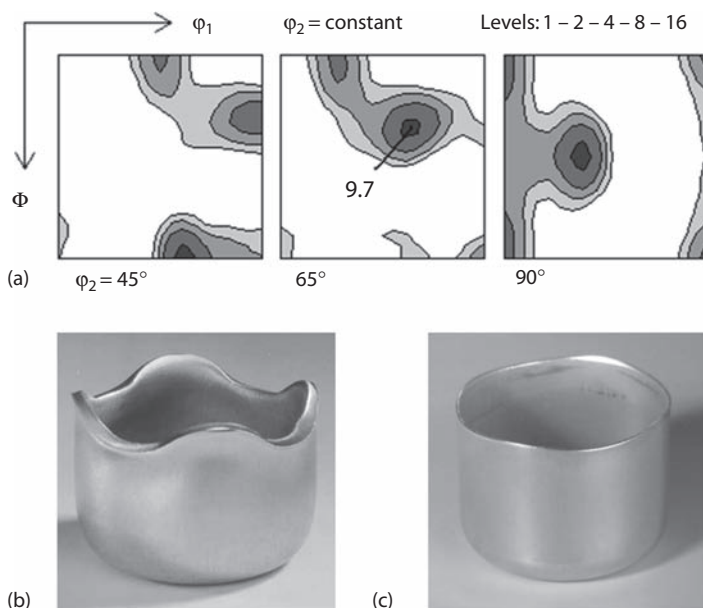
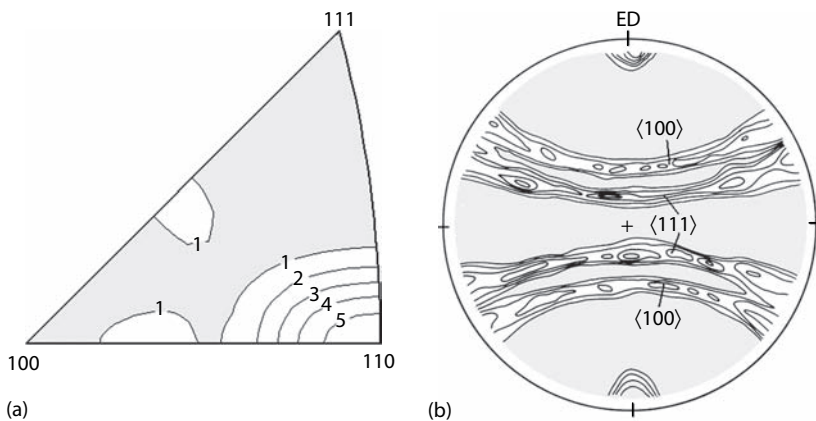


FIGURE 5.19

Correlation of texture and earing in AA 3104 can body stock. (a) Texture at final gauge (H19), showing a rolling texture superimposed on a cube texture retained from the recrystallized hot strip; (b) cup drawn from hot strip, showing pronounced $0^\circ/90^\circ$ earing; (c) cup drawn from final gauge sheet, showing very weak earing with mixed $0^\circ/90^\circ$ and 45° ears. (Adapted from Engler, O. and Hirsch, J., *Mater. Sci. Eng.*, A452-453, 640, 2007.)

**FIGURE 5.20**

(a) Inverse pole figure of the compression direction of copper after compression to a strain of ~ 1 ; (b) pole figure of the extrusion texture of an Al-Li alloy. (Courtesy of J. Hirsch.)

(Figure 5.19b) are able to balance the newly forming 45° ears up to rather high rolling reductions, typically ranging between 80% and 90% (Hutchinson et al., 1989; Engler et al., 2007). Figure 5.19a shows an example of the texture of final gauge can stock, which consists of a mixture of a retained cube texture and the newly formed rolling texture components. The resulting cup height profile reveals a characteristic six-ear profile with ears under 0° , 45° , 135° , 180° , 225° , and 315° to the RD (Figure 5.19c).

Uniaxial deformation—tension, compression, wire drawing, or extrusion—usually leads to simpler textures than rolling. Since only one deformation axis is prescribed, invariably fiber textures form, which are often represented as inverse pole figures. Figure 5.20a shows the compression texture of pure copper, which consists of a $\langle 110 \rangle$ fiber with some scatter toward $\langle 221 \rangle$ (Stout et al., 1988). In low-SFE materials, $\langle 111 \rangle$ components may also form. After tension or uniaxial extrusion of fcc materials, the textures can be described by two fibers with $\langle 111 \rangle$ and $\langle 100 \rangle$ parallel to the deformation axis. Figure 5.20b shows an example of this double fiber texture in an extruded Al alloy. The relative proportion of the two fibers may vary with initial texture, deformation mode, and SFE (English and Chin, 1965).

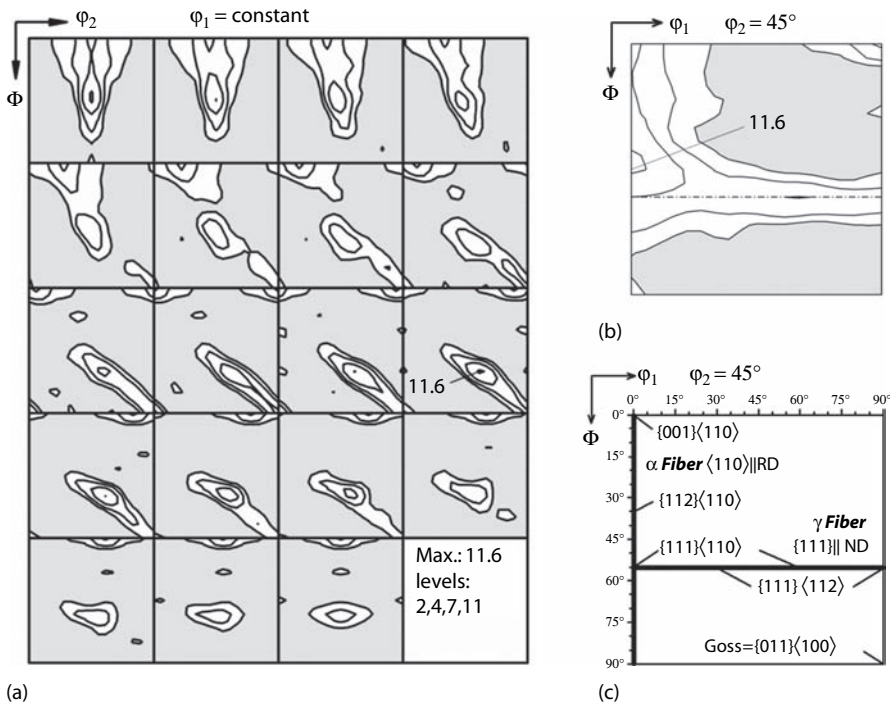
5.5.2 Deformation Textures of bcc Metals

Despite the importance of steel industry, deformation textures in bcc metals and alloys have been less extensively investigated. In general, bcc metals and alloys tend to form fiber textures, which means that most orientations are assembled along two characteristic fibers through orientation space. These are summarized in Table 5.3 (Hutchinson, 1984; Von Schlippenbach et al., 1986). Figure 5.21a shows a typical cold-rolling texture of a microalloyed

TABLE 5.3

Characteristic Fibers in bcc Metals and Alloys

Fiber	Fiber Axis	Euler Angles ^a
α	$\langle 011 \rangle // RD$	$0^\circ, 0^\circ, 45^\circ - 0^\circ, 90^\circ, 45^\circ$
γ	$\langle 111 \rangle // ND$	$60^\circ, 54.7^\circ, 45^\circ - 90^\circ, 54.7^\circ, 45^\circ$
η	$\langle 001 \rangle // RD$	$0^\circ, 0^\circ, 0^\circ - 0^\circ, 45^\circ, 0^\circ$
ζ	$\langle 011 \rangle // ND$	$0^\circ, 45^\circ, 0^\circ - 90^\circ, 45^\circ, 0^\circ$
ε	$\langle 110 \rangle // TD$	$90^\circ, 0^\circ, 45^\circ - 90^\circ, 90^\circ, 45^\circ$
β	^b	$0^\circ, 35^\circ, 45^\circ - 90^\circ, 54.7^\circ, 45^\circ$

^a Typical values without symmetry considerations.^b Defined by the maximum intensity rather than by exact crystallographic position.**FIGURE 5.21**

Rolling texture of a Ti and Nb microalloyed interstitial-free steel in the Euler space (90% rolling reduction). (a) Conventional representation of the ODF in φ_1 sections; (b) $\varphi_2 = 45^\circ$ section displaying the intensity distribution of the α - and γ -fiber orientations; (c) schematic representation of the most important orientations in bcc materials in the $\varphi_2 = 45^\circ$ section. (Courtesy of M.Y. Huh.)

interstitial-free (IF) steel, plotted in φ_1 sections. The, mostly partial, α fiber comprises the orientations with a common $\langle 110 \rangle$ crystal axis parallel to the RD, that is, the orientations $\{hkl\}\langle 110 \rangle$, which include the orientations $\{001\}$

$\langle 110 \rangle$, $\{112\}\langle 110 \rangle$, and $\{111\}\langle 110 \rangle$. In the Euler space, the α fiber can be found between $(\phi_1, \Phi, \phi_2) = (0^\circ, 0^\circ, 45^\circ)$, $(0^\circ, 35^\circ, 45^\circ)$, and $(0^\circ, 54.7^\circ, 45^\circ)$ (note that, because of the cubic crystal symmetry, these orientations also appear at other, symmetrically equivalent locations in the Euler space). The γ fiber comprises the orientations with $\{111\}$ parallel to the ND, that is, the orientations $\{111\}\langle uvw \rangle$, including $\{111\}\langle 110 \rangle$ and $\{111\}\langle 112 \rangle$. This fiber runs from $(0^\circ, 54.7^\circ, 45^\circ)$ to $(90^\circ, 54.7^\circ, 45^\circ)$ in Euler space but, because of the cubic crystal symmetry, the range $60^\circ \leq \phi_1 \leq 90^\circ$ is sufficient for a representation of the full γ fiber. As already alluded to in Section 5.4.2, the characteristic texture changes during rolling can readily be visualized by plotting the orientation density along the most important texture fibers. Figure 5.22 displays the typical texture evolution upon cold rolling of a low-carbon steel in the form of the intensity density along the α and γ fibers (Hölscher et al., 1991). It is evident that, starting from the almost random hot strip texture (see the following text), there is a significant texture sharpening with increasing strain. Furthermore, increasing rolling deformation tends to shift the texture maxima from $\{001\}\langle 110 \rangle$ along the α fiber over $\{112\}\langle 110 \rangle$ toward $\{111\}\langle 110 \rangle$ and $\{111\}\langle 112 \rangle$ in the γ fiber.

As already mentioned, the textures of bcc materials are often represented in ϕ_1 sections, though ϕ_2 sections offer some advantages. In Figure 5.21b, the

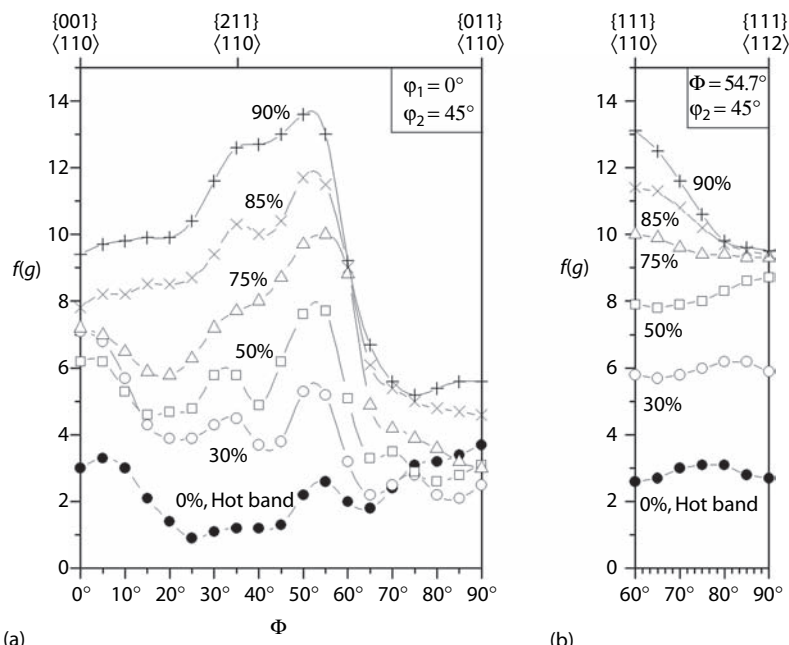


FIGURE 5.22

Development of the rolling texture fibers of a low-carbon steel with increasing rolling reduction. (Data from Hölscher, M., Raabe, D., and Lücke, K., *Steel Res.*, 62, 567, 1991.)

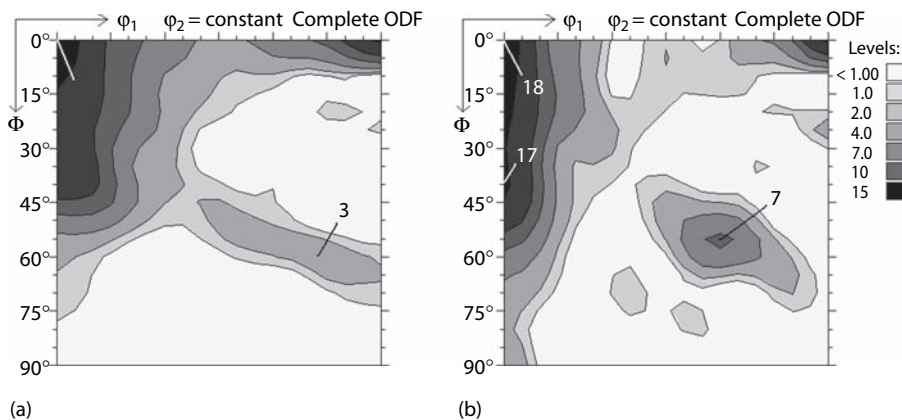
texture of Figure 5.21a is represented in the $\varphi_2 = 45^\circ$ section, and it is seen that the most important texture features—including both the α fiber $\langle 011 \rangle // RD$ and the γ fiber $\{111\} // ND$ —can all be found in this section (Figure 5.21c).

Unlike in fcc metals, the rolling texture evolution in iron and low-carbon steels is largely independent of composition and processing (except the described general texture sharpening with strain). During hot rolling and subsequent coiling, recrystallization and the phase transformation from γ to α iron take place, leading to grain refinement and a randomization of the texture (Ray et al., 1994). As a consequence, the hot bands of low-carbon steels comprise fairly small grains with a random texture, which constitutes quite constant starting conditions for the subsequent cold rolling and recrystallization.

This is different in highly alloyed steel grades, like Fe–Si transformer steel or Cr-containing ferritic stainless steel (Seidel et al., 1989; Raabe, 1996; Huh and Engler, 2001). Such steel undergo no or merely a limited phase transformation during hot rolling, which restricts the opportunities for a texture randomization through a γ -to- α -phase transformation during the thermomechanical processing. The as-cast ingots usually comprise a columnar grain structure with the fast-growing $\{001\}$ crystal directions aligned parallel to the normal direction of the ingot. Accordingly, the hot bands of ferritic stainless steels commonly display pronounced textures and strong through-thickness gradients in both microstructure and texture. Small recrystallized grains with a weak shear texture form at the outer surface layers, and highly elongated very large pancake-shaped grains with $\{001\}\langle 110 \rangle$ are often observed in the sheet center (Figure 5.23a). This inhomogeneous hot strip has a marked impact on the evolution of texture and properties during the subsequent cold rolling and recrystallization. Because of the preferred $\{001\}\langle 110 \rangle$ component in the hot strip, the cold-rolling textures usually comprise higher α -fiber intensities, whereas the γ fiber is less well developed than in plain low-carbon steel (Figure 5.23b).

Other bcc materials, like tantalum, molybdenum, and niobium, show similar α - and γ -fiber rolling textures as steel. As discussed for the highly alloyed Fe–Si and Fe–Cr steel grades, usually the component $\{001\}\langle 110 \rangle$, which is retained from the hot strip texture, is quite strong (Raabe and Lücke, 1994; Raabe et al., 1994). Moreover, refractory metals have been reported to develop pronounced through-thickness texture gradients (Vandermeer and Ogle, 1969; Klein et al., 1994; Wright et al., 1994b).

In uniaxial tension or wire drawing, bcc materials form $\langle 110 \rangle$ fiber textures, as fcc materials deformed in compression. Vice versa, in compression of bcc metals, mixed $\langle 100 \rangle$ and $\langle 111 \rangle$ fiber texture form, which resemble the typical fcc tension textures (Section 5.5.1). For the resemblance of fcc and bcc deformation textures due to reversing slip plane and slip direction, see Hölscher et al. (1994) and Rollett and Wright (1998). A notable difference between tensile deformation of fcc and bcc structures, however, is the phenomenon of *grain curling* (Hosford, 1964; Gil Sevillano et al., 2007). Upon drawing of bcc

**FIGURE 5.23**

Texture of (a) hot strip and (b) cold strip of ferritic stainless steel Fe-17%Cr (ODF $\varphi_2 = 45^\circ$ section, sheet center). (Data from Huh, M.Y. and Engler, O., *Mater. Sci. Eng.*, A308, 74, 2001.)

wires, grains tend to form ribbons and wrap around one another, rather than deforming uniaxially. This is attributed to the formation of a $\langle 110 \rangle$ fiber texture, which—at variance to the macroscopic uniaxial strain state—favors a plane strain deformation on the grain level.

5.5.3 Deformation Textures of Hexagonal Metals

Compared to cubic metals (both fcc and bcc), studies on the texture evolution in hexagonal materials are very limited. Nevertheless, hexagonal textures are of interest because of the use of zirconium alloys Zircaloy in nuclear reactors and titanium and magnesium sheet in transportation applications (see reviews by Tenckhoff, 1988; Philippe, 1994; Wang and Huang, 2003). Note that for hexagonal structures, two different conventions for the definition of crystal axes are used in the literature (Section 2.3.1; Appendix I). All examples in this chapter are based on the definition in Equation 2.2a.

With a view to the evolution of deformation textures, hexagonal materials are different from cubic metals in that, besides dislocation slip, twinning is almost always required to accommodate the external plastic strain state (Kocks and Westlake, 1967). Fcc materials have 12 equivalent slip systems of type $\{111\}/\langle 110 \rangle$ (i.e., slip plane/slip direction) that can be activated, so that there will always be enough slip systems to accommodate plastic deformation. In bcc materials the slip direction is $\langle 111 \rangle$, whereas the slip planes are not so clearly defined. In most bcc materials, $\{110\}$ planes are activated, whereas in some cases, additional slip occurs on $\{112\}$ or $\{123\}$ planes. Thus, bcc metals have 12, 24, or even 48 possible slip systems to

accommodate plastic strain. In hexagonal structures, basal slip $\{0002\}/\langle1120\rangle$ is the easy glide system and, as such, activated most often. However, there are only three slip systems of this type (and only two mutually independent ones), which in most cases is not sufficient to accommodate plastic deformation. Additionally, the prismatic slip systems $\{1010\}/\langle1120\rangle$ and the pyramidal slip systems $\{1011\}/\langle1120\rangle$ and $\{1012\}/\langle1120\rangle$ may be activated, but they have the same slip direction as the basal glide (cross slip). Pyramidal slip $\{1122\}/\langle1123\rangle$ is the only slip system that has a slip direction *not* parallel to the basal plane. That is to say, pyramidal $(c+a)$ glide is the only mechanism that permits the accommodation of deformation along the c axis. Because of this general lack of slip systems, slip cannot continue as the only deformation mode but twinning becomes significant already at rather low strains. The most important twinning system is $\{1012\}/\langle1011\rangle$, but in materials with a low c/a ratio, other twinning systems may be activated as well. The shears achieved by twinning are quite low, typically between 0.1 and 0.2 (Grewen, 1973). Therefore, hexagonal materials usually contain a large volume of twins, which reorient the structure and hence facilitate further dislocation slip.

The deformation textures of hexagonal materials can roughly be subdivided into three groups in accordance with their c/a ratio (Wassermann and Grewen, 1962; Grewen, 1973; Barrett and Massalski, 1980; Philippe et al., 1988). For metals like magnesium or cobalt with a close-to-ideal c/a ratio of ~ 1.633 , the rolling textures are dominated by a pronounced $\{0001\}$ fiber texture (Figure 5.24a). This is a direct consequence of the dominant basal slip that leads to a rapid rotation of the grain orientations toward $\{0001\}$ and, therewith, readily exhausts the possibility to activate other slip systems or twinning systems. This severely limits the possibility for both further cold rolling and subsequent forming operations of Mg sheet (Agnew et al., 2003; Barnett et al., 2004; Gehrmann et al., 2005; Yang et al., 2005). Upon hot deformation,

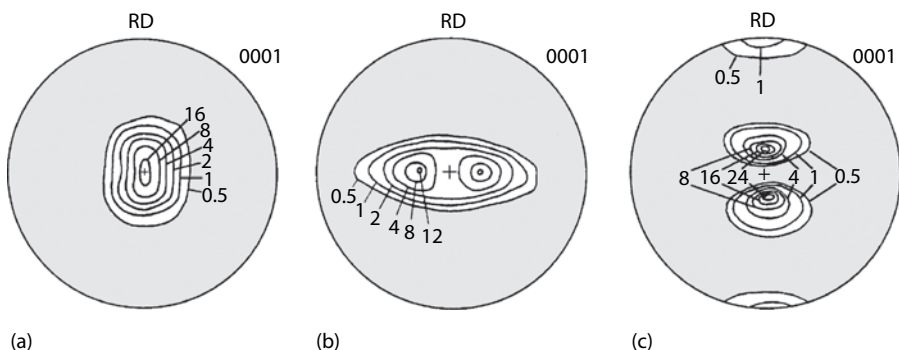


FIGURE 5.24

{0001} Pole figures for rolled hexagonal metals as a function of the c/a ratio. (Adapted from Grewen, J., Proc. 3ème Colloq. Europ. sur les Textures des Métaux et leurs Application Industrielle, Pont-à-Mousson, Soc. Franç. Métal., Nancy, France, 1973.)

other slip systems (prismatic slip as well as pyramidal $c+a$ slip) are activated much more easily; furthermore, recovery or recrystallization are enhanced (Ion et al., 1982; Del Valle et al., 2003; Backx et al., 2004; Walde and Riedel, 2007; Al-Samman and Gottstein, 2008). Figure 5.25 shows the ODF of hot-rolled Mg alloy AZ31 sheet ($Mg-3\%Al-1\%Zn$). Note that because of crystal symmetry, the angular range of φ_2 is limited to 60° , whereas there is no three-fold symmetry as in the case of cubic structures (Section 2.6.2; Table 2.3). The ODF shows a rather weak $\{0001\}$ fiber texture with some scatter toward $\{0112\}$ $\langle 2110 \rangle$. Sheet formability is likewise greatly enhanced at elevated temperature (Doege and Dröder, 2001).

For metals with a lower c/a ratio than ideal (titanium, zirconium), the basal planes are rotated by $\pm 30^\circ$ to 40° about the rolling direction, RD (Figure 5.24b). Figures 5.26a and 5.26b show the evolution of the cold-rolling texture of titanium sheet for two different rolling degrees. The textures are displayed in two important φ_2 sections of the ODF, $\varphi_2 = 0^\circ$ and $\varphi_2 = 30^\circ$ (Figure 5.26c). After medium rolling degrees, the orientations tend to align along a fiber along Φ at $\varphi_1 = \varphi_2 = 0^\circ$, which are all orientations having a common $\langle 1010 \rangle$ direction parallel to the RD, plus minor intensities of $\{0001\}\langle uvt0 \rangle$

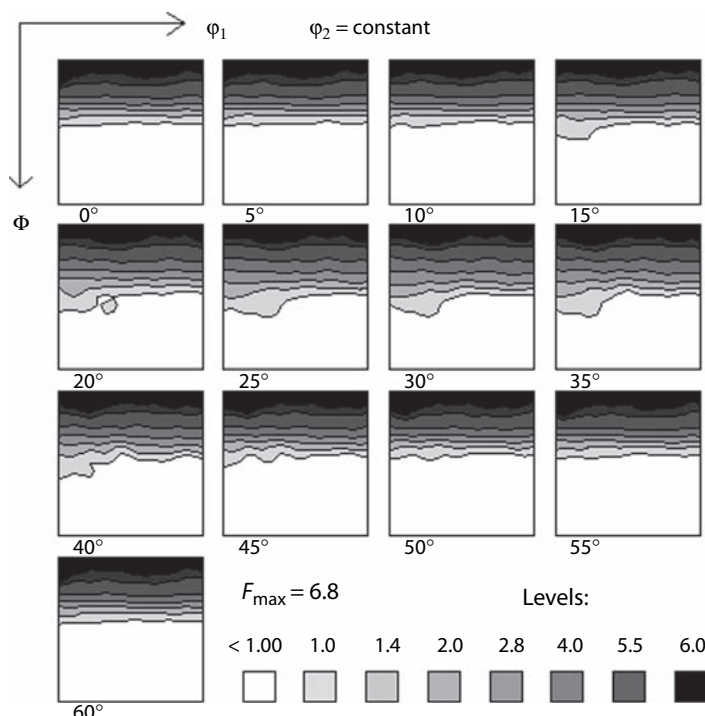
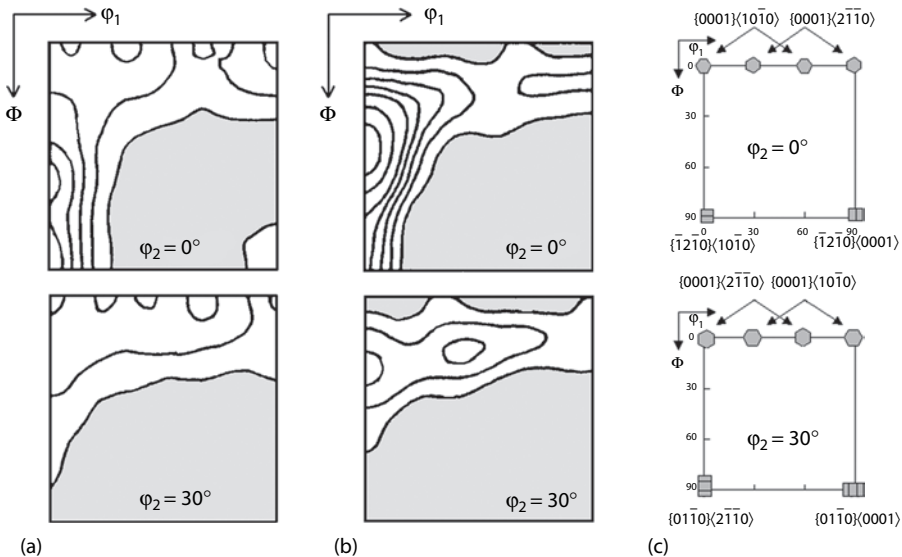


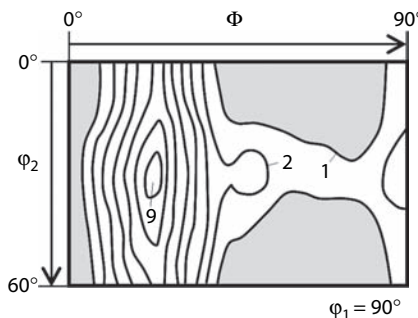
FIGURE 5.25
Hot-rolling texture of Mg alloy AZ31. (Courtesy of T. Al-Samman.)

**FIGURE 5.26**

Rolling texture of titanium sheet: (a) 50% cold rolled, (b) 90% cold rolled, (c) position of important orientations of hexagonal materials in Euler space ($ODF \varphi_2 = 0^\circ$ and 30° sections, intensity levels 1–2–3–4–5–7–9). (Adapted from Inoue, H. and Inakazu, N., *Proc. ICOTOM 8*, TMS, Warrendale, PA, 1988.)

(Figure 5.26a). At higher rolling degrees, the texture sharpens whereas the orientations concentrate at $\Phi \sim 35^\circ$ – 40° , that is, at $\langle 1214 \rangle\langle 1010 \rangle$ (Figure 5.26b) (Inoue and Inakazu, 1988; Lee et al., 1988; Singh and Schwarzer, 2000; Wagner et al., 2002). Such textures form through prevalent $\langle 1010 \rangle/\langle 1120 \rangle$ prismatic slip, whereas pyramidal and basal cross slip as well as pyramidal ($c+a$) slip are less important. Furthermore, there is significant contribution from two twinning systems: $\{1012\}$ tension twinning and $\{1122\}$ compression twinning (Tomé et al., 1988).

In zinc and cadmium with higher c/a ratios, the basal orientation is split up in that the basal planes are tilted symmetrically by $\pm 20^\circ$ to 30° about the transverse direction, TD, toward the rolling direction, RD (Figure 5.24c); the $\langle 1010 \rangle$ directions are aligned with the TD (Dillamore and Roberts, 1965; Philippe et al., 1994; Carmichael et al., 1996). Figure 5.27 shows an example of the ODF of a ZnCuTi alloy after 80% cold rolling, plotted in the section $\varphi_1 = 90^\circ$. The texture is composed of a fiber along φ_1 at $\varphi_1 = 90^\circ$ and $\Phi = 20^\circ$, with a texture maximum at $\varphi_2 = 45^\circ$, corresponding to crystallites with the c axes tilted by $\sim 20^\circ$ from ND in the ND–RD plane. This texture can be interpreted by a combination of basal slip and significant contributions of prismatic and pyramidal ($c+a$) slip systems, whereas $\{1012\}$ twinning, though present, is less significant.

**FIGURE 5.27**

Rolling texture of 80% cold-rolled ZnCuTi alloy sheet (ODF $\varphi_1 = 90^\circ$ section). (Adapted from Philippe, M.J., Wagner, F., Mellab, F.E., Esling, C., and Wegria, J., *Acta Metall. Mater.*, 42, 239, 1994.)

Of course the categorization by the c/a ratio is quite crude, and other factors, including initial texture, strain rate, deformation temperature, and chemical composition—both intentional alloying and impurities—will also impact texture development of hexagonal metals. For instance, the oxygen content has been reported to have a strong effect on the rolling texture evolution through changes of the critical resolved shear stress of the various slip systems and, most notably, through suppression of twin activities (Philippe et al., 1988).

After wire drawing or extrusion, Zr and Ti usually form $\langle 1010 \rangle$ fiber textures; an example for this has already been given in Section 5.2.2 (Figure 5.3). Extruded Mg develops $\langle 1010 \rangle$ and $\langle 1120 \rangle$ double fiber textures, where the intensity ratio between the two fibers depends on the deformation conditions (Müller et al., 2006). Zn wires have a so-called “spiral texture,” with $\langle 0001 \rangle$ approximately 70° from the wire axis. This difference is attributed to twinning, which leads to significant reorientations of material from a position in which the basal plane is parallel to the wire axis (Dillamore and Roberts, 1965; Barrett and Massalski, 1980).

5.5.4 Recrystallization Textures of fcc Metals

Recrystallization of deformed metallic materials is accomplished by the nucleation of new undeformed grains and their subsequent growth into the deformed matrix (Humphreys and Hatherly, 1995). These processes are characterized by the formation and the movement of high-angle grain boundaries. Therefore, recrystallization gives rise to a change in the distribution of the crystallographic orientations and, consequently, to a change in the crystallographic texture of a metallic material.

The rolling textures of fcc materials are mainly governed by two fibers, the α fiber and, most pronounced, the β fiber. It has been shown in Section 5.5.1 that

the addition of alloy elements mainly alters the intensity distribution along these fibers, most notably through affecting the materials' SFE. While the rolling textures of Cu alloys show a rather smooth, continuous transition as a function of alloy composition (Figure 5.17b), the recrystallization textures change more drastically, however, and several points have been established on how alloying elements may potentially affect recrystallization textures. In correspondence to the two fundamental steps of recrystallization, nucleation and growth, the texture changes during recrystallization are traditionally interpreted in terms of the two rival theories of oriented nucleation and oriented growth (Doherty et al., 1988).

In the case of the *oriented nucleation* argument, it is assumed that the preferred formation of special orientations determines the final recrystallization texture. With the emergence of the techniques for local texture analysis available today—analysis of Kikuchi diffraction patterns in the TEM and EBSD—nucleus orientations can be readily studied and, therewith, the occurrence of oriented nucleation in the sense of the preferred formation of special orientations at each nucleation site has been established.

In the case of *oriented growth* or *growth selection* arguments, it is assumed that, starting from a broad spectrum of nucleus orientations, those with the best growth conditions with respect to the deformed matrix grow fastest and, therefore, dominate the recrystallization texture. The well-known work by Liebmann et al. (1956) and, more recently, detailed bicrystal experiments performed by Molodov et al. (1995) have proven that in aluminum, grain boundaries with a rotation relationship of approximately 40° about a $\langle 111 \rangle$ axis depict maximum mobility.

It must be emphasized here that each of these two theories describes only one aspect of recrystallization as a limiting case, such that a discussion solely based on either of these two theories will be incomplete. Instead, in the majority of cases, a combination of both theories in the sense of a $40^\circ \langle 111 \rangle$ growth selection out of a limited spectrum of preferentially formed nucleus orientations takes place, which explains well the recrystallization textures of many fcc metals and alloys.

Materials with a high SFE like Al, Ni, and Cu typically form a cube recrystallization texture $\{001\}\langle 100 \rangle$; an example is shown in Figure 5.28a. The

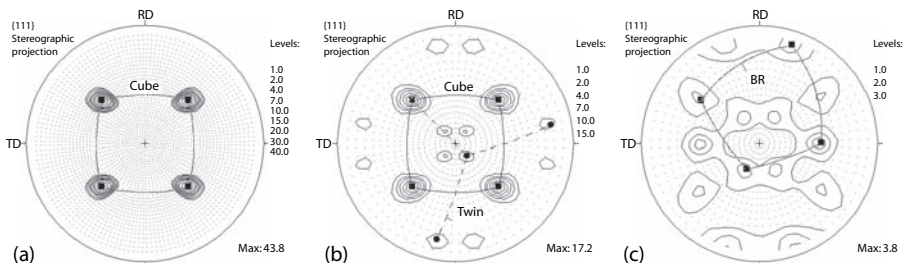


FIGURE 5.28

Recrystallization texture of cold-rolled fcc metals: (a) aluminum, (b) copper, and (c) brass (Cu-37%Zn) ($\{111\}$ pole figure).

mechanisms leading to the cube recrystallization texture have been subject to debate for more than six decades; a systematic review of this research is given by Hu (1986). Only with the advent of techniques for microtexture analysis, the nucleation and growth mechanisms of cube-oriented grains have been understood quite comprehensively. In brief, cube-oriented nuclei emerge from bandlike structures, the so-called cube bands, which are part of the deformed microstructure (Ridha and Hutchinson, 1982; Dons and Nes, 1986; Hjelen et al., 1991). These cube bands are either transition bands (Dillamore and Katoh, 1974) or deformed grains with retained cube orientation (Vatne et al., 1996). During the subsequent growth, grains with the cube orientation prevail, which is due to their optimum growth conditions into the rolling texture (Lücke, 1974).

With an increasing amount of alloying elements, the SFE of most Cu alloys decreases. Because of the decrease in SFE, recrystallization twinning may become an important mechanism for providing new orientations, thus leading to recrystallization texture components that are not present in the as-deformed state. For instance, copper has a lower SFE than Al. Although the SFE of Cu is not low enough to allow for deformation twinning (Section 5.1), growth twins may emerge. Accordingly, the recrystallization texture of pure Cu is composed of the cube orientation and its first-generation twins (Figure 5.28b).

Usually very weak recrystallization textures are observed in Cu alloys with medium contents of Zn, Al, or Ge, which contain twins of the cube and Goss orientation as well as a few new orientations, including the transition or U orientation $\{258\}\langle 121 \rangle$ and the P orientation $\sim\{011\}\langle 122 \rangle$ (Figure 5.29a; Table 5.4). In such materials, the SFE is not sufficiently reduced so as to promote mechanical twinning and subsequent shear band formation and,

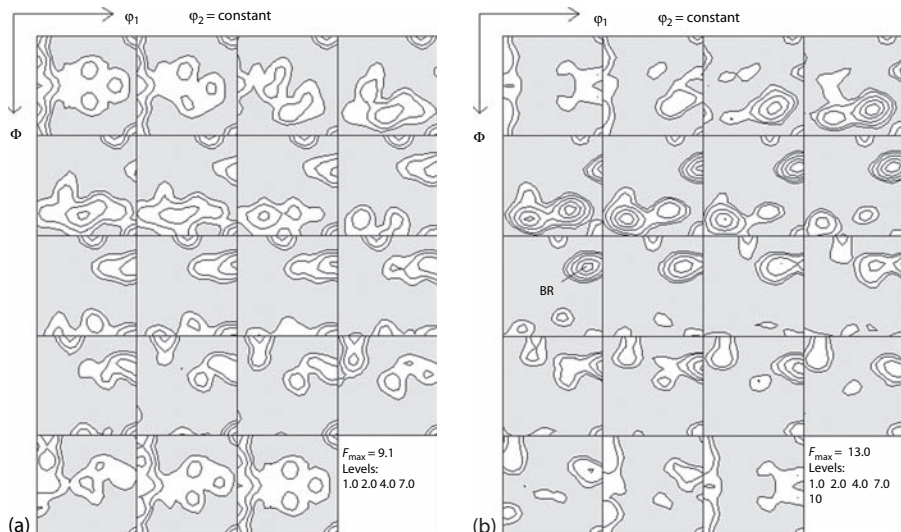


FIGURE 5.29

Recrystallization texture of cold-rolled copper alloys. (a) Cu-8%Mn, (b) Cu-37%Zn.

TABLE 5.4

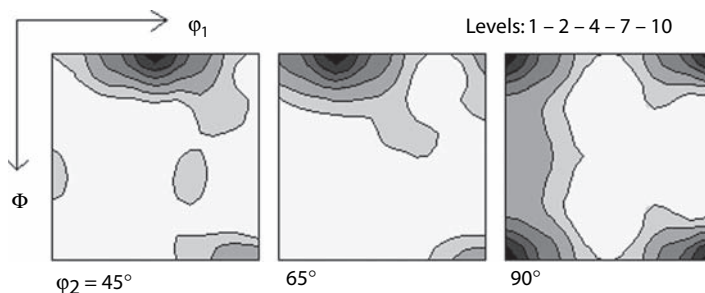
Miller Indices and Euler Angles of the Most Important Recrystallization Texture Orientations of fcc Metals and Alloys (Approximated)

Designation	Miller Indices $\{hkl\}\langleuvw\rangle$	Euler Angles $\varphi_1 \Phi \varphi_2$
Cube	$\{001\}\langle100\rangle$	$0^\circ 0^\circ 0^\circ / 90^\circ$
Cube _{RD}	$\{013\}\langle100\rangle$	$0^\circ 22^\circ 0^\circ / 90^\circ$
Cube _{ND}	$\{001\}\langle310\rangle$	$22^\circ 0^\circ 0^\circ / 90^\circ$
Cube-twin (first generation)	$\{122\}\langle212\rangle$	$27^\circ 48^\circ 27^\circ \text{ or } 63^\circ$ $48^\circ 63^\circ$
Goss	$\{011\}\langle100\rangle$	$0^\circ 45^\circ 0^\circ / 90^\circ$
BR	$\{236\}\langle385\rangle$	$80^\circ 31^\circ 35^\circ$
U (transition)	$\{258\}\langle121\rangle$	$45^\circ 35^\circ 20^\circ$
R	$\{124\}\langle211\rangle$	$53^\circ 36^\circ 60^\circ$
P	$\{011\}\langle122\rangle$	$65^\circ 45^\circ 0^\circ / 90^\circ$
Q	$\{013\}\langle231\rangle$	$45^\circ 15^\circ 10^\circ$

consequently, provide additional nucleation sites. However, SFE is small enough to facilitate recrystallization twinning, which explains the increased occurrence of the twin orientations in the corresponding textures. Moreover, the alloying elements in solid solution interfere with the grain boundary motion, which retards the growth of the recrystallized grains, slows down recrystallization kinetics, and counteracts the formation of a well-defined recrystallization texture (Schmidt and Lücke, 1979; Eichelkraut et al., 1984; Savoie and Lücke, 1991).

A further decrease in the SFE leads to changes in the as-deformed microstructure, especially by promoting profuse shear band formation. Upon subsequent annealing, this gives rise to nucleation of recrystallization at the shear bands, which can substantially alter the resulting recrystallization textures. As an example, the recrystallization texture of brass is dominated by the so-called brass recrystallization texture component “BR” $\{236\}\langle385\rangle$, as displayed in Figures 5.28c and 5.29b. The BR orientation is the characteristic recrystallization texture component of materials with low SFE, like silver or Cu alloys with high Zn, Al, or Ge contents (Schmidt and Lücke, 1979; Engler et al., 1995b). Grains with the BR orientation emerge from shear bands through subsequent twinning. Furthermore, the BR orientation has an approximate $40^\circ\langle111\rangle$ orientation relationship to the Bs orientation, the main rolling texture component in such low-SFE alloys (Figure 5.16b), which favors it for a successful growth.

In the field of Al alloys, texture investigations are of great interest since the texture determines the plastic anisotropy that is important for practical

**FIGURE 5.30**

Cube-recrystallization texture of hot-rolled aluminum (can stock alloy AA 3104, recrystallized hot strip, ODF $\phi_2 = 45^\circ, 65^\circ, 90^\circ$ sections).

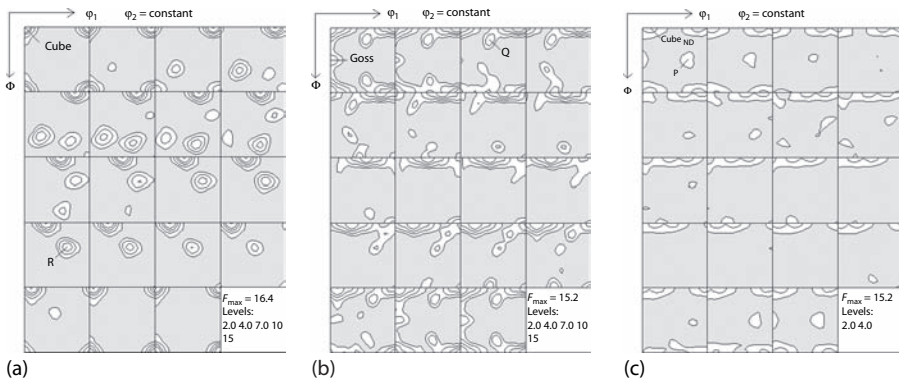
applications, for example, for good deep-drawing properties. Furthermore, with a view to recrystallization, the occurrence of specific texture components yields viable information about the underlying mechanisms of recrystallization, namely, formation and growth of the nuclei. In Al alloys, the SFE is too high to allow for significant twin formation. Nonetheless, there is quite a variety of recrystallization textures, which is caused by the interplay of preferred nucleation and growth effects (Engler, 1996).

Hot-rolled Al usually shows a more or less strong cube recrystallization texture (Daaland and Nes, 1996). Figure 5.30 shows an example of the hot strip texture of aluminum alloy AA 3104 can stock, where a strong cube recrystallization texture is key to the formation of Al sheet suited for the production of beverage cans (Section 5.5.1). Pronounced cube recrystallization textures are also observed in cold-rolled high-purity Al (Figure 5.28a; see also Figure 4.7), for example, in Al foil for high-voltage electrolytic capacitors (Kneijnsberg et al., 1985; Kernig et al., 1989).

In commercial purity Al, the cube component is frequently accompanied by the R orientation, which is quite similar to the rolling texture S orientation (Figure 5.31a). R-oriented grains presumably form through nucleation at the preexisting high-angle grain boundaries and subsequent growth into the as-deformed matrix (Engler, 1999).

On cold rolling of Al alloys with high amounts of solute, Cu or Mg, shear bands may form (Wagner et al., 1995). On subsequent recrystallization annealing, these shear bands are viable nucleation sites because of their strong local lattice rotations and highly localized strains. As shown in Figure 5.31b, nucleation at shear bands leads to the formation of two new orientations, the Goss orientation $\{011\}\langle100\rangle$ and the Q orientation $\{013\}\langle231\rangle$ (Lücke and Engler, 1990; Engler, 2001). During the growth of the nuclei, both Q and Goss-oriented grains are regarded as being preferred owing to a $40^\circ\langle111\rangle$ orientation relationship to the main rolling texture orientations.

In Al alloys containing large particles ($>1 \mu\text{m}$), nucleation of recrystallization takes place in the deformation zones that form around these large

**FIGURE 5.31**

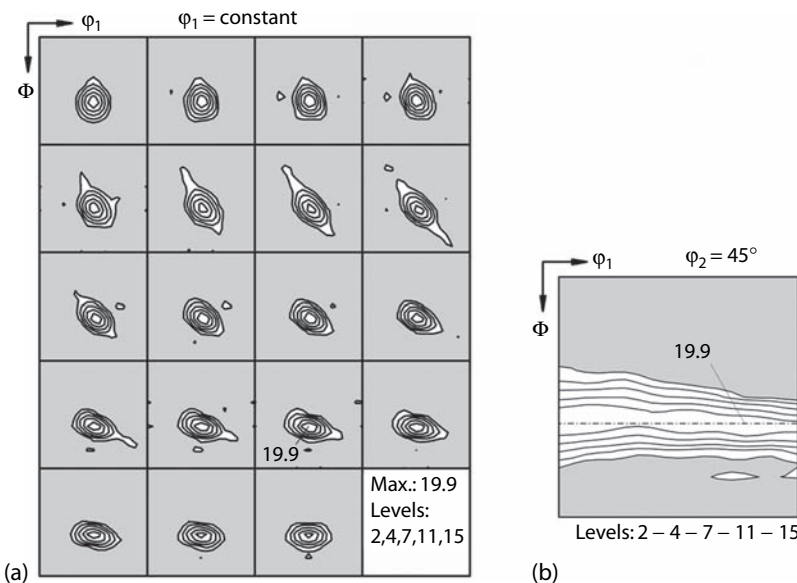
Characteristic recrystallization texture of cold-rolled aluminum alloys. (a) Cube + R texture of commercial purity Al; (b) Goss + Q texture of Al-3%Mg; (c) weak PSN recrystallization texture of AlFeSi with large second-phase particles.

particles during deformation, which is commonly referred to as *particle stimulated nucleation* (PSN) (Humphreys, 1977). PSN typically results in rather weak recrystallization textures with some preference of the P orientation $\langle 011 \rangle \langle 122 \rangle$ and a characteristic scatter of the cube orientation about the sheet normal direction toward $\langle 001 \rangle \langle 310 \rangle$ (Figure 5.31c).

5.5.5 Recrystallization Textures of bcc Metals

Analysis of recrystallization textures in bcc steels is of major industrial importance because of the correlation of texture and formability, especially, deep drawability. Compared to fcc materials, bcc metals usually exhibit a narrower range of recrystallization textures. Figure 5.32 shows the recrystallization texture of an IF steel optimized for deep-drawing applications. Evidently, the grain orientations assemble along the characteristic α and γ fibers and, as such, the recrystallization texture of ferritic steel sheets resembles the corresponding rolling textures (Figures 5.21 and 5.22). The main effect of recrystallization is sharpening of the γ fiber at the expenses of the α fiber (Emren et al., 1986; Kern et al., 1986; Därmann-Nowak and Engl, 1991; Samajdar et al., 1997). For other bcc materials, only limited information is available in the literature, but, generally, similar recrystallization textures consisting of α and γ fibers with varying ratios have been reported (Raabe et al., 1994; Briant et al., 2000; Hünsche et al., 2004).

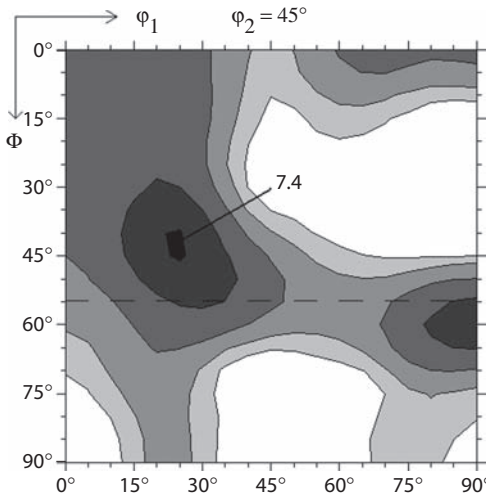
The typical γ fiber recrystallization texture of bcc materials is attributed to the preferred formation of recrystallized nuclei at the preexisting high-angle grain boundaries between the deformed grains, where optimum conditions for nucleation prevail (Hutchinson, 1989; Inagaki, 1994; Tse et al., 2000). Because of the nucleation within the as-deformed microstructure, the new grains will retain orientations of the former rolling texture. However,

**FIGURE 5.32**

Recrystallization texture of a Ti-alloyed interstitial-free steel showing a pronounced γ fiber: (a) φ_1 sections; (b) $\varphi_2 = 45^\circ$ section (90% cold rolled, annealed for 1 h at 700°C). (Courtesy of M.Y. Huh.)

the different rolling texture components differ in density and local arrangement of the dislocations, and, thus, in driving force for recrystallization. The γ -fiber orientations between $\{111\}\langle110\rangle$ and $\{111\}\langle112\rangle$ are commonly believed to have higher stored energy than the competing rolling texture orientations (Samajdar et al., 1997; Rajmohan et al., 1997). Therefore, nuclei form preferably in grains with γ -fiber orientations, which then grow at the expense of other orientations, including the α -fiber orientations.

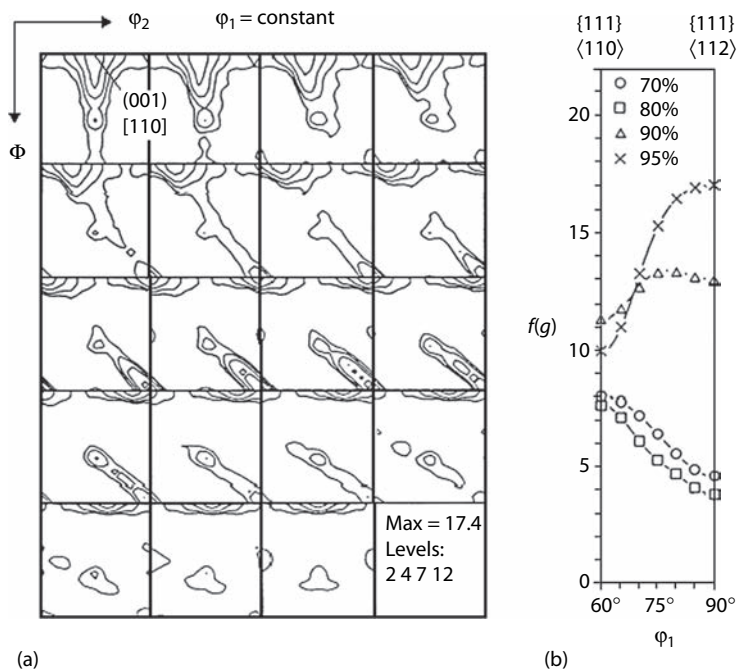
It has further been argued that because of deformation inhomogeneities and local strain gradients that persist in the vicinity of the grain boundaries, the nuclei forming in those regions may be subjected to substantial rotations about the ND with regard to the matrix at a distance from the grain boundary (Hutchinson, 1989; Tse et al., 2000). This means that regions close to the grain boundaries between two symmetrically equivalent components of $\{111\}\langle110\rangle$ may actually comprise $\{111\}\langle112\rangle$, and vice versa. Thus, in the presence of a dominant $\{111\}\langle110\rangle$ rolling texture, $\{111\}\langle112\rangle$ will nucleate preferably and, consequently, eventually prevail in the recrystallization texture. It is noted that good deep-drawing properties demand both high intensities of the γ -fiber orientations and a uniform intensity distribution along the γ fiber. Thus, optimization of deep drawability entails control of texture and microstructure during rolling and subsequent recrystallization so as to achieve a uniform intensity distribution along the γ fiber (Figure 5.32b).

**FIGURE 5.33**

Texture of recrystallization annealed ferritic stainless steel Fe-17%Cr (ODF $\varphi_2 = 45^\circ$ section, sheet center). (Data from Huh, M.Y. and Engler, O., *Mater. Sci. Eng.*, A308, 74, 2001.)

For ferritic stainless steels, once again, different recrystallization textures are found. Figure 5.33 displays the texture of 80% rolled Fe-17%Cr sheet after the final recrystallization anneal (see Figure 5.23b). The recrystallization texture is quite weak, consisting of γ -fiber orientations with a fairly uneven intensity distribution. The texture maximum is notably shifted by approximately 8° from $\{111\}\langle112\rangle$ on the γ fiber to an orientation $\{334\}\langle4\bar{8}3\rangle$ with the Euler angles $(\varphi_1, \Phi, \varphi_2) = (26^\circ, 48^\circ, 45^\circ)$. The occurrence of this orientation is explained in terms of a growth preference into $\{112\}\langle110\rangle$ through a mechanism termed “selective particle drag” (Raabe and Lücke, 1992). Finely dispersed microcarbides exert a retarding force on grain boundary motion. The amount of this so-called Zener drag depends, among others, on the specific energy of a given grain boundary. Thus, in materials with a fine particle dispersion, CSL boundaries with a low specific energy experience less Zener drag than ordinary high-energy boundaries, which, in turn, favors them for growth on recrystallization.

A direct consequence of the limited $\gamma \rightarrow \alpha$ -phase transformation during the thermomechanical processing of ferritic stainless steel sheets (Section 5.5.2) is the propensity of some grades of chromium steel to develop an undesirable surface phenomenon known as *ridging* (or *roping*) when the sheets are deformed in tension or deep drawing. During hot and cold rolling, the columnar grain structure of the as-cast slab is converted into highly elongated bands with a sharp texture. On the final recrystallization annealing, these bands transform into grain colonies of similar orientations (Brochu et al., 1997; Park et al., 2002; Huh et al., 2005). During the subsequent forming operation, these orientation

**FIGURE 5.34**

Annealing texture of cold-rolled tantalum showing strong recovery. (a) 80% rolled, annealed for 1 h at 1000°C (φ_1 sections); (b) rolled by various rolling degrees, annealed for 1 h at 1000°C (γ -fiber plots). (Courtesy of D. Raabe.)

clusters are likely to show different plastic behavior than their surroundings. At the free sample surface, these variations result in different strains in the sheet normal direction and, therewith, in ridging (Engler et al., 2005b).

An important effect of annealing of samples with low rolling strains or annealing at low temperatures is the occurrence of extended recovery, which is of particular importance for the orientations around $\{001\}\langle 110 \rangle$. Compared to the other rolling texture orientations, $\{001\}\langle 110 \rangle$ is distinguished by minimum stored energy as well as a very homogeneous microstructure. Accordingly, both nucleation and growth of $\{001\}\langle 110 \rangle$ are retarded with respect to the competing α - and γ -fiber orientations (Vandermeer and Snyder, 1979; Raabe, 1995). This effect of extended recovery is of particular importance for bcc transition metals, for example, tantalum and tungsten. Figure 5.34a shows an example of a tantalum sheet, which was 80% cold rolled and then annealed for 1 h at 1000°C. Apparently, besides the sharpened γ -fiber orientations, significant intensities of $\{001\}\langle 110 \rangle$ are retained from the rolling texture (Raabe et al., 1994). In specimens with stronger deformation or higher annealing temperatures, a pronounced $\{111\}$ γ -fiber texture is formed through discontinuous recrystallization (Figure 5.34b).

5.5.6 Recrystallization Textures of Hexagonal Metals

In contrast to the quite well-established recrystallization textures of cubic metals, recrystallization of hexagonal material has been studied much less extensively. Early studies on recrystallization textures of hexagonal metals reported that the former rolling textures were often retained (Wassermann and Grewen, 1962; Barrett and Massalski, 1980). More detailed ODF analysis proves that at high strains and high annealing temperatures, there are distinct texture changes. Often, however, recrystallization and rolling textures are related through a $30^\circ\langle 0001 \rangle$ orientation relationship that—for hexagonal crystal symmetry—is not easy to discern, in particular in $\{0001\}$ fiber textures like those commonly found in Mg alloys (Figure 5.25).

At high strains and high annealing temperatures in both Ti and Zr alloy sheets, a preferred orientation $\sim\{1013\}\langle 1210 \rangle$ ($\varphi_1, \Phi, \varphi_2$) = $(0^\circ, 30^\circ, 30^\circ)$ has been described (Inoue and Inakazu, 1988; Singh and Schwarzer, 2000; Zhu et al., 2007). This orientation has a $30^\circ\langle 0001 \rangle$ orientation relationship to the rolling texture orientation $\sim\{1214\}\langle 1010 \rangle$ ($\varphi_1, \Phi, \varphi_2$) = $(0^\circ, 35^\circ \dots 40^\circ, 0^\circ)$, as exemplified in Figure 5.35 by way of the rolling and recrystallization textures of 80% cold-rolled Zr sheet. There is some evidence that nucleation of recrystallization starts in the deformed grains where twinning during the preceding rolling deformation is important. A large fraction of the microstructure

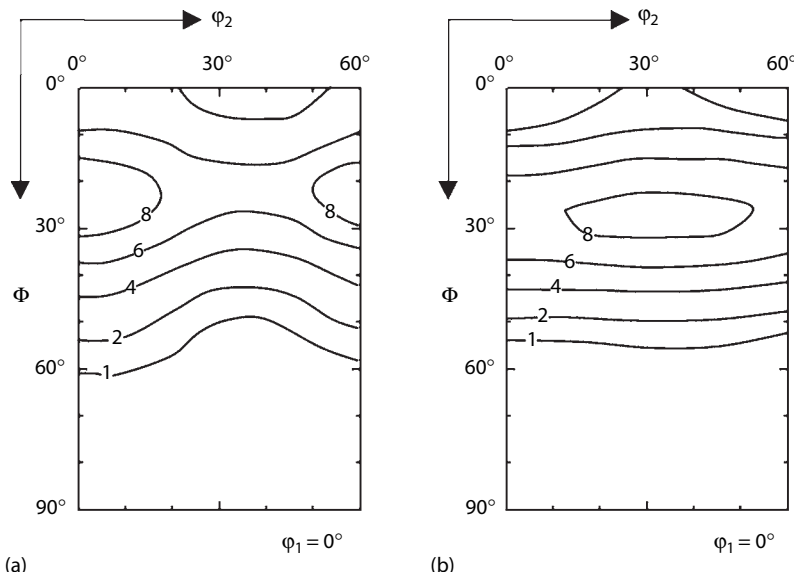


FIGURE 5.35

(a) Rolling and (b) recrystallization texture of zirconium (90% cold rolled, annealed for 350 min at 650°C , ODF $\varphi_1 = 0^\circ$ section). (Adapted from Zhu, K.Y. et al., *Mater. Sci. Forum*, 550, 545, 2007.)

(approximately 75%) recrystallizes without any orientation change, however, suggesting extended recovery or *in situ* recrystallization. More significant texture changes toward the described annealing textures then only occur after finalization of (primary) recrystallization through a selective grain growth that is influenced by the inheritance of the texture and microstructure developed during the first stage of recrystallization annealing (Wagner et al., 2002).

5.6 Summation

In this chapter, the most common methods to represent and evaluate macrotexture data have been introduced and their main advantages and disadvantages addressed.

The most well-known way of representing macrotextures is to project the crystal orientations into the sample coordinate system in a *pole figure*. Since the density distribution in a pole figure is the direct output from most techniques to determine textures experimentally, pole figures are well suited to a critical assessment of the experimental data. *Inverse pole figures*, the projection of the sample coordinate system into the crystal coordinate system, are used frequently to represent the orientation distribution of the main sample axis in the case of uniaxial sample symmetry. Although for analysis of fiber textures representation of one reference direction may suffice, for the evaluation of misorientations the full orientation information must be considered, however, which renders inverse pole figures inferior to the pole figures for the representation of texture data.

The projection of the 3-D orientation onto a 2-D pole figure results in a loss in information, so that for a quantitative evaluation of macrotextures a 3-D representation (the ODF) is required. However, ODFs cannot be measured directly in x-ray or neutron diffraction experiments but have to be calculated from several pole figures, known as *pole figure inversion*. An analytical solution to this problem of pole figure inversion is unfortunately not possible. A variety of numerical approaches to derive the ODF have been developed, which can basically be subdivided into two groups.

- The harmonic method is based on a series expansion of ODF and pole figures. This method inherently suffers from the so-called ghost error, which is caused by the impossibility to derive the odd-order C coefficients from diffraction experiments. This means that the odd-order C coefficients must be determined based on additional assumptions, for example, the condition that the ODF must be nonnegative for all orientations. In combination with an appropriate method to correct for the ghost error, the series expansion method

is a fast, reliable method that is rather insusceptible to experimental scatter in the pole figures. The resulting C coefficients represent a condensed manner to characterize the texture; furthermore, they disclose information on texture-related properties.

- In direct methods, the ODF is computed in an iterative procedure directly in the orientation space; not in a Fourier space as in the harmonic method. The condition of nonnegativity and the handling of the ghost problem are usually implicitly fulfilled and no truncation error arises. Analysis of incomplete pole figures as well as different sample or crystal symmetries is straightforward to accomplish.

A comparison of the various methods to compute ODFs from pole figure data proves that nowadays all methods are able to yield reliable and reproducible quantitative results, but because of the systematic differences between methods, it is suggested to stay with a given method within a series of experiments.

To represent the orientation density in dependence on the three Euler angles, that is, the ODF, an appropriate 3-D orientation space is necessary. Traditionally, textures are represented in sections through an orthogonal orientation space whose axes are formed by the three Euler angles, that is, the *Euler space*. However, this Cartesian Euler space depicts strong distortions at small angles Φ , which renders a visualization of the orientations and textures complicated. These distortions can be reduced by representing the textures in polar rather than orthogonal coordinates—similar as in pole figures—which results in a cylindrically shaped Euler space.

Texture analysis can greatly be facilitated by suitable ways to condense the data. In many cases, texture representation can be confined to characteristic regions of the Euler space, which contain the texture information of interest rather than showing the entire ODF. For instance, if material processing affects only a few sections of the Euler space, the representation of these sections may be sufficient to visualize important texture changes. Many textures can be represented by plotting the orientation intensity along certain characteristic paths or distinct crystallographic fibers through the orientation space versus an angle defining the position along this path or fiber.

The chapter concludes with a guide to the most typical texture types of fcc, bcc, and hexagonal metallic materials as well as the underlying formation mechanisms during deformation and recrystallization.

Part III

Microtexture Analysis

6

The Kikuchi Diffraction Pattern

6.1 Introduction

There is a basic divide between macrotexture techniques (based on x-ray or neutron diffraction; Chapters 4 and 5) and microtexture techniques (based usually on electron diffraction; Chapters 7 through 11), which relates to the scale of the inquiry and hence affects the nature of the primary output data. For macrotexture techniques, the primary output is a profile of diffracted intensities, which is characteristic of a large contiguous sample volume, whereas for microtexture—individual grain—techniques, the primary output is a diffraction pattern from each sampled volume. Such a pattern embodies the complete crystallographic information inclusive of the orientation of the respective sampled volume, which usually is an individual crystallite wherein the orientation can be taken to be uniform. For a vast majority of microtexture works in both TEM and SEM, this type of pattern is a Kikuchi diffraction pattern. Other techniques occasionally used are SAD, which still has applications in TEM (Section 8.3), and the micro-Kossel technique, which has applications in SEM (Section 7.2).

This chapter addresses the formation of Kikuchi patterns (Section 6.2). Since the principles of pattern formation and the crystallographic information embodied in them are equivalent for TEM or SEM generation, they can all be evaluated according to the same principles. The interpretation of a Kikuchi pattern, that is, the determination of the crystallographic orientation of the sampled volume, is performed in two consecutive steps. First, the pattern is indexed by identifying the crystallographic indices of the poles and bands/lines in the pattern. Second, the relative position of the poles or bands/lines with respect to an external reference frame—and therewith the crystal orientation—is determined.

Although interpretation of Kikuchi patterns is theoretically straightforward, consistent indexing and subsequent orientation calculation was time-consuming when it was performed manually. Nowadays computer codes strongly facilitate the procedure. This chapter introduces various levels of dedicated computer support from assistance with matrix handling during manual, offline microtexture analysis up to fully automated systems for

pattern indexing and orientation determination in online applications (Section 6.3). Another parameter that can be derived from the Kikuchi pattern is a measure of its “quality” or diffuseness, which is significant because it can provide information on plastic deformation in the lattice (Section 6.4). Although this is not strictly texture analysis, it is included here because the pattern quality is obtained concurrently with the orientation, and it can augment interpretation of the data (Section 10.4.4).

6.2 The Kikuchi Diffraction Pattern

A *Kikuchi diffraction pattern* arises by application of the following electron diffraction techniques (Dingley, 1981; Gottstein and Engler, 1993):

- SAC in SEM (Section 7.3)
- EBSD in SEM (Sections 7.4 through 7.8)
- Microdiffraction or convergent beam electron diffraction (CBED) in TEM (Section 8.4)

Nowadays it is common for Kikuchi patterns to be analyzed automatically, especially in SEM, often using commercially available software packages. This is a tremendous benefit since data can be acquired very rapidly by an operator who needs only a rudimentary knowledge of crystallography. On the other hand such a “black box” approach can be detrimental if data must be checked or the principles of the calibration routine understood. For these reasons, a description of the formation, meaning, and interpretation of the geometry of Kikuchi patterns, which relates directly to the crystal orientation, is included here.

6.2.1 Formation of Kikuchi Patterns

To understand the principles of orientation determination, the formation of Kikuchi lines can be explained in terms of a simplified model that considers only their geometrical aspects (Kikuchi, 1928). Although Kikuchi diffraction occurs in both TEM and SEM, the geometry is easier to illustrate for TEM, so this is considered first. When an electron beam enters a crystalline solid, it is diffusely scattered in all directions. This means that there must always be some electrons arriving at the Bragg angle θ_B at every set of lattice planes, and these electrons can then undergo elastic scattering to give a strong, reinforced beam. Figure 6.1a illustrates the situation for just one set of lattice planes. Since diffraction of the electrons through the Bragg angle is occurring in all directions, the locus of the diffracted radiation is the surface of a cone (Kossel cone) that extends about the normal of the reflecting atomic

planes with half apex angle $90^\circ - \theta_B$. The source of electron scattering can be considered to be between lattice planes, as shown in Figure 6.1a, and hence two cones of radiation result from each family of planes—viewed simplistically as one from “either side” of the source.

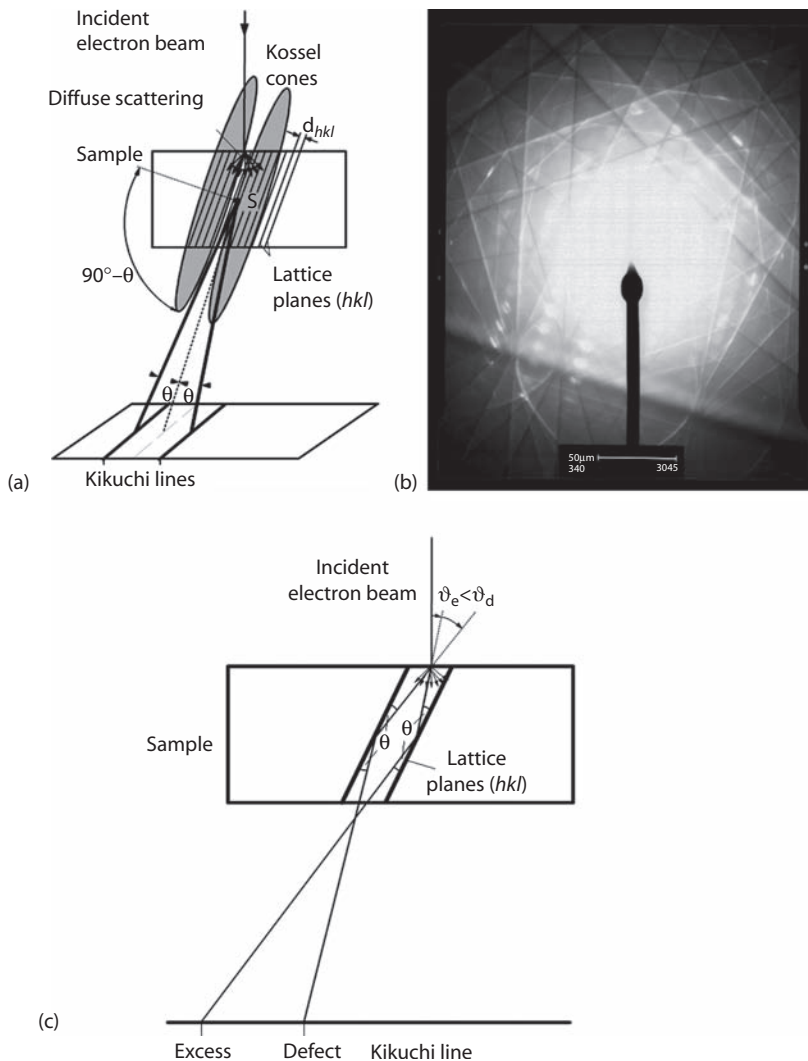


FIGURE 6.1

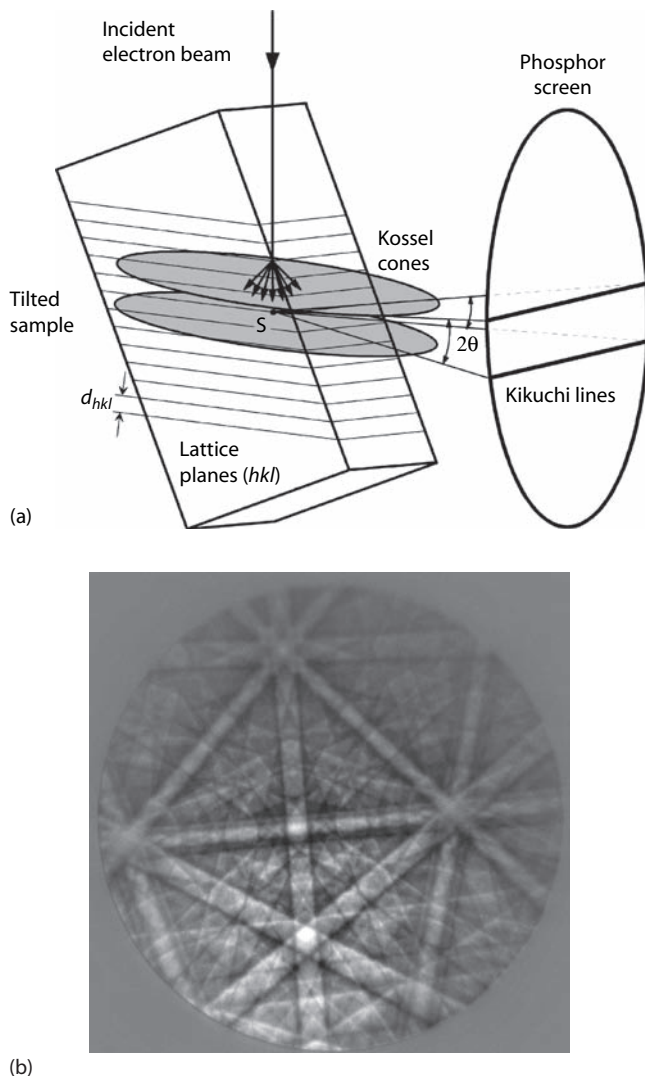
Formation of Kikuchi patterns in transmission geometry in TEM. (a) Origin of Kikuchi lines by inelastic scatter of the electrons, giving Bragg diffraction at source S on lattice planes (hkl) . (b) Kikuchi pattern from austenitic steel (accelerating voltage 200 kV). (Courtesy of S. Zaefferer.) (c) Formation of excess and defect Kikuchi lines.

From substitution of typical values for electron wavelength (Equation 3.15) and lattice interplanar spacing into Bragg's law (Equation 3.4), the Bragg angle θ_B is found to be approximately 0.5° . Consequently the apex angle of a diffraction cone is close to 180° , that is, the cones are almost flat. If some sort of recording medium—a phosphor screen interfaced to a camera or a piece of cut film—is positioned so as to intercept the diffraction cones, a pair of parallel conic sections results, which are so nearly straight that they generally appear to be parallel lines. These are Kikuchi lines, and it can be seen that their spacing is an angular distance of $2\theta_B$, which in turn is proportional to the interplanar spacing.

Thus, the whole Kikuchi pattern consists of pairs of parallel lines where each pair, or "band," has a distinct width and corresponds to a distinct crystallographic plane. The intersection of bands corresponds to a zone axis (pole), and major zone axes are recognized by intersection of several bands. The Kikuchi pattern therefore essentially embodies all the angular relationships in a crystal—both the interzonal and interplanar angles—and hence implicitly contains the crystal symmetry. Figure 6.1b shows a TEM Kikuchi pattern from austenitic steel (fcc). The orientation of the pattern and hence of the volume from which it has arisen is evaluated by "indexing," that is, identifying the poles and bands in the pattern, and calculating the relationship between these and some chosen reference axes. This process is described in detail in Section 6.3.

Figure 6.1b shows that the two lines forming a given Kikuchi band in general have different intensities; typically the line that is closer to the primary beam is darker (the "defect" line) than the background, whereas the other one is brighter (the "excess" line). The formation of dark and bright Kikuchi lines is illustrated in Figure 6.1c. In general, the angle ϑ_e between the primary beam and the diffracted beam that gives rise to the excess line is smaller than the angle ϑ_d between the primary beam and the beam diffracted toward the defect line. As discussed in Section 3.2, the scattering amplitude of electrons strongly decreases with increasing scattering angle ϑ (Figure 3.2). Thus, low-intensity defect lines will occur in the direction of the incident electron beam, where Bragg's law is satisfied, since there the electrons are scattered away and hence do not contribute to the transmitted intensity. Lines of higher intensity (the excess lines) are obtained in the direction into which the electron beam is diffracted since there the electrons add to the background intensity.

Figure 6.1 shows the diffracted electron beams passing through the specimen, which is the case for TEM. For EBSD in SEM, diffraction occurs from the interaction of primary "backscattered" electrons with lattice planes close to the specimen surface (Sections 7.4 through 7.8). Tilting the specimen by angles of typically 60° – 70° allows more electrons to be diffracted and escape toward the detector or recording medium. Figure 6.2a shows the modified diagram for formation of one pair of Kikuchi lines for the tilted specimen EBSD geometry, rather than the TEM-transmission geometry.

**FIGURE 6.2**

Formation of backscattered Kikuchi patterns by EBSD in SEM. (a) Origin of Kikuchi lines from the EBSD (i.e., tilted specimen) perspective. (b) EBSD pattern from copper (accelerating voltage 15 kV). (Courtesy of S. Zaefferer.)

Kikuchi patterns can also be produced in SEM by changing the direction of the incident beam, for example, by rocking the electron beam at a given sample site, which is SAC (Section 7.3). Although the exact formation mechanisms of the resulting bands are slightly different (pseudo-Kikuchi bands), both their geometry and crystallographic information are equivalent to the Kikuchi patterns, and consequently they can be evaluated according to the same principles (Section 6.3).

6.2.2 Comparison between Kikuchi Patterns Arising from Different Techniques

Figure 6.2b is an EBSD Kikuchi pattern from copper. If this is compared with the TEM Kikuchi pattern from a very similar material (Figure 6.1b), there are two main differences:

- The capture angle is about five times greater for the EBSD pattern than for the TEM pattern. This is a consequence of the experimental setup in both cases, and facilitates pattern indexing and identification of the symmetry elements for EBSD compared to TEM.
- The Kikuchi lines are sharper in the case of TEM than in that of EBSD, such that defect and excess lines can be distinguished in the former. This is a consequence of the different electron transfer functions in the two cases and means that greater precision in measurements from the diffraction pattern is obtained in TEM.

Figure 6.3 shows a comparison between Kikuchi patterns from TiAl obtained by SAC and EBSD, respectively, which again shows the much greater capture angle of the latter. On the contrary, there is more fine detail visible in the SAC than in the EBSD pattern, including superlattice lines (Simkin et al., 2003). However, this detail is redundant as far as orientation measurement is concerned but is an advantage for other applications such as elastic/plastic strain measurement and residual stress measurement (Dingley, 1981; Troost et al., 1993; Joy, 1994; Wilkinson, 1996).

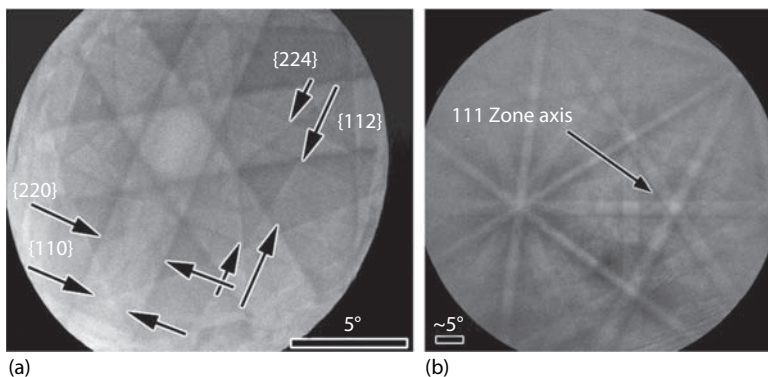


FIGURE 6.3

Comparison between (a) SAC and (b) EBSD patterns of a $\langle 111 \rangle$ zone axis in TiAl. The EBSD pattern has a much greater capture angle, whereas the SAC pattern contains more fine detail, for example, $\{110\}$ and $\{112\}$ superlattice bands. (Courtesy of M.A. Crimp.)

6.2.3 Projection of the Kikuchi Pattern

The Kikuchi diffraction pattern is essentially a *projection* onto a flat surface, that is, a film or screen, of a spherical projection of the angular relationships in the crystal. Figure 6.4a demonstrates the spherical projection. Both a single experimental EBSD pattern is mapped onto the surface of the sphere (left) and several montaged patterns (right) are shown with black outlines. Appendix IV comprises a description of the use of projection techniques in texture analysis.

For projection of the Kikuchi pattern onto a flat surface, we visualize the sampled volume of a crystal residing at the center of a reference sphere with radius ON , where ON is the distance between the specimen and the projection plane that is positioned so as to be the tangent plane at the “north pole” N . N is referred to as the *diffraction pattern center*, as shown in

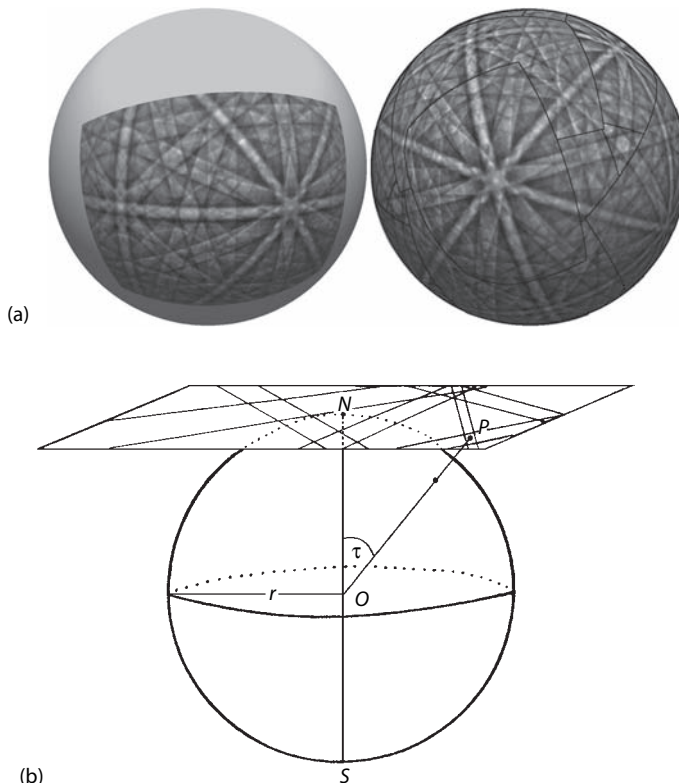


FIGURE 6.4

(a) A single experimental EBSD pattern mapped onto the surface of a sphere (left) and several montaged EBSD patterns (right) shown with black outlines. (Courtesy of A. Day.) (b) Illustration of a Kikuchi pattern as a gnomonic projection, showing the reference sphere (radius r) and a projected pole P . The projection point is O and the origin of the projection (pattern center) N .

Figure 6.4b. Diffracted rays from the specimen intersect the sphere and from there project out to the recording medium. Since the projection source point is at the center of the sphere, the position of a point P on the projection plane will be given by $\hat{O}N(\tan \tau)$, where τ is the angular displacement of P from the pattern center. For large values of τ ($>60^\circ$), the projection takes on a “stretched” appearance because the tangent function increases rapidly as it approaches 90° . This effect is not apparent in TEM or SAC patterns where the angular range of the patterns is small, but it is encountered in EBSD patterns. The type of projection illustrated in Figure 6.4b is called a *gnomonic projection* (Phillips, 1971). Appendix VII shows standard Kikuchi maps constructed from the most prominent reflectors for fcc, bcc, and hexagonal crystal structures. Such maps are very helpful during manual indexing or to check automatic indexing of Kikuchi patterns (Section 6.3).

6.2.4 Qualitative Evaluation of the Kikuchi Pattern

A Kikuchi diffraction pattern contains a wealth of information, as indicated in the previous sections. Although the pattern can be quantitatively interpreted to obtain an exact orientation (Section 6.3), other information, which may be valuable to the investigation, is available from rapid qualitative, that is, visual, evaluation of the pattern. This information includes the following:

- *Lattice strain* can be identified by diffuseness in the diffraction pattern, which is a consequence of lattice plane bending. In general, the pattern blurredness is used as a guide to strain in the lattice, for example, to pick out recrystallization nuclei from a cold-worked matrix or to formulate one type of orientation map (Section 10.4.4). There has been some success in evaluating quantitatively the amount of lattice strain from pattern diffuseness (Wilkinson, 1996; Troost et al., 1993). Methods to describe the pattern quality in a more quantitative way are described in Section 6.4.
- *Grain/phase boundaries* can be identified from the change in the real-time diffraction pattern that accompanies a traverse of the sampling probe over the specimen surface. With some experience, tasks such as distinguishing low-angle boundaries from high-angle types, checking the integrity of single crystals, or estimating the grain size distribution can be carried out.
- *Certain orientations* such as the cube orientation $\{001\}\langle100\rangle$ can be rapidly identified by visual appraisal, facilitated by overlaying a computer simulation of the target diffraction pattern for the exact orientation on top of the real-time patterns.

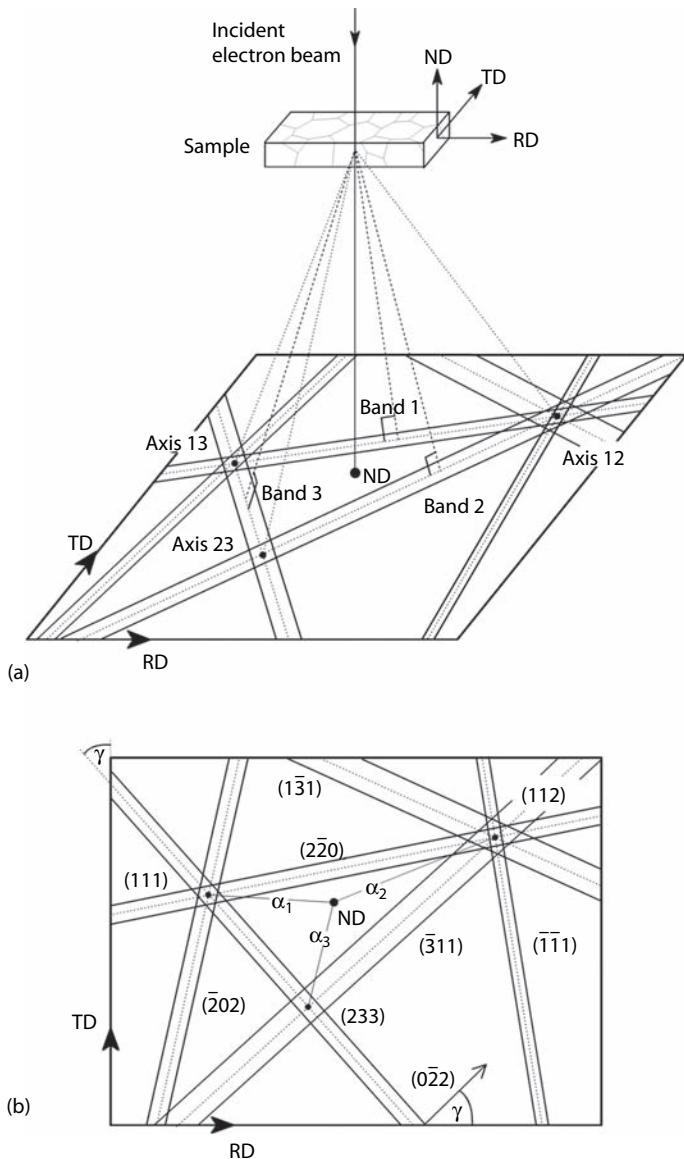
6.3 Quantitative Evaluation of the Kikuchi Pattern

As described in Section 6.2.1, the Kikuchi lines are linked directly to the arrangement of the reflecting lattice planes in the crystal and hence Kikuchi patterns are perfectly suited for determination of the crystallographic orientation. Interpretation of the Kikuchi patterns, which gives the determination of the crystallographic orientation of the sampled volume, is performed in two consecutive steps. First, the pattern has to be indexed, which means that the crystallographic indices of the Kikuchi bands and poles (more precisely, of the corresponding lattice planes) have to be determined. After the indexing, in the second step the relative positions of the bands or poles with respect to an external reference frame, that is, the crystallographic orientation of the sampled volume with respect to the specimen axes, are derived. Figure 6.5 illustrates this procedure for the TEM case. The basic principles of orientation calculation for the case of manual evaluation of TEM Kikuchi patterns are outlined in Section 6.3.1. Section 6.3.2 introduces a more rigorous approach to derive the orientation matrix, together with the methods for automatic indexing of EBSD patterns.

With the advent of EBSD for large-scale microtexture analysis, the demand for support by dedicated computer codes increased, which eventually led to the development of fully automated, online systems for pattern indexing and orientation determination (Figure 7.7). Nowadays, such systems are commercially available from several vendors.

In order of dependence on the degree of automation, the operation modes for evaluating Kikuchi patterns are as follows:

- *Manual, nonautomated.* Traditionally, Kikuchi patterns were recorded on photographic films and then evaluated “offline” after developing the films. In most cases, pattern indexing is assisted by comparison with standard patterns, and then the crystallographic orientation of the sample volume can be derived as described in Section 6.3.1.
- *Interactive, semiautomated.* For an interactive orientation evaluation of a Kikuchi pattern, the coordinates of a number of bands or axes in the pattern are marked by the user and transferred to a computer, which automatically indexes the pattern and computes the corresponding orientation. Section 6.3.2 describes some approaches for semiautomated pattern indexing and orientation determination.
- *Fully automated.* Complete automation means that the crystallographic features in the Kikuchi patterns are automatically detected by means of appropriate pattern recognition codes, thus avoiding

**FIGURE 6.5**

Diagrams illustrating the evaluation of a TEM Kikuchi pattern. (a) Correlation between the reference frame of the specimen and a Kikuchi pattern. (b) Indexed Kikuchi pattern, drawn to scale, from which the crystallographic orientation is derived.

the time-consuming manual marking of zones or axes (Section 6.3.3). Such fully automated codes are an essential prerequisite for performing orientation microscopy (Chapter 10).

6.3.1 Principles of Orientation Determination

Interpretation of Kikuchi patterns that are obtained in TEM, or by SAC in SEM, is still performed in many cases by evaluation of photographic films. Both TEM and SAC Kikuchi patterns can mostly be indexed by visual appraisal, particularly for cubic crystals, or by comparison with standard patterns (Appendix VII). In cubic crystal structures, when the indices of two intersecting bands are (h_1, k_1, l_1) and (h_2, k_2, l_2) , the corresponding zone axis $[uvw]$ can be derived from the cross product, $(h_1, k_1, l_1) \times (h_2, k_2, l_2)$, and vice versa. For example, in Figure 6.5 the cross product of band 1 and band 2, $(\bar{2}\bar{2}0)$ and $(\bar{3}11)$, gives the zone axis labeled axis 12, which is [112]. In noncubic crystal structures, the crystallographic indices have first to be transformed into an orthonormal coordinate system via multiplication by the inverse crystal matrix (Equation 2.3).

For both TEM and SAC, the photographic plate is arranged parallel to the specimen surface itself, so that the primary electron beam direction, usually referred to as the *beam normal*, BN, corresponds to the specimen normal direction, ND. Thus, to derive the crystallographic orientation, the angles between the indexed bands or poles and the sample normal can readily be determined by measuring their distances to the beam normal, $\alpha_1, \alpha_2, \alpha_3$, in Figure 6.5b. The scaling factor to transform these distances into angles is derived from the distance between two indexed poles or from the bandwidth of a Kikuchi band, which is related through 2θ to its indices. Although the diffraction pattern is a gnomonic projection (Section 6.2.3 and Appendix IV), distances near the pattern center can be considered to scale linearly with projection angle.

From the information about the crystallographic indices $q^i = (q_1^i, q_2^i, q_3^i)$, with $i = 1, 2 \dots n$ (where n is the number of identified bands or poles) and the angles α_i between each band or pole i and the beam normal, the orientation of the sample normal in terms of its crystallographic indices (hkl) can be expressed as

$$\begin{pmatrix} q_1^i \\ q_2^i \\ q_3^i \end{pmatrix} \cdot \begin{pmatrix} h \\ k \\ l \end{pmatrix} = \cos \alpha_i \cdot \sqrt{(q_1^i)^2 + (q_2^i)^2 + (q_3^i)^2} \quad (6.1)$$

The root term in Equation 6.1 normalizes the indices of the bands or axes, which are typically given as integer numbers, for example, (022) or [112], to unity. Hence the resulting vector (hkl) is directly normalized to unity. It is seen that three equations are necessary to determine the vector (hkl) , which means that three bands or poles have to be indexed. In the example given in Figure 6.5b, the angles α_i were determined to be $\alpha_1 = 8.5^\circ$, $\alpha_2 = 11.6^\circ$, and $\alpha_3 = 7.2^\circ$. Solving Equation 6.1 for the corresponding three poles [111], [112], and [233], we find $(hkl) = (0.486, 0.541, 0.686)$, which means that the beam normal is approximately 2° away from (567).

The method outlined in the preceding text yields the axis of the crystal under investigation, which is parallel to the beam normal, that is, the normal direction ND of the sample. To derive the full orientation matrix with respect to the specimen, the indices of one further reference axis have to be determined as well. This is more complicated, and typically less accurate, and therefore such procedures are omitted in many textbooks. Nevertheless, although determination of the beam direction may be sufficient for some applications, it must be emphasized that in many cases the absolute orientation with respect to the macroscopic specimen geometry is relevant. Note that for computation of orientation relationships or misorientations, specification of a particular axis in the specimen is not necessary; only *the same* reference direction in a pair of crystals in the same specimen is required. For this purpose, a direction such as that defined by the edge of the photographic plate (provided that there is no specimen tilt or rotation between measurements from each of the crystal pair) suffices as the reference axis.

To derive the complete or *absolute orientation* matrix, specific reference axes must be chosen in the specimen. One of these is the specimen normal direction (ND) and the second is the rolling direction (RD) or the transverse direction (TD) (Figure 6.5). Determination of any reference axis in the specimen other than its normal requires that this axis can still be identified after specimen preparation. For TEM samples and, in particular, after inserting the sample into the TEM, typically the sample is positioned with its reference direction parallel to the edge of the specimen holder. Image rotations can be taken into account by calibration of the reference direction with the help of a copper net that is inserted in the specimen holder in a similar manner. It is clear that these difficulties of identifying the reference direction account for the inferior accuracy in TEM of orientation determination of specimen reference axes other than the beam normal. Provided that the direction of the reference axis in the specimen surface—the edge of the photographic plate or the rolling direction—is known in the final Kikuchi pattern, its crystallographic indices $[uvw]$ can be determined by tilting the sample around this axis and determining the new beam normal $(h'k'l')$ as described earlier. $[uvw]$ is then given by $(hkl) \times (h'k'l')$.

In a more rigorous approach, the information necessary to derive the complete orientation matrix can also be obtained from the angle between one indexed Kikuchi band and the reference axis in the specimen surface (Figure 6.5b). Following the method proposed by Young et al. (1973) and Heilmann et al. (1982), we define an intermediate pattern frame with the z axis parallel to the beam normal BN and the y axis parallel to any of the (indexed) Kikuchi bands with the normal hkl , which means y is given by $BN \times hkl$. Thus, the rotation matrix R_{CP} from the crystal frame C to the intermediate pattern frame P becomes

$$R_{CP} = ((BN \times hkl) \times BN \quad BN \times hkl \quad BN) \quad (6.2)$$

The pattern frame P contains the information of the indexed beam normal BN and differs from the outer reference frame, that is, the sample frame S , only by a rotation of angle γ around $BN = z$, where γ is the angle between the Kikuchi band and the sample y direction. This is equivalent to the angle between the *normal* to that Kikuchi band and the sample x direction (Figure 6.5b). The corresponding matrix R_{PS} for a rotation by angle γ about $BN = z$ is

$$R_{PS} = \begin{pmatrix} \cos \gamma & -\sin \gamma & 0 \\ \sin \gamma & \cos \gamma & 0 \\ 0 & 0 & 1 \end{pmatrix} \quad (6.3)$$

Combination of the two rotation matrices R_{CP} and R_{PS} yields the rotation R_{CS} between the crystal and the sample frame, that is, the desired orientation matrix g :

$$g = R_{CS} = R_{PS} \cdot R_{CP}^T \quad (6.4)$$

In the present example, the angle γ between the $(0\bar{2}\bar{2})$ band normal and the rolling direction RD is 41.5° . Substituting this information and the indices of BN into Equations 6.2 through 6.4, we get a rolling direction $[uvw] = [-0.616, -0.345, 0.707]$, approximately 4° away from $[2\bar{1}2]$, and a transverse direction $[qrs] = [0.620, -0.766, 0.165]$, approximately 0.7° away from $[4\bar{5}1]$. Note that the Miller indices rounded to integer values are no longer perpendicular, which demonstrates one of the main disadvantages of this kind of orientation representation (Section 2.4).

Although such methods to determine the orientation from a Kikuchi pattern are theoretically straightforward, they are quite challenging to apply and very tedious when analyzing a large number of orientations, if no dedicated computer software is available. In the simplest case, the position of three Kikuchi bands or poles, together with their crystallographic indices as well as the angle between one of these Kikuchi bands and the reference direction, is input into a computer, which then calculates the 3-D orientation matrix g . From this orientation matrix, eventually the Miller indices, Euler angles, Rodrigues vectors, or misorientation parameters (Chapter 2) can be computed according to standard algorithms, and the results can be stored for further evaluation and representation of the data (Chapter 9).

In the case of EBSD, pattern indexing is usually easier, which is due to the larger steric angle, which in turn allows a much larger portion of the gnomonic projection to be surveyed in one pattern (Section 6.2.2; Figure 6.2b). However, subsequent determination of the orientation is much more complicated, which is a consequence of the different geometry of experimental setups to obtain EBSD patterns. As illustrated in Figures 6.2a and 6.6, for EBSD the specimen is tilted to approximately 70° in the SEM chamber. Moreover, the microscope hardware may dictate that the camera that records the diffraction pattern cannot always be positioned in a simple geometrical relationship

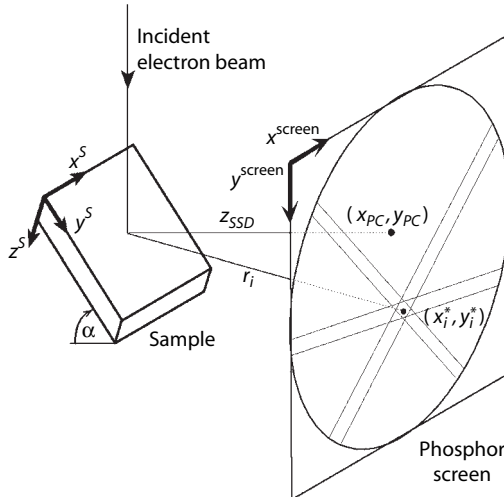
**FIGURE 6.6**

Diagram illustrating the evaluation of an EBSD pattern.

with respect to the specimen—only rarely is the camera parallel to the specimen surface as for TEM or SAC. These additional considerations for EBSD mean that distances in the pattern cannot be transformed into angles by a simple relationship. Furthermore, the beam normal typically lies out of the plane of the recorded pattern itself. Therefore, EBSD patterns are usually not evaluated manually, but dedicated computer software was developed already at an early stage in EBSD evolution (Section 7.4) (Dingley et al., 1987).

6.3.2 Automation of Pattern Indexing and Orientation Determination by Electron Backscatter Diffraction

Section 6.3.1 introduced the principles of orientation determination from Kikuchi patterns. For high-symmetry materials, and where the geometrical relationship between the microscope and the EBSD camera is simple, patterns can usually be indexed by visual appraisal or by comparison with standard Kikuchi maps. Even so, consistent indexing and subsequent calculation of the orientation is a tedious procedure. In particular, the problems caused by the geometrical distortions of EBSD patterns led to the development of a number of different approaches to automatize pattern indexing and orientation determination.

One of the main prerequisites for such an automatized evaluation of Kikuchi patterns is that the coordinates of the bands or zone axes in the pattern must be entered directly into a computer, thus avoiding the time-consuming preparation and evaluation of photographic films. As mentioned in Section 6.3.1, three bands or zone axes are required for orientation determination, but later

in this section it will be seen that more information may be necessary for unambiguous indexing, especially for noncubic systems.

EBSL patterns are usually captured with a camera and displayed on a monitor (Section 7.6.1). To transfer the necessary information into a computer, in earlier setups the computer was interfaced to the camera such that a mouse-controlled cursor could be superimposed on the live EBSD patterns (Dingley et al., 1987; Hjelen et al., 1993) or, vice versa, the position of a cursor generated by the image processor was automatically fed into the computer through a serial interface (Engler and Gottstein, 1992). Thus, the coordinates of several Kikuchi bands or zone axes were entered directly into the computer and no video grabber card was required. By contrast, in most current setups, the EBSD pattern captured by the camera is entirely transferred pixel by pixel to the computer by means of a video grabber card. There, the bands or poles can directly be marked by the user with the computer mouse and then used to determine the orientation of the sampled volume.

The main steps necessary for automated pattern indexing and orientation determination will now be outlined following the approach that was implemented at the Institut für Metallkunde und Metallphysik in Aachen for evaluation of EBSD patterns (Engler et al., 1996a). Algorithms for automatic pattern recognition are described in Section 6.3.3, and the procedure for calibrating the specimen-to-screen distance and origin of the gnomonic projection is given in Section 7.7.

To relate the characteristic features of an EBSD pattern—typically zone axes or bands—from the 2-D computer screen to the 3-D sample coordinate system (denoted by the superscript s in Equation 6.5), the 2-D screen coordinates (x_i^*, y_i^*) are transferred into 3-D vectors r_i by

$$r_i = \begin{pmatrix} x_i^* \\ y_i^* \\ z_i^* \end{pmatrix} = A \cdot \begin{pmatrix} x_i \\ y_i \\ z_i \end{pmatrix} = A \cdot \begin{pmatrix} x_i^* - x_{PC} \\ y_i^* - y_{PC} \\ z_{SSD} \end{pmatrix} \quad (6.5)$$

With an appropriate calibration of the hardware setup (Section 7.7), the coordinates of the pattern center (x_{PC}, y_{PC}) and the specimen-to-screen distance z_{SSD} are known (Figure 6.6). The rotation matrix A contains all necessary geometrical corrections, most notably the tilting angle α of the sample (usually 60° – 75°) as well as additional angles between sample and phosphor screen, which may occur in the various EBSD setups.

Thus, for an interactive orientation determination, the user has to mark several zone axes on the computer screen, whose coordinates are then transferred to 3-D vectors r_i as described previously. Alternatively, the user identifies several EBSD bands, usually by selecting two points in the band center or by appropriate marking of the band edges. The marked screen coordinates are again transferred to 3-D vectors r_i , with the cross product of these vectors defining the normal to the EBSD band in the sample frame.

Now, the mutual angles between all marked bands or zone axes can be calculated from the dot product between the corresponding vectors r_i and compared to a look-up table that contains all angle combinations possible in the given crystal structure. Some small measuring uncertainty (typically of the order of 1°) must be tolerated, of course. Besides the interplanar or inter-zonal angles, the widths of the Kikuchi bands can be considered as well. Since the bandwidth is related to the Bragg angle of the corresponding lattice plane (Section 6.2.1), it can be exploited to index the bands or check the indexing by identifying wrong solutions. For EBSD, however, the measurement of the bandwidth is not very accurate, which is due to the low signal-to-noise ratio of the patterns. However, in case of high-symmetry materials (cubic, hexagonal), virtually all EBSD patterns can be unequivocally indexed, so that the bandwidths are usually not considered for orientation determination. In contrast, for materials with lower symmetry, the bandwidths yield valuable additional information to ensure unequivocal indexing that is particularly important for TEM or SAC where a much smaller portion of the gnomonic projection is visible.

After indexing the pattern, the orientation of the sampled crystal volume with respect to the external specimen coordinate system can be determined (Schwarzer and Weiland, 1984; Dingley et al., 1987; Schmidt et al., 1991; Wright and Adams, 1992; Engler and Gottstein, 1992). The crystallographic orientation is usually given in terms of its orientation matrix g (Section 2.3) that transforms the specimen coordinate system into the coordinate system of the crystal (indexed by the superscript c in the following equations):

$$r_i^c = g \cdot r_i^s \quad (6.6)$$

Thus, for each vector r_i (zone axis or band normal), its vector in the sample frame $r_i^s = (x_i^s, y_i^s, z_i^s)$ (Equation 6.5) and, after the indexing, its crystallographic direction $r_i^c = (x_i^c, y_i^c, z_i^c)$ are known. For noncubic crystal structures, the crystallographic vectors r_i^c have to be transformed into an orthonormal coordinate system by multiplication with the inverse crystal matrix (Equation 2.3), but then they can equally well be examined. It follows from the definition of g (with $i \in 1,2,3$):

$$\begin{pmatrix} x_1^c & x_2^c & x_3^c \\ y_1^c & y_2^c & y_3^c \\ z_1^c & z_2^c & z_3^c \end{pmatrix} = g \cdot \begin{pmatrix} x_1^s & x_2^s & x_3^s \\ y_1^s & y_2^s & y_3^s \\ z_1^s & z_2^s & z_3^s \end{pmatrix} \text{ or } g = \begin{pmatrix} x_1^c & x_2^c & x_3^c \\ y_1^c & y_2^c & y_3^c \\ z_1^c & z_2^c & z_3^c \end{pmatrix} \cdot \begin{pmatrix} x_1^s & x_2^s & x_3^s \\ y_1^s & y_2^s & y_3^s \\ z_1^s & z_2^s & z_3^s \end{pmatrix}^{-1} \quad (6.7)$$

For computation of the orientation matrix g , the second matrix in Equation 6.7 must be inverted, which requires its determinant to be different from zero (i.e., the matrix must be regular). Matrix inversion is much easier for orthogonal matrices, where $A^{-1} = A^T$, so that only the rows and columns of the matrix must be exchanged. To obtain an orthogonal matrix, three new

vectors r_1^s in the sample frame and r_1^c in the crystallographic frame are formed according to

$$\tilde{r}_1^s = r_1^s \times r_2^s, \tilde{r}_2^s = \tilde{r}_1^s \times r_3^s, \tilde{r}_3^s = \tilde{r}_1^s \times \tilde{r}_2^s \quad (6.8)$$

and correspondingly

$$\tilde{r}_1^c = r_1^c \times r_2^c, \tilde{r}_2^c = \tilde{r}_1^c \times r_3^c, \tilde{r}_3^c = \tilde{r}_1^c \times \tilde{r}_2^c \quad (6.9)$$

An easier orthogonal arrangement can be gained just by setting $r_1^s = r_1^c$ and correspondingly combining the other vectors, as proposed by Wright et al. (1991). In that case, two bands or axes would theoretically be sufficient to compute g . However, with only two vectors, indexing is never unequivocal—even if no tolerance needed to be considered, the corresponding two solutions could equally well be exchanged. Moreover, the use of three vectors introduces some averaging during the computation of g .

Finally, a pattern can be recalculated from the orientation matrix g and overlaid on the original pattern. If the solution is judged by the operator to be correct, the orientation matrix g is stored in a computer file for further evaluation and representation of the data (Chapter 9).

6.3.3 Automated Evaluation of Electron Backscatter Diffraction Patterns

The main problem of automatic pattern indexing codes is the recognition of the low-contrast bands in the patterns. In the first attempt of automatic pattern recognition, direct detection of zone axis positions was tried (Wright et al., 1991). This was carried out by convolution of the pattern with a filter in the shape of a “Mexican hat” to detect regions with high intensity compared to their neighborhood, that is, the zone axes. However, it turned out that this method is too sensitive to calibration errors and camera distortions. Therefore, algorithms have been developed to detect the positions of the bands rather than the zone axes, Juul Jensen and Schmidt (1990) scanned the patterns line by line, searching for local maxima, which then yielded the band positions. Wright and Adams (1992) tried to detect the band edges from the local intensity gradients in the pattern by means of the Burns algorithm (Burns et al., 1986). Krieger Lassen et al. (1992) and, later, Kunze et al. (1993) transformed the EBSD pattern by means of the *Hough transform* (or alternatively the Radon transform, see the following text), as has already been applied to the automatic evaluation of Laue patterns by Gottstein (1988). By this procedure, which has been reviewed by Krieger Lassen (1996), lines in the original image are transformed into points, which can be detected much more easily by computer codes. A careful comparison of these two pattern recognition codes has shown that the Burns and the Hough algorithms seem to be equally reliable, although both algorithms have their own advantages (Kunze et al., 1993). In general, for poorer pattern quality, the Hough transform yields

slightly more accurate results, whereas the Burns algorithm is advantageous for high-quality patterns. Furthermore, the velocity of the Hough transform does not depend on the pattern quality, which favors it for automated systems.

In the following text, the main steps of automatic interpretation of EBSD patterns are outlined. Codes for the automatic indexing of TEM Kikuchi patterns by means of the Hough transform have been developed as well, and this is addressed in Section 6.3.4.

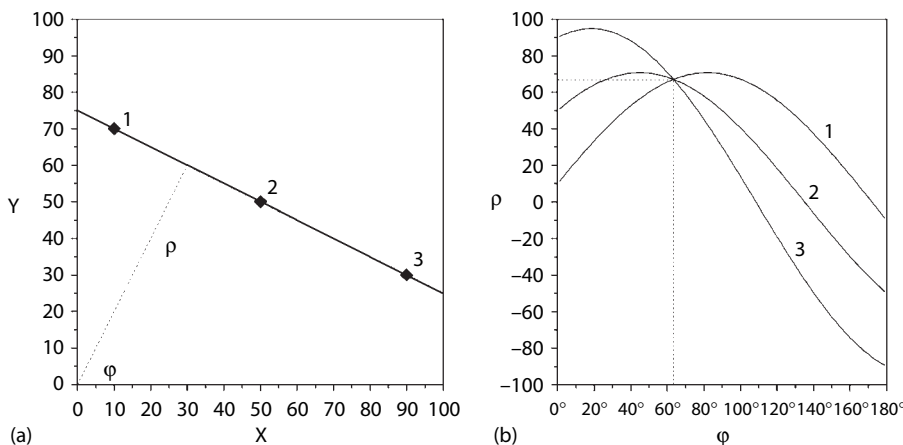
After recording the pattern from the video grabber card, first, several steps of preprocessing of the original pattern are taken to obtain optimum conditions for the subsequent pattern recognition codes. Typically, the first steps in the image processing are background subtraction/division, contrast enhancement, and, if necessary, pattern averaging (Section 7.6.6 and Figure 7.13). The size of the pattern is generally reduced so as to increase the speed of the analysis by reducing the number of pixels, and also affords some integration of intensities over local blocks of pixels, which improves the signal to-noise ratio. A pattern size of 100×100 pixels typically represents a good compromise between sufficient angular resolution of the EBSD pattern and satisfactory computation time.

The next step of the procedure is the transformation of the pattern and, as already stated in this section, the method that most workers have now settled on involves forming a Hough transform of the pattern (Hough, 1962). During the Hough transform, each point (x_i, y_i) of the original image is transformed into a sinusoidal curve in an accumulation space, commonly called *Hough space*, which is characterized by the coordinates ρ and θ according to the relation:

$$\rho = x_i \cdot \cos \theta + y_i \cdot \sin \theta, \quad \theta \in (0^\circ, 180^\circ), \rho \in (-R, R) \quad (6.10)$$

This relation specifies a line by the angle θ between its normal and the pattern x axis as well as its distance ρ from the origin—here, the center of the image with radius R . The principle of the Hough transformation is schematically illustrated in Figure 6.7 for a straight line that is defined by three points. It is seen that all collinear points in the original image (Figure 6.7a) will map to sinusoidal curves intersecting in a common point in Hough space (Figure 6.7b), which is defined by the coordinates ρ and φ of the original line. Hence, the Hough transform converts the difficult problem of detecting lines in the original image into a more easily solved problem of detecting points in the Hough space.

For a transformation of a gray-tone image such as an EBSD pattern, each point of the original image (x_i, y_i) is transformed into the accumulation space (ρ, θ) under consideration of its intensity (Figure 6.8). That is to say, the intensity $I(x, y)$ at each pixel in the EBSD image is added to the value of pixels $I(\rho, \theta)$ in the transform, which are all initially set at zero. This procedure is referred to as gray-tone weighted Hough transform or, more precisely, a *Radon*

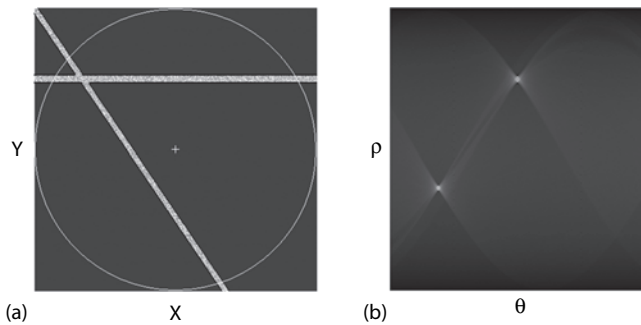
**FIGURE 6.7**

Schematic representation of the Hough transform. (a) Line with three points in the original image; (b) all the corresponding three Hough-transformed curves from (a) meet in one point in Hough space whose coordinates p and θ then specify the original line.

transform (Radon, 1917). For obtaining a homogeneously transformed image without shading effects, only a circle with a diameter of $2R$ from the square pattern is considered during the transform (Figure 6.8a).

The next step is the identification of the peaks in Hough space, that is, the bands in the original pattern. A bright line with a width of one pixel in the original image would become a single bright point in the Hough transform, which could easily be found by standard peak locating methods. In real EBSD patterns, however, the finite width of the bright EBSD bands produces peaks of finite extent in the transform, and these peaks have a characteristic butterfly-like shape in the transformed image, as shown in Figures 6.8b and 6.9b (Krieger Lassen et al., 1992). Hence, rather than simply searching for the largest peaks, the transform is first filtered with a kernel designed to output high intensities wherever the butterfly motif is located in the transform. The size of this so-called *butterfly filter* is dependent on the width of the Kikuchi bands, so that different-sized filters are used as the microscope voltage is altered. Once the peaks are located in the filtered Hough transform, this gives the Hough parameters and, in turn, the locations of the prominent bands in the EBSD pattern. Figure 6.9 shows an example of an EBSD pattern, where a number of bands are marked with the same color in both the original image and the Hough space.

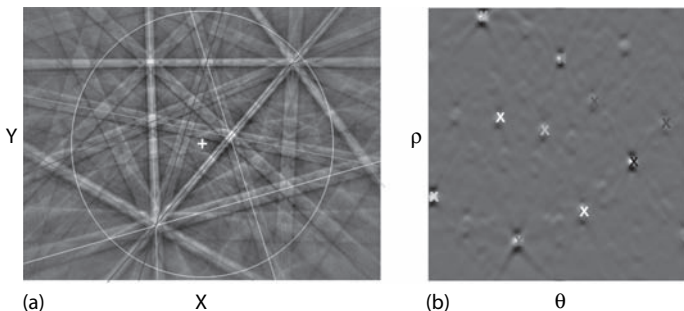
Krieger Lassen (1998) has further refined the peak detection procedure in the Hough transform to determine location and particularly width of EBSD bands with improved accuracy. The new procedure applies a special back-mapping technique to generate two separate Hough images for the bright and dark lines in the EBSD patterns. A coordinated search for peaks in the

**FIGURE 6.8**

Gray-tone weighted Hough transform, or Radon transform, of two bands of distinct width in a gray-tone image. (a) Original image; (b) Radon-transformed image, showing the development of the characteristic butterfly shape of transformed EBSD bands.

two Hough images then leads to an improvement in the accuracy of determination of both the position and the width of the bands in the original EBSD pattern. The back-mapping techniques were adopted by Zaefferer (2002) for automatic pattern recognition in TEM (Section 6.3.4).

The detected bands are listed according to their relative intensity, and the bands with the highest intensities are used for further orientation computation as described in Section 6.3.2. Occasionally wrong lines are detected, and consequently no solution is obtained. In other cases ambiguous solutions may be found, particularly for patterns with symmetrical poles (Nowell and Wright, 2005). Here, additional consideration of bands with lower intensity may eliminate the wrong solutions. In an interactive operating mode, the user can intervene by manually rejecting wrong lines or adding new lines. In fully automated systems this is not possible, of course, so that wrongly solved or nonindexed patterns end up being stored in the results files. However, this is not really a problem because many of the unsolved points can be filled

**FIGURE 6.9**

(See color insert following page 240.) Gray-tone weighted Hough transform, or Radon transform, of an EBSD pattern of aluminum with overlaid bands. (a) Original EBSD pattern; (b) pattern after the Radon transform. (Courtesy of A. Gholinia.)

in during subsequent cleanup routines, as long as the overall indexing rate is sufficiently large (Section 10.4).

In conclusion, automated evaluation of EBSD patterns has been a vital step forward in the development of microtexture analysis, since the unreasonable time burden on operators and microscopes that are inherent in manual EBSD is reduced or eliminated. Furthermore, automation is a necessary prerequisite for the full potential of EBSD being realized through the subsequent development of orientation microscopy and orientation mapping (Chapter 10).

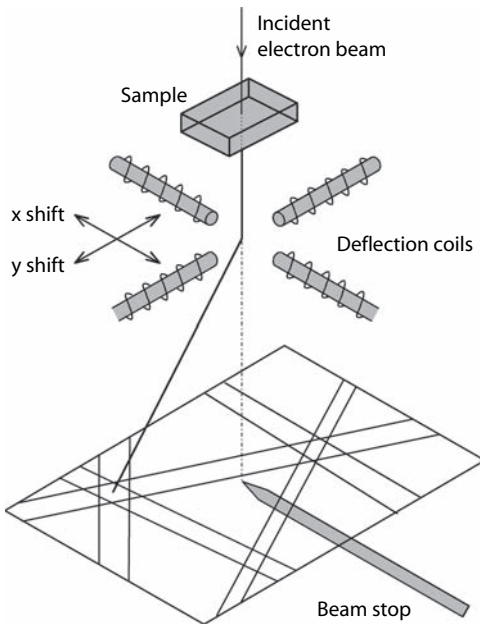
6.3.4 Automated Evaluation of Transmission Electron Microscopy Kikuchi Patterns

As discussed in Section 6.2.1, TEM Kikuchi patterns rely on the same physical and crystallographic principles as the EBSD patterns in SEM, and therefore they can be evaluated according to analogous methods. In fact, we have introduced the principles of interpretation of Kikuchi patterns for TEM geometry, as this is easiest to illustrate.

Schwarzer and Weiland (1984) developed a method to interpret Kikuchi patterns *in situ* at the viewing screen of TEM. For this interactive online analysis, the pattern is shifted across the viewing screen using the TEM deflection coils until the points to be measured—which may be poles in a Kikuchi pattern or, alternatively, points in a SAD pattern (Section 8.3.1)—successively coincide with a reference mark on the screen, for example, the primary beam stop (Figure 6.10). The voltages needed to shift the pattern are a measure for the position of the respective points on the screen. They can be transferred to a computer through an analog-to-digital converter board and can then be evaluated to yield the crystallographic orientation of the crystal under investigation. In the approach by Schwarzer and Weiland (1984), the positions of minimum three Kikuchi bands are characterized by marking four points for each band, and this information is used in an automated code for pattern indexing and orientation determination, similar to that described in Section 6.3.2.

Recently, based on the success of the automatic indexing of EBSD patterns (Section 6.3.3), there have been several attempts to adapt the respective computer codes for evaluation of Kikuchi patterns in TEM (Zaefferer and Schwarzer, 1994; Weiland and Field, 1994; Krieger Lassen, 1995; Engler et al., 1996a; Schwarzer, 1997b; Schwarzer and Sukkau, 1998; Zaefferer, 2000, 2002; Fundenberger et al., 2005). In these developments, likewise the entire camera image is transferred to the computer through a video grabber card (Section 8.4). However, for TEM Kikuchi patterns, more serious problems had to be overcome and the EBSD codes had to be substantially modified to yield satisfactory results. These problems include the following:

- TEM Kikuchi patterns have a much higher *dynamic range* due to variations in background intensity as well as the superposition of SAD diffraction spots and the primary beam.

**FIGURE 6.10**

Online acquisition of Kikuchi patterns in TEM. (Adapted from Schwarzer, R.A. and Weiland, H., *Proc. ICOTOM 7*, Netherlands Soc. for Mater. Sci., Zwijndrecht, 1984.)

- TEM Kikuchi patterns usually consist of pairs of *bright and dark Kikuchi lines* as opposed to the bands with rather homogeneous intensity in EBSD.
- *Unambiguous indexing* of TEM Kikuchi patterns is more complicated because of both the small steric angle and the large number of visible high-index bands.

6.3.4.1 Dynamic Range

The contrast range of TEM Kikuchi patterns is much larger than that of EBSD patterns. Furthermore, the Kikuchi patterns are frequently superimposed by high-intensity SAD diffraction spots and, particularly, by the primary beam, whose intensity may exceed that of the Kikuchi lines by several orders of magnitude. Therefore, cameras with higher resolution are advantageous to handle this large dynamic range of TEM Kikuchi patterns. For instance, 12- or even 14-bit digitization, respectively, yields more than 4,000 or even 16,000 gray values as opposed to the 256 gray values of the old 8-bit cameras. Alternatively, a continuous gradation filter inserted in front of the camera has been used to level out the uneven background intensity (Zaefferer and Schwarzer, 1994). Because of the high dynamic range and the stronger

variations in background intensity in TEM Kikuchi patterns, additional steps of image processing are required in comparison to EBSD patterns. For instance, strongly localized high intensities can be searched for and replaced by the average value of their neighborhood, since such regions are likely to correspond to the SAD spots. The area affected by the primary beam spot can similarly be smoothed, or it is simply neglected during the Hough transform.

6.3.4.2 Bright and Dark Kikuchi Lines

TEM Kikuchi patterns usually consist of pairs of bright and dark lines (Section 6.2.1), which means that an offset has to be introduced during determination of the background intensity to ensure that the defect Kikuchi lines with intensities below that of the background are not removed. In contrast, EBSD patterns mainly comprise bands with a higher intensity than their surroundings, and only occasionally sharp bright and dark lines are observed at the band edges (Section 6.2.2). Furthermore, low-index lines in TEM are frequently associated with parallel high-order diffraction lines. For these reasons, the routines for line detection via the Hough-transformed image had to be adapted as well (Zaefferer and Schwarzer, 1994; Krieger Lassen, 1995; Engler et al., 1996a).

6.3.4.3 Unambiguous Indexing

Owing to the smaller steric angle, but larger number of high-index bands, unambiguous indexing is more complicated for TEM than for EBSD. For instance, in EBSD patterns of fcc materials usually only bands up to (311) or maximum (331) are clearly visible, whereas in TEM Kikuchi patterns bands like (244) and higher are obtained and hence must be considered during the indexing procedure. However, the widths of the Kikuchi bands can be determined much more accurately, and hence they can also be used to index the bands or at least to identify wrong solutions (Section 6.3.2). The large number of different, widespread data that is needed to index the patterns results in the necessity of an appropriate handling of erroneous data. In many cases, still several solutions are obtained which require interaction by the user.

To sum up, automated indexing of TEM Kikuchi patterns is by far more complicated and less developed than that of EBSD patterns, although it is nowadays possible to solve automatically Kikuchi patterns and perform orientation mapping in TEM, analogous to EBSD (Section 10.5). An alternative technique for automated orientation determination of separate small volumes in TEM—which is based on the examination of a large series of dark-field images—is also described in Section 10.5.

Recently, another simple method has been introduced, which allows a fast and accurate interpretation of TEM Kikuchi patterns using a double-tilt specimen holder (Liu, 1995, 1996). To determine the orientation of the

sampled volume, the sample is tilted so that a low-index zone axis is close to the beam direction. The tilting angles as well as three features (zone axes or points on the Kikuchi lines) that clearly define the Kikuchi pattern in this position are marked using the post-specimen deflection coils and evaluated to yield the crystallographic orientation. This method is particularly well suited to the determination of misorientations in a given sample region with similarly oriented crystals—in a deformed and recovered subgrain structure (Wert et al., 1995). If the misorientation angle is less than, say, 15°, the low-index zone axis is mostly still visible, so that only the relative position of the actual Kikuchi pattern with regard to the reference pattern has to be determined. For the determination of misorientations in terms of misorientation angle and axis, the accuracy is stated to be 0.3° and 3°, respectively.

6.3.5 Automated Evaluation of Selected Area Channeling Patterns

It has been stated in Section 6.2 that the geometry of the diffraction patterns as obtained by SAC is akin to the TEM Kikuchi patterns, although their formation mechanisms are slightly different. Furthermore, both the geometrical arrangement and the capture angle of both techniques are comparable; hence, SAC patterns can generally be evaluated according to the same principles as TEM Kikuchi patterns (Joy et al., 1982; Lorenz and Hougardy, 1988; Schmidt and Olesen, 1989).

SAC patterns form on the viewing screen of the SEM and are usually recorded on photographic films as conventional SEM micrographs. Hence, there is again the problem of transferring the pattern information into a computer for the automatic analysis. Schwarzer and Zaefferer (1994) used the SEM image cursor to mark the bands and transfer the data through a serial interface to a computer. Alternatively, in modern digital SEMs, the entire screen image—thus also the SAC patterns—can be stored and used by an external computer to derive the crystallographic orientation of the sampled volume.

However, due to the advantages of the competitive EBSD technique (Sections 7.4 through 7.8), SAC is increasingly less used for the determination of individual orientations in SEM (Section 7.3). Accordingly, nowadays little effort is put into the automatization of interpreting SAC patterns.

6.4 Pattern Quality

Besides the crystallographic orientation (Section 6.3), there is another parameter that can be derived from the patterns by means of image analysis, namely, the sharpness or quality of the patterns. Since the Kikuchi line broadening, and indeed the whole pattern quality, is related to the number of lattice defects in the sampled volume, it yields information about the state

of deformation and internal stresses. Pattern quality is also affected by artifacts such as inappropriate specimen preparation (Section 7.5) or occlusion of the specimen surface by surface layers (Figure 7.8).

The first attempt to relate the pattern quality to plastic strain in a specimen was when Quested et al. (1988) determined the magnification at which the pattern quality in spot mode and image mode of the SEM was same. The larger the value of this magnification, the smaller is the sample area in the image mode that contributes to the pattern, where the pattern is not yet affected by lattice distortions. This provides a brief estimate of the dislocation density and, consequently, of internal stresses.

In detailed studies on differently deformed aluminum samples, Wilkinson and Dingley (1991) developed a more meaningful method for a quantitative evaluation of the pattern quality. By means of a discrete Fourier analysis, they showed that with increasing deformation the sharpness of the edges of the bands in the patterns decreased, which resulted in a continuous reduction of the high-frequency parts of the bands in the Fourier spectrum. The pattern quality could be derived in a quantitative manner from the first moment of the Fourier-transformed pattern. However, this method is based on the analysis of patterns that were recorded photographically, and is restricted to one particular zone axis ($\langle 112 \rangle$), so that it is not suitable for routine applications.

For a quantitative characterization of the pattern quality, which is routinely applicable during large-scale microtexture measurements, a quality parameter IQ , "image quality," is derived directly from the pattern. Kunze et al. (1993) defined a quality parameter IQ as the sum over the peak sharpness of all detected peaks. For a homogeneous, gray pattern, IQ becomes zero. The upper limit of IQ is given for each pattern by the minimum peak sharpness and the maximum possible number of peaks, so that this definition yields data whose absolute values cannot be compared quantitatively.

Krieger Lassen et al. (1994) adapted the Fourier transform for use in fully automated evaluation codes. As this method appears to be the most general one, it is described here in more detail. First, a Fourier transform of the entire pattern $I(x,y)$ is performed. To achieve minimum computation time, the fast Fourier transform (FFT) is used:

$$F(u, v) = \frac{1}{n^2} \sum_{x=0}^{n-1} \sum_{y=0}^{n-1} I(x, y) \exp\left(-i2\pi \frac{ux + vy}{n}\right) \quad (6.11)$$

where i is the imaginary number. For the FFT, n must be a multiple of 2 so that only a part of the pattern, for example, 64×64 pixels ($64 = 2^6$), is considered. A pattern of poor quality has a more homogeneous frequency spectrum than a pattern of higher quality (Figures 6.11a and 6.11b). This means that sharper patterns comprise a larger fraction of low frequencies, whereas poor patterns approach the frequency spectrum of white noise (Figures 6.11c and 6.11d).

(Note that Wilkinson and Dingley [1991] analyzed the Fourier spectrum of the *edges* of the bands, not the entire pattern.) A measure for the uniformity of the frequency spectrum is the inertia I of the Fourier spectrum normalized to the total energy of the Fourier spectrum. With increasing concentration of the Fourier spectrum in the lower frequencies, that is, with better patterns, I becomes smaller. To obtain values that are quantitatively comparable, I is related to the value I_{\max} for a completely homogeneous spectrum. The image quality is then given by

$$IQ = 1 - \frac{I}{I_{\max}} \quad (6.12)$$

This definition of the image quality IQ yields normalized values between 0 and 1. For white noise $I = I_{\max}$, thus $IQ = 0$. The better the pattern, the larger the part of low frequencies will be. Consequently, I decreases and IQ increases up to $IQ = 1$, but in practice, usually patterns with $IQ < 0.6$ are obtained. The completely automated procedure to derive IQ , combined with very short computation times, favors incorporating this—or a similar—method into codes for automated evaluation of Kikuchi patterns. The use of image quality parameters to produce orientation maps is described in detail in Section 10.4.4.

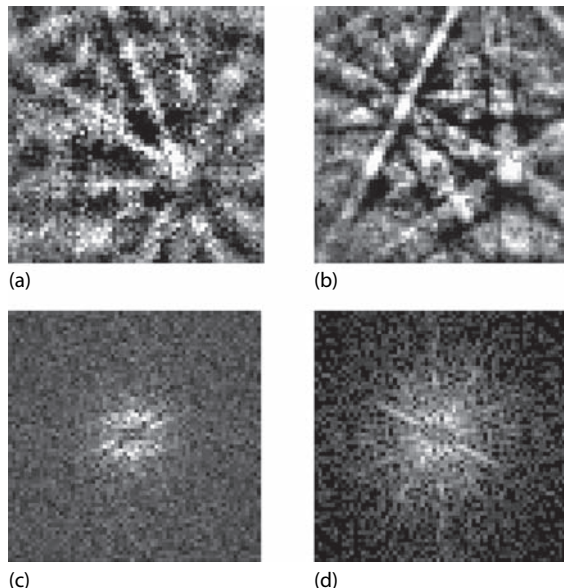


FIGURE 6.11

Original and Fourier-transformed EBSD patterns with different quality to derive the image quality IQ . (a) Original poor-quality EBSD pattern; (b) original high-quality EBSD pattern; (c) Fourier spectrum of (a) ($IQ = 0.29$); (d) Fourier spectrum of (b) ($IQ = 0.43$).

It has already been mentioned that the pattern quality is strongly affected by the experimental setup, so that the absolute values of IQ of different set-ups cannot be compared unambiguously. For instance, changes in experimental parameters like accelerating voltage and beam current as well as other factors like vacuum or quality and alignment of the filament will strongly influence degradation of the pattern. However, during one scan the experimental parameters should remain more or less constant, so that at least a semiquantitative evaluation of the pattern quality can be achieved. For instance, with the help of the image quality parameter, Krieger Lassen et al. (1994) could distinguish between deformed and recrystallized grains in a sample of partially recrystallized aluminum with a very high reliability.

It should be noted that the pattern quality IQ may also depend on the orientation of the sampled volume itself. Despite the large steric angle covered by EBSD, patterns representing different orientations will depict different regions of the stereogram (Nowell and Wright, 2005). Therefore, regardless of the strain state, the numerical value of IQ will vary, to some extent, for different orientations.

A new parameter, called the “modified crystal deformation,” has been defined to quantify the spread of crystal orientation within individual grains, arising due to dislocation accumulation during plastic deformation (Kamaya et al., 2006). This parameter has a good correlation with the degree of plastic strain. Until recently, measurement of elastic strain had been beyond the scope of EBSD. However, small shifts in the positions of zone axes in EBSD patterns can now be detected and measured with sufficient sensitivity to enable elastic strain measurement (Wilkinson et al., 2006). The technique has been used to measure strains across the interface in a Si–Ge epilayer on a Si substrate. Other workers have exploited the strain-sensitive parameters in EBSD patterns to evaluate the elastically distorted regions in GaN epilayers (Luo et al., 2006). A strain range from 100 to 200 nm was detected.

6.5 Summation

Almost all microtexture work relies on the interpretation of Kikuchi patterns. Both the Kikuchi patterns in TEM and the EBSD patterns in SEM form by Bragg reflection of inelastically scattered electrons at the lattice planes of the illuminated crystal. Accordingly, the Kikuchi pattern is directly related to the orientation of the reflecting planes in the specimen and is hence perfectly suited to crystal orientation determination. Although the formation mechanisms of SAC patterns in SEM are slightly different, all these patterns embody the same geometry and crystallographic information, and consequently can be evaluated according to the same principles. The spatial resolution and angular accuracy is compared for these techniques in Table 12.1.

The large steric angle covered by EBSD means that the resulting patterns can usually be indexed in an unequivocal manner. As the EBSD patterns furthermore comprise a rather homogeneous contrast range, they are very well suited to automatic pattern recognition codes (Hough or Radon transform), which automatically detect the Kikuchi bands. Accordingly, fully automated systems to index the patterns and evaluate the corresponding crystallographic orientation have been developed with great success and are widely available. Automation has allowed the full potential of EBSD to be realized through the subsequent development of orientation microscopy and orientation mapping (Chapter 10). In contrast, for TEM Kikuchi patterns and SAC patterns much smaller regions of the stereogram, but more high-index bands, are visible so that unequivocal indexing is much more complicated. Here, the additional information provided by the bandwidth must be considered to attain unequivocal solutions. Furthermore, the much higher dynamic range of TEM Kikuchi patterns renders automated indexing of TEM Kikuchi patterns more difficult than for EBSD.

7

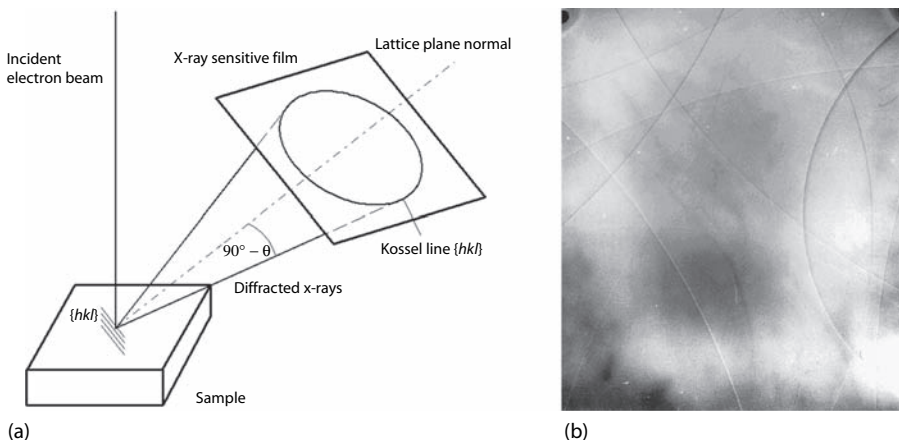
Scanning Electron Microscopy-Based Techniques

7.1 Introduction

The scanning electron microscope (SEM) is a powerful instrument for acquiring microtexture data and characterizing the local crystallography of materials (Wilkinson and Hirsch, 1997). EBSD is the technique that has become almost universally used to obtain such data, so most of this chapter is devoted to a description of the principles and practice of EBSD. Although EBSD has now become a mainstream and powerful experimental tool for a whole range of microstructure characterization, the focus throughout this book is on its application to *microtexture* analysis. Two other SEM-based techniques, micro-Kossel and electron channeling diffraction or SAC, were fore-runners of EBSD and, although they are comparatively less used nowadays, they are included here for completeness.

7.2 Micro-Kossel Technique

The basis of the Kossel technique is the diffraction of x-rays at the crystal lattice, where the x-ray source is situated *within* the sample under investigation. For crystallographic studies—including orientation determination—by means of this technique an electron beam is focused on the sample. Through interaction of the incident electron beam with the electron shells of the atoms, characteristic x-rays are emitted, which then interfere with the surrounding crystal lattice. Kossel et al. (1935) first used this method to achieve diffraction patterns for macroscopically large samples. To investigate local orientations in microscopic regions (micro-Kossel x-ray diffraction [MKXD]), Kossel measurements are usually performed in a microprobe (Peters and Ogilvie, 1965; Bevis and Swindells, 1967; Inokuti and Doherty, 1977) or an SEM (Dingley and Steeds, 1974; Dingley, 1978).

**FIGURE 7.1**

(a) Diagram illustrating the formation of Kossel patterns in reflection. (b) Kossel pattern from titanium. (Courtesy of F. Friedel.)

Part of the x-radiation, which forms through the interaction of the electron beam with the sample material, is subject to subsequent reflection at the lattice planes of the sample in accordance with Bragg's law (Equation 3.4). Because the lattice planes are irradiated with x-rays coming virtually from all directions, the reflected x-rays form cone-shaped planes, the Kossel cones, with a half apex angle $90^\circ - \theta$. The reflected x-ray intensity along these cones can be recorded on an x-ray sensitive film that is usually placed several centimeters before (reflection geometry) or behind (transmission geometry) the sample within the microscope chamber (Figure 7.1a). In comparison to Kikuchi electron diffraction (Section 6.2.1), the wavelength of the x-rays analyzed by the Kossel technique is much larger. Therefore, all Bragg angles θ between 0° and 90° may occur, so that the resulting projection lines on the film plane are strongly curved (Figure 7.1b).

In order to obtain Kossel patterns, the accelerating voltage of the electrons must be about two to three times larger than the critical voltage to produce the characteristic x-ray $K\alpha$ radiation (Section 4.3.1), which is not possible for all materials. By contrast, in the case of light elements (e.g., aluminum), the characteristic wavelength of the $K\alpha$ radiation of the sample material is too large to yield reflection according to Bragg's law. In both cases x-radiation of a suitable wavelength can be produced by an external x-ray source that is placed as close as possible to the surface of the sample (pseudo-Kossel technique). For example, a thin layer of a different material can be deposited on the sample surface (Peters and Ogilvie, 1965; Ferran et al., 1971) or the sample can be covered with fine particles of another metal (Ullrich and Schulze, 1972).

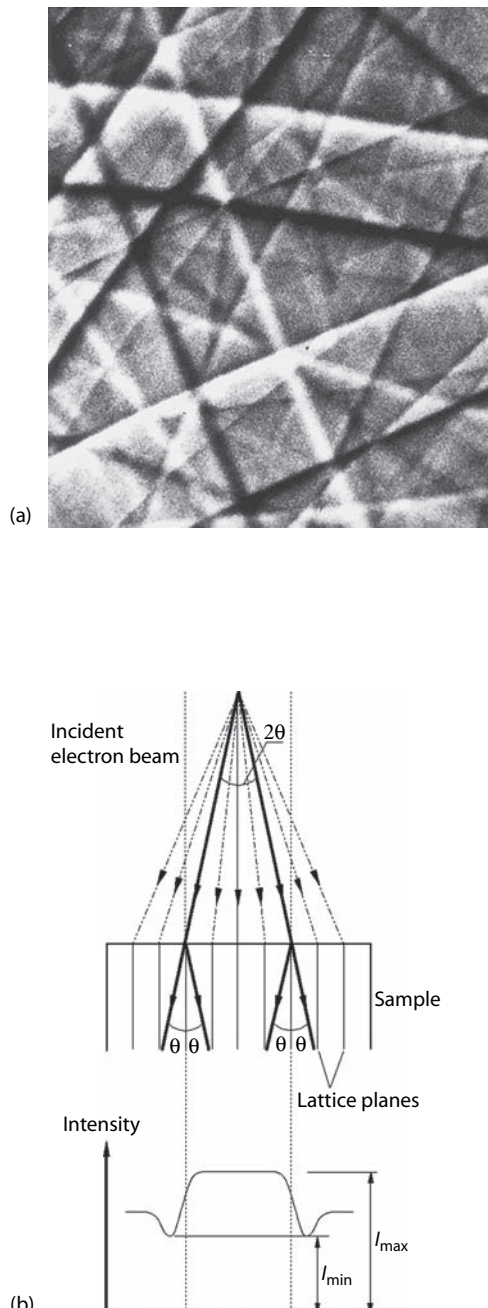
Although Kossel patterns have been achieved from volumes of only a few microns (Dingley and Steeds, 1974), the spatial resolution is, in general cases, limited to 5–10 μm , so that only rather coarse-grained samples can

be analyzed. In case of the transmission technique, the spatial resolution is correlated with the transmitted sample thickness, which generally results in poorer spatial resolution (Ferran et al., 1971). Only with extremely thin samples has a spatial resolution of 10–20 μm been realized (Bellier and Doherty, 1977). Furthermore, Kossel patterns have a very high background and, consequently, a low signal-to-noise ratio. This is caused by the nonreflected x-rays as well as the Bremsstrahlung (continuous radiation) and complicates evaluation of the patterns. In particular, for this reason, Kossel patterns cannot be digitally recorded to date, rendering an automated evaluation impossible (as in the case of Kikuchi patterns; Section 6.3). For these reasons, and with the advent of EBSD, the Kossel technique is no longer competitive for orientation determination. Rather, nowadays Kossel patterns are mainly used for analysis of unknown crystal structures (Tixier and Wache, 1970; Ullrich and Schulze, 1972; Ullrich et al., 1992) and high-precision internal stress measurements (Ellis et al., 1964; Bauch and Ullrich, 2004), as lattice constants a can be derived with an accuracy of better than $\Delta a/a = 10^{-5}$.

It is noted that since the 1990s, Kossel experiments are also performed using the fluorescent radiation excited by the highly collimated x-ray beam of synchrotron facilities (Section 10.2). Here, the high beam intensity together with the absence of the continuous radiation leads to an appreciably better signal-to-noise ratio; hence, synchrotron Kossel patterns can be recorded with image plates (Ullrich et al., 1994, 1999).

7.3 Electron Channeling Diffraction and Selected-Area Channeling

Electron channeling diffraction has been a more common method for local orientation determination in the SEM than has Kossel diffraction. It is based on the diffraction of the electron beam in an SEM at the crystal lattice. The intensity of the reflected electrons depends not only on the site in the sample but also on the angular direction of the incident electron beam with respect to the lattice planes. Thus if one changes the direction of the incident beam at a constant sample site—in a given grain—the anisotropy of backscattered electrons gives rise to *electron channeling patterns* (ECP) (Coates, 1967). These ECP patterns, which are composed of bright bands of a given thickness representing distinct crystallographic planes (Figure 7.2a), are akin to TEM Kikuchi patterns and EBSD patterns in both their geometry and the crystallographic information that they contain (Section 6.2). Consequently, they can be evaluated according to the same principles (Section 6.3). The exact formation mechanisms of ECP bands, however, differ slightly from that of Kikuchi lines in TEM (for a comprehensive treatment, see Joy et al., 1982); therefore, ECP bands are often referred to as “pseudo-Kikuchi bands” (Figure 7.2b).

**FIGURE 7.2**

(a) SAC pattern of a recrystallized grain in partially recrystallized aluminum. (Courtesy of H.W. Erbslöh.) (b) Formation of pseudo-Kikuchi bands in SAC.

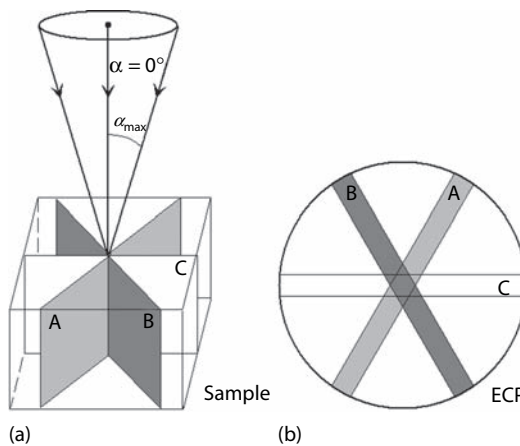


FIGURE 7.3
Formation of SAC patterns.

To use ECP for orientation determination, the electron beam in the SEM is focused on the sample site to be analyzed. Then, the beam is tilted at this position by an angle α either in two perpendicular directions or on concentric circles with angles $0^\circ < \alpha \leq \alpha_{\max}$ (Figure 7.3a), without leaving the corresponding sample site. If the electron beam fulfills Bragg's condition for reflection at a given set of lattice planes, that is, $\alpha = 0$, it will be reflected, and will contribute to a band in the ECP pattern (Figure 7.3b). In practical applications the angle α_{\max} is limited to 5° – 10° , which means that the angular diameter of the ECP pattern is only 20° maximum. Hence, only a small region of the gnomonic projection can be recorded, which makes pattern indexing slightly more complicated than in EBSD.

To achieve optimum spatial resolution, minimum probe diameter is required. For that purpose, the beam diameter is usually reduced by suitable apertures to a size of a few microns (*selected area electron channeling diffraction* [SAC] or [SAECD]; van Essen et al., 1970, 1971). In general the spatial resolution is still limited to ~ 10 μm , which is caused by the necessity to tilt the electron beam without leaving the corresponding measuring site. Only with the application of dynamic corrections of the electromagnetic lenses can the spatial resolution be improved to 1 – 2 μm (van Essen, 1971; Joy and Newbury, 1972). Another drawback of the SAC technique is its high sensitivity to lattice defects, so that only recrystallized or strongly recovered microstructural regions can be analyzed. In principle, ECP can be obtained in a TEM as well, when scanning equipment is available (Section 8.4). In that instance, the spatial resolution is approximately 1 μm (Joy et al., 1982; Humphreys, 1984). A very detailed survey on ECP and SAC, including a list of literature that has appeared to that date, can be found in Joy et al. (1982).

7.4 Evolution of Electron Backscatter Diffraction

EBSD in an SEM has become the most widely used technique for the determination of microtexture (Randle, 2003). As mentioned in Section 1.2.2, the steps necessary to produce an EBSD pattern in an SEM are as follows:

- Tilt the specimen so that its surface makes an angle $\sim >60^\circ$ with the horizontal
- Turn off the scan coils to obtain a stationary electron beam
- Place a recording medium in front of the tilted specimen to capture the diffraction pattern

The main effect of tilting the specimen is to reduce the path length of electrons that have been backscattered by lattice planes as they enter the specimen, thus allowing a far greater proportion of these electrons to undergo diffraction and escape from the specimen (having lost virtually none of their energy) before being absorbed. When the specimen is flat, which is the case for conventional SEM, the path length and hence absorption of the backscattered electrons is too great to produce detectable diffraction. Figure 7.4 shows how the electron-specimen interaction volume is modified from the well-documented “tear drop” shape to a volume having a very small depth when the specimen is tilted (Schwarzer, 1993). The total effect on the backscatter process of tilting the specimen is more complex than described here, but a simple explanation based on electron path length is adequate for the present purposes. More details on the physics of EBSD can be found elsewhere (Venable and Bin-Jaya, 1977; Dingley, 1981; Dingley et al., 1987; Wilkinson and Hirsch, 1997; Reimer, 1998; Zaefferer, 2007).

The observation of high-angle Kikuchi patterns from “reflected” electrons, which was the forerunner of the EBSD technique, was reported as early as 1933 (von Meibom and Rupp, 1933) and 1937 (Boersch, 1937). A report on systematic analysis of high-angle Kikuchi patterns was published in 1954 (Alam et al, 1954). Here, a special apparatus consisting of an electron source, a specimen chamber and a camera was used and specimens of cleaved LiF, KI, NaCl and PbS₂ were examined. This arrangement captured very wide angle Kikuchi patterns (up to 164°) that were found to have lost almost no energy in the scattering process and to be in agreement with Bragg’s law.

It was nearly twenty years later before the discovery of wide-angle Kikuchi patterns was pursued further. At this stage an SEM was used to provide the electron source, and the diffraction patterns from the tilted specimen were captured by a fluorescent screen interfaced to a closed-circuit TV camera. The patterns were named “electron backscattering patterns” since they comprised the angular distribution of the backscattered electrons after diffraction. Several advantages of the technique over SAC for obtaining crystallographic

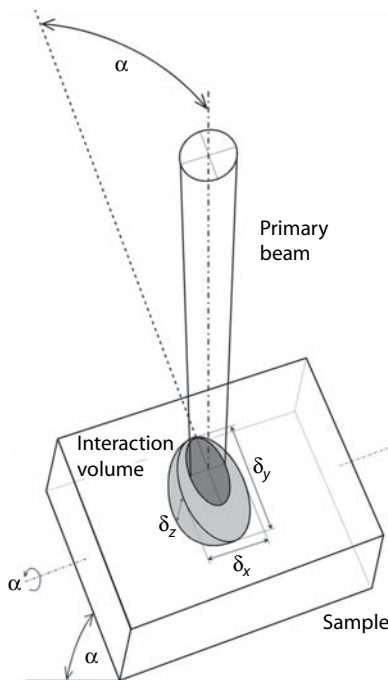
**FIGURE 7.4**

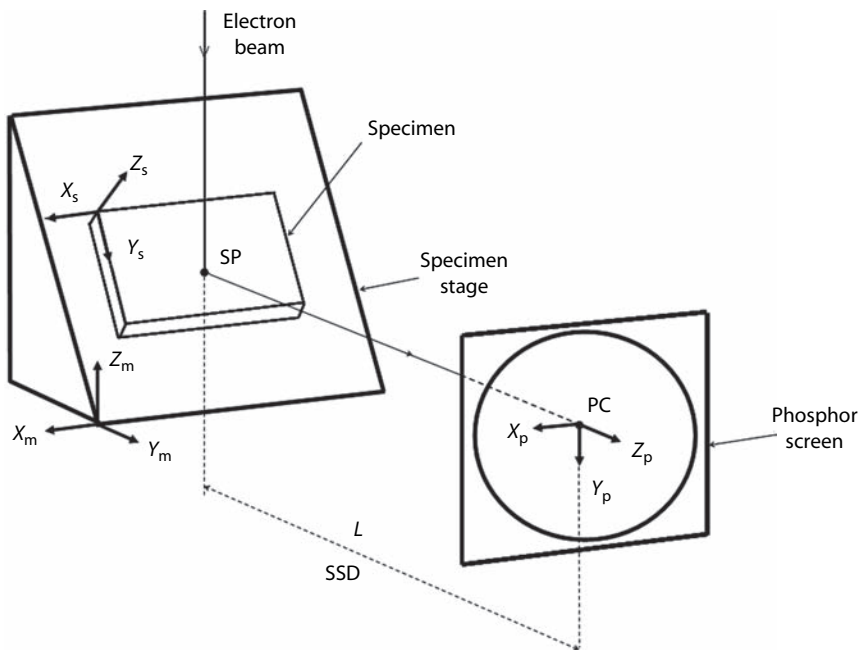
Diagram showing the specimen–beam interaction volume in a specimen tilted for EBSD.

information in the SEM were cited: the smaller sampled volume, much larger angular view of the diffraction pattern, and simpler modifications to the microscope (Venables and Harland, 1973). EBSD patterns were obtained from materials such as tungsten, silicon, and aluminum.

To make orientation measurements from EBSD patterns, it is essential to identify the following parameters (Venables and Bin-Jaya, 1977), which are illustrated in Figure 7.5 (Randle, 2003):

- The coordinates of the *pattern center*, PC , defined in Section 6.2.3
- The specimen-to-screen distance Z_{SSD} or L in Figure 7.5
- The relationship between reference directions in the microscope $X_mY_mZ_m$, specimen $X_sY_sZ_s$, and screen/pattern xyz

These parameters depend on the relative positions of the camera and specimen within the microscope, and are discussed in Sections 6.3 (pattern evaluation) and 7.7 (EBSD calibration). The first method to obtain the coordinates of the pattern center and the specimen-to-screen distance involved measuring the axes of elliptical shadows cast onto the pattern by three fixed spheres (Venables and Bin-Jaya, 1977). Although this method was cumbersome and

**FIGURE 7.5**

Parameters required for EBSD orientation measurements. Pattern source point on the specimen, SP ; pattern center on the recording screen, PC ; specimen-to-screen distance L (or Z_{SSD}); and three sets of orthogonal axes, xyz (screen/pattern axes), $X_sY_sZ_s$ (specimen axes), and $X_mY_mZ_m$ (microscope axes).

slow, it was an accurate means of calibration such that individual orientations could be obtained by photographing the diffraction pattern and spheres assembly and subsequently analyzing it offline.

The next advances in the evolution of EBSD occurred in the early 1980s. These were as follows:

- A more convenient method of calibration
- Online interaction with the diffraction pattern
- Software that gave a rapid evaluation of the orientation
- Hardware improvements

The calibration method involved use of a silicon crystal cleaved so as to reveal $\{001\}$ and mounted at a predetermined inclination angle so that the known geometry allowed the pattern center and specimen-to-screen distance to be evaluated. The diffraction pattern could be interrogated in real time on a monitor screen, and the first versions of software to accomplish this were for cubic materials only (Dingley et al., 1987). The operator was required to move

the computer cursor to identify certain zones axes— $\langle 112 \rangle$ and either $\langle 114 \rangle$ or $\langle 111 \rangle$ —from which information the orientation was calculated. The indices of all major poles were superimposed on the pattern and, if the indexing was correct, the orientation was stored in a data file. Performance of these steps required the operator to have an adequate knowledge of crystallography.

The hardware improvements included substituting a silicon intensified target (SIT) low-light camera for the earlier TV camera. This camera required a lower probe current in the SEM (down to 0.5 nA compared to 20 nA) and so provided greater sensitivity (Hjelen et al., 1994). An image-processing system was also employed, which allowed the live image to be frozen and for a background subtraction/averaging routine to be implemented to improve the quality of the raw EBSD pattern (Section 7.6.6).

From the early 1980s onward, EBSD was also being developed as a tool for crystallographic phase identification via measurement of the symmetry elements in the diffraction pattern (Dingley et al., 1994). These measurements require as much detail in the pattern and as wide an angular view as possible, and so patterns were recorded on film introduced into the microscope chamber in front of the tilted specimen. Recording the pattern directly onto film is a very sensitive means of producing high-contrast, detailed hard copies of diffraction patterns. However, the recording process is tedious and it is not required for orientation determination. Nowadays, phase identification can be performed on digitally stored EBSD patterns (Section 7.6.4).

The progression of EBSD described so far, as summarized in Figure 7.6, has involved step changes in the technology. Subsequent evolution, which occurred from the early 1980s to the early 1990s, was less dramatic, involving instead refinements of the fundamental components and routines. It included the following:

- Further improvements to EBSD hardware, particularly better cameras—intensified silicon-intensified target (ISIT) cameras that offer further enlarged light sensitivity and CCD cameras that offer less distortion. Diffraction pattern processing also improved, and a forward-mounted backscatter detector (FMBSD) became available for convenient viewing of the image when it is highly tilted (Section 7.6.1).
- Extension of the calibration options for greater accuracy and convenience (Section 7.7).
- Continuing improvements to the EBSD software, including indexing routines for any crystal system; mouse-driven interrogation of diffraction patterns no longer involving identification of zones; more sophisticated and faster data handling; and a choice of options for data output (Section 7.8).
- Availability of commercial EBSD systems.

- Recognition and awareness in the scientific and engineering community of the benefits of EBSD for microtexture measurement through early publication of EBSD-generated data (Randle and Ralph, 1988; Hjelen and Nes, 1988; Juul Jensen and Randle, 1989; Engler and Gottstein, 1992).

In the early 1990s, two more major step changes occurred in EBSD technology—the implementation of computer interpretation and indexing of diffraction patterns without operator input (Section 6.3). These were followed by coupling this facility with beam or stage control to automate totally the EBSD

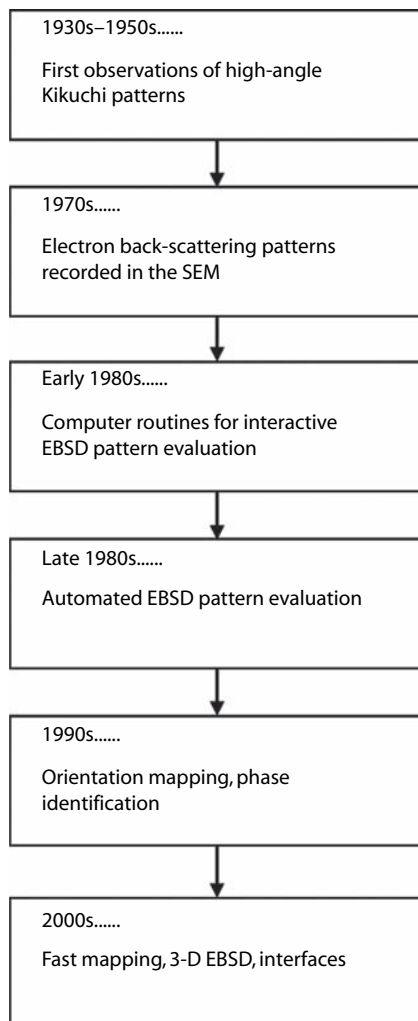
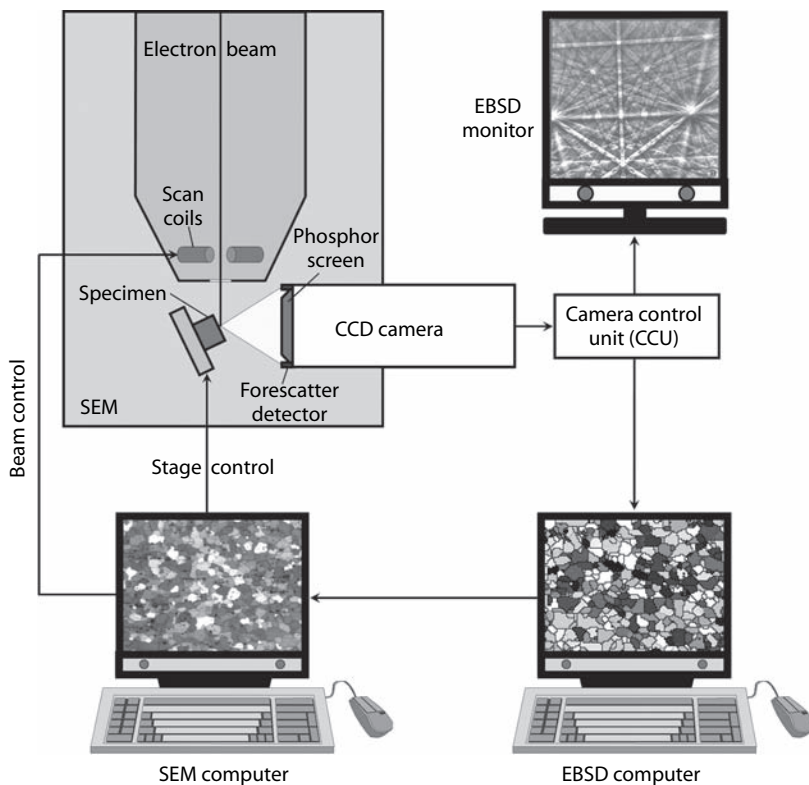


FIGURE 7.6

Timeline of the most significant EBSD developments.

**FIGURE 7.7**

Components of a state-of-the-art EBSD system.

operation, which finally led to orientation mapping (Section 10.4). By the end of the 1990s, most crystal structures could be successfully indexed, although for some lower symmetries this remains quite a challenging task. From 2000 up to the present day, the most significant improvement in EBSD has been in terms of increased speed of mapping (Section 7.6.2), with other developments also in interface characterization (Section 11.3.3), 3-D EBSD (Section 11.3.4), phase identification (Section 7.6.4), and strain measurement (Section 6.4) (Randle, 2007). Figure 7.7 illustrates the essential components of a typical EBSD system.

7.5 EBSD Specimen Preparation

One of the attractions of EBSD is that specimen preparation is straightforward, often similar to that for optical microscopy. This is in contrast to the requirements for other electron diffraction-based techniques, in particular

TEM and also SAC in the SEM, both of which require complex preparation procedures.

The specimen preparation objective for EBSD can be stated very simply: the top 10–50 nm of the specimen should be representative of the region from which crystallographic information is sought, since it is only from this surface region that diffraction occurs. The shallowness of the diffraction volume results from the highly tilted specimen position in the SEM chamber and the consequent reduction of the mean free path length for electrons (Section 7.4; Figure 7.4). The practical upshot of this, and indeed the only crucial aspect of specimen preparation for EBSD, is that the specimen surface must not be obscured in any way—by mechanical damage (e.g., grinding), surface layers (e.g., oxides and most coatings), or contamination.

The standard metallographic preparation route for most specimens, especially metals and alloys, is mounting, grinding, and polishing (Katrakova and Mücklich, 2001). The adaptation of this route for EBSD is discussed first, since metallic materials are currently the most common group to which EBSD is applied. Mounting the specimens in a conducting medium is clearly advantageous for SEM work; otherwise, electrical contact with the specimen can be established by using silver or carbon paint or conductive tape, or simply by cutting the specimen from the mount after the preliminary preparation stages.

It is the final preparation step that ensures suitability for EBSD. Diamond polishing is not an appropriate final stage because of the remnant mechanical damage entailed. However, many common electropolishes or etchants that are used to reveal the microstructure for optical microscopy do so by attacking the specimen surface. This has the concurrent effect of removing polishing damage. Hence, for many metals and alloys the route used for optical metallography, with minimized diamond polishing to avoid surface damage, is all that is needed for EBSD. A useful guide is that the same electrolytes that are used to prepare TEM thin foils can often also be used to prepare the surfaces of bulk specimens for EBSD. Brittle specimens (typically, minerals, ceramics, and semiconductors) may be fractured, cleaved, or mounted and polished for EBSD. Specimens that contaminate or oxidize rapidly may need to be prepared immediately before SEM examination or alternatively ultrasonically cleaned and stored under solvent (e.g., white tin). Particularly difficult specimens can be ion milled for a few hours (Michael and Kotula, 2008).

A highly recommended method for preparing a variety of specimens for EBSD is final polishing in colloidal silica, since this medium does not introduce the harsh mechanical damage associated with diamond polishing (Nowell et al., 2006; Wynick and Boehlert, 2005). In general, it is not necessary to prepare simple metals and alloys in this way because they respond readily to conventional polishing and etching. However, large particles (e.g., carbides and nitrides) in metallic matrices, low-melting-point

metals and alloys, ceramics, composites, and minerals are all amenable to polishing for up to several hours in colloidal silica (Katrakova and Mücklich, 2002).

Inadequate or inappropriate specimen preparation could give rise to misleading data interpretation. For example, the diffuseness of an EBSD pattern is a guide to the amount of plastic strain in the lattice (Section 6.4); however, if a specimen contained diamond polish damage prior to etching, the pattern might be interpreted erroneously as arising from a deformed specimen. Furthermore, the absence of an EBSD pattern in a sampled region is evidence either that it is noncrystalline, or highly strained, or that the grain size is smaller than the probe size. However, these interpretations are only valid after correct specimen preparation.

Although the primary aim of EBSD specimen preparation is to obtain diffraction patterns, a secondary objective may be to reveal the microstructure. This can be done either by orientation microscopy (Section 10.3) or by conventional electropolishing or etching. Often, orientation microscopy is carried out in conjunction with either of the other two methods used to reveal microstructure. However, etching time should be kept short to minimize topographical effects that may affect collection of diffraction patterns, particularly close to grain boundaries.

The actual depth of the surface layer that gives rise to EBSD patterns is a function of both the accelerating voltage and the atomic number of the specimen. Higher accelerating voltages allow deeper penetration of the electron beam, whereas higher atomic numbers are associated with lower elastic mean free paths of electrons, and thus shallower penetration (Section 7.6.5). The sensitivity of EBSD patterns to coating thickness has been explored by coating single crystals of silicon with various thicknesses (from 5 to 40 nm) of aluminum, nickel, or gold (Michael and Goehner, 1994). Figure 7.8 illustrates the effect of coating silicon with 5 nm of nickel. An EBSD pattern from the underlying silicon is easily observed when an accelerating voltage of 40 kV is used, yet for an accelerating voltage of 10 kV, the beam hardly penetrates through 5 nm of nickel. It was confirmed that the interaction thickness is approximately twice the elastic mean free path (Joy, 1994), giving critical interaction depths—the maximum thickness of surface material that can be penetrated by the electron beam at 40 kV accelerating voltage—of 100, 20, and 10 nm for aluminum, nickel, and gold, respectively.

For nonconducting specimens, which includes minerals, diffraction patterns can usually be obtained if very small specimens are embedded in conducting paint. Low accelerating voltages may be needed to reduce charging or beam damage. Otherwise, a conductive coating that is only a few nanometers thick, such that the electron beam can penetrate to the specimen beneath, could be deposited prior to EBSD. If a coating has been deposited, it may be helpful to increase the accelerating voltage of the SEM to enhance beam penetration as described earlier.

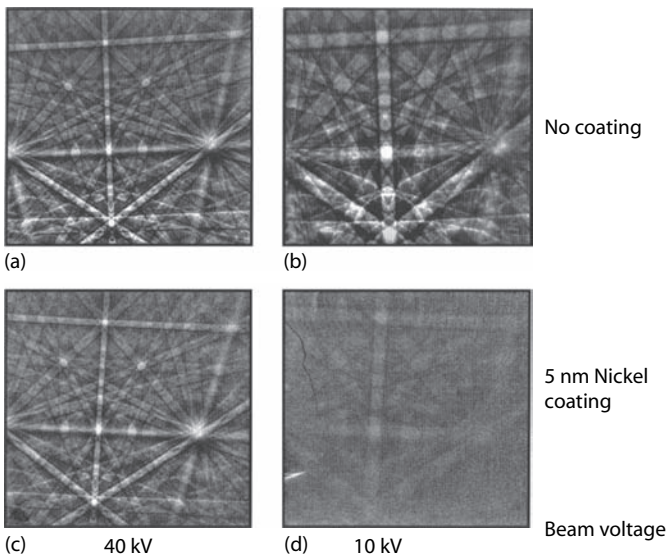
**FIGURE 7.8**

Illustration of the penetration depth of the electron beam in a silicon EBSD specimen. (a) No coating, 40 kV accelerating voltage; (b) no coating, 10 kV accelerating voltage; (c) coating with 5 nm of nickel, 40 kV accelerating voltage; (d) coating with 5 nm nickel, 10 kV accelerating voltage. There is less beam penetration at 10 kV since the underlying silicon pattern is indistinct. (Courtesy of J.R. Michael.)

A few examples of preparation methods used for EBSD are given here, to illustrate some of the points made in this section.

- *Commercially pure aluminum, titanium alloys.* Electropolish in 5% perchloric acid in ethanol at -25°C. Etchants that deposit a film on aluminum are unsuitable for EBSD.
- *Aluminum-lithium alloys.* Immerse for several seconds in Keller's reagent, slightly warmed.
- *Mild steel.* Swab with 2% nital for several seconds.
- *Many rocks and minerals.* Diamond polish block specimens followed by colloidal silica polishing for several hours.
- *Polysilicon.* Wash in detergent and immerse for 1 min in 10% hydrofluoric acid in a plastic beaker.

In summary, specimen preparation for EBSD is generally uncomplicated, and for most cases, it is based on standard metallographic routes. Diffraction patterns arise from a surface region that is of the order of tens of nanometers thick, the exact thickness varying with microscope conditions such as accelerating voltage and atomic number.

7.6 Experimental Considerations for EBSD

There are many choices for the methodology and microscope operating conditions used in a microtexture determination, reflecting the versatility of EBSD. These are discussed in Sections 7.6.1 through 7.6.6.

7.6.1 Hardware

An EBSD system can be added as an attachment to practically any SEM. A tungsten-filament SEM is standard in many laboratories, which is satisfactory for many EBSD applications and also the most cost-effective option. A LaB₆ emission source has advantages in terms of available beam current. Field emission gun SEMs (FEGSEMs) have become increasingly popular for EBSD because an increase in spatial resolution of two to three times that of a tungsten-filament SEM can be obtained (Humphreys et al., 1999; El-Dasher et al., 2003). A slow-scan charge-coupled device (SSCCD) video camera with solid-state sensors is now used for EBSD, replacing the first generation of SIT cameras. For most microtexture work, rapid data acquisition is a primary consideration, and a TV rate camera combines sufficient speed with adequate pattern contrast and definition. EBSD can now also be applied in an environmental SEM (Sztwiertnia et al., 2006; Karlsen et al., 2008).

Although in the earlier standard setups, the diffraction camera was mounted horizontally in the rear of the microscope, other geometries with either a tilted camera (in a positive or negative sense) or entry through a side port of the microscope are now more common. Since most of the electrons are diffracted in the forward direction from the tilted specimen, the most favorable capture geometry is to have the camera also tilted so as to be below the horizontal. However, this poses additional problems for maintaining the camera in a stable position, and so is not generally adopted. The most common reason for mounting the camera in a side port of the microscope is to take advantage of the resident tilt of the eucentric stage. Which of these options is more convenient will depend on the microscope column layout.

The most important item of EBSD hardware is of course the camera. A CCD camera is usually cooled to reduce the buildup of thermally generated charge during operation. The advantages of the CCD camera over the earlier tube-type models are as follows (Hjelen et al., 1994; Drake and Vale, 1995):

- The patterns are of a consistent quality over a wide range of microscope operating conditions, unlike tube cameras where the diffraction pattern becomes noisy if the accelerating voltage or probe current is reduced.

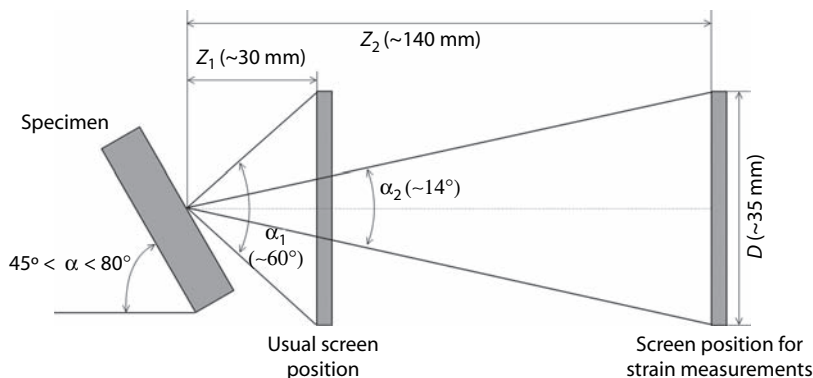
- There is no geometric distortion of the diffraction pattern, whereas tube cameras may introduce considerable distortion.
- They are more robust, since they are not damaged by normal illumination, whereas low-light tube cameras are susceptible to damage.
- The lifetime of a CCD camera is longer than that of a tube camera, and furthermore the CCD camera is smaller and lighter.

There are two options for accommodating the camera/screen assembly. In older setups, the camera viewed the specimen in the microscope through a lead glass window, with a port in the microscope chamber purpose modified to house the window. The phosphor screen resided inside the microscope column, independent of the camera that was outside the vacuum system. A more advanced approach, which takes advantage of the smaller and lighter CCD camera, has the phosphor screen mounted on the front of the camera, and the whole camera/screen assembly is inserted or retracted through a vacuum seal into the SEM chamber. The phosphor screen itself is fragile, and touching, cleaning, or collision with any object should be avoided. It may be possible to tolerate some screen blemishes because pattern enhancement routines can minimize their effect. Damaged or degraded screens can also be easily replaced.

The position of the camera in the column is generally dictated in the first instance by the space available in the microscope specimen chamber, and is usually approximately 15–30 mm from the specimen. The camera may not be maintained at a fixed position for several reasons:

- If large specimens for non-EBSD application are accommodated in the microscope chamber, the camera will need to be retracted to prevent collision damage to it.
- One of the EBSD calibration routines requires the camera to be operated in two positions (Section 7.7.2).
- If the camera is placed further away from the specimen than is usual, the capture angle for the diffraction pattern will be reduced. Figure 7.9 shows that the capture angle is reduced to 14° if the screen is placed 140 mm from the specimen. This configuration gives an increased accuracy and has been used to measure small orientation changes (Wilkinson, 1996). However, there is a concomitant reduction in light level captured by the camera (approximately 1/20 of that usually encountered for the 30 mm specimen-to-screen distance).

The other main components of an EBSD system are a computer and dedicated software to control the camera, data processing, pattern indexing, analysis, and output. In addition to a mechanism for controlling the position of the beam, there will also be a stage motor to position the specimen, as shown in Figure 7.7.

**FIGURE 7.9**

Effect of retracting the phosphor screen in an EBSD system to give a smaller convergence angle α and hence better resolution in the diffraction pattern. (Courtesy of A. Wilkinson.)

Finally, an FMBSD, which is also referred to as a forward-scattered electron detector or, in short, forescatter detector, may be included in the EBSD system. This detector fulfills the same function as a backscattered electron detector in conventional imaging; namely, it uses the primary (backscattered) electrons and a form of amplification to image the microstructure on the basis of changes in topography, composition, or orientation. The modification that is required for EBSD is to mount the detector in a *forward* position (Figure 7.7), either on the camera or phosphor screen itself or on the specimen holder, so as to be in the optimum position to detect the backscattered electrons and use them for imaging. Since the inclination of the specimen gives a much higher yield of backscattered electrons than if the specimen were flat, backscattered imaging is improved by tilting the specimen, particularly for predominantly low-atomic-number specimens such as minerals, rocks, or aluminum alloys.

If the SEM is additionally equipped with a heating stage, *in situ* EBSD annealing measurements can be performed to analyze microstructure and orientation changes during annealing, most prominently, during recovery, recrystallization, and grain growth (Mirpuri et al., 2006; Lens et al., 2005) and during phase transformations (Seward et al., 2004; Lischewski et al., 2008). High-speed EBSD is of particular interest so as to allow for sufficiently high heating rates (Field et al., 2007). One of the potential problems with *in situ* annealing experiments is that the free surface may influence the microstructural changes (Nakamichi et al., 2008); hence, it must be ascertained that the microstructure and texture effects observed at the surface are representative of the bulk behavior. Also, pattern quality may degrade at elevated temperature, and emission of thermal electrons may interfere with the imaging of microstructure. It is also possible to combine EBSD with *in situ* deformation by uniaxial tension, compression, or bending (Han et al., 2003; Scherian and Pippin, 2008). At present the applied deformation is halted to obtain an

EBSD map (Karlsen et al., 2008). Combined *in situ* EBSD annealing and deformation studies offer experimental advantages in the study of topics such as phase transformations and microstructure evolution.

7.6.2 Data Collection Efficiency

Efficient data collection is an advantage in an EBSD investigation. The total time required per map pixel is the sum of the time taken to move to the map coordinates and to site the electron probe, the time taken to collect a diffraction pattern, and the time taken to analyze the pattern. Data points are acquired manually or, more usually, automatically stepping the electron beam across the specimen surface within the field of view on the SEM image. This is the basis of orientation microscopy and orientation mapping as described in Chapter 10. Thereafter, new fields of view on the same or different specimens can be automatically sampled according to inputted specimen coordinates, and the orientation maps can be subsequently montaged if required. In this way maps are generated over many hours or even days, provided the microscope conditions remain stable. This method provides an efficient means of automated data collection.

The greatest gains in data collection speed are a result of the improvements in camera technology, which have occurred in the past few years. The improved quality of the captured diffraction pattern is due in part to an improved dynamic range of the camera, that is, the number of distinguishable gray levels, which has increased 10-fold with a CCD camera compared to an SIT camera. The improvement is also due to the recent technological advance whereby groups of pixels in the diffraction pattern can be grouped together into “super pixels” (*binning*), which increases the sensitivity of the camera. For example, a block of 8×8 pixels can be grouped together to produce the same increase in camera sensitivity, that is, $8 \times 8 = 64$. In turn, this gives the same reduction in diffraction pattern collection time.

The gain in pattern collection speed brought about by binning is further enhanced by recent improvements in electronic processing, such as frame averaging, and amplification of the captured diffraction pattern (Section 7.6.6) as well as computer and software improvements. This has led to faster and faster mapping rates, depending on the material. For example, in 2004 a map was acquired from a nickel superalloy at a rate of 70 points per second, with 99% of the data indexed correctly (Dingley, 2004). At the time of writing, a new generation of digital EBSD cameras is being introduced, which enables another order of magnitude increase in scanning rates—up to about several hundred patterns per second on suitable materials (Nowell et al., 2006; Wright et al., 2007; Ghosh, 2008). To the authors’ best knowledge, the highest recording speed published to date is 770 patterns per second (Schwarzer, 2008; Søfferud et al., 2008), and it is expected that rates of as much as 1000 patterns per second will be feasible shortly. However, it is important that gains in speed do not incur any loss in indexing accuracy or spatial resolution

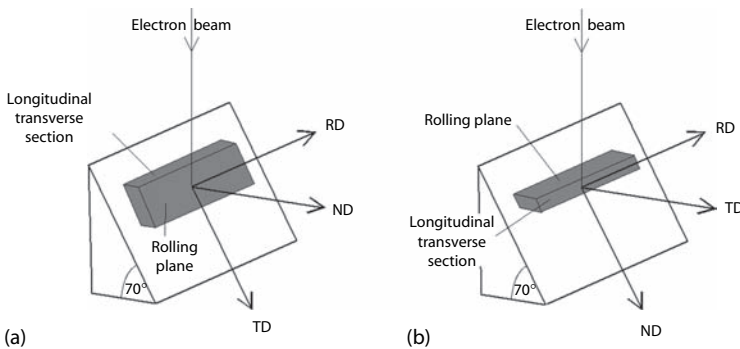
(Trimby et al., 2002). The data collection speed achievable in individual cases depends on the type of SEM, EBSD camera, operating parameters, and specimen type. For example, backscattered electron signal increases with atomic number; therefore, high-atomic-number materials yield stronger diffraction patterns and, in general, can be analyzed faster than low-atomic-number species. Diffraction patterns from lower crystal symmetry groups or multiphase specimens require longer processing time than those from cubic materials. Degraded diffraction patterns increase analysis time; therefore, specimen preparation routines must always be meticulous.

The latest generation of cameras also has the advantage of distortion-free lenses and a rectangular phosphor screen, replacing the circular screen, so that the whole diffraction pattern is captured and used. This camera is also shaped so that it can be moved close to the specimen, which increases both the camera sensitivity and the spatial resolution.

Having collected the diffraction pattern, the speed of pattern analysis and indexing depends on the processing speed of the computer and selections made in the pattern-solving algorithm. The resolution of the Hough transform and the number of Kikuchi bands used to recognize the pattern (typically three to eight) are the main influential variables. The pattern-indexing rate is increased by a low-resolution Hough transform and few Kikuchi bands. However, these selections must be tempered by the requirement to optimize the proportion of indexable patterns, sometimes called the "hit rate." Some issues of indexing ambiguity are discussed elsewhere (Nowell and Wright, 2005). Unsolved patterns result from either positioning the electron probe on a region where the diffraction pattern is corrupted (typically at a grain boundary or a surface blemish) or from setting the Hough transform resolution and/or Kikuchi band number too low. Finally, the operator must select judiciously the level of acceptance criterion for correct indexing, which will impact not only the speed of map generation but also the solve accuracy. In practice, for meticulously prepared specimens that give high-quality diffraction patterns, achievement of the optimum mapping speed for a particular EBSD camera and system is influenced mostly by the balance between a suitable choice of binning level, diffraction pattern "noise reduction," and hit-rate tolerance. Note that the hit rate does not have to be maximized because many of the unsolved points can be filled in during subsequent cleanup routines (Section 10.4).

7.6.3 Experiment Design Philosophy

The first point to consider when designing an EBSD investigation is the actual choice of analysis technique itself. The range of EBSD applicability is increasing to encompass more investigations that have traditionally been the province of other techniques (TEM or x-ray diffraction). Having established that EBSD is to be used, the material needs to be sectioned so that an appropriate surface can be prepared. In most cases, there is an obvious choice for

**FIGURE 7.10**

Examples of choices for mounting an EBSD specimen to sample either (a) the rolling plane or (b) longitudinal-transverse section.

this surface, although its selection may need some thought. For example, a specimen that has been cut from a rolled product may be mounted so as to sample microtexture from the “side” of the sheet—the RD–ND plane rather than the more obvious RD–TD plane as shown in Figure 7.10 (Davies and Randle, 1996; Huh et al., 1998).

The orientation sampling schedule can be performed either manually or automatically. In general, some preliminary exploration in manual mode to establish the scale of the orientations and how they relate to the microstructure (e.g., the grain size distribution) will clarify the requirements. A step size of one-tenth of the average grain size is often used as a starting point for microtexture and grain misorientation measurements. If EBSD is used to gain a representation of the overall texture, then consideration must be given to the location and sample population size of the constituent orientations (Section 9.3.3).

Once the parameters for the *location* of the region of interest, that is, its *area* plus the *step size* or *individual coordinates* needed for orientation measurements (usually orientation maps), have been determined by trial runs, most investigations can then proceed automatically, usually as an orientation map (Section 10.3). Sometimes further manual interaction is required, such as where there are very large differences in the spatial scale of the orientation distribution (e.g., the sampling of fine twins in polysilicon that has a grain size of many millimeters; Wagner et al., 1996).

In summary, although there is a great diversity in application of EBSD for microtexture-related investigations, the basic steps of experiment design and procedure are generic. These are as follows:

1. Selection of a suitable candidate material and specimens for analysis
2. Optimum specimen preparation

3. Manual checking of diffraction patterns for clarity and expected phase match
4. Appraisal of microstructure for grain size and phase distribution
5. Test run of data collection
6. Data collection, usually via automated orientation mapping

7.6.4 Phase Identification

Multiphase materials and phase identification is a growing area of application for EBSD. For the purposes of microtexture measurement, it is necessary first to identify unknown phases present before measuring, concurrently, the texture of each phase. An unknown phase can be identified by analysis of the symmetry elements in the diffraction pattern, coupled with elemental analysis in the SEM and consultation of a library of possible phase matches (Michael, 2000). The resulting system, nicknamed "PIA" (phase identification analysis), was applied for identification of small crystalline particles of micrometer and submicrometer size (Small and Michael, 2001). Several commercial systems are now available for dedicated phase identification by EBSD.

A high-sensitivity EBSD camera is used for dedicated phase identification work (Goehner and Michael, 1996), although for phase identification as a precursor to microtexture determination, the standard EBSD camera is used. The principle of phase identification by EBSD is that the full crystal symmetry of the specimen is embodied in the symmetry of the diffraction patterns (Wilkinson and Hirsch, 1997). If an experimentally acquired, unknown EBSD pattern is indexed using the correct phase match, a consistent and accurate match will be achieved with all parts of the pattern simulation of the phase match candidate. Phase match candidates are selected from compiled or existing external crystallographic databases. Chemical composition analysis of the phase by energy-dispersive spectroscopy (EDS) is used as a filter in selection of candidate phases.

The EDS and EBSD analyses can be performed as two separate steps. For example, very small intergranular Bi-In phases have been identified in Zn powders (Perez et al., 2006), and calcium compounds have been identified in aluminum alloys (Zaldívar-Cadena and Flores-Valdés, 2007). A recent advance is the integration of both these steps into a single interface such that chemical and crystallographic data are acquired simultaneously (Nowell and Wright, 2004; Dingley, 2004). This requires conjoint data collection from a highly tilted specimen (for EBSD), no shadowing from either the EDS detector or the EBSD camera, and rationalization of the different dwell times to acquire EDS and EBSD data. The dedicated phase identification package compares automatically collected diffraction patterns from an unknown phase with simulated patterns from reference phases, using chemical composition from the EDS spectra to filter

out impossible solutions. Links to a number of external databases, such as the International Center for Diffraction Data (ICDD), are used to find the candidate reference phases and then to simulate diffraction patterns from the crystallographic parameters, including full structure factor calculations. Often such databases were originally compiled for x-ray diffraction, and conversions are applied for electron diffraction. Phases from all seven crystal systems can be identified by the combined method. For example, complex phase compositions in the Cr–Si–Nb system have been identified, including orthorhombic $(\text{Cr},\text{Nb})_{11}\text{Si}_8$ and orthorhombic $(\text{Cr},\text{Nb})_6\text{Si}_5$ (<http://www.oxinst.com>, 2008). Orientation mapping from multiphase materials is discussed briefly in Section 10.4.5.

7.6.5 Resolution and Operational Parameters

Resolution, with regard to EBSD, can refer either to *spatial resolution* on the specimen or to *angular resolution*, that is, the orientation measurement accuracy. The *angular resolution* or *accuracy* of EBSD relates directly to the precision with which the diffraction pattern can be indexed, which in turn is influenced by the calibration of the system (Section 7.7), the effectiveness of the software solve routine (Section 6.3), the pattern quality (Section 6.4), and the magnification of the diffraction pattern as determined by the camera position. The accuracy is usually determined by measuring the misorientation between adjacent sampling points in a single crystal. Note that this gives the inherent accuracy of the measurement technique, and does not take account of the relationship between the orientation of the diffraction pattern and the specimen axes, which introduces a greater error than the inherent measurement accuracy. The accuracy for orientation measurement by EBSD has been found experimentally to be approximately 0.5° – 1.0° , and better for the best case in FEGSEM (El-Dasher et al., 2003). This precision applies for patterns of optimum quality and will reduce significantly for poor-quality patterns.

The fundamental factor that governs the theoretical *spatial resolution* of EBSD, and indeed of SEM in general, is the interaction volume of the electron beam in the specimen. The effective spatial resolution is larger than the theoretical spatial resolution (see the following text). Because of the very thin surface layer from which the EBSD pattern originates, the interaction volume approximates to the area of the incident beam, that is, the spot size. The large angle of specimen tilt means that the interaction volume is anisotropic (Figure 7.4); therefore, the interaction volume is often quoted as the product of the resolution parallel and perpendicular to the tilt axis, or an average of these two values. The spatial resolution of EBSD is influenced by

- Microscope parameters
- Material
- Specimen/microscope geometry

- Accelerating voltage
- Probe current
- Pattern clarity

7.6.5.1 Microscope Parameters

The type of SEM has a major effect on the interaction volume and hence on the spatial resolution: An FEGSEM is capable of some threefold improvement in spatial resolution compared to a tungsten-filament SEM, with a LaB₆ SEM performance in between the two. A recent advance in EBSD has been that better spatial resolutions are obtainable: first due to the use of an FEGSEM rather than a conventional SEM, and second due to improvements in camera technology as described in Section 7.6.1. There are several investigation types for which this improved resolution is an advantage, including deformed materials, nanocrystals, and measurements close to grain boundaries. The move to the use of FEGSEM has therefore extended the range of EBSD applications, especially into areas that were traditionally the province of TEM. For example, the size of the structure elements in severely deformed copper has been determined and found to be larger than those determined by TEM (Dobatkin et al., 2007).

7.6.5.2 Material

The amount of backscattered signal increases with atomic number; hence, often there is more detail and greater clarity in patterns from high-atomic-number elements than from those with low atomic numbers.

7.6.5.3 Specimen/Microscope Geometry

The three main parameters that can be altered in the microscope/EBSD setup are the specimen-to-screen distance, the specimen tilt, and the specimen height (working distance) in the microscope. Values for all these parameters are necessary to calibrate the system (Section 7.7) and hence to index the diffraction pattern (Section 6.3). Often for EBSD data collection, the *specimen-to-screen distance* remains fixed. With regard to *specimen tilt*, EBSD patterns have been observed for specimen tilt angles $>45^\circ$. However, as mentioned in Section 7.1, the path length of the backscattered electrons in the specimen decreases with increased specimen tilt, which leads to better contrast in the EBSD pattern with increased tilt angle (Venables and Harland, 1973). Tilt angles $>80^\circ$ are impracticable because of the excessive anisotropy of the sampled volume and distortion in the uncorrected image. A tilt angle of 70° is obligatory for one calibration routine (Section 7.7), and since this value represents a good compromise with regard to convenience and pattern contrast, it is used as a standard angle for EBSD. For a flat specimen, the

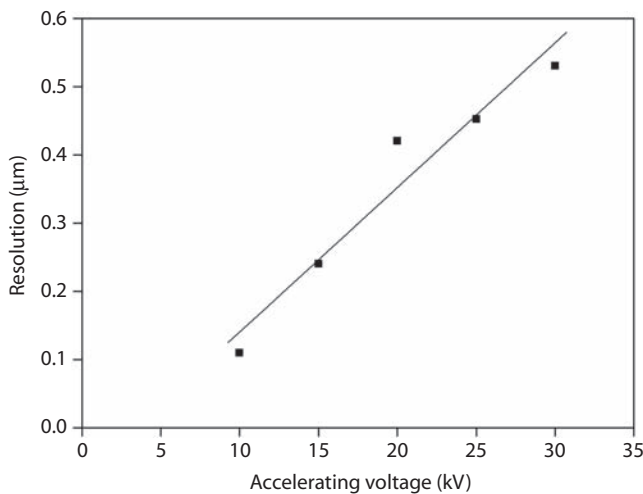
sampled volume would project as a circle on the surface of the specimen, but for EBSD, the high specimen tilt angle distorts this shape into an ellipse having an aspect ratio of $\tan 70^\circ : 1$ (3:1). In other words, the probe area on the specimen surface is three times smaller parallel to the tilt axis than when it is perpendicular to it.

Although for standard SEM work best resolution and minimized focusing distortions are obtained from a short *working distance*, for EBSD the major consideration when choosing the working distance is to position the specimen so that electrons are backscattered from the specimen toward the camera. Often a limiting factor is also the risk of collision with microscope hardware, particularly the pole piece, at small working distances. The optimum specimen position will depend, therefore, on the geometry of the microscope. It is also convenient, if possible, to choose a working distance that locates the pattern center near the center of the phosphor screen. Taking all these factors into consideration, an optimum working distance is often in the range 15–25 mm. Some calibration routines or eucentric sample stages dictate a fixed working distance.

7.6.5.4 Accelerating Voltage

There is a linear relationship between accelerating voltage and interaction volume for a specific element. Hence a low accelerating voltage is chosen if good spatial resolution is required. Since the size of the interaction volume also correlates with the atomic number of the element, in general a higher accelerating voltage can be chosen for high-atomic-number specimens. Figure 7.11 shows the relationship between accelerating voltage and average lateral spatial resolution in nickel as determined in a standard tungsten-filament SEM (Drake and Vale, 1995). It is clear that where good resolution is required, for example, for fine-grained or deformed material, significant improvements in resolution are attained by reducing the accelerating voltage.

In addition to resolution, several other factors should be considered when selecting an accelerating voltage for a particular inquiry. There are advantages of using a high accelerating voltage (30–40 kV). The efficiency of the phosphor screen increases with electron energy (i.e., higher accelerating voltage), which results in a brighter diffraction pattern. Moreover, there is less interference from stray electromagnetic fields. Finally, the electron beam penetrates further and, thus, the diffraction pattern originates from a region below the surface such that surface contamination or surface damage effects are minimized (Drake and Vale, 1995; Schwarzer et al., 1996b). The disadvantages of using a high accelerating voltage are that the beam–specimen interaction volume increases, thus strongly reducing spatial resolution, and specimens that are poor conductors or susceptible to beam damage cannot be examined, unless the specimen is lightly coated with a conductor (Section 7.5).

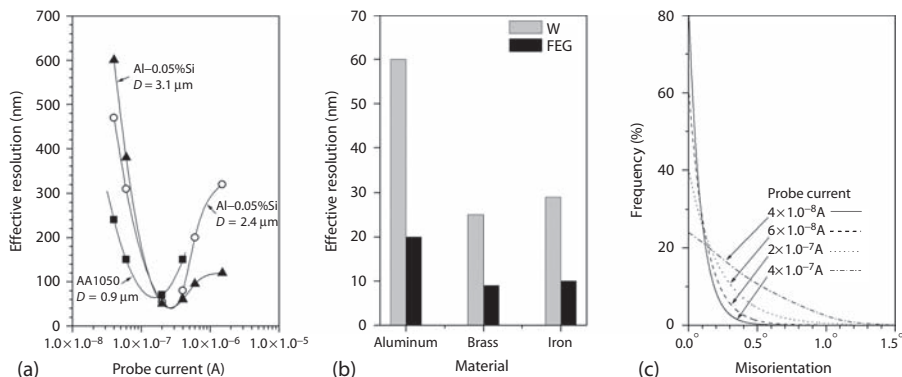
**FIGURE 7.11**

Spatial resolution of EBSD in nickel as a function of accelerating voltage. (Adapted from Drake, A. and Vale, S.H., *Inst. Phys. Conf. Ser.* 147, 137, Inst. Phys. Pub. Inc., Bristol, 1995.)

A change in accelerating voltage changes the electron wavelength, which in turn changes the spacing of the Kikuchi bands according to Bragg's law (Equation 3.4). This effect can be seen in Figure 7.8 where the accelerating voltage is varied from 10 to 40 kV. However, neither the interplanar nor inter-zonal angles are affected, and so the principles of orientation measurement (Section 6.3) are independent of accelerating voltage.

7.6.5.5 Probe Current

The probe current is selected in accordance with the light sensitivity of the camera and the requirement of imaging the specimen surface. A typical probe current used is 0.1 nA. The spatial resolution is less sensitive to probe current than to accelerating voltage, but if it is convenient to work at a particular accelerating voltage, then the probe current can be used to manipulate the resolution. Although the best theoretical resolution corresponds to the smallest interaction volume, small interaction volumes affect adversely the pattern clarity and hence the ability of the software to locate the Kikuchi lines and index the pattern. However, if the probe is too large, more than one diffraction pattern may be sampled concurrently. Hence the best working resolution is not achieved with the smallest probe size, as illustrated in Figure 7.12a (Humphreys et al., 1999; Humphreys, 2004). There are minima in the curves relating effective spatial resolution to probe current, indicating that there is a compromise situation between interaction volume and acceptable pattern clarity. The number of frames over which the diffraction pattern is averaged increases the quality of the diffraction pattern, and hence improves the effective resolution, albeit with a time penalty (Section 7.6.6).

**FIGURE 7.12**

(a) The effect of probe current on effective resolution for several aluminum specimens. The minima in the plots are caused by the reduced pattern-solving accuracy at low probe currents. (From Humphreys, F. J. et al., *J. Microsc.*, 195, 212, 1999.) (b) Effective EBSD spatial resolution for various metals in tungsten filament and FEG SEMs. (From Humphreys, F.J., *Scripta Mater.*, 51, 771, 2004.) (c) Misorientation measurements between adjacent points on a single-crystal silicon specimen for four different probe currents (in amperes). The highest-probe current provides the most accurate result. (Courtesy of F. J. Humphreys.)

The best resolutions are obtained with an FEGSEM rather than with a conventional tungsten-filament SEM due to the small size of the electron beam. Resolution in the FEGSEM is much less sensitive to probe current than that in a tungsten-filament SEM. Figure 7.12b shows effective resolutions for aluminum, brass, and iron in both a tungsten-filament SEM and an FEGSEM. Although in a tungsten SEM, the accelerating voltage is typically 20 kV, the latest FEGSEMs provide sufficient beam current at typically 5–10 kV, hence allowing further gains in resolution.

7.6.5.6 Pattern Clarity

Pattern clarity is influenced by the innate quality of the pattern arising from the sampled volume of specimen, itself caused by the presence of lattice defects (Section 6.4). Clarity is also influenced by “noise” introduced during pattern capture and processing. Degradation of this type will result when the pattern is averaged over too few frames or digitized to too few points, or when the backscattered electron signal is reduced. Since the backscattered signal is proportional to the atomic number, higher-atomic-number materials give inherently clearer patterns than their low-atomic-number counterparts. Use of large probe currents increase significantly the amount of backscattered signal generated, as shown in Figure 7.12a, because of the larger sample volume entailed, thus improving the pattern quality. This effect is further illustrated and quantified in Figure 7.12c for single-crystal silicon. For the largest probe current used, 87% of the misorientations measured to assess

the accuracy were $<0.1^\circ$, whereas for the smallest probe current only 20% were $<0.1^\circ$ (although they were virtually all $<1^\circ$, the quoted accuracy for EBSD) (Humphreys et al., 1999).

The clarity of the diffraction pattern affects the precision with which Kikuchi lines can be located by the pattern-solving algorithm, which in turn degrades the accuracy of the measurement. There are also hardware considerations that affect the clarity of the pattern and hence the accuracy of EBSD measurements. A more highly magnified pattern will result in increased accuracy in the location of the Kikuchi lines, provided enough of the pattern is visible to facilitate unambiguous indexing. This option is achieved by withdrawing the camera as discussed in Section 7.6.1. Alternatively, a high-clarity pattern is achieved by capturing it on photographic film in the microscope chamber (Dingley et al., 1994) using slow-scan CCD cameras (Michael and Goehner, 1994) or, with a standard EBSD setup, using long processing times. Although any of these options could be used for special circumstances where optimum accuracy is paramount, they are not suitable for routine microtexture applications where a balance must be maintained among speed, convenience, and accuracy.

In summary, the best spatial resolution for a material such as brass is 25–50 nm for a tungsten-filament SEM and 9–22 nm for an FEGSEM, both measured parallel to the tilt axis (Harland et al., 1981; Dingley, 2000; Humphreys, 2001). A spatial resolution of 6–9 nm in a nickel superalloy has been quoted (Dingley, 2004). The depth resolution has been quoted as approximately 40 nm for silicon and 10 nm for nickel (Harland et al., 1981; Dingley, 2004; Borbely et al., 2008). It has further been reported that for 15 kV SEM accelerating voltage in iron, half the electrons emerge from a depth of 2 nm (Zaefferer, 2007).

7.6.6 Diffraction Pattern Enhancement

The real-time or “raw” diffraction pattern—obtained straight from the specimen—is typically rather noisy, blemished, uneven, blurred, or dim. Lack of sharpness can be caused by material properties (e.g., lattice strain; see Section 6.4) or experimentally induced artifacts formed mainly by inappropriate specimen preparation, with some contribution from electron energy spread in the phosphor screen (Day, 2008). All EBSD systems include forms of diffraction pattern enhancement to improve the quality and so facilitate indexing on the processed pattern.

The diffuse background, plus minor screen blemishes, is stripped from a pattern by employing a *background correction* routine. This routine involves obtaining an image of the background intensity on the phosphor by integrating over the patterns obtained from a number of differently oriented grains such that the various patterns “cancel out.” In a typical as-deformed or finely recrystallized microstructure, this can readily be accomplished by switching from spot to image mode—if necessary at a lower magnification

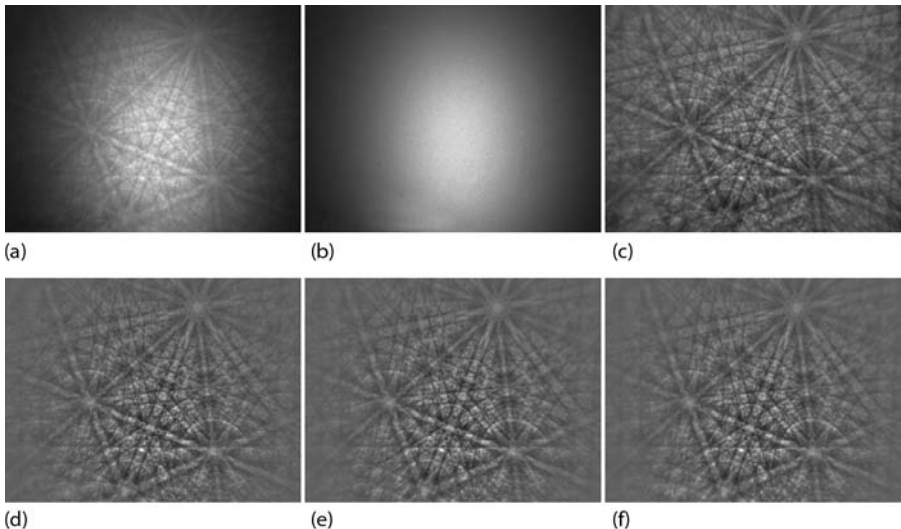


FIGURE 7.13

Example of EBSD image processing. (a) A raw EBSD pattern from tungsten carbide. (b) The EBSD pattern background signal. (c) The corrected EBSD pattern produced by dividing the raw pattern by the background and then adjusting the brightness and contrast of the resulting image to fit the available gray-level range. (d) Pattern after single frame averaging. (e) Pattern after frame averaging over three frames. (f) Pattern after frame averaging over 20 frames. (Courtesy of K. Mingard and A. Day.)

on the specimen—so that the orientations of a multitude of grains contribute to the background image. If the number of grains is too small to yield a uniform background, especially in single-crystal materials, a background can be obtained either by defocusing the objective lens extensively or by rotating the sample during background acquisition. The background image is then electronically subtracted from the diffraction pattern. Alternatively, the diffraction pattern can also be divided by the background image, which results in a better correction of shading differences of the processed pattern. A new image of the background intensity is collected every time a new specimen is placed into the microscope, or when the operating conditions are changed.

Figure 7.13 illustrates the improvement in diffraction pattern quality, which can be obtained compared to the raw pattern. Figure 7.13a shows a raw EBSD pattern from tungsten carbide. Dark corners, poor contrast, and CCD/phosphor flaws are apparent. The background signal from the diffraction pattern, formed by rapidly scanning many different orientations, is shown in Figure 7.13b. The corrected EBSD pattern produced by dividing the raw pattern by the background and then adjusting the brightness and contrast of the resulting image to fit the available gray-level range is shown in Figure 7.13c. Furthermore, the diffraction pattern is usually *averaged* over a large number of frames to reduce the amount of noise present. A long averaging time improves the pattern quality but it will noticeably slow down

data acquisition. Frame averaging is illustrated in Figures 7.13d through 7.13f, showing averaging over 1 frame, 3 frames, and 20 frames, respectively. The noise in the pattern reduces with increasing frame averaging. Note that the frame-averaged patterns shown in Figures 7.13d through 7.13f have been corrected by subtraction of the background rather than division by it. Comparison with Figure 7.13c shows that background division appreciably improves the Kikuchi band contrast at the periphery of the pattern.

7.7 Calibration of an EBSD System

EBSL calibration involves a transformation between the 2-D distances (given in pixels) in the diffraction pattern and the corresponding 3-D crystallographic angles in the specimen. Careful calibration is most important if accurate orientations are to be measured. Although standard commercial EBSD packages have calibration routines that include step-by-step instructions, it is useful to understand the principles on which the calibration is based, and to have an appreciation of the various methods that can be used to obtain the calibration parameters, both of which are discussed in the following text. The calibration methods, including those that have now become historical, are as follows:

- Shadow casting
- Known crystal orientation
- Pattern magnification
- Iterative pattern fitting

7.7.1 Calibration Principles

The objective of EBSD calibration is to provide a transformation between angles in the diffraction pattern expressed as screen pixels and the same angles in the specimen. Only two parameters are required for this transformation, and both of them can be described in terms of the gnomonic projection (Appendix IV):

- The origin of the gnomonic projection, labeled N in Figure 6.4b and referred to as the pattern center, PC
- The radius of the reference sphere, labeled ON in Figure 6.4b and referred to as the specimen-to-screen distance, Z_{SSD}

The specimen-to-screen distance is the line that connects the PC with the point of incidence of the electron beam on the specimen, known as the

pattern source point, SP (although strictly SP is a volume, not a point, as shown in Figure 7.4). PC , SP , and Z_{SSD} are illustrated in Figure 7.5 (Randle, 2003). It is worth mentioning that although in Figure 7.5 the PC is shown coinciding with the physical center of the EBSD pattern, this is not usually the case in reality for two reasons. First, the y (vertical) coordinate of the PC depends on height of the SP on the specimen, which in turn depends on the height at which the specimen is positioned in the microscope. Second, the x (horizontal) coordinate of the PC depends on the location of the optic axis of the microscope, which for some models is displaced from a central position. (These considerations are not valid for TEM or SAC diffraction patterns, since for these techniques the electron beam is concentric with the PC .)

The orthogonal axes xyz , $X_sY_sZ_s$, and $X_mY_mZ_m$ in Figure 7.5 refer to the reference axes of the diffraction pattern, specimen, and microscope, respectively. Calibration of the system presupposes that X_s and X_m are parallel, which implies selection of a reference direction in the specimen, usually a specimen edge. This in turn may be important for the particular investigation, for example, a cleaved edge, a facet, or a direction of processing. Where X_s does correspond to a significant direction in the specimen, it is clearly important to align it carefully parallel to X_m .

Any alteration in the microscope to the diffraction pattern collection geometry will change the calibration parameters. Possible alterations are as follows:

- The tilt angle of the specimen stage
- The position of the detecting screen/camera
- The position of the specimen (more specifically the SP on the specimen)

In practice, the first two of these do not usually apply because a fixed specimen tilt is chosen to conserve the calibration geometry and, once calibration is completed, the screen/camera assembly remains in a fixed position during data collection. However, the position of the SP on the specimen will move if the focusing controls are used because essentially this operation changes the working distance (objective lens setting). Once the system is calibrated, if refocusing of the image is necessary, it is achieved by changing the height of the specimen using the microscope "Z" stage control; hence, the specimen moves but the SP remains fixed (Dingley et al., 1987).

Another way in which the position of SP can move between calibration and data collection is through beam deflection at very low magnifications (Day, 1994), which may become an issue in orientation microscopy (Section 10.3). At a magnification of $\times 75$, the total beam deflection across the screen is approximately 1 mm in the x -direction and 3 mm in the y -direction if the specimen is tilted to 70° . This means that if sampling points are chosen by moving the beam away from the original SP , large inaccuracies in the PC will result. At higher magnifications ($\times 1000$), the scanning area on the specimen is very small and discrepancies between the SP , as defined in the calibration

routine, and sampled volumes defined by moving the beam become negligible. If it is necessary to work at low magnification, for example, if a specimen has a very large grain size, then the beam position should remain at the calibration position and individual grains should be sampled by translating the specimen. In this way, the coordinates of the *PC* and the value of Z_{SSD} are maintained between calibration and data collection.

On the whole, the accuracy of calibration feeds through to give an error of approximately 0.5° on an orientation measurement relative only to the calibration parameters and not to the external specimen geometry. Where it is necessary to quote an orientation relative to the external specimen geometry, sometimes called the "absolute orientation," the accuracy degrades to approximately 2° because of specimen location errors. Individual EBSD packages may claim slightly different estimated calibration accuracies. An improved calibration accuracy results if Z_{SSD} is increased since the angular resolution is improved (Figure 7.9). The angle subtended by 1 mm on the screen at the *PC* is reduced from approximately 2° to 0.4° by increasing Z_{SSD} from 30 to 140 mm. However, as discussed in Section 7.6.1, this camera configuration is not only usually inconvenient because of the reduction in signal that ensues, but also because the small capture angle of the diffraction pattern may hinder automatic indexing.

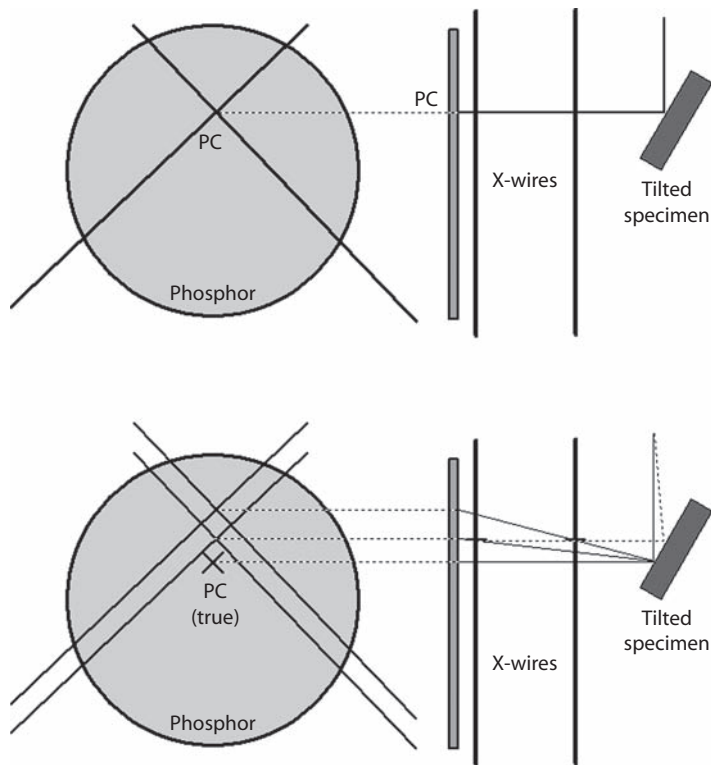
7.7.2 Calibration Procedures

7.7.2.1 Shadow Casting

Objects placed between the specimen and the camera will cast a shadow on the recording screen. If the objects are regular in shape, the shadows cast can be used to find the *PC* and Z_{SSD} . As alluded to in Section 7.4, this was the principle of the first calibration used for EBSD, when the patterns were recorded onto film. Three spheres mounted in front of the specimen cast elliptical shadows onto the screen. The major axes of the ellipses, when extended, intersected at the *PC*. Another shadow-casting method uses a fine square mesh attached to the phosphor screen (Schwarzer et al., 1996b). The shadow images of the mesh are trapezoids having their long axes pointing toward the *PC*.

A variant of the shadow-casting method is to have two shadow-casting objects, one behind the other, between the phosphor screen and the specimen. These can then be lined up in a similar manner to gun sights to define the *PC* and *SP*. Figure 7.14 demonstrates that when the shadows of both sighting wires are superimposed on the image of the diffraction pattern, the *PC* and *SP* are defined (Day, 1994).

The *advantages* of the shadow-casting method are that it is accurate and repeatable, and may offer some protection from collision between the specimen and the screen; the *disadvantages* are that it requires additional, precision-made hardware and, unless the shadow-casting devices can be retracted, it interferes with automatic pattern recognition.

**FIGURE 7.14**

Location of the pattern center, *PC*, on the phosphor screen by alignment of two sets of cross wires located between the specimen and the screen. (Courtesy of A. Day.)

7.7.2.2 Known Crystal Orientation

The “known crystal orientation” method was inaugurated as part of the original computer software that analyzed EBSD patterns online (Dingley et al., 1987). It survived for several years as the main method for EBSD calibration. Essentially a single crystal of silicon, cleaved so as to reveal {001}, was mounted in the microscope and tilted so as to make an angle of 19.5° with respect to the electron beam. This specimen geometry means that the *PC* must lie 19.5° vertically below the specimen normal direction, [001], which is [114]. Hence for a [001] cleaved silicon standard, tilted at 70.5° ($90^\circ - 19.5^\circ$), the *PC* is given by the position of the [114] zone axis. Z_{SSD} is then obtained by measuring the distance in pixels on screen between two zone axes—[011] and [001]—and relating it to the known angle between them, which is 45° in this case, via the following relationship:

$$\cos \phi = \frac{\begin{pmatrix} x_1 - x_{PC} \\ y_1 - y_{PC} \\ Z_{SSD} \end{pmatrix} \cdot \begin{pmatrix} x_2 - x_{PC} \\ y_2 - y_{PC} \\ Z_{SSD} \end{pmatrix}}{\sqrt{(x_1 - x_{PC})^2 + (y_1 - y_{PC})^2 + Z_{SSD}^2} \cdot \sqrt{(x_2 - x_{PC})^2 + (y_2 - y_{PC})^2 + Z_{SSD}^2}} \quad (7.1)$$

where ϕ = angle between the two chosen zone axes, x_1, x_2, y_1, y_2 = coordinates of both chosen zone axes, respectively, x_{PC}, y_{PC} = coordinates of the PC, and Z_{SSD} is then the only unknown in Equation 7.1.

Figure 7.15 shows an EBSD pattern of (001) silicon with the specimen normal direction labeled A and the pattern center labeled B. Note that if the edge of the silicon is cleaved along $\langle 110 \rangle$, and mounted with this edge parallel to the X_m , then the x axis of the system is defined by the $\langle \bar{1}10 \rangle$ direction in the diffraction pattern. In other words, the Kikuchi band (zone) that contains $[114]$ and $[001]$ should be vertical. The fortuitous features of this method are that a specimen tilt angle of approximately 70° is optimal for a compromise between backscattered contrast and tilt of the image and the $[114]$ zone axis is easy to recognize as the PC. The operator is required to input the position of $[114]$ and the location of two identified zone axes plus the angle between them. The specimen must be mounted

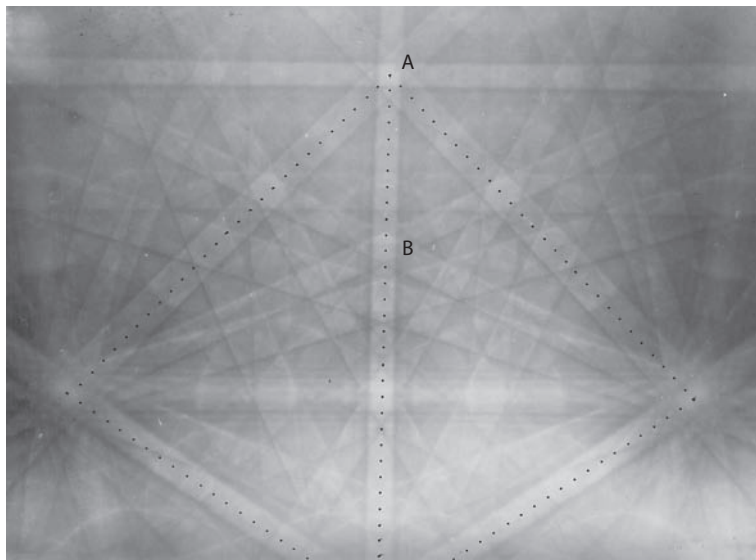


FIGURE 7.15

An EBSD pattern of (001) silicon with the specimen normal direction labeled A and the pattern center labeled B.

with exactly the same geometry as the calibration crystal, and usually this is achieved by mounting them together.

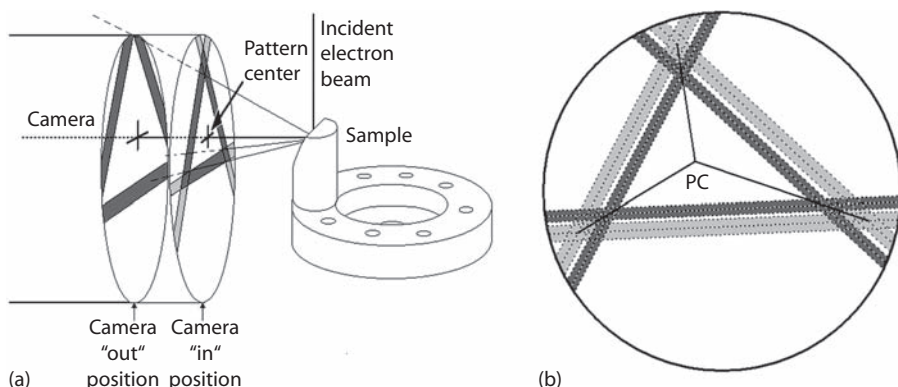
{001} Single-crystal silicon is widely used for the known crystal calibration method since the material is readily available, stores well, and gives clear diffraction patterns. Germanium or gallium arsenide are also used, or lead sulfide that has the additional advantage of exhibiting natural {001} facets. Errors are introduced into the method if the single crystal is not exactly {001}, which is undetectable in the SEM and would necessitate checking by independent means, such as x-ray methods. Since silicon calibration specimens are usually made by mechanical cutting along {001}, which is not a natural cleavage plane in silicon, a slightly misaligned calibration crystal is a real possibility. The other main error that can occur relates to rotation of the calibration crystal, which can be checked from the ratios of [114]:[112], [112]:[111], and [100]:[101] measured in pixels in the diffraction pattern.

The *advantage* of the known orientation method is its simplicity. The main *disadvantages* are that care has to be taken to mount the calibration crystal carefully, and even then there may be “hidden” errors, which are difficult to take into account. Furthermore, some knowledge of crystallography or ability to recognize elements of the diffraction pattern is required.

7.7.2.3 Pattern Magnification

The effect of increasing Z_{SSD} (ON in the gnomonic projection, Figure 6.4b) is to increase the distance of a projected point in the diffraction pattern from the pattern origin or *PC*. In other words, the pattern is more magnified. However, increasing Z_{SSD} and magnifying the pattern does not change the position of the origin of the gnomonic projection, the *PC*. Thus, the *PC* is identified as the only point that does not shift when the diffraction pattern is magnified, and hence “zooming” the pattern offers another method for calibrating the *PC*. Practically, this means that the camera/screen assembly must be capable of retraction to increase Z_{SSD} so that the pattern can be viewed at a minimum of two magnifications, which can be called the “in” and “out” positions. The easiest way to locate the pattern center is to outline three Kikuchi bands that form a triangle in the “in” camera position, and then outline the *same* three bands in the “out” position on the magnified diffraction pattern, as shown in Figure 7.16a. The coordinates of each triangle corner for the “in” and “out” positions lie on a line on which the *PC* also lies. The intersection of the three lines from each triangle corner therefore defines the *PC* (Figure 7.16b; Hjelen et al., 1993).

The specimen-to-screen distance Z_{SSD} is found by the same method as that described earlier—when the camera is in the “in” position ready for data collection, the distance in screen pixels between two known zone axes is measured and the angle between them inputted. The pattern magnification method does not require a standard crystal and can be applied to any well-defined diffraction pattern. However, determination of Z_{SSD} requires

**FIGURE 7.16**

Principle of the “pattern magnification” method of EBSD calibration. (Courtesy of K. Dicks.)

recognition of two zone axes, and it may be convenient to keep a specimen with an easily identified EBSD pattern such as {001} silicon to facilitate this procedure.

The *advantage* of the pattern magnification method is that it requires no special equipment beyond a “stop” to prevent the camera being wound in too far when locating the “in” position. There are no great disadvantages, except that, as for the previous case, some pattern recognition capability is needed to input the parameters to find Z_{SSD} .

7.7.2.4 Iterative Pattern Fitting

Calibration via iterative pattern fitting requires only an EBSD pattern of reasonable quality in which at least three bands or zone axes can be identified. Equation 7.1 can then be formulated $n(n-1)/2$ times, where n is the number of identified zone axes, substituting in the known indices of two of the poles in turn. These equations have to be solved numerically to obtain x_{PC} , y_{PC} , and Z_{SSD} (Schmidt et al., 1991; Krieger Lassen et al., 1992; Krieger Lassen and Bilde-Sørensen, 1993). The numerical method needs a “first guess” for the values of the PC coordinates and Z_{SSD} . If the first guess is reasonably good, less iterations will be required to converge toward the right solution.

Another iterative fitting model uses a comparison between a diffraction pattern from a known material and a simulated pattern. Approximately 10 zones (band centers) are required to be input by the operator, and the method will calculate the rotation of the simulated pattern required to bring it into alignment with the real pattern (Day, 1994). Again, a reasonably good “first guess” is required.

The *advantages* of the iterative pattern fitting method are that the need for any special attachments or standards is eliminated and it is insensitive to the geometry of the setup. Hence it is very suitable for nonstandard

TABLE 7.1

Summary of EBSD Calibration Options

Method	Advantages	Disadvantages
Shadow casting	Accurate and repeatable; some protection against screen collision	Requires precision hardware that interferes with automatic pattern recognition
Known crystal orientation	Simplicity	Errors associated with crystal and mounting; some pattern recognition required
Pattern magnification	No special equipment or standards required	Some pattern recognition required
Iterative pattern fitting	No special equipment or standards required	Requires sophisticated programming and a "first guess" solution

equipment. Moreover, iterative pattern fitting works for any good-quality pattern without operator interaction, which qualifies this method for recalibration during automatic EBSD runs (Section 10.3.1). A *disadvantage* of this method is that it requires sophisticated programming (although this is not really a disadvantage for the user of a commercial package) and a "first guess" solution. However, in most cases unless the experimental setup has been completely changed, the "old" calibration parameters can be used as the first guess.

Table 7.1 summarizes the pertinent features of the calibration routines described earlier. The optimum approach to calibration is to exploit the best features from the different methods and form a combination procedure. For example, most commonly iterative calibration is used to refine the calibration parameters after they have been obtained by other means.

7.8 Operation of an EBSD System and Primary Data Output

Most modern EBSD packages evaluate the diffraction pattern automatically, as described in Section 6.3.3. The parameters that need to be passed to the software are as follows:

- The unit cell dimensions, interplanar angles, crystal system, lattice type, atom types, and positions.
- The calibration parameters as described in Section 7.7. The microscope operating conditions, accelerating voltage and probe current, may be selected during calibration.

- The specimen geometry with respect to the camera—the specimen tilt and rotation angles and the directions of the specimen reference axes.
- The pattern acquisition conditions, that is, suitable background correction conditions.

Patterns are normally solved and stored in a fraction of a second. Sampling points are selected either manually in real time, or by automatically moving the beam or stage (Section 10.3.1). The automatic route samples either at pre-set intervals so as to form a grid of sampling points on the specimen, or by moving the stage/beam to pre-programmed individual coordinates on the specimen. Many EBSD packages offer a numerical assessment indicating the goodness of fit between the experimental pattern and the solution. Examples are a “mean angular deviation” or a “confidence index.”

Once a population of orientations has been evaluated from the diffraction patterns, they can be displayed and output in the following formats (Chapter 9), which are available as standard in most commercially available EBSD packages:

- *Orientation matrices* that can be exported for further mathematical manipulation (Section 2.3.2)
- *Pole figures* that is the most popular display method for EBSD data (Sections 2.5.1 and 9.2)
- *Inverse pole figures* (Sections 2.5.2 and 9.2)
- *Ideal orientation* for each individual orientation, that is, $\{hkl\}\langleuvw\rangle$ (Section 2.4)
- *Euler angles* plotted in Euler space (Sections 2.6, 9.3, and 9.6.1)
- *Rodrigues vectors* for orientations or misorientations plotted in RF space (Sections 2.8, 9.4, and 9.6.3)
- *Misorientation parameters*, which comprise typically the angle/axis of misorientation (Sections 2.7 and 9.5.1) and CSL designations (Section 11.2.1)
- *Crystal orientation maps* and their derivatives such as grain boundary maps and image quality maps (Section 10.4)

The preceding descriptors of orientation and representation methods are described in detail in Chapters 2 and 9. Orientation mapping differs from the other output methods in that it conveys spatial rather than statistical information, which is discussed in detail in Chapter 10. The information contained in the orientation matrix can be further manipulated to determine specific crystallographic directions in the specimen, such as in the analysis of facets, cracks, or interfaces. These topics are discussed in Chapter 11.

7.9 Summation

A commercial EBSD system is designed to be operated with minimal knowledge of the underpinning principles. However this chapter, which has concentrated mainly on EBSD rather than on other less versatile SEM techniques, has aimed to provide sufficient depth of information for an EBSD user to have a basic appreciation of the operating principles of the technique. Procedures for evaluation of the EBSD pattern are described in Chapter 6.

In recent years, the biggest driver in terms of EBSD hardware and software development has been speed of data collection. This is because a major asset of EBSD has always been that data is acquired in large, statistically significant quantities from bulk specimens. This advantage is expedited if these large data sets can be obtained rapidly, allowing cost-effective use of the SEM resource and even more reliable statistics for microtexture determination and other EBSD applications. At the time of writing, the maximum pattern solve rate, on suitable materials, is up to approximately 500 patterns per second.

In parallel with improvements to indexing speed, there have also been progressive improvements in other aspects of data collection, particularly spatial resolution as described in Section 7.6. Figure 7.17 summarizes both these improvements for a range of microdiffraction techniques, including EBSD (Day, 2008). By fitting the data to best-fit lines, it is evident that the spatial resolution is improving by a factor of 2 every 4 years, and the acquisition speed is improving by a factor of 2 every 2 years. These improvements have facilitated extension of the range of EBSD microtexture applications, allowing EBSD to challenge some areas where other techniques, notably TEM and x-rays, have traditionally been used to obtain orientation information. Section 10.4 discusses some examples.

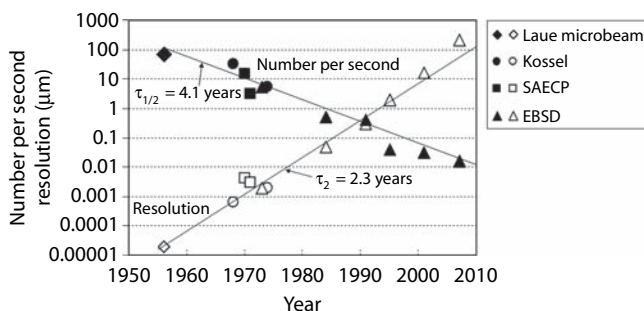


FIGURE 7.17

Improvements in spatial resolution and indexing speed as a function of year for several microdiffraction techniques. (Courtesy of W.B. Hutchinson.)

8

Transmission Electron Microscopy-Based Techniques

8.1 Introduction

Chapter 7 discussed the current techniques to determine local orientations in an SEM. Compared with those methods, in particular EBSD, it turns out that TEM-based techniques can contribute most valuable information in cases where their much higher spatial resolution is a significant factor, such as where the diffraction volume elements are less than approximately 200 nm in size. Furthermore, the TEM yields a wealth of concurrent information on the microstructure of the sample under investigation, such as small precipitates, dislocation substructures, and associated measurements, that cannot be obtained in the SEM.

This chapter gives an overview of the techniques that can be used to determine orientations in a TEM. These techniques are as follows:

- High-resolution electron microscopy (HREM) (Section 8.2)
- Analysis of selected area diffraction (SAD) spot patterns (Section 8.3)
- Microdiffraction and CBED (Section 8.4)

To date HREM is certainly only of peripheral interest for orientation determination, whereas SAD has historically been widely used to analyze orientations in a TEM. Recently, SAD has regained some interest since use of a slightly convergent rather than parallel electron beam leads to an appreciable improvement in spatial resolution (Section 8.3.3). In contrast to other techniques that yield only orientations of individual crystals, SAD also offers the possibility to measure directly pole figures of small volumes in the TEM (Section 8.3.2). However, for the determination of individual orientations, the evaluation of Kikuchi patterns, which are obtained by microdiffraction or, if highest spatial resolution is required, by CBED, is much better suited, as this method combines highest spatial and angular resolutions and is easy to perform (Section 8.4). For details on the principles of electron diffraction, dynamic diffraction theory, and operation of the TEM and also the

scanning-transmission electron microscope (STEM), the reader is referred to standard textbooks: Edington, 1975, 1976; Wenk, 1976; Hirsch et al., 1977; von Heimendahl, 1980; Thomas and Goringe, 1979; Loretto, 1994; Williams and Carter, 1996; Reimer, 1997; Goodhew et al., 2001.

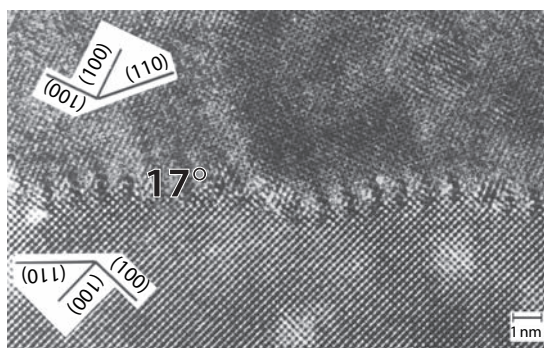
Preparation of specimens for TEM examination involves electropolishing for metallic materials and other procedures such as ion beam milling for nonmetallics. The standard methods used to prepare electron-transparent (i.e., less than approximately 200 nm thick) specimens that are representative of the bulk material are quite exacting, but they are well established and documented in several texts (Goodhew et al., 2001). Almost always the preparation of TEM specimens is more difficult than preparation of the same materials for EBSD analysis in the SEM (Section 7.5).

8.2 High-Resolution Electron Microscopy

A fascinating technique for determination of local orientations in the very smallest volumes is the use of HREM. In this technique, the positions of atoms (more precisely, columns of atoms) are imaged by means of an interference method, which enables one to draw directly conclusions on the crystallographic features. HREM is best suited for determination of misorientations as well as for investigation of grain or phase boundaries. As an example, Figure 8.1 is an HREM image of a $17^\circ/\langle 100 \rangle$ grain boundary in gold, showing subtle details of the grain boundary structure. For routine orientation measurement, however, HREM is not appropriate for the following reasons (Schwarzer, 1989, 1993):

- Handling of the microscope is complicated.
- At present the spatial resolution of TEMs is restricted to ~ 0.15 nm, so that only low-index lattice planes can be imaged and analyzed.
- Sample preparation is very difficult because HREM requires extremely thin samples (~ 20 nm).
- Using such thin samples raises the question of whether the orientations determined are actually representative for the sample volume of interest.
- Interpretation of the results is complicated and requires the use of dedicated software.

In conclusion, although the HREM technique yields impressive images of the atomistic structures, particularly of interfaces, use of this technique for mainstream microtexture purposes is clearly inappropriate.

**FIGURE 8.1**

HREM photograph of a $17^\circ/\langle 100 \rangle$ grain boundary in gold in which the interfacial structure can be resolved. (Courtesy of W. Wunderlich.)

8.3 Selected Area Diffraction

The traditional method for orientation determination in TEM is the use of SAD. However, although electron microscopes have been in use since 1930, only with the appearance of more powerful TEMs with accelerating voltages of 100 kV in about 1950 could thin metal foils be irradiated and their crystallographic orientations analyzed (Hirsch et al., 1977). For texture analysis, this technique was first utilized by Pitsch et al. (1964) and Haefner et al. (1964). Nowadays, as TEMs with microdiffraction facilities become more prevalent, standard SAD has been superseded by the more accurate modern techniques for microtexture analysis described later in this chapter (Sections 8.3.3 and 8.4); nevertheless, the principles of SAD pattern generation are included here for completeness (Section 8.3.1). A complete treatise on SAD, as well as its advantages and disadvantages, can be found elsewhere (Edington, 1975; Duggan and Jones, 1977; Humphreys, 1984; Schwarzer, 1989, 1993).

8.3.1 Selected Area Diffraction Patterns

To utilize diffraction of electrons at the crystal lattice for orientation determination, the volume of interest is irradiated with a parallel electron beam in the TEM. To achieve a high resolution, the transmitted volume must be very thin (of the order of the mean free path of the electrons in the material), so that multiple diffraction effects are avoided. For analysis of small sampled regions, the area of view is reduced by inserting an appropriate aperture in the plane of the first magnified image that has a magnification of typically $\times 25$. Thus, a $50 \mu\text{m}$ aperture will select an area of size $2 \mu\text{m}$ in the sample. The diffraction pattern that appears in the back focal plane of the microscope is then focused onto the main viewing screen or a photographic plate.

**FIGURE 8.2**

SAD pattern of an aluminum crystal with a zone axis near $\langle 110 \rangle$.

Investigation of diffraction from single-crystal volumes yields characteristic patterns that are composed of a regular arrangement of individual diffraction spots, as shown in Figure 8.2, which can be evaluated for orientation determination.

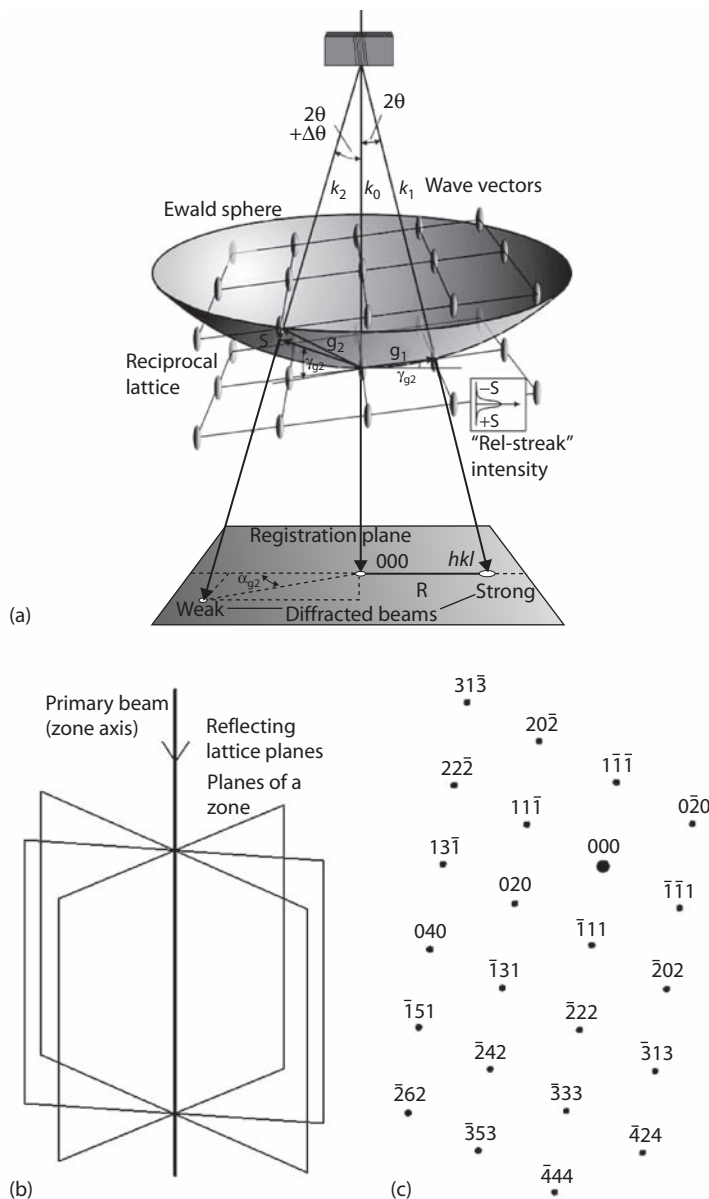
The diffraction spots are formed by coherent elastic scatter of the electrons at the crystal lattice (Figure 8.3a). Because of the very short wavelength of the electron radiation, the diffraction angles between the reflecting lattice planes and the primary beam are very small as well—at the most approximately 2° (Section 3.6.3). This means that all the reflecting planes are situated almost parallel to the primary beam or, in other words, the primary beam is a zone axis of the reflecting planes (Figure 8.3b). Owing to the very small Bragg angles $\sin \theta \approx \theta$, Bragg's law (Equation 3.4) can be written as

$$n\lambda = 2d \sin \theta \approx 2d\theta = \frac{2dR_{hkl}}{2L} \quad (8.1)$$

where L is the distance between sample and photographic plate and R_{hkl} is the distance between primary beam and diffraction spot hkl as shown in Figure 8.3a. With $n = 1$, it follows:

$$\lambda L = R_{hkl} d \text{ or } R_{hkl} = \frac{\lambda L}{d} \quad (8.2)$$

The expression λL that describes the magnification of the diffraction patterns is constant for monochromatic radiation, which is approximately the case in the TEM, and is called the *camera constant*. As an example, for

**FIGURE 8.3**

Schematic diagrams showing the formation of SAD patterns. (a) Formation of diffraction spots. (Courtesy of S. Zaeferer.) (b) Primary beam as a zone axis for several diffracting planes. (c) Indexed diffraction pattern of a [101] zone axis (see Figure 8.2).

a TEM operating at 200 kV (which results in a wavelength $\lambda = 0.00251$ nm; Equation 3.15) and a camera length of 500 mm, the camera constant $\lambda L = 1.255$ mm \times nm.

For a general description of the diffraction effects during SAD, the construction of the *reciprocal lattice* is used. Briefly, the distance between a diffraction spot in the diffraction pattern and the primary beam, that is, the length of the vector R_{hkl} , is inversely proportional to the lattice spacing d (Equation 8.2). R_{hkl} is perpendicular to the reflecting lattice planes, the position of which can be assumed to lie in the origin of the diffraction pattern. These two conditions correspond to the definition of a point in the reciprocal lattice (except for a scaling factor). It follows that each diffraction spot represents the reciprocal lattice point of the corresponding set of lattice planes $\{hkl\}$. Thus, the diffraction patterns can be interpreted as intersections between the points in the reciprocal lattice and the reflection sphere or *Ewald sphere* (Figure 8.3a). As samples that can be transmitted by electrons in the TEM must be very thin, the points in the reciprocal lattice are elongated parallel to the foil normal and get an ellipsoidal shape in reciprocal space. Furthermore, as the radius of the reflection sphere, $1/\lambda$, is approximately two orders of magnitude larger than the inverse lattice constant $1/d$, the plane of intersection with the reflection sphere is almost flat. Thus, the ellipsoids or “spikes” around the points in the reciprocal lattice can intersect with the reflection sphere even when the Bragg condition for diffraction is not exactly met. Therefore, several planes that belong to a given zone axis can contribute simultaneously to the diffraction pattern, as illustrated in Figures 8.3b and 8.3c, whereas under the strict application of Bragg’s law only one individual diffraction spot would be expected. The concept of the reflection sphere and reciprocal lattice is explained in detail in the standard texts listed in Section 8.1.

Unfortunately, the spatial resolution of SAD cannot be improved to any extent just by using a smaller aperture. A reduction of the aperture size causes defocusing and lens errors as a result of which the TEM image formed by the primary beam and the SAD pattern formed by the diffracted beam do not coincide in the image plane (Riecke, 1961; Ryder and Pitsch, 1967, 1968; Edington, 1975). In older TEMs, this displacement error limits the application of SAD to an area of approximately 1 μm . In modern microscopes, lens and defocusing errors are smaller, and in particular the higher accelerating voltages (200 kV and more) result in smaller diffraction angles, so that the displacement error is smaller. Nowadays, the availability of sufficiently small apertures (5–10 μm) limits the spatial resolution to approximately 0.2–0.5 μm (Schwarzer, 1989, 1993; Williams and Carter, 1996).

Indexing SAD patterns, which is often carried out by comparison with known patterns, is a standard TEM technique and is described elsewhere (Edington, 1975). Analysis of more complicated patterns—with overlapping zone axes or of unknown crystal structures—is more difficult, but can be performed with the help of dedicated computer software (Stadelmann, 1987). However, SAD patterns invariably comprise a twofold symmetry, so that an orientation cannot be distinguished from the equivalent one formed by a rotation of 180° around the primary beam. Hence if exact orientation

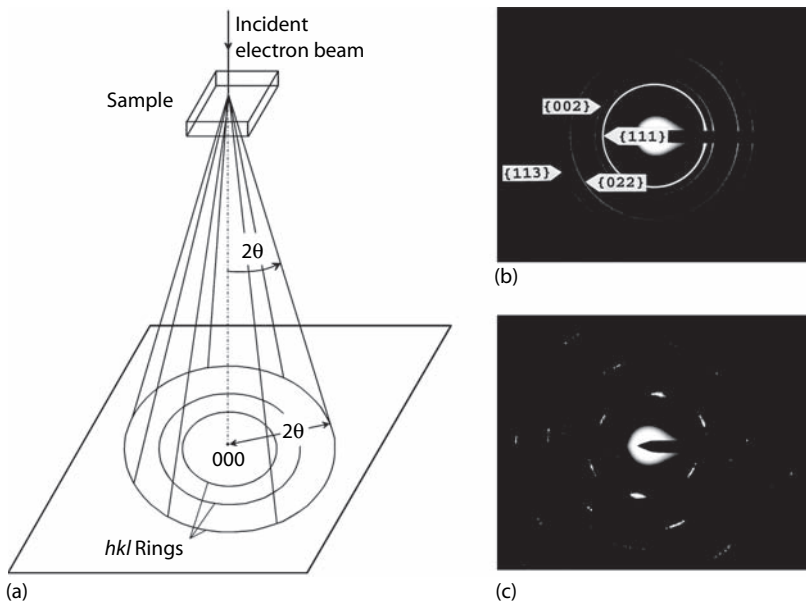
determination is required (e.g., for orientation relations), diffraction spots of more than one zone axis must be analyzed (Ryder and Pitsch, 1967).

Rotations around the direction of the primary beam can be detected very accurately, whereas the diffraction patterns are much less sensitive to rotations around other, nonparallel rotation axes (Laird et al., 1966; Ryder and Pitsch, 1968). This means that the accuracy of orientation determination strongly depends on the given orientation itself, which in turn feeds through as an error for orientation determination by SAD of 5°–10°. This value can substantially be improved to better than 1° by considering the relative intensities of the diffraction spots in addition to their positions in the diffraction patterns (Laird et al., 1966; Zaefferer, 2000, 2002). Analysis of several zone axes also improves the accuracy (Ryder and Pitsch, 1967, 1968). These methods, however, are time-consuming and not well suited for routine applications. Therefore, SAD patterns should not be used for microtexture analysis nowadays, since interpretation of Kikuchi patterns (Sections 6.3 and 8.4) offers analysis of individual orientations with much higher spatial and angular resolutions.

8.3.2 Selected Area Diffraction Pole Figures

When recording diffraction patterns of polycrystalline sample regions with SAD, concentric ring patterns arise that resemble the Debye–Scherrer diagrams obtained from x-ray analysis (Section 3.4). Each of these rings forms by accumulating the hkl reflections from a multitude of differently oriented $\{hkl\}$ planes in the sample, and the ring diameters are related through 40 to the Bragg angle of the corresponding hkl reflection (Figure 8.4a). As an example, Figures 8.4b and 8.4c show the SAD diffraction patterns obtained in two aluminum samples, depending on the texture. Although a random texture yields uniform intensities along the Debye–Scherrer rings (Figure 8.4b), in the case of a pronounced texture—as in the case of a sample deformed by rolling—the intensities are very irregularly distributed (Figure 8.4c). Thus, the intensity distribution along the individual Debye–Scherrer rings is a measure for the alignment of the corresponding lattice planes $\{hkl\}$, which can be exploited for determination of the local texture of the irradiated volume. Such techniques for measuring local pole figures have been developed independently by Schwarzer (1983) and Humphreys (1983). For experimental details, see also Schwarzer and Weiland (1986) and Weiland and Panchanadeeswaran (1993).

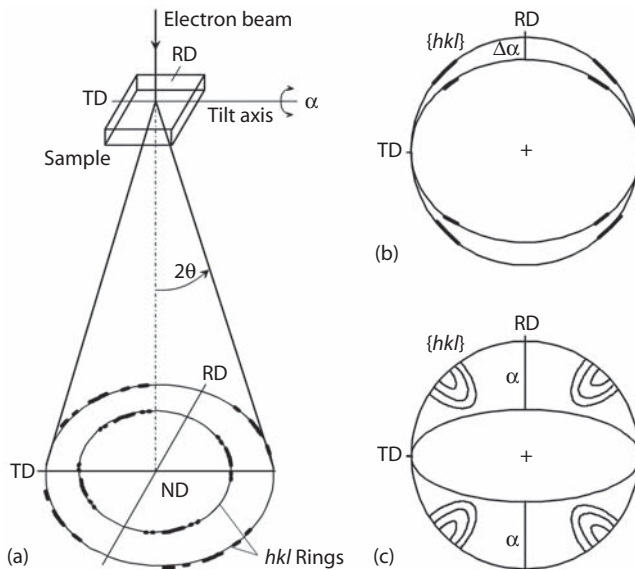
The diffraction rings only reveal the spread of orientations around the incident beam, and hence one diffraction pattern does not comprise the full information on the texture of the sampled volume. Since the Bragg angle of electron diffraction is usually below 1°, under perpendicular irradiation of the sample the reflecting planes are all arranged approximately parallel to the incident beam (see Figure 8.3b), so that the measured points fall on the outer circle ($\alpha=90^\circ$) of the pole figure (Figures 8.5a and 8.5b). To obtain larger

**FIGURE 8.4**

- (a) Schematic illustration of formation of SAD ring patterns in polycrystalline assemblies.
 (b) SAD diffraction pattern of evaporated aluminum with random texture. (c) SAD diffraction pattern of cold-rolled aluminum with strong texture. (Courtesy of H. Weiland.)

coverage of the pole figure, the sample has to be tilted similarly to conventional x-ray texture analysis (Section 4.3). Tilting of the sample through angle $\Delta\alpha$ in both directions around an axis perpendicular to the incident beam allows one to record great circles that are situated in the interior of the pole figure as shown in Figures 8.5b and 8.5c.

To derive the complete orientation distribution, for each pole figure point the intensity along the corresponding Debye–Scherrer ring has to be recorded. For that purpose, the diffraction pattern is deflected by the post-specimen deflection coils on a circle such that the selected Debye–Scherrer ring passes across a suitable detector (a Faraday cage) in the final image plane. Alternatively, the primary beam is deflected along a cone of apex angle 2θ pointing at the sample volume. In that case, the diffracted beam whose intensity has to be recorded is parallel to the optic axis of the microscope, which increases the lateral resolution of the technique. In the latter mode, the reflected intensities along the Debye–Scherrer rings can also be obtained from the current of the dark-field image on the final image screen. With an appropriate computer control of the TEM for sample tilting, scanning of the Debye–Scherrer rings, and intensity recording, it is possible to determine the local pole figures of very small regions of the microstructures. A major drawback of the quantitative evaluation of these SAD pole figures is caused by the fact that the intensity distribution along the Debye–Scherrer

**FIGURE 8.5**

(a) Formation of SAD pole figures in a TEM; (b) and (c) coverage of the pole figure as the angle α is gradually increased.

rings is not directly proportional to the pole density in the pole figures, which requires relatively complicated additional experimental or analytical corrections, including background intensity and an increase in diffracting volume and absorption with increasing sample tilt (Schwarzer, 1983, 1989, 1993; Humphreys, 1984).

With an appropriate computer control, a pole figure scan can typically be performed within about half an hour, and several pole figures can be acquired simultaneously. However, this time may exceed the long-term stability of a TEM. Hence, to reduce the recording time, it has been proposed to record simultaneously several complete hkl rings for a given sample tilt α by using a CCD camera as an area detector (Schwarzer et al., 1996a; Schäfer and Schwarzer, 1998). The diffraction patterns are stored in a computer, and after the scans are finalized, the intensity distributions along the rings can be retrieved either interactively or automatically with the help of suitable image processing algorithms. This parallel recording technique drastically reduces the measuring time to approximately 1 min.

In most TEMs, the tilting angle is limited to a range of 0° to approximately $\pm 60^\circ$, so that only incomplete pole figures with a large nonmeasured "white" region in the pole figure center are obtained (Figure 8.5c). This white region can be reduced by a second scan where the sample is tilted around an axis perpendicular to the first one. To receive complete information about the texture, several incomplete pole figures can be determined and, similarly to

x-ray texture analysis (Section 5.3), from these an ODF is computed (Weiland and Panchanadeeswaran, 1993; Helming and Schwarzer, 1994). If required, complete pole figures can then be recalculated.

The minimum measured volume that can be analyzed by this technique is given by the spatial resolution of the SAD technique; SAD pole figures can be derived from regions of approximately 1 μm in diameter. In practice, however, mostly larger regions of several microns, up to say 20 μm , are chosen to determine local textures of characteristic microstructural regions. Applications include the microtextures in the deformation zones around particles (Humphreys, 1977) or within deformation or shear bands (Schwarzer, 1988).

8.3.3 Small Convergence Beam Electron Diffraction

The spatial resolution of spot pattern analysis can greatly be improved by illuminating the specimen with a slightly focused rather than parallel electron beam. The convergence is achieved by focusing the electron beam in the TEM onto the specimen, and the angle of convergence is controlled by the size of the probe on the sample and the size of the condenser aperture. Since the diffraction pattern arises only from the illuminated volume, the spherical aberration, which results from the aperture selecting only a portion of an illuminated area, does not interfere here. Hence, the spatial resolution is only limited by the spot size of the probe, which can be focused down to a few nanometers (Ralph and Ecob, 1984; Zaefferer, 2000, 2002).

Thus, the electrons enter the specimen under a range of different directions, which is defined by the width of the illumination cone; diffraction occurs within this range of directions. Convergent illumination results in the formation of diffraction disks instead of sharp diffraction spots under parallel illumination, with the diameter of the diffraction disks being proportional to the convergence angle. When the convergence angle of the primary beam is not too large, the disks are still small, however, and comprise uniform intensities as in standard parallel SAD. Accordingly, the Ewald sphere construction can be applied for the orientation determination. This technique is referred to as *microbeam spot diffraction* (MBSD) or *small convergence beam electron diffraction* (SCBED) (Zaefferer, 2000, 2002).

The angular resolution of SCBED is akin to that of standard parallel SAD. SCBED patterns can likewise be affected by the 180° ambiguity. Thus, as described in Section 8.3.1, precise orientation determination mandates consideration of the intensities of the spots in addition to their positions. In SCBED, spot intensities can be determined by integration over the whole disk area. Then, an angular resolution of better than 1° can be achieved. The main advantage of SCBED is that the technique is relatively insensitive to lattice defects, so that orientations in highly deformed materials can be analyzed. An example of the application of this technique is given in Section 10.5.

8.4 Kikuchi Patterns, Microdiffraction, and Convergent Beam Electron Diffraction

When the diffraction effects in a TEM are analyzed in a sample with increasing thickness, one observes that the SAD diffraction spots increasingly attenuate, and instead a system of bright and dark lines, the Kikuchi lines (Kikuchi, 1928), are formed on the main viewing screen (Figure 6.1b). Since similar patterns are also formed in SEM (SAC and EBSD; Chapter 7), the formation principles as well as the crystallographic information embodied in the Kikuchi patterns have already been described generically in Chapter 6. To recap briefly, an electron beam entering a crystalline solid is subject to elastic or diffuse scattering. The *elastic* scattering gives rise to distinct diffraction spots in the back focal plane, which can be utilized for SAD (Section 8.3.1). In case of *diffuse* scattering, the atomic planes of a crystalline specimen are showered by electrons arriving from all directions, and these electrons can then undergo elastic (Bragg) scattering to give a strong, reinforced beam that eventually gives rise to the Kikuchi lines. Thus, the Kikuchi lines are directly linked to the orientation of the reflecting planes in the specimen and, as such, Kikuchi patterns are well suited for crystal orientation determination (von Heimendahl et al., 1964). Figure 8.6 illustrates the great sensitivity of Kikuchi patterns to the crystal orientation by comparing (simulated) SAD and Kikuchi electron diffraction patterns for a 100 zone axis (simulated with program TOCA by Zaefferer, 2002). In Figure 8.6b, the pattern is shown after a slight rotation by 2°. It appears that the Kikuchi lines have shifted significantly, showing the high accuracy of Kikuchi patterns to crystal orientation. The SAD diffraction spots, in contrast, do not change their position and their intensity alters only slightly before falling to zero intensity as the crystal is tilted so that the reflection sphere no longer cuts the corresponding spikes around the reciprocal lattice points (Section 8.3.1). For this reason, the interpretation of Kikuchi patterns is superior to SAD analysis in the determination of the local orientation of small single crystalline regions in TEM.

When Kikuchi patterns are created under parallel irradiation of the sample as in the SAD operation mode, the spatial resolution is limited to approximately 1 μm as discussed for the SAD spot patterns (Section 8.3.1). Furthermore, the angular distribution of electrons, which are eventually scattered elastically according to Bragg's law to form the Kikuchi patterns, is provided by inelastic scattering in the sample material (Section 6.2.1). Accordingly, Kikuchi diagrams are usually observed in thick TEM samples (Figure 8.7a). Although the resulting spatial resolution of ~1 μm may be sufficient to analyze the orientations of individual grains in most metallic samples, such inquiries can be addressed much more easily by EBSD in an SEM. For other applications such as analysis of the orientation, or orientation relationships of small precipitates, or orientation gradients within a grain, finer resolution is required. In particular, for the analysis of deformed samples, the spatial resolution

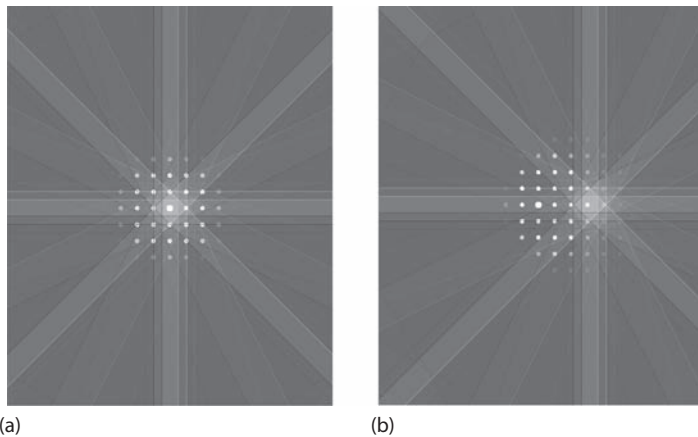


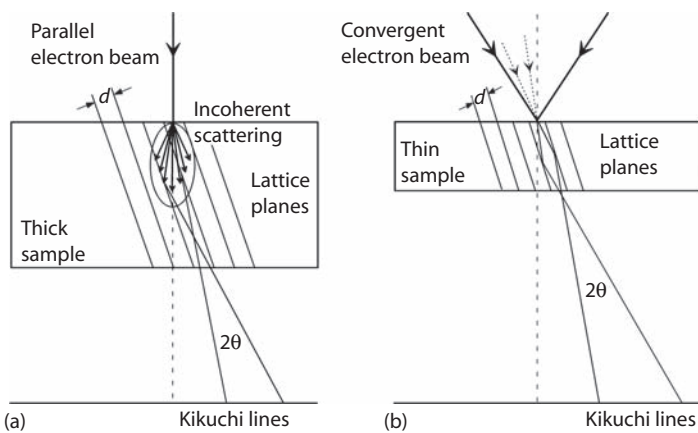
FIGURE 8.6

Simulated diffraction patterns for a [100] axis showing both SAD spots and Kikuchi lines for (a) untilted, that is, exact [100] orientation and (b) 2° tilted orientation. These patterns show that Kikuchi lines have much greater sensitivity to crystal orientation than SAD spots (simulation program TOCA by Zaefferer, 2002).

must be so high that the small undistorted volume elements necessary for formation of Kikuchi patterns can be resolved. To overcome these limitations, several techniques have been developed to achieve Kikuchi patterns of small region of the order of nanometers. These techniques are commonly termed as *microdiffraction* (Warren, 1979; Williams and Carter, 1996) and are briefly summarized in the following text.

Focused aperture microdiffraction uses the same objective lens as that used for scanning-transmission mode (STEM), but it images the sample in the same manner as conventional SAD. For the former, however, a strongly demagnifying upper objective lens allows a small (<10 µm) condenser aperture to be imaged on the sample plane itself, such that only a small portion of the sample is illuminated, and it is this small area alone that forms the diffraction pattern (Riecke, 1962). Thus, the role of spherical aberration, which limits the spatial resolution in SAD, is confined to a slight distortion of the diffraction pattern. This technique permits a quick and effective way to produce microdiffraction patterns from areas down to 50 nm in diameter.

In *rocking beam* microdiffraction, the electron beam is rocked over the sample by the STEM scanning coils (Van Oostrum et al., 1973; Geiss, 1975). The diffraction pattern is created by the varying intensity that falls in the STEM detector at the base of the microscope as the beam changes its angle of incidence to the sample, and is recorded on the STEM display screen. With this technique, diffraction patterns from crystals smaller than 10 nm have been obtained. It should be mentioned that the rocking beam technique can also be utilized to produce transmission channeling patterns (Fujimoto et al., 1972),

**FIGURE 8.7**

Formation of Kikuchi patterns in a TEM for (a) parallel beam, thick sample and (b) convergent beam, thin sample.

similarly as described for the SEM in Section 7.3. In this case, however, the spatial resolution is again controlled by the spherical aberration of the objective lens, that is, it is limited to approximately 1 μm (Warren, 1979).

By far the most widely used technique for producing Kikuchi patterns from small volumes is *focused-beam* microdiffraction. As described in the preceding section, the best spatial and angular resolutions can be obtained not by using parallel irradiation, but by using a slightly convergent beam. The electron beam in the TEM is focused by additional coils or by scanning equipment (STEM) to converge at the region of interest. Hence, the spatial resolution is only limited by the spot size of the probe, which can readily be focused down to a few nanometers (Ralph and Ecob, 1984); even subnanometer analysis is possible (Williams and Carter, 1996). Furthermore, owing to the increased spot intensity, and in particular to the convergence of the incident beam itself, Kikuchi patterns are formed even in very thin sample regions, since the incident electrons hit the lattice planes directly at the Bragg angle (Figure 8.7b). Although in such cases the exact mechanisms of formation of the diffraction patterns are slightly different (see below), they yield the same crystallographic information and, accordingly, they can be interpreted by the same principles as those described in Chapter 6. Thus, under convergent illumination, sharp Kikuchi lines are almost invariably seen in the resulting diffraction patterns (Figure 8.8). Because the very small volume contributing to the diffraction pattern under convergent illumination usually contains little or no strain, even highly deformed materials can be analyzed (Heilmann et al., 1983).

In standard experimental setups, the Kikuchi pattern, recorded on a photographic film, can finally be indexed to determine the crystallographic

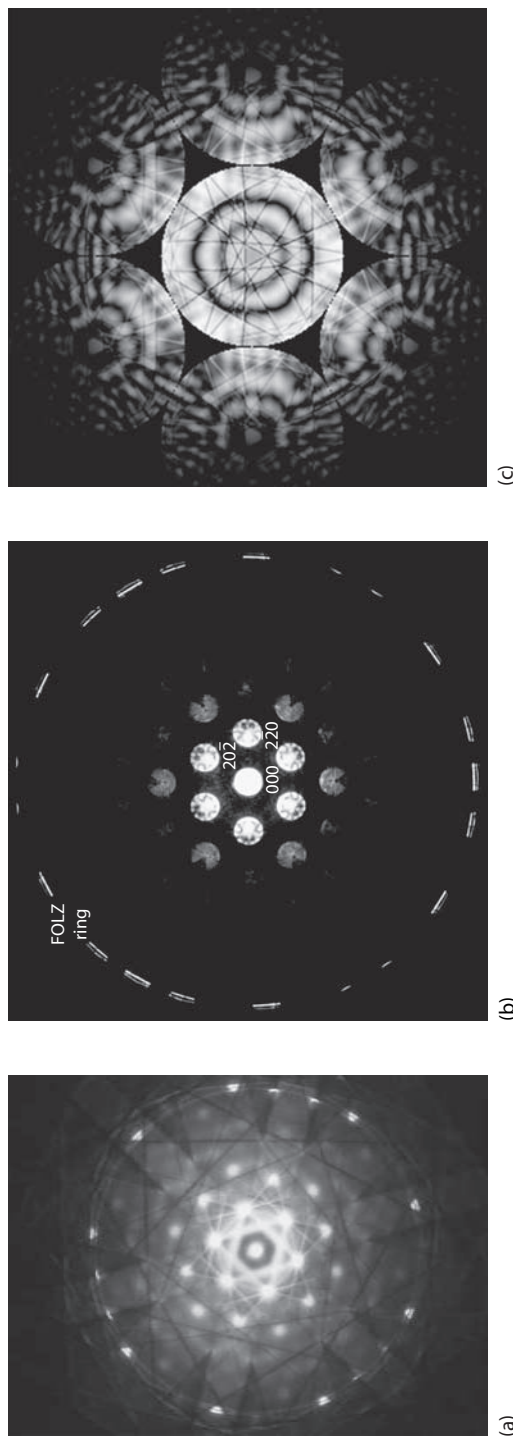


FIGURE 8.8
Microdiffraction patterns from [111]-oriented crystals obtained with increasing convergence of the electron beam. (a) Kikuchi lines and HOLZ lines in the zero-order Laue zone (ZOLZ) (Nimonic PE16). (b) Widened ZOLZ disks with intensity variations plus first-order Laue zone (FOLZ) lines (silicon). (Courtesy of K. Tsuda.) (c) Central diffraction spot with HOLZ lines (simulated). (Courtesy of R. Holmestad.)

orientation of the corresponding crystal. Of course this method is very time-consuming and not suited to online measurements. Rather, similarly as described for the EBSD patterns in Section 7.6.1, for online orientation determination the Kikuchi patterns can be captured with a low-light CCD camera and then transferred through a video grabber card to a computer for storage and orientation determination. The camera can be attached outside the TEM and can record the pattern either from the (tilted) main viewing screen (Høier et al., 1994) or from an additional screen that has to be moved into the electron beam (Zaefferer and Schwarzer, 1994). In another setup, the chip of a Peltier-cooled slow scan CCD camera is inserted into the electron beam slightly above the main viewing screen of the TEM (Krieger Lassen, 1995; Engler et al., 1996a); here the advantage is that the recorded Kikuchi pattern is undistorted. Alternatively, the camera is mounted inside the TEM below the main viewing screen (Weiland and Field, 1994). The subsequent automatic indexing and evaluation of TEM Kikuchi patterns by means of image analysis codes is described in Section 6.3.4.

As described in Section 8.3.3, with increasing convergence of the incident electron beam, the diffracted disks widen, with their diameter being controlled by the convergence angle. This gives rise to the term CBED (Steeds, 1979; Spence and Zuo, 1992; Williams and Carter, 1996), sometimes also referred to as Kossel–Möllenstedt diffraction. Within the disks, additional diffraction features arise, including the high-order Laue zone (HOLZ) lines. Figure 8.8 illustrates the effect of increasing the angle of convergence on the resulting diffraction patterns for the [111] zone axis. Figure 8.8a shows a conventional focused-beam Kikuchi pattern, with Kikuchi lines and Kikuchi bands in the zero-order Laue zone (ZOLZ). These patterns are enhanced by increasing the beam convergence angle, typically to approximately 0.5°. Figure 8.8b shows an example of a CBED pattern from a [111]-oriented silicon crystal, showing widened ZOLZ diffraction disks with some intensity variations plus the first-order Laue zone (FOLZ) ring (Ogata et al., 2008). Kikuchi bands are easily visible. Finally, Figure 8.8c shows the central diffraction disk from a simulated CBED pattern in [111] orientation with sharp HOLZ lines. If the convergence angle is further increased, the individual disks overlap and the individual diffraction maxima can no longer be discerned. For these patterns the term Kossel patterns is sometimes used, although this must not be confused with the Kossel x-ray patterns described in Section 7.2.

Although CBED is not directly used for microtexture measurements, it provides a wealth of allied microstructural and crystallographic information, including specimen thickness (Allen and Hall, 1982), unit cell and precise lattice parameters (Ayer, 1989; Randle et al., 1989), symmetry changes (Ecob et al., 1981), and point group/space group (Steeds, 1979; Tanaka et al., 1983; Steeds and Vincent, 1983), as well as information on lattice defects (dislocations, stacking faults, etc.).

8.5 Summation

This chapter has described the techniques to determine local orientations in a TEM. The main *advantages* of TEM-based microtexture techniques are as follows:

- Excellent spatial resolution, down to the subnanometer range
- Fine detail in the Kikuchi pattern, which facilitates analysis from complex crystal structures
- Wealth of additional microstructural and crystallographic information available, for example, on precipitates or dislocations
- No requirement for complex calibration routines

The main *disadvantages* of TEM-based microtexture techniques are as follows:

- Demanding and laborious specimen preparation
- Very small area of view in a single specimen, and therefore low statistics
- Difficulty in relating viewing area to the macroscopic specimen geometry
- Less potential for automation (Section 6.3.4) and orientation microscopy (Section 10.5)

It is fortuitous that microtexture analysis in the TEM has its most important applications in cases where EBSD fails, which include heavily deformed materials, nanocrystals, or complex crystal structures.

Considering the more common techniques for orientation determination in TEM, best results in terms of spatial resolution and accuracy are achieved by the interpretation of Kikuchi patterns obtained by microdiffraction or, if highest spatial resolution is required, by CBED. In contrast, SAD should not nowadays be used for orientation determination, as this technique suffers from much poorer spatial resolution ($\sim 1 \mu\text{m}$) and, particularly, since errors of as much as 5° – 10° may frequently occur. However, SAD is still of great interest as this technique offers the unique possibility to directly measure pole figures of small polycrystalline volumes, such as shear bands or deformation zones.

9

Evaluation and Representation of Microtexture Data

9.1 Introduction

A microtexture is, essentially, a population of individual orientations that can be linked to their location in a specimen and are obtained usually by an electron diffraction technique as described in Chapters 7 and 8. These two factors—the discrete nature of the orientation data and their direct link to the microstructure—introduce a much broader and more complex scenario for data evaluation and representation than that for macrotextures, since in the latter case the orientation data evaluation usually involves only direct representation in the form of pole figures and subsequently calculation of an ODF (Chapter 5). The large variety of situations that can be addressed by means of individual orientation measurements and orientation mapping requires many more formats for the representation and interpretation of the measurements.

The nature of microtexture gives rise to two lines of inquiry: statistical distribution of orientation/misorientation data and orientation/misorientation data related to the microstructure. For most investigations both these analyses are required. Chapter 10 describes orientation mapping in detail, whereas this chapter discusses statistical representation of data. There are also many examples in the literature of investigations that involve both orientation mapping and statistical representation of the entailed data. Such investigations are not catalogued here; rather, the principles of data representation are described.

There are two ways in which orientation and misorientation microtexture data can be displayed in a space: as discrete data points or as a continuous density distribution. For simplicity in the case of the latter we will use the terminology “orientation (or misorientation) distribution function” for *all* continuous distributions, without distinguishing if the function applied involves the series expansion method (as for macrotexture data) or the more simple case of a direct contouring function. This has the advantage of allowing generic terminology to be used for both macrotexture and all

continuous microtexture data. Some texts, however, reserve use of the term “(mis)orientation distribution function” [(M)ODF] in microtexture for series expansion methods only, and refer to direct contouring as a “(mis)orientation distribution.”

This chapter considers data processing for orientations and misorientations separately, since the different physical applications of the measurements in both cases lead to a dichotomy in approach. For example, the angle/axis descriptor (Section 2.7) has direct relevance to misorientations at interfaces, whereas it is inconvenient for orientation descriptions. Hence, Sections 9.2 through 9.4 and 9.5 through 9.7 deal with orientation and misorientation representations, respectively. For further information see Randle (1992, 2003); Gerth and Schwarzer (1993); and Engler et al. (1994a). The representation methods described could be applied to microtexture data generated from EBSD or TEM, although the vast majority of investigations are EBSD and only a few are TEM (Paul et al., 2007).

9.1.1 Statistical Distribution of Orientation and Misorientation Data

For this type of microtexture representation, the chief aim is only to represent and quantify the orientation distribution in a region of interest in the microstructure, either by sampling every orientation present or by statistical sampling throughout a large region of the specimen. If only a single orientation is sampled at each point, then there is no access to misorientation or microstructure information—in fact this is equivalent to an “average” texture, that is, the microtexture counterpart to a macrotexture. Some investigations use a combination of macrotexture and microtexture measurements (Rafaja et al., 2008).

Sometimes, since automated EBSD is very rapid and is able to measure directly the “true” grain orientation, the statistical analysis mode is used advantageously in place of a traditional macrotexture technique to generate a measure of the overall texture. However, it is of prime importance to consider both the *size* and the *distribution* of the sample population to obtain a statistically reliable result. The number of grains encountered may be smaller than the number of grains contributing to x-ray or neutron pole figure measurements, depending on the size of the specimen, the grain size and the mapping speed. Assuming a typical sampling area of $10 \times 10 \text{ mm}^2$ and an average penetration depth of approximately 0.05 mm (Section 4.3), an x-ray macrotexture of a sample with an average grain size of 25 μm represents the orientation information of approximately 300,000 grains. In the case of neutron diffraction, this number is even higher by two orders of magnitude, which is due to the much higher penetration depth in the order of 10 mm (Sections 3.5 and 4.4). In EBSD, despite the large number of orientation data that can nowadays be obtained by fully automated EBSD systems, the number of grains encountered is usually much smaller, which raises the question of the statistical relevance of the data with regard to the description of the

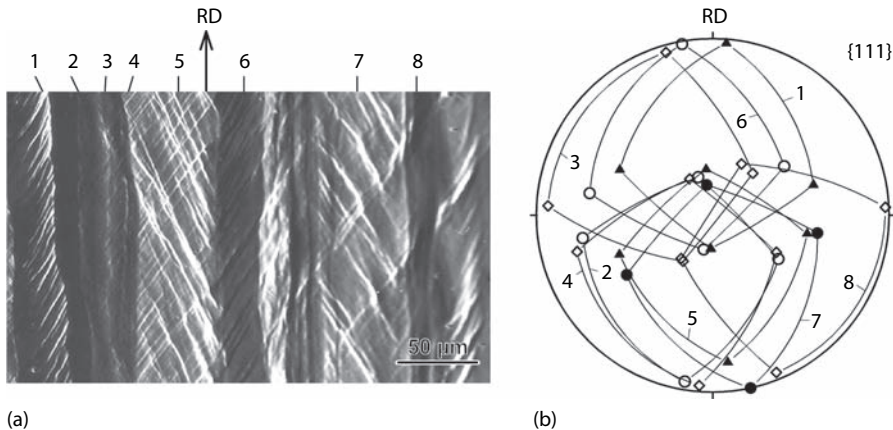
orientation distribution of the volume of interest. The success of using EBSD for overall texture estimation, therefore, depends on the ability to assess how many orientation measurements are required and an appropriate sampling schedule. This is discussed in Section 9.3.3.

Turning now to general evaluation of statistical microtexture data in the form of either orientations or misorientations, it is usual to display first the population using one of the methods described in Chapter 2. Secondary processing steps can then be applied to extract quantified information appropriate to the investigation, for example, what proportion of specified orientations within a certain angular tolerance are present, either by number or by projected grain area (Section 9.2.2). Many of these processing steps are available as part of commercial software packages or, alternatively, the user can design customized options. Some of the representation options are those traditionally used for macrotexture, for example, the pole figure/inverse pole figure (Section 2.5) and Euler space (Section 2.6), whereas other options such as Rodrigues space (Section 2.8) and misorientation evaluation (Section 2.7) derive directly from microtexture data. However, the fundamental differences between data collection for microtexture (Chapters 7, 8, and 10) and macrotexture (Chapters 4 and 5) feed through to necessitate different approaches for data handling in both cases.

Although a “raw” microtexture population comprises discrete individual orientations, which are usually displayed as such, when the number of data points is very large (which is often the case for mapping, Chapter 10) or the texture is very sharp, it becomes inconvenient to display the data—in any space—individually because the representation will soon become unacceptably crowded and lucidity will be lost. Instead the data can be shown as density distribution contours (Sections 9.2.2. and 9.3.2).

9.1.2 Orientation and Misorientation Data Related to the Microstructure

The most valuable aspect of microtexture is the direct link that it provides between orientation and microstructure. Consideration of the statistical orientation distribution of the sampled region(s) (or subsets of them), as described in Section 9.1.1, is usually only part of the total microtexture investigation. Almost always an orientation distribution is derived from an orientation map or a selected subset of the map. Several figures in Chapter 10 depict orientation maps accompanied by statistical microtexture output (Figures 10.3 through 10.9). Sometimes orientation data are accompanied by a manual record of sampling coordinates in the microstructure, and the location of these individual data points is marked on the representation, which is usually a pole figure or inverse pole figure. A similar strategy has traditionally been common practice in TEM. Clearly, this method is only viable for relatively small data subsets. Figures 9.1 and 9.2 depict this strategy, as described in Section 9.2.

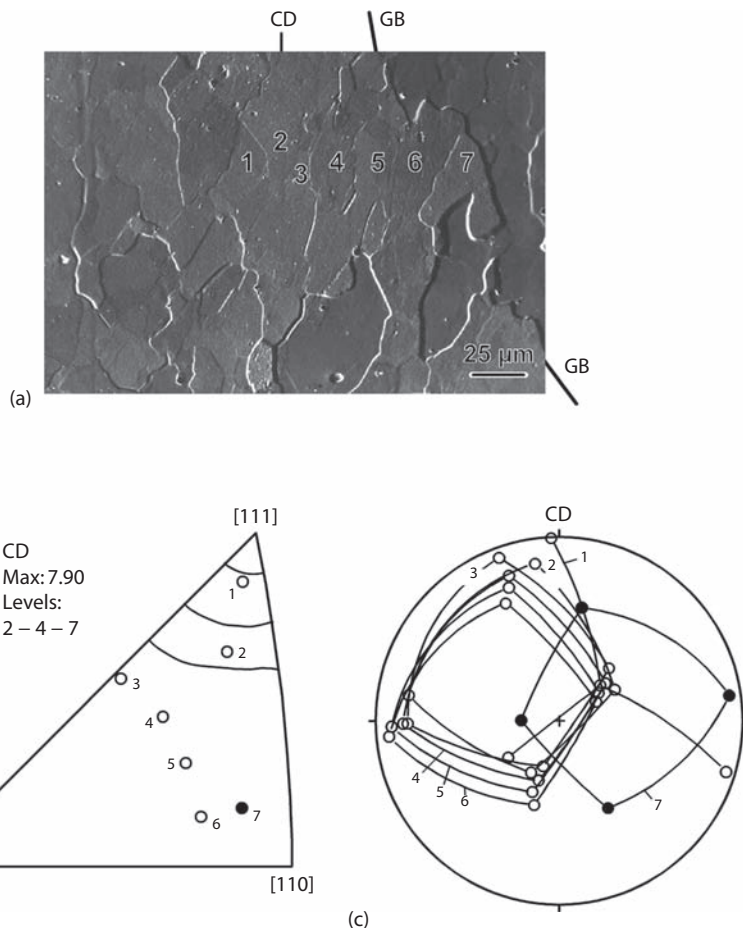
**FIGURE 9.1**

Example of the presentation of microtexture data in a pole figure, showing the influence of the matrix orientation on shear band formation in polycrystalline Al–3%Mg, 90% cold rolled. (a) Microstructure; (b) orientations of (a). Filled symbols—grains with shear bands; open symbols—grains without shear bands.

Another asset of microtexture is the access it provides to interfacial parameters, orientation relationships, and orientation connectivity in the microstructure. This area gives rise to a further range of data processing and representation options (Section 1.2.1). Even though the representation spaces are the same for orientations and misorientations, they are utilized differently in both cases to highlight the required physical features in the data. Chapter 11 discusses further processing of the crystallography of interfaces and also aspects of microtexture that encompass the way in which the orientation components are distributed in space, that is, orientation connectivity.

9.2 Representation of Orientations in a Pole Figure or Inverse Pole Figure

The most obvious method of representing a microtexture is in a pole figure. This is convenient since only a single graphic is required to embody the entire texture information. Local orientation data can be marked in the pole figure (or inverse pole figure) with different symbols or numbers with respect to their location in the microstructure, and the corresponding symbols/numbers are marked on a depiction of the microstructure (Section 9.2.1). This method allows a direct correlation of orientation and site in the

**FIGURE 9.2**

(a) Microstructure of NiAl deformed at 900°C by 70% in compression, showing a coarse sub-grain structure in the vicinity of a grain boundary marked GB. (b) Inverse pole figure of the subgrain orientations shown in (a). The x-ray macrotexture of the sample mainly showed intensities close to [111], as indicated by the iso-intensity lines. EBSD single-grain orientation measurements of subgrains 1–7 close to the GB depict remarkable orientation changes. (c) Pole figure of the subgrain orientations 1–7 showing that the orientations of subgrains 6 and 7 were quite different. (Courtesy of L. Löchte and J. Fischer-Bühner.)

microstructure but, as mentioned in Section 9.1.2, its application is limited to a quite small number of individual points. For the representation of larger numbers of orientations with statistical relevance in a pole figure, a continuous density distribution is superior (Section 9.2.2), though in this case the direct correlation of orientation and site in the microstructure is lost.

9.2.1 Individual Orientations

An example of pole figure/microstructure correspondence for individual orientations is illustrated in Figure 9.1, which shows a micrograph of several deformed grains in a cold-rolled Al–Mg alloy (Figure 9.1a) and an accompanying pole figure (Figure 9.1b), where the orientations of these grains were determined by EBSD. In Figure 9.1b, the orientations are further distinguished whether or not the corresponding grains developed shear bands during deformation. Orientations of grains that developed shear bands during deformation are marked with filled symbols and those of homogeneously deforming grains with open symbols. From this study it has been concluded that shear band formation is restricted to grains with orientations close to the $\{112\}\langle111\rangle$ orientation, whereas grains with other orientations deform homogeneously (Engler et al., 1992).

Inverse pole figures are often used for axial symmetric samples, where only one of the sample axes is defined (Section 2.5.2). For instance, for compression or tensile samples the orientation changes of the compression/tensile axis are plotted in the crystal coordinate system. According to the crystal symmetry, it is not necessary to show the entire inverse pole figure—one stereographic triangle will suffice. In the case of cubic crystal symmetry, the well-known stereographic triangle [100], [110], and [111] is shown. Figure 9.2a shows the compression axis inverse pole figure of the intermetallic compound NiAl that has been deformed at 900°C. EBSD single-grain orientation measurements close to a grain boundary depict remarkable orientation changes as shown from the position of the subgrain orientations 1–6 in the inverse pole figure, whereas the macrotexture of that sample showed a pronounced $\langle111\rangle$ texture. In the inverse pole figure (Figure 9.2b) the two subgrains 6 and 7 on different sites of the high-angle grain boundary are very similar, but note that this does not unequivocally prove that these subgrains actually have the same orientation. This is because the inverse pole figure only shows the orientation of *one* reference axis—here the compression axis CD—but rotations about this axis are not considered. In fact, the full grain orientations of subgrains 6 and 7 were quite different as becomes obvious when plotting the same orientations in a pole figure (Figure 9.2c). Hence, for a complete representation of the 3-D orientation information, two inverse pole figures showing two of the three different reference axes are required. (The third reference axis is redundant because it is defined by a cross product of the first two.)

9.2.2 Density Distributions

Whether to get more quantitative information on the relative density of microtexture data or to relieve a congestion of individual data points, it is beneficial to represent the density distribution from single-grain orientation data as density levels in the pole figure. Then, however, the direct correlation of

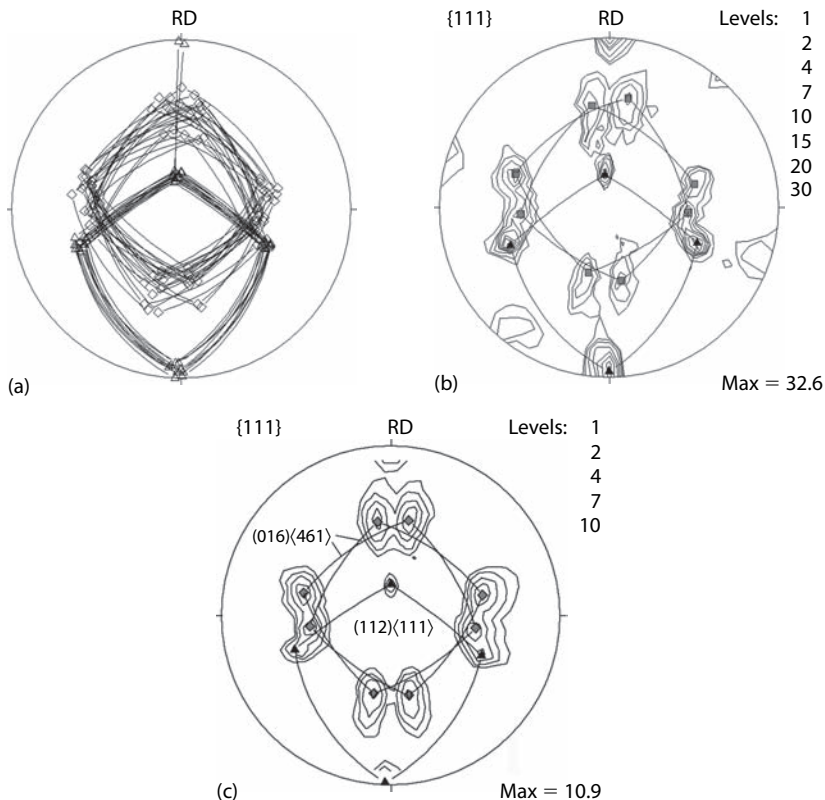
orientation and site is lost. Density distributions resulting from a given set of single orientations can readily be determined by subdividing the pole figure into a grid with distinct angular cells, for example, $\alpha \times \beta = 5^\circ \times 5^\circ$. For each orientation g (where g denotes the rotation matrix between the sample and the crystal coordinate system; Section 2.3.2), the pole figure angles α_i and β_i for each pole $(h_i k_i l_i)$ (e.g., (111) and $(\bar{1}\bar{1}1)$) are given by (Section 2.5.1)

$$\begin{pmatrix} \sin \alpha_i \cos \beta_i \\ \sin \alpha_i \sin \beta_i \\ \cos \alpha_i \end{pmatrix} = g^{-1} \cdot \begin{pmatrix} h_i \\ k_i \\ l_i \end{pmatrix} \quad (9.1)$$

In the case of an inverse pole figure, the inverse orientation matrix g^{-1} in Equation 9.1 is replaced by the orientation matrix g , and the vector $(h_i k_i l_i)$ is replaced by a vector $(X_S Y_S Z_S)$ of the sample coordinate system, for example, $X_S = RD = (100)$, $Y_S = TD = (010)$, $Z_S = ND = (001)$ (Section 2.5.2). If only one inverse pole figure is presented, then this means that just one axis is considered, that is, $i = 1$. The angles α and β now define the position of the orientation g in the inverse pole figure.

After calculation of the angles α_i and β_i , the value of the corresponding cell (α_i, β_i) is incremented by one. Finally, the data are normalized with the total number of orientations N and the number of poles i . The data can then be plotted in a pole figure or inverse pole figure. As an example, Figure 9.3 displays micro- and macrotexture results of a cold-rolled and partially recrystallized aluminum single crystal. Initially, this single crystal had a $\{112\}\langle 111 \rangle$ orientation, which was found to remain stable during deformation by cold rolling. Subsequent recrystallization annealing led to the formation of two symmetrical variants of the orientation $\{016\}\langle 461 \rangle$ (Engler et al., 1993a). In Figure 9.3a, some single-grain orientations, as measured by EBSD in the deformed and the recrystallized regions, are plotted in the stereographic projection. Figure 9.3b shows the density distribution calculated from approximately 500 individual orientations as described earlier. Figure 9.3c presents the x-ray macrotexture of the sample.

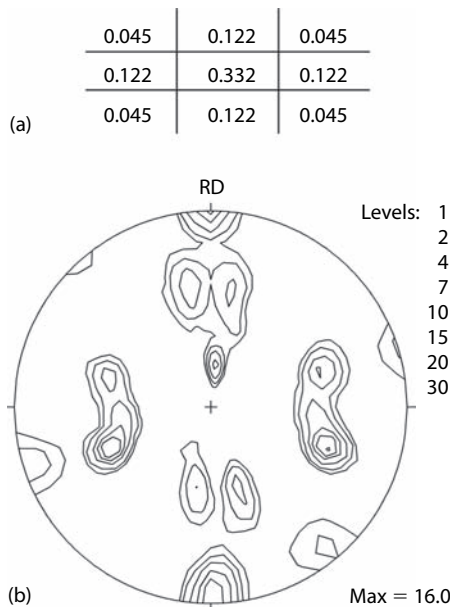
A comparison of microtexture (Figure 9.3b) and macrotexture (Figure 9.3c) shows very good correspondence in the positions of the main peaks. A quantitative comparison of the orientation density, however, is not possible, as already evident from the different heights of the texture maxima (32.6 in Figure 9.3b compared to 10.9 in Figure 9.3c). This difference in intensity distribution is caused by the different measuring procedures applied: x-ray pole figures are *textures by volume* (Bleck and Bunge, 1981), which means that each orientation contributes to the texture according to its volume. By contrast, during the EBSD single-grain orientation measurements, the orientation of large recrystallized grains was measured only once, yielding a *texture by number*. Therefore, in comparison to the x-ray texture the intensity of these large grains is underestimated. Of course, it is entirely possible to measure

**FIGURE 9.3**

Comparison of EBSD microtexture and x-ray macrotexture pole figures of a partially recrystallized Al-1.8%Cu single crystal (rolled to 80% reduction, annealed for 300 s at 300°C). (a) Examples of EBSD single-grain orientation measurements in the as-deformed matrix and the new recrystallized grains; (b) continuous density distribution as computed from approximately 500 orientations similar as in (a); (c) x-ray macrotexture of the same sample.

textures by volume using single-grain orientation measurements, for example, by correction of the data with respect to the corresponding grain size. Similarly, orientation mapping as applied during orientation microscopy (Section 10.3) directly yields textures by volume, as in this case the number of measurements per grain is a measure for the volume or, more precisely, the area of the respective grain.

If the number of orientations is smaller or the orientation scatter is larger than that in the example in Figure 9.3, the pole figures may look rather unsystematic or “spiky.” In that case, it might be appropriate to represent only the discrete data or to smooth the pole figure data by convolution of the intensity data in the pole figures with a suitable filter. Figure 9.4a shows an appropriate 2-D filter with an approximate Gauss-shape. Application of

**FIGURE 9.4**

Smoothing of pole figure data. (a) Two-dimensional filter with approximate Gauss-shape to smooth pole figures; (b) pole figure as derived from pole figure data as in Figure 9.3c but smoothed with the filter in (a).

this filter considers the intensity of the current pole figure position α and β with 33%, the intensities of direct neighboring cells with 12%, and that of second-next neighbors with 4.5%. These values do not change the integral intensity (i.e., the normalization) of the pole figure, but in general they reduce the maximum intensity. Figure 9.4b displays the pole figure of Figure 9.3c after smoothing according to this procedure. Another way to derive continuous pole figure or inverse pole figure plots from single-grain orientation data is to calculate an ODF (Section 9.3.2) and then to recalculate the desired (inverse) pole figure (Section 5.3.2). Provided the series expansion method is applied, the pole figure data are automatically smoothed.

9.3 Representation of Orientations in Euler Space

Since single-grain orientations already contain the entire orientation information in an unequivocal manner, no further information is yielded if a microtexture is plotted in a 3-D space, such as Euler space or Rodrigues space, than if it is plotted in a pole figure. However, representation in a 3-D

orientation space could be advantageous for complex data sets, and also if direct comparison to x-ray macrotexture data, where the ODF in Euler space is the traditional representation method, is required. This is discussed in Sections 9.3.1 and 9.3.2, and in particular direct and indirect methods to derive a continuous ODF from single-grain orientations are compared.

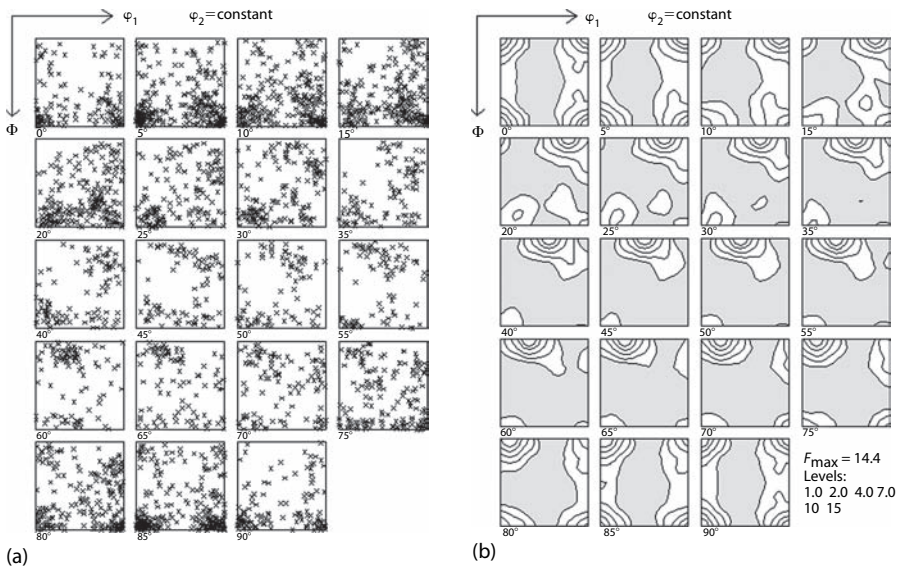
9.3.1 Individual Orientations

As discussed in Section 2.6, a given orientation can be assigned a point with the coordinates $(\varphi_1, \Phi, \varphi_2)$ in the 3-D Euler angle space. Thus, a set of orientations determined by single-grain orientation measurements can be expressed in terms of the Euler angles and, after appropriate reduction with regard to sample and crystal symmetry, displayed as points or with appropriate symbols in the Euler space. Similarly as discussed for the representation of macrotextures (Section 5.4), microtextures are likewise usually represented as a set of 2-D sections along φ_1 or φ_2 through the Euler space. Orientations that do not fall exactly in one of the sections—virtually all orientations—are plotted in the adjacent section. The resulting error can slightly be reduced by projecting the orientations under the condition $\varphi_1 + \varphi_2 = \text{constant}$ (which in this strict form only applies for $\Phi = 0$).

Another problem relates to the fact that usually only a subspace of the full Euler space is used for presentation of orientations. For cubic crystals and orthonormal sample symmetry, this is $0^\circ \leq (\varphi_1, \Phi, \varphi_2) \leq 90^\circ$ (1/32 of the full Euler space) that still does not take the threefold axis of cubic crystal symmetry into account (Section 2.6.2). Hence, each individual orientation has to appear three times in this subspace, but the single-grain orientation measurement of course provides only one variant. The two missing variants can readily be generated by successive $120^\circ\langle111\rangle$ rotations from the original orientation. Figure 9.5a shows an example of the orientations of 1000 grains in a recrystallized aluminum sample plotted in the Euler angle space. The main textural features strongly resemble the macrotexture of the same sample as obtained by x-ray diffraction (Figure 9.5b), though fine details and smaller intensity variations cannot be resolved.

9.3.2 Continuous Distributions

The easiest way to determine a continuous orientation distribution in Euler space from single-grain orientation data is to apply a *direct method* (cell method) similar to that described earlier for the pole figures. As shown in Section 9.3.1, a point in Euler space is obtained for each orientation. If one now subdivides the Euler angle space into small cells of an appropriate size, the number of points in each cell can be counted and a continuous distribution function is derived. This method was first applied by Perlwitz et al. (1969) to single orientations determined by SAD in a TEM.

**FIGURE 9.5**

Presentation in Euler space of microtexture data of a recrystallized aluminum sample. (a) Orientations of 1000 grains as obtained by EBSD; (b) continuous intensity function (ODF) as derived from x-ray pole figure measurements of the same sample, showing good reproducibility of the main texture features.

In the direct methods, the orientations are associated with discrete cells of finite size in the orientation space, so that a direct method provides a discrete ODF. Typically, the Euler angle space is subdivided into cells of size $\Delta\phi_1 = \Delta\Phi = \Delta\phi_2 = 5^\circ$ or 10° . For each individual orientation, g_i , the content of the corresponding cell j with the orientation $g_j - 2.5^\circ < g_i < g_j + 2.5^\circ$ is incremented. Finally, the value of each cell is normalized to the total number of single-grain orientation measurements N and to the cell size Δg_j . If necessary, a filter can be applied to smooth the resulting orientation distribution, as discussed earlier for the pole figures. It is seen that the presentation corresponds to a histogram of orientation densities $\Delta n_j / (N\Delta g_j)$ defined by the number of orientations Δn_j falling into the j th cell and normalized by the number N of measured orientations with regard to the cell size Δg_j .

Although this method appears easy and straightforward, it has several drawbacks. First, the number of measured orientations is often too low for statistical relevance (see Section 9.3.3). As an example, for a cell size of 10° and a statistical reliability of 80%, approximately 25 points per cell must be considered, which for cubic crystals would require approximately 3000 single-grain orientation measurements (Bunge, 1982). Consequently, in the case of a smaller number of orientations the cell size would become very

large, which would result in a falsification of the ODF. Therefore, it may be necessary to use the series expansion method to derive an interpolation function as discussed later in this section.

A second drawback is that in direct methods it is very complicated to take the strong distortion at small angles Φ properly into account, and therefore this is in general not done. This means that an ODF, as derived by means of a direct method from single-grain orientation data, could comprise a strong peak at a given orientation having small Φ , though continuous densities obeying the condition $\varphi_1 + \varphi_2 = \text{constant}$ would be more appropriate.

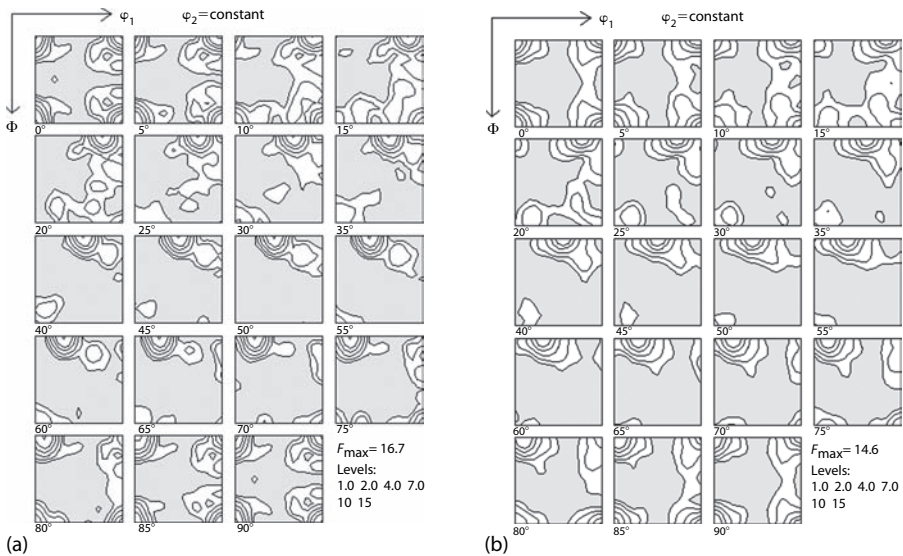
Because of these problems, an *indirect method* might be advantageous (Pospiech and Lücke, 1975; Wagner et al., 1981; Bunge, 1982). Each single-grain orientation g_i is associated with a Gauss-type distribution in Euler angle space with the (half) scatter width ψ_0 . The distribution of the orientation density S as function of the angular distance ψ from the exact orientation can be computed according to

$$S(\psi) = S_0 \cdot \exp\left[-\left(\frac{\psi}{\psi_0}\right)^2\right] \quad (9.2)$$

For single-grain orientation measurements, density S_0 is equal to 1. For a texture consisting of N individual orientations, the ODF can be determined by superposition of the corresponding N Gauss peaks. The main advantage of this method is that it provides an easy computation of the C coefficients of the series expansion method by

$$C_l^{mn} = \frac{1}{N} \cdot \frac{\exp(-l^2\psi_0^2/4) - \exp(-(l+1)^2\psi_0^2/4)}{1 - \exp(-\psi_0^2/4)} \cdot \sum_{i=1}^N T_l^{mn}(g_i) \quad (9.3)$$

With regard to the discussion of the ghost error caused by the lack of odd-order C coefficients in macrotexture experiments (Section 5.3.2), note that Equation 9.3 yields both odd- and even-order C coefficients so that the microtexture approach does not suffer from this error. For a microtexture ODF calculated according to Equation 9.3, each individual orientation i contributes to the final texture with the same weight of $1/N$, that is, it yields a texture by number. To determine textures by volume, the term $1/N$ has to be replaced by a term that takes the volume of each grain into account. The same would also apply for the scatter widths ψ_0 if it turned out that the ψ_0 is different for different orientations or orientation classes, for example, for the as-deformed matrix and recovered subgrains (Engler et al., 1996b). As an example for calculation of an ODF from single-grain orientation data, Figures 9.6a and 9.6b show the ODFs of a recrystallized aluminum sample, which have been derived from 100 and 1000 EBSD measurements, respectively (the latter ODF

**FIGURE 9.6**

ODFs of recrystallized aluminum, as in Figure 9.5, calculated from different numbers N of EBSD single-grain orientation measurements, (a) $N = 100$, (b) $N = 1000$.

corresponds to the individual data shown in Figure 9.5a). In this example $N = 100$ orientations already yield a fairly good qualitative estimate of the corresponding x-ray texture (Figure 9.5b), whereas $N = 1000$ orientations reproduce the macrotexture with high accuracy.

If the C coefficients are available for microtexture ODFs, then parallel calculations to those derived for macrotexture ODF evaluation can be carried out (Bunge, 1982). For example, plots of individual texture component profiles, volume fractions and scatter widths, subordinate functions such as (inverse) pole figures, and, furthermore, mechanical properties and anisotropic behavior can be predicted (Bunge and Esling, 1982; Bunge, 1988; Wenk and Van Houtte, 2004).

An immediate comparison of ODFs as derived from the direct and indirect methods is difficult for the following reasons. In the case of the (discrete) cell method, the intensities depend on the dimension of the cells and are further locally affected by the distortion of the orientation space. In the continuous representation, the density values strongly depend on the chosen scatter width ψ_0 . Moreover, they are locally influenced by the error introduced by the truncation of the series expansion, which is generally the more severe the higher the local concentration of the measured single-grain orientations is.

Both the size of the cells in the discrete presentation and the scatter width in the continuous case cannot be chosen arbitrarily, but they should be

carefully defined in connection with the resolution of the measurement as well as the computation procedure. In the literature, values ranging from 2° to 10° have been proposed, although larger values should be avoided as this would cause undue smearing of the peaks and errors in the textures (Engler et al., 1994a). As a lower limit for both cell size and scatter width, the absolute accuracy of single-grain orientation measurements, for example, 5°, has been proposed (Engler et al., 1994c). Wagner et al. (1981) have discussed that the scatter width ψ_0 of the series expansion method should depend on the maximum series expansion coefficient l_{\max} , which means that for $l_{\max} = 22$ and $l_{\max} = 34$, ψ_0 should not be smaller than 8° and 5°, respectively. However, Hutchinson et al. (1999) have pointed out that there is some instrumental broadening of approximately 3° in x-ray diffraction techniques as well. They recommend only small amounts of smoothing of the same order of magnitude (i.e., 2°–4°), if any, to be applied to EBSD data. In general, the degree of smoothing should decrease with increasing number of measurements.

9.3.3 Statistical Relevance of Single-Grain Orientation Measurements

Despite the relatively large number of orientation data, which can nowadays be obtained by the various techniques for single orientation measurements the number of grains encountered is still small compared to the number of grains contributing to x-ray or neutron pole figure measurements. Even in the case of fully automated EBSD measurements, usually less than 10,000 grains are recorded, which raises the question of the statistical relevance of the data with regard to the description of the orientation distribution of the volume of interest.

The number of single-grain orientation measurements, which is necessary to represent adequately the texture, depends on crystal and sample symmetry and, most of all, on the texture sharpness. Although in the ideal case of a single crystal one measurement is sufficient, for weak textures several thousand individual orientations must be measured. As alluded to earlier, Bunge (1982) stated that for determination of an ODF with statistical relevance (i.e., statistical reliability of 80%) approximately 25 points per cell must be considered. For cubic crystal and orthonormal sample symmetry (i.e., ODF size 90° × 90° × 90°) and a cell size of 5°, this would require approximately 10,000 orientation measurements. In a recent experimental study on rolled stainless steel having a medium strength texture, it has also been stated that of the order of 10,000 grain orientations were needed to provide a texture characterization equivalent to that obtained by x-ray diffraction (Wright et al., 2007). In an analytical study by Jura et al. (1996), it was concluded that for weak textures even several tens of thousands of orientations must be considered. Note that in this discussion the number of single-grain orientation measurements N is to be understood as the number of measured *grains*, whereas modern automated EBSD systems usually record many orientations per grain. This will be discussed at the end of this section.

In the early 1990s, several experimental studies were undertaken to estimate the number of single-grain orientation measurements necessary to achieve the statistics of conventional macrotexture measurement techniques using x-ray diffraction. In these studies the texture of a given sample was determined from 100, 200, 300, ..., N individual orientations and compared with the corresponding x-ray macrotextures (Wright and Adams, 1990; Baudin and Penelle, 1993; Engler et al., 1994c). It turned out that for cubic materials, the ODFs derived from only 100 orientations already comprised the main characteristics of the textures, whereas a statistically sound representation of the textures required 500–1000 orientations.

Because of the strong influence of the texture sharpness on the accuracy of reproducing an ODF from single-grain orientation measurements, it is necessary to develop a quantitative measure for the minimum number of single-grain orientation measurements N_C , which is required to represent adequately the texture of a given sample. Although in all experimental investigations of this problem so far the texture as derived from the single-grain orientation data has been compared with x-ray macrotextures, such a criterion must as well hold for the reproduction of a microtexture of a given part of the microstructure.

As such, Pospiech et al. (1994) proposed to analyze the convergence of the statistical parameter ρ , which represents the relative mean square deviation between two textures. To determine the minimum number of single-grain orientation measurements N_C necessary to reproduce appropriately the corresponding texture, ODFs are computed for an increasing number N of single-grain orientation measurements, for example, in successive steps of 100 orientations. A parameter $\rho_{0,N}$ comparing the intensity values f_N of the ODF as computed from N single-grain orientation data with the values f_0 of a reference ODF, for example, the macrotexture, is then calculated according to

$$\rho_{0,N} = \frac{\oint (f_0 - f_N)^2 dg}{\oint f_0^2 dg} \cdot 100\% \quad (9.4)$$

If the two ODFs, f_0 and f_N , are identical, ρ becomes zero. It is noted that the given definition of the parameter ρ is equivalent to the measure introduced by Van Houtte et al. (2004) to assess texture simulations, namely, the texture index $I(\Delta f)$ of the difference ODF Δf between experimental and modeled texture, divided by the texture index I_{exp} of the former.

Single-grain orientation measurements are used more frequently to determine local microtextures rather than bulk textures, so that no data of a reference texture f_0 may be available. In such cases, a parameter $\rho_{N',N}$ can be calculated from the ODF values $f_{N'}$ and f_N for two consecutive stages of

the single-grain orientation measurement procedure, say for $N' = 300$ and $N = 400$. Equation 9.4 is then modified to

$$\rho_{N',N} = \frac{\oint (f_{N'} - f_N)^2 dg}{\oint f_N^2 dg} \cdot 100\% \quad (9.5)$$

To illustrate the behavior of the statistical parameters ρ with the number of single-grain orientation measurements N , Figure 9.7a displays the evolution of both $\rho_{0,N}$ and $\rho_{N',N}$ for three different samples that are differentiated by their texture sharpness. (i) As an example, for a sharp texture, a heavily cold-rolled copper sheet was recrystallization annealed. The resulting

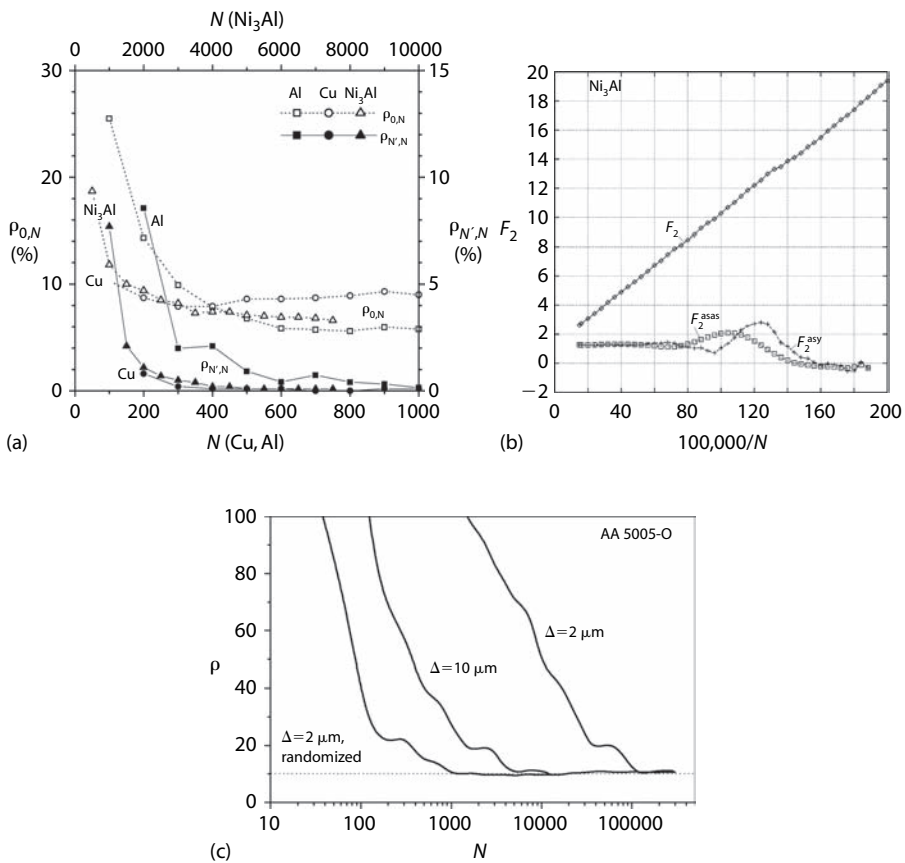


FIGURE 9.7

Statistical assessment of single-grain orientation measurements. Evolution of (a) the statistical parameters $\rho_{0,N}$ and $\rho_{N',N}$ with increasing number of single-grain orientation measurements N for different texture examples, (b) F_2 with $1/N$ for recrystallized Ni_3Al , and (c) $\rho_{0,N}$ with N for different scanning procedures in recrystallized Al-Mg.

texture consisted of a very sharp cube component $\{001\}\langle100\rangle$ with an intensity as high as $f(g) \approx 120$ plus a minor recrystallization twin component. (ii) Medium texture sharpness with $f(g) \approx 15$ was obtained in a recrystallized aluminum alloy. (iii) A sample of recrystallized Ni₃Al revealed a very weak texture with a maximum intensity of only $f(g) \approx 3.5$, corresponding to a random fraction in excess of 85%.

Analysis of the evolution of the preceding statistical parameters illustrates that, for the Al sample, $\rho_{0,N}$ rapidly decreases with N to values of approximately 6%; convergence is reached at approximately 700 single-grain orientations. For the parameter $\rho_{N,N}$, a similar evolution is observed. Thus, it is concluded that an ODF computed with $N_C = 700$ orientations should be representative of the corresponding macrotexture (Figure 9.5b). The very sharp cube-texture of the Cu sample has already been derived with statistically sufficient accuracy from 100 to 200 orientations. For the weaker twin orientations larger N is required, however, which is reflected in the rather slow convergence of $\rho_{0,N}$ and $\rho_{N,N}$. In contrast, for an adequate reproduction of the weak texture of Ni₃Al, obviously much more orientations are needed ($N_C \approx 4000$).

In an alternative procedure, Matthies and Wagner (1996) developed a parameter $F_2(1/N)$ that approaches linear behavior when the number of orientations N is sufficiently large. Using a discrete structure of the orientation space (e.g., $M 5^\circ \times 5^\circ \times 5^\circ$ cells at g_i with volume v_i), N measured single orientations can be sorted into these cells. From the resulting "hit-numbers" h_i formally a "hit-ODF" $f_N(g)$ can be constructed as a staircase function:

$$F_m(N) = \int_G [f_N(g)]^m dg = \sum_{i=1}^M \left(\frac{h_i}{v_i N} \right)^m v_i, \quad (9.6)$$

with $\sum_{i=1}^M v_i = 1$ and $\sum_{i=1}^M h_i = N$

Laws of statistics prescribe a mean linear dependence of the texture index F_2 on $1/N$. Only if this tendency is reached for N greater than the critical number N_C , it makes sense to represent the N orientations in the form of an ODF. From the extrapolation of the asymptote of the least-square fitted $F_2(1/N)$ -line to $1/N = 0$ (i.e., $N = \infty$), the unknown "true" F_2 of the sample can be determined, yielding the value $F_2^{\text{asy}}(N)$. Similarly as discussed earlier for the parameter ρ , N_C depends on the chosen grid, crystal and sample symmetry, and, most notably, the texture of the sample. Sharp textures with a small isotropic background are equivalent to a lower number of cells that can be hit at all. This means the linear dependency of F_2 on $1/N$ will be reached for lower N than in the case of weak textures. Figure 9.7b shows the $F_2(1/N)$ curves as well as the F_2^{asy} values as derived from the fitted asymptotic $F_2(1/N)$ -line for the Ni₃Al specimen described earlier in this section. The fit always considers the last 10 $F_2(1/N)$ points to the right. A second smoothing

over the last 10 $F_2^{\text{asy}}(1/N)$ values yields $F_2^{\text{asas}}(1/N)$. The plot displays a clean $1/N$ tendency with a stable F_2^{asy} of approximately 1.3. Here, $N = 100,000/60 \approx 1,700$ grain orientations would suffice for a reasonable ODF.

To summarize the discussion on how many orientation measurements are needed to describe an ODF with statistical relevance, the convergence of the statistical parameters $\rho_{0,N}$ and $\rho_{N;N}$ with increasing number of single-grain orientation measurements N and the linear behavior of the texture index F_2 as a function of the inverse $1/N$ can be analyzed. Among the three quantities described, the parameter $\rho_{0,N}$ comparing the ODF as computed from N single orientations with a reference texture—typically the x-ray macrotexture of the sample—turned out to be most rigid in the sense that it yielded the largest values of N_C . Qualitatively, however, the evolution of $\rho_{N;N}$ and the F_2 versus $1/N$ analysis give very similar results, so that analysis of either parameter yields valuable information on the statistical relevance of single-grain orientation data. In conclusion, it is strongly suggested to implement one of these procedures as a mandatory step to assess the statistical significance of microtexture data.

The statistical relevance of microtexture results is also affected by the measurement procedure, which becomes particularly important in the context of automated EBSD measurements. In the preceding discussion, the number of single-grain orientation measurements N is to be understood as the number of measured *grains*, but automated EBSD systems usually record many orientations per grains so as to allow reconstruction of the corresponding microstructure with sufficient accuracy. To illustrate this effect, a recrystallized Al–Mg sample was scanned with a fine step size of 2 μm . Figure 9.7c shows the evolution of the parameter ρ with increasing number of EBSD data points N . Obviously, ρ decreases rather slowly, and it is only at N in excess of 150,000 that the ρ value levels at approximately 10%. Apparently, this value of N_C is larger by several orders of magnitude than the values of the order of 1000 grains necessary to provide a reasonable macrotexture description reported earlier. The average grain size of the material was approximately 25 μm . Thus, a highly simplified estimate yields that each grain is on average measured 100 times, producing a very large number of redundant data. Despite the quite large number of measurement points (in excess of 300,000), the number of actual *grains* was below 3,000. Obviously, although a 2 μm scan produces a very detailed orientation map, the statistical relevance of the data is not that good, which is reflected in the rather slow convergence of the parameter ρ (Figure 9.7c).

To substantiate this point, the sample was scanned again on a 5× coarser grid, that is, with a step size of 10 μm . Figure 9.7c displays that for the 10 μm scan the parameter ρ drops much faster, reaching values of approximately 10% already after 5000 measurement points. The ratio of 5,000 to 150,000 agrees well with the factor 25 (i.e., 5^2) by which the second map was accelerated. This procedure reduces the number of redundant data, which leads to an increased statistical relevance of the data set. Of course, this procedure is

not suited for generation of high-quality orientation maps or computation of misorientation parameters, where spatial resolution is important, but it gives a good *statistical* representation of the orientation distribution, that is, the macrotexture (Engler et al., 1999; Schwarzer, 2000; Wright et al., 2007).

A similar effect of breaking up the effect of redundant neighboring data can be achieved by randomizing the arrangement of the EBSD data. For that purpose, the fine EBSD data set (2 μm step width) was reshuffled with a random generator, and the evolution of ρ with N was again computed for these randomized data. Here, ρ converges much faster, and only ~ 1000 orientations are required to get a sound description of the corresponding macrotexture (Figure 9.7c). This procedure is obviously applicable to all data files, and will work as long as enough *grains* (i.e., not measured points) have been recorded in the EBSD scan.

9.4 Representation of Orientations in Rodrigues Space

Use of Rodrigues space, otherwise known as *Rodrigues–Frank space*, wherein a population of R vectors resides (Section 2.8), is a relatively new field compared with the long-established Euler space approach for representation of orientations. The explanation for the late introduction of Rodrigues space is that its application is intimately connected with microtexture, that is, discrete orientation measurements, whereas representation of texture in Euler space relates traditionally to the representation of continuous orientation distributions as calculated from pole figures (Section 5.4). As already stated, microtexture data can be represented in either Euler space or Rodrigues space, whereas macrotexture data tend to be represented only in Euler space because most commercial systems are configured for this approach. Although Rodrigues space, which is particularly well suited to analysis of misorientations (Section 9.6.3), has not been very widely used to date, it has many advantages over Euler space (Section 2.8.3) and so may well be adopted more in the future (Cho, 2007).

Orientations are usually best displayed in the whole of the fundamental zone of Rodrigues space (Section 2.8). Since for orientation representation the axes of the zone are coupled to the axes of the specimen, the zone could be divided according to the symmetry of the specimen itself. For example, a rolled specimen has three axes of symmetry, and so in an appropriate reference frame the RD, TD, and ND should be parallel to the X, Y, and Z axes of the fundamental zone, respectively. For this case, one-eighth of the fundamental zone could be used. The advantage of using this reduced volume is that if the sample population is small, texture trends are more discernable in the smaller volume. However, valuable information can be lost in that the assumed symmetry of the material may not be borne out in practice.

For example, a rolling process could bias the textures on one side of the strip or plate more than on the other and this would be evident if the whole fundamental zone were used to represent the data (Section 5.4.2).

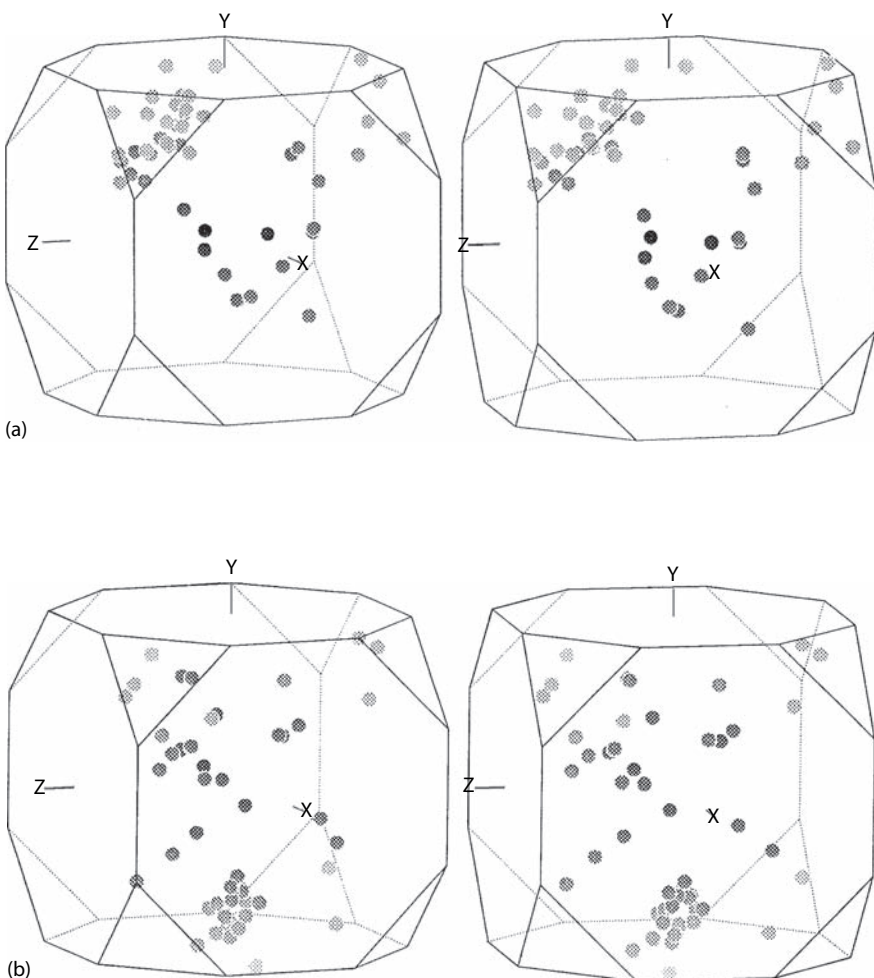
Another, and often more important, consideration to be taken into account if orthonormal sample symmetry is enforced by collapsing the fundamental zone into a reduced volume is that related texture variants having the same Miller indices families are not distinguished (Becker, 1991). There are, in the most general case, four different orientations having the same Miller indices families (Section 2.4). As an example, the variants of the S orientation are $(123)[6\bar{3}4]$, $(\bar{1}\bar{2}3)[634]$, $(123)[6\bar{3}4]$, and $(\bar{1}23)[6\bar{3}4]$ (Table 2.2 and Appendix III), quoted in their lowest-angle forms. These are distinct orientations even though they feature common families of planes that are only symmetrical with regard to orthonormal sample symmetry. The whole of the zone is required to display correctly these distinct variants whose R vectors are

$$\begin{aligned} &(0.254, -0.235, -0.291) \\ &(-0.254, 0.235, -0.291) \\ &(-0.254, -0.235, 0.291) \\ &(0.254, 0.235, 0.291) \end{aligned}$$

Figure 9.8 shows textures from an aluminum–lithium alloy where two different near-S orientations were observed in two different parts of the sheet (Randle and Day, 1993). There are 50 grains in each sample population. In the first set (Figure 9.8a), the microtexture comprises 68% near-S1 orientations, and in the second set (Figure 9.8b) there is 42% near-S2 orientations. Both have $\{001\}\langle 100 \rangle$ and $\{013\}\langle 100 \rangle$ as secondary components. We can see that the clusters that represent these two textures are occurring in different regions in Rodrigues space. This information would have been lost if the data had been compressed into a single octant.

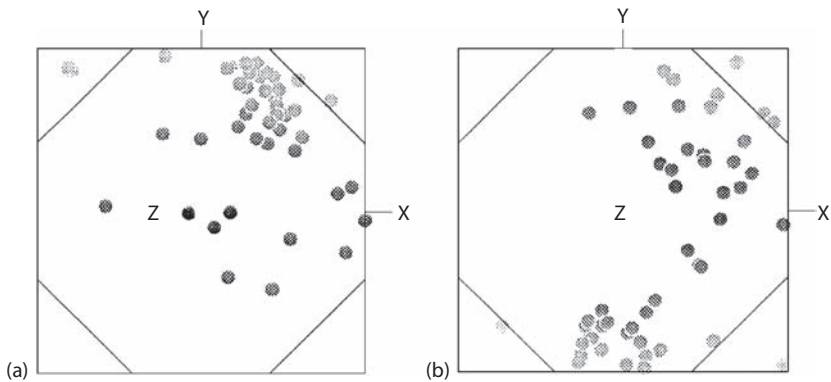
Distributions of orientations in Rodrigues space are usually generated by a computer program such that the zone can be rotated on-screen to gain maximum visual appraisal of orientation clusters. However, like any other 3-D space, Rodrigues space is problematic to display in the 2-D medium of a printed page. Several options have been tried. The first method to be used was to view the whole fundamental zone as a stereo pair (Frank, 1988; Ashbee and Sargent, 1990; Randle and Day, 1993). This is not a very convenient method because most people need a stereo viewer to appreciate the 3-D depth perspective (Figure 9.8). Viewing the whole zone in perspective is a feasible option for gaining an appraisal of the data spread especially if either different colors/sizes/shading are attributed to the data points to give pseudodepth information (Neumann, 1991a,b) or contouring is used (Hughes and Kumar, 1996).

A useful perspective of Rodrigues space is to view all the data by looking directly down one of the reference axes. The Z-axis perspective is

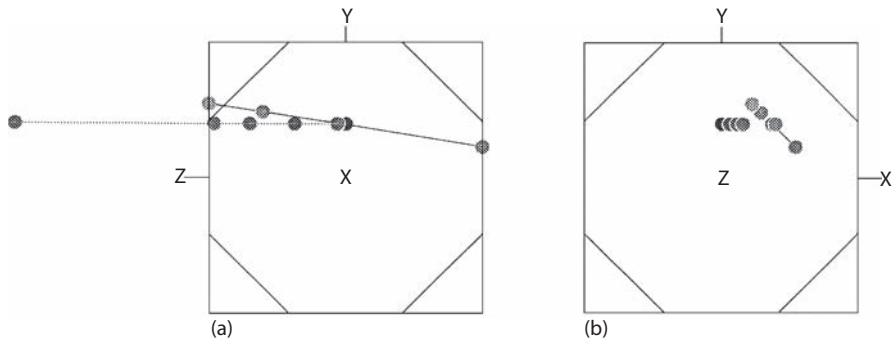
**FIGURE 9.8**

Textures from an aluminum-lithium alloy displayed in Rodrigues space as stereo pairs. Data sets are of 50 grains having (a) predominantly S1 orientation and (b) predominantly S2 orientation. (Adapted from Randle, V. and Day, A., *Mater. Sci. Technol.*, 9, 1069, 1993.)

then equivalent to a standard {100} pole figure. Figures 9.9a and 9.9b show the Z-axis perspective partners to the views in Figures 9.8a and 9.8b. It can be informative to study more than one perspective view. For example, two fiber textures, $(103)[uvw]$ and $(\bar{1}13)[uvw]$, are shown by three different perspectives in Rodrigues space in Figure 9.10, and it can be seen that the X-axis rather than the Z-axis perspective is better for appreciating the pattern of how the textures lie on straight lines. The R vectors for these, and other, fiber textures are listed in Table 9.1. Note that one of the orientations, $(103)[010]$, is located

**FIGURE 9.9**

Rodrigues space Z-axis perspective view of the microtextures in Figures 9.8a and 9.8b, respectively. (Adapted from Randle, V. and Day, A., *Mater. Sci. Technol.*, 9, 1069, 1993.)

**FIGURE 9.10**

Fiber textures in Rodrigues space for $\{103\}\langle hkl \rangle$ (dotted line) and $\{\bar{1}13\}\langle hkl \rangle$ (dashed line). Both (a) the X-axis perspective and (b) the Z-axis perspective are shown. (Adapted from Randle, V. and Day, A., *Mater. Sci. Technol.*, 9, 1069, 1993.)

outside the fundamental zone to preserve the feature that fiber textures map onto a straight line in Rodrigues space. This point could alternatively be reexpressed in its lowest-angle form (Section 2.3.3) so that it would then plot within the zone.

Rodrigues space can be represented by sections through it, as for Euler space, and the sections reconstructed into a 3-D format by eye (Engler et al., 1994a; Sarma and Dawson, 1996). Figure 9.11 shows an example of such a representation for cubic symmetry (Becker and Panchanadeeswaran, 1989). The dimensions of Rodrigues space can be represented in absolute R vectors or normalized so that the length of the major axis is unity,

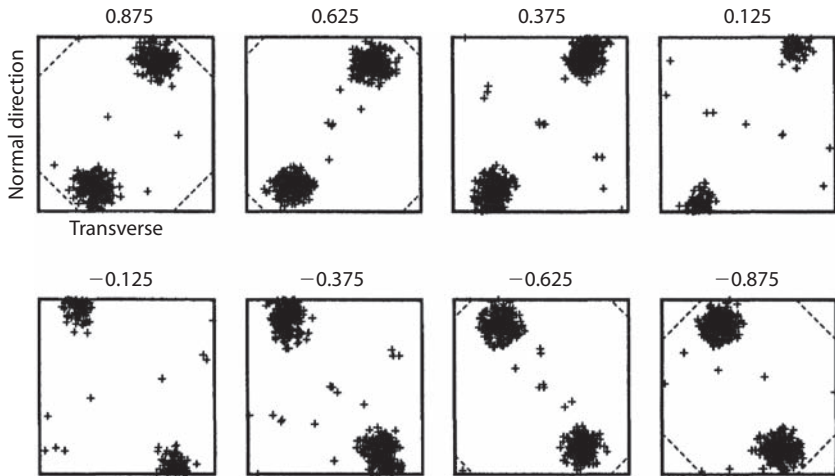
TABLE 9.1

Components of the Rodrigues Vector for Orientations uvw along Various Fiber Axes

uvw	R_1	R_2	R_3
<i>001 fiber axis</i>			
100	0	0	0
3̄10	0	0	0.162
2̄10	0	0	0.236
32̄0	0	0	0.303
110	0	0	0.414
<i>1̄01 fiber axis</i>			
101	0	0.414	0
212	0.071	0.414	-0.172
111	0.132	0.414	-0.318
121	0.214	0.414	-0.518
131	0.263	0.414	-0.634
<i>1̄11 fiber axis</i>			
1̄12	0.214	0.518	0.414
101	0.318	0.414	0.132
312	0.379	0.353	-0.036
211	0.414	0.318	-0.132
110	0.518	0.214	-0.414
<i>103 fiber axis</i>			
010	0.162	0.162	1
33̄1	0.065	0.162	0.399
32̄1	0.047	0.162	0.290
31̄1	0.025	0.162	0.154
301	0	0.162	0
<i>1̄13 fiber axis</i>			
3̄32	0.093	0.224	0.414
2̄11	0.119	0.198	0.251
301	0.154	0.162	0.025
110	0.224	0.093	-0.414

Source: Data from Randle, V. and Day, A., *Mater. Sci. Technol.*, 9, 1069, 1993.

and the R vectors scaled accordingly. As for any other representation of microtexture, contouring of the data may be substituted for discrete data points.

**FIGURE 9.11**

Example of orientation distributions in Rodrigues space displayed as sections in R_3 : copper rolling texture and cubic symmetry. (Data from Becker, R. and Panchanadeeswaran, S., *Text. Microstruct.*, 10, 167, 1989.)

9.5 General Representation of Misorientation Data

The formulation of a misorientation from pairs of orientations is described in Section 2.7. The following categories of misorientation populations can be distinguished:

- Misorientations between nearest-neighbor grains, that is, grain boundary misorientation (also sometimes called *mesotexture*). This is by far the most common case.
- Misorientations between a single, specific grain and other grains, for example, a large grain and all small grains (Shimizu et al., 1990).
- Intragrain misorientations or misorientations sampled from several sites within neighboring grains (Section 9.5.2). It has been shown that even in recrystallized materials small orientation changes, that is, lattice rotation or bending, exist within a grain.
- MODFs and their derivatives (Section 9.7).
- Orientation relationships between different phases (Section 11.5).

Analysis of misorientations at interfaces also gives rise to a further level of processing and crystallographic analysis, for instance, categorizing the statistics according to the CSL model. These methodologies are discussed in detail in Chapter 11.

9.5.1 Representations Based on the Angle/Axis Descriptor

The angle/axis descriptor is the most popular method for representation of a misorientation. As described in Section 2.3.3, there are a number of crystallographically related, mathematically equivalent solutions for a misorientation—for example, 24 and 12 for cubic and hexagonal crystal symmetry, respectively. To avoid confusion it has become common practice to select, from all the solutions, the angle/axis pair that has the minimum misorientation angle to represent the misorientation. This solution has been named the *disorientation* to conveniently distinguish it from the remaining ones (Warrington and Boon, 1975). The angle of misorientation and axis of misorientation provide different physical information: A low-angle or high-angle grain boundary is recognized from the angle alone, and certain misorientation axes are considered to be important in processes such as recrystallization. The angle and axis of misorientation can be represented separately, both for convenience on the printed page and to focus on either the angle or axis alone. Alternatively, both parameters can be displayed in cylindrical angle/axis space (Section 9.6.2). A combination of angle and axis is used for representation in Rodrigues space (Section 9.6.3).

Considering first the representation of disorientation axes, these are conveniently represented on the stereographic projection or, more compactly, on a single unit triangle of the stereographic projection since the density of axes becomes multiplied by the number of unit triangles, as for an inverse pole figure. The probability density distribution of disorientation axes $[hkl]$ in a unit triangle has been calculated for cubic crystals (Mackenzie, 1958, 1964) and is shown in Figure 9.12a. The plot consists of density contours centered on both $[100]$ and $[111]$. The density rises as the arc AB of the great circle $2^{1/2} \cdot h = k + l$, where $h \geq k \geq l$, is approached. A more useful form of the

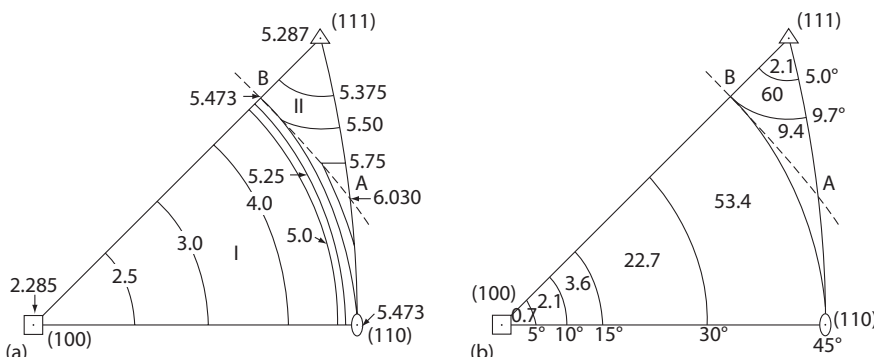


FIGURE 9.12

Distribution of disorientation axes $[hkl]$ for cubic crystals in a single unit triangle of the stereographic projection. (a) Probability density plot; (b) percentage of disorientation axes lying in the various regions. (Data from Mackenzie, J.K., *Acta Metall.*, 12, 223, 1964.)

probability distribution is shown in Figure 9.12b, which shows the percentages of disorientation axes that are expected to lie in each marked region if the distribution is random. This has come to be known as the “Mackenzie axis distribution” or “Mackenzie triangle,” and is used to display disorientation axes and assess the degree of departure from randomness of a sample population.

Frequently disorientation axis distributions are shown in angle ranges. An example is shown in Figure 9.13. Here, the disorientation axis distribution for copper, which has been processed to give a high proportion of CSL boundaries (Section 11.2.1), is shown. There are peaks in the sections, which correspond to $38.9^\circ/\langle 110 \rangle$ ($\Sigma 9$) misorientation and $60^\circ/\langle 111 \rangle$ ($\Sigma 3$) misorientation, as well as a large peak of low-angle boundaries. Another option, although not the one that is used frequently, is to display misorientation axes relative to some external axes, rather than those of the crystal, that is, a major stress axis or a dominant axis associated with the specimen processing, for instance, a rolling direction. Such a distribution is analogous to choosing a pole figure representation rather than an inverse pole figure for orientations (Heidelbach et al., 1996).

Figure 9.14 shows the disorientation angle distribution for copper, which partners the disorientation axis distribution in Figure 9.13. The peaks for low-angle boundaries, $\Sigma 3$ and $\Sigma 9$, are evident. The probability distribution for disorientation angles in cubic polycrystals has been derived (Warrington and Boon, 1975), and it has a maximum at 45° and a cutoff at 62.8° . This distribution, often called simply the “Mackenzie distribution,” is also shown in Figure 9.14. Similarly to the case for the axis distribution, the Mackenzie angle distribution is used to assess the departure from randomness in a sample population of disorientation angles (Uhbi and Bowen, 1996). The

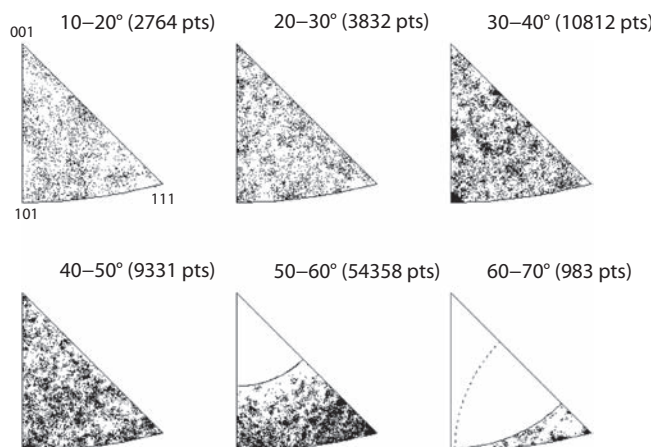
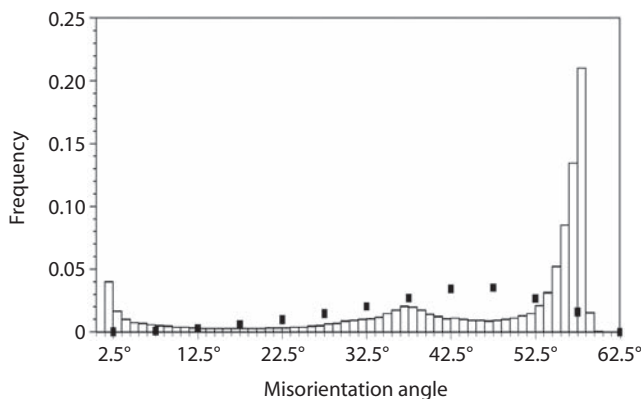


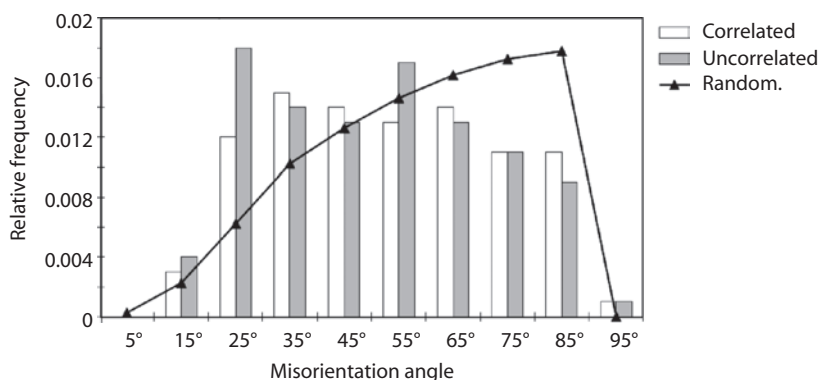
FIGURE 9.13

Distribution of disorientation axes for copper in 10° angle sections.

**FIGURE 9.14**

Distribution of disorientation angles for copper; same data set as in Figure 9.13. The distribution for randomly misoriented crystal pairs that have cubic symmetry (the “Mackenzie distribution”) is also included.

probability distribution for disorientation angles for all point-symmetry groups has also been derived (Morawiec, 1995), and it can be used to assess the departure from randomness, similarly to the case for cubic crystals. For example, Figure 9.15 shows the random distribution for hexagonal crystals, which accompanies an experimental distribution of misorientation angles from commercially pure titanium (Hu and Randle, 2007). The experimental distribution is plotted as “correlated,” that is, misorientations as they occur in the microstructure, and “uncorrelated,” that is, random pairs selected from the experimental sample population. Section 9.7 addresses normalization of misorientations and correlation functions.

**FIGURE 9.15**

Disorientation angle distribution histogram for correlated and uncorrelated misorientation pairs in commercially pure titanium. The disorientation angle distribution for randomly misoriented crystal pairs is also included (with triangles).

It is important to bear in mind that, although it may sometimes be sound to separate the angle and axis of misorientation to concentrate on particular physical aspects of the data, the *total* misorientation embodies three independent variables (Section 2.7). These can be expressed by the same parameters as orientations, and the angle/axis pair is only one descriptor (Chapter 2). Hence, when comparing *amounts* of misorientation it can be misleading to compare angles of misorientation alone, unless the misorientation axis is constant. Furthermore, it may be relevant to assess if the misorientation is in a positive or negative sense, for example, in the evaluation of cumulative misorientations (Driver et al., 1996).

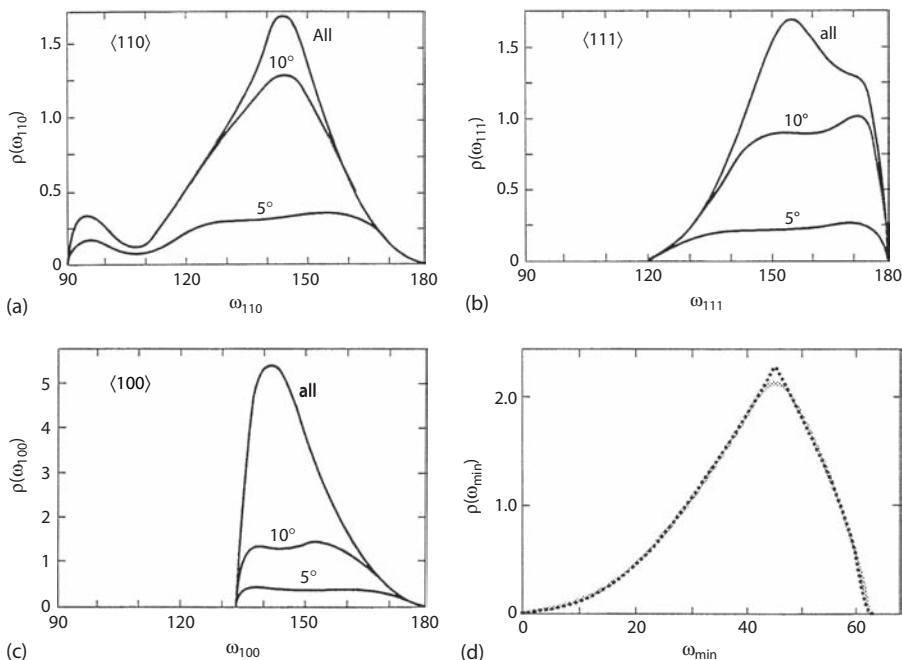
As stated at the beginning of this section, it is common practice to select the disorientation from all the symmetry-related solutions to describe a misorientation. Although this convention simplifies the data processing, there is a risk that insights into the physics of misorientation-related phenomena may be overlooked if only one angle/axis pair is examined. It is probably true to say that if the misorientation angle alone is of interest in an investigation, it will almost always be the lowest-angle solution that is most meaningful. However, if an investigation concerns the misorientation axis, it may not be that of the disorientation which is of interest (Hutchinson et al., 1996). For example, in bcc metals it is reported that high-mobility grain boundaries are misoriented on $\langle 110 \rangle$. For such investigations, it is clearly better to choose, from the 24 crystallographically related solutions, the one having a misorientation axis closest to $\langle 110 \rangle$. The distribution of 10,000 random computer-generated misorientations is displayed as those misorientation angles having axes closest to $\langle 110 \rangle$, $\langle 111 \rangle$, and $\langle 100 \rangle$ in Figures 9.16a, 9.16b, and 9.16c, respectively, which can be compared with the distribution for the disorientation angles for a random distribution shown in Figure 9.16d. Plots for misorientations within 5° and 10° of the given axis are included. It is clear that even for random misorientations there are peaks in the distributions of misorientation axes, which must be taken into account during data interpretation (Cross and Randle, 2003).

A second reason for examining misorientations from the standpoint of particular misorientation axes is that where three (or more) grain boundaries adjoin at a grain junction they share a common axis of misorientation (Section 11.4). For example (Randle, 1990, 1993),

$$180^\circ/\langle 210 \rangle \leftrightarrow 106.6^\circ/\langle 210 \rangle + 73.4^\circ/\langle 210 \rangle \quad (9.7a)$$

refers to the relationship of three grain boundaries at a junction misoriented on $\langle 210 \rangle$, according to the “addition rule” (Section 11.4). None of these are in the lowest-angle form and this relationship could not have been recognized from the disorientation since for that case the axes are all different:

$$53.1^\circ/\langle 001 \rangle \leftrightarrow 43.3^\circ/\langle 133 \rangle + 38.3^\circ/\langle \bar{1}\bar{1}1 \rangle \quad (9.7b)$$

**FIGURE 9.16**

Distributions of computer-generated misorientation angles for a random distribution plotted for misorientation axes closest to (a) $\langle 110 \rangle$, (b) $\langle 111 \rangle$, (c) $\langle 100 \rangle$, and (d) disorientation axes. (Courtesy of W.B. Hutchinson.)

9.5.2 Intragrain Misorientations

Measurements of intragrain misorientations in metals and alloys have revealed the presence of local variations in orientation (Liu and Chakrabarti, 1996). Although this is well known from TEM observations of deformed materials (Hughes and Kumar, 1996), EBSD can be used to study subgrain misorientation and show the presence of local “lattice bending,” or intra-grain misorientation, even in recrystallized materials (Adams et al., 1993; Thomson and Randle, 1997a). Orientation mapping to reveal intra-grain misorientations is discussed briefly in Section 10.4. As far as data processing of intragrain misorientations is concerned, it is important to choose a relevant sampling step size to reveal orientation changes. A suitable step size will depend on the scale of the microstructure: Typically, a recrystallized microstructure might require a step size of $1 \mu\text{m}$, whereas a deformed material might be sampled every $0.01\text{--}0.1 \mu\text{m}$ using EBSD or TEM.

A useful combination of intragrain spatial and numerical information is to show a linear scan of orientation changes across one or more grains. The simplest approach is to use only the misorientation angle. This technique has been used to show, for example, that there is a direct contribution of texture

evolution to misorientation accumulation with strain in bcc steel (Kang et al., 2007). Another example is that the technique has been used to show the misorientation profile across banded areas in deformed niobium single crystals (Sandim et al., 2007). This display method has the advantage of both focusing attention on the area of interest and providing concurrently quantification of the orientation change. A disadvantage of the approach is that a compromise must be made to represent compactly the three independent variables that describe the misorientation, in addition to the positional information.

When misorientations between neighboring sampling points are calculated, different values may be obtained depending on the spacing of the sampling points. Although this approach of calculating misorientations between nearest-neighbor points may be valid for some cases, for example, to monitor cumulative misorientations (Hjelen et al., 1991), the ambiguous effect of the sampling step size can be circumvented by plotting an orientation, rather than a misorientation, parameter. Such a parameter can be calculated for each sampling point with reference to a starting point or an average orientation. Alternatively, a compressed orientation parameter can be calculated using either Euler angles or Rodrigues vectors (Randle et al., 1996). The compressed orientation parameter D in Rodrigues space is given by

$$D = 2 \tan^{-1} [(R_1 - R_{1R})^2 + (R_2 - R_{2R})^2 + (R_3 - R_{3R})^2]^{1/2} \quad (9.8)$$

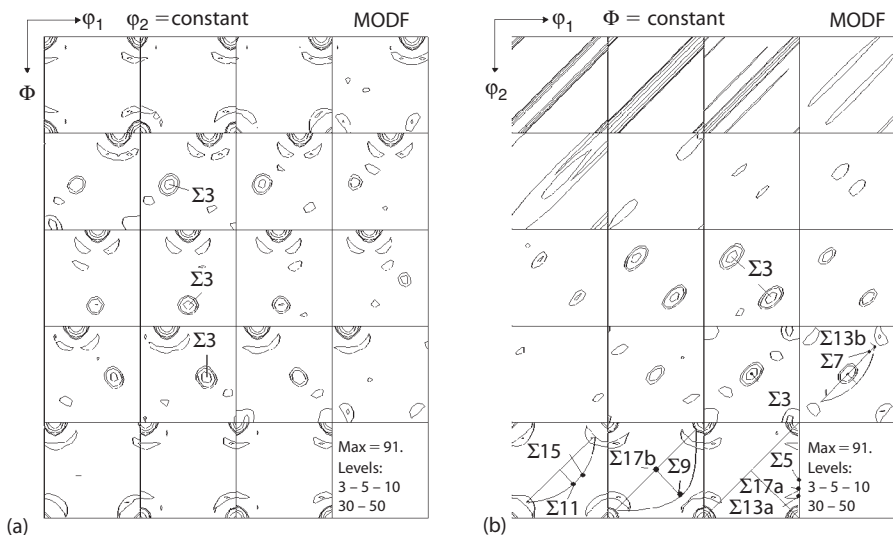
where R_1, R_2, R_3 and R_{1R}, R_{2R}, R_{3R} are the components of the R vector at the measuring point and the reference point (e.g., the grain center), respectively. An inevitable disadvantage of the compressed orientation parameter D is that occasionally different orientations can have the same D value.

9.6 Representation of Misorientations in Three-Dimensional Spaces

Misorientations can be displayed in Euler-space (Section 9.6.1) or spaces based on the angle/axis pair, namely, cylindrical angle/axis space (Section 9.6.2) and Rodrigues space (Section 9.6.3). It turns out that representation in Rodrigues space is the most advantageous.

9.6.1 Representation of Misorientations in Euler Space

For representation of misorientations in the Euler angle space, from the misorientation matrices M , the Euler angles $\varphi_1, \Phi, \varphi_2$ are calculated according to standard procedures (Section 2.7). As has been described in more detail in Section 9.3, for the representation of orientations, the resulting set of Euler angles

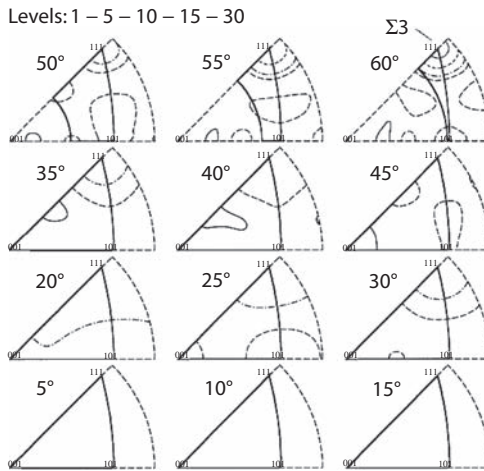
**FIGURE 9.17**

Representation of the MODF of a cyclically deformed nickel specimen in Euler space. (a) $\varphi_2 = \text{constant}$; (b) $\Phi = \text{constant}$.

can be transposed in the Euler space either by direct cell methods or by the series expansion method. As an example, Figure 9.17 shows a misorientation distribution that was derived from EBSD single-grain orientation measurements in cyclically deformed nickel. The sample was deformed at 600°C in 300 cycles with a frequency of $13 \times 10^{-3} \text{ s}^{-1}$ under a strain amplitude of 0.5%. Under such circumstances the grain boundaries tend to rearrange, and particularly $\Sigma 3$ -twin grain boundaries were observed to remain stable in the microstructure (Brodesser and Gottstein, 1993). Besides the $\Sigma 3$ -peak in the distribution, strong intensities close to the origin of the Euler space, that is, at $\varphi_1 = \Phi = \varphi_2 = 0^\circ$, prevail, representing the low-angle grain boundaries (Figure 9.17). (The same data will also be shown in other spaces in Figures 9.18 and 9.19b.)

The main advantages of the representation of misorientation distributions in Euler space are that the computation is relatively easy and the MODF and its derivatives can be obtained, if required (Section 9.7). However, the technique suffers from several disadvantages:

- The Euler angle representation does not yield direct information on the crystallographic orientation relation between the two considered orientations, which means it is difficult to visualize. Thus, evaluation of MODFs in the Euler space needs detailed legends or marking of special misorientation as done in Figure 9.17.
- The orientation space exhibits strong distortions for small angles Φ (Section 5.4.1), as it becomes most evident from representing the

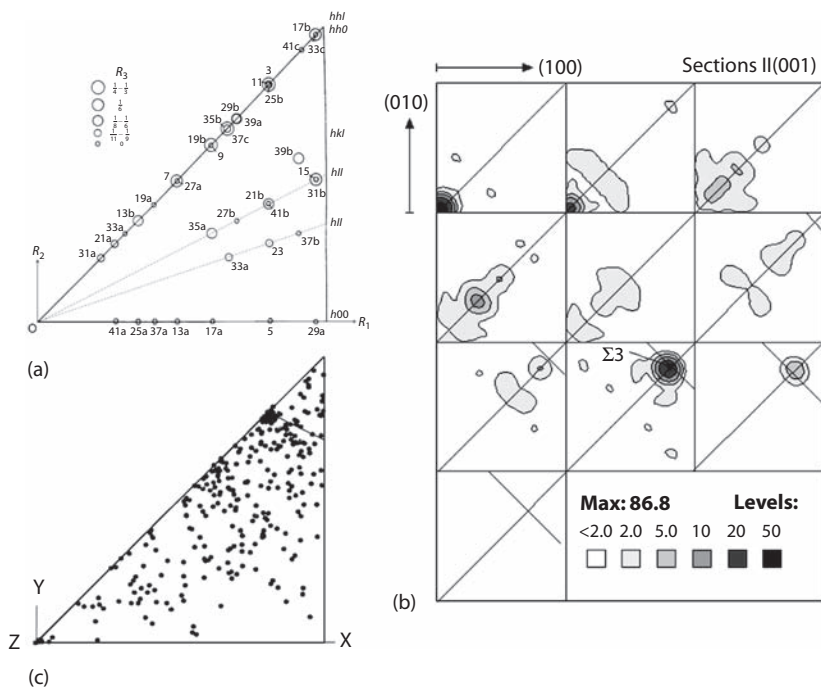
**FIGURE 9.18**

MODF of a cyclically deformed nickel specimen in cylindrical angle/axis space (see Figure 9.17).

MODF in the—rather unusual— Φ sections (Figure 9.17b). To overcome this shortcoming, Zhao and Adams (1988) proposed to use a subspace with very high Φ angles ($\Phi \geq 70^\circ$), where the distortions are minimal. The borders of this subspace are marked in Figure 9.17b. As the two orientations that define the mutual misorientation can be treated equivalently (Section 2.7.2), this subspace can be further subdivided into two equivalent asymmetric domains, as also indicated in Figure 9.17b. Furthermore, the positions of the special grain boundary orientation relationships with $\Sigma \leq 17$ are marked in Figure 9.17b. It can be seen that each Σ position can be found exactly once in this subspace.

- The surfaces between the various basic domains of the cubic/cubic symmetry are strongly curved (which is induced by the threefold axis), causing difficulties in identification. The $\Sigma 3$ -twin relation that is located on the interface between adjacent subspaces is visible three times in the standard Euler angle space. Note that all orientation relationships with low Σ lie at the border surfaces of the subspaces rather than in their interior (Figure 9.17b). This is due to the rotation about symmetrical $\langle h k 0 \rangle$ or $\langle h l l \rangle$ axes for such orientation relationships.

For all these reasons the representation of misorientations in Euler space is very difficult to visualize, which may cause uncertainties in evaluation of

**FIGURE 9.19**

Representation of misorientations in Rodrigues space. (a) \$R\$ vectors for CSLs having \$\Sigma \leq 45\$ in a Z-axis perspective of the subvolume. (Adapted from Randle, V., *Proc. R. Soc. Lond.*, 431, 61, 1990.) (b) \$R\$-vector density distribution, displayed in sections through a left- and right-handed subvolume, for cyclically deformed nickel. (c) Z-axis perspective of misorientations in an austenitic steel, indicating a high proportion of \$\Sigma 3\$ s. (Adapted from Randle, V., and Day, A., *Mater. Sci. Technol.*, 9, 1069, 1993.)

misorientations in the Euler space. Rather, misorientations are better represented in angle/axis spaces.

9.6.2 Representation of Misorientations in the Cylindrical Angle/Axis Space

Misorientations can conveniently be represented in an orientation space given by the parameters of the angle/axis pair description. For that purpose, the rotation axis \$r\$ is expressed in terms of two angles \$\vartheta\$ and \$\psi\$ (Equation 2.23), such that the misorientation is now given by the three angles \$\vartheta\$, \$\psi\$, and \$\theta\$. All possible orientations and misorientations are given in the interval \$(0^\circ \leq \theta \leq 360^\circ, 0^\circ \leq \vartheta \leq 90^\circ, 0^\circ \leq \psi \leq 360^\circ)\$ and, as shown in Figure 2.15, can be represented in a cylindrically shaped 3-D space with the cylinder axis parallel

to the θ axis. In this arrangement, the base plane of the cylinder corresponds to a stereographic projection of the rotation axis r , which means that the rotation axes can readily be evaluated.

Figure 9.18 shows the misorientation distribution of a cyclically deformed nickel sample (also shown in Euler angle space, Figure 9.17) in sections parallel to θ ($\Delta\theta = 5^\circ$) through a subsection of the cylindrical orientation space. The basic domain, that is, the smallest subspace in which each possible misorientation would exist exactly once, is marked with thick lines (for cubic/cubic symmetry). The main advantage of this space is given by the fact that for each θ section, the rotation axis r can readily be derived from its position in the stereographic triangle. This is a very familiar way to evaluate misorientation data. Another example of an MODF represented in the cylindrical angle/axis space is given in Section 11.5.

A major disadvantage of the cylindrical angle/axis space is caused by the relatively large distortion of this space. For decreasing θ angles, the resolution for the position of the rotation axis becomes increasingly smaller and is indefinite for $\theta = 0^\circ$ (Pospiech et al., 1986). Since the Rodrigues space described in Section 9.6.3 offers several advantages, the cylindrical angle/axis space will not be discussed here any further.

9.6.3 Representation of Misorientations in Rodrigues Space

When analyzing misorientations, the coordinate frame of Rodrigues space is parallel to the crystal axes. If all the misorientation axes are expressed in the same form—that is, $h \geq k \geq l$ —and all are positive, the whole of the fundamental zone does not need to be used to display misorientations. For the cubic system, for instance, the fundamental zone can be divided up along planes of symmetry into 48 identical and equivalent subvolumes (Randle, 1990; Field, 1995). This process is identical to the division of the reference sphere and hence the stereogram into unit triangles (Appendix IV), or division of Euler space into asymmetric domains (Section 9.6.1). The subvolume of the fundamental zone is also sometimes called the *Mackenzie cell* after the Mackenzie triangle that shows the distribution of random misorientations for the cubic system (Section 9.5.1). Table 2.4 includes the size of the subvolume as a fraction of the fundamental zone for each crystal system.

Figure 2.16 shows how the fundamental zone for cubic lattices is divided along the surfaces equivalent to planes perpendicular to the symmetry axes, that is, $\langle 100 \rangle$, $\langle 111 \rangle$, and $\langle 110 \rangle$. The $\langle 100 \rangle$, $\langle 111 \rangle$, and $\langle 110 \rangle$ axes are shown radiating from the origin along edges of the subvolume. All misorientations can be constrained to lie either within the subvolume or on a surface, edge, or vertex. Misorientations that lie on the boundary of the subvolume are “geometrically special,” by having a rational, low-index axis of misorientation.

Three types of boundary can be recognized readily in the subvolume of Rodrigues space—low-angle boundaries, boundaries with preferred misorientation axes, and CSL-type boundaries (Section 11.2). Low-angle

boundaries are recognized by their proximity to the origin of Rodrigues space, whereas preferred misorientation axes lie along straight lines in the subvolume, analogous to the case of orientation fiber textures. Often, preferred misorientation axes are low-index types, $\langle 100 \rangle$, $\langle 111 \rangle$, or $\langle 110 \rangle$, and so coincide with the edges of the space. It should be noted that distributions of misorientations in Rodrigues space take account only of the lowest-angle solution, and so alternative descriptions, which may show up common misorientation axes, are not recognized. For example, in CSL notation $\Sigma 3$, $\Sigma 5$, and $\Sigma 15$ are all misoriented on a $\langle 210 \rangle$ axis (Equation 9.7), yet only $\Sigma 15$ is in its lowest-angle form.

Rodrigues space is especially apposite for the representation of low- Σ CSL misorientations in cubic systems since the Rodrigues vectors are rational fractions and therefore easy to recognize when plotted (Randle, 1990). The representation of CSLs in Rodrigues space for crystal systems other than cubic has been addressed little as yet and so will not be discussed here. R vectors for CSLs up to $\Sigma = 45$ are listed in Table 9.2 and shown as a Z-axis perspective in the subvolume of the fundamental zone in Figure 9.19a.

The subvolume of the fundamental zone is usually displayed as sections parallel to the XY plane. Either a single subvolume is used that gives a triangular base, or two subvolumes are displayed that give a square base and would allow both right- and left-handed misorientations to be displayed, if required. Figure 9.19b shows a sample population of misorientations from the cyclically deformed nickel sample that has already been shown in the Euler angle space (Figure 9.17) and the cylindrical angle/axis space (Figure 9.18). In Figure 9.19b, the MODFs are plotted with contour lines in one-eighth of the fundamental zone by sectioning Rodrigues space perpendicular to the [001] axis in equal distances of $\tan \theta/2$. In comparison to constant sections with $\Delta\theta = 5^\circ$ this yields a maximum error of 0.9° , which demonstrates the small distortions of this space. This kind of representation of a cubic space comprising one-eighth of the fundamental zone, which differs from the Mackenzie cell, was chosen because of its similarity to the well-known sections through the Euler space (Engler et al., 1994a). Figure 9.19c shows a distribution of misorientations from austenitic steel, again having a high proportion of $\Sigma 3$ boundaries, in a single subvolume.

Rodrigues space has been used to characterize orientation and misorientation distributions of island grains in an iron–silicon alloy (Bennett et al., 2007). It has also proved beneficial for representation of orientation relationships between dissimilar lattices, for example, fcc–bcc or bcc–hcp, which renders it useful for the study of phase transformations or precipitation. The formalism of this approach is discussed in detail by He and Jonas (2007). For example, phase transformations in a meteorite have been studied by He et al. (2005). Attempts have been made to superimpose Rodrigues space and real-space coordinates to provide an orientation/microstructure link (Hughes and Kumar, 1996; Weiland et al., 1991), and orientation maps can be colored according to Rodrigues vectors.

TABLE 9.2Rodrigues Vectors for CSLs up to $\Sigma = 45$

Axis/Σ	R_1	R_2	R_3	Axis/Σ	R_1	R_2	R_3
$\langle 100 \rangle$							
				$\langle 311 \rangle$			
5	$\frac{1}{3}$	0	0	23	$\frac{3}{9}$	$\frac{1}{9}$	$\frac{1}{9}$
13a	$\frac{1}{5}$	0	0	33b	$\frac{3}{11}$	$\frac{1}{11}$	$\frac{1}{11}$
17a	$\frac{1}{4}$	0	0				
25a	$\frac{1}{7}$	0	0	$\langle 111 \rangle$			
29a	$\frac{2}{5}$	0	0	3	$\frac{1}{3}$	$\frac{1}{3}$	$\frac{1}{3}$
37a	$\frac{1}{6}$	0	0	7	$\frac{1}{5}$	$\frac{1}{5}$	$\frac{1}{5}$
41a	$\frac{1}{9}$	0	0	13b	$\frac{1}{7}$	$\frac{1}{7}$	$\frac{1}{7}$
				19b	$\frac{1}{4}$	$\frac{1}{4}$	$\frac{1}{4}$
$\langle 210 \rangle$							
				21a	$\frac{1}{9}$	$\frac{1}{9}$	$\frac{1}{9}$
15	$\frac{2}{5}$	$\frac{1}{5}$	0	31a	$\frac{1}{11}$	$\frac{1}{11}$	$\frac{1}{11}$
27b	$\frac{2}{7}$	$\frac{1}{7}$	0	37c	$\frac{3}{11}$	$\frac{3}{11}$	$\frac{3}{11}$
41b	$\frac{2}{6}$	$\frac{1}{6}$	0	39a	$\frac{1}{6}$	$\frac{1}{6}$	$\frac{1}{6}$
43b	$\frac{2}{9}$	$\frac{1}{9}$	0	43a	$\frac{1}{13}$	$\frac{1}{13}$	$\frac{1}{13}$
$\langle 310 \rangle$							
				$\langle 221 \rangle$			
37b	$\frac{3}{8}$	$\frac{1}{8}$	0	17b	$\frac{2}{5}$	$\frac{2}{5}$	$\frac{1}{5}$
				29b	$\frac{2}{7}$	$\frac{2}{7}$	$\frac{1}{7}$
$\langle 321 \rangle$							
				45b	$\frac{2}{9}$	$\frac{2}{9}$	$\frac{1}{9}$
39b	$\frac{3}{8}$	$\frac{2}{8}$	$\frac{1}{8}$	45c	$\frac{2}{6}$	$\frac{2}{6}$	$\frac{1}{6}$
$\langle 110 \rangle$							
				$\langle 331 \rangle$			
9	$\frac{1}{4}$	$\frac{1}{4}$	0	25b	$\frac{3}{9}$	$\frac{3}{9}$	$\frac{1}{9}$
11	$\frac{1}{3}$	$\frac{1}{3}$	0	35b	$\frac{3}{11}$	$\frac{3}{11}$	$\frac{1}{11}$
19a	$\frac{1}{6}$	$\frac{1}{6}$	0				
27a	$\frac{1}{5}$	$\frac{1}{5}$	0	$\langle 332 \rangle$			
33a	$\frac{1}{8}$	18	0	43c	$\frac{3}{8}$	$\frac{3}{8}$	$\frac{2}{8}$
33c	$\frac{2}{5}$	$\frac{2}{5}$	0				
41c	$\frac{3}{8}$	$\frac{3}{8}$	0				
$\langle 211 \rangle$							
21b	$\frac{2}{6}$	$\frac{1}{6}$	$\frac{1}{6}$				
31b	$\frac{2}{5}$	$\frac{1}{5}$	$\frac{1}{5}$				
35a	$\frac{2}{8}$	$\frac{1}{8}$	$\frac{1}{8}$				

9.7 Normalization and Evaluation of the Misorientation Distribution Function

In analogy to the continuous distribution of the orientations, the ODF, a continuous distribution function of misorientations can be defined, that is, the

MODF or, sometimes, MDF (Pospiech et al., 1986, Adams, 1986). Thus, the MODF is constituted of the misorientations g_{ij} between all grains i and all their neighbors j in a given sampling volume. Similarly as described previously for the ODF, continuous misorientation distributions can be derived from the individual misorientations g_{ij} , either by direct methods in an appropriate 3-D (mis)orientation space or by the series expansion method in Fourier space. The functions for the series expansion have originally been defined in terms of the Euler angles (Section 5.3.1), whereas comparable functions for the angle/axis and Rodrigues vector parameters have not yet been developed. Therefore, although the angle/axis and Rodrigues vector descriptions of misorientations are generally considered superior to the Euler angle description, the computations are usually performed in Euler space and then the results are transformed into other spaces (Pospiech et al., 1986). Alternatively, the MODF can directly be derived by superposition of the corresponding misorientations in the desired (mis)orientation space (Engler et al., 1994a; Matthies and Vinel, 1994).

Under the assumption of a random arrangement of the orientations in the microstructure, the MODF can directly be derived from the ODF, that is, it can be computed from macrotexture data. The resulting MODF, the so-called texture-derived MODF, statistical MODF, or, following the nomenclature introduced by Pospiech et al. (1993), orientation difference distribution function (ODDF) can be used to normalize the MODF, but it does not contain any valuable information on the spatial arrangement of the individual orientations. In real microstructures, the orientations are not randomly arranged such that the “real” MODF generally differs from the “statistical” ODDF. Thus, determination of the measured, or physical, MODF requires analysis of the orientations of the corresponding grains in the microstructures together with their spatial arrangements, which can only be accomplished by techniques for microtexture analysis.

The difference between MODF and ODDF is illustrated schematically in Figure 9.20. The MODF is constituted of the misorientations g_{ij} between all

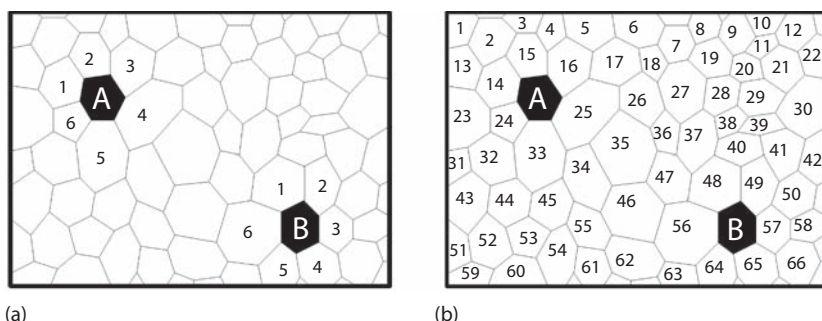


FIGURE 9.20

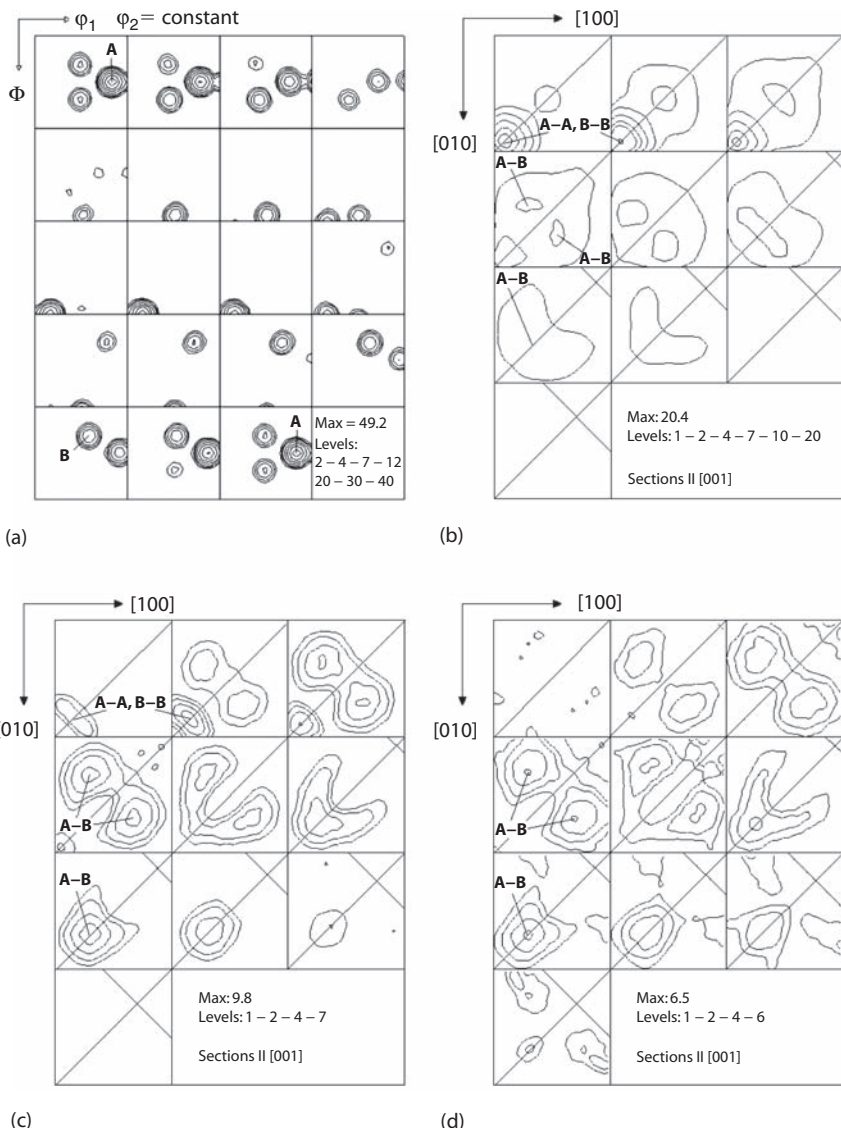
Schematic sketch of the topological features forming the basis of (a) MODF and (b) ODDF.

grains i and all their *direct* neighbors j . Thus, in the schematic sketch in Figure 9.20a the MODF is made up of the misorientations g_{Aj} between grain A and its neighbors $j = 1, \dots, 6$ plus the misorientations g_{Bj} between grain B and its neighbors $j = 1, \dots, 6$, and so on. The ODDF, by contrast, is composed of the mutual misorientations between *all* grains i and j (with $i, j = 1, \dots, 66$), completely disregarding their actual location in the microstructure (Figure 9.20b).

To distinguish between the features in the MODF that arise from a given local arrangement of the corresponding orientations in the microstructure and the features that are controlled by the macrotexture of the sample, the measured MODF has to be normalized with respect to the macrotexture, which can be accomplished by dividing the MODF by the ODDF (Plege, 1987; Schwarzer and Weiland, 1988; Zhao et al., 1988; Pospiech et al., 1993; Mainprice et al., 1993; Heidelbach et al., 1996). The resulting texture-reduced MODF discloses features arising from a correlation in nearest-neighbor orientation relationships, which gives rise to correlated MODF or orientation correlation function (OCF).

To illustrate the potential applications of MODFs most clearly, in the following paragraphs the various possibilities of normalization of the MODF and the resulting information are discussed using an example with a model distribution of two texture components with a mutual misorientation of $35^\circ\langle112\rangle$ (Engler et al., 1994a). The model texture was composed of two components labeled A and B at the Euler angles $(75^\circ, 45^\circ, 0^\circ)$ and $(54^\circ, 29^\circ, 78^\circ)$; both components were associated with a Gauss-type scatter in Euler angle space with volume fraction $M = 50\%$ and a half scatter width $\psi_0 = 8.5^\circ$. Figure 9.21a shows the corresponding ODF, which was calculated as described in Section 9.3.2. Subsequently, this ODF was discretized, yielding a set consisting of approximately 500 single-grain orientations. With this data set, three different calculations were performed:

1. The ODDF was computed by determination of the orientation difference—that is, the misorientation—between each individual orientation and all other orientations of the entire data set. Thus, the ODDF yields statistical information on the potential misorientations between all orientations in a specimen, without consideration of the actual spatial arrangement of the corresponding grains in the microstructure, in particular of their neighborhood. Thus, the ODDF is only influenced by the macrotexture of the given sample and, as such, it can also be computed directly from macrotexture data (Plege, 1987; Zhao et al., 1988; Pospiech et al., 1993), though it is typically derived from the microtexture data by computing the misorientations between each grain and all other grains irrespective of their local arrangement. The ODDF of the present example—represented in Rodrigues space in Figure 9.21b—comprises two maxima at the position of low-angle grain boundaries (near the origin), indicating A-A and B-B relationships, and at the A-B orientation relationship $35^\circ\langle112\rangle$.

**FIGURE 9.21**

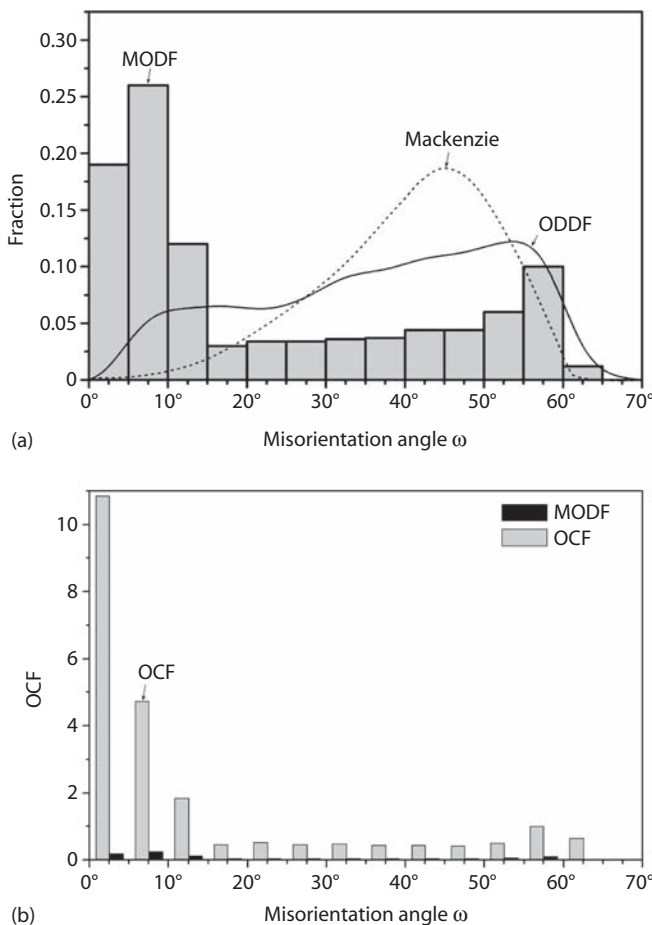
(a) Model ODF consisting of two components A and B with a $35^\circ/\langle 112 \rangle$ orientation relationship, used to illustrate the normalization of MODFs. (b) ODDF, (c) MODF, and (d) OCF of the model texture in (a).

2. An MODF was computed by artificially “arranging” the grains in such a way that A–B high-angle grain boundaries were preferred over low-angle grain boundaries A–A and B–B. This means that A grains are preferentially surrounded by B grains and vice versa.

The corresponding Rodrigues plot reveals a peak at $35^\circ\langle112\rangle$ (Figure 9.21c), which is significantly stronger than the corresponding peak in the ODDF (Figure 9.21b). However, there remains a strong peak near the origin, which indicates the presence of still a large number of low-angle grain boundaries. In the case of such a strong macrotexture as in the present example despite the favorization of A–B misorientations, many A–A and B–B grain boundaries will still arise, which is simply due to their statistical frequency. Thus, the MODF yields information about the frequency of orientation relations between neighboring grains in the microstructure. This particularly favors the MODF for problems related to grain boundaries, such as grain boundary diffusion and grain boundary sliding (Pumphrey, 1976). In that context, the special treatment of a material to achieve an optimum grain boundary distribution is referred to as *grain boundary engineering or design* (Watanabe, 1988; Palumbo and Aust, 1992; Randle, 2004).

3. For an analysis of the orientation correlation, as for example the preferred occurrence of A–B grain boundaries, the MODF is not suited, however, since it is influenced by the texture of the sample. To yield information on orientation correlations, the MODF is divided by the ODDF. This way one obtains a texture-reduced form of the misorientation function, namely, the correlated MODF or OCF. In contrast to the MODF, the OCF yields information about the texture-reduced spatial correlation of misorientations, for example, whether deformation or recrystallization leads to a preferred development of distinct neighborhood relations. Occurrence of a given misorientation with $f > 1$ (or $f < 1$) in the OCF indicates its stronger (or weaker) occurrence compared to a statistical arrangement of grains in the microstructure. Hence, the OCF is suitable to allow conclusions to be drawn on the underlying physical mechanisms of microstructure and microtexture development. In the present example, no low-angle grain boundaries arise in the OCF; only the peak at $35^\circ\langle112\rangle$ (A–B) remains (Figure 9.21d), which exactly reflects the distribution that is to be expected from the artificial arrangement of the orientations A and B.

The applicability of MODF, ODDF, and OCF is now illustrated by way of an example pertaining to the occurrence of continuous recrystallization in aluminum (Engler and Huh, 1999). High-purity aluminum foil was recrystallization annealed and an EBSD orientation map with size $280 \times 220 \mu\text{m}$ was measured in steps of $1 \mu\text{m}$. For each point of the orientation map, the misorientations with regard to the six next neighbors were evaluated in terms of misorientation angle ω and misorientation axis, though the latter will be ignored in the following. Figure 9.22a shows the misorientation distribution as fraction of boundaries in dependence on the misorientation

**FIGURE 9.22**

(a) MODF, ODDF, and Mackenzie distribution and (b) MODF and OCF in terms of fraction of grain boundaries as a function of the misorientation angle ω obtained in high-purity aluminum foil, which had undergone continuous recrystallization. (Data from Engler, O. and Huh, M.Y., *Mater. Sci. Eng.*, A271, 371, 1999.)

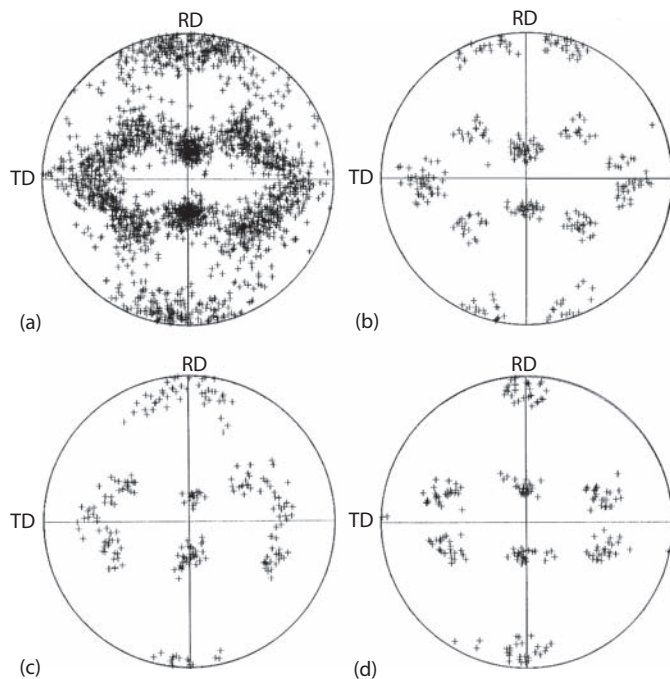
angle ω . The distributions obtained for both the as-deformed state and the recrystallized state were very similar, and in both examples, the majority of boundaries have misorientation angles below 20° and can therefore be classified as low-angle grain boundaries. For an appraisal of the misorientation distribution with regard to the occurrence of continuous recrystallization, these data had to be compared to the average misorientation distribution of the same sample without consideration of the spatial arrangement of the corresponding grains and subgrains in the microstructure, that is, the ODDF. In the present example, the ODDF was derived from

the corresponding x-ray macrotexture data and was again expressed in terms of the fraction of misorientation angles ω . Comparison of the resulting curve with the actual misorientation distribution in Figure 9.22a shows that small misorientations, representing low-angle grain boundaries, are much more frequent than they would be in a sample with the same texture but a random spatial arrangement of the orientations. Finally, the OCF was computed, simply by dividing the MODF histogram values by the corresponding values of the ODDF (Figure 9.22a). The resulting OCF, displayed in Figure 9.22b, reveals a very high peak with $f > 10$ at low misorientation angles, whereas all other columns are below 1. This implies that low-angle grain boundaries are strongly preferred over medium- and high-angle boundaries, which proves that recrystallization proceeded by continuous subgrain coarsening rather than the discontinuous growth of some distinct recrystallization nuclei, that is, by continuous recrystallization (Engler and Huh, 1999).

Figure 9.22a shows that the ODDF is quite different from the standard Mackenzie distribution, which is the probability distribution for disorientation angles in randomly oriented cubic polycrystals (Section 9.5.1; Figure 9.14). The difference between ODDF and Mackenzie distribution lies in the occurrence of texture: The Mackenzie distribution is valid for a random orientation distribution, whereas the ODDF is derived for a given texture, though under the assumption of a random topological arrangement of the texture constituents. The MODF does incorporate both orientation distribution (i.e., texture) and topological arrangement of the texture constituents, whereas the OCF yields information about the texture-reduced spatial correlation of the texture constituents.

9.8 Extraction of Quantified Data

Display of orientation or misorientation data in an appropriate space is only a part of data evaluation. Secondary processing is needed to extract quantified information from the data. As far as statistical information is concerned, one way to do this is mentioned in Section 9.3.2, namely, calculate the C coefficients of the series expansion method and call upon the analysis methods derived for macrotexture. However, this route may be unnecessarily complicated, especially for small data sets. Proportions of grains having specified texture components, within a predetermined tolerance angle, can be extracted directly from the orientation matrices. Indeed, these statistics could be output directly without recourse to any orientation space, but it is convenient to have a depiction of the texture distribution to facilitate qualitative characterization by eye.

**FIGURE 9.23**

(a) {111} Pole figure from deformed and part annealed aluminum. Some of the texture components are extracted onto separate pole figures, using a 15° spread. (b) {123}(634), (c) {211}(111), (d) {436}(323). See also Table 9.3. (Data from Davies, R. and Randle, V., *Mater. Char.*, 37, 131, 1996.)

Figure 9.23a shows a {111} microtexture pole figure comprising a small data set of 300 grains from a deformed and partially recrystallized aluminum alloy (Davies and Randle, 1996). The texture components extracted, using an angular tolerance of 15° , are shown in Table 9.3 and some of the main extracted components are shown separately on pole figures in Figures 9.23b through 9.23d. These are {123}(634), {211}(111) and a 11° rotated component of {211}(111), {436}(323). A comparison of Figures 9.23c and 9.23d shows that on the basis of the pole figure these last two components are hard to separate. However, analytically they can be readily distinguished. A few orientations could be classified as either {211}(111) or {436}(323), based on a 15° spread. For these cases, the orientation was classified according to the smaller deviation angle. The analytical procedure involved a search through a look-up table of specified textures. Many commercial software packages include routines for similar calculations. Note that each crystallographically related solution was

TABLE 9.3

Proportion (%) of Grains Representative of Each Main Texture Component from the Data in Figure 9.23a

Orientation	{001}	{001}	{103}	{101}	{211}	{123}	{436}	Random
	$\langle 100 \rangle$	$\langle 310 \rangle$	$\langle 311 \rangle$	$\langle 111 \rangle$	$\langle 111 \rangle$	$\langle 634 \rangle$	$\langle 323 \rangle$	
Proportion [%]	8.7	3.3	4.3	4.7	21.0	28.0	19.3	10.7

Source: Data from Davies, R. and Randle, V., *Mater. Char.*, 37, 131, 1996.

searched for separately and, although all the variants are included together in Table 9.3, it turned out that each variant was not represented evenly. For example, for the {436}⟨323⟩ component only two of the four variants were present.

9.9 Summation

The aim of this chapter has been to provide a guide to the broad array of choices that exist for evaluation and representation of microtexture data, by giving a concise exposition of the principles and methodology of each. Formalism has been deliberately kept to a minimum, and the reader can obtain fuller information elsewhere (see General Bibliography). There is a host of examples in the literature to illustrate microtexture investigations where the representation methods described in this chapter have been used.

Selection of a method for data representation and analysis will depend on the nature of the inquiry and the user's preference. A key point is that single-grain orientation measurements are *directly 3-D* and therefore their representation (and subsequent extraction of statistics) in pole figures, Euler space, or Rodrigues space is equivalent. As far as direct representation of misorientations is concerned, axis/angle representations, including those in Rodrigues space, offer significant advantages over use of Euler space. When analyzing microtexture data, it must always be borne in mind that the quantification can be by *volume* (or area for interfaces) or by *number*.

As a consequence of the speed of EBSD analysis, this technique is now capable of providing an acceptable alternative to macrotexture for the measurement of overall texture, provided that attention is paid to appropriate sampling schemes and population size (Wright et al., 2007). The EBSD-based

method is free from the errors introduced in the series expansion method (Section 5.3.2), and the cost of a standard SEM plus EBSD system is considerably less than a full x-ray texture goniometer. Furthermore, EBSD gives access to a whole range of local orientation studies, which is usually the main focus.

However, potential disadvantages of EBSD to measure overall texture are that only surface grains are sampled (although sequential surface depths could be prepared), all grains must provide indexable patterns, which restricts deformation levels, and x-ray macrotexture determination is faster. It is probable, therefore, that in the future both techniques will be used to generate overall textures. Neutron diffraction, with its greater depth of penetration (Section 4.4), offers considerable advantages over EBSD, although these are offset by the inconvenience associated with the nature of neutron production. Often, it is expedient to use a multiscale approach in an investigation and combine more than one texture technique (Section 12.4).

10

Orientation Microscopy and Orientation Mapping

10.1 Introduction

The concepts of orientation microscopy and orientation mapping were introduced in Section 1.2.3. *Orientation microscopy* refers to the automated measurement and storage of orientations according to a predefined pattern of coordinates on the sampling plane of the specimen. Once this basic information (orientation plus position) is stored, it can be processed and output in a numbers of ways, which is the topic of this chapter. The pictorial output of these orientations with reference to the sampling coordinates provides an *orientation map* of the spatial orientation distribution; that is, it derives the “orientation topography.”

Not only does an orientation map have great visual appeal, but it also gives access to fully quantified orientation statistics. In this chapter, we first consider the historical evolution of orientation mapping (Section 10.2) followed by some experimental aspects of orientation microscopy using EBSD (Section 10.3). The types of orientation mapping output and the information entailed are discussed in detail in Section 10.4, concentrating on application of orientation mapping to microtexture. Simple examples are used to show the basic types of microtexture parameters that are most commonly used in the maps to convey and depict aspects of the orientation topography. It should be emphasized that only a few examples, illustrating the main principles of orientation mapping to display microtexture, are shown. There are many more examples, of varying complexity, in the recent literature. The microtexture constituents in orientation maps are quantified and analyzed in the ways described in Chapter 9, and the examples show how the maps, or subsets of them, link to the statistical output.

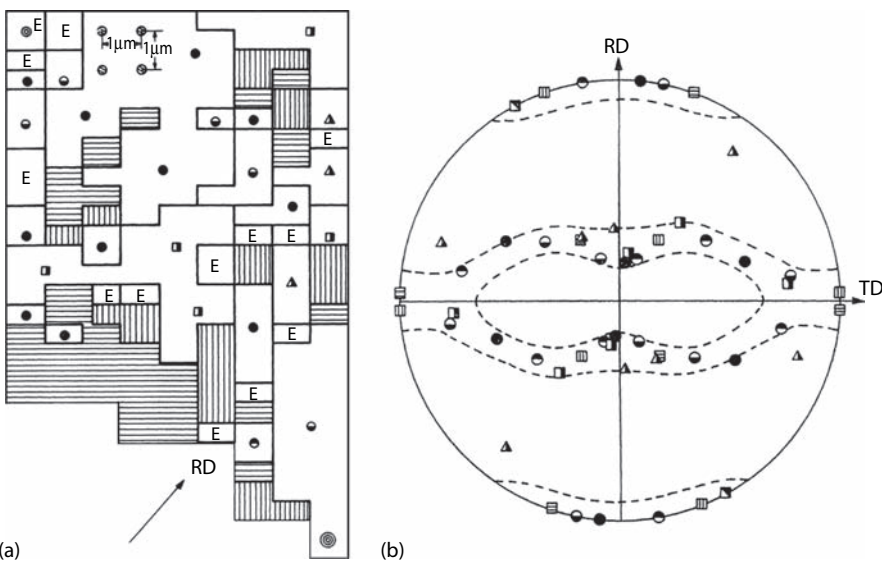
Orientation microscopy and orientation mapping are almost always based on EBSD in SEM. Some orientation microscopy techniques in TEM are also available, which are described briefly in Section 10.5. Less effort has been put into the development of orientation mapping in TEM than in SEM because there are limitations with the TEM approach and there are fewer applications than there are for SEM.

10.2 Historical Evolution

The practice of linking microstructure and orientation in a map has existed ever since individual orientation measurements have been made, although it has not been reported frequently. A typical procedure would have been to observe or record the grain structure, measure orientations of individual grains—usually one orientation per grain—then compile a map of the orientations (or grain boundary misorientations) superimposed on a diagram of the grain structure. Early examples of colored grain orientation maps derived by the Kossel technique (Section 7.2) were published by Inokuti et al. (1987). Although this method fulfilled the criterion of linking microstructure and orientation, the components of the microstructure and the orientations were first identified separately and then combined to produce a map. True orientation mapping takes a fundamentally different approach: Diffraction patterns are collected according to a grid, and the spatial arrangement of the orientations thus obtained constitutes directly the map.

To the best of the authors' knowledge, the first time a true orientation map was published was in the 1960s; the technique was referred to as *orientation topography* (Haefner et al., 1966). The maps, consisting of approximately 25 data points, were collected from rolled copper using SAD in the TEM, with a square grid spacing of 1.8 μm . All in all, 900 SAD diffraction patterns were photographed from 14 different areas of the material. Figure 10.1a shows one of the larger contiguous maps composed of 100 individual orientations together with a pole figure (Figure 10.1b) which provides an orientation key to the symbols used (Gotthardt et al., 1972). The map, which relied on manual diffraction pattern evaluation, is certainly crude but it does embody the fundamental orientation mapping principle of constructing a diagram of the microstructure based on orientation measurements collected on a regular grid-sampling schedule. Furthermore, each measurement encompasses quantification of the orientation, which is conveyed in this case by a pole figure.

Acquisition of a modern orientation map can only be achieved realistically by an automated system, that is, one in which both the sampling coordinates are located automatically and the diffraction patterns are solved automatically. For example, a square grid of 1 μm step sampling points measuring 100 $\mu\text{m} \times 100 \mu\text{m}$ requires 10^4 orientation measurements. The key stage in the development of orientation microscopy has been the provision of a reliable routine to solve diffraction patterns online, which was not achieved for EBSD patterns until the beginning of the 1990s (Section 6.3.3) and was achieved for TEM a few years later (Section 6.3.4). By the mid-1990s orientation mapping was realized as an extension to EBSD and various systems became commercially available.

**FIGURE 10.1**

(a) Early orientation map, collected manually in the TEM from rolled copper using a square grid size of 1 μm . The symbols on the map refer to the pole figure in (b). (Adapted from Gotthardt, R., Hoschek, G., Reimold, O., and Haefner, F., *Texture*, 1, 99, 1972.)

10.3 Orientation Microscopy

The principal issues concerning orientation microscopy by EBSD (i.e., the actual collection of the raw data to produce a map) are as follows:

- Mechanisms to locate sampling points (Section 10.3.1)
- Sampling schedule (Section 10.3.2)
- Data storage and output (Section 10.3.3)

10.3.1 Mechanisms to Locate Sampling Points

There is a choice of two basic approaches for location of the sampling spots on a specimen surface. Either the specimen is moved with respect to the stationary incident beam by means of a computer controlled specimen stage, that is, *stage control* (Adams et al., 1993), or the electron beam itself is deflected across the stationary sample surface, similar to conventional SEM, that is, *beam control* (Schwarzer et al., 1995).

Stage control can be realized by a high-precision specimen stage that positions the sample relative to the electron beam. In a modern computer-controlled

SEM, motorized sample motion is often a standard feature, so no additional hardware is required. The main advantage of stage control is its ease of performance. The sample is always located at the position for which calibration and focusing were derived, and so a constant beam–specimen–detector geometry is maintained, even for low magnifications. Despite this feature, stage control on its own is little used nowadays to locate sampling points because it is very slow compared to beam control operation.

Precise movement of the beam is achieved via algorithms in the EBSD software, which control the SEM deflection coils. The attraction of beam control is that the electron beam can be positioned much more precisely, and much faster, than by mechanical movement of the microscope stage. As the resolution of an SEM depends only on the spot size and not on the magnification, in principle large sampling areas can be scanned at low magnifications. However, scanning at low magnifications necessitates large deflections of the electron beam away from the image center. For regions well away from the image center the calibration of the EBSD setup is no longer accurate. Updating of the current calibration parameters can be accomplished by an automated calibration routine (Section 7.7.2) or, more easily, by interpolation of the parameters obtained for the start and end points of the scan. However, if the sampling area is limited to SEM images obtained at magnifications exceeding $\times 500$, focusing corrections are largely unnecessary. Because the specimen is highly tilted (e.g., 70°), the electron image of the sampling area is distorted and a dynamic focusing correction is applied to account for the foreshortening effect and to produce an undistorted map.

Considering the advantages and disadvantages of stage versus beam control, it turns out that the optimum solution for large maps is a combination of both. Using stage control the sample is positioned at the region of interest, whereupon diffraction patterns from within the field of view on the microscope screen in a specified step size are automatically acquired by movement of the beam. The specimen stage is then automatically moved to another user-defined region on the specimen and the process is repeated. If data acquired in this way are from contiguous regions on the specimen, the beam-scanned maps can subsequently be montaged in a postprocessing step. By this procedure, many beam-scanned maps can be stitched together to cover a wide area of specimen surface.

10.3.2 Sampling Schedule

The data for an orientation map are collected from a user-defined grid of regularly spaced sampling positions on the specimen. The lower limit of the grid step size is defined by the spatial resolution of EBSD; hence steps of down to $0.1\text{ }\mu\text{m}$ are typical in a tungsten filament SEM and approximately three times smaller in an FEGSEM (Section 7.6.1). However, it is important to select appropriately the step size of the grid, and the step size chosen will depend on the nature of the inquiry and effective use of resources. For

example, the spatial distribution of microtexture components in a region can be obtained by using a step size equal to the smallest grain size class, whereas a more detailed map, in terms of microstructure morphology, will require a smaller step size with respect to the grain size. Fine detail of subtle orientation shifts within grains also requires a small step size. However, an overview of the texture, equivalent to macrotexture, can use a larger step size (Section 9.3.3). Use of a step size that is too small is an inefficient use of resources because the map would take longer to complete than is necessary and would require excessive computer storage and postprocessing time.

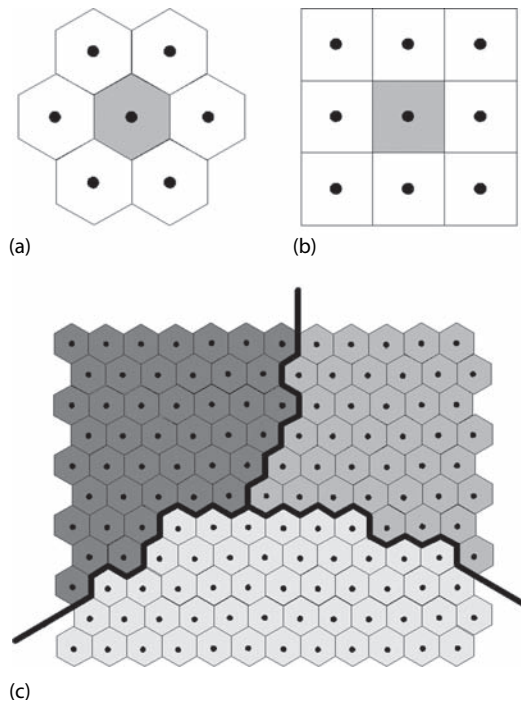
Choice of a pertinent step size usually involves both a certain amount of preliminary experimental work to gauge the scale of the microstructure and thoughtful consideration of the inquiry to make the best decision. For example, several maps of an area could be collected using different step sizes. Generally, the sampling area is scanned by a horizontal raster, and the orientation map builds up pixel by pixel as each orientation is measured. Stable microscope operating conditions should prevail while the orientation map is being collected.

Orientation microscopy methodology employs either a square or a hexagonal sampling grid. The hexagonal grid has the advantage that each measuring point has six nearest neighbors, whereas in a square grid four nearest neighbors plus four second nearest neighbors must be considered as shown in Figure 10.2. Furthermore, the hexagonal grid facilitates delineation of interfaces.

10.3.3 Data Storage and Output

After diffraction pattern indexing each sampling point is stored with its phase identity, orientation (usually as Euler angles), spatial coordinates, measure of fit or confidence index, and diffraction pattern quality metric(s). The phase identification and spatial coordinates of unsolved points are also recorded. The record file is usually in text format for potential input to a number of external packages such as various microstructural modeling applications. Diffraction patterns can also be stored for further offline analysis, for example, to rerun the indexing using different solve parameters. However, data storage issues can arise when large numbers of patterns are stored.

The data file can then be used to output a variety of user-defined map formats, as described in Section 10.4. It is important to realize that the orientation data that comprise the map are quantitative and usually accompanied by one or more statistical microtexture output, as described in Chapters 2 and 9. It may be appropriate to select all or only part of the orientation map for statistical output. For example, if all the data points are included, the microtexture thus obtained is weighted according to the projected grain area in the section plane—it represents “texture by volume.” If one orientation per grain is selected then the texture is weighted according to the number of grains (texture by number) (Section 9.2.2). Grain boundary misorientation

**FIGURE 10.2**

(a) Hexagonal grid and (b) square grid, where orientation microscopy sampling points have six and eight nearest neighbors, respectively. (c) Orientation microscopy recognition of a grain boundary as a region between neighboring pixels having an orientation difference greater than a preset value.

can be similarly treated. Also, a subset of the map can be selected for statistical output according to various user-defined factors such as a certain texture component or grain size. Examples are shown in the following section.

10.4 Orientation Mapping and Its Applications

Depending on the information that is being sought, the main applications of orientation mapping to microtexture can be categorized as follows:

1. Spatial distribution of microtexture components (Section 10.4.1)
2. Misorientations and interfaces (Section 10.4.2)
3. True grain size/shape distributions (Section 10.4.3)
4. Pattern quality maps (Section 10.4.4)
5. Phase maps (Section 10.4.5)

More complex parameters, such as Taylor factors or other user-defined functions such as geometrically necessary dislocations (GND) (El-Dasher et al., 2003) or r values (Huh et al., 2005), can also be displayed in orientation maps.

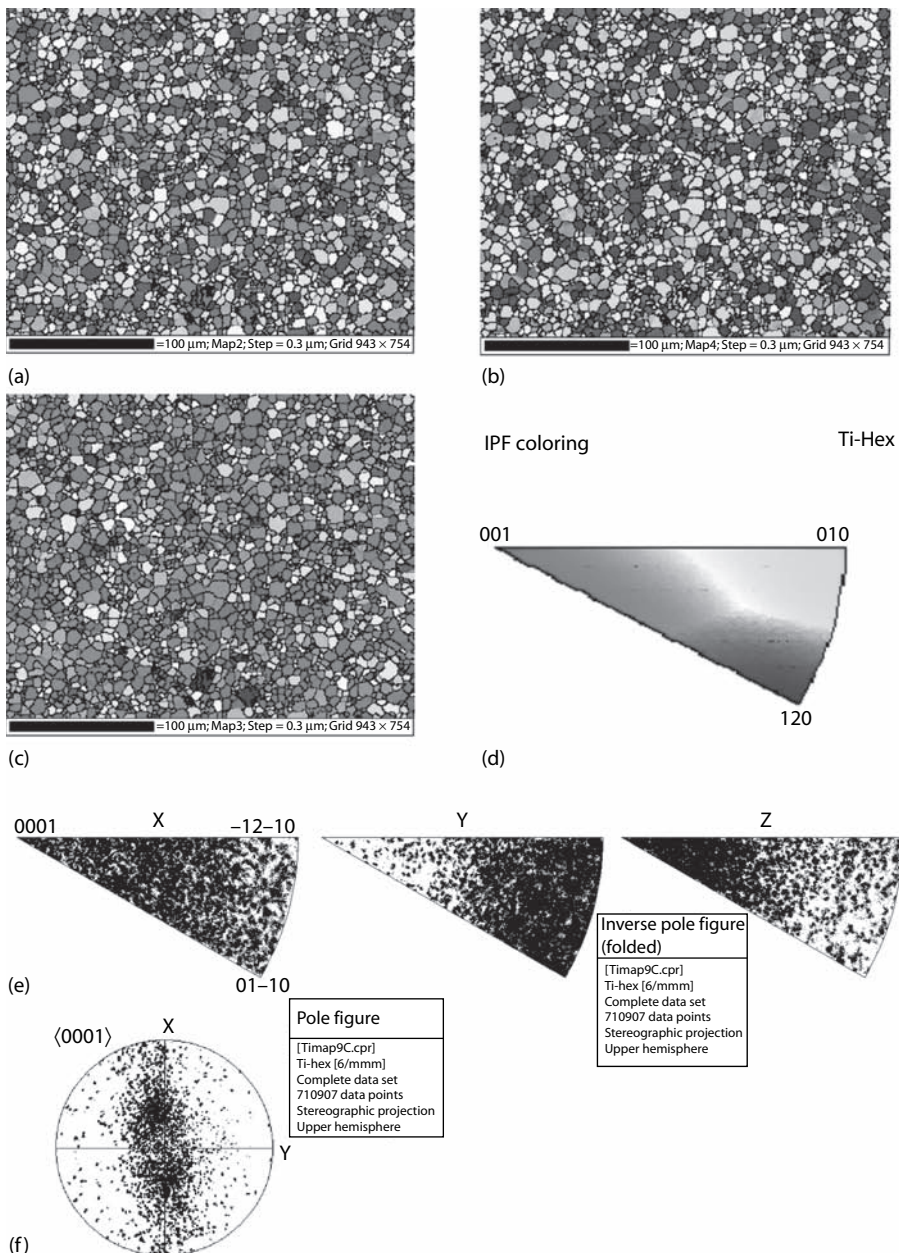
Various noise filtering or “cleanup” algorithms are used to reduce the number of null pixels in the map by extrapolating data into adjacent regions of poor pattern solve success, or by replacing single orientations that are obviously wrong. Reduced solve success will occur at grain boundaries, because two patterns might be sampled together or there is distortion in the sample volume, and because it is appropriate to use filter routines so that grain boundaries are displayed as continuous lines in maps. Use of cleanup routines should be carefully controlled to avoid introduction of artifacts into the data.

10.4.1 Spatial Distribution of Microtexture Components

Different texture components can be represented in a map using colors, gray scale, or patterns. This attribute is particularly useful for picking out the distribution of particular components with respect to grain size, shape, or position, for example, newly recrystallized grains in a deformed matrix or $\langle 111 \rangle$ grains with respect to their position within the steel sheet. Another area of interest since the advent of automated EBSD is the *connectivity* or grouping of orientations into spatially linked clusters (Larsen and Juul Jensen, 2003; Lewis et al., 2006). Orientation mapping indicates such clusters very graphically (Mason and Adams, 1994; Huh et al., 2005).

Color output is either linked directly to the orientation or user-defined. It is accompanied by a key to the use of colors. A popular output is based on assigning red, green, and blue to the 001, 011, and 111 corners, respectively, of the stereographic unit triangle for crystal directions that are parallel to a selected specimen direction. Note that, as for an inverse pole figure (Sections 2.5.2 and 9.2), this representation displays only one direction of the 3-D orientation information, and so rotations about this axis are not seen. For a complete interpretation, maps for one (or both) of the two other specimen reference directions can also be viewed. An example of this type of output is shown in Figure 10.3, which is an orientation map from commercially pure titanium in the specimen X, specimen Y, and specimen Z directions (Figures 10.3a through 10.3c, respectively). The stereographic unit triangle color key for the maps is included in Figure 10.3d. The microtexture data from the maps are represented as inverse pole figures from the X, Y, and Z direction maps in Figure 10.3e. Finally, Figure 10.3f shows the equivalent {0001} pole figure representation.

Euler angles (Section 2.6) or Rodrigues vectors (Section 2.8), each comprising three components, can be represented in maps by three colors. Only one map is necessary to display the full orientation distribution, rather than at least two maps, which is the case when the orientation color coding is linked

**FIGURE 10.3**

(See color insert following page 240.) Orientation map from commercially pure titanium in (a) the specimen X, (b) the specimen Y, and (c) the specimen Z directions. (d) Color key for the maps; (e) inverse pole figures from the X, Y, and Z directions; (f) $\langle 0001 \rangle$ pole figure.

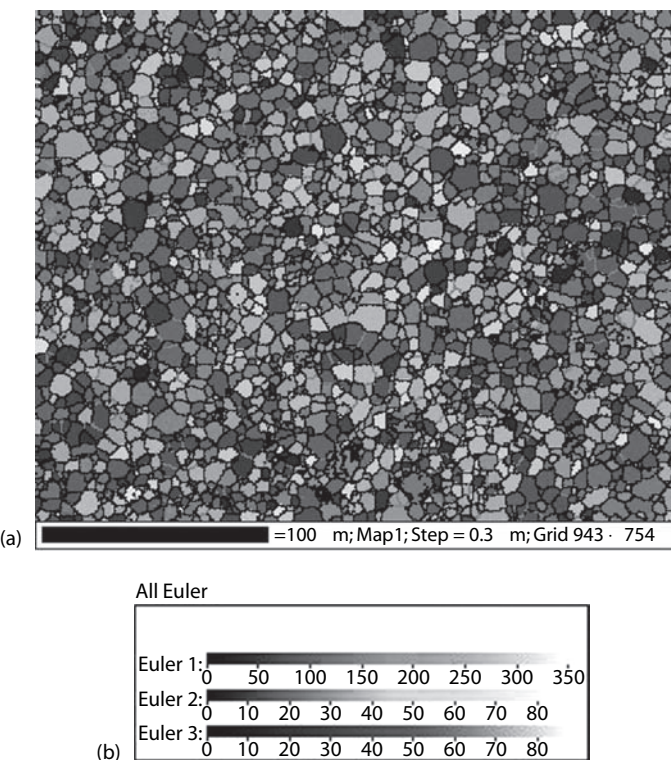


FIGURE 10.4
 (See color insert following page 240.) (a) Euler angle orientation map from commercially pure titanium. (b) Euler angle color key.

to the specimen direction as in Figure 10.3. Figure 10.4a is the same map as Figure 10.3, but displayed with Euler angle coloring. The map is accompanied by a color key for the Euler angles (Figure 10.4b).

There is a very wide range of user-defined choices for depicting various microtexture subsets on maps. For example, choices can be based on a particular texture parameter, a grain size range, or both. These examples are illustrated by orientation maps obtained from silicon iron. Figure 10.5a shows an orientation map from silicon iron with grains colored blue if the specimen Z (normal) direction is $<20^\circ$ from $\langle 111 \rangle$, which comprises 45% of the map area. The depth of color diminishes with increasing deviation from exact $\langle 111 \rangle$. High-angle grain boundaries are depicted by black lines and low-angle grain boundaries by gray lines. Figure 10.5b is the $\{111\}$ pole figure from the entire map in Figure 10.5a, shown as density contours.

Figure 10.6a shows another orientation map from silicon iron where large grains have arisen from abnormal grain growth. Here, the user-defined color

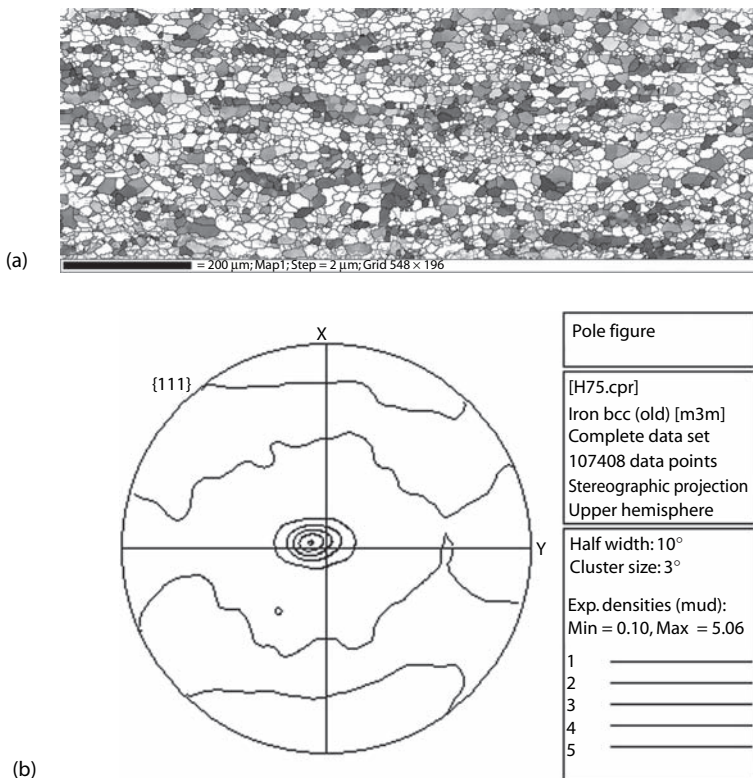
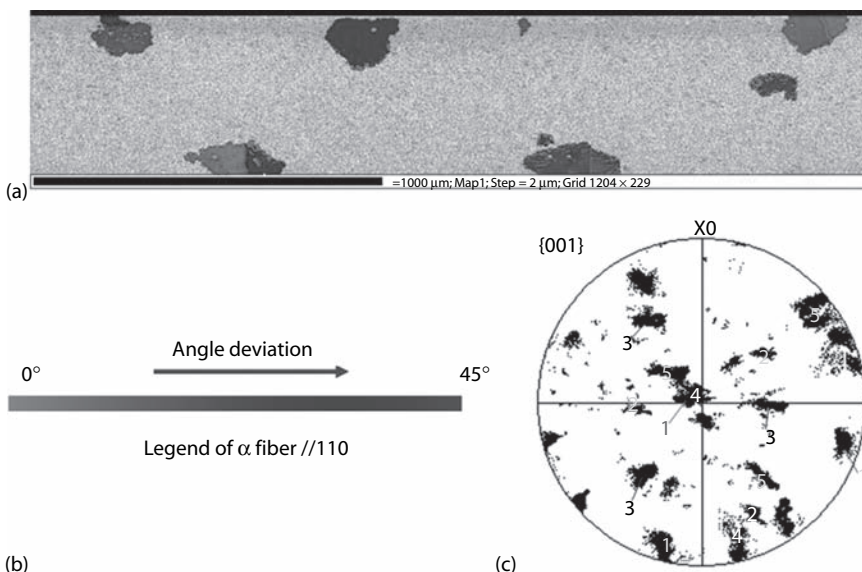


FIGURE 10.5

(See color insert following page 240 for Figure 10.5a.) (a) Orientation map from silicon iron showing grains colored in blue if the specimen Z (normal) direction is $<20^\circ$ from $\langle 111 \rangle$. The depth of color diminishes with increasing deviation from exact $\langle 111 \rangle$. High-angle grain boundaries are depicted by black lines and low-angle grain boundaries by gray lines. (b) $\{111\}$ Pole figure from the map in (a), shown as density contours. The rolling direction is horizontal (parallel to the specimen X direction).

key (Figure 10.6b) refers to proximity to the “ α fiber,” that is, $\langle 110 \rangle$ parallel to the direction of rolling during processing (Section 5.5.2). Red depicts the exact α fiber, changing to blue for orientations having the maximum deviation from the α fiber, that is, 45° . The $\{001\}$ pole figure is shown in Figure 10.6c. The pole figure is linked to the map via numbering of the data points associated with large grains.

Orientation mapping has highlighted that, although a grain is defined as a unit of microstructure having a single orientation, in reality it has an *average* orientation since even undeformed materials may show some lattice curvature close to grain boundaries, and deformed grains exhibit a whole range of substructures that are accompanied by orientation shifts. Orientation mapping with a very small step size provides a means of studying these orientation perturbations (Adams et al., 1993; Bastos et al., 2006; Sandim et al., 2007). The results of such studies help to pinpoint mechanisms of strain

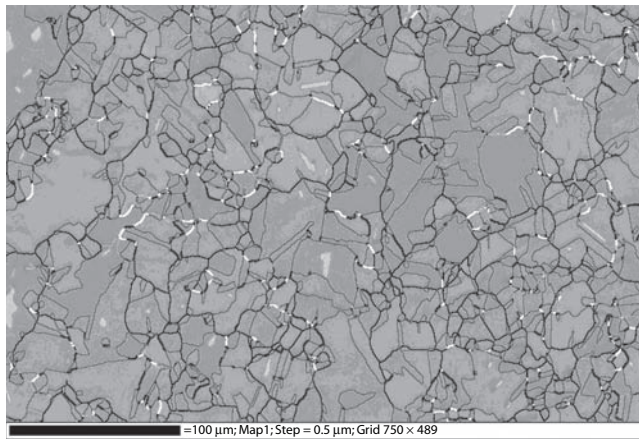
**FIGURE 10.6**

(See color insert following page 240.) (a) Orientation map from silicon iron showing large grains (numbered) arising from abnormal grain growth. (b) User-defined color key for the map in (a); grains are colored according to proximity to the “ α fiber,” that is, $\langle 110 \rangle$ parallel to the rolling direction. Red depicts the exact α fiber, changing to blue for orientations having the maximum deviation from the α fiber (45°). (c) $\{001\}$ Pole figure showing the orientations of the large grains, numbered accordingly, in (a). The rolling direction is horizontal (parallel to the specimen X direction).

accommodation, which in turn have a large influence over a wide range of thermomechanical processes, including commercial fabrication of materials, and geological studies. For example, a new parameter, called the “modified crystal deformation,” has been defined to quantify the spread of crystal orientation within individual grains arising due to dislocation accumulation during plastic deformation (Kamaya et al., 2006).

10.4.2 Misorientations and Interfaces

Regions of orientation change are immediately obvious in a standard orientation map because they are associated with a color change. The presence of these orientation changes is enhanced if a line is drawn between all neighboring points where the misorientation exceeds a certain value, as shown schematically in Figure 10.2c. Often, a black line is chosen if the misorientation exceeds 15° to denote a high-angle boundary; a low-angle boundary can then be depicted by a gray line or a thinner line, as shown in Figure 10.7. Phase boundaries can be represented similarly (Section 10.4.5). Alternatively, misorientation axes can be shown rather than misorientation angle ranges (Schwarzer, 1997a). Intragrain variations can also be represented. Often these

**FIGURE 10.7**

(See color insert following page 240.) Orientation map made from an austenitic steel showing various grain boundary misorientation types. High-angle grain boundaries are depicted by black lines and low-angle grain boundaries by gray lines. Σ_3 , Σ_9 , and Σ_{27} boundaries (in CSL notation) are colored red, blue, and yellow, respectively. The background to the map is shaded gray according to a diffraction pattern quality parameter.

are displayed as a misorientation profile along a specific line in a map, typically in a deformed region (Sandim et al., 2007) (Section 9.5.2). If small misorientations between neighboring pixels are mapped, typically $\sim 2^\circ$, it is possible to represent the local deformed state of the microstructure (Randle et al., 1996; Bastos et al., 2006).

Selected special grain boundary types such as low-angle boundaries or CSL (or Σ) boundaries (Section 11.2.1) can be assigned particular colors in a map. Similarly to orientation connectivity, the linking of certain boundary types is then apparent. Figure 10.7 is an orientation map from austenitic steel showing various grain boundary types. High-angle grain boundaries are depicted by black lines and low-angle grain boundaries by gray lines. Σ_3 , Σ_9 , and Σ_{27} boundaries (in CSL notation) are colored red, blue, and yellow, respectively. The background to the map is shaded gray according to a diffraction pattern quality parameter. Use of orientation maps to depict orientation changes at interfaces, and other aspects of interface crystallography, represents a substantial application of EBSD and is described in detail in Chapter 11.

10.4.3 True Grain Size/Shape Distributions

Grain size distribution statistics can be readily computed by the EBSD software via the recognition of grain boundaries and hence grains. The map is digital and can therefore be input directly to various image analysis routines.

Because it relies only on crystallographic characterization to determine a grain rather than etching or other traditional methods, the orientation map has the capacity to replace optical microscopy for characterization of grain size. Microtexture measurements can hence also be linked to grain size. For example, the effect of second-phase particles on the rate of grain refinement has been studied by EBSD in an aluminum alloy (Apps et al., 2003). A weaker texture was found in the particle-containing alloy than in a similar alloy without particles. The link between grain size and texture has also been investigated by EBSD in a friction-stir processed Mg–Al–Zn alloy (Wang et al., 2006).

The misorientation used to define a high-angle and a low-angle grain boundary from an orientation map is user-defined and will affect the grain size calculation. Typically, a high-angle boundary has a misorientation of more than 15°. A more subtle consequence of use of orientation mapping to define grains is that the specification of a “grain” in the orientation map is based on the orientation of neighboring points being within a certain, small, tolerance of each other. However, the cumulative spread of orientation within a grain can be relatively large, especially for deformed materials (Kamaya et al., 2006).

10.4.4 Pattern Quality Maps

Besides the orientations of the individual sampling points, EBSD systems provide a numerical estimate of the pattern blurredness or image quality (Section 6.4). To display this information in a map, the available range of gray scale values (typically 256) is normalized to the range of image quality values in the given map, so that unindexed points are shaded dark and increasing brightness indicates increasing pattern quality. Color can be used instead of gray scale, although gray scale is a popular choice. Patterns obtained at grain and phase boundaries are typically characterized by poor pattern quality and hence appear as dark lines in the map. The pattern quality index may be different for different phases in a specimen, which can sometimes be exploited to distinguish between phases having the same crystal structure (Petrov et al., 2007). An additional advantage of the pattern quality map is that the pattern quality can be displayed even if the pattern cannot be indexed subsequently. Figure 10.7 includes both image quality shading and grain boundary types. Figure 10.8a shows an image quality map obtained in a two-phase nickel–tungsten material, displaying well the different microstructural features. The bcc tungsten phases generally have different pattern qualities than their surroundings but, as mentioned in Section 6.4, differently oriented grains of the nickel matrix may also depict differences in pattern quality, so that various grains and phases can readily be distinguished. Furthermore, patterns obtained at grain and phase boundaries are typically characterized by poor pattern quality and hence appear as dark lines in the map.

The representation using pattern quality is of particular interest for deformed materials. A degradation of pattern quality within a single phase is an indication of lattice strain. Although not a widespread application of EBSD, analyses connected with lattice strain are noteworthy because they allow insights into deformation and some other physical characteristics of materials. Some aspects of strain-related exploitation of EBSD have

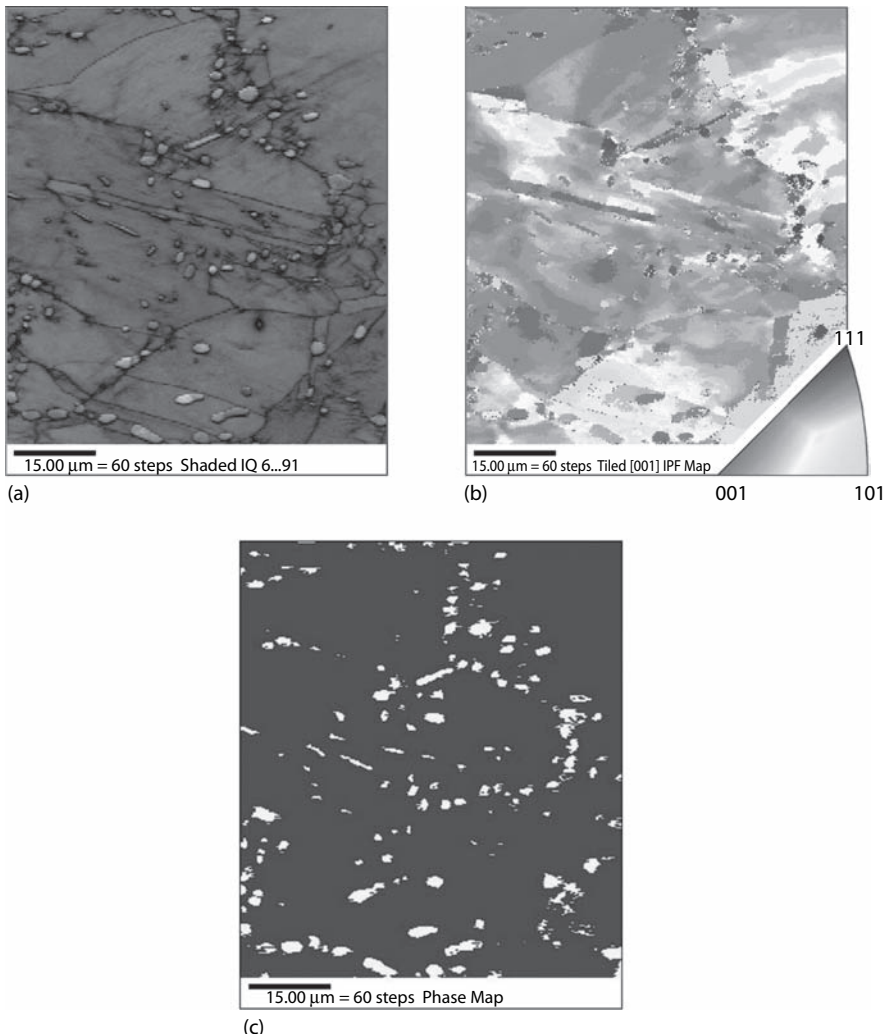


FIGURE 10.8

(See color insert following page 240.) EBSD analysis of a mildly deformed two-phase nickel-tungsten specimen. (a) Image quality map (darker shading corresponds to poorer image quality. Note that grain and phase boundaries are not specially marked, but show up due to their low image quality.); (b) orientation map; (c) phase map (blue—nickel; yellow—tungsten). (Data taken from Sinclair, C.W. et al., *Mater. Sci. Technol.*, 19, 1321, 2003.)

concentrated on visualization of plastic deformation or measurement of dislocation content. An algorithm has been developed to map plastic deformation, which has been used to study deformation zones around high strain gradient microstructural features such as crack tips and indentations in an austenitic steel (Brewer et al., 2006). Analysis of grain boundary maps or misorientation gradient maps has been adapted to connect the observed deformation with the local density of GND. The long-range accumulation of dislocations near grain boundaries has been obtained by this method (El-Dasher et al., 2003). Another approach to visualization and quantification of strain involves the average orientation deviation angle approach (Field et al., 2005).

As far as microtexture analysis is concerned, the pattern quality parameter can be a means of distinguishing recrystallized grains from unrecrystallized grains on the basis of good and poor pattern quality, respectively. Subsequently, the microtexture of the recrystallized and unrecrystallized fractions can be measured separately (Džubinský et al., 2004; Wagner et al., 2002). The pattern quality parameter is also used to separate out phases that have the same or similar crystal structures for subsequent microtexture determination. For example, bcc ferrite and bainite have been distinguished by measurement of image quality and confidence index in undeformed steel specimens (Petrov et al., 2007).

10.4.5 Phase Maps

Microtexture can be determined simultaneously from known phases in multiphase materials. Section 7.6.4 described dedicated phase identification by EBSD. Orientation mapping and microtexture determination when applied to multiphase materials require some additional considerations regarding the simultaneous automatic pattern recognition of two or more phases (Field et al., 1996). These issues include the following:

- The “background” diffraction signal may vary for each phase, which can be addressed by various hardware or software solutions.
- The computer algorithm needs to recognize correctly each phase. To search simply for the “best-fit” solution may have an unacceptable time penalty, and so a “confidence index” approach may be used. This requires some preliminary work to assess the confidence index parameters of each phase in the material.
- Multiphase materials where the phases have the same crystal structures can only be analyzed with the help of other parameters such as pattern quality (Section 10.4.4).
- Specimen preparation of multiphase materials, where the constituent phases polish at different rates, may be more complicated than that of a single-phase matrix.

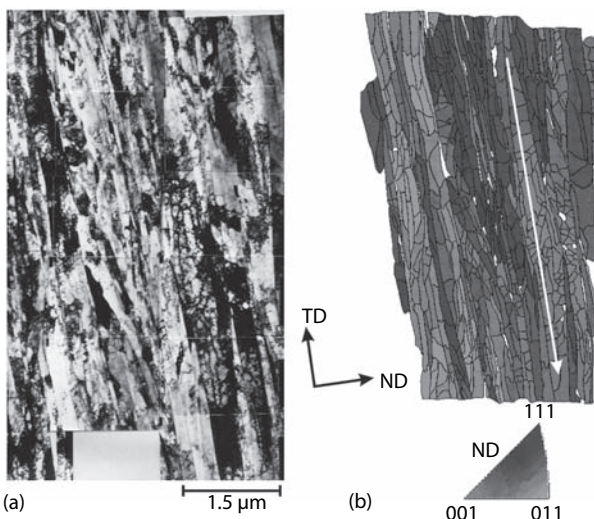
Various steels and titanium alloys are typical examples of multiphase systems that have been analyzed by EBSD orientation mapping (Schwarzer et al., 2000; Seward et al., 2004; Garzón and Tschiptschin, 2006). Not only is the microtexture of each phase obtained, but the output is a potent tool in the study of phase transformations (Gourgues-Lorenzon, 2007).

As an example, Figure 10.8 shows three different orientation microscopy maps obtained in a two-phase nickel–tungsten material, namely, an image quality map (Figure 10.8a; Section 10.4.4), an orientation map (Figure 10.8b), and a phase map (Figure 10.8c). As for the latter, orientations that could better be indexed for fcc crystal structure—those that are more likely to belong to the nickel—are colored blue, whereas the bcc orientations (i.e., tungsten) are colored yellow. Furthermore, high-angle boundaries are marked with black lines. This representation displays well the topographic arrangement of the two phases, and estimates the respective volume fractions. In the present example, it turns out that the minority component, the tungsten, is situated preferentially at the nickel grain boundaries (Sinclair et al., 2003). The phase orientation relationship between the two phases can also be determined, which is addressed in Section 11.5.

10.5 Orientation Microscopy in the TEM

TEM diffraction patterns can be solved automatically online, which is discussed in detail in Section 6.3.4 (Zaefferer and Schwarzer, 1994; Weiland and Field, 1994; Krieger Lassen, 1995; Engler et al., 1996a; Zaefferer, 2000). An orientation map can be acquired by several methods, as described in the following text. SEM methods relying on application of a Hough transform for Kikuchi line detection can be adapted for TEM (Krieger Lassen, 1995; Schwarzer, 1997b; Schwarzer and Sukkau, 1998; Fundenberger et al., 2003, 2005). However, difficulties are encountered, mainly because the background varies across the diffraction pattern, diffraction spots are superimposed on the pattern, and excess/defect (bright/dark) Kikuchi bands have to be considered. Another problem arises from the TEM drift during the measuring time. At a rate of 10 orientations per second, the time to produce a map with sufficient data points, say 65,000, is of the order 2 h; during this time a sample in the TEM is likely to drift by 100 nm (Dingley, 2006).

Another group of techniques is based on the analysis of spot diffraction patterns. The SCBED technique analyzes spot patterns, both position and intensity, from very small volumes of crystal (Zaefferer, 2002; Section 8.3.3). Figure 10.9 displays an application of this procedure, taken from a study on the mechanisms of nucleation of recrystallization in heavily deformed Fe–36% Ni (Zaefferer et al., 2001). The TEM micrograph of the 94% cold-rolled material shows regions with dislocation cells and others with thin and

**FIGURE 10.9**

(See color insert following page 240.) Example of orientation microscopy in the TEM. (a) TEM micrograph of Fe-36% Ni deformed 94% by cold rolling (longitudinal section, i.e., ND-TD plane); (b) orientation map of (a). The colors correspond to crystal directions parallel to the normal direction (ND) of the sheet. (From Zaefferer, S., Baudin, T., and Penelle, R., *Acta Mater.*, 49, 1105, 2001. With permission.)

elongated lamellae and microbands (Figure 10.9a). The orientation map shows that the dislocation cell structure appears in cube-oriented grains, whereas crystals with orientations typical for the deformed state show lamellae and microbands (Figure 10.9b). An offshoot of the SCBED technique uses template matching for accelerated pattern indexing (Rauch and Dupuy, 2005; Rauch and Duft, 2005). This technique uses a comparison of the experimental pattern with precalculated template patterns to find the correct crystal orientation.

Fully automated orientation microscopy in the TEM—by analyzing either Kikuchi patterns or SAD point patterns—requires the automatic translation of the electron beam across the (stationary) specimen in regular steps (Section 10.3). In the TEM, the beam can be directed across the sampling area by the current in the beam-deflecting coils, which is controlled through the computer (Kunze et al., 1994).

The final group of techniques, which at present is the most commonly used, is partly based on earlier work (Schwarzer, 1983; Humphreys, 1983; Section 8.3.2) to reconstruct spot diffraction patterns from dark field images obtained by conical scanning of the primary beam (Wright and Dingley, 1998; Dingley, 2006). This technique is particularly interesting for TEM orientation microscopy as it is very quick and is capable of very high resolution. The technique is based on the fact that, for a given incidence angle of the primary electron beam onto the specimen, those crystals that are in a Bragg

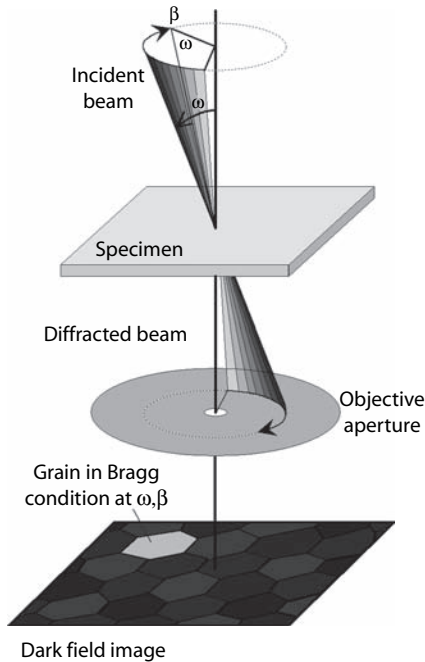


FIGURE 10.10

Illustration of the conical scan technique developed by Wright and Dingley (1998) and Dingley (2006). The primary electron beam is conically scanned to cover all possible beam incidence angles ω and β , and the related dark field images are recorded. For a given incidence angle of the electron beam, those crystals that are in a Bragg reflection position light up in the corresponding dark field image. From the intensities in the dark field images, the spot diffraction patterns that would have been obtained at these positions can be reconstructed.

reflection position light up in the corresponding dark field image. The parallel primary beam is now conically scanned to cover all possible beam incidence angles and the related dark field images are recorded (Figure 10.10). From the intensities obtained at each pixel position in these dark field images, the spot diffraction patterns that would have been obtained at these positions can be reconstructed. The reconstruction process is regarded as an inversion of the ray path of an SAD pattern. In SAD patterns the sample is illuminated from one direction and the electrons are diffracted by the crystal according to Bragg's law (Section 8.3.1). However, in the conical scan technique the sample is illuminated successively from different directions and only those electrons fulfilling Bragg's law contribute to the dark field image.

All positions of a given observation area are recorded simultaneously in dark field image series; therefore the technique is very robust against drift problems. Most of the analysis (i.e., reconstruction and indexing of the patterns) can be done offline, which considerably reduces the measurement

time in the TEM. In total some 5000 images are recorded in approximately 15 min (Dingley, 2006). The resolution is restricted only by the resolution of the dark field image and the pixel resolution of the recording camera. However, due to misalignment of the microscope, the area illuminated on the sample will always change slightly with the variation of the beam incidence angle and deteriorate the actual resolution.

10.6 Summation

Orientation mapping has opened up many new possibilities for microtexture investigations of materials, and indeed microstructure characterization in general. Its central strengths are as follows:

- The *visualization* aspect of orientation mapping is a compelling feature. The type of map is selected by the operator: orientations, grain boundary parameters, strain (from pattern quality), or combinations of these.
- The most significant merit of orientation mapping is that it embodies total *quantification* of the orientation aspects of microstructure, which complements the visual appraisal aspects. Hence, microtexture or grain boundary statistics can be accessed from a map and represented by the methods described in Chapter 9.
- Orientation mapping offers the ability to *compact* into one data set measurements that had previously been obtained by disparate methods (e.g., grain structure, texture distributions, and grain boundary types) or indeed had been virtually inaccessible (e.g., maps of local deformation within grains). Hence the need for elaborate correlation techniques between various separately determined parameters is obviated.
- The *speed* of data acquisition has impacted on the popularity and usefulness of orientation mapping, as described in Chapter 7.
- The *morphology* of grains is depicted using orientation mapping, which allows a direct measure of the true grain size and distribution on the particular section through the microstructure. This feature is especially relevant to materials whose grain interfaces are difficult to observe in an image (e.g., low-angle or “special” boundaries), such as superconductors, which are unresponsive to etchants, and aluminum, whose microstructures are best revealed by deposition processes such as anodizing, which is unsuitable for EBSD.
- The information contained in an orientation map depends on the *scale of the measurements* and the nature of the inquiry, both of which

are under operator control. For example, the basic microtexture distribution in a specimen can be obtained by using a sampling step size of the order of the smallest grains over a region encompassing many grains, whereas fine details of orientation shifts close to grain boundaries can be studied in the same region of the specimen by preparing a map that has a much smaller step size, typically one-tenth of the grain size. By collecting an orientation map in an FEGSEM very fine-scale microstructure can be mapped, to encompass nanocrystalline materials and deformed states.

11

Crystallographic Analysis of Interfaces, Surfaces, and Connectivity

11.1 Introduction

A spin-off to the spatial specificity of microtexture measurements is that planar surfaces or facets can be analyzed in some crystallographic detail. These surfaces include grain boundaries, phase boundaries, slip traces, cracks, and external surfaces of the specimen, such as facets or fracture surfaces. Although grain/phase boundaries and slip traces can be analyzed in TEM, there are considerable disadvantages, mainly in terms of statistical reliability. Furthermore, analysis of cracks or external specimen surfaces is not possible in TEM because of specimen preparation restrictions. However, SEM is ideal for studying the morphology of surfaces and so it is mainly EBSD that has been adapted to crystallographic studies of surfaces.

Application of EBSD to interfaces has allowed the misorientation of grain boundaries to be characterized for large sample populations of boundaries. Typically such characterization has been linked to evolution of the misorientation distribution as a consequence of processing or properties (Tan et al., 2007). Representation of grain and phase boundaries in terms of misorientation alone is achieved via the usual orientation parameters, namely, the Euler angles, angle/axis pair, or Rodrigues vector (Chapter 2). The CSL model is used widely as a characterization tool (Section 11.2.1). Over the past decade or so a research area known as Grain Boundary Engineering (GBE) has emerged. GBE aims to use processing regimes to alter the crystallography of grain boundaries to achieve better properties. The development of EBSD and orientation mapping has been a key driver in this area because it has allowed the routine collection of statistically significant quantities of misorientation data (Randle, 2004, 2007).

Five independent variables are required to specify the crystallographic orientation of a surface, whereas the misorientation supplies only three. Section 11.2.2 describes these five parameters and the relationship between them. Knowledge of all five parameters is required to specify a plane or surface in the specimen. A full analysis of a planar surface requires spatial information, in addition to the grain orientation, to calculate the crystallographic

indices. The various methodologies in connection with such investigations are described in detail in Section 11.3. These methodologies include some relatively new extensions of EBSD, such as the “five-parameter” stereological method and focused ion beam (FIB) tomography, which are not yet mainstream applications in commercial EBSD packages as is the case for studies involving only orientations and misorientations.

Sometimes it is pertinent to examine how the various orientations and misorientations are connected in the microstructure. This is discussed in Section 11.4. Finally, the topic of Orientation Relationships (ORs) between phases is discussed in Section 11.5.

11.2 Crystallographic Analysis of Grain Boundaries

In this section we describe the theoretical aspects of grain boundary crystallographic analysis.

11.2.1 The Coincidence Site Lattice

The categorization of grain boundary misorientations as angle/axis pairs is often supplemented by further classification according to the CSL model, especially for cubic materials. This is the most commonly used classification tool for grain boundaries in cubic materials, although there is increasing realization that it is simply a geometrical model and is only linked to grain boundary properties in certain cases. It owes its popularity both to convenience, since the analysis is easy to apply, and to the fact that *some* CSLs (Randle, 1996, 2001) may be the so-called special boundaries, that is, those often having beneficial properties associated with them, such as resistance to intergranular degradation, which is a major cause of component failure in service.

A “coincidence plot”—the interpenetration of two lattices of the same crystal structure as shown in Figure 11.1—is the most visual way to illustrate the concept of a CSL. For certain discrete misorientations between interpenetrating lattices a proportion of lattice sites will coincide, forming a periodic superlattice in three dimensions (Grimmer et al., 1974). The parameter Σ is the volume ratio of the unit cell of the CSL to that of the crystal lattice, or equivalently Σ is described as the reciprocal density of coinciding sites. In Figure 11.1b, one in five lattice sites are coinciding, so this is described as a $\Sigma 5$ relationship. The actual grain boundary surface or *boundary plane* itself is realized as a plane running through the CSL, as shown in Figure 11.1a. On average, the plane will intercept 1 in Σ atoms. $\Sigma 3$ boundaries, of which annealing twins are a subset, are of especial significance because they are ubiquitous in some materials and they are very strongly associated with special properties (Lin et al., 1995; Randle, 2004).

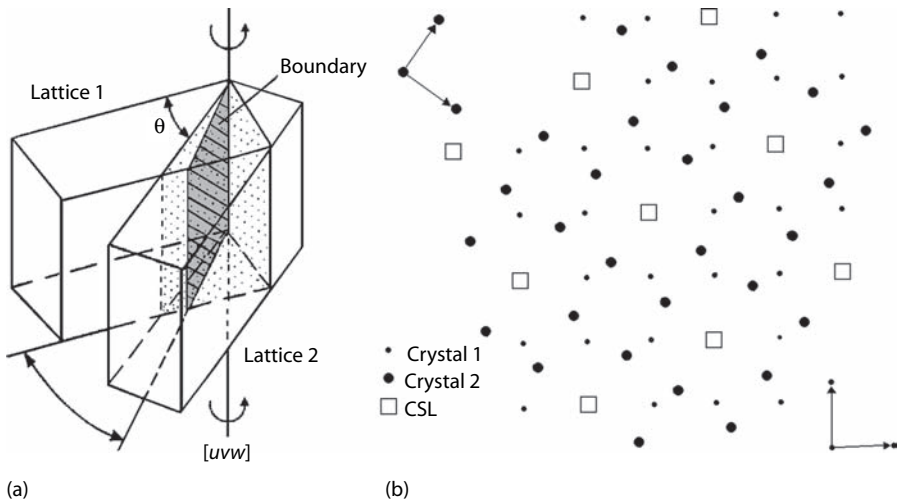


FIGURE 11.1

Formation of a coincidence site lattice (CSL) boundary. (a) Notional interpenetration of two neighboring lattices misoriented by θ/uvw , where θ and uvw are the angle and axis of misorientation, respectively (for simplicity, a tilt boundary is represented). (b) 2-D representation of a lattice interpenetration showing how a misorientation of $36.9^\circ/\langle 100 \rangle$ leads to the creation of a $\Sigma 5$ CSL; that is, one in five lattice sites from each crystal coincide.

The requirement for a CSL analysis of a population of misorientations is to identify all misorientations that are “close to” low- Σ CSLs in terms of an angular deviation. The structural analogies between low-angle boundaries and CSLs led to the adoption for the CSL case of the following well-known Read–Shockley relationship, which links the dislocation density d in the boundary with the Burgers vector b and the angular misorientation δ :

$$\delta = \frac{b}{d} \text{ (low angle)} \quad (11.1a)$$

$$v_m = \frac{b}{d} \text{ (CSL)} \quad (11.1b)$$

Thus, v_m , the maximum deviation from an exact CSL, corresponds to the highest density of dislocations possible in the boundary. The density of dislocations that can be accommodated in a CSL is related to its periodicity, Σ . The variation of v_m with Σ is usually taken to be as $\Sigma^{-1/2}$, called the *Brandon criterion*, which corresponds to a relationship based on periodicity alone (Brandon, 1966). Hence

$$v_m = v_0 \Sigma^{-1/2} \quad (11.2)$$

where v_0 is a proportionality constant based on the angular limit for a low-angle boundary, which is typically 15° . If $\Sigma = 1$ is substituted into

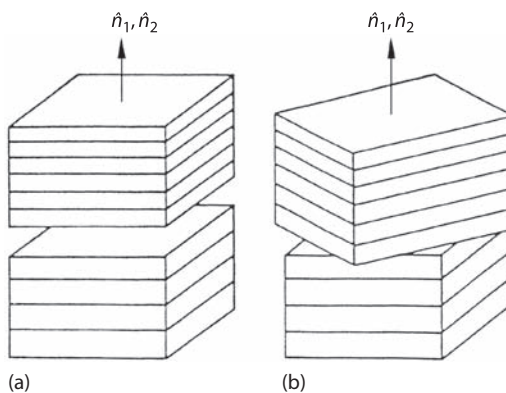
Equation 11.2, v_m is 15° , which is the low-angle boundary limit. Hence a low-angle boundary can be described as $\Sigma 1$. The Brandon criterion has been adopted almost universally for deciding v_m . Although other criteria exist for v_m and arguably the Brandon criterion may not be the most accurate descriptor on a physical basis, for reasons mainly of consistency between investigations it is used almost universally as the CSL deviation cutoff. Another criterion suggests a narrower $\Sigma^{-5/6}$ dependency (Palumbo and Aust, 1992).

As for all other aspects of microtexture analysis, both statistical and spatial information regarding CSLs needs to be available for a full interpretation of the data. The statistics of CSLs, either as numbers of boundaries or weighted according to projected grain boundary length, can be conveniently displayed in angle/axis space or Rodrigues space (Section 9.6; Figure 9.19) or as frequency distributions according to Σ value. Although CSLs can also be displayed in the asymmetric domain of Euler space (Zhao and Adams, 1988), this method is cumbersome compared to other methods and so is little used. Orientation mapping allows connectivity between various CSLs to be evaluated according to numbers, grain boundary projected length, and grain boundary type (Section 10.4.2).

More information on CSL formalism and application to materials can be found elsewhere (Brandon, 1966; Grimmer et al., 1974; Aust, 1994; Gertsman, 2001a), as can details of other grain boundary descriptors such as the O-lattice (Bollmann, 1970). These are not included here because the CSL is by far the most popular method for grain boundary misorientation analysis. The CSL model can be applied directly to cubic materials and modified according to the “near” or “constrained” CSL for application to materials having more complex crystal structures (Chan, 1994).

11.2.2 The Interface–Plane Scheme

A more advanced method of grain boundary analysis, which usually includes CSL classification, focuses on crystallographic analysis of the grain boundary plane. Five degrees of freedom are required to specify the boundary, and these are most familiarly approached from the angle/axis of misorientation viewpoint, sometimes including the boundary plane expressed in one grain. An alternative viewpoint is to use 4° of freedom to specify the Miller indices or direction cosines of the boundary plane in the coordinate systems of both interfacing grains and 1° of freedom to specify the twist angle Φ of both plane stacks normal to the boundary plane, as illustrated in Figure 11.2. This is known as the *interface–plane scheme* for describing grain boundary crystallography (Wolf and Lutsko, 1989; Wolf, 1992). The interface–plane scheme is particularly powerful for CSL boundaries where it is especially relevant to identify tilt and twist components, since these types are thought to have lower free volumes than

**FIGURE 11.2**

Notional formation of a grain boundary by the joining of plane stacks from adjacent grains, that is, the interface-plane scheme. (a) An asymmetrical tilt boundary; (b) an asymmetrical twist or general boundary. (Courtesy of D.P. Wolf.)

boundaries having a totally random structure. Four classes of boundaries are identified:

- $\{h_1k_1l_1\} = \{h_2k_2l_2\}$ and $\Phi = 0$; a symmetrical tilt grain boundary (STGB)
- $\{h_1k_1l_1\} \neq \{h_2k_2l_2\}$ and $\Phi = 0$; an asymmetrical tilt grain boundary (ATGB)
- $\{h_1k_1l_1\} = \{h_2k_2l_2\}$ and $\Phi \neq 0$; a twist grain boundary (TWGB)
- $\{h_1k_1l_1\} \neq \{h_2k_2l_2\}$ and $\Phi \neq 0$; a general or random boundary

where $h_1k_1l_1$ and $h_2k_2l_2$ are the indices of the boundary plane expressed in the coordinate systems of both interfacing grains, grain 1 and grain 2, respectively. The tilt and twist boundaries are described in more detail in Sections 11.2.2.1 and 11.2.2.2.

11.2.2.1 Tilt Boundaries

A tilt boundary has the tilt axis parallel to the axis of misorientation. An STGB has planes from the same family (i.e., the same form of Miller indices) on either side of the boundary, whereas an ATGB has different plane types interfacing the boundary. Both of these tilts are recognized in the interface-plane scheme by $\Phi = 0$. For a particular CSL there are up to two STGBs; for example, the $\Sigma 3$ system has STGBs on $\{111\}$ and $\{211\}$. There are an unlimited number of ATGBs, although it is practical to consider only those with planes having low Miller indices.

If $\Phi = 0$ and $\{h_1k_1l_1\}, \{h_2k_2l_2\}$ are different but commensurate, the boundary is an ATGB. A commensurate boundary arises when the ratio of the planar grain boundary unit cells is an integer G . The planar grain boundary unit cell area is proportional to the separation of planes parallel to the boundary. G is

therefore given by the square root of the ratio of the sum of the squares of the Miller indices. For example, {751} and {111} are commensurate planes because

$$G = \left(\frac{(7^2 + 5^2 + 1^2)}{(1^2 + 1^2 + 1^2)} \right)^{1/2} = 5 \quad (11.3)$$

that is, an integer. These two planes constitute an ATGB in the $\Sigma 5$ system.

Since a CSL can give rise to two STGBs at the most but many ATGBs, this is one of the reasons why ATGBs have been found to be ubiquitous in polycrystals.

11.2.2.2 Twist Boundaries

A TWGB has the twist axis perpendicular to the axis of misorientation, and is characterized by the condition $h_1 k_1 l_1 = h_2 k_2 l_2$ and $\Phi > 0$. All the TWGBs for a particular CSL are given by the misorientation axis for each of the 24 crystallographically related solutions (Section 2.3.3). An asymmetric TWGB is in fact better known as a random or general high-angle boundary. Figure 11.2a shows a representation of an ATGB, and Figure 11.2b depicts an asymmetric TWGB.

There is evidence that boundary planes that are near quite densely packed lattice planes (i.e., those with low Miller indices) are significant in polycrystals, particularly noncubic ones (Randle, 1997, 1998; Rohrer et al., 2004; Randle et al., 2006). Such boundaries may be tilt or twist types (e.g., the ATGB in the $\Sigma 3$ system having {110}₁{411}₂ indexed in both grains), or they may not have a periodic (i.e., CSL) structure at all (e.g., {111}₁{100}₂). Conversely, some misorientations such as CSL may be periodic in nature, but the boundary planes are irrational. Provided it is known whether a boundary is an STGB, ATGB, or TWGB, it is generally sufficient to specify the Miller indices of the plane in both grains alone, and omit Φ .

In conclusion to this section, the central tenet of the interface–plane scheme as applied to grain boundaries in polycrystals is to focus primarily on the crystallography of the *plane*, with the misorientation being a secondary consideration. More details can be found elsewhere (Wolf, 1992; Randle, 1998). The practical aspects of how the indices of boundary planes, and also cracks and facets, are determined experimentally are discussed in Section 11.3.

11.3 Crystallographic Analysis of Surfaces

The measurement of grain orientation is made from a flat surface, giving the orientation of the crystallographic direction that is normal to this surface and two other directions that are mutually perpendicular to the surface normal. The orientation of other surfaces in the specimen may also be of

interest. Such surfaces include *microcracks*, either intergranular or transgranular (Liu et al., 1992); *fracture surfaces or facets*, that is, external surfaces of the specimen (Slavik and Gangloff, 1996; Randle and Hoile, 1998; Randle, 2000; Ro et al., 2005; Ayer et al., 2006); the plane of *grain or phase boundaries* (Randle, 1995a; Pan et al., 1996; Randle et al., 2006); and *slip traces* (Blochwitz et al., 1996; Lin and Pope, 1996; Raabe et al., 1996).

It is possible to extend techniques for measuring single orientations, most especially EBSD, to obtain the crystallographic indices of flat surfaces (i.e., planes) associated with the specimen. This strategy requires some kind of sectioning or photogrammetric (fractographic) technique to obtain the spatial coordinates of the surfaces, which is then coupled with orientation information. As mentioned in Section 11.1, TEM is not well suited to the crystallographic analysis of surfaces, although it is sometimes used to give detailed information on individual or small numbers of boundaries. Specimen preparation restrictions preclude examination of facets or cracks, and usually only a few suitable grain/phase boundaries are found in each foil. By far the most convenient technique for crystallographic analysis of surfaces is EBSD, since all the relevant imaging capabilities are encompassed in the SEM (large depth of field, specimen tilt, stereo imaging). The remainder of these sections on crystallographic analysis will therefore pertain mainly to EBSD-based analysis.

Surfaces associated with polycrystals are of two types, as far as investigation methodology is concerned: exposed and unexposed. Exposed facets, such as a fracture surface, can be viewed directly in the SEM, whereas unexposed facets, such as grain boundaries or slip traces, are first revealed as an etched trace on a polished surface, by a change of contrast in a backscattered image or by various orientation mapping options. Different experimental approaches are required to deal with each type of facet.

This section is organized as follows. Section 11.3.1 provides details of experimental methodologies to obtain flat sections through the microstructure. Section 11.3.2 briefly describes the well-established technique of photogrammetry, largely used to examine fracture facets. Section 11.3.3 describes in detail a new means of obtaining distributions of grain boundary planes in addition to misorientation, called the “five-parameter” analysis. Finally, Section 11.3.4 describes new methods to obtain information in three dimensions, namely, FIB tomography coupled with EBSD.

11.3.1 Sectioning Technique Principles

The principle of using sectioning techniques to obtain the orientation of a planar surface (e.g., a grain boundary or an exposed facet) relies on the trace of the plane being evaluated on at least two sections through the specimen. There are three stages in the analysis (Randle, 1993, 1995b):

- Acquisition of the inclination of the plane with respect to reference axes in the specimen

- Measurement of the orientation of the grain(s) that abut the plane, relative to the *same* reference axes as the inclination measurement
- Calculation of the direction cosines of the plane from the orientation and inclination parameters

The plane inclination is described by the angles α and β , which are shown in Figure 11.3a with respect to the orthogonal reference axes XYZ in the specimen. Clearly, the evaluation applies only to surfaces that actually are planar, and not to curved surfaces such as grain boundaries immediately following recrystallization. For convenience, X is horizontal in the microscope and EBSD measurements are made on the XY reference surface. Where the plane is exposed, for example, a fracture surface, the right-hand part of Figure 11.3a is missing.

Experimentally, the sectioning process is usually carried out by the standard metallographic technique of mounting the specimen in a suitable medium, grinding down the exposed surface of the specimen, followed by appropriate polishing/finishing steps. These procedures can be performed manually or automatically using equipment designed for that purpose. A potential alternative to the traditional grinding method for sectioning is ultramicrotomy, that is, sectioning with a diamond knife. This technique is a mainstay of TEM specimen preparation in the life sciences, and has been adapted for some materials applications (Malis and Steele, 1990).

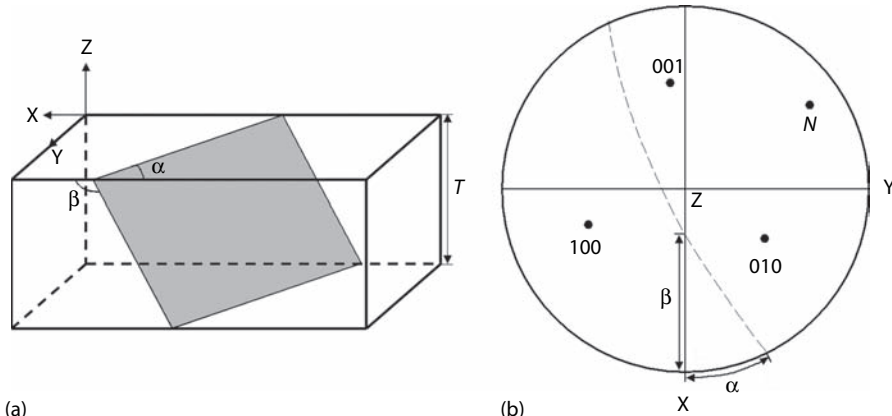


FIGURE 11.3

(a) Parameters required to measure the orientation of a surface. XYZ are the specimen axes, α and β are the angles relating the surface trace to the X axis, and T is the experimental section depth. For an exposed rather than an unexposed facet, the right-hand part of the diagram is missing. (b) Stereographic projection showing the relationship among XYZ, α , and β , from (a), the crystal axes of one grain, and the boundary plane normal N.

11.3.1.1 Two-Surface Sectioning

Relatively hard materials can be polished on two mutually perpendicular and adjoining surfaces so that the plane trace is revealed on both surfaces, as shown in Figure 11.3a. α and β can easily be measured in the SEM by tilting the specimen about the X axis so that both angles are visible together. The true angles, α_T and β_T , are corrected to account for the microscope tilt angle θ as follows (Randle and Dingley, 1989):

$$\alpha_T = \tan^{-1} \left(\frac{\tan \alpha_M}{\cos \theta} \right) \quad (11.4a)$$

$$\beta_T = \tan^{-1} \left(\frac{\tan \beta_M}{\cos(90^\circ - \theta)} \right) \quad (11.4b)$$

where α_M and β_M are the measured angles after tilting. An example of the application of the two-surface sectioning approach to interface crystallography is a study of fatigue crack initiation in copper (Liu et al., 1992). Fatigue cracks often initiate as a result of impingement of persistent slip bands against grain boundaries, and application of this method allowed the grain boundary crystallography to be determined and related to the slip band interaction.

11.3.1.2 Calibrated Serial Sectioning

The second procedure that can be used to obtain plane inclinations is to section the specimen parallel to the EBSD measurement surface—the XY surface in Figure 11.3a. If the section depth is known, then the plane inclination can be calculated from accurate measurement of the trace of the plane on the XY surface before and after sectioning. The section depth, where a layer of material is removed by grinding, can be measured by inserting hardness indents into the specimen surface at the start of the procedure. The reduced size of the indent after sectioning, coupled with the knowledge that the angle between opposite faces of the diamond indenter is 136° , allows the depth of material removed to be calculated. The image of the hardness indents also facilitates accurate alignment between serial sections, which is crucial. The thickness of specimen removed, T , is given by

$$T = \frac{(D_b - D_a)}{\tan(136^\circ / 2)} \quad (11.5)$$

where D_b and D_a are the average distance from the center to the closest point on the edge of the indent before and after grinding, respectively. If the offset on the specimen surface of a grain boundary before and after grinding is O , then β is given by

$$\beta = \tan^{-1} \left(\frac{O}{T} \right) + 90^\circ \quad (11.6a)$$

or

$$\beta = 90^\circ - \tan^{-1} \left(\frac{O}{T} \right) \quad (11.6b)$$

depending on the sense of the plane inclination in the specimen. The trace angle α is measured directly from the boundary trace on the specimen surface.

The principal disadvantage of the calibrated serial sectioning method is that, for an unexposed surface, planarity within the measurement depth is assumed. Several small depth sections can be made to validate this assumption, although the procedure then becomes very time-consuming. To minimize measurement errors, the total depth of material removed should be maximized while remaining within the same grain. Hence there is a lower restriction on grain size of approximately 50 μm . The reliability of this method has been estimated to be $\pm 4^\circ$, including the orientation measurement (Randle et al., 1997). Recently, the technique has been improved and automated, as described in Section 11.3.3.

Once the grain orientation has been measured near to the plane, its crystallographic indices are calculated as follows. Two vectors that lie in the boundary plane are given by A and B , which are obtained from α and β , respectively. The coordinates of A and B are given by

$$A = \begin{pmatrix} \cos \alpha \\ \cos(90^\circ - \alpha) \\ 0 \end{pmatrix}, \quad B = \begin{pmatrix} \cos \beta \\ \cos(90^\circ - \beta) \\ 0 \end{pmatrix} \quad (11.7)$$

The cross product of A and B gives N , the plane normal, which can then be related to the crystal axes of the grains through the orientation matrix. The whole procedure is illustrated on the stereogram in Figure 11.3b.

For the case of the crystallographic analysis of slip traces, the slip plane family has been identified by a one-surface trace analysis, which can be adopted for other surfaces. This is carried out by aligning a set of slip traces in an individual grain with the X axis in the microscope. The first column of the orientation matrix then gives the slip plane. By this method, slip traces in Ni_3Al were found using EBSD to be on {111} (Lin and Pope, 1996). Alternatively, if the angle between the slip trace and the X axis is measured, the identity of the slip plane—assuming that the slip band is perpendicular to the specimen surface—can be calculated. Such an analysis cannot give full information without this assumption but nonetheless is useful for some applications and has the advantage of not requiring sectioning.

11.3.1.3 Thin Sections: TEM Methods

The most straightforward way to obtain a plane normal in TEM is to tilt the foil until the plane is upright in it, and then obtain the plane normal from the cross product of the foil normal and the direction of the boundary

trace. However, the projected grain boundary width has a minimum value over several degrees, which degrades the accuracy of this method. The most convenient and accurate method to obtain a plane normal in the TEM is to measure the projected width of a highly inclined plane in the foil, coupled with measurement of the foil thickness and grain orientations, both using microdiffraction. More details of these methods can be found in the book by Randle (1993).

11.3.2 Photogrammetric Techniques

Photogrammetry in the SEM is a well-established technique for determining the coordinates of an exposed facet plane relative to a fixed coordinate system in the microscope (Hilliard, 1972). These data can then be coupled with diffraction data to give the crystallographic orientation of the facet.

The photogrammetric procedure involves producing a series of micrographs of the facet using at least two tilt angles (e.g., 0°, 10°, and 20°) and identifying the projected (x, y) coordinates of point features in the plane, relative to the reference axes, at the various tilt angles. If the coordinates of one point at tilt angles θ_1 and θ_2 are (x_1, y_1) and (x_2, y_2) , then the true coordinates x_T, y_T, z_T of the point in space are given by (Themelis et al., 1990)

$$x_T = \frac{(x_1 \sin \theta_2 - x_2 \sin \theta_1)}{\sin(\theta_2 - \theta_1)} \quad (11.8a)$$

$$y_T = y_1 = y_2 = \frac{(y_1 + y_2)}{2} \quad (11.8b)$$

$$z_T = \frac{(-x_1 \cos \theta_2 + x_2 \cos \theta_1)}{\sin(\theta_2 - \theta_1)} \quad (11.8c)$$

The coordinates of three points on the plane can then be used to compute the equation of the plane normal. This brief description of the photogrammetric procedure is amplified by Themelis et al. (1990) and Slavik et al. 1993). An extension of the photogrammetry technique is computer-assisted stereophotogrammetry, where a 3-D reconstructed image of the facet is coupled with EBSD diffraction information (Davies and Randle, 2001; Davies et al., 2002).

The crystallographic orientation of the grain containing the facet is then obtained as a separate step, taking care to ensure that the specimen coordinate system is identical for both photogrammetry and diffraction. A key point, similar to the sectioning technique described earlier, is that diffraction is performed on a surface *adjacent to the facet*, rather than on the facet itself. This allows the fracture surface to remain undisturbed while a full metallographic procedure is used to prepare the adjacent surface for diffraction.

Once the equations of both the plane normal and the grain orientation have been obtained, the crystallographic orientation of the plane is obtained by adapting the principle illustrated in the stereogram in Figure 11.3b.

The crystallography of facet planes is an important subset of materials studies, concerning, for example, brittle fracture, fatigue, and stress corrosion cracking. Examples of the combined EBSD and photogrammetric approach to these studies are with respect to fracture surfaces in Cu–Bi bicrystals, using Laue back-reflection (Themelis et al., 1990), and fatigue fracture in Al alloys, using EBSD (Slavik and Gangloff, 1996). The technique has also been used to show that fatigue fracture surface facets in an Al–Cu–Li alloy were close to, but not identical to, {111} (Ro et al., 2005). It is occasionally possible to align the facet surface so that diffraction information can be obtained from it directly. However, this method is only feasible for large surfaces, and often the deformation processes associated with the formation of the facet interfere with the clarity of the diffraction pattern. This method is therefore not suitable for general analysis.

In summary, EBSD can also be used to determine the orientation of facets, for example, on a fracture surface (Randle and Hoile, 1998; Ayer et al., 2006). However, this is an awkward procedure because there are uncertainties in the facet alignment with respect to the microscope geometry and surface preparation is not viable. Recently the technique has been improved, such that the stereological measurements and the EBSD data are both collected *in situ*, without the need for specimen replacement and associated errors. The uncertainty in facet crystallography determination was found to be 2°–5° (Ro et al., 2005). It has also been coupled with Auger electron spectroscopy to investigate the correlation between grain boundary segregation and grain boundary plane orientation in Nb-doped TiO₂ (Peng and Wynblatt, 2005).

11.3.3 “Five-Parameter” Analysis and Stereological Techniques

As mentioned in Section 11.1, whereas characterization of a grain boundary frequently refers only to its misorientation parameters, expressed usually as an angle and axis of misorientation, this is an incomplete description. Five independent parameters (degrees of freedom) are required to parameterize a grain boundary, namely, three for the misorientation and a further two for the boundary plane or surface between two neighboring grains. These five parameters give rise to a huge number of possible grain boundary geometries. For example, between two cubic crystals there are 10⁵ possible different boundaries, assuming a 5° resolution (Saylor et al., 2003).

The crystallographic orientation of the boundary plane has a strong influence on boundary properties. For example, the Σ3 misorientation, 60°⟨111⟩, is well known to have boundary planes that include {111} (the “coherent twin”) and {112} (the “incoherent twin”). Although the misorientation is the same in both cases, the Σ3 on {111} is almost immobile, whereas the Σ3 on {112} is highly mobile. It is now thought that the boundary plane is often more

important for determining boundary properties than is the misorientation (Randle et al., 2006).

Given the importance of the boundary plane, it is at first sight surprising that it has been largely omitted from EBSD data. This is because the serial sectioning techniques involved are quite tedious, as described in Sections 11.3.1 and 11.3.2. In recent years, interest has been generated in using the information obtained from the grain boundary trace direction on the specimen surface, and dispensing with the serial sectioning step, which has ultimately led to the “five-parameter” stereological method for determination of grain boundary crystallography, as described in the following text.

The crystallographic boundary trace direction plus the misorientation between neighboring grains provides four out of the five boundary parameters. These can be used to check if certain well-defined criteria are met, for example, if the boundary is a twin (Randle and Davies, 2002). The basis for this calculation is that the trace vector T must lie in the boundary plane, which has normal N . For the case of a coherent annealing twin boundary, N is $\langle 111 \rangle$. Hence the product of N and T will determine whether or not it is possible for the boundary to be a twin. For example, Figure 11.4 shows $\Sigma 3$ boundaries depicted in white. For grain boundary 1/2 the angle between T and $\langle 111 \rangle$ is 88.3° and 87.8° in both neighboring grains, respectively, and the boundary is 0.3° deviated from the $\Sigma 3$ reference misorientation. This boundary is therefore probably a coherent twin, and similarly for boundary 3/4. However, for boundary 5/6, the angle between T and $\langle 111 \rangle$ is 76.6° and 73.8° in both neighboring grains, respectively; therefore, it is impossible for this boundary to be a coherent twin.

The methodology for identifying the possibility of twinning in this way has been automated by use of an algorithm that automatically extracts the

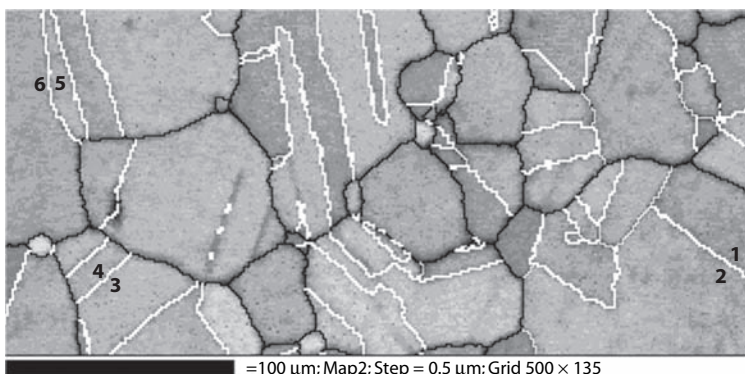


FIGURE 11.4

$\Sigma 3$ boundaries (white) in a nickel-based superalloy. The boundaries selected for trace analysis are numbered.

boundary trace position from EBSD orientation maps (Wright and Larsen, 2002). This algorithm has been used to investigate twinning in zirconium, nickel, and copper, but most importantly it is used as part of a procedure to determine automatically all five boundary parameters from a single section (see the following text).

The boundary trace reconstruction routine works on an orientation map in which grains have been identified as groups of similarly oriented points, from which grain boundaries are defined according to a predefined tolerance. Triple junctions, where three grains meet, are then identified by the software. If one of the boundary segment paths is followed until the next triple junction is encountered, a first attempt at reconstructing a boundary trace can be made by joining the two neighboring triple junctions, as shown in Figure 11.5a. However, the grain boundary is rarely a straight line between the two junctions, and so the reconstructed trace needs to be segmented to follow more closely the true boundary. This is done by locating the point

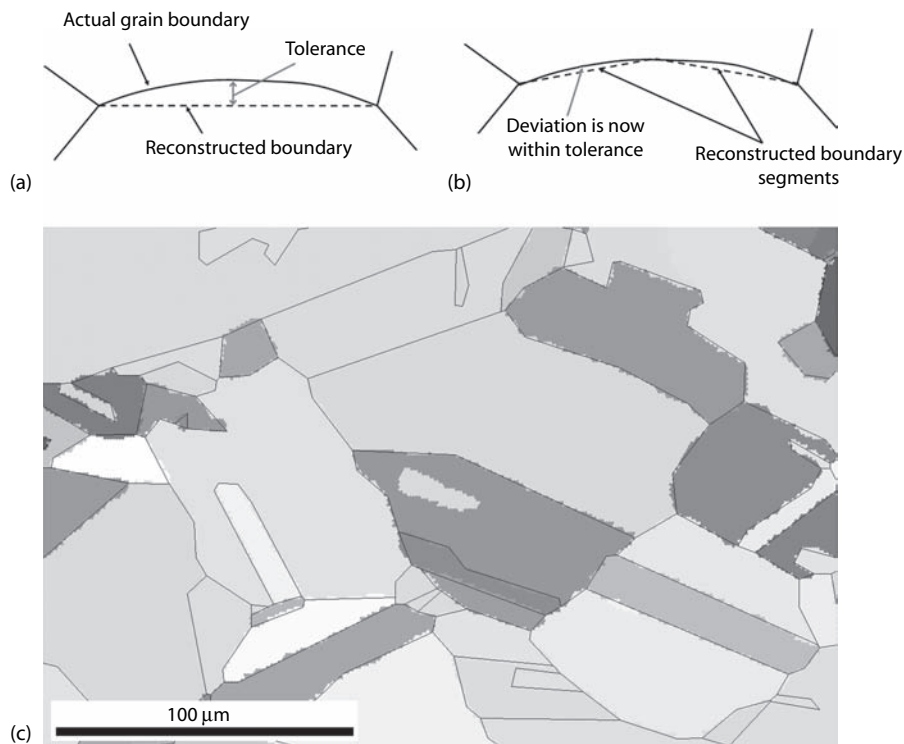


FIGURE 11.5

(See color insert following page 240.) Illustration of the boundary trace reconstruction routine. (a) First reconstruction attempt by joining adjacent triple junctions. (b) Segmentation of the reconstructed trace. (c) Small map wherein reconstructed boundaries are superimposed on true boundaries. Grains are colored randomly.

on the true boundary furthest from the reconstructed boundary. If the perpendicular distance between this point and the reconstructed boundary exceeds a predefined tolerance then the reconstructed boundary is split into two line segments, as shown in Figure 11.5b. This procedure is repeated until all points on the reconstructed boundary are within the tolerance distance of the true boundary.

Figure 11.5c shows a small map wherein reconstructed boundaries are superimposed on true boundaries. To minimize errors, a small step size needs to be used to generate the map to reproduce the boundary positions as faithfully as possible, given the discrete nature of the measurement grid. Then the segmenting process must aim to reproduce the true boundary rather than any “noise” on the boundary length. It is therefore essential that a small tolerance, for example, twice the map step size, is chosen to reconstruct boundaries. The expected error for a boundary of length six times greater than the scan step size would be $\pm 2^\circ$ (Wright and Larsen, 2002). Finally, an average orientation from each neighboring grain is associated with each segment of the reconstructed boundary trace. Measurement points between one and five steps from the boundary are used in the averaging.

Recently, a method has been devised to measure the “five-parameter” grain boundary distribution. This is defined as the relative frequency of occurrence of a grain boundary in terms of misorientation and boundary plane normal, expressed in units of multiples of a random distribution (MRD). The original five-parameter analysis schedule did not use automatically reconstructed boundaries, but rather used SEM images to determine the boundary positions coupled with serial sectioning. One of the first materials to be analyzed was a hot-pressed MgO polycrystalline specimen (Saylor et al., 2003). Grain boundaries were manually digitized using a program that allowed the operator to trace and hence skeletonize the boundaries with a computer mouse. A coarse orientation map of the same region was obtained, which was matched to the SEM image to allow an orientation to be assigned to each grain. Information on the inclination of each boundary was then obtained by sequential, high-precision, serial sectioning. Data from three to five layers were collected. Once the geometry and orientation of all grains on all the layers had been determined, adjacent layers were aligned to establish the connectivity of grains between the layers. So finally a meshed surface between adjacent layers was created. Eventually for each mesh element the area of boundary plane, the misorientation across the plane, and the crystallographic normal to the plane were specified.

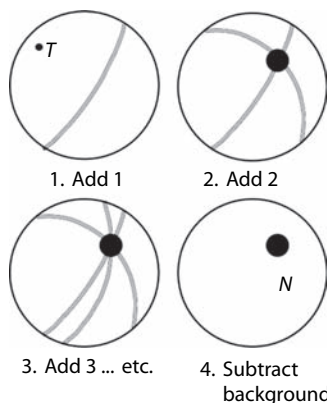
The procedure outlined earlier allows the complete five-parameter grain boundary distribution function, encompassing the misorientation and the plane, to be calculated. Details of how the 5-D domain of misorientations and planes is parameterized, taking into account that crystal symmetries lead to numerous symmetrically equivalent boundaries, are given by Saylor et al., (2003). Essentially, the domain is normalized and partitioned into cells of equal volume, such that the grain boundary distribution that falls in each

cell is an MRD. For the case of MgO, it was shown that grain boundaries most frequently adopted asymmetric configurations with the boundary plane parallel to {100} in one of the two neighboring grains.

Considerable technical challenges were involved in the original experimental procedure summarized earlier to obtain the grain boundary distribution. These are mainly due to the need for serial sectioning. Account must be taken of errors that arise in both montaging neighboring images in a single-section layer and, more specifically, aligning adjacent layers in the same global reference frame. The resolution of the sectioning process is far less than that of the microscopy, leading to further errors. Furthermore, serial sectioning preferentially reveals planes that are perpendicular to the analysis surface, and so a sampling bias is introduced. Finally, the whole procedure is time-consuming. For these reasons, the five-parameter methodology has recently been refined so that the grain boundary distribution is estimated from a single section through the microstructure, and the need for *ex situ* serial sectioning is obviated. However, recently *in situ* serial sectioning of small regions via FIB has become viable for serial sectioning, and is still under development (Section 11.3.4).

The stereological procedure to extract boundary plane data from a single section has been adapted from established methods to determine habit planes from embedded crystals. The details of the method are described by Saylor et al. (2004); only a brief summary of the principles is given here. The procedure uses EBSD mapping both to obtain grain orientations and to reconstruct the boundary segment traces, as described earlier. This provides four out of the five independent parameters to describe the grain boundary. Only the boundary inclination angle is unknown. However, what is known is that the boundary plane must be in the set of planes whose normals are perpendicular to the boundary trace on the single section. These normals lie on a great circle in the stereographic projection, as shown in Figure 11.6. Because the sample population of boundary traces is large, comprising at least 50,000 trace segments for a material with cubic symmetry, many crystal pairs have the same misorientation but different boundary planes. The boundary trace generates a set of possible boundary planes. The probability that the set contains the true boundary plane is 1, whereas the probability that other false planes are included in the set is less than 1. Therefore, if a sufficiently large number of observations are made, the true boundary plane will accumulate more than the false planes and form a peak in the distribution. The background (false planes) is then removed, based on the assumption of random sampling. This is illustrated schematically in Figure 11.6. From the remaining peaks, the ratios of the observed line lengths specify the relative areas of each boundary type, that is, the five-parameter grain boundary distribution.

The new, single-section method for estimating the five-parameter boundary distribution has been tested against both simulated data and known boundary distributions obtained by serial sectioning (Saylor et al., 2004). The comparison was very favorable provided that sufficient data are included

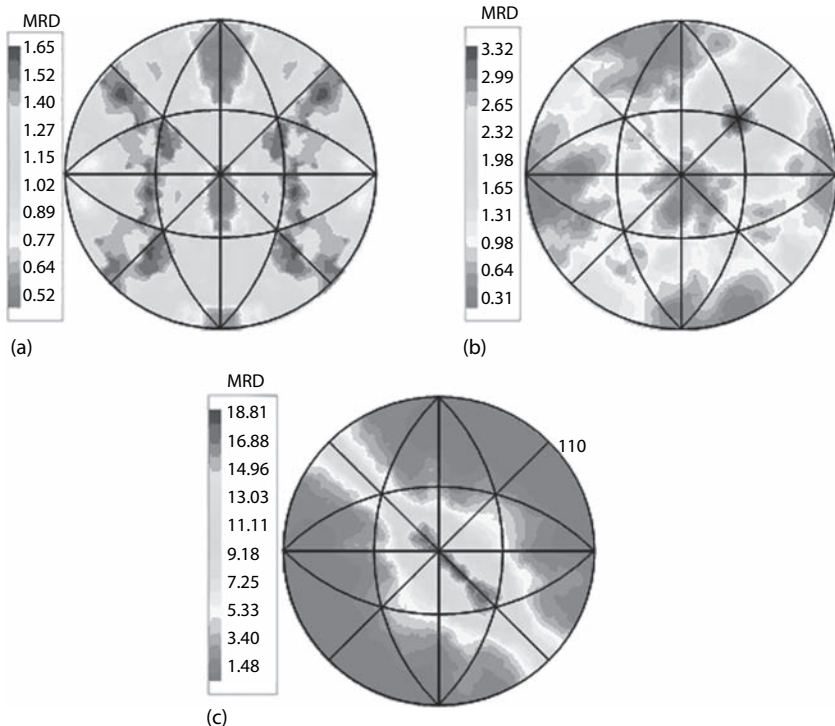
**FIGURE 11.6**

Schematic illustration of the principle of the five-parameter stereology method. T is the boundary trace direction, and N is the boundary plane normal. If a sufficiently large number of observations are made, the true boundary plane will accumulate more than the false planes and form a peak in the distribution at N . (Courtesy of G. Rohrer.)

in the stereological analysis—at least 50,000 boundary segments for cubic materials, and more for noncubics. With the advent of rapid EBSD orientation mapping, as described in Section 7.6, such quantities of data, obtained with high spatial resolution, can be collected easily; hence it is preferable to traditional serial sectioning with its inherent difficulties.

Analysis of the 5-D grain boundary distribution function is achieved by visual examination of various sections through the 5-D space. It is convenient physically to maintain the distinction between misorientation (three parameters) and boundary plane (two parameters). Misorientation axes and angles, and combinations thereof, can be displayed using standard facilities available in EBSD packages. Data specifically from the five-parameter analysis (boundary plane distributions) are shown in stereographic projection, where the stereogram has the axes of the crystal and the resolution is usually 10° . The five-parameter grain boundary analysis technique is illustrated by an example from annealed brass in Figure 11.7.

To view the distribution of boundary planes in some detail, certain misorientations of interest are selected. A starting point is to select those misorientations that have a low-index misorientation axis. From the data in Figure 11.7, it can be concluded that there were few misorientations on [100], but more on [111] and [110]. Although originally the entire misorientation angle range was inspected, here just one angle/axis combination for each misorientation axis is shown, for illustration purposes. Figure 11.7a shows $30^\circ/[100]$, which includes very few planes. Figure 11.7b shows $30^\circ/[111]$, which reveals that (111) TWGBs are prevalent because there is a maximum at (111) with an MRD value of 3.32. Finally, Figure 11.7c shows $30^\circ/[110]$, where it is seen that asymmetrical tilt boundaries are prevalent because the plane density is distributed along the

**FIGURE 11.7**

(See color insert following page 240.) Distribution of boundary planes for selected misorientations in a brass specimen expressed as multiples of a random distribution (MRD) and shown in standard stereographic projection. (a) 30°/[100] misorientation; (b) 30°/[111] misorientation; (c) 30°/[110] misorientation. The [110] misorientation axis is marked in (c).

(110) zone, with multiple peaks having a high MRD value of 18.81. (The [110] misorientation axis is marked.) These distributions show that there is anisotropy in the distribution of boundary planes. Since tilt and twist boundaries have lower energies than a random configuration, here energy considerations have had a role in the choice of boundary planes.

It needs to be emphasized that here EBSD has been used to make a big step forward in grain boundary studies. This is the first time that data on which boundary planes exist in polycrystals are available, which has paved the way for expanding knowledge on grain boundary structure and how it links to properties.

11.3.4 Three-Dimensional EBSD

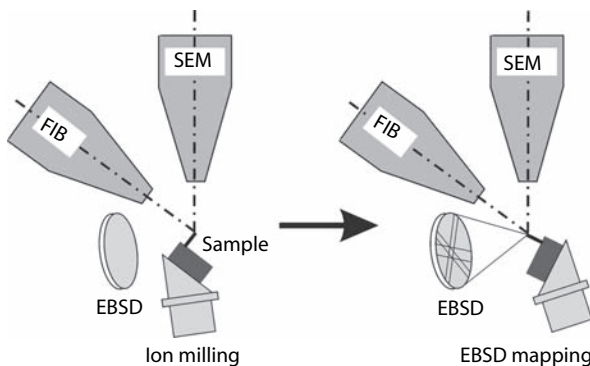
The most common way to characterize the 3-D microstructure is by depth-calibrated serial sectioning. Section 11.3.3 described automated precision serial sectioning to obtain a population of boundary plane inclinations. There

are further examples where EBSD can be supplemented by other techniques for 3-D studies. EBSD measurements have been coupled with synchrotron x-ray microtomography to study the interaction of fatigue cracks with grain boundaries in cast Al alloys (Ludwig et al., 2003). Here grains were visualized in three dimensions by decoration of the grain boundaries with liquid gallium, whereas EBSD was used on the sample surface to obtain grain orientations. The 3-D structure of diamond films has been studied by acquisition of an EBSD map followed by ion milling to remove a layer of the film and repeated mapping (Chen and Rudolph, 2003). A final example is that serial sectioning has been combined with EBSD to give a methodology for 3-D microstructure reconstruction, as demonstrated on austenitic steel (Lewis et al., 2006). Although sectioning is usually performed in a parallel manner, a series of oblique double sections can also be obtained and combined with EBSD data, which can offer better representation of the bulk microstructure and certain experimental advantages compared to serial sectioning (Homer et al., 2006).

Having obtained the 3-D data, reconstruction and visualization in three dimensions is a further step, and there are several commercial or in-house programs available for this 3-D rendering (Lewis et al., 2006). Such data, apart from giving insights into the true microstructure, provide input for various computer models.

FIB tomography is a relatively new technique, which is used to section and shape specimens on a nanometer scale. An exciting extension to this technique has been the recent integration of FIB technology with an SEM, to give a “dual beam” instrument capable of both precision sectioning and high-resolution imaging. An added benefit of the dual beam configuration is that EBSD is possible. The applications of this equipment fall into two main categories: analysis of certain delicate specimens and acquisition of 3-D data. Delicate specimens include those that degrade readily so that a freshly milled surface is advantageous for diffraction pattern collection, or where the specimen form renders preparation awkward, such as thin wires and nanomaterials. For example, FIB-SEM has been used to record the microtexture and microstructure of gold interconnect wires and tungsten lamp filaments (<http://www.oxinst.com>, 2007).

It is possible to obtain a 3-D EBSD data set by removing successive slices with the FIB column and then manually switching to the electron column to obtain successive EBSD maps. However, a real step forward in efficiency occurred recently when the whole process was automated using software that communicates with both the dual beam for controlled sectioning and the EBSD system. Maps from up to 200 slices have been obtained (<http://www.oxinst.com>, 2007). The best spatial resolution of the 3-D pixels (voxels) is 100 nm × 100 nm × 100 nm, the angular resolution is 0.5°, and the maximum observable volume is 50 µm × 50 µm × 50 µm. A slice from nickel measuring 15 µm × 8 µm × 200 nm would be removed in approximately 25 min, using a 30 kV ion beam and a current of 3 nA (<http://www.oxinst.com>, 2007).

**FIGURE 11.8**

Schematic illustration of the geometry of the FIB column, the SEM column, the EBSD detector, and the specimen stage. (Courtesy of M. Ferry.)

The integration of EBSD and FIB-SEM is experimentally challenging because of obstruction by the various detectors and the need to collect EBSD patterns at the crossover point of the electron and ion beams, which occurs at a very short working distance (5–8 mm). Figure 11.8 illustrates the combined geometry of the FIB column, the SEM column, the EBSD detector, and the specimen stage. An EDS detector may also be required. The specimen surface has to be maintained first parallel to the ion beam for milling, and then at 20° (typically) to the electron beam for EBSD. It is therefore necessary to precision rotate and position the specimen between successive operations.

The ion beam is Ga^+ ions with typical energies between 5 and 30 keV. Further experimental and technical details can be found elsewhere (Zaafarani et al., 2006; Konrad et al., 2006; Xu et al., 2007; Zaefferer et al., 2008). The Ga^+ beam produces some surface damage, depending on the atomic number of the material and the operating conditions. This, in turn, can have a knock-on effect on the clarity and hence solve efficiency of the diffraction patterns. Metals with low atomic numbers are more affected than those with high atomic numbers (Ferry et al., 2007).

Figure 11.9 shows an example of FIB/EBSD data, taken from an investigation that was able to reveal particle-stimulated nucleation in a nickel alloy. This would have been hard to detect in a 2-D section. Figure 11.9a shows EBSD maps of consecutive FIB sections through partly recrystallized Ni-0.3wt% Si. The slices represent section depths of $0.2 \mu\text{m} \pm 0.05 \mu\text{m}$. SiO_2 particles and recrystallized grains containing annealing twins are seen in the deformed matrix. A 3-D rendering of the sections in Figure 11.9a is shown in Figure 11.9b.

There are few examples in the literature of the application of FIB/EBSD to materials research. One example shows the evaluation of microstructure and microtexture below a nanoindent, and how these measurements compare to finite element simulations (Zaafarani et al., 2006). In another

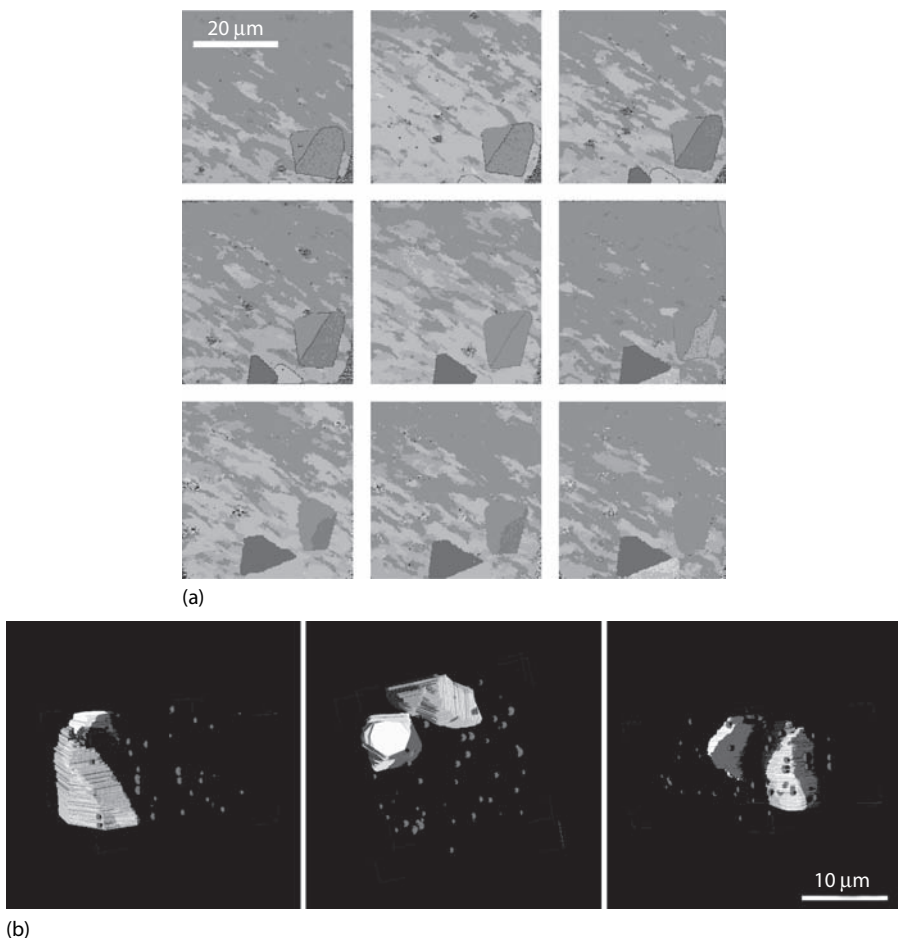


FIGURE 11.9
(See color insert following page 240.) (a) EBSD maps of consecutive FIB sections through part-recrystallized Ni-0.3wt% Si. The slices represent section depths of $0.2 \mu\text{m} \pm 0.05 \mu\text{m}$. SiO_2 particles and recrystallized grains containing annealing twins are seen in the deformed matrix. (b) 3-D rendering of (a). (Courtesy of M. Ferry.)

example, orientation gradients around a hard Laves particle in a warm-rolled Fe_3Al -based alloy were analyzed (Konrad et al., 2006). Similarly to the case for conventional serial sectioning, a variety of *ex situ* packages are used to compile and manipulate 3-D renderings from the 2-D section maps.

It is notable that there are few publications in the literature on combined sectioning and EBSD for 3-D microstructure characterization using only a conventional SEM. This perhaps reflects both the labor-intensive nature of the process and the more exciting attractions of FIB. FIB/EBSD is complementary to the serial sectioning or stereological methods of 3-D characterization because FIB/EBSD is still a relatively slow process and is only viable

for small volumes, whereas serial sectioning or stereology methods provide statistical data from much larger specimens. However, FIB/EBSD is still developing, and many improvements and output of data are expected over the next years.

11.4 Orientation Connectivity and Spatial Distribution

The topological parameters associated with polycrystals—numbers of grains, grain surfaces, edges, and corners—have been studied for many years. Stereological techniques (i.e., the reconstruction of 3-D information based on that accrued from 2-D sections) have generally been used to investigate the topological connectivity of grains aggregated in a polycrystal (Rhines et al., 1976). The sectioning planes can be random, which gives a statistical result, or parallel to build up an accurate impression of the spatiality of the microstructure. These topological aspects of microstructure have traditionally been studied separately from crystallographic considerations. However, the advent of EBSD allows large regions of microstructure to be accessed in a single section in terms of both the crystallography *and* areal topology. These studies access the way in which grains having various orientations connect together—*orientation connectivity*.

Another aspect of orientation connectivity is the spatial distribution of orientations with respect to some features of the microstructure; for example, how grain textures relate to grain size (Vogel and Klimanek, 1996; Engler, 1998; Bastos et al., 2006) or the clustering of grains that are separated by low-angle boundaries, where a single cluster is enclosed by high-angle boundaries (West and Adams, 1997). Quantitative cluster structure analysis is carried out using aspects of percolation theory, such as fractal analysis. Examples of specific orientation connectivity topics include the following:

- Grain shape, distribution, and orientation
- Particle distribution with regard to grains of particular orientations
- “Decision trees” for crack paths throughout the microstructure
- Grain boundary connectivity
- Clustering of orientation elements

Any of these examples can be explored on a single section through the microstructure; if sectioning techniques are employed then 3-D aspects of orientation connectivity can be addressed, which render the data much more powerful, as described in Section 11.3.4. Other metrics are beginning to be used to assess the connectivity and topology of the grain boundary network. Percolation theory is relevant to the length of connected intergranular

pathways or “clusters” through the microstructure. A simple approach is to consider that such pathways consist only of boundaries with random geometries. A “skeletonized” EBSD mapping can be used to show the evolution of connected random boundaries with processing and the data subsequently exported to other applications to quantify the percolation characteristics. This has been carried out, for example, on a grain boundary engineered nickel-base alloy (Schuh et al., 2003).

Aspects of orientation connectivity that relate to *grain junctions*, that is, where more than two grains meet, are often called a “triple line.” An “addition rule” applies, which predicts the geometry of the third boundary from the relationship:

$$M_1 M_2 M_3 = I \quad (11.9)$$

where M_{1-3} are the misorientation matrices of three boundaries at a common junction and I is the identity matrix. This rule has the most significant consequences for conjoining CSL boundaries since they share a common misorientation axis; the sum of two of the misorientation angles gives the third multiplied by a common factor, and the product or quotient of two of the Σ values gives the third (Ranganathan, 1966; Gertsman, 2001b; Reed and Kumar, 2006). For example,

$$60^\circ/\langle 111 \rangle - 21.8^\circ/\langle 111 \rangle = 38.2^\circ/\langle 111 \rangle \quad (11.10a)$$

that is, $\Sigma 3 - \Sigma 21a = \Sigma 7$

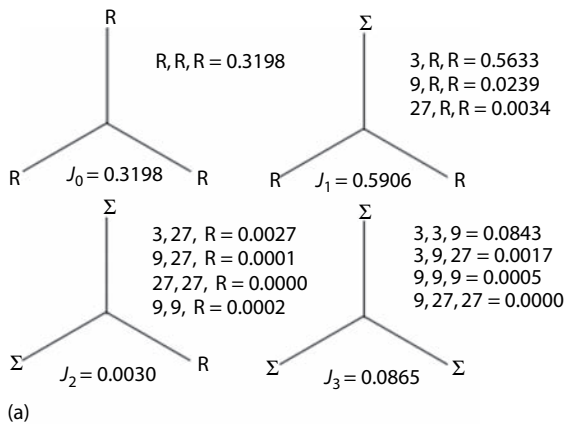
or more generally

$$\Sigma_A \Sigma_B = k^2 \Sigma_C \quad (11.10b)$$

where k is a common factor of Σ_A and Σ_B . The interest in grain junctions from a practical point of view is that any interfacial propagation phenomenon (diffusion, corrosion, cracking, etc.) is controlled by the juxtaposition of boundaries at grain junctions. The phenomenon will only be likely to propagate along nonspecial boundaries; therefore, it is pertinent to categorize grain junctions in terms of the combinations of special/nonspecial types (Garbacz et al., 1995; Thomson and Randle, 1997b). In recent years, statistics on triple junctions have begun to appear in reports alongside grain boundary proportions (Schuh et al., 2003). For example, Figure 11.10 shows the constitution of triple junctions in nickel, in terms of twin-related boundaries (Σ) and random boundaries (R), before and after GBE. The statistics demonstrate that processing has increased the proportion of triple junctions that contain twin-related CSLs.

Although orientation connectivity aspects of the microstructure can be addressed partially via a single section through the microstructure, far more in-depth data can be obtained from incorporating sectioning techniques to

N_i ref: Total number of TJs = 43473
 Total number of TJs analyzed = 43088



N_i gbe: Total number of TJs = 30488
 Total number of TJs analyzed = 30197

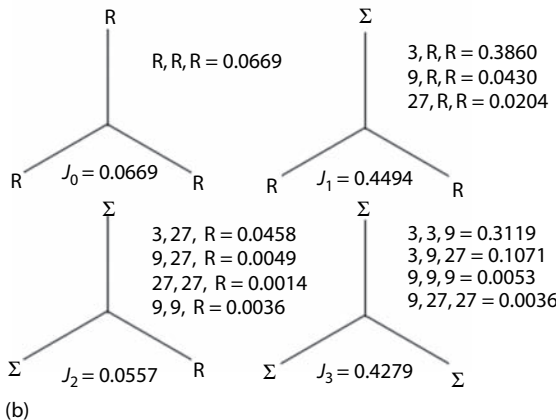


FIGURE 11.10

Constitution of triple junctions in nickel, in terms of twin-related boundaries (Σ) and random boundaries (R): (a) before and (b) after grain boundary engineering. (Courtesy of G. Rohrer.)

gain a 3-D viewpoint. This can be done either statistically or specifically. The *intercrystalline structure distribution function* (ISDF) and related *interface damage function* (IDF) (Adams et al., 1990) take a statistical approach to couple the spatial distribution of grain boundaries with the MODF (Section 9.7). In one series of experiments, grain misorientations were measured on four section planes, for example, in plate material at 0° , 10° , 30° , and 60° to the plane of the plate. From these data, MODFs for various interface normal inclinations could be plotted in Euler space, which would yield peaks of preferred

boundary misorientation. Note that here the attention is focused on *probabilities* rather than on the crystallography of individual boundaries, and that the boundary orientation data relate to specimen, rather than crystal, geometry. This methodology has been used to analyze creep damage in copper (Adams et al., 1990).

11.5 Orientation Relationships between Phases

Over the past few years, EBSD has become more frequently used to investigate crystallographic relationships between phases, which in turn has contributed toward understanding of phase transformations. This application of EBSD, which is a natural outcome of the increased efficiency of orientation mapping from multiphase materials (Section 10.4.5), has recently been reviewed in detail by Gourgues-Lorenzon (2007). EBSD allows the “crystallographic units” in a phase microstructure to be distinguished from the “morphological units” that are observed in an image. Usually, the crystallographic units are more complex than implied by the image.

Often, a crystallographic orientation relationship, OR, exists between two phases that have a parent/product relationship in a phase transformation. The most frequently investigated ORs involve either the decomposition of austenite in steel to form ferrite or other products such as martensite or bainite (Cabus et al., 2007; Petrov et al., 2007; Lischewski et al., 2008), or the α/β (hcp/bcc) phase transformation in titanium and titanium alloys (Seward et al., 2004). All of these phase transformations are technologically important. The OR may have several variants, depending on the crystallography of the system. Various EBSD investigations have recently shown that “variant selection” usually operates and those variants that either obey the OR with both parent grains or that have a special OR with the boundary plane are favored (Gourgues-Lorenzon, 2007).

The phase transformations between austenite (fcc γ) and ferrite (bcc α or δ) in steel have been analyzed most widely, and usually the mutual ORs are observed to cluster around the classical Bain OR $45^\circ/\langle 100 \rangle$. Table 11.1 lists the ORs with the possible misorientation descriptors for the most well-known fcc/bcc phase relationships: Pitsch, Kurdjumov–Sachs, and Nishiyama–Wassermann. There is still much debate about the relationship between OR and the displacive or diffusive character of phase transformations in steel, in particular concerning acicular ferrite, Widmanstätten ferrite side plates, and bainite (Gourgues-Lorenzon, 2007).

For the transformation between bcc (β) and hcp (α) structures, often the so-called Burgers phase relationship is observed, where both close-packed planes and close-packed directions in the hcp/bcc transformation are parallel, that is, $\{100\}_\beta \parallel \{0001\}_\alpha$ and $\langle 111 \rangle_\beta \parallel \langle 1120 \rangle_\alpha$. This relationship produces

TABLE 11.1

Possible Orientation Relationships between γ and α Phases in fcc/bcc Duplex Structures

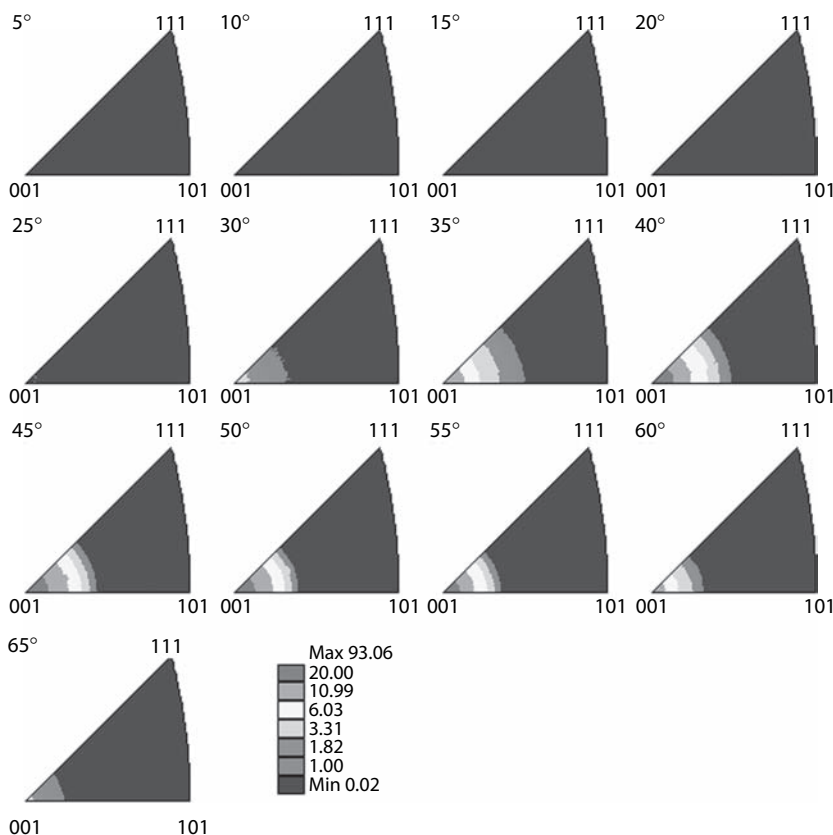
Orientation Relationship	Parallelism	Angle/Axis Pair $\omega \langle hkl \rangle$	RF Vector $\langle r_1 \ r_2 \ r_3 \rangle$	Euler Angles $\varphi_1 \ \Phi \ \varphi_2$
Bain	$\{001\}_\gamma \parallel \{001\}_\alpha$ $\langle 100 \rangle_\gamma \parallel \langle 110 \rangle_\alpha$	$45^\circ \langle 100 \rangle$	$\langle 0.414 \ 0.0 \ 0.0 \rangle$	$0.0^\circ \ 45.0^\circ \ 0.0^\circ$
Kurdjumov–Sachs	$\{111\}_\gamma \parallel \{110\}_\alpha$ $\langle 110 \rangle_\gamma \parallel \langle 111 \rangle_\alpha$	$42.85^\circ \langle 0.968 \ 0.178 \ 0.178 \rangle$	$\langle 0.380 \ 0.07 \ 0.07 \rangle$	$5.77^\circ \ 48.19^\circ \ 5.77^\circ$
Nishiyama–Wassermann	$\{111\}_\gamma \parallel \{110\}_\alpha$ $\langle 112 \rangle_\gamma \parallel \langle 110 \rangle_\alpha$	$45.98^\circ \langle 0.976 \ 0.083 \ 0.201 \rangle$	$\langle 0.414 \ 0.035 \ 0.085 \rangle$	$9.74^\circ \ 45.0^\circ \ 0.0^\circ$
Pitsch	$\{100\}_\gamma \parallel \{110\}_\alpha$ $\langle 011 \rangle_\gamma \parallel \langle 111 \rangle_\alpha$	$45.98^\circ \langle 0.083 \ 0.201 \ 0.976 \rangle$	$\langle 0.035 \ 0.085 \ 0.414 \rangle$	$0.0^\circ \ 45.0^\circ \ 9.74^\circ$

Source: Data from He, Y., Godet, S., and Jonas, J.J., *Acta Mater.*, 53, 1179, 2005; Nolze, G., *Cryst. Res. Technol.*, 43, 61, 2008.

six crystallographically equivalent variants. For the α/β phase transformation in pure titanium, it has been found that plates of β have a Burgers OR with the parent α (Seward et al., 2004). Several variants tended to occur in one grain. The Burgers relationship in zirconium alloys has also been investigated (Chauvy et al., 2006). Recently, EBSD has also been used on several systems to retrieve by calculation the orientation of the parent phase from measurement of the orientation of the product (Cayron et al., 2006; Germain et al., 2007).

Phase relationships of an increasingly complex nature are being investigated by EBSD. For example, the phases in the Nb–Si system have been studied (Miura et al., 2007). It was found that there were several ORs between the Nb and Nb_5Si_3 phases formed during the eutectoid reaction, some of which show good atomic matching. In another investigation, the relationship between NbC and ZrO_2 was elucidated (Faryna, 2003). Misorientations in the composite systems $\text{Al}_2\text{O}_3/\text{WC}$ and $\text{Al}_2\text{O}_3/\text{W}$ have also been studied in an ESEM (Šztwiertnia et al., 2006).

Just like the misorientation between two different grains, the ORs between different phases can also be expressed in the form of a misorientation distribution and displayed in the corresponding spaces (Section 9.6), most advantageously in Rodrigues space (Brückner et al., 2001; Kestens et al., 2005). In the case of two cubic phases—fcc and bcc—the computation and representation of an MODF proceeds analogous to single-phase materials, whereas in all other conceivable phase combinations, the different crystal symmetries render determination and evaluation of MODFs a complicated task. Schwarzer and Weiland (1988) studied orientations and phase relationships in a ferrite/martensite duplex steel by Kikuchi-pattern analysis in a TEM. From the orientations of contiguous ferrite and martensite grains, an MODF was computed and represented in Euler space. The MODF showed

**FIGURE 11.11**

(See color insert following page 240.) MODF between two different phases in a nickel/tungsten composite. The MODF was computed from the misorientations between adjacent grains of fcc nickel and bcc tungsten, which were obtained by EBSD (see also Figure 10.8).

low-angle boundaries and $45^\circ/\langle 100 \rangle$ misorientations, pointing at a Bain OR between ferrite and martensite (Table 11.1). Field et al. (1996) determined the MODF between ferrite and retained austenite by means of EBSD and presented it in Rodrigues space; they likewise observed a Bain-like OR between the two phases.

Figure 11.11 displays an example of the MODF between bcc tungsten and fcc nickel in a W/Ni composite material. The orientations of both phases were determined by means of automated EBSD orientation microscopy (Section 10.4.5), and the resulting maps—image quality map, orientation map, and phase map—are shown in Figure 10.8. Subsequently, the misorientations between tungsten and nickel across the phase boundaries were determined, expressed in terms of the mutual misorientation axis r and angle θ , and represented in the form of θ sections through the cylindrical angle/axis

space (Section 9.6.2). As in the previous two examples, the resulting MODE, displayed in Figure 11.11, shows a strong maximum of $45^\circ/\langle 100 \rangle$ misorientations, which indicates a Bain OR between the two phases (Sinclair et al., 2003). Note that in most cases more complex ORs between bcc ferrite and fcc austenite are obtained, however, which are usually expressed in terms of one of the phase relationships: Pitsch, Kurdjumov–Sachs, or Nishiyama–Wassermann (Table 11.1).

11.6 Summation

This chapter has shown how microtexture analysis can be extended to obtain crystallographic characterization of other features, particularly grain and phase boundaries, cracks and facets, and the whole connectivity of the microstructure. Such analyses, which have mainly arisen from EBSD, involve non-standard, multistage methodologies. No doubt over the next few years there will be an increase in sophistication and availability of these approaches, which in turn will enhance our understanding of microstructure and properties.

12

Synchrotron Radiation, Nondiffraction Techniques, and Comparisons between Methods

12.1 Introduction

In this chapter we introduce methods for texture determination that do not fit into the earlier sections on x-ray or neutron macrotexture or electron microscope-based microtexture techniques.

Although x-ray diffraction is usually associated with macrotexture (Section 4.3), such methods can in principle also be used for individual-grain (microtexture) measurements if it can be arranged that the necessary small volumes in a sample are irradiated with a sufficiently fine x-ray beam. X-rays generated in a synchrotron offer this possibility since they are characterized by an intensity several orders of magnitude higher than those generated by conventional x-ray tubes, combined with a high brilliance, that is, low angular divergence. Accordingly, Laue patterns from individual grains or Debye–Scherrer patterns from small polycrystalline volumes can be obtained (Section 12.2). Although the underlying methods, Laue and Debye–Scherrer, have been known for decades (Section 3.4), the application of synchrotron radiation in texture research is a quite new, rapidly emerging field.

All techniques for texture analysis mentioned so far are founded on the diffraction of radiation—electrons, x-rays, or neutrons—at the crystal lattice (Chapter 3). Besides those diffraction-based techniques, there are methods (e.g., ultrasonic or magnetic measurements or optical methods) to derive macrotextures or microtextures that are not based on diffraction of radiation. Since such techniques may still be of some interest for special applications, a short discussion is warranted (Section 12.3). Finally, Section 12.4 includes a summary of the various techniques used to determine macrotextures and local orientations, which have been discussed in this book, and a comparison of their main advantages and disadvantages.

12.2 Texture Analysis by Synchrotron Radiation

Modern electron synchrotrons with energies of 60 keV and more yield a white spectrum of x-rays with intensities of six to seven orders of magnitude higher than conventional x-ray tubes, combined with minimum angular divergence of less than 2 mrad. This unique combination of high photon flux, small beam size, and free choice of wavelength opens a wide range of possibilities for texture analysis. Short-wavelength synchrotron x-rays have similar penetration depths as neutrons, which allow global textures of big centimeter-sized specimens to be measured similarly as in neutron diffraction (Section 4.4). However, because of the local resolution of a high-energy synchrotron beam, measurements can also be performed on a local basis. Especially, the high brilliance of third-generation synchrotron radiation sources with x-ray intensities exceeding 100 keV enables new applications in x-ray microdiffraction with submicrometer beam sizes, where mesoscopic length scales of 0.1–100 μm can be studied. The strongly focused, high-intensity, polychromatic radiation favors synchrotron x-rays for local analysis of individual crystallites by means of the Laue technique (Section 3.4), which is discussed in Section 12.2.1. Alternatively, monochromatic radiation can be produced by using a monochromator crystal, and then synchrotron radiation can be used to generate Debye–Scherrer patterns in polycrystalline volumes (Section 12.2.2).

In brief, interesting applications of synchrotron radiation may include (Garbe et al., 1996)

- Nondestructive local texture measurements
- High-resolution texture analysis
- Investigation of texture gradients
- *In situ* texture measurements of texture transformations
- Determination of misorientation and characterization of grain boundaries, including boundary plane
- Internal strain characterization in selected local volumes
- Study of textures of noncentrosymmetric crystals by means of observations near the absorption edge (Section 3.6.1) with high anomalous scattering where Friedel's law does not apply (Bunge and Esling, 1981), since it is possible to tune the synchrotron x-ray wavelength in a wide range, although this has not been tested so far

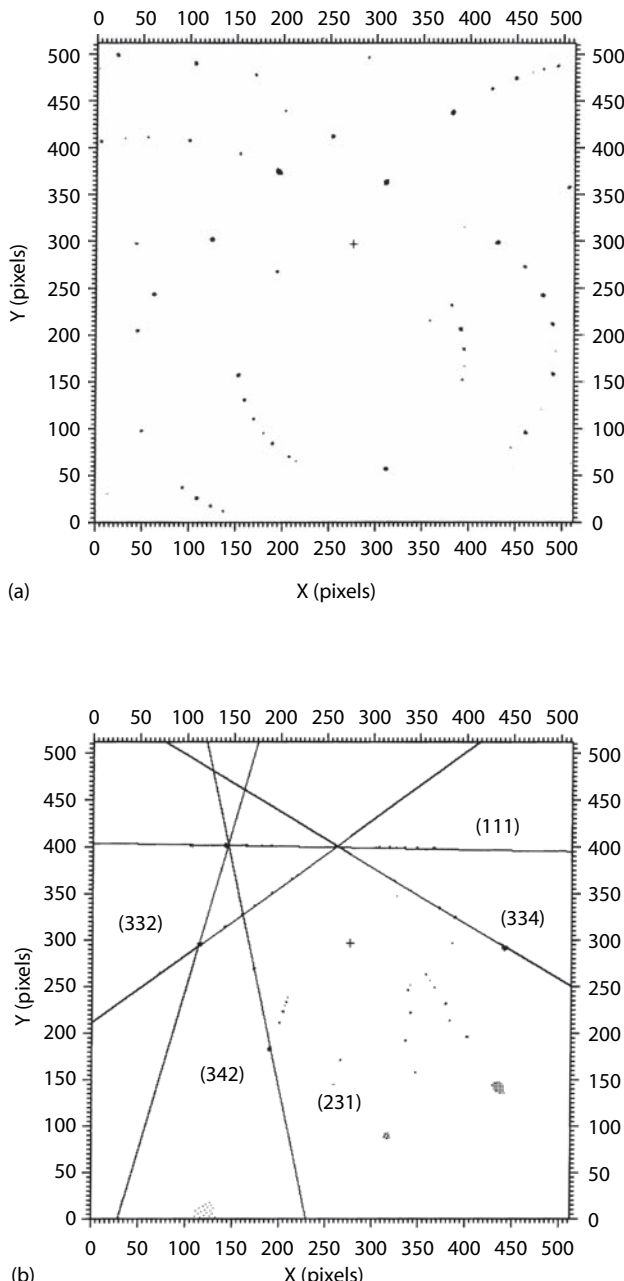
The main drawback of the synchrotron techniques is very limited availability of synchrotron sources in large-scale research facilities, similar to the case of neutron diffraction. Furthermore, interpretation of the data is much more complicated than for standard x-ray or electron diffraction techniques.

Finally, unlike in electron microscopy, the microstructure of the sample cannot be imaged simultaneously with the orientation measurements, so that the microstructure has to be recorded before the synchrotron investigation. Thus, experiments using synchrotron radiation will most likely be limited to special cases that cannot be accomplished by conventional x-ray or electron diffraction techniques.

12.2.1 Individual Orientations from Laue Patterns

The most common technique to determine the orientation of single crystallites by means of x-ray diffraction is the Laue method, which has been introduced in Section 3.4. In this method, the use of white (polychromatic) radiation ensures that for each set of lattice planes, x-rays will exist that fulfill Bragg's condition for diffraction. On intersection with a recording medium, the diffracted beams generate characteristic point patterns (Figure 3.9) that can be evaluated to derive the crystallographic orientation of the sampled volume. However, the beam diameter of conventional x-ray tubes is approximately 1 mm. As x-rays cannot be focused easily, small beam diameters of the order of microns—which would be necessary to achieve spatial resolution competitive with electron diffraction techniques—can only be obtained by a collimation of the primary beam. This, however, results in a strong reduction in intensity and, consequently, in unacceptably long times to record the diffraction patterns. Even under application of rotating anode x-ray tubes, a beam diameter of 10 μm would require illumination times of the order of 10 h, which makes large-scale microtexture analysis an unrealistic task (Gottstein, 1988). Therefore, the Laue technique is usually only applied for analysis of single crystals or very coarse-grained structures with a grain size exceeding 100 μm (Ferran et al., 1971).

To overcome these limitations, Gottstein (1986, 1988) suggested the use of the enormous intensity of synchrotron x-rays for Laue orientation determination. With a collimation of the synchrotron beam to a size of $5 \times 5 \mu\text{m}^2$ (sufficiently fine for many microtexture applications), illumination times of the order of 1 s could be realized. The sample was mounted in back-reflection geometry on a motorized x/y stage, which allowed scanning of the sample surface in a constant grid with steps of 10 μm . Fairly large numbers of orientations could be determined by recording the diffraction patterns on photographic films or x-ray-sensitive image plates, digitization of the patterns, and a subsequent, automated evaluation similar to that described for Kikuchi patterns (Brodesser et al., 1991). With the advent of CCD cameras, it became possible to record and interpret Laue patterns online (Wenk et al., 1997). For this purpose, the Laue patterns (Figure 12.1a) are converted into gnomonic projection (Appendix IV) where cozonial poles (hkl) lie on straight lines (Figure 12.1b). Next the Hough transform is applied, converting lines into points (Section 6.3.3). The computer then detects the points and calculates the

**FIGURE 12.1**

Laue patterns obtained with polychromatic synchrotron x-radiation. (a) Digitized Laue pattern from an olivine crystal (the small cross represents the pattern center). (b) Pattern from (a) transformed into a gnomonic projection with overlaid zones that were identified by a Hough transform. (Courtesy of H.R. Wenk.)

interzonal angles that are used to index the patterns, so that finally the orientation can be determined. As an alternative, a template-matching scheme for rapid indexing of Laue diffraction patterns has been developed, which was shown to offer good indexing rates even for low-quality patterns (Gupta and Agnew, 2009).

The sampling area investigated by this method is given by the selected beam diameter that can be reduced to as little as a few microns. However, considering the large penetration depth of the high-energy synchrotron x-rays, this means that highly elongated volumes of $10 \times 10 \times 1000 \mu\text{m}^3$ contribute to the Laue patterns, which prevents high-resolution local texture analysis in bulk materials. To overcome this limitation, thin sections of the materials can be analyzed in transmission geometry (Wenk et al., 1997). This results in a spatial resolution of the order of $10 \mu\text{m}$ that is sufficient for analysis of many geological materials and many metals in the recrystallized state, but is definitely inferior to electron microscopy-based techniques for orientation determination. However, the signal-to-noise ratio of the synchrotron Laue technique is superior, and furthermore, sample preparation is easy and nonconductive materials can readily be analyzed.

Recently, Larson and coworkers developed a technique based on Laue diffraction, which is capable of probing local crystal structure, grain orientation, and strain tensors with submicrometer spatial resolution (Larson et al., 2002; Yang et al., 2004). This so-called differential-aperture x-ray microscopy (DAXM) technique was installed at the Advanced Photon Source (APS) at Argonne National Laboratory. In contrast to the Debye–Scherrer techniques (Section 12.2.2), the use of a Laue-based technique with polychromatic radiation eliminates the need for sample rotation, which facilitates the spatial mapping below $5 \mu\text{m}$ and provides a truly 3-D probe for nondestructively investigating polycrystalline structures on mesoscopic length scales of $0.1\text{--}100 \mu\text{m}$.

In DAXM, a highly focused, high-energy polychromatic synchrotron x-ray beam with size of $0.5 \times 0.5 \mu\text{m}^2$ is directed onto the test sample. The x-ray beam penetrates the sample material and generates Laue diffraction spots over a distance of up to approximately $100 \mu\text{m}$. Laue diffraction patterns, emanating from the region of the sample lying in the path of the incident x-ray beam, are detected with a CCD camera located at 90° to the incident beam. A $50 \mu\text{m}$ platinum wire—acting as a knife-edge profiler—is traversed across the face of the sample so that Laue diffraction spots are systematically obscured from the CCD camera by the moving wire. In this manner, it is possible to establish the location in the sample from which the Laue spots originate. A computer program collates and reconstructs the Laue diffraction images from each microregion of the sample material along the path of the x-ray beam. By moving the sample with respect to the incident x-ray beam and, at each position, scanning the Pt wire across the sample, the local crystallographic orientation and residual deviatoric strain tensor can be determined with a spatial resolution of approximately $0.5 \times 0.5 \times 1.0 \mu\text{m}^3$ (Larson et al., 2002; Yang et al., 2004).

12.2.2 Local Textures from Debye–Scherrer Patterns in Polycrystalline Regions

For texture analysis in fine-grained polycrystalline samples by means of the Debye–Scherrer method with synchrotron radiation, a narrow beam of monochromatic x-rays is required. To achieve monochromatic radiation, the beam first passes a cooled copper plate that absorbs radiation with long wavelengths, and then a monochromator crystal selects the desired wavelength in the range of 0.01–0.1 nm (Poulsen and Juul Jensen, 1995). Finally, the monochromatic beam is collimated to the desired size and falls onto the sample, where the Debye–Scherrer patterns are generated in transmission geometry (Figure 12.2a). Szpunar and Davies (1984) have demonstrated that

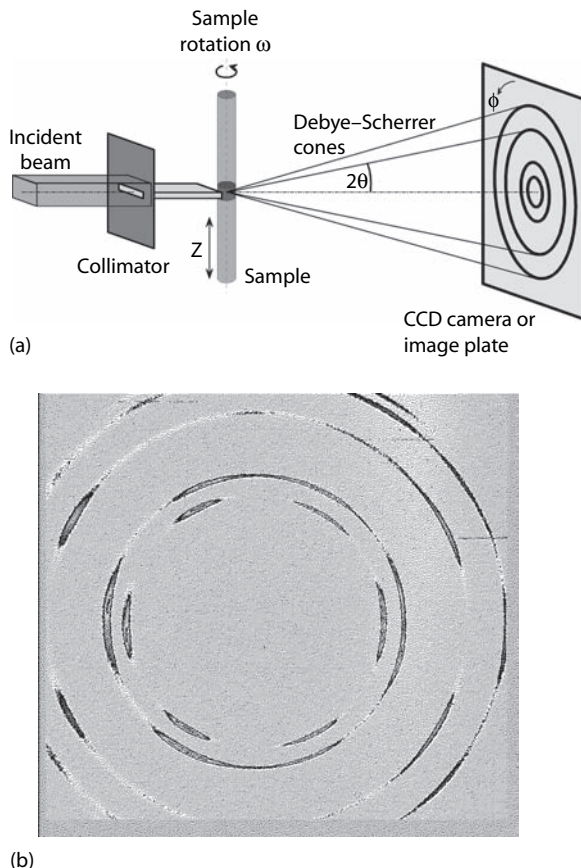


FIGURE 12.2

Texture analysis by the Debye–Scherrer method with monochromatic synchrotron radiation. (a) Schematic view of the experimental setup. 2θ is the scattering angle, ω describes the sample rotation, and ϕ denotes the angle along the Debye–Scherrer ring. (b) Example from a cold-rolled aluminum sheet (38% reduction, layer 2850 μm from the surface). (Courtesy of O. Mishin and D. Juul Jensen.)

it is possible to obtain reliable texture information from the Debye–Scherrer patterns that they recorded on photographic films. Nowadays, the diffraction patterns are recorded either with image plates or with a CCD camera (Section 4.3.4). For online analysis, CCD cameras are superior as they provide digitized intensities with a high spatial resolution and a wide dynamic range within a few seconds (Wenk and Grigull, 2003).

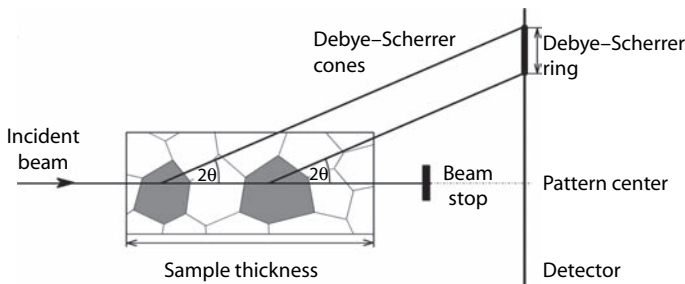
As discussed in Section 3.4, diffraction from a powder sample with random texture gives rise to a set of homogeneous concentric Debye–Scherrer rings that are related to the various reflecting lattice planes (hkl) through the Bragg angle θ . If the sample has a pronounced texture, the rings display intensity variations that are characteristic of the texture of the sampled volume (Wever, 1924). As an example, Figure 12.2b illustrates the diffraction pattern recorded with a CCD camera from a cold-rolled aluminum sheet. After appropriate intensity corrections, the texture can be derived from the analysis of the intensity variations along the Debye–Scherrer rings.

If samples with axially symmetric textures, such as wires, are analyzed in transmission with the fiber axis normal to the incident x-ray beam, then a single set of Debye–Scherrer rings contains already the necessary texture information. By this method, texture variations in small rods of Ni–Fe alloys, prepared by electroforming techniques, have been documented and represented in inverse pole figures (Bäckström et al., 1996). For nonaxial textures, one set of Debye–Scherrer rings is not sufficient, but, in analogy to SAD pole figures in TEM (Section 8.3.2), the sample needs to be rotated by an angle ω (Figure 12.2a) and in each setting a pattern has to be recorded. Geometric expressions for the transformation of the angles φ , θ , and ω into the pole figure coordinates α and β have been given by Poulsen and Juul Jensen (1995) and Heidelbach et al. (1999).

Hard synchrotron x-rays with short wavelengths of approximately 0.01 nm have similar penetration depths as neutrons, so that global textures of centimeter-sized specimens can be measured (Brokmeier, 2006). Investigations on metals such as iron, titanium, copper, aluminum, and magnesium have been carried out up to 35 mm sample thickness. Because of the high photon flux, the total counting times for texture measurements can be very short, allowing *in situ* experiments on a short timescale to measure the texture changes under applied load or at high temperatures (Yi et al., 2006).

However, the high brilliance of a synchrotron source makes it ideally suited for measurements on a local scale. With appropriate focusing/collimation of the incident beam, the textures from small mesoscopic volumes can be analyzed. For instance, as sketched in Figure 12.2a, through-thickness texture heterogeneity in a cylindrical sample can be studied by measuring the texture with a finely collimated x-ray beam at several positions along the z axis of the sample (Mishin et al., 2000; Skrotzki et al., 2003).

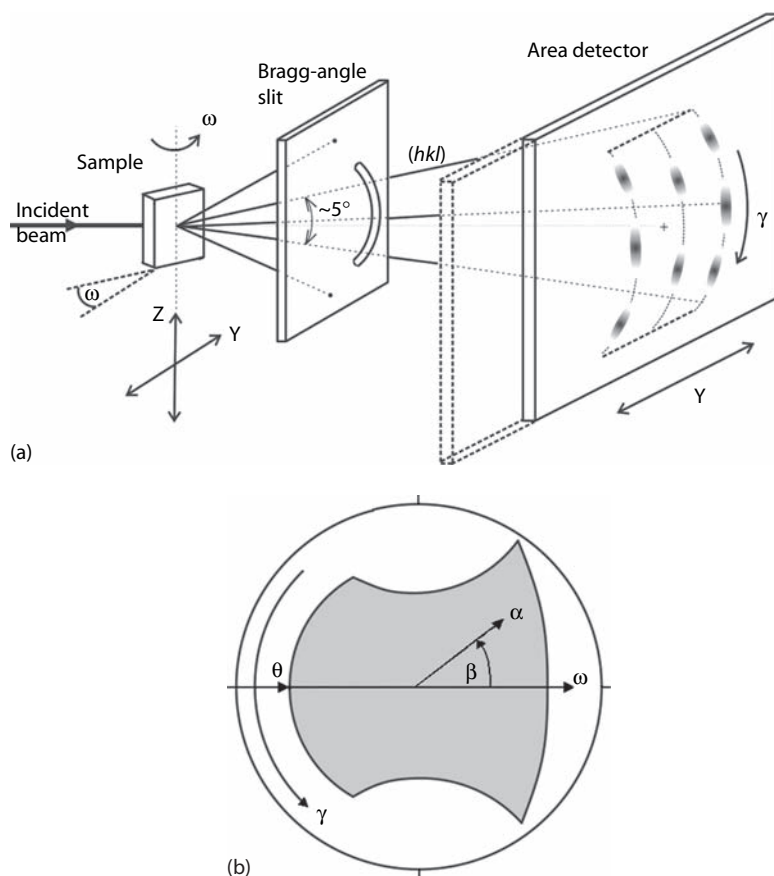
Because of the extremely small divergence of the incident beam in synchrotron diffraction experiments, such diffraction patterns can be exploited to yield information on microstructure and texture of small volumes (tenths

**FIGURE 12.3**

Analysis of local textures within bulk samples with monochromatic synchrotron radiation. Broadening of the Debye–Scherrer rings diffracted in two grains with identical orientations at different positions along the beam path. (Adapted from Reeves, A. et al., *Mater. Sci. Forum*, 217–222, 595, 1996.)

of millimeters), within bulk samples of centimeter size (Black et al., 1991). As illustrated in Figure 12.3, the radial width of the Debye–Scherrer rings is linked to the sample thickness along the beam path. For a Bragg angle of 5° and a sample thickness of 10 mm, the width of the Debye–Scherrer rings is of the order of 2 mm, and the different parts of the Debye–Scherrer rings disclose the texture information of different layers within the sample volume. Thus, the spatial resolution in terms of the volume analyzed along the beam path is determined by the radial resolution of the Debye–Scherrer rings. Provided a CCD camera with a resolution of 100 μm is used, small volumes with a length of the order of 500 μm along the beam direction can be resolved. By this method, Reeves et al. (1996) were able to differentiate diffraction patterns from three different through-thickness layers in a 15 mm aluminum plate. Garbe et al. (1996) refined this method by introducing a conical Debye–Scherrer slit system in combination with a pinhole to define the local volume. With this setup, pole figures of small volumes with size down to $50 \times 50 \times 600 \mu\text{m}^3$ could be distinguished and the disappearance of the shear texture component at the surface of a 3 mm aluminum sheet could be traced through the depths of 50–850 μm.

Bunge and coworkers have installed a “sweeping” technique at the high-energy (short-wavelength) beamline BW5 at HASYLAB/DESY in Hamburg, Germany (Wcislak et al., 2002; Bunge et al., 2003; Bunge, 2005). This instrument is essentially the advancement of standard diffractometry with an area detector (Wassermann and Grewen, 1962; see Section 4.3.4), where the use of a high-brilliance, high-intensity synchrotron beam allows spatially resolved measurements of textures of materials with very high orientation resolution. The sweeping technique is based on the continuous movement of an area detector during exposure. That is to say, the detector undergoes a vertical translation motion in direction Y with the velocity synchronized with the velocity of sample rotation about angle ω (Figure 12.4a). The sweeping technique yields a continuous 2-D image of a pole figure (Figure 12.4b), without

**FIGURE 12.4**

Texture diffractometer with the sweeping detector and the Bragg-angle slit system. (a) The Debye–Scherrer rings passing through a diffraction angle slit are continuously registered by the sweeping area detector; (b) continuous coverage of a pole figure. (Adapted from Bunge, H.-J. et al., *J. Appl. Crystallogr.*, 36, 1240, 2003.)

the necessity of interpolation as in the discontinuous step-scan technique of conventional pole figure measurements (Section 4.3.3). Similar sweeping modes can be applied to obtain images of other sections through the 6-D orientation–location space $\{x, y, z, \varphi_1, \Phi, \varphi_2\}$, that is, two orientation coordinates, two location coordinates, or a combination thereof. Both the orientational as well as lateral resolution of the instrument is better by at least two orders of magnitude than that of conventional texture goniometers (Wcislaw et al., 2002), so that, in many cases, the individual grains of a polycrystalline material can be resolved. Although location resolution is generally limited by the width of the entrance slit to typically $100\text{ }\mu\text{m}$, finer resolution of the order of $10\text{ }\mu\text{m}$ can be achieved by using other slit systems or a focused incident beam

(Figure 12.4a). Then, under certain conditions, the position of individual grains in the polycrystalline structure, and hence the complete 6-D “orientation stereology” of grain-resolved microstructures, can be obtained.

Over the past 10 years a novel technique, referred to as 3-D x-ray diffraction (3-D XRD), has been developed for measuring local crystallographic orientations and thereby generating a truly 3-D map of the microstructure (Poulsen et al., 2001; Poulsen and Juul Jensen, 2002; Poulsen, 2004; Juul Jensen et al., 2006). The 3-D XRD microscope has been developed by Risø National Laboratory, Denmark, in cooperation with the European Synchrotron Radiation Facility (ESRF) in Grenoble, France, and is operating at the ESRF materials science beamline (ID11). A similar facility was established at the APS of Argonne National Laboratory (Pantleon et al., 2004). Based on the use of highly penetrating hard x-rays and a “tomographic” approach to diffraction, the method enables a nondestructive 3-D description of the microtexture and microstructure within polycrystals. Hence, the 3-D XRD concept can be thought of as a 3-D equivalent of orientation microscopy in SEM (Juul Jensen et al., 2006).

Figure 12.5 illustrates the principal components of the 3-D XRD microscope. The incoming beam is a monochromatic focused x-ray beam tunable to energies in the range 45–100 keV. The focusing is obtained by means of a bent Laue crystal or multilayer mirrors (Lienert et al., 1999). The specimen is mounted on a sample tower that allows translations (x , y , z), rotation (ω), and tilting of the sample with an absolute accuracy of 1 μm . At present, four CCD detectors are available, covering a range of pixel sizes from 1.2 to 225 μm . Detectors with a small pixel size are typically placed close to the sample for optimal spatial resolution, whereas those with a large pixel size are placed

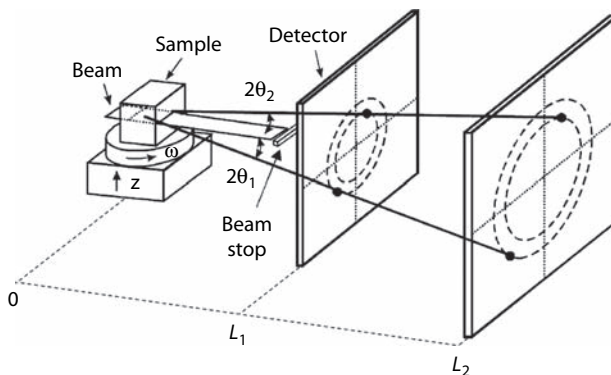


FIGURE 12.5

Sketch of the 3-D XRD microscope. The diffraction spots appearing in exposures of the area detector at different sample-detector distances are projected back into the illuminated plane in the sample. (Adapted from Poulsen, H.F. et al., *J. Appl. Crystallogr.*, 34, 751, 2001.)

far from the sample for strain characterization. For *in situ* measurements of the microtexture and microstructure evolution, a cryostat, a tensile machine, and several furnaces are available.

The incoming monochromatic beam penetrates the sample, and all microstructural volume elements within the illuminated gauge volume that fulfill the Bragg condition generate diffracted beams. The incoming beam is confined by focusing, possibly in combination with slits. It determines the gauge volume, which is typically a plane or a volume within the sample. To probe the complete crystal structure within the illuminated layer or volume, the sample is rotated around the ω axis perpendicular to the incoming beam (Figure 12.5).

A critical issue is the determination of the exact position of the diffracting volume within the gauge volume. The conventional approach for this is to limit the gauge volume to a point by slit(s) and scan the sample with respect to this point. However, in general, this approach is too slow for dynamic studies. Hence, in the 3-D XRD concept, it is replaced by a tracking method that allows diffraction from large gauge volumes (Lauridsen et al., 2001). Diffraction patterns are recorded at two or more distances between the sample and the detector(s) (distances L_1, L_2, \dots , etc. in Figure 12.5). The position of the diffracting volume element is then determined by back-extrapolating a straight line through the corresponding diffraction spots at different distances L_i all the way back to the originating volume within the sample.

At present the mapping precision is $\sim 5 \times 5 \times 1 \mu\text{m}^3$, provided that there is a sufficiently large orientation difference to the neighboring volumes to avoid overlap of diffraction spots. Fewer diffracting grains may be achieved by reducing the beam size or by inserting a conical slit between the sample and the detector (Nielsen et al., 2000). For comparison, the 3-D crystal microscope DAXM described in Section 12.2.1 has better spatial resolution but shorter penetration depths and much worse time resolution than the 3-D XRD microscope at ESRF.

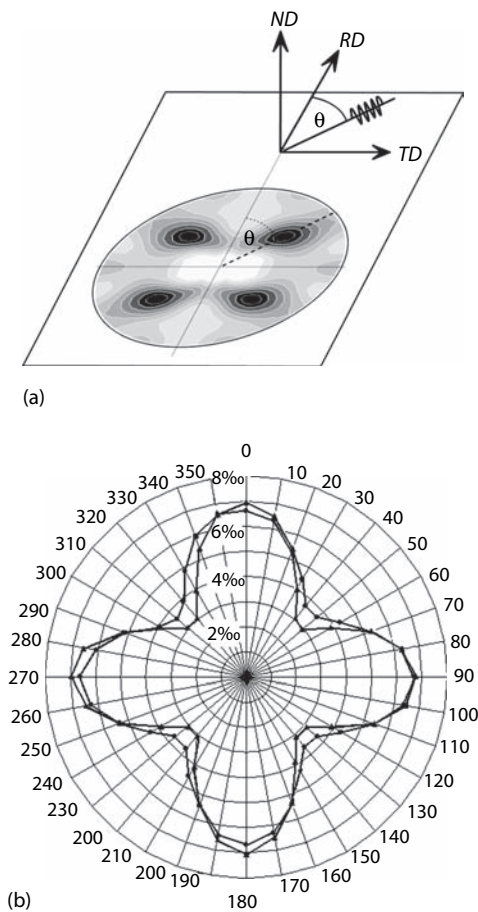
12.3 Texture Analysis by Nondiffraction Techniques

A vast majority of techniques that are in use for texture analysis are based on the diffraction of radiation at the crystal lattice planes (Chapter 3). However, besides those diffraction-based techniques there are a few other methods to derive either macrotextures or microtextures that may be of some interest for special applications. In general, such techniques make use of a crystal property being anisotropic in different crystallographic directions. For instance, measurements of ultrasonic velocity or magnetism yield information on the integral orientation distribution (macrotexture) of the sample analyzed (Section 12.3.1). The optical reflectivity of a crystal depends on the

12.3.1 Ultrasonic Velocity

通过超声波测量来推导晶格学纹理的方法是基于超声波在不同晶格学方向传播速度不同的事实，即，利用超声波在不同晶格学方向传播速度不同的特性。无论是激光超声波（LUS）方法还是更常见的电磁声学换能器（EMAT）都可以用来分析片材的纹理并推导出结果的各向异性属性（Lu et al., 1996; Moreau et al., 2002）。超声波纹理测量涉及测量板模速度的角变化。为了这个目的，EMAT发送和接收超声波在各种方向 θ 在片材平面内（Figure 12.6a）。LUS依赖于光束进行换能。该技术使用一个脉冲激光（几纳秒）来生成超声波，并使用一个较长的脉冲（持续数微秒），或一个第二连续激光，与光学干涉仪一起用于检测超声波。特别是，LUS是一个实用的解决方案，用于远程测试，特别是在大距离下，生产线上快速移动部件的检查，以及在恶劣环境下的检查（Hutchinson et al., 2002）。Figure 12.6b展示了铝热带在不同方向上的超声波传播时间（即，它们的速度或“慢速”）的极坐标图。很明显，在 $\pm 45^\circ$ 和 $\pm 135^\circ$ 时，波速更快，这归因于立方体纹理的再结晶化热带。

通过超声波速度的测量，只能获得第四阶系数C，这给出了一种相当差、低分辨率的ODF描述。然而，第四阶系数C已经包含了片材的全弹性及塑性各向异性（Bunge, 1993）；因此，超声波方法在工业应用中对于快速非破坏性测试及在线确定片材质量具有兴趣。例如，在钢片中，超声波速度与成形参数r及 Δr 之间建立了相关性（Kawashima et al., 1993; Thompson et al., 1993; Moreau et al., 2002; Davis et al., 2008a）。在铝中，不同晶格学方向上的超声波速度差异较小，但无论如何，纹理及由此产生的各向异性在r值及弹性模量方面都有可能被确定（Spies and Salama, 1990; Thompson et al., 1993; Schneider and Österlein, 1996; Davis et al., 2008b）。此外，已证明超声波纹理测量可以很容易地区分滚动和再结晶化纹理。

**FIGURE 12.6**

(a) Anisotropy of the velocity of an ultrasonic wave in different in-plane directions in a textured sheet; (b) directional variation of travel time (slowness) of an SH_0 wave in an aluminum hot strip with a mild cube texture (two different locations; polar plot). (Courtesy of J. Hirsch.)

of aluminum alloys and hence can be used for nondestructive online analysis of the progress of recrystallization (Anderson et al., 1994; Kruger et al., 2003). In conclusion, within some limitations, ultrasonic methods have been developed to yield quantitative texture data and, in particular, information on the elastic and plastic anisotropy of sheet materials.

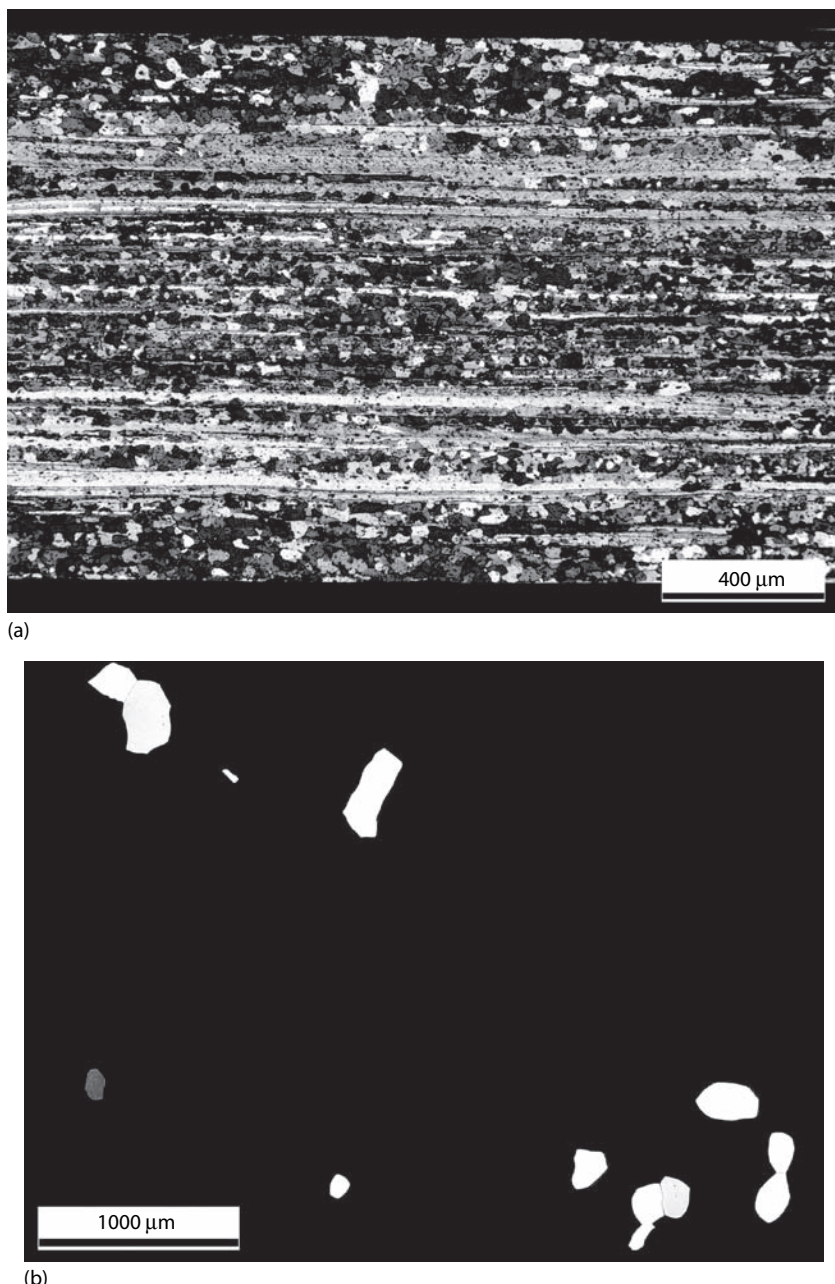
12.3.2 Optical Methods

When optically anisotropic crystals are studied with polarized light in an optical microscope, the color and the intensity of the reflected or transmitted light are dependent on the crystal orientation. To use this effect for

orientation determination, thin sections of the sample are mounted on a microscope with the so-called universal stage (U stage) that allows rotation of the sample about four or five axes (similar to the texture goniometer). The crystal under investigation is rotated until its optical axis is aligned parallel to the microscope axis. The required rotation angles then yield the crystallographic orientation with regard to the external sample frame. This method finds wide applications in geology where most materials have low crystal symmetry and, hence, are optically anisotropic (Wenk, 1985; Bunge et al., 1994; Ullemeyer et al., 2000).

Owing to their high symmetry, most metals are optically isotropic, which precludes investigations with the U stage. In some cases, however, an appropriate chemical etch can introduce an anisotropy of the optical properties, which then can be used to derive the orientation of the individual crystallites (Nauer-Gerhardt and Bunge, 1986). Especially, anodical oxidation of aluminum causes the epitactical growth of an optically anisotropic oxide layer on the sample surface ("Barker etch," Barker, 1950). For pure aluminum and many aluminum alloys, anodization for approximately 1 min in a reagent of 49% H_3O , 49% methanol, and 2% HF with a voltage of 60–70 V yields good results. Under polarized light, the grains then appear with different brightness in accordance with their crystallographic orientation (Sætre et al., 1986; Kröger et al., 1988). Accordingly, this method can be used for a rapid appraisal of the microstructure (Figure 12.7a) and measurements of quantitative grain size data. Anodical oxidation is also applied to assess the quality of aluminum foil for electrolytic capacitors, where the capacitance of the final product is determined by the fraction of cube-oriented grains. Under polarized light, the cube orientation $\{001\}\langle100\rangle$ can easily be distinguished from the other recrystallization texture components, mostly the R orientation $\{124\}\langle211\rangle$ (Ibe et al., 1984; Hasenclever and Scharf, 1996): Because of its symmetry the cube orientation always appears black, independent of sample rotation, whereas grains with other orientations are usually brighter and furthermore change their brightness on sample rotation (Figure 12.7b).

Another optical method to determine individual orientations, which has been known for many decades, is based on the evaluation of etch pits (Kostron, 1950; Tucker and Murphy, 1952/53; Nauer-Gerhardt and Bunge, 1986). Here, the etching attack is concentrated at points where dislocations intersect with the sample surface. Only those crystallographic planes whose normals correspond to the direction of minimum dissolution velocity are attacked. In the metallographic micrographs, the etch pits appear as characteristic polygons, whose shape is determined by the crystallographic orientation (Figure 12.8). In the 1990s, this technique regained some interest via analyzing the evolution of the Goss orientation during secondary recrystallization in iron–silicon transformer steel (Abbruzzese et al., 1991; Böttcher et al., 1992; Baudin et al., 1994; Lee et al., 1995). However, both the spatial resolution and the accuracy of orientation determination by this technique are limited, so that generally only qualitative or semiquantitative conclusions can be drawn.

**FIGURE 12.7**

Examples of the anodical oxidation of aluminum alloys (Barker etch, investigated with polarized light). (a) Microstructure of recrystallized aluminum, enabling easy analysis of grain size and shape, (b) high-purity aluminum condenser foil, where bright areas indicate noncube-oriented grains. (Courtesy of W.D. Finkelnburg.)

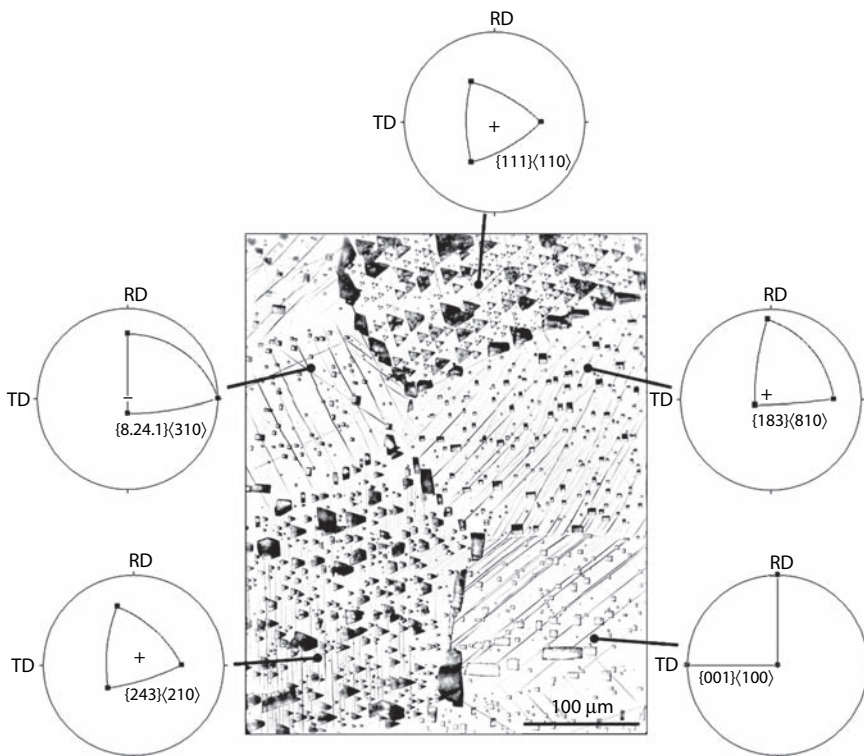
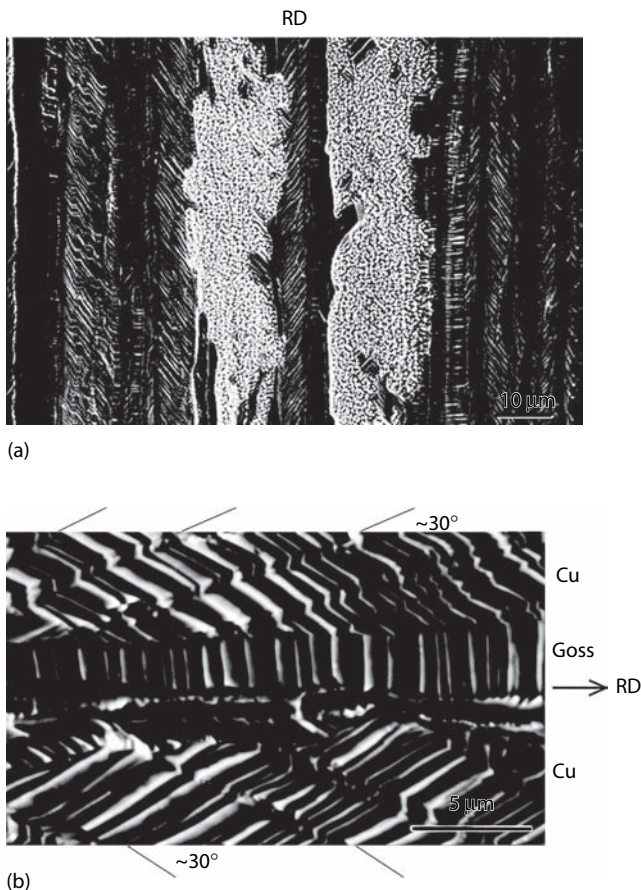


FIGURE 12.8
Etch pits in as-cast aluminum. (Courtesy of K. Kuhnke.)

For copper and some copper alloys, very satisfactory results can be obtained with a more recent method, the “{111}-etching” (Köhlhoff et al., 1988). If copper is etched in hot concentrated HNO_3 , only the {111} planes are attacked. The $\langle 110 \rangle$ directions along which the corresponding {111} planes intersect form the valleys and rims of the deep-etched surface. As an example, Figure 12.9a shows a micrograph obtained from a partially recrystallized copper sheet. It is obvious that the etch patterns differ in the various deformed grains, which is a result of their different crystallographic orientations. Furthermore, some layers of the sheet reveal a totally different etching pattern. Here, recrystallization has started, leading to the formation of cube-oriented regions (Engler et al., 1993). Studying such samples in an SEM permits analysis of structures down to sizes of the order of 1 μm . Figure 12.9b shows an SEM micrograph obtained at a higher magnification ($\times 5000$), revealing the existence of grain-scale shear bands in Cu-oriented matrix grains (Engler, 2000). Even within the shear bands, etch patterns can be resolved. By comparing the etch patterns with an atlas that contains the patterns of all possible orientations, the local orientations can be evaluated

**FIGURE 12.9**

Examples of the {111}-etching technique to reveal the orientation topography in copper alloys (SEM). (a) Partially recrystallized copper. (b) Shear bands in a 90% cold-rolled copper–manganese alloy. (From Engler, O., *Acta Mater.*, 48, 4827, 2000. With permission.)

to an accuracy of 5°–10° (Wang et al., 1995). A major advantage of this newly developed technique is the quasicontinuous imaging of orientations in the microstructure, which enables one to draw conclusions on the orientation topography.

The main drawback of the {111}-etching technique—and in general of all chemical techniques for orientation determination—is its strong material dependence. Suitable etchants to evaluate crystallographic features are only available for a few materials. Methods based on the diffraction of radiation, in contrast, are not only much less material sensitive but in general also much more precise, and therefore superior for orientation determination.

12.4 Summation: Comparison and Assessment of the Experimental Methods for Texture Analysis

This book introduces a variety of common techniques to derive the crystallographic texture of crystalline samples. A vast majority of techniques for texture analysis are based on the diffraction of radiation—neutrons, x-rays, or electrons—at the crystal lattice (Chapter 3); these techniques are summarized in Figure 3.15. A few other techniques make use of a crystal property being anisotropic in different crystallographic directions (Section 12.3). In the following text, all the various techniques are summarized and their main advantages and disadvantages compared.

Techniques to obtain the texture of a polycrystalline sample by means of x-ray or neutron diffraction provide the integral texture of the polycrystalline array (Chapter 4). This macrotexture discloses information about the volume fraction associated with each orientation, which can be used to predict texture-related anisotropy of polycrystalline behavior during elastic and plastic straining, and also physical properties such as magnetic permeability and thermal expansion (Chapter 1). Furthermore, analysis of the texture changes during the thermomechanical treatment of materials yields valuable, statistically relevant information about the mechanisms of the underlying metallurgical processes, particularly deformation, recrystallization, or phase transformations. In geology, macrotexture analysis can provide insight into the geological mechanisms that have led to rock formation millions of years ago.

Because of the very limited access to neutron beam lines, macrotexture measurements will, in most cases, be performed by x-ray diffraction. However, the much greater depth of penetration into the sample by neutrons offers some distinct advantages for texture analysis in large grained or irregularly shaped specimens, small volume fractions of a second phase, samples with low crystal symmetry, or multiphase systems (Sections 4.4 and 4.5). However, with a view to determine textures of small volumes, x-rays are superior. In neutron diffraction the entire specimen volume of typically several cubic centimeters contributes to the diffracted intensities, whereas in standard x-ray techniques only volumes of the order of cubic millimeters are sampled, so that the textures of specific layers in a sheet can be discriminated.

Synchrotron sources yield a white spectrum of x-rays with intensities many orders of magnitude higher than conventional x-ray tubes combined with minimum angular divergence. This combination of high intensity, small beam size, and free choice of wavelength opens a wide range of possibilities for texture analysis (Section 12.2). Experiments that make use of synchrotron diffraction represent a hybrid between the macrotexture techniques covering large bulk samples and the microtexture techniques (see the following text) that record the texture of volumes down to the individual grain level. As in the case of neutron diffraction, the main drawback of synchrotron-based

techniques is the very limited availability of synchrotron sources so that experiments using this radiation will most likely be limited to special cases that cannot be accomplished by other techniques but necessitate one of the characteristic advantages of synchrotron radiation.

In contrast to the macrotecture methods, microtexture or local texture analysis is performed by sampling the orientations of individual single crystallites—grains and subgrains. (The only exception to this is the SAD pole figure technique [Section 8.3.2] that records the texture in a small contiguous polycrystalline volume.) The main requirements for an experimental technique to determine local, usually individual, orientations are as follows:

- The technique yields the crystallographic orientation unambiguously and with high accuracy.
- The spatial resolution of the applied technique is higher than the size of the microstructural regions of interest.
- It is possible to locate and image specific regions of interest in the microstructure of the specimen, from which orientation measurements can be obtained.
- Orientation measurement and evaluation is automated to allow orientation mapping.

The main characteristics that can be addressed by the methods for local texture analysis are as follows:

- The spatial arrangement of the crystallographic orientations in the microstructure, that is, orientation topography
- The intensity distribution of orientations in specific subregions of the microstructure
- Orientation correlations, that is, misorientations, between (usually) neighboring grains in the microstructure

The most popular techniques for local orientation determination are summarized in Table 12.1. This table and other work on this subject (Dingley, 1981; Humphreys, 1984; Schwarzer, 1989; Gottstein and Engler, 1993) clearly show that individual orientations are determined most easily and with maximum accuracy from electron diffraction patterns in an electron microscope (SEM and TEM). Table 12.1 distinguishes these methods from others with great accuracy—errors of only a few degrees—and a high spatial resolution in the submicrometer range. A further advantage of electron microscopy techniques is based on the fact that orientation and microstructure of the site of interest are analyzed simultaneously with the same spatial resolution. The corresponding evaluation methods are nowadays highly standardized and automated (Chapter 6), so that local orientation and microtexture determination can be used for routine purposes. Use of other methods, such

TABLE 12.1

Overview of the Most Common Techniques for Determination of Local Orientations

Method	Technique	Spatial Resolution ^a	Angular Accuracy	Application
TEM	CBED	1 nm	0.1°	Polycrystals (grains, subgrains, deformed microstructure, inhomogeneities, recrystallization nuclei, ...)
	MBED	10 nm	0.2°	
	SAD	1 μm	5°	
SEM	EBSD	<0.1 μm	0.5°	Polycrystals (grains, subgrains)
	SAC	10 μm	0.5°	Polycrystals (grains)
	Micro-Kossel	10 μm	0.5°	Polycrystals (grains)
X-ray diffraction	Conventional Laue	100 μm	2°	Single crystals, very coarse grains
	Synchrotron based	0.1–100 μm	0.1°	Polycrystals (grains)
Optical techniques	Selective ((111)) etching	1 μm	5°–10°	Polycrystals (grains)
	Etch pits	20–100 μm	>10°	Polycrystals (coarse grains)

^aDiameter of the minimum detectable sample area.

as selective etching techniques (Section 12.3), Laue x-ray diffraction (Section 3.4), and the micro-Kossel technique (Section 7.2), is restricted to some special applications.

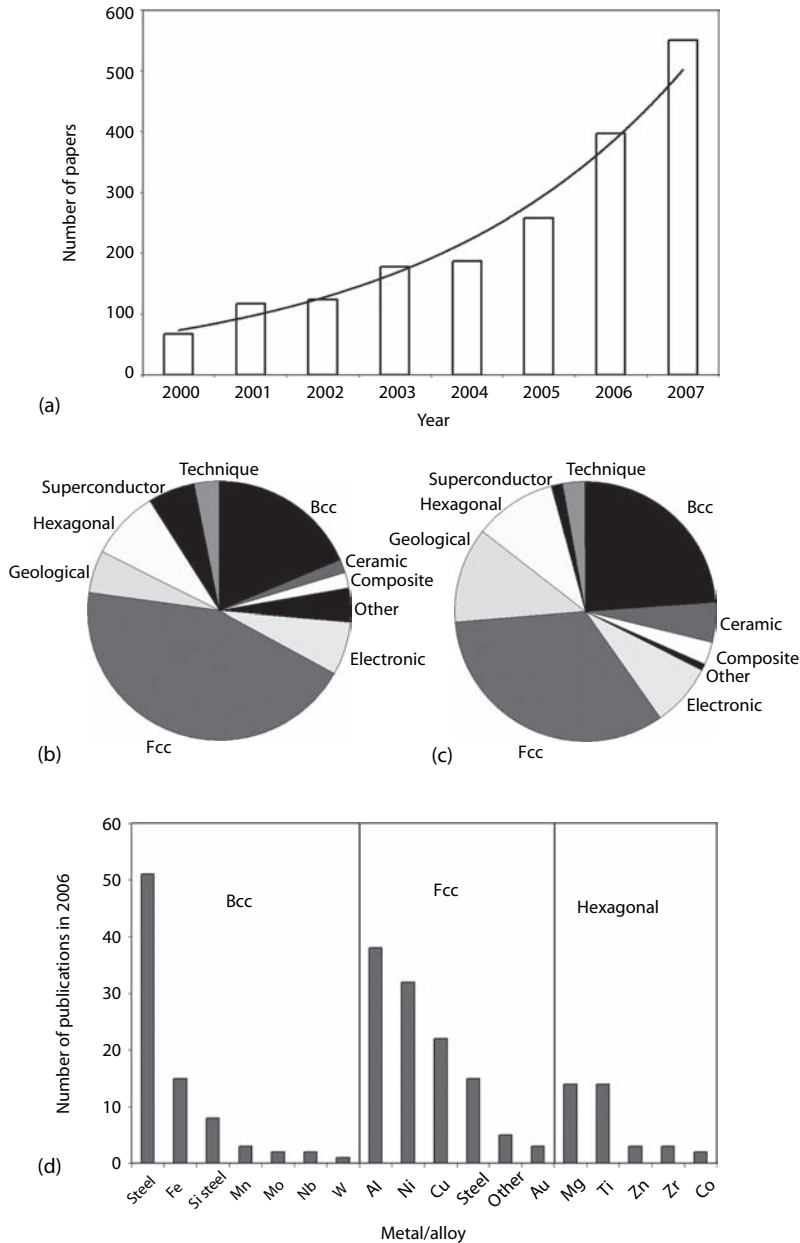
The main advantage of TEM-based techniques (Chapter 8) is obviously their excellent spatial resolution, which is at least one order of magnitude better than that for SEM. With regard to the different techniques for determination of local orientations, evaluation of Kikuchi patterns obtained by means of microdiffraction (MBED or CBED) is advantageous compared to the SAD technique, as the former yields higher spatial resolution as well as much higher angular accuracy. However, only SAD allows direct measurement of pole figures of small volumes in TEM. With CBED, Kikuchi patterns from regions as small as a few nanometers can be obtained. This high spatial resolution also allows investigation of orientations in highly deformed samples. Finally, TEM offers much more additional information on the microstructure—precipitates, dislocations, and dislocation arrangements—than SEM. The major disadvantages of TEM are the difficult and laborious sample preparation and the very small area of view, which is usually much less than 100 μm in diameter. This generally restricts the application of TEM to few

selected examples with only limited information on the statistical relevance of the effects observed.

The limitations of TEM provided great incentive to develop SEM-based techniques to perform single-grain orientation measurements in thick bulk samples; the available techniques—micro-Kossel diffraction, SAC, and EBSD—are described in Chapter 7. A comparison of these three techniques clearly proves that the EBSD technique offers by far the most advanced possibilities due to its ease of performance combined with high accuracy and high spatial resolution, and is the principal technique used in SEM nowadays. Sample preparation is not critical; electrolytic polishing or slight chemical etching is usually sufficient. The evaluation of the patterns is very much facilitated by the large steric angle obtained, which speeds up evaluation and reduces ambiguity of the determined orientation. A spatial resolution better than 0.1 μm even allows investigation of deformed samples, if the microstructure comprises undistorted (dislocation-free) volumes—cells or subgrains—in excess of this size. Because of the lower signal-to-noise ratio of the EBSD patterns, the accuracy of orientation determination is somewhat inferior to TEM, but with an accurate calibration a relative error of 0.5°–1° can be obtained, which is sufficient for most texture applications.

The development of fully automated EBSD has led to the implementation of orientation microscopy and orientation mapping (Chapter 10). The ability to produce automatically an orientation map, in other words, a depiction of the microstructure in terms of its orientation constituents, has greatly enhanced the application of EBSD. Although the visualization aspects of mapping contribute to its appeal, the opportunity for quantification of the orientation/microstructure relationship on a very fine scale is scientifically a much more powerful feature. Fast mapping of more than 100 data points per second on suitable materials has rendered EBSD a very powerful characterization technique indeed.

The trends in EBSD usage have been assessed and quantified by an analysis of the published papers in 2 years, 2003 and 2006. The total number of publications has doubled in the period 2003–2006 (Figure 12.10a). In 2003, the emphasis was particularly on fcc metals, accounting for nearly half the publications at that time. The most noticeable trend between 2003 and 2006 is the upsurge in application of EBSD to crystal structures and material groups other than fcc metals, particularly those more complex. The number of papers on geological materials has increased more than four times, and that on hexagonal, bcc, and electronic materials has more than doubled. This is evidence that EBSD is becoming more widely applicable to the entire range of crystalline materials. Furthermore, although a few years ago the main application of EBSD was to microtexture, it is shown in Figure 12.10a that the rate of increase of texture-related EBSD papers is less than that of all EBSD investigations. Now, the range of applications has broadened to include a whole range of microstructure characterization.

**FIGURE 12.10**

(See color insert following page 240.) (a) Numbers of papers published in the period 2000–2007, which report EBSD, showing an approximately exponential increase. (From ScienceDirect.com.) (b) Breakdown of EBSD application according to material type based on publications in 2003. (c) Breakdown of EBSD application according to material type based on publications in 2006. (d) Breakdown of EBSD applications according to metals (or alloys based on that metal) in 2006.

Increasingly, applications of EBSD may include combination with other characterization techniques. For example, EBSD can be combined with EDS so that chemical and crystallographic data are acquired simultaneously (Nowell and Wright, 2004; Dingley, 2004; see Section 7.6.4). Coupling of EBSD with FIB tomography in a dual beam instrument capable of both precision sectioning and high-resolution imaging enables acquisition of microtexture information in three dimensions (Zaefferer et al., 2008; see Section 11.3.4). EBSD has also been linked with atomic force microscopy (AFM) to correlate crystallography with surface evolution (Chandrasekaran and Nygård, 2003; Schuh et al., 2003). Another aspect is the use of EBSD data as input for finite element modeling and other simulations (Engler et al., 2005b; Zhang et al., 2007). These and many other applications are augmenting and enriching the use of EBSD as an investigative tool.

Figures 12.10b and 12.10c show a breakdown of EBSD usage in 2003 and 2006, respectively, according to material type. There is also a group labeled “technique,” which refers to publications that describe aspects of EBSD methodology, rather than being material specific. Metals are overwhelmingly the largest category, and they are further divided into fcc, bcc, and hexagonal crystal structures. In 2006, fcc metals remained the biggest single group for EBSD-related investigations. This group was composed mainly of aluminum, copper, or nickel alloys. The bcc group is the second largest group, mainly representing steel. The hexagonal metals group is the smallest of the metals groups and represents mainly titanium and magnesium alloys. The proportions of all these, and other, metals and alloys are shown in Figure 12.10d.

A further key feature of microtexture determination is that crystallographic analysis of surfaces can be undertaken (Chapter 11). Such surfaces include grain or phase boundaries, cracks, slip traces, and external surfaces such as facets or fracture surfaces. A limited amount of analysis of grain/phase boundaries can be carried out in TEM, but most analysis, because of the 3-D nature of the surface/specimen geometry, is the province of SEM and EBSD. Recently crystallographic analysis of surfaces by EBSD, especially in three dimensions, has become viable and will be a growth area in the future.

Hence it can be summarized that nowadays basically two techniques have prevailed for measurement of local orientations: TEM and EBSD in SEM. Maximum spatial resolution is obtained by evaluation of Kikuchi patterns in a TEM. However, as soon as the microstructural regions exceed a size of approximately 1 μm , the EBSD technique in SEM is most suitable. Thus, EBSD is able to fill the gap between the TEM-based techniques, which have the highest spatial resolution but mostly lack statistics, and the x-ray macrotextures, which yield statistically reliable data but have no information on the spatial arrangement of the orientations. Already much work has been done to expand further the capabilities of EBSD for microtexture analysis, and also to introduce EBSD as an alternative to macrotexture analysis to

obtain overall texture data. This includes improving the spatial resolution, accuracy, and speed of operation using FEGSEM, improved solve algorithms, and faster processors, respectively (Section 7.6). Hence, EBSD will find more application in areas that have traditionally been the province of either TEM or x-rays.

It should be emphasized that different techniques should not be considered as competitive but should be applied in a complementary manner. A combination of different techniques for orientation determination with increasing spatial resolution yields much more valuable information on the underlying mechanisms than that accessible by the sole use of the individual techniques.

Appendices

Appendix I

MILLER AND MILLER-BRAVAIS INDICES

Within the crystal coordinate system, both crystallographic directions and lattice planes are commonly described in terms of integer indices, called the *Miller indices*, which are derived as follows.

A crystallographic direction is given by the vector r in the crystal:

$$r = ua + vb + wc \quad (\text{I.1})$$

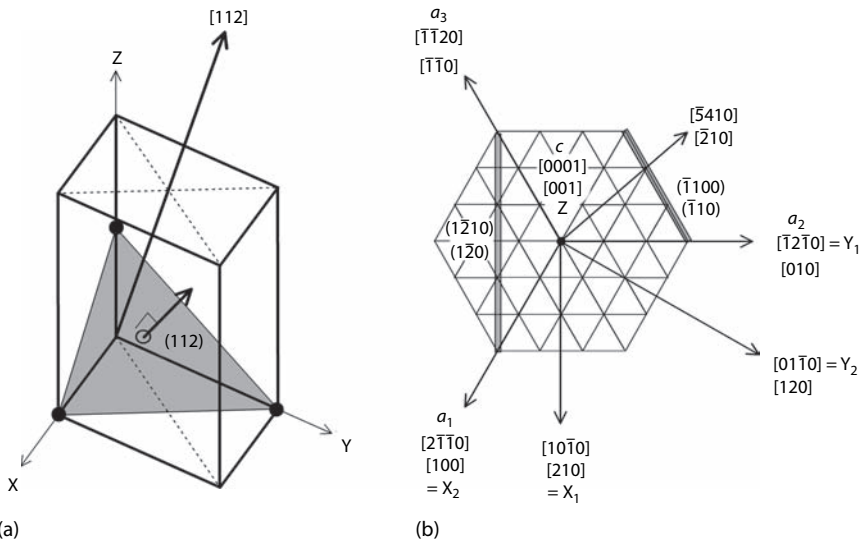
where a , b , and c are the base vectors of the unit cell (Figure 2.1b); thus, the direction is unambiguously described by the values of u , v , and w . It is common practice to characterize a direction by the triplet of smallest integers having the same ratios, which is denoted by the symbol $[uvw]$. A lattice plane is described according to

$$h\frac{x}{a} + k\frac{y}{b} + l\frac{z}{c} = 1 \quad (\text{I.2})$$

where x , y , and z are the coordinates of any point on that plane. Crystal planes are usually denoted by the reciprocal multiples of the axis intercepts h , k , and l , again reduced to the smallest integers with the same ratios; these are the *Miller indices* (hkl).

Figure I.1a shows the (112) plane in an orthorhombic crystal. The normal to this plane—called its *pole*—is also commonly indexed (112) . Note that this normal (112) is not parallel to the direction $[112]$. Only in cubic crystals are plane normals and directions with same indices parallel, whereas for other crystals this only holds for special cases. Because of the symmetry elements of most crystal structures, a lattice direction or a lattice plane is symmetrically equivalent to some others. For instance, planes like (112) , (121) , and $(1\bar{2}1)$ all have the same atomic arrangement, lattice spacing, and so on; thus they are summarized by the family $\{112\}$ —denoted by curly brackets rather than parentheses. Likewise, a generic set of symmetrically equivalent directions is denoted by angular brackets $\langle uvw \rangle$.

Though directions and planes can be described by the Miller indices in *all* crystal structures, for hexagonal and trigonal crystals it is often more convenient to use a coordinate system with four axes. Commonly, the z axis is chosen along the sixfold or threefold c axis such that the x and y axes come to lie in the basal plane. To account for the symmetry of the basal plane, an

**FIGURE I.1**

Example of the crystallographic indices for directions and planes. (a) (112) plane and [112] direction in an orthorhombic crystal. Note that the (112) plane normal is not parallel to the [112] direction. (b) Planes and directions in the (0001) basis plane of a hexagonal lattice expressed as both Miller–Bravais and Miller indices.

additional, redundant axis is introduced in such a way that the three axes, a_1 , a_2 , and a_3 , all lie at 120° to each other in the basal plane (Figure I.1b), leading to the description of directions and planes by a four-index notation, the *Miller–Bravais indices*. Lattice planes can still be described by their reciprocal intercepts on all four axes; they are denoted by the Miller–Bravais indices $(hkil)$ with $h + k + i = 0$. When directions are described by the Miller–Bravais indices $[uvtw]$ (with $u + v + t = 0$), the third index has to be considered as an additional vector component (Figure I.1b). Since the third index can readily be derived, it is often replaced by a dot— $(\bar{2}\bar{1}.0)$ —or sometimes even completely omitted— $(\bar{2}\bar{1}0)$. However, the resulting three-index set is not to be confused with the Miller indices.

The four-index Miller–Bravais notation has the advantage that symmetrically equivalent directions and planes have similar indices and hence can easily be recognized. As an example, the directions $a_1 = [2\bar{1}\bar{1}0]$, $a_2 = [\bar{1}2\bar{1}0]$, and $a_3 = [\bar{1}\bar{1}20]$ would be indexed in the Miller notation as $[100]$, $[010]$, and $[\bar{1}\bar{1}0]$ so that symmetry is no longer apparent (Figure I.1b). However, some calculations that are important for indexing Kikuchi patterns, including determination of a common zone from two planes, a plane from two directions, and interzonial angles (Section 6.3.1), can be more easily performed by

using the three-index Miller indices. The transformations linking the two conventions are (Partridge, 1969):

For planes, that is, $(hkil) \rightarrow (HKL)$:

$$H = h; K = k; L = l \quad (\text{I.3a})$$

$$h = H; k = K; i = -H - K; l = L \quad (\text{I.3b})$$

For directions, that is, $[uvtw] \rightarrow [UVW]$:

$$U = u - t; V = v - t; W = w \quad (\text{I.4a})$$

$$u = 2U - V; v = 2V - U; t = -U - V; w = 3W \quad (\text{I.4b})$$

Appendix II

CRYSTALLOGRAPHICALLY RELATED OPERATIONS

As discussed in Section 2.3.3, there are a number of *crystallographically related solutions* for an orientation or misorientation, depending on the crystal system. These crystallographically related solutions are generated by premultiplying the orientation or misorientation matrix M by a symmetry operator T_i :

$$M' = T_i M \quad (\text{II.1})$$

where the value of i depends on the symmetry of the crystal system. The 24 matrices T_i for cubic symmetry are

$$\begin{array}{cccc} \begin{pmatrix} 1 & 0 & 0 \\ 0 & 1 & 0 \\ 0 & 0 & 1 \end{pmatrix} & \begin{pmatrix} 0 & 0 & \bar{1} \\ 0 & \bar{1} & 0 \\ \bar{1} & 0 & 0 \end{pmatrix} & \begin{pmatrix} 0 & 0 & \bar{1} \\ 0 & 1 & 0 \\ 1 & 0 & 0 \end{pmatrix} & \begin{pmatrix} \bar{1} & 0 & 0 \\ 0 & 1 & 0 \\ 0 & 0 & \bar{1} \end{pmatrix} \\ \begin{pmatrix} 0 & 0 & 1 \\ 0 & 1 & 0 \\ \bar{1} & 0 & 0 \end{pmatrix} & \begin{pmatrix} 1 & 0 & 0 \\ 0 & 0 & \bar{1} \\ 0 & 1 & 0 \end{pmatrix} & \begin{pmatrix} 1 & 0 & 0 \\ 0 & \bar{1} & 0 \\ 0 & 0 & \bar{1} \end{pmatrix} & \begin{pmatrix} 1 & 0 & 0 \\ 0 & 0 & 1 \\ 0 & \bar{1} & 0 \end{pmatrix} \\ \begin{pmatrix} 0 & \bar{1} & 0 \\ 1 & 0 & 0 \\ 0 & 0 & 1 \end{pmatrix} & \begin{pmatrix} \bar{1} & 0 & 0 \\ 0 & \bar{1} & 0 \\ 0 & 0 & 1 \end{pmatrix} & \begin{pmatrix} 0 & 1 & 0 \\ \bar{1} & 0 & 0 \\ 0 & 0 & 1 \end{pmatrix} & \begin{pmatrix} 0 & 0 & 1 \\ 1 & 0 & 0 \\ 0 & 1 & 0 \end{pmatrix} \\ \begin{pmatrix} 0 & 1 & 0 \\ 0 & 0 & 1 \\ 1 & 0 & 0 \end{pmatrix} & \begin{pmatrix} 0 & 0 & \bar{1} \\ \bar{1} & 0 & 0 \\ 0 & 1 & 0 \end{pmatrix} & \begin{pmatrix} 0 & \bar{1} & 0 \\ 0 & 0 & 1 \\ \bar{1} & 0 & 0 \end{pmatrix} & \begin{pmatrix} 0 & 1 & 0 \\ 0 & 0 & \bar{1} \\ \bar{1} & 0 & 0 \end{pmatrix} \\ \begin{pmatrix} 0 & 0 & \bar{1} \\ 1 & 0 & 0 \\ 0 & \bar{1} & 0 \end{pmatrix} & \begin{pmatrix} 0 & 0 & 1 \\ \bar{1} & 0 & 0 \\ 0 & \bar{1} & 0 \end{pmatrix} & \begin{pmatrix} 0 & \bar{1} & 0 \\ 0 & 0 & \bar{1} \\ 1 & 0 & 0 \end{pmatrix} & \begin{pmatrix} 0 & 1 & 0 \\ 1 & 0 & 0 \\ 0 & 0 & \bar{1} \end{pmatrix} \\ \begin{pmatrix} \bar{1} & 0 & 0 \\ 0 & 0 & 1 \\ 0 & 1 & 0 \end{pmatrix} & \begin{pmatrix} 0 & 0 & 1 \\ 0 & \bar{1} & 0 \\ 1 & 0 & 0 \end{pmatrix} & \begin{pmatrix} 0 & \bar{1} & 0 \\ \bar{1} & 0 & 0 \\ 0 & 0 & \bar{1} \end{pmatrix} & \begin{pmatrix} \bar{1} & 0 & 0 \\ 0 & 0 & \bar{1} \\ 0 & \bar{1} & 0 \end{pmatrix} \end{array}$$

The 12 symmetry operation matrices for hexagonal symmetry are (Hagege et al., 1980)

$$\begin{array}{cccc}
 \begin{pmatrix} 1 & 0 & 0 \\ 0 & 1 & 0 \\ 0 & 0 & 1 \end{pmatrix} & \begin{pmatrix} 0.5 & 0.87 & 0 \\ -0.87 & 0.5 & 0 \\ 0 & 0 & 1 \end{pmatrix} & \begin{pmatrix} -0.5 & 0.87 & 0 \\ -0.87 & -0.5 & 0 \\ 0 & 0 & 1 \end{pmatrix} & \begin{pmatrix} -1 & 0 & 0 \\ 0 & -1 & 0 \\ 0 & 0 & 1 \end{pmatrix} \\
 \begin{pmatrix} -0.5 & -0.87 & 0 \\ 0.87 & -0.5 & 0 \\ 0 & 0 & 1 \end{pmatrix} & \begin{pmatrix} 0.5 & -0.87 & 0 \\ 0.87 & 0.5 & 0 \\ 0 & 0 & 1 \end{pmatrix} & \begin{pmatrix} 1 & 0 & 0 \\ 0 & -1 & 0 \\ 0 & 0 & -1 \end{pmatrix} & \begin{pmatrix} 0.5 & 0.87 & 0 \\ 0.87 & -0.5 & 0 \\ 0 & 0 & -1 \end{pmatrix} \\
 \begin{pmatrix} -0.5 & 0.87 & 0 \\ 0.87 & 0.5 & 0 \\ 0 & 0 & -1 \end{pmatrix} & \begin{pmatrix} -1 & 0 & 0 \\ 0 & 1 & 0 \\ 0 & 0 & -1 \end{pmatrix} & \begin{pmatrix} -0.5 & -0.87 & 0 \\ -0.87 & 0.5 & 0 \\ 0 & 0 & -1 \end{pmatrix} & \begin{pmatrix} 0.5 & -0.87 & 0 \\ -0.87 & -0.5 & 0 \\ 0 & 0 & -1 \end{pmatrix}
 \end{array}$$

The 4 symmetry operation matrices for orthorhombic symmetry are

$$\begin{array}{cccc}
 \begin{pmatrix} 1 & 0 & 0 \\ 0 & 1 & 0 \\ 0 & 0 & 1 \end{pmatrix} & \begin{pmatrix} 1 & 0 & 0 \\ 0 & \bar{1} & 0 \\ 0 & 0 & \bar{1} \end{pmatrix} & \begin{pmatrix} \bar{1} & 0 & 0 \\ 0 & 1 & 0 \\ 0 & 0 & \bar{1} \end{pmatrix} & \begin{pmatrix} \bar{1} & 0 & 0 \\ 0 & \bar{1} & 0 \\ 0 & 0 & 1 \end{pmatrix}
 \end{array}$$

Appendix III

CRYSTALLOGRAPHICALLY RELATED SOLUTIONS FOR THE FOUR S-TEXTURE VARIANTS

S1	S2	S3	S4
(123)[634] ^a	(123)[$\bar{6}\bar{3}4$]	(213)[364]	(213)[$\bar{3}\bar{6}4$]
(321)[$\bar{4}3\bar{6}$]	(321)[4 $\bar{3}6$]	(31 $\bar{2}$)[$\bar{4}6\bar{3}$]	(31 $\bar{2}$)[4 $\bar{6}3$]
($\bar{1}2\bar{3}$)[$\bar{6}34$]	($\bar{1}2\bar{3}$)[634]	($\bar{2}1\bar{3}$)[$\bar{3}64$]	($\bar{2}1\bar{3}$)[$\bar{3}\bar{6}4$]
($\bar{3}21$)[436]	($\bar{3}21$)[$\bar{4}36$]	($\bar{3}12$)[463]	($\bar{3}12$)[$\bar{4}\bar{6}3$]
(13 $\bar{2}$)[64 $\bar{3}$]	(13 $\bar{2}$)[$\bar{6}43$]	(23 $\bar{1}$)[3 $\bar{4}6$]	(23 $\bar{1}$)[$\bar{3}46$]
(1 $\bar{2}\bar{3}$)[6 $\bar{3}4$]	(1 $\bar{2}\bar{3}$)[$\bar{6}34$]	(2 $\bar{1}\bar{3}$)[3 $\bar{6}4$]	(2 $\bar{1}\bar{3}$)[$\bar{3}\bar{6}4$]
(132)[643]	(132)[$\bar{6}\bar{4}3$]	(231)[346]	(231)[$\bar{3}46$]
(2 $\bar{1}3$)[364]	(2 $\bar{1}3$)[$\bar{3}64$]	(1 $\bar{2}3$)[$\bar{6}\bar{3}4$] ^a	(1 $\bar{2}3$)[$\bar{6}34$]
($\bar{1}2\bar{3}$)[$\bar{6}3\bar{4}$]	($\bar{1}2\bar{3}$)[634] ^a	($\bar{2}1\bar{3}$)[$\bar{3}6\bar{4}$]	($\bar{2}1\bar{3}$)[364]
($\bar{2}1\bar{3}$)[$\bar{3}64$]	($\bar{2}1\bar{3}$)[$\bar{3}6\bar{4}$]	($\bar{1}2\bar{3}$)[$\bar{6}34$]	($\bar{1}2\bar{3}$)[$\bar{6}\bar{3}4$] ^a
(231)[3 $\bar{4}6$]	(231)[$\bar{3}4\bar{6}$]	(132)[643]	(132)[$\bar{6}4\bar{3}$]
(312)[$\bar{4}63$]	(312)[4 $\bar{6}3$]	(321)[436]	(321)[$\bar{4}36$]
($\bar{2}3\bar{1}$)[$\bar{3}4\bar{6}$]	($\bar{2}3\bar{1}$)[346]	($\bar{1}3\bar{2}$)[$\bar{6}4\bar{3}$]	($\bar{1}3\bar{2}$)[643]
($\bar{3}1\bar{2}$)[$\bar{4}6\bar{3}$]	($\bar{3}1\bar{2}$)[$\bar{4}63$]	($\bar{3}2\bar{1}$)[4 $\bar{3}6$]	($\bar{3}2\bar{1}$)[$\bar{4}3\bar{6}$]
($\bar{3}1\bar{2}$)[$\bar{4}63$]	($\bar{3}1\bar{2}$)[$\bar{4}6\bar{3}$]	($\bar{3}2\bar{1}$)[436]	($\bar{3}2\bar{1}$)[$\bar{4}36$]
(23 $\bar{1}$)[34 $\bar{6}$]	(23 $\bar{1}$)[$\bar{3}46$]	(1 $\bar{3}2$)[$\bar{6}4\bar{3}$]	(1 $\bar{3}2$)[$\bar{6}43$]
($\bar{2}3\bar{1}$)[$\bar{3}46$]	($\bar{2}3\bar{1}$)[346]	($\bar{1}3\bar{2}$)[$\bar{6}43$]	($\bar{1}3\bar{2}$)[643]
(31 $\bar{2}$)[$\bar{4}6\bar{3}$]	(31 $\bar{2}$)[$\bar{4}63$]	($\bar{3}2\bar{1}$)[4 $\bar{3}6$]	($\bar{3}2\bar{1}$)[$\bar{4}3\bar{6}$]
($\bar{3}1\bar{2}$)[$\bar{4}63$]	($\bar{3}1\bar{2}$)[$\bar{4}6\bar{3}$]	($\bar{3}2\bar{1}$)[436]	($\bar{3}2\bar{1}$)[$\bar{4}36$]
(23 $\bar{1}$)[34 $\bar{6}$]	(23 $\bar{1}$)[$\bar{3}46$]	(1 $\bar{3}2$)[$\bar{6}4\bar{3}$]	(1 $\bar{3}2$)[$\bar{6}43$]
($\bar{2}3\bar{1}$)[$\bar{3}46$]	($\bar{2}3\bar{1}$)[346]	($\bar{1}3\bar{2}$)[$\bar{6}43$]	($\bar{1}3\bar{2}$)[643]
(31 $\bar{2}$)[$\bar{4}6\bar{3}$]	(31 $\bar{2}$)[$\bar{4}63$]	($\bar{3}2\bar{1}$)[4 $\bar{3}6$]	($\bar{3}2\bar{1}$)[$\bar{4}36$]
(21 $\bar{3}$)[364]	(21 $\bar{3}$)[$\bar{3}64$]	(12 $\bar{3}$)[634]	(12 $\bar{3}$)[$\bar{6}34$]
($\bar{1}3\bar{2}$)[$\bar{6}4\bar{3}$]	($\bar{1}3\bar{2}$)[$\bar{6}43$]	($\bar{2}3\bar{1}$)[$\bar{3}46$]	($\bar{2}3\bar{1}$)[$\bar{3}4\bar{6}$]
(321)[$\bar{4}36$]	(321)[436]	(31 $\bar{2}$)[$\bar{4}63$]	(31 $\bar{2}$)[$\bar{4}6\bar{3}$]
($\bar{2}1\bar{3}$)[$\bar{3}64$]	($\bar{2}1\bar{3}$)[364]	(12 $\bar{3}$)[$\bar{6}34$]	(12 $\bar{3}$)[$\bar{6}\bar{3}4$]
($\bar{1}3\bar{2}$)[$\bar{6}4\bar{3}$]	($\bar{1}3\bar{2}$)[$\bar{6}43$]	($\bar{2}3\bar{1}$)[$\bar{3}46$]	($\bar{2}3\bar{1}$)[$\bar{3}4\bar{6}$]
($\bar{3}2\bar{1}$)[$\bar{4}36$]	($\bar{3}2\bar{1}$)[436]	(31 $\bar{2}$)[$\bar{4}63$]	(31 $\bar{2}$)[$\bar{4}6\bar{3}$]

^aThe lowest angle solution.

Appendix IV

SPHERICAL PROJECTION AND THE STEREOGRAPHIC, EQUAL-AREA, AND GNOMONIC PROJECTIONS

Projection is used in many branches of crystallography to represent the key features of crystals, namely, the relationships between lattice planes and directions. The subject of this book, texture, is an aspect of crystallography, and to understand such attributes as Kikuchi patterns (Chapter 6) and pole figures (Sections 2.5, 5.2, and 9.2), it is crucial to gain an elementary knowledge of projection geometry.

A crystal can be represented by a set of normals, one from each crystallographic plane. Angular relationships between planes are therefore the same as those between their respective normals. If a sphere having the same origin as the crystal itself is circumscribed on the crystal, the intersections of the plane normals, known as *poles*, with the sphere surface form a *spherical projection*, otherwise known as a *reference sphere* (Figure IV.1). The symmetry of the crystal itself is carried through to the representation on the reference sphere. This means that the reference sphere is divided, by the crystal

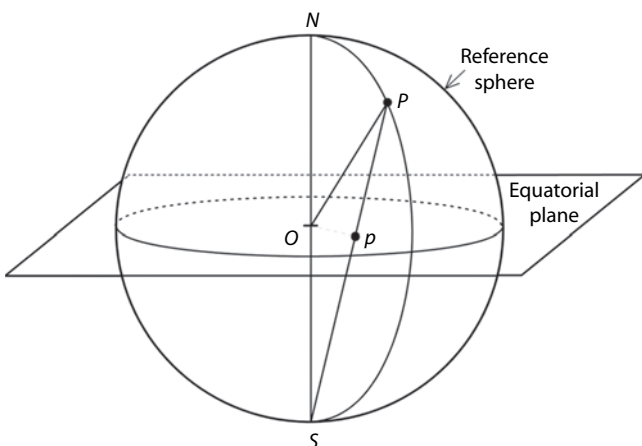


FIGURE IV.1

A spherical projection (reference sphere) with origin, "North Pole," and "South Pole" labeled O , N , and S , respectively. A crystal is imagined to lie at O . The normal of a plane in the crystal intersects the reference sphere at P . P is projected from the South Pole onto the equatorial plane at p ; this is the stereographic projection of P .

symmetry planes, into spherical triangles. For example, the cubic, hexagonal, and orthorhombic systems have 48, 24, and 8 crystallographically equivalent *stereographic unit triangles*, respectively. Various other projections are then introduced to project the 3-D reference sphere onto a more manageable 2-D flat form.

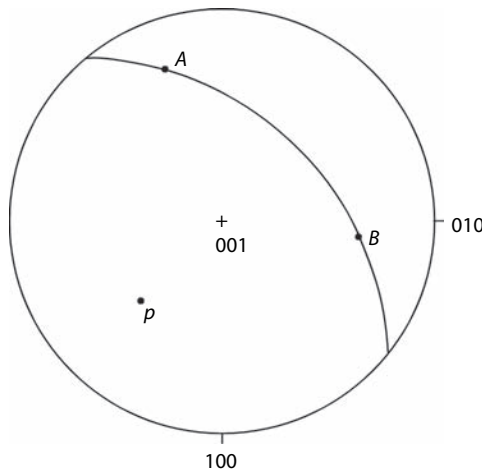
IV.1 The Stereographic Projection

The *stereographic projection* is a means of representing 3-D angular relationships in two dimensions. In the present context, the angular relationships of interest are those between crystallographic plane normals or between crystallographic directions. The main application of the stereographic projection in texture analysis is that pole figures/inverse pole figures, misorientations (Section 9.5.1), and especially one angle/axis space (Sections 2.7.3 and 9.6.2) are usually presented in stereographic projection (although equal-area projections [Section IV.2] are also sometimes used).

The intermediate stage in the construction of a stereographic projection is spherical projection of poles onto the reference sphere as described earlier. Using terminology relating to the Earth, the point of projection is the South Pole and the plane of projection is the equatorial plane as shown in Figure IV.1. It can be seen that poles in the Northern Hemisphere fall inside the equator or primitive circle, poles on the primitive circle project onto themselves, and poles in the Southern Hemisphere fall outside the primitive circle. It is more convenient to project poles in the Southern Hemisphere from the North Pole so that they also fall inside the primitive circle. They are denoted in the stereographic projection by open circles to distinguish them from poles arising from the Northern Hemisphere, which are denoted by smaller, filled circles. In Figure IV.1, the projection p of the pole P onto the equatorial plane is given by $r \tan \angle OSP$, where r is the radius of the sphere and $\angle OSP = \frac{1}{2} \angle NOP$.

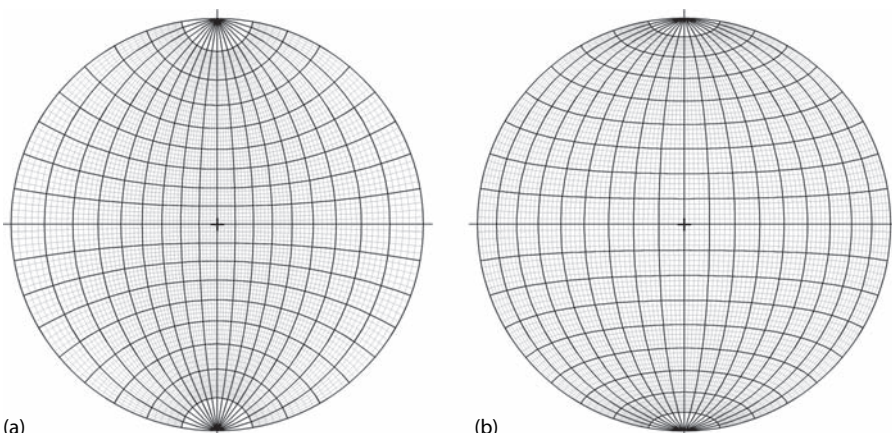
The main attraction for crystallographers of the stereographic projection is that angular relationships in the crystal are preserved in the projection. Consideration of the projection geometry shows that the angle between the center of the projection, O , and the primitive circle is 90° . For crystals with orthogonal symmetry, it is conventional to denote the “axes” of the standard stereogram (i.e., the three crystal axes 100, 010, and 001) in the positions shown in Figure IV.2. This figure shows a standard stereographic projection, that is, the equatorial plane, illustrating some of its basic features. p is a pole of a plane, and the trace of the plane itself is a “great circle.” A great circle is the projection of any plane that passes through the origin of the reference sphere (whereas a plane that does not pass through the origin projects as a “small circle”).

A plane is usually represented by its normal (pole), although sometimes it is more convenient to represent it by the trace of the plane, that is, the great

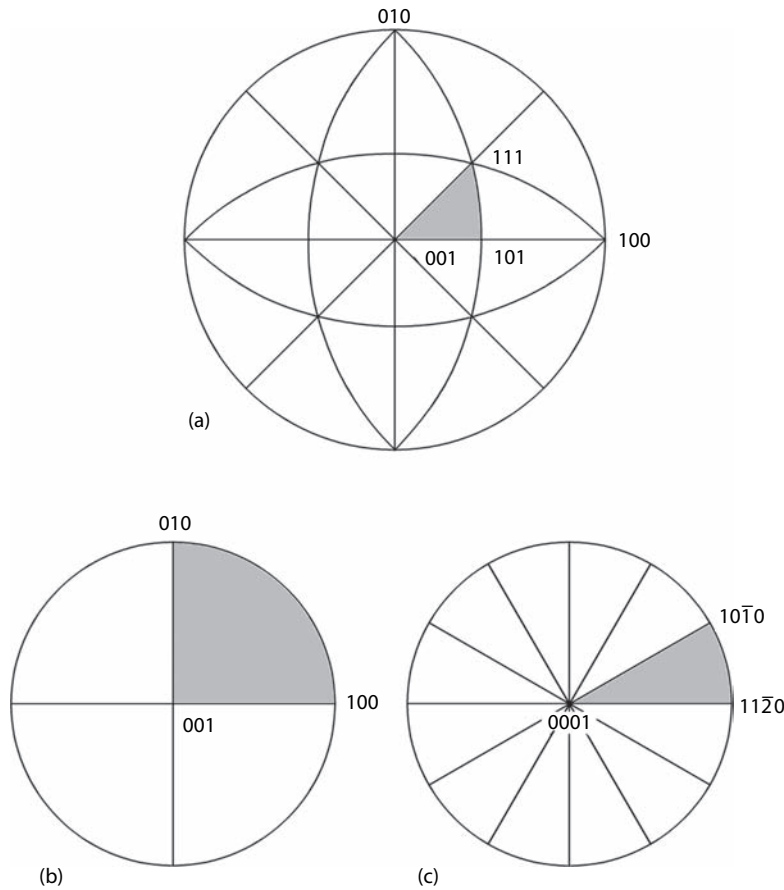
**FIGURE IV.2**

Stereographic projection showing the projection of the great circle (zone) of which p is the pole. A and B lie on the zone of p , and the angle between them is measured along the great circle that connects them.

circle or *zone* (Figures 11.5 and IV.2). The angle between two poles/directions is measured along a great circle that passes through both of them. For example, in Figure IV.2, A and B are directions that lie in the same plane, and the angle between them is measured along the great circle connecting them. Since p is the plane normal, the angle between p and any points on the plane (e.g., A and B) is 90° . Angles on the stereogram are measured with the aid of a grid known as a *Wulff net* that is marked in 2° intervals as shown in Figure IV.3a.

**FIGURE IV.3**

(a) Wulff net for measuring angles in stereographic projection. (b) Schmidt net for measuring angles in equal-area projection (thick lines— 10° intervals; thin lines— 2° intervals).

**FIGURE IV.4**

Unit triangles in stereographic projection for (a) cubic, (b) orthorhombic, and (c) hexagonal crystal symmetry. The apices of one triangle are labeled.

The projection of the stereographic unit triangles for the cubic system is shown in Figure IV.4a. There are 24 each of right- and left-handed triangles. A single stereographic unit triangle is usually used for an inverse pole figure (Sections 2.5.2, 5.2.2, and 9.2) and misorientation axis distributions (Section 9.5.1) or interface plane distributions (Sections 11.2 and 11.3.3). In general, if the specimen axis that is to be plotted in the inverse pole figure is a mirror (symmetry) plane of the specimen, a single unit triangle suffices. Otherwise, right- and left-handed triangles should be used. A pole figure is usually plotted in the whole of the stereographic projection, although sometimes “reduced” pole figures in one-quarter of the stereogram are seen. For the sake of completeness, Figures IV.4b and IV.4c show the 4 and 12 stereographic unit triangles of the orthorhombic and hexagonal crystal structures, respectively.

The construction of a stereographic projection and some of its features that are pertinent to texture analysis are amplified and discussed rigorously by Johari and Thomas (1969) and McKie and McKie (1974).

IV.2 The Equal-Area Projection

In the *equal-area projection*, equal areas on the reference sphere have equal areas in projection. Such a projection is particularly appropriate for the measurement of population densities. For example, a random distribution of points (orientations) appears as a uniform density of points on the equal-area projection, whereas this distribution is distorted on the stereographic projection. With reference to Figure IV.1, in an equal-area projection, the projection of P onto the equatorial plane is given by $r\sqrt{2}\sin\angle OSP$. Figure IV.3b shows the *Schmidt net* that is used to determine angular relationships in equal-area projection and comparison between it and the Wulff net in Figure IV.3a illustrates the equal-area characteristics of the former. Here, the size of the net units represents correctly the fraction of orientation space covered by each.

Figure IV.5 shows the projection of 500 randomly oriented poles in both stereographic and equal-area projections. In the stereographic projection the poles are clearly clustered in the central regions of the pole figure (Figure IV.5a), whereas in the equal-area projection they appear homogeneously distributed (Figure IV.5b). Disadvantages of the equal-area projection

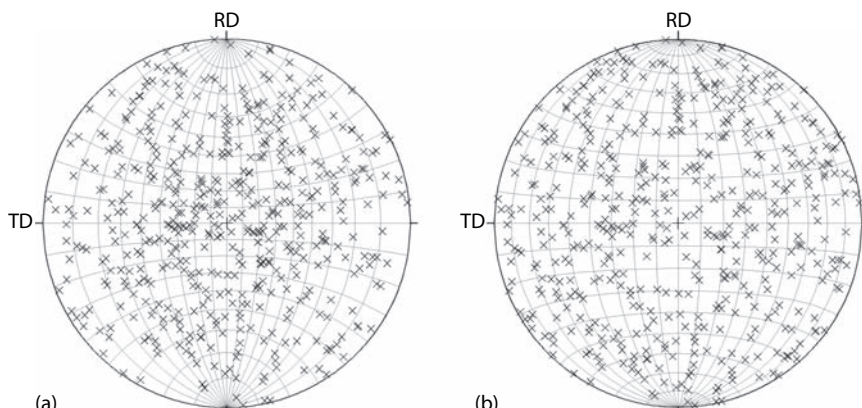


FIGURE IV.5

Projection of a random distribution of 500 poles on the surface of a sphere. (a) Stereographic projection with superimposed Wulff net; (b) equal-area projection with superimposed Schmidt net.

are that circles on the sphere do not appear as circles in the projection and angles between great circles are not preserved.

Despite the advantages of equal-area projection for assessing population densities, stereographic projection remains popular in metallurgy and equal-area projection is most widely used in geology (Wenk and Kocks, 1987).

IV.3 The Gnomonic Projection

In the *gnomonic projection*, poles are projected from the center of the reference sphere to a tangent plane at the North Pole, as shown in Figure IV.6 (McKie and McKie, 1974). Since every great circle passes through the projection point O , all zones project as straight lines. The projection of P is now given by $r \tan \angle NOP$. This has the disadvantage that as $\angle NOP$ approaches 90° , the distance NP in the projection becomes unmanageably large, until when $\angle NOP = 90^\circ$ P projects at infinity. The link between the gnomonic projection and texture analysis is that a Kikuchi diffraction pattern is a gnomonic projection. The distortion at large projection angles is particularly apparent in EBSD patterns, since they have a capture angle of approximately 60° (Section 6.2; Figure 6.4a).

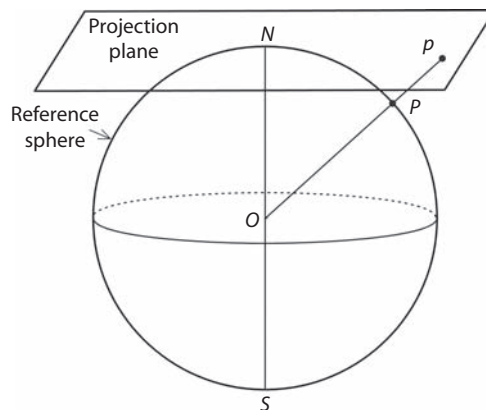


FIGURE IV.6

The relationship between the reference sphere and the projection plane for gnomonic projection. The pole P is projected from O to a tangent plane at the North Pole.

Appendix V

INDEXING A POLE FIGURE

This appendix describes the methodology for indexing a pole figure, measured by x-ray or neutron diffraction techniques, and evaluating the corresponding orientation. Figure V.1a shows the {111} pole figure of a single crystal with an unknown orientation. To determine this orientation in terms of its Miller indices (hkl)[uvw], the four {111} poles of the orientation have to be indexed first. As described in Section 2.4, in the cubic crystal system there are 48 different possibilities to do so, one of which is applied in Figure V.1b. Remember the crystal orientation (hkl)[uvw] is given by the specimen rolling direction (RD) expressed in crystal coordinates, [uvw], and the specimen normal direction (ND) expressed in crystal coordinates, (hkl). Hence, to determine the crystal orientation, it is necessary to express the specimen axes RD and ND in crystal coordinates. For that purpose, the angles between the four (indexed) {111} poles and the sample axes RD and ND are determined. As described in Appendix IV, this can be done with the help of a Wulff net (Figure IV.3a) or a Schmidt net if an equal-area pole figure is analyzed (Figure IV.3b). The resulting angles are marked in Figure V.1b with dashed lines for the RD and dotted lines for the ND.

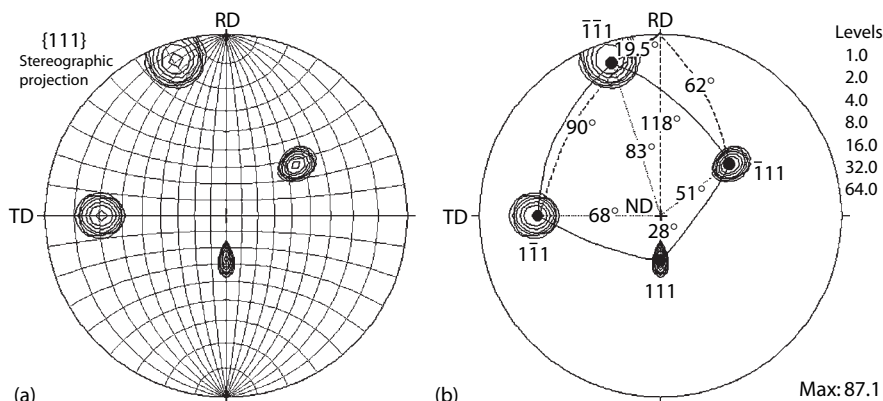


FIGURE V.1

(a) {111} Pole figure of a single crystal, plotted in stereographic projection. (b) Indexed poles and angles between the poles and sample axes RD and ND to determine the single-crystal orientation of (a).

To determine the orientation of the RD in crystal coordinates, $[uvw]$, the angles between the $\{111\}$ poles and the RD are analyzed. For instance, for the (111) pole this reads:

$$\cos \angle((111), [uvw]) = \frac{\begin{pmatrix} 1 \\ 1 \\ 1 \end{pmatrix} \cdot \begin{pmatrix} u \\ v \\ w \end{pmatrix}}{\sqrt{3}} = \frac{u+v+w}{\sqrt{3}} \quad (\text{V.1})$$

The factor $\sqrt{3}$ is necessary to normalize the vector (111) to unity, whereas the resulting $[uvw]$ will automatically be normalized to unity. This equation is set up three times for three of the four possible $\{111\}$ poles so as to yield the three unknowns u , v , and w ; for example,

$$\begin{aligned} 111: \quad & u + v + w = \sqrt{3} \cdot \cos 118^\circ \\ 1\bar{1}1: \quad & u - v + w = \sqrt{3} \cdot \cos 90^\circ \\ \bar{1}\bar{1}1: \quad & -u - v + w = \sqrt{3} \cdot \cos 19.5^\circ \end{aligned} \quad (\text{V.2})$$

In the present example, the RD is $[uvw] = [-0.816, -0.407, 0.440] \approx [\bar{2}\bar{1}1]$. This procedure is repeated for the ND, (hkl) :

$$\begin{aligned} 111: \quad & h + k + l = \sqrt{3} \cdot \cos 28^\circ \\ 1\bar{1}1: \quad & h - k + l = \sqrt{3} \cdot \cos 68^\circ \\ \bar{1}\bar{1}1: \quad & -h - k + l = \sqrt{3} \cdot \cos 83^\circ \end{aligned} \quad (\text{V.3})$$

These three equations yield $(hkl) = (0.219, 0.440, 0.870) \approx (124)$. Thus, the unknown single-crystal orientation displayed in Figure V.1a is $(hkl)[uvw] = (124)[\bar{2}\bar{1}1]$.

Appendix VI

X-RAY COUNTERS AND PULSE HEIGHT ANALYSIS

This appendix describes the different types of counters that may be used for recording the diffracted intensities in x-ray diffraction experiments—Geiger, scintillation, proportional, and semiconductor counters—as well as the use of pulse height analyzers to improve the peak-to-background ratio. (For a more thorough treatment, see Cullity [1978] and Barrett and Massalski [1980].) All electrical counters suitable for x-ray diffraction experiments depend on the power of the x-rays to ionize atoms, either of a gas (Geiger and proportional counters) or of a solid (scintillation and semiconductor counters). With regard to quantitative texture analysis, mainly three aspects of the different counters are of importance:

- An incoming x-ray quantum results in an electrical pulse of the counter. With increasing number of x-ray quanta, that is, with increasing counting rates, however, the time interval between the pulses decreases and may become so small that successive pulses can no longer be resolved by the counter, which leads to *counting losses* at high counting rates.
- The counter *efficiency* describes the fraction of x-ray quanta that is indeed able to initiate an electrical pulse in the counter. Both absorption of x-rays in the counter window and passing of x-rays through the entire counter without being absorbed by the recording medium decrease the efficiency.
- In most counters, the output voltage is proportional to the energy of the x-ray photon (see below), and the *energy resolution* is a measure for this proportionality between the size of the voltage pulse generated by the counter and the energy of the absorbed x-ray quantum.

VI.1 Geiger Counters

The *Geiger counter* (also called Geiger–Müller counter) was the first electrical counter used to detect radiation. A Geiger counter consists of a wire electrode in a gas-filled chamber with a voltage at the wire that is high enough (~1500 V) to attract an electron in the gas so strongly that it would

ionize many atoms of the gas along its path (Figure VI.1a). Thus, an ionization effect by a single incident x-ray photon results in a chain of ionizing events that culminate in a strong discharge through the gas. The number of such pulses in a given time interval is a measure of the radiation intensity. The main disadvantage of the Geiger counters for x-ray texture analysis is the long dead-time of $\sim 10^{-4}$ s between initiation of the ionization chain

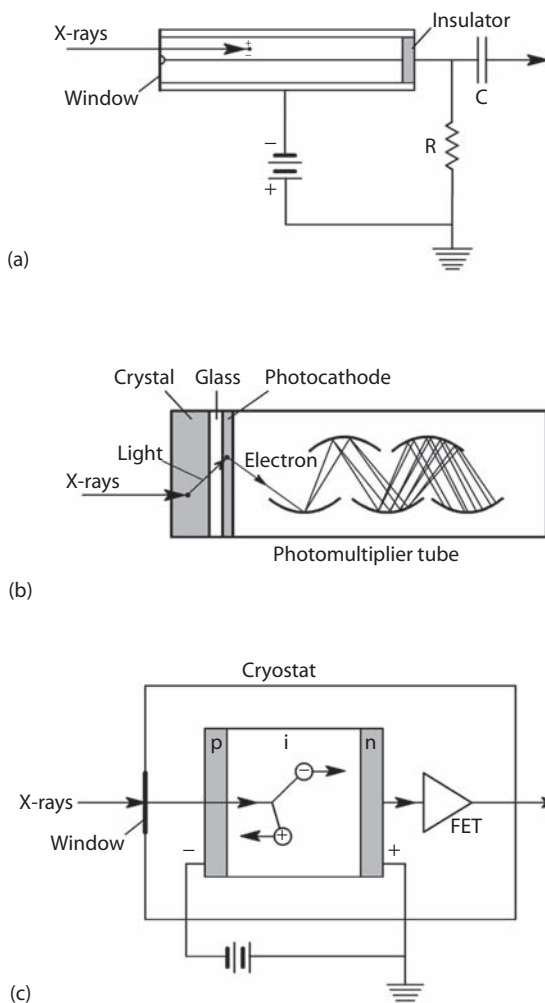


FIGURE VI.1

Schematic representation of x-ray counters: (a) Geiger counter, (b) scintillation counter, (c) semiconductor detector. (Adapted from Cullity, B.D., *Elements of X-ray Diffraction* (2nd edition), Addison-Wesley, Reading, MA, 1978.)

and resetting of the counter, which may lead to losses in the order of 10% at counting rates of only 500 s^{-1} . Another drawback is that the output of Geiger counters does not depend on the incident wavelength, that is, it is not proportional; therefore, Geiger counters are today virtually obsolete in diffractometry.

VI.2 Scintillation Counters

Much more often *scintillation counters* are in use, which consist of a fluorescent crystal mounted at the end of a photomultiplier tube (Figure VI.1b). An x-ray photon absorbed in this crystal—typically a sodium iodide crystal containing ~1% thallium—ejects photoelectrons that energize fluorescence of the thallium ions. The fluorescent light ejects electrons in the photomultiplier tube, which are multiplied and finally transferred to the measuring electronics. Scintillation detectors stand out by a constant, very high efficiency throughout the range of wavelengths used in x-ray diffractometry and by a short dead time of only 10^{-7} s caused by the decay of the fluorescence induced by photon absorption. Thus, x-ray data with rates of $10,000\text{ s}^{-1}$ can be counted with losses below 1%. The output voltage is proportional to the energy of the x-ray photon, so that the reflected peak intensity can be distinguished from background and fluorescent radiation with different wavelengths by setting an appropriate energy window of a subsequent pulse height analyzer (Section VI.5).

VI.3 Proportional Counters

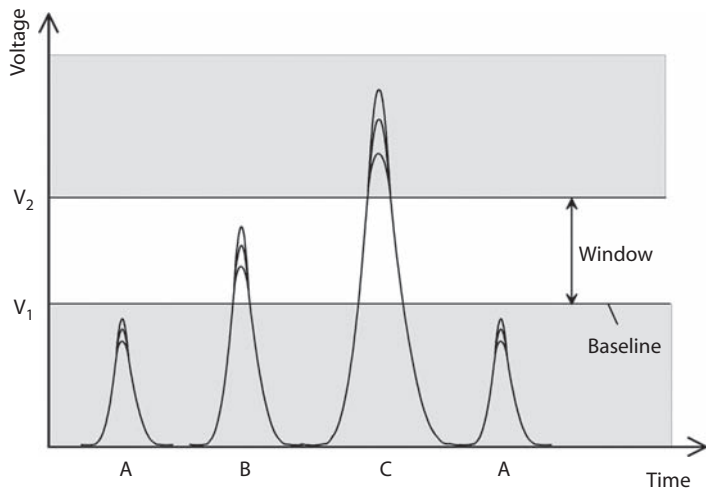
In principle, a *proportional counter* resembles a Geiger counter, but it works at a lower voltage of $\sim 1000\text{ V}$ to ensure proportionality between the energy of the absorbed photon and the amplitude of the output signal. The dead time of proportional counters is comparable to that of scintillation counters, permitting similar counting rates. Their efficiency is lower, however, and depends more strongly on the wavelength of the x-rays. Their amplification is smaller, requiring stronger amplification by the subsequent electronics. The main advantage of proportional counters is that for monochromatic radiation, the distribution of amplitudes of the pulses is narrower than with scintillation counters, thus allowing a better separation of diffracted peak and background intensity.

VI.4 Semiconductor Detectors

Nowadays, increasingly solid-state *semiconductor detectors* are used, since they produce pulses proportional to the absorbed x-ray energy with better energy resolution than any other counter. Furthermore, they stand out by a high efficiency and by low counting losses. A semiconductor detector basically consists of a silicon single crystal containing small amounts of lithium, and therefore these counters are designated Si(Li). Germanium counters are in use for detection of radiation with shorter wavelengths. The crystal is produced so as to comprise very thin surface layers of *n*-type on one side, meaning it contains free electrons from donor impurities, and *p*-type on the opposite side, meaning it contains free holes from acceptor impurities (Figure VI.1c). The central region is neither *n*- nor *p*-type; that is, it is intrinsic (*i*), which means that it has a very high resistivity because only few electrons are thermally excited from the valence band across the energy gap into the conduction band. However, an incident x-ray quantum can cause excitation and create a multitude (approximately 1000) of pairs of free electrons (–) in the conduction band and free holes (+) in the valence band. If a high voltage is applied to the opposite faces of the crystal, the electrons and holes will be swept to these faces, creating a small electrical pulse. Subsequently, these very small pulses are amplified by a field-effect transistor (FET). Disadvantages are that the semiconductor counters must be cooled with liquid nitrogen or with a Peltier cooler and they require more complex electronics.

VI.5 Pulse Height Analyzers

In all counters that are commonly used today (scintillation, proportional, and semiconductor), the output voltage depends on the wavelength of the x-ray photon in so far as the size of the resulting pulses is proportional to the energy of the triggering x-ray quanta. This means that if an x-ray quantum of CuK α radiation ($E = h\nu = 9$ keV) generates a pulse of 1 mV, then an MoK α quantum ($h\nu = 20$ keV) would produce a pulse of $(20/9) = 2.2$ mV. Therefore, electrical units that distinguish between pulses of different size, the so-called *pulse height analyzers*, can distinguish between x-rays of different energy and, therewith, background and fluorescent radiation with different wavelengths can be reduced. Let us assume that x-rays with three different wavelengths $a > b > c$ are detected by a counter, which in turn produces pulses of different sizes $A < B < C$ (Figure VI.2). If an electronic circuit that transmits only pulses with size larger than a certain value (given by the voltage V_1) is inserted between counter and rate meter, then pulses with larger wavelengths (pulse A) are not counted. This can be used to reduce

**FIGURE VI.2**

Pulse height analysis. (Adapted from Cullity, B.D., *Elements of X-ray Diffraction* (2nd edition), Addison-Wesley, Reading, MA, 1978.)

background intensities resulting from the continuous spectrum as well as fluorescence with long wavelengths. If the device is additionally able to reject pulses with size larger than a voltage V_2 (pulse C) then diffracted intensities from low wavelengths will be ignored as well (Figure VI.2). Thus, with a proper setting of the baseline and the window of the pulse height analyzer, the peak-to-background ratio can markedly be improved.

Appendix VII

KIKUCHI MAPS OF FCC, BCC, AND HEXAGONAL CRYSTAL STRUCTURES

This appendix comprises Kikuchi maps for fcc, bcc, and hexagonal crystal structures, which can be used to aid manual indexing or check automatic indexing of Kikuchi patterns (Section 6.3). The maps are constructed from the most prominent reflectors usually visible in EBSD patterns of reasonable quality. Note, however, that SAC and TEM Kikuchi patterns usually contain higher-index reflectors as well (Sections 6.2 and 6.3). Figure VII.1a shows the Kikuchi map for fcc crystal structures, constructed from the four most prominent reflectors $\{111\}$, $\{200\}$, $\{220\}$, and $\{311\}$. The map covers one stereographic unit triangle ($[001]-[011]-[111]$), which approximately corresponds to the capture angle in standard EBSD applications. The corresponding Kikuchi map for bcc crystal structures—constructed from the reflectors $\{110\}$, $\{200\}$, $\{211\}$, and $\{310\}$ —is shown in Figure VII.1b.

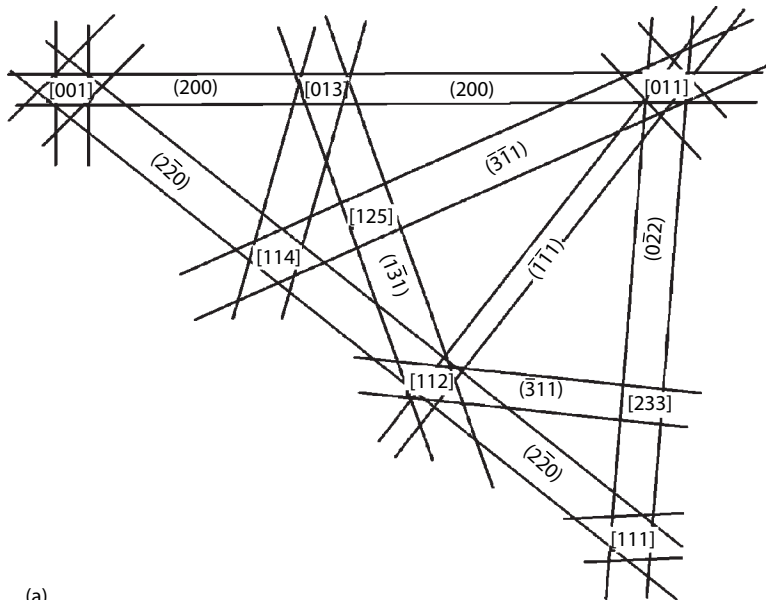


FIGURE VII.1

Kikuchi maps for (a) fcc and (b) bcc crystal structures (one stereographic triangle).

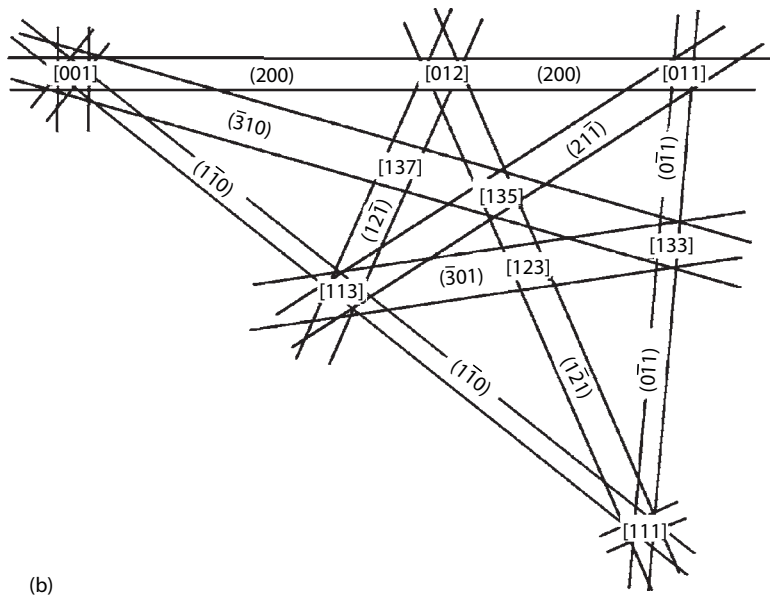


FIGURE VII.1 (Continued)

The Kikuchi map for hexagonal crystal structures (Figure VII.2) covers two stereographic triangles so as to facilitate indexing. Here, the seven most prominent reflectors $\{0001\}$, $\{1\bar{1}00\}$, $\{2\bar{2}01\}$, $\{1\bar{1}01\}$, $\{1\bar{1}03\}$, $\{11\bar{2}0\}$, and $\{11\bar{2}2\}$ (in Miller–Bravais notation) that can usually be observed in good-quality EBSD patterns are considered. Note that interplanar and interzonal angles in hexagonal structures depend on the c/a ratio; Figure VII.2 is derived for $c/a \approx 1.59$ (titanium). EBSD patterns of other hexagonal metals with different c/a ratios therefore look slightly different, though the main geometrical features remain unaffected.

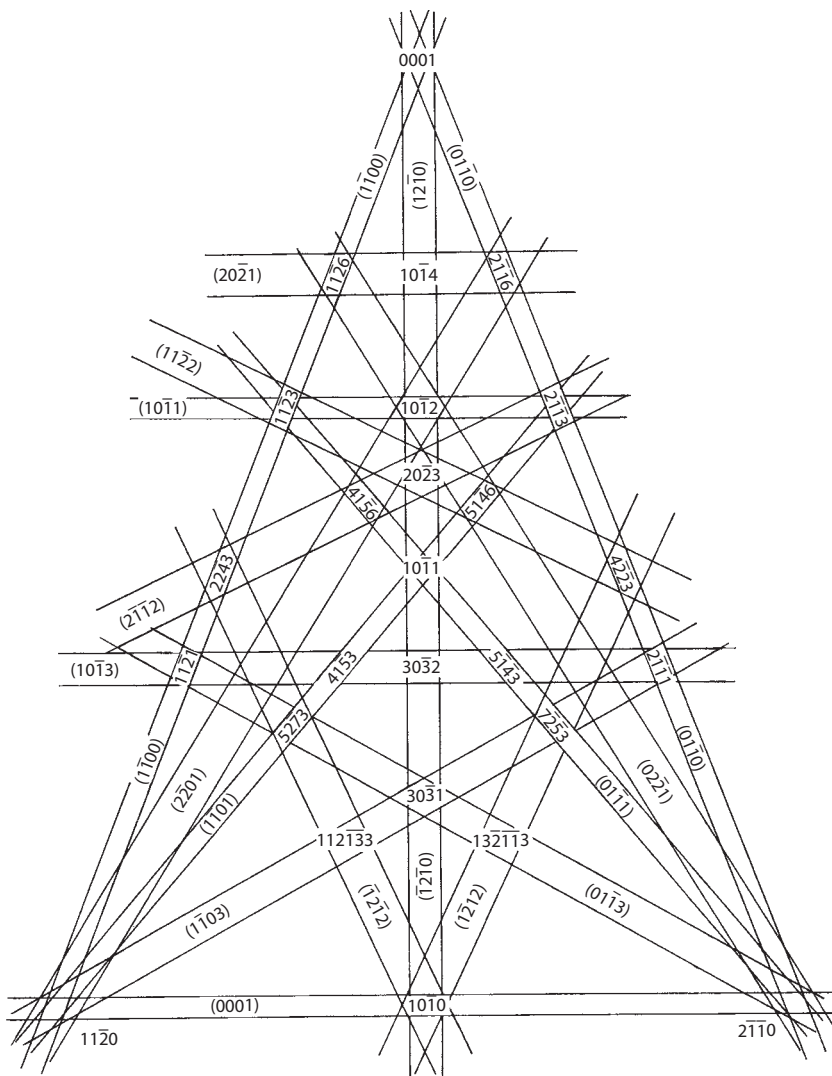


FIGURE VII.2

Kikuchi map for hexagonal crystal structures (Ti, $c/a \approx 1.59$, two stereographic triangles).

Glossary

absolute orientation: *see* crystallographic orientation

absorption edge: drop in the absorption of x-rays of a given wavelength between certain elements, caused by the efficiency of the x-rays in emitting photoelectrons from the electron shells of the sample material

angle and axis of misorientation: transformation between the crystal coordinate systems of two grains via rotation through an angle about a specific axis

angle and axis of rotation: transformation between the crystal coordinate system and the specimen coordinate system via rotation through an angle about a specific axis

angle/axis pair: *see* angle and axis of rotation

angle/axis space: three-dimensional space wherein angle/axis pairs reside (*see also* cylindrical angle/axis space)

angular-dispersive diffractometry: conventional technique to separate different reflectors according to their reflection angle for monochromatic radiation

anisotropy: phenomenon of a directionally dependent materials property, that is, the property has different values when measured in different crystal directions; for polycrystals, the property then depends on the crystallographic texture

arbitrary defined cell (ADC) method: direct method for ODF computation, similar to the WIMV method but based on the use of projection tubes in orientation space

area detector: two-dimensional position-sensitive detector

asymmetric domain of Euler space: portion of Euler space defined such that every interior point in it represents a physically distinct orientation or misorientation

automated crystal orientation mapping (ACOM): *see* orientation mapping

background: intensities in the diffraction spectra that are caused by incoherent scattering, fluorescence, and reflection of x-rays with other wavelengths that do not contribute to the diffracted information

backscatter Kikuchi Diffraction (BKD): *see* EBSD

camera constant: distance between sample and photographic plate times electron wavelength in the TEM; measure for the magnification of diffraction patterns

coincidence site lattice (CSL): lattice formed by notional superposition of lattice sites from two crystals and used in the context of texture analysis to categorize grain boundary geometry

component method: description of the ODF by a set of a number of Gauss-shaped components

continuous scan: method to scan the pole figure continuously integrating over a range of pole figure angles

convergent beam electron diffraction (CBED): electron diffraction occurring under irradiation with a convergent rather than parallel electron beam; allows orientation determination with best spatial and angular resolutions in the subnanometer range

crystal coordinate system: coordinate system chosen as the edges of the crystal unit cell

crystal matrix: 3×3 matrix to transform the crystal axes into an orthonormal frame

crystal orientation mapping (COM): *see* orientation mapping

crystallographic orientation: orientation of the crystal coordinate system of a volume of crystal with respect to the specimen coordinate system

crystallographically related solutions (of an orientation): equivalent representations of an orientation depending on the crystal system symmetry

cylindrical angle/axis space: three-dimensional orientation space wherein angle/axis pairs reside such that the axis and angle are represented perpendicular and parallel to the long axis of the cylinder, respectively

Debye–Scherrer method: technique for orientation determination in polycrystalline volumes, which is based on the diffraction of monochromatic x-rays

defocusing error: decrease in recorded intensity in pole figure measurements with increasing tilting angle, which is caused by broadening of the reflected peak

direct methods of ODF calculation: methods to calculate the ODF from pole figure data in real space by an iterative fitting procedure

disorientation: the lowest-angle crystallographically related solution of a misorientation

electron backscatter diffraction (EBSD): an SEM-based technique for obtaining diffraction information from volumes of crystal down to about 200 nm diameter

electron channeling pattern (ECP): *see* selected-area channeling (SAC)

energy-dispersive diffractometry: technique to separate different reflectors according to the energy (or wavelength) of the reflected radiation for polychromatic radiation

equal-area projection: projection of a reference sphere onto its equatorial plane such that equal areas on the sphere retain their equality in projection

etch pits: characteristic polygons that form via etching and whose shape is determined by the crystallographic orientation of the etched grain

Euler angles: a description of orientation involving sequential rotations of the crystal coordinate system through three angles with respect to the specimen coordinate system

Euler space: three-dimensional (usually Cartesian) space wherein Euler angles are represented

Friedel's law: radiation is diffracted in the same fashion from both sides of a set of lattice planes, so that diffraction patterns are always

centrosymmetric, even if the crystals are not; this also causes the “ghost error” during ODF computation

fundamental zone of Rodrigues space: volume of Rodrigues space in which the lowest-angle crystallographically related solution of an orientation (or misorientation) resides

Geiger counter: counter to detect x-rays that is based on the potential of x-rays to ionize gas—today virtually obsolete in diffractometry

ghost error: error in ODF calculation by the series expansion method caused by the unavailability of the odd-order C coefficients

gnomonic projection: projection of a reference sphere in which the center of the sphere is the projection point and a plane tangential to the North Pole is the projection plane

goniometer: diffractometer to position the sample and the detector with respect to the incident beam

harmonic method of ODF calculation: *see* series expansion method

high-resolution electron microscopy (HREM): technique for determination of local orientations and orientation relationships based on direct imaging of the atoms

Hough transform: transformation of points in an image into sinusoidal curves in an accumulation space; a line in the original image is transformed into a point characterized by the angle θ and the distance ρ of the line in the original image

ideal orientation/Miller indices representation: orientation representation having the nearest Miller (or Miller–Bravais) indices of the crystal directions parallel to the specimen Z and X directions, respectively

interface-plane scheme: methodology for characterizing interfaces on the basis of the crystallographic orientation of the planar surface of the interface

interplanar angle: angle between two crystallographic planes

interzonal angle: angle between two crystallographic directions

inverse pole figure: angular distribution of a chosen specimen direction with respect to the crystal coordinate system

K β filter: foil positioned between sample and detector in x-ray diffractometry and made of a material whose absorption edge lies just between the K α and the K β peak of the x-ray tube; used to produce quasimonochromatic x-radiation

Kikuchi diffraction pattern: system of bright and dark lines (the Kikuchi lines) that form by the elastic (Bragg) reflection of diffusely scattered electrons at the atomic planes of a single crystalline volume in TEM; similar patterns form in SEM by SAC and EBSD; very well suited for orientation determination with the highest angular resolution

Kikuchi line: *see* Kikuchi diffraction pattern

Laue group: eleven crystal classes out of the possible 32 point groups that contain an inversion center

Laue method: technique for orientation determination in single-crystal volumes, which is based on the diffraction of polychromatic x-rays

Mackenzie distribution: distribution of disorientation angles and axes, where the latter are located in a stereographic unit triangle, for cubic crystals misoriented at random

macrotexture: an average texture determined from many grains obtained without reference to the location of individual grains within a specimen, or the experimental technique used to obtain this information

maximum entropy method: method for the correction of the ghost error in the series expansion method based on the assumption that, out of the possible range of complete ODFs, the solution with maximum entropy has the smoothest distribution with minimum additional information, that is, ghosts

mesotexture: the texture between grains, that is, the texture associated with grain boundaries

micro-Kossel diffraction: an SEM-based technique for obtaining crystallographic information from volumes of crystal down to approximately 10 μm , and based on the diffraction of x-ray generated within the sample under investigation

microdiffraction: generic term for techniques used to generate Kikuchi diffraction patterns in small volumes, with a spatial resolution beyond the limit of SAD, $\sim 1 \mu\text{m}$

microtexture: a sample population of orientation measurements that can be linked individually to their location within a specimen, or the experimental technique used to obtain this information

misorientation: the orientation difference between two individual orientation measurements, usually of the same phase (*see also* orientation relationship)

misorientation distribution function (MODF; MDF): continuous density distribution of misorientations, calculated either from discrete data or from a series expansion method

monochromator: crystal used in x-ray or neutron diffractometry to produce monochromatic radiation of a certain wavelength in accordance with Bragg's law

normalization of pole figures: normalization of the pole figure intensities recorded in numbers of counts to standard units, commonly referred to as multiples of a random distribution independent of the experimental parameters

orientation correlation function (OCF): texture-reduced form of the MODF, derived by division of the MODF by the ODDF; yields information about the texture-reduced spatial correlation of misorientations

orientation difference distribution function (ODDF): statistical distribution of misorientations in a sample without consideration of the actual location of the orientations, only governed by the texture; used to normalize the MODF, but does not contain valuable information on the spatial arrangement of the individual orientations

orientation distribution function (ODF): continuous density distribution of orientations, calculated either from discrete data or from a series expansion method

orientation imaging microscopy (OIMTM): *see* orientation mapping

orientation mapping: depiction of the microstructure in terms of its orientation constituents

orientation matrix: cosines of angles between axes of the specimen coordinate system and the crystal coordinate system, arranged to form a 3×3 matrix

orientation microscopy: automated measurement and storage of orientations according to a predefined pattern of coordinates on the sampling plane of the specimen

orientation relationship: the difference between two individual orientation measurements, usually of different phases (*see also* misorientation)

orientation topography: spatial arrangement of the crystallographic orientations in the microstructure

orthonormal coordinate system: right-handed Cartesian coordinate system chosen as three mutually perpendicular unit vectors

peak separation: the means to separate intensities stemming from closely spaced reflectors, either experimentally or numerically

penetration depth: depth of the specimen from where the diffracted information arises

pole: normal to a set of crystallographic planes

pole figure: angular distribution of a chosen crystal direction (usually a set of plane normals) with respect to the specimen coordinate system

pole figure inversion: calculation of the ODF from the data of (typically several) pole figures

position-sensitive detector (PSD): one-dimensional location-sensitive counter that simultaneously records a part of the diffraction spectrum

positivity method: iterative method for the correction of the ghost error in the series expansion method based on a generalization of the zero-range method

proportional counter: counter to detect x-rays that is based on the potential of x-rays to ionize a gas

pseudo-Kossel diffraction: an SEM-based technique for obtaining crystallographic information by Kossel diffraction, where the x-radiation is generated in a target layer of an appropriate material deposited on the sample under investigation

pulse-height analyzer: device that distinguishes between electrical pulses of different size and that is used to distinguish between x-rays of different energy, thus reducing background and fluorescent radiation

Radon transform: Hough transform under consideration of the gray values of the individual pixels

random texture: sample population of orientations having no preferred crystallographic orientation

reflection geometry: geometrical setup to study diffraction effects on thick bulk samples where the incident radiation is reflected in the surface layers

Rietveld texture analysis (RITA): a method for quantitative texture analysis by an iterative combination of crystallographic Rietveld profile analysis of diffraction spectra and ODF calculation

Rodrigues space: three-dimensional Cartesian space wherein Rodrigues vectors are represented

Rodrigues vector (R vector): combination of the angle and axis of rotation into one mathematical entity

Rodrigues–Frank space (RF space): see Rodrigues space

rotation matrix: see orientation matrix

scintillation counter: counter to detect x-rays that is based on the potential of x-rays to ionize a solid crystal

selected-area channeling (SAC): an SEM-based technique for obtaining diffraction information from volumes of crystal down to approximately 10 µm

selected-area diffraction pole figures: technique to derive the orientation distribution of smallest polycrystalline volumes in the TEM

selected-area electron diffraction (SAD): characteristic point patterns generated by electron diffraction in thin metallic foils, or the experimental technique to generate those patterns; the traditional method for orientation determination in the TEM before the advent of TEMs with microdiffraction facilities

semiconductor counter: counter to detect x-rays that is based on the possibility of x-rays to ionize a semiconductor crystal

series expansion method: method to calculate the ODF from pole figure data in Fourier space by fitting pole figures and ODF by a series expansion with spherical harmonic functions

skeleton line: representation of the relative intensity maxima in the various ODF sections in the Euler space as a function of the corresponding Euler angle

spallation source: neutron source where the neutrons are produced by spallation, that is, the interaction of a high-energy proton beam with a target material; interesting for time-of-flight (TOF) applications because of the possibility to pulse the neutron beam

specimen coordinate system: coordinate system chosen as the geometry of the specimen

spiral scan: method to scan the pole figure on a spiral by a coupled changing of both pole figure angles (outdated)

step scan: method to scan the pole figure in distinct pole figure angles

stereographic projection: projection of a reference sphere onto its equatorial plane such that equal angles between lines on the surface of the sphere retain their equality in the projection

structure factor: unit cell equivalent of the atomic scattering amplitude; summation over the waves scattered by each of the atoms in the unit cell gives the amplitude of the wave being reflected at a given plane

subvolume of the fundamental zone of Rodrigues space: volume obtained by subdivision of the fundamental zone such that the absolute value of the axis of rotation is given by $H > K > L$, where HKL are its Miller indices

synchrotron radiation: x-radiation generated in an electron synchrotron that is characterized by a high intensity and low angular divergence and which can be used for local texture analysis by means of the Laue and Debye–Scherrer methods

texture: distribution of the crystallographic orientations of a given sample

texture fibers: intensity distribution along certain predefined paths through the Euler space

time-of-flight (TOF) measurements: method to separate several reflectors by determining the flight time of the neutrons, which depends on their energy or wavelength (*see also* energy-dispersive diffractometry); requires a pulsed neutron source

transmission geometry: geometrical setup to study diffraction effects on thin samples that are penetrated by the incident radiation

truncation error: error in ODF calculation by the series expansion method caused by the necessity to truncate the series expansion of pole figure and ODF expansion

universal stage (U stage): sample stage that allows rotation of an optically anisotropic crystal until its optical axis is aligned parallel to the microscope axis; the rotation angles then yield the crystallographic orientation of the crystal

vector method: direct method for ODF computation based on subdivision of both pole figures and orientation space into small subregions, which are considered as components of vectors

WIMV method: direct method for ODF computation; acronym for the authors Williams, Imhof, Matthies, and Vinel

zero-range method: method for the correction of the ghost error in the series expansion method based on the assumption that ranges with zero intensity in the pole figures yield an approximation to the indeterminable part of the *entire* ODF

References

- Abbruzzese, G., Campopiano, A., and Fortunati, S., *Textures Microstruct.* 14–18 (1991) 775.
- Adams, B.L., *Metall. Trans.* A17 (1986) 2199.
- Adams, B.L., Wright, S.I., and Kunze, K., *Metall. Trans.* 24A (1993) 819.
- Adams, B.L., Zhao, J., and O'Hara, D., *Acta Metall. Mater.* 38 (1990) 953.
- Agnew, S.R., Tomé, C.N., Brown, D.W., Holden, T.M., and Vogel, S.C., *Scr. Mater.* 48 (2003) 1003.
- Alam, M.N., Blackman, M., and Pashley, D.W., *Proc. Roy. Soc. Lond.* 221A (1954) 224.
- Allen, S.M. and Hall, E.L., *Phil. Mag.* A46 (1982) 243.
- Al-Sammam, T., and Gottstein, G., *Mater. Sci. Eng.* A490 (2008) 411.
- Anderson, A., Thompson, R.B., and Bolingbroke, R., *Mater. Sci. Forum* 157–162 (1994) 295.
- Antoniadis, A., Berruyer, J., and Filhol, A., *Acta Crystallogr.* A46 (1990) 692.
- Apps, P.J., Bowen, J.R., and Prangnell, P.B., *Acta Mater.* 51 (2003) 2811.
- Ashbee, K.H.G. and Sargent, J.P., *Metall. Trans.* 21A (1990) 253.
- Aust, K.T., *Can. Met. Quart.* 33 (1994) 265.
- Ayer, R., *J. Electron Micr. Technol.* 13 (1989) 16.
- Ayer, R., Mueller, R.R., and Neeraj, T., *Mater. Sci. Eng.* A417 (2006) 243–248.
- Bäckström, S.P., Riekel, C., Abel, S., Lehr, H., and Wenk, H.R., *J. Appl. Crystallogr.* 29 (1996) 118.
- Backx, P., Barnett, M.R., and Kestens, L., *Mater. Sci. Forum* 467–470 (2004) 429.
- Bacon, G.E., *Neutron Diffraction* (3rd edition), Clarendon Press, Oxford (1975).
- Bacroix, B., Chaveau, T., Gargano, P., and Pochettino, A.A., *Mater. Sci. Forum* 157–162 (1994) 301.
- Barker, L.J., *Trans. Am. Soc. Metals* 42 (1950) 347.
- Barnett, M.R., Nave, M.D., and Bettles, C.J., *Mater. Sci. Eng.* A386 (2004) 205.
- Barrett, C.S. and Massalski, T.B., *Structure of Metals: Crystallographic Methods, Principles and Data*, McGraw-Hill, New York (1980).
- Bastos, A., Zaefferer, S., Raabe, D., and Schuh, C., *Acta Mater.* 54 (2006) 2451.
- Bauch, J. and Ullrich, H.J., *MP Materialprüfung (Materials Testing)* 46 (2004) 53.
- Baudin, T., Paillard, P., Cruz, F., and Penelle, R., *J. Appl. Crystallogr.* 27 (1994) 924.
- Baudin, T. and Penelle, R., *Metall. Trans.* 24A (1993) 2299.
- Bauer, G.S., *J. Fusion Energy* 8 (1989) 169.
- Becker, R., *Acta Metall. Mater.* 39 (1991) 1211.
- Becker, R. and Panchanadeeswaran, S., *Textures Microstruct.* 10 (1989) 167.
- Bellier, S.P. and Doherty, R.D., *Acta Metall.* 25 (1977) 521.
- Bennett, T.A., Kalub, P.N., and Rollett, A.D., *Scr. Mater.* 57 (2007) 41.
- Bessières, J., Heizmann, J., and Eberhardt, J., *Textures Microstruct.* 14–18 (1991) 157.
- Bevis, M. and Swindells, N., *Phys. Stat. Sol.* 20 (1967) 197.
- Birsan, M., Szpunar, J.A., Tun, Z., and Root, J.H., *Phys. Review* 53B (1996) 6412.
- Black, D.R., Burdette, H.E., Kuriyama, M., and Spal, R.D., *J. Mater. Res.* 6 (1991) 1469.
- Bleck, W. and Bunge, H.-J., *Acta Metall.* 29 (1981) 1401.
- Blochwitz, C., Brechbühl, J., and Tirschler, W., *Mater. Sci. Eng.* A210 (1996) 42.
- Boersch, H., *Z. Techn. Phys.* 18 (1937) 574.
- Bollmann, W., *Crystal Defects and Crystalline Interfaces*, Springer-Verlag, Berlin (1970).
- Bolmaro, R.E. and Brokmeier, H.G., in *Proceedings of ICOTOM 12* (Ed. J.A. Szpunar) NRC Research Press, Ottawa (1999) 211.
- Borbély, A., Maurice, C., and Driver, J.H., *J. Appl. Crystallogr.* 41 (2008) 747.

- Böttcher, A., Gerber, T., and Lücke, K., *Mater. Sci. Technol.* 8 (1992) 16.
- Bourgeois, D., Moy, J.P., Svensson, S.O., and Kvick, Å, *J. Appl. Crystallogr.* 27 (1994) 868.
- Bowen, D.K. and Wormington, M., *Adv. X-ray Anal.* 36 (1992) 171.
- Bragg, W.L., *Proc. Camb. Phil. Soc.* 17 (1913) 43.
- Brandon, D.G., *Acta Metall.* 14 (1966) 1479.
- Brewer, L.N., Othon, M.A., Young, L.M., and Angeliu, T.M., *Microsci. Microanal.* 12 (2006) 85.
- Briant, C.L., MacDonald, E., Balliett, R.W., and Luong, T., *Int. J. Refr. Metals Hard Mater.* 18 (2000) 1.
- Brochu, M., Yokota, T., and Satoh, S., *ISIJ Int.* 37 (1997) 872.
- Brockhouse, B.N., *Can. J. Phys.* 31 (1953) 339.
- Brodesser, S., Chen, S., and Gottstein, G., *Textures Microstruct.* 14–18 (1991) 829.
- Brodesser, S. and Gottstein, G., *Textures Microstruct.* 20 (1993) 179.
- Brokmeier, H.-G., *Textures Microstruct.* 10 (1989) 325.
- Brokmeier, H.-G., *Physica B* 234 (1997) 977.
- Brokmeier, H.-G., *Physica B* 385–386 (2006) 623.
- Brokmeier, H.-G. and Bunge, H.-J., *Textures Microstruct.* 10 (1988) 1.
- Brokmeier, H.-G. and Ermrich, M., *Mater. Sci. Forum* 157–162 (1994) 119.
- Brokmeier, H.-G. and Ostwaldt, D., in *Proceedings of ICOTOM 11* (Eds. Z. Liang, L. Zou, and Y. Chu), International Academic Publishers, Beijing (1996) 75.
- Brückner, G. and Pospiech, J., in *Proceedings of ICOTOM 11* (Eds. Z. Liang, L. Zou, and Y. Chu), International Academic Publishers, Beijing (1996) 598.
- Brückner, G., Pospiech, J., Seidl, I., and Gottstein, G., *Scr. Mater.* 44 (2001) 2635.
- Bunge, H.-J., *Z. Metallkd.* 56 (1965) 872.
- Bunge, H.-J., *Texture Analysis in Materials Science: Mathematical Methods*, Butterworths, London (1982).
- Bunge, H.-J., in *Preferred Orientation in Deformed Metals and Rocks: An Introduction to Modern Texture Analysis* (Ed. H.-R. Wenk), Academic Press, Orlando FL (1985a) 73.
- Bunge, H.-J., *Z. Metallkd.* 76 (1985b) 92.
- Bunge, H.-J., *Int. Met. Rev.* 32 (1987) 265.
- Bunge, H.-J. (Ed.), *Directional Properties of Materials*, DGM Inf. Ges., Oberursel, Germany (1988).
- Bunge, H.-J., *Textures Microstruct.* 10 (1989a) 265.
- Bunge, H.-J., *Textures Microstruct.* 11 (1989b) 75.
- Bunge, H.-J., *J. Nondestructive Eval.* 12 (1993) 3.
- Bunge, H.-J., *Mater. Sci. Forum* 495–497 (2005) 87.
- Bunge, H.-J. and Esling, C., *J. Phys. Lett.* 40 (1979) 627.
- Bunge, H.-J. and Esling, C., *J. Appl. Crystallogr.* 14 (1981) 253.
- Bunge, H.-J. and Esling, C. (Eds.), *Quantitative Texture Analysis*, DGM Inf. Ges., Oberursel, Germany (1982).
- Bunge, H.-J. and Esling, C., in *Preferred Orientation in Deformed Metals and Rocks: An Introduction to Modern Texture Analysis* (Ed. H.-R. Wenk), Academic Press, Orlando, FL (1985) 109.
- Bunge, H.-J. and Klein, H., *Z. Metallkd.* 87 (1996) 465.
- Bunge, H.-J. and Puch, K.H., *Z. Metallkd.* 75 (1984) 124.
- Bunge, H.-J. and Roberts, W.T., *J. Appl. Crystallogr.* 2 (1969) 116.
- Bunge, H.-J., Siegesmund, S., Skrotzki, W., and Weber, K. (Eds.), *Textures in Geological Materials*, DGM Inf. Ges., Oberursel, Germany (1994).
- Bunge, H.-J. and Tobisch, J., *Z. Metallkd.* 59 (1968) 471.

- Bunge, H.-J., Wcislaw, L., Klein, H., Garbe, U., and Schneider, J.R., *J. Appl. Crystallogr.* 36 (2003) 1240.
- Bunge, H.-J., Wenk, H.-R., and Pannetier, J., *Textures Microstruct.* 5 (1982) 153.
- Buras, B., Staun, O.J., Gerward, L., Selsmark, B., and Lindegaard-Andersen, A., *Acta Crystallogr.* A31 (1975) 327.
- Burns, J.B., Hanson, A.R., and Riseman, E.M., *IEEE Trans. PAMI* 8 (1986) 425.
- Cabus, C., Réglé, H., and Bacroux, B., *Mater. Char.* 58 (2007) 332.
- Carmichael, C.M., Malin, A.S., and Hatherly, M., in *Proceedings of ICOTOM 11* (Eds. Z. Liang, L. Zou, and Y. Chu), International Academic Publishers, Beijing (1996) 254.
- Cayron, C., Artaud, B., and Briottet, L., *Mater. Char.* 57 (2006) 386.
- Chan, S., *J. Phys. Chem. Sol.* 55 (1994) 1137.
- Chandrasekaran, D. and Nygård, M., *Acta Mater.* 51 (2003) 5375.
- Chateigner, D., Germi, P., and Pernet, M., *J. Appl. Crystallogr.* 27 (1994) 278.
- Chauvy, C., Barberis, P., and Montheillet, F., *Mater. Sci. Eng.* A431 (2006) 59.
- Chen, H.-W. and Rudolph, V., *Diamond Relat. Mater.* 12 (2003) 1633.
- Cho, J.-H., *Mater. Sci. Eng.* A465 (2007) 228.
- Coates, D.G., *Phil. Mag.* 16 (1967) 1179.
- Cross, I., and Randle, V., *Scr. Mater.* 48 (2003) 1587.
- Cullity, B.D., *Elements of X-ray Diffraction* (2nd edition), Addison-Wesley, Reading, MA (1978).
- Daaland, O. and Nes, E., *Acta Mater.* 44 (1996) 1389.
- Dąbrowski, W., Gryboś, P., Hottowy, P., Świentek, K., and Wiącek, P., *Nucl. Instrum. Methods* A512 (2003) 213.
- Dahms, M., *J. Appl. Crystallogr.* 25 (1992) 258.
- Dahms, M., Beaven, P.A., Tobisch, J., Bermig, G., and Helming, K., *Z. Metallkd.* 85 (1994) 536.
- Dahms, M. and Bunge, H.-J., *Textures Microstruct.* 6 (1986) 167.
- Dahms, M. and Bunge, H.-J., *Textures Microstruct.* 10 (1988) 21.
- Dahms, M. and Bunge, H.-J., *J. Appl. Crystallogr.* 22 (1989) 439.
- Därmann-Nowak, C., and Engl, B., *Steel Res.* 62 (1991) 576.
- Davies, G.J., Kallend, J.S., and Morris, P.P., *Acta Mater.* 24 (1976) 159.
- Davies, P., Novikov, M., Bowen, P., and Randle, V., *J. Microsc.* 205 (2002) 278.
- Davies, P. and Randle, V., *J. Microsc.* 204 (2001) 29.
- Davies, R. and Randle, V., *Mater. Char.* 37 (1996) 131.
- Davis, C.L., Mukhopadhyay, P., Strangwood, M., Potter, M., Dixon, S., and Morris, P.F., *Ironmaking Steelmaking* 35 (2008a) 359.
- Davis, C.L., Strangwood, M., Potter, M., Dixon, S., and Morris, P.F., *Metall. Mater. Trans.* A39 (2008b) 679.
- Day, A., *PhD Thesis*, University of Bristol, U.K. (1994).
- Day, A., *J. Microsc.* 230 (2008) 472.
- Debye, P. and Scherrer, P., *Physikal. Zeitschrift* 17 (1916) 277; 18 (1917) 291.
- Decker, B.F., Asp, E.T., and Harper, D., *J. Appl. Phys.* 19 (1948) 388.
- Del Valle, J.A., Pérez-Prado, M.T., and Ruano, O.A., *Mater. Sci. Eng.* A355 (2003) 68.
- Dillamore, I.L. and Katoh, H., *Metal Sci.* 8 (1974) 73.
- Dillamore, I.L. and Roberts, W.T., *Metall. Rev.* 10 (1965) 271.
- Dingley, D.J., *Scanning* 1 (1978) 79.
- Dingley, D.J., in *Scanning Electron Microscopy*, SEM Inc., Chicago (1981/IV) 273.
- Dingley, D.J., in *Scanning Electron Microscopy*, SEM Inc., Chicago (1984/II) 569.

- Dingley, D.J., in *Electron Backscatter Diffraction in Materials Science* (Eds. A.J. Schwartz, M. Kumar, and B.L. Adams), Kluwer Academic/Plenum Publishers, New York (2000) 1.
- Dingley, D.J., *J. Microsc.* 213 (2004) 214.
- Dingley, D.J., *Microchim. Acta* 155 (2006) 19.
- Dingley, D.J., Baba-Kishi, K., and Randle, V., *Atlas of Backscatter Kikuchi Diffraction Patterns*, Institute of Physics Publishing, Bristol (1994).
- Dingley, D.J., Longden, M., Weinbren, J., and Alderman, J., *Scan. Elect. Microsc.* 1/2 (1987) 451.
- Dingley, D.J., and Steeds, J.W., in *Quantitative Scanning Electron Microscopy* (Eds. D.B. Holt et al.), Academic Press, London (1974) 487.
- Dobatkin, S.V., Szpunar, J.A., Zhilyaev, A.P., Cho, J.-Y., and Kuznetsov, A.A., *Mater. Sci. Eng. A*462 (2007) 132.
- Doege, E. and Dröder, K., *J. Mater. Proc. Technol.* 115 (2001) 14.
- Doherty, R.D., Gottstein, G., Hirsch, J., Hutchinson, W.B., Lücke, K., Nes, E., and Willbrandt, P.J., in *Proceedings of ICOTOM 8* (Eds. J.S. Kallend and G. Gottstein), TMS, Warrendale, PA (1988) 563.
- Dons, A.L. and Nes, E., *Mater. Sci. Technol.* 2 (1986) 8.
- Dorner, D., Zaefferer, S., and Raabe, D., *Acta Mater.* 55 (2007) 2519.
- Doyle, P.A. and Turner, P.S., *Acta Crystallogr. A*24 (1968) 390.
- Drake, A., and Vale, S.H., *Inst. Phys. Conf. Ser.* 147, Institute of Physics Publishing, Bristol (1995) 137.
- Driver, J.H., Theyssier, M.-C., and Maurice, C., *Mater. Sci. Technol.* 12 (1996) 851.
- Duggan, B.J. and Jones, I.P., *Texture Cryst. Sol.* 2 (1977) 205.
- Dunst, D. and Mecking, H., *Z. Metallkd.* 87 (1996) 498.
- Džubinský, M., Husain, Z., and van Haaften, W.M., *Mater. Char.* 52 (2004) 93.
- Ecob, R.C., Shaw, M.P., Porter, A.J., and Ralph, B., *Phil. Mag.* 44A (1981) 1117, 1135.
- Edington, J.W., *Electron Diffraction in the Electron Microscope*, MacMillan, London (1975).
- Edington, J.W., *Practical Electron Microscopy in Materials Science*, Van Nostrand Reinhold, New York (1976).
- Eichelkraut, H., Hirsch, J., and Lücke, K., *Z. Metallkd.* 75 (1984) 113.
- El-Dasher, B.S., Adams, B.L., and Rollett, A.D., *Scr. Mater.* 48 (2003) 141.
- Elf, F., Schäfer, W., Höfler, S., and Will, G., *Textures Microstruct.* 13 (1990) 55.
- Ellis, T., Nanni, L.F., Shrier, A., Weissmann, S., Padawer, G.E., and Hosokawa, N., *J. Appl. Phys.* 35 (1964) 3364.
- Emren, F., Von Schlippenbach, U., and Lücke, K., *Acta Metall.* 34 (1986) 2105.
- Engler, O., *Textures Microstruct.* 23 (1995) 61.
- Engler, O., *Mater. Sci. Technol.* 12 (1996) 859.
- Engler, O., *Textures Microstruct.* 28 (1997) 197.
- Engler, O., *Mater. Sci. Forum* 273–275 (1998) 483.
- Engler, O., *Metall. Mater. Trans.* 30A (1999) 1517.
- Engler, O., *Acta Mater.* 48 (2000) 4827.
- Engler, O., *Scr. Mater.* 44 (2001) 229.
- Engler, O., Crumbach, M., and Li, S., *Acta Mater.* 53 (2005a) 2241.
- Engler, O., Escher, C., and Gottstein, G., *Mater. Sci. Forum* 113 (1993a) 127.
- Engler, O., Escher, C., and Gottstein, G., *Textures Microstruct.* 26–27 (1996a) 337.
- Engler, O. and Gottstein, G., *Steel Res.* 63 (1992) 413.
- Engler, O., Gottstein, G., Pospiech, J., and Jura, J., *Mater. Sci. Forum* 157–162 (1994a) 259.
- Engler, O., Heckelmann, I., Rickert, T., Hirsch, J., and Lücke, K., *Mater. Sci. Technol.* 10 (1994b) 771.

- Engler, O. and Hirsch, J., *Mater. Sci. Eng.* A452–453 (2007) 640.
- Engler, O., Hirsch, J., and Lücke, K., *Acta Metall.* 37 (1989) 2743.
- Engler, O., Hirsch, J., and Lücke, K., *Acta Metall. Mater.* 43 (1995a) 121.
- Engler, O., Hirsch, J., and Lücke, K., *Z. Metallkd.* 86 (1995b) 475.
- Engler, O. and Huh, M.Y., *Mater. Sci. Eng.* A271 (1999) 371.
- Engler, O., Huh, M.Y., and Tomé, C.N., *Metall. Mater. Trans.* A36 (2005b) 3127.
- Engler, O. and Juul Jensen, D., *Scr. Mater.* 30 (1994) 25.
- Engler, O., Jura, J., and Matthies, S., in *Proceedings of ICOTOM 12* (Ed. J.A. Szpunar), NRC Research Press, Ottawa (1999) 68.
- Engler, O., Löchte, L., and Hirsch, J., *Acta Mater.* 55 (2007) 5449.
- Engler, O., Palacios, J., Schäfer, W., Jansen, E., Lücke, K., and Will, G., *Textures Microstruct.* 21 (1993b) 195.
- Engler, O., Renoux, C., and Gottstein, G., in *Proceedings of ICAA3* (Eds. L. Arnberg et al.), NTH, Trondheim, Vol. II (1992) 203.
- Engler, O., Sachot, E., Ehrström, J.C., Reeves, A., and Shahani, R., *Mater. Sci. Technol.* 12 (1996b) 717.
- Engler, O., Yang, P., Pospiech, J., Jura, J., and Gottstein, G., *Mater. Sci. Forum* 157–162 (1994c) 933.
- English, A.T. and Chin, G., *Acta Metall.* 13 (1965) 1013.
- Ermrich, M., Hahn, F., and Wölfel, E.R., *Textures Microstruct.* 29 (1997) 89.
- Esling, C., Bechler-Ferry, E., and Bunge, H.-J., *J. Phys. Lett.* 42 (1981) 141.
- Faryna, M., *Mater. Chem. Phys.* 81 (2003) 301.
- Feldmann, K., *Textures Microstruct.* 10 (1989) 309.
- Feldmann, K., Betz, M., Andreef, A., Hennig, K., Kleinstück, K., and Matz, W., *Texture Cryst. Sol.* 4 (1980) 1.
- Ferran, G.L., Doherty, R.D., and Cahn, R.W., *Acta Metall.* 19 (1971) 1019.
- Ferry, M., Xu, W., Mateescu, N., Cairney, J.M., and Humphreys, F., *Mater. Sci. Forum* 550 (2007) 55.
- Field, D.P., *Scr. Metall. Mater.* 32 (1995) 67.
- Field, D.P., Bradford, L.T., Nowell, M.M., and Lillo, T.M., *Acta Mater.* 55 (2007) 4233.
- Field, D.P., Trivedia, P.B., Wright, S.I., and Kumar, M., *Ultramicroscopy* 103 (2005) 33.
- Field, D.P., Wright, S.I., and Dingley, D.J., in *Proceedings of ICOTOM 11* (Eds. Z. Liang, L. Zou, and Y. Chu), International Academic Publishers, Beijing (1996) 94.
- Fionova, L., Kononenko, O., Materveev, V., Priester, L., Lartigue, S., and Dupau, F., *Int. Sci. 1* (1993) 207.
- Frank, F.C., *Metall. Trans.* 19A (1988) 24.
- Friedel, G., *Comp. Rend.* 157 (1913) 1533.
- Fujimoto, F., Komaki, K., and Tagaki, S., *Z. f. Naturforschung* 27a (1972) 441.
- Fundenberger, J.J., Morawiec, A., Bouzy, E., and Lecomte, J.S., *Ultramicroscopy* 96 (2003) 127.
- Fundenberger, J.J., Morawiec, A., and Bouzy, E., *Sol. State Phenom.* 105 (2005) 37.
- Gale, B. and Griffiths, D., *Brit. J. Appl. Phys.* 11 (1960) 96.
- Gallagher, P.C.J., *Metall. Trans.* 1 (1970) 2429.
- Garbacz, A., Ralph, B., and Kurzydłowski, K.J., *Acta Metall. Mater.* 43 (1995) 1541.
- Garbe, S., Poulsen, H.F., and Juul Jensen, D., in *Proceedings of ICOTOM 11* (Eds. Z. Liang, L. Zou, and Y. Chu), International Academic Publishers, Beijing (1996) 100.
- Garzón, C.M. and A.P. Tschiotschin, *Mater. Sci. Eng.* A441 (2006) 230.
- Gehrman, R., Frommert, M., and Gottstein, G., *Mater. Sci. Eng.* A395 (2005) 338.

- Geiss, R.H., *Appl. Phys. Lett.* 27 (1975) 174.
- Germain, L., Gey, N., and Humbert, M., *Ultramicroscopy* 107 (2007) 1129.
- Gerth, D. and Schwarzer, R.A., *Textures Microstruct.* 21 (1993) 177.
- Gertsman, V.Y., *Acta Crystallogr.* A57 (2001a) 649.
- Gertsman, V.Y., *Acta Crystallogr.* A57 (2001b) 369.
- Gerward, L., Lehn, S., and Christiansen, G., *Texture Cryst. Sol.* 2 (1976) 95.
- Gholinia, A., *Technical Brochure Nordlys F+*, Oxford Instruments Analytical Ltd., High Wycombe, England (2008).
- Giessen, B.C. and Gordon, G.E., *Science* 159 (1968) 973.
- Gil Sevillano, J., González, D., and Martínez-Esnaola, J.M., *Mater. Sci. Forum* 550 (2007) 75.
- Goehner, R.P. and Michael, J.R., *J. Res. Natl. Inst. Stand. Technol.* 101 (1996) 301.
- Goodhew, P.J., Humphreys, F.J., and Beanland, R., *Electron Microscopy and Analysis* (3rd edition), Taylor and Francis, London (2001).
- Gotthardt, R., Hoschek, G., Reimold, O., and Haeßner, F., *Texture* 1 (1972) 99.
- Gottstein, G., *Scr. Metall.* 20 (1986) 1791.
- Gottstein, G., in *Proceedings of ICOTOM 8* (Eds. J.S. Kallend and G. Gottstein), TMS, Warrendale, PA (1988) 195.
- Gottstein, G. and Engler, O., *J. de Physique IV Coll. C7* 3 (1993) 2137.
- Gourgues-Lorenzon, A.-F., *Int. Mater. Rev.* 57 (2007) 65.
- Grewen, J., in *Proc. 3ème Colloq. Europ. sur les Textures des Métaux et leurs Application Industrielle, Pont-à-Mousson* (Ed. R. Penelle), Société Française de Métallurgie, Nancy, France (1973) 195.
- Grimmer, H., Bollmann, W., and Warrington, D.H., *Acta Crystallogr.* A30 (1974) 197.
- Groves, J.R., Yashar, P.C., Arendt, P.N., DePaula, R.F., Peterson, E.J., and Fitzsimmons, M.R., *Physica C* 355 (2001) 293.
- Guilmeau, E., Chateigner, D., Noudem, J., Funahashi, R., Horii, S., and Ouladdiaf, B., *J. Appl. Crystallogr.* 38 (2005) 199.
- Gupta, V.K. and Agnew, S.R., *J. Appl. Cryst.* 42 (2009) 116.
- Haeßner, F., Jakubowski, U., and Wilkens, M., *Phys. Stat. Sol.* 7 (1964) 701.
- Haeßner, F., Jakubowski, U., and Wilkens, M., *Acta Metall.* 14 (1966) 454.
- Hahn, T. (Ed.), *International Tables for Crystallography Vol. A*, Springer-Verlag, Dordrecht, The Netherlands (2005).
- Han, J.H., Jee, K.K., and Oh, K.H., *Int. J. Mech. Sci.* 45 (2003) 1613.
- Hansen, J., Pospiech, J., and Lücke, K., *Tables for Texture Analysis of Cubic Crystals*, Springer-Verlag, Berlin (1978).
- Hansen, N. and Juul Jensen, D., *Mater. Sci. Forum* 157–162 (1994) 1211.
- Hansen, N., Leffers, T., and Kjems, J.K., *Acta Metall.* 29 (1981) 1523.
- Harland, C.J., Akhter, P., and Venables, J.A., *J. Phys.* E14 (1981) 175.
- Harris, G.B., *Phil. Mag.* 43 (1952) 113.
- Hartig, C., Vogel, S.C., and Mecking, H., *Mater. Sci. Eng.* A437 (2006) 145.
- Hasenclever, J. and Scharf, G., *Mater. Sci. Forum* 217–222 (1996) 565.
- Hatherly, M. and Hutchinson, W.B., *An Introduction to Textures in Metals* (Monograph no. 5), The Institute of Metals, London (1979).
- He, B.B., *Powder Diffraction* 18 (2003) 71.
- He, Y., Godet, S., and Jonas, J.J., *Acta Mater.* 53 (2005) 1179.
- He, Y. and Jonas, J.J., *J. Appl. Crystallogr.* 40 (2007) 559.
- Heidelbach, F., Riekel, C., and Wenk, H.-R., *J. Appl. Crystallogr.* 32 (1999) 841.
- Heidelbach, F., Wenk, H.-R., Muenchhausen, R.E., Folty, S., Nogar, N., and Rollett, A.D., *J. Mater. Res.* 7 (1992) 549.

- Heidelbach, F., Wenk, H.R., Chen, S.S., Pospiech, J., and Wright, S.I., *Mater. Sci. Eng.* A215 (1996) 39.
- Heilmann, P., Clark, W.A.T., and Rigney, D.A., *Ultramicroscopy* 9 (1982) 365.
- Heilmann, P., Clark, W.A.T., and Rigney, D.A., *Acta Metall.* 31 (1983) 1293.
- Heinicke, F., Brokmeier, H.-G., Dahms, M., Bunge, H.-J., Pannetier, J., Ritter, C., and De Wall, H., *Textures Microstruct.* 14–18 (1991) 403.
- Heinz, A. and Neumann, P., *Acta Crystallogr.* A47 (1991) 780.
- Heizmann, J.J. and Laruelle, C., *J. Appl. Crystallogr.* 19 (1986) 467.
- Helming, K., in *Proceedings of ICOTOM 11* (Eds. Z. Liang, L. Zou, and Y. Chu), International Academic Publishers, Beijing (1996) 106.
- Helming, K., *Mater. Sci. Forum* 273–275 (1998) 125.
- Helming, K. and Eschner, T., *Cryst. Res. Technol.* 25 (1990) K203.
- Helming, K. and Prechwinkel, U., *Sol. State Phenom.* 105 (2005) 71.
- Helming, K. and Schwarzer, R.A., *Mater. Sci. Forum* 157–162 (1994) 1219.
- Helming, K., Schwarzer, R.A., Rauschenbach, B., Geier, S., Leiss, B., Wenk, H.-R., Ullemeier, K., and Heinitz, J., *Z. Metallkd.* 85 (1994) 545.
- Helming, K., Voitus, W., and Walther, K., *Physica B* 180–181 (1992) 1025.
- Hilliard, J.E., *J. Microsc.* 95 (1972) 45.
- Hirsch, J., Burmeister, G., Hoenen, L., and Lücke, K., in *Experimental Techniques of Texture Analysis* (Ed. H.-J. Bunge), DGM Inf. Ges., Oberursel, Germany (1986) 63.
- Hirsch, J. and Lücke, K., *Acta Metall.* 36 (1988) 2863.
- Hirsch, J., Lücke, K. and Hatherly, M., *Acta Metall.* 36 (1988) 2905.
- Hirsch, P.B., Howie, A., Nicholson, R.B., Pashley, D.W., and Whelan, M.J., *Electron Microscopy of Thin Crystals*, Krieger Publishers, Malabar, FL (1977).
- Hjelen, J. and Nes, E., in *Proceedings of ICOTOM 8* (Eds. J.S. Kallend and G. Gottstein), TMS, Warrendale, PA (1988) 597.
- Hjelen, J., Ørsund, R., and Nes, E., *Acta Metall. Mater.* 39 (1991) 1377.
- Hjelen, J., Orsund, R., Hoel, E., Runde, P., Furu, T., and Nes, E., *Textures Microstruct.* 20 (1993) 29.
- Hjelen, J., Qvale, A.H., and Gomo, O., *Mater. Sci. Forum* 157–162 (1994) 137.
- Høier, R., Bentdal, J., Daaland, O., and Nes, E., *Mater. Sci. Forum* 157–162 (1994) 143.
- Hölscher, M., Raabe, D., and Lücke, K., *Steel Res.* 62 (1991) 567.
- Hölscher, M., Raabe, D., and Lücke, K., *Acta Metall. Mater.* 42 (1994) 879.
- Homer, E.R., Adams, B.L., and Fullwood, D.T., *Scr. Mater.* 54 (2006) 1017.
- Hosford, W.F., *Trans. Metall. Soc. AIME* 230 (1964) 12.
- Hough, P.V.C., US Patent 3 069.654 December 18 (1962). <http://www.oxinst.com/products/microanalysis/ebsd/Pages/ebsd.aspx>, October 2008.
- Hu, H., in *Proceedings of the 7th Risø International Symposium* (Eds. N. Hansen et al.), Risø National Laboratory, Roskilde, Denmark (1986) 75.
- Hu, Y. and Randle, V., *Scr. Mater.* 56 (2007) 1051.
- Hughes, D.A. and Kumar, A., in *Proceedings of ICOTOM 11* (Eds. Z. Liang, L. Zou, and Y. Chu), International Academic Publishers, Beijing (1996) 1376.
- Huh, M.Y., Cho, Y.S., and Engler, O., *Mater. Sci. Eng.* A247 (1998) 152.
- Huh, M.Y. and Engler, O., *Mater. Sci. Eng.* A308 (2001) 74.
- Huh, M.Y., Lee, J.H., Park, S.H., Engler, O., and Raabe, D., *Steel Res. Int.* 76 (2005) 797.
- Humbert, M., in *Experimental Techniques of Texture Analysis* (Ed. H.-J. Bunge), DGM Inf. Ges., Oberursel, Germany (1986) 29.
- Humbert, M. and Bergmann, H.W., *J. Appl. Crystallogr.* 13 (1980) 500.
- Humphreys, F.J., *Acta Metall.* 25 (1977) 1323.

- Humphreys, F.J., *Textures Microstruct.* 6 (1983) 45.
- Humphreys, F.J., in *Proceedings of the 5th Risø International Symposium* (Eds. N. Hessel Andersen et al.), Risø National Laboratory, Roskilde, Denmark (1984) 35.
- Humphreys, F.J., *J. Mater. Sci.* 36 (2001) 3833.
- Humphreys, F.J., *Scr. Mater.* 51 (2004) 771.
- Humphreys, F.J. and Hatherly, M., *Recrystallisation and Related Annealing Phenomena*, Pergamon, Oxford (1995).
- Humphreys, F.J., Huang, Y., Brough, I., and Harris, C., *J. Microsc.* 195 (1999) 212.
- Hünsche, I., Oertel, C.G., Tamm, R., Skrotzki, W., and Knabl, W., *Mater. Sci. Forum* 467–470 (2004) 495.
- Hutchinson, B., Moss, B., Smith, A., Astill, A., Scruby, C., Engberg, G., and Björklund, J., *Ironmaking Steelmaking* 29 (2002) 77.
- Hutchinson, W.B., *Int. Met. Rev.* 29 (1984) 25.
- Hutchinson, W.B., *Acta Metall.* 37 (1989) 1047.
- Hutchinson, W.B., Duggan, B.J., and Hatherly, M., *Metals Technol.* 6 (1979) 398.
- Hutchinson, W.B., Oscarsson, A., and Karlsson, A., *Mater. Sci. Technol.* 5 (1989) 1118.
- Hutchinson, W.B., Ryde, L., Bate, P.S., and Bacroix, B., *Scr. Mater.* 35 (1996) 579.
- Hutchinson, W.B., Lindh, E., and Bate, P., in *Proceedings of ICOTOM 12* (Ed. J.A. Szpunar), NRC Research Press, Ottawa (1999) 34.
- Ibe, G., Grzemba, B., Hannibal, W.D., and Scharf, G., in *Proceedings of ICOTOM 7* (Eds. C.M. Brakman, P. Jongenburger, and E.J. Mittemeijer), Netherlands Society for Material Science, Zwijndrecht (1984) 503.
- Imhof, J., *Z. Metallkd.* 68 (1977) 38.
- Inagaki, H., *ISIJ Int.* 34 (1994) 313.
- Inokuti, Y. and Doherty, R.D., *Texture Cryst. Sol.* 2 (1977) 143.
- Inokuti, Y., Maeda, C., and Ito, Y., *Trans. ISIJ* 27 (1987) 139, 302.
- Inoue, H. and Inakazu, N., in *Proceedings of ICOTOM 8* (Eds. J.S. Kallend and G. Gottstein), TMS, Warrendale, PA (1988) 997.
- Inoue, H. and Takasugi, T., *Z. Metallkd.* 92 (2001) 82.
- Ion, S.E., Humphreys, F.J., and White, S.H., *Acta Metall.* 30 (1982) 1909.
- Jansen, E., Schäfer, W., and Will, G., *J. Appl. Crystallogr.* 21 (1988) 228.
- Jansen, E., Schäfer, W., and Will, G., *Textures Microstruct.* 30 (1998) 145.
- Jones, J.L., Vogel, S.C., Slamovich, E.B., and Bowman, K.J., *Scr. Mater.* 51 (2004) 1123.
- Joy, D.C., *Microscopy Society of America 52nd Annual Meeting* (Eds. G.W. Bailey and A.J. Garratt-Read), San Francisco Press, San Francisco, CA (1994) 592.
- Joy, D.C. and Newbury, D.E., *J. Mater. Sci.* 7 (1972) 714.
- Joy, D.C., Newbury, D.E., and Davidson, D.L., *J. Appl. Phys.* 53 (1982) R81.
- Jura, J. and Pospiech, J., *Texture Cryst. Sol.* 3 (1978) 1.
- Jura, J., Pospiech, J., and Gottstein, G., *Z. Metallkd.* 87 (1996) 476.
- Juul Jensen, D. and Kjems, J.K., *Textures Microstruct.* 5 (1983) 239.
- Juul Jensen, D., Lauridsen, E.M., Margulies, L., Poulsen, H.F., Schmidt, S., Sørensen, H.O., and Vaughan, G.B.M., *Mater. Today* 9 (2006) 18.
- Juul Jensen, D. and Leffers, T., *Textures Microstruct.* 10 (1989) 361.
- Juul Jensen, D. and Randle, V., in *Proceedings of the 10th Risø International Symposium on Annealing Processes* (Eds. J.B. Bilde-Sørensen et al.), Risø National Laboratory, Roskilde, Denmark (1989) 103.
- Juul Jensen, D. and Schmidt, N.-H., in *Proceedings of Recrystallisation '90* (Ed. T. Chandra), TMS, Warrendale, PA (1990) 1219.

- Kallend, J.S., in *Texture and Anisotropy, Preferred Orientations in Polycrystals and their Effect on Materials Properties* (Eds. U.F. Kocks, C.N. Tomé, and H.-R. Wenk), Cambridge University Press, Cambridge, UK (1998) 102.
- Kallend, J.S., Kocks, U.F., Rollett, A.D., and Wenk, H.-R., *Mater. Sci. Eng.* A132 (1991a) 1.
- Kallend, J.S., Morris, P.P., and Davies, G.J., *Acta Metall.* 24 (1976) 361.
- Kallend, J.S., Schwarz, R.B., and Rollett, A.D., *Textures Microstruct.* 13 (1991b) 189.
- Kamaya, M., Wilkinson, A.J., and Titchmarsh, J.M., *Acta Mater.* 54 (2006) 539.
- Kang, J.Y., Bacroix, B., Regle, H., Oh, K.H., and Lee, H.C., *Acta Mater.* 55 (2007) 4935.
- Karlsen, M., Hjelen, J., Grong, Ø., Rørvik, G., Chiron, R., Schubert, U., and Nilsen, E., *Mater. Sci. Technol.* 24 (2008) 64.
- Katrakova, D. and Mücklich, F., *Pract. Metallogr.* 38 (2001) 547.
- Katrakova, D. and Mücklich, F., *Pract. Metallogr.* 39 (2002) 644.
- Kawashima, K., Hyoguchi, T., and Akagi, T., *J. Nondestructive Eval.* 12 (1993) 71.
- Kelly, A.M., Bingert, S.R., and Reiswig, R.D., *Microstructural Sci.* 23 (1996) 185.
- Kern, R., Lee, H.P., and Bunge, H.-J., *Steel Res.* 57 (1986) 563.
- Kernig, B., Scharf, G., and Rixen, R., *Aluminium* 65 (1989) 274.
- Kestens, L., Verbeken, K., Decocker, R., Petrov, R., Gobernado, P., and Offerman, S.E., *Mater. Sci. Forum* 495–497 (2005) 157.
- Kikuchi, S., *J. Appl. Phys.* 5 (1928) 83.
- Kleber, W., Bautsch, H.J., and Bohm, J., *Einführung in die Kristallographie* Oldenbourg Wissenschaftsverlag, München, Germany (2002).
- Klein, H., Bunge, H.-J., and Nauer-Gerhardt, C.U., in *Proceedings of ICOTOM 11* (Eds. Z. Liang, L. Zou, and Y. Chu), International Academic Publishers, Beijing (1996) 122.
- Klein, H., Heubeck, C., and Bunge, H.-J., *Mater. Sci. Forum* 157–162 (1994) 1423.
- Kleinstück, K. and Tobisch, J., *Kristall u. Technik* 3 (1968) 455.
- Kleinstück, K., Tobisch, J., Betz, M., and Schläfer, U., *Kristall u. Technik* 11 (1976) 409.
- Klinkenberg, C., Schmitz, H.P., and Tamler, H., in *Proceedings of ICOTOM 12* (Ed. J.A. Szpunar), NRC Research Press, Ottawa (1999) 475.
- Kneijnsberg, H.P., Verbraak, C.A. and ten Bouwhuijs, M.J., *Mater. Sci. Eng.* 72 (1985) 171.
- Knorr, D.B., Weiland, H., and Szpunar, J.A., *J. Metals* September (1994) 32.
- Koblischka-Veneva, A., Koblischka, M.R., Qu, T., Han, Z., and Mücklich, F., *Physica C* 468 (2008) 174.
- Kocks, U.F., in *Proceedings of ICOTOM 8* (Eds. J.S. Kallend and G. Gottstein), TMS, Warrendale, PA (1988) 31.
- Kocks, U.F., in *Texture and Anisotropy, Preferred Orientations in Polycrystals and their Effect on Materials Properties* (Eds. U.F. Kocks, C.N. Tomé, and H.-R. Wenk), Cambridge University Press, Cambridge, UK (1998) 10, 44.
- Kocks, U.F. and Westlake, D., *Trans. AIME* 239 (1967) 1107.
- Köhlhoff, G.D., Sun, X., and Lücke, K., in *Proceedings of ICOTOM 8* (Eds. J.S. Kallend and G. Gottstein), TMS, Warrendale, PA (1988) 183.
- Konrad, J., Zaefferer, S., and Raabe, D., *Acta Mater.* 54 (2006) 1369.
- Kopinek, H.J., *Mater. Sci. Forum* 157–162 (1994) 1929.
- Kossel, W., Loeck, V., and Voges, H., *Z. Phys.* 94 (1935) 139.
- Kostron, H., *Z. Metallkd.* 41 (1950) 370.
- Krieger Lassen, N.C., in *Proceedings of 16th Risø International Symposium: Microstructural and Crystallographic Aspects of Recrystallisation* (Eds. N. Hansen et al.), Risø National Laboratory, Roskilde, Denmark (1995) 405.

- Krieger Lassen, N.C., *Mater. Sci. Technol.* 12 (1996) 837.
- Krieger Lassen, N.C., *J. Microscopy* 190 (1998) 375.
- Krieger Lassen, N.C. and Bilde-Sørensen, J.B., *J. Microsc.* 170 (1993) 125.
- Krieger Lassen, N.C., Juul Jensen, D., and Conradsen, K., *Scan. Microsc.* 6 (1992) 115.
- Krieger Lassen, N.C., Juul Jensen, D., and Conradsen, K., *Mater. Sci. Forum* 157–162 (1994) 149.
- Kröger, S., Dahlem-Klein, E., Weiland, H., and Bunge, H.-J., *Textures Microstruct.* 10 (1988) 41.
- Kruger, S.E., Moreau, A., Militzer, M., and Biggs, T., *Mater. Sci. Forum* 426–432 (2003) 483.
- Kunze, K., Wright, S.I., Adams, B.L., and Dingley, D.J., *Textures Microstruct.* 20 (1993) 41.
- Kunze, K., Zaefferer, S., and Schwarzer, R., *Beitr. elektronenmikr. Direktabb. Oberfl. (BEDO)* 27 (1994) 169.
- Laird, C., Eichen, E., and Bitler, W.R., *J. Appl. Phys.* 37 (1966) 2225.
- Lange F.F., *Acta Metall.* 15 (1967) 311.
- Larsen, A.W. and Juul Jensen, D., *Mater. Char.* 51 (2003) 271.
- Larson, B.C., Yang, W.G., Ice, G.E., Budai, J.D., and Tischler, J.Z., *Nature* 415 (2002) 887.
- Laue, M., Friedrich, W., and Knipping, P., *Sitzungsbericht der Bayr. Akad. D. Wiss. Math.-Phys.* (1912/1913).
- Lauridsen, E.M., Schmidt, S., Suter, R.M., and Poulsen, H.F., *J. Appl. Crystallogr.* 34 (2001) 744.
- Lee, H.P., Esling, C., and Bunge, H.-J., *Textures Microstruct.* 7 (1988) 317.
- Lee, K.T., de Wit, G., Morawiec, A., and Szpunar, J.A., *J. Mater. Sci.* 30 (1995) 1327.
- Leffers, T. and Bilde-Sørensen, W.B., *Acta Metall. Mater.* 38 (1990) 1917.
- Leffers, T. and Juul Jensen, D., *Textures Microstruct.* 6 (1986) 231.
- Lens, A., Maurice, C., and Driver, J.H., *Mater. Sci. Eng. A*403 (2005) 144.
- Lewis, A.C., Bingert, J.F., Rowenhorst, D.J., Gupta, A., Geltmacher, A.D., and Spanos, G., *Mater. Sci. Eng. A*418 (2006) 11.
- Liebmann, B., Lücke, K., and Masing, G., *Z. Metallkd.* 47 (1956) 57.
- Lienert, U., Poulsen, H.F., Honkimäki, V., Schulze, C., and Hignette, O., *J. Synchrotron Rad.* 6 (1999) 979.
- Lin, H. and Pope, D.P., *Mater. Sci. Forum* 204–206 (1996) 399.
- Lin, P., Palumbo, G., Erb, U., and Aust, K.T., *Scr. Metall. Mater.* 33 (1995) 1387.
- Lins, J.F.C., Sandim, H.R.Z., Kestenbach, H.-J., Raabe, D., and Vecchio, K.S., *Mater. Sci. Eng. A*457 (2007) 205.
- Lischewski, I., Kirch, D.M., Ziemons, A., and Gottstein, G., *Texture, Stress and Microstructure* (2008) Article ID 294508 (on-line journal).
- Lisowski, P.W., Bowman, C.D., Russell, G.J., and Wender, S.A., *Nuclear Sci. Eng.* 106 (1990) 208.
- Liu, J. and Chakrabarti, D.J., *Acta Mater.* 44 (1996) 4647.
- Liu, Q., *Ultramicroscopy* 60 (1995) 81.
- Liu, Q., in *Proceedings of ICOTOM 11* (Eds. Z. Liang, L. Zou, and Y. Chu), International Academic Publishers, Beijing (1996) 128.
- Liu, W., Bayerlein, M., Mughrabi, H., Day, A., and Quested, P.N., *Acta Metall. Mater.* 40 (1992) 1763.
- Liu, W., Liu, Y., Suo, H., and Bunge, H.-J., *Mater. Sci. Forum* 273–275 (1998) 503.
- Lorenz, W. and Hougardy, H., *Textures Microstruct.* 8&9 (1988) 579.
- Loretto, M.H., *Electron Beam Analysis of Materials* (2nd edition), Chapman & Hall, London/New York (1994).
- Lücke, K., *Can. Met. Quart.* 13 (1974) 261.

- Lücke, K., Därmann, C., and Hirsch, J., *Trans. Ind. Inst. Met.* 38 (1985) 496.
Lücke, K. and Engler, O., *Mater. Sci. Technol.* 6 (1990) 1113.
Lücke, K., Pospiech, J., Virnich, K.H., and Jura, J., *Acta Metall.* 29 (1981) 167.
Lücke, K., Pospiech, J., Jura, J., and Hirsch, J., *Z. Metallkd.* 77 (1986) 312.
Lu, W., Hughes, D., and Min, S., in *Proceedings of ICOTOM 11* (Eds. Z. Liang, L. Zou, and Y. Chu), International Academic Publishers, Beijing (1996) 134.
Ludwig, W., Buffière, J.-Y., Savelli, S., and Cloetens, P., *Acta Mater.* 51 (2003) 585.
Luo, J.F., Ji, Y., Zhong, T.X., Zhang, Y.Q., Wang, J.Z., Liu, J.P., Niu, N.H., Han, J., Guo, X., and Shen, G.D., *Microelectron. Reliab.* 46 (2006) 178.
Lutterotti, L., Matthies, S., Wenk, H.-R., Schultz, A.J., and Richardson Jr. J.W., *J. Appl. Phys.* 81 (1997) 594.
Mackenzie, J.K., *Biometrika* 45 (1958) 229.
Mackenzie, J.K., *Acta Metall.* 12 (1964) 223.
Mainprice, D., Lloyd, G.E., and Casey, M., *J. Struct. Geol.* 15 (1993) 1169.
Malis, T.F. and Steele, D., *Proceedings of Material Research Society* 199 (Ed. R. Anderson), MRS, Pittsburgh, PA (1990).
Mao, W., Hirsch, J., and Lücke, K., in *Proceedings of ICOTOM 8* (Eds. J.S. Kallend and G. Gottstein), TMS, Warrendale, PA (1988) 613.
Mason, T.A. and Adams, B.L., *J. Metals* (October 1994) 43.
Matthies, S., *Phys. Stat. Sol. (b)* 92 (1979) K135.
Matthies, S., *Phys. Stat. Sol. (b)* 112 (1982) 705.
Matthies, S., in *Proceedings of ICOTOM 7* (Eds. C.M. Brakman, P. Jongenburger, and E.J. Mittemeijer), Netherlands Society Mater. Sci., Zwijndrecht (1984) 737.
Matthies, S., *Mater. Sci. Forum* 408–412 (2002) 95.
Matthies, S., Helming, K., and Kunze, K., *Phys. Stat. Sol. (b)* 157 (1990) 71, 489.
Matthies, S., Lutterotti, L., and Wenk, H.-R., *J. Appl. Crystallogr.* 30 (1997) 31.
Matthies, S. and Vinel, G.W., *Phys. Stat. Sol. (b)* 112 (1982) K111, K115.
Matthies, S. and Vinel, G.W., *Mater. Sci. Forum* 157–162 (1994) 1641.
Matthies, S., Vinel, G.W., and Helming, K., *Standard Distributions in Texture Analysis*, Akademie-Verlag, Berlin (1987).
Matthies, S. and Wagner, F., *Phys. Stat. Sol. (b)* 196 (1996) K11.
Matthies, S. and Wenk, H.-R. in *Preferred Orientation in Deformed Metals and Rocks: An Introduction to Modern Texture Analysis* (Ed. H.-R. Wenk), Academic Press, Orlando, FL (1985) 139.
Matthies, S. and Wenk, H.-R., *Phys. Stat. Sol. (a)* 133 (1992) 253.
Matthies, S., Wenk, H.-R., and Vinel, G.W., *J. Appl. Crystallogr.* 21 (1988) 285.
Maurice, C. and Driver, J.H., *Acta Mater.* 45 (1997) 4627.
McKie, C. and McKie, D., *Crystalline Solids*, Nelson, London (1974).
Michael, J., in *Electron Backscatter Diffraction in Materials Science* (Eds. A.J. Schwartz, M. Kumar, and B.L. Adams), Kluwer Academic/Plenum Publishers, New York (2000) 75.
Michael, J.R. and Goehner, R.P., in *Proceedings of Microscopy Society of America 52nd Annual Meeting* (Eds. G.W. Bailey and A.J., Garratt-Read), San Francisco Press, San Francisco, CA (1994) 596.
Michael, J.R. and Kotula, P.G., *Microsc. Microanal.* 14 Suppl. S2 (2008) 976.
Mirpuri, K., Wendrock, H., Menzel, S., Wetzig, K., and Szpunar, J., *Thin Solid Films* 496 (2006) 703.
Mishin, O.V., Lauridsen, E.M., Krieger Lassen, N.C., Brückner, G., Tschenetscher, T., Bay, B., Juul Jensen, D., and Poulsen, H.F., *J. Appl. Crystallogr.* 33 (2000) 364.

- Miura, S., Ohkubo, K., and Mohri, T., *Intermetallics* 15 (2007) 783.
- Molodov, D.A., Czubayko, U., Gottstein, G., and Shvindlerman, L.S., *Scr. Metall. Mater.* 32 (1995) 529.
- Montesin, T. and Heizmann, J.J., *J. Appl. Crystallogr.* 25 (1992) 665.
- Moreau, A., Lévesque, D., Lord, M., Dubois, M., Monchalin, J.-P., Padoleau, C., and Bussière, J.F., *Ultrasonics* 40 (2002) 1047.
- Morawiec, A., *J. Appl. Crystallogr.* 28 (1995) 289.
- Morawiec, A. and Field, D.P., *Phil. Mag.* 73A (1996) 1113.
- Morris, P.R., *J. Appl. Phys.* 30 (1959) 595.
- Morris, P.R. and Heckler, A.T., *Adv. X-Ray Anal.* 11 (1968) 454.
- Morris, P.R. and Hook, R.E., *Textures Microstruct.* 19 (1992) 75.
- Mücklich, A., Hennig, K., Bouillot, J., and Matthies, S., in *Proceedings of ICOTOM 7* (Eds. C.M. Brakman, P. Jongenburger, and E.J. Mittemeijer), Netherlands Society for Material Science, Zwijndrecht (1984) 657.
- Müller, S., Müller, K., Rosumek, M., and Reimers, W., *Aluminium* 82 (2006) 438.
- Mykura, H., in *Grain Boundary Structure and Kinetics*, ASM, Ohio, Metals Park (1980) 445.
- Nakamichi, H., Humphreys, F.J., and Brough, I., *J. Microsc.* 230 (2008) 464.
- Nauer-Gerhardt, C.U. and Bunge, H.-J., in *Experimental Techniques of Texture Analysis* (Ed. H.-J. Bunge), DGM Inf. Ges., Oberursel, Germany (1986) 125, 147.
- Neumann, P., *Steel Res.* 62 (1991a) 560.
- Neumann, P., *Textures Microstruct.* 14–18 (1991b) 53.
- Nielsen, S.F., Wolf, A., Poulsen, H.F., Ohler, M., Lienert, U., and Owen, R.A., *J. Synchrotron Rad.* 7 (2000) 103.
- Nolze, G., *Cryst. Res. Technol.* 43 (2008) 61.
- Norton, J.T., *J. Appl. Phys.* 19 (1948) 1176.
- Nowell, M.M., Chui-Sabourin, M., and Carpenter, J.O., *Microscopy Today* 14 (2006) 6.
- Nowell, M.M. and Wright, S.I., *J. Microsc.* 213 (2004) 296.
- Nowell, M.M. and Wright, S.I., *Ultramicroscopy* 103 (2005) 41.
- Obst, B., Nast, R., Schlachter, S., de Boer, B., Holzapfel, B., Nemetschek, R., and Prusseit, W., *Z. Metallkd.* 94 (2003) 580.
- Ogata, Y., Tsuda, K., and Tanaka, M., *Acta Crystallogr. A*64 (2008) 587.
- Okamoto, M., Matersuo, M., Motegi, M., and Tanino, M., *Trans. ISIJ* 25 (1985) B110.
- Palumbo, G. and Aust, K.T., in *Materials Interfaces: Atomic Level Structure and Properties* (Eds. D. Wolf and S. Yip), Chapman & Hall, London (1992) 190.
- Pan, Y., Adams, B.L., Olson, T., and Panayotou, N., *Acta Mater.* 44 (1996) 4685.
- Pantleon, W., Poulsen, H.F., Almer, J., and Lienert, U., *Mater. Sci. Eng.* A387–389 (2004) 339.
- Park, N.J. and Bunge, H.-J., *Mater. Sci. Forum* 157–162 (1994) 563.
- Park, S.H., Kim, K.Y., Lee, Y.D., and Park, C.G., *ISIJ Int.* 42 (2002) 100.
- Partridge, P.G., *Met. Rev.* 118 (1969) 169.
- Paul, H., Driver, J.H., Maurice, C., and Piątkowski, A., *Acta Mater.* 55 (2007) 575.
- Pawlak, K., *Phys. Stat. Sol (b)* 134 (1986) 477.
- Pawlak, K., *Mater. Sci. Forum* 157–162 (1994) 401.
- Pawlak, K., Pospiech, J., and Lücke, K., *Textures Microstruct.* 14–18 (1991) 25.
- Peng, Y. and Wynblatt, P., *J. Am. Ceram. Soc.* 88 (2005) 2286.
- Perez, M.G., Kenik, E.A., O'Keefe, M.J., Miller, F.S., and Johnson, B., *Mater. Sci. Eng.* A424 (2006) 239.
- Perlitz, H.J., Lücke, K., and Pitsch, W., *Acta Metall.* 17 (1969) 1183.
- Peters, E.T. and Ogilvie, R.E., *Trans. AIME* 233 (1965) 89.

- Petrov, R., Kestens, L., Wasilkowska, A., and Houbaert, Y., *Mater. Sci. Eng.* A447 (2007) 285.
- Philippe, M.J., *Mater. Sci. Forum* 157–162 (1994) 1337.
- Philippe, M.J., Esling, C., and Hocheid, B., *Textures Microstruct.* 7 (1988) 265.
- Philippe, M.J., Wagner, F., Mellab, F.E., Esling, C., and Wegria, J., *Acta Metall Mater.* 42 (1994) 239.
- Phillips, F.C., *An Introduction to Crystallography* (4th edition), Longman Group, London (1971).
- Pitsch, W., Perlwitz, H.J., and Lücke, K., *Phys. Stat. Sol.* 7 (1964) K105 733.
- Plege, P., in *Theoretical Methods of Texture Analysis* (Ed. H.-J. Bunge), DGM Inf. Ges., Oberursel, Germany (1987) 393.
- Pospiech, J., *Kristall und Technik* 7 (1972) 1057.
- Pospiech, J., in *Quantitative Texture Analysis* (Eds. H.-J. Bunge and C. Esling), DGM Inf. Ges., Oberursel, Germany (1982) 293.
- Pospiech, J. and Jura, J., *Z. Metallkd.* 65 (1974) 324.
- Pospiech, J. and Jura, J., *Kristall Technik* 10 (1975) 783.
- Pospiech, J., Jura, J., and Gottstein, G., *Mater. Sci. Forum* 157–162 (1994) 407.
- Pospiech, J. and Lücke, K., *Acta Metall.* 23 (1975) 997.
- Pospiech, J. and Lücke, K., *Z. Metallkd.* 70 (1979) 567.
- Pospiech, J., Lücke, K., and Sztwiertnia, K., *Acta Metall. Mater.* 41 (1993) 305.
- Pospiech, J., Sztwiertnia, K., and Haefner, F., *Textures Microstructures* 6 (1986) 201.
- Poulsen, H.F., *Crystall. Rev.* 10 (2004) 29.
- Poulsen, H.F. and Juul Jensen, D., in *Proceedings of the 16th Risø International Symposium* (Eds. N. Hansen et al.), Risø National Laboratory, Roskilde, Denmark (1995) 503.
- Poulsen, H.F. and Juul Jensen, D., *Mater. Sci. Forum* 408–412 (2002) 49.
- Poulsen, H.F., Nielsen, S.F., Lauridsen, E.M., Schmidt, S., Suter, R.M., Lienert, U., Margulies, L., Lorentzen, T., and Juul Jensen, D., *J. Appl. Crystallogr.* 34 (2001) 751.
- Prince, E. (Ed.), *International Tables for Crystallography Vol. C*, Springer-Verlag, Dordrecht, The Netherlands (2004).
- Pumphrey, P.H., in *Grain Boundary Structure and Properties* (Eds. G.A. Chadwick and D.A. Smith), Academic Press, London (1976) 139.
- Quested, P.N., Henderson, P.J., and McLean, M., *Acta Metall.* 36 (1988) 2743.
- Raabe, D., *Dissertation*, RWTH Aachen, Germany (1992).
- Raabe, D., *Steel Res.* 66 (1995) 222.
- Raabe, D., *J. Mater. Sci.* 31 (1996) 3839.
- Raabe, D., Keichel, J., Mao, W., Sun, Z., and Gottstein, G., in *Proceedings of ICOTOM 11* (Eds. Z. Liang, L. Zou, and Y. Chu), International Academic Publishers, Beijing (1996) 1027.
- Raabe, D. and Lücke, K., *Scr. Metall.* 26 (1992) 19.
- Raabe, D. and Lücke, K., *Z. Metallkd.* 85 (1994) 302.
- Raabe, D., Schlenkert, G., Weisshaupt, H., and Lücke, K., *Mater. Sci. Technol.* 10 (1994) 229.
- Radon, J., *Ber. Sächs. Akad. Wiss. Leibzig Math.-Phys. Klasse* 69 (1917) 262.
- Rafaja, D., Dopita, M., Masimov, M., Klemm, V., Wendt, N., and Lengauer, W., *Int. J. Ref. Met. Hard Mater.* 26 (2008) 263.
- Rajmohan, N., Hayakawa, Y., Szpunar, J.A., and Root, J.H., *Acta Mater.* 45 (1997) 2485.
- Ralph, B. and Ecob, R.C., in *Proceedings of the 5th Risø International Symposium* (Eds. N. Hessel Andersen et al.), Risø National Laboratory, Roskilde, Denmark (1984) 109.

- Randle, V., *Proc. Roy. Soc. Lond.* 431 (1990) 61.
- Randle, V., *Microtexture Determination and its Applications*, The Institute of Materials, London (1992).
- Randle, V., *Grain Boundary Geometry in Polycrystals*, Institute of Physics Publishing, Bristol (1993).
- Randle, V., *Acta Metall. Mater.* 43 (1995a) 1741.
- Randle, V., *Mater. Char.* 34 (1995b) 29.
- Randle, V., *The Role of the Coincidence Site Lattice in Grain Boundary Engineering*, Institute of Materials, London (1996).
- Randle, V., in *Proceedings of the Materials Research Society Meeting No. 458* (Eds. C.L. Briant et al.), MRS, Pittsburgh, PA (1997) 41.
- Randle, V., *Acta Mater.* 46 (1998) 1459.
- Randle, V., in *Electron Backscatter Diffraction in Materials Science* (Eds. A.J. Schwartz, M. Kumar, and B.L. Adams), Kluwer Academic/Plenum Publishers, New York (2000) 291.
- Randle, V., *Mater. Char.* 47 (2001) 411.
- Randle, V., *Microtexture Determination and its Applications* (2nd edition), Institute of Materials, London (2003).
- Randle, V., *Acta Mater.* 52 (2004) 4067.
- Randle, V., *Adv. Imag. Electron Phys.* 151 (2007) 363.
- Randle, V., Barker, I., and Ralph, B., *J. Electron Microsc. Technol.* 13 (1989) 51.
- Randle, V., Caul, M.C., and Fiedler, J., *Microsc. Anal.* 3 (1997) 224.
- Randle, V. and Davies, H., *Ultramicroscopy* 90 (2002) 153.
- Randle, V. and Day, A., *Mater. Sci. Technol.* 9 (1993) 1069.
- Randle, V. and Dingley, D.J., *Scr. Metall.* 23 (1989) 1565.
- Randle, V. and Hoile, C., *Mater. Sci. Forum* 273–275 (1998) 183.
- Randle, V., Juul Jensen, D., and Hansen, N., *Phil. Mag.* 73 (1996) 265.
- Randle, V. and Ralph, B., *Proc. Roy. Soc. Lond.* 415A (1988) 239.
- Randle, V., Rohrer, G., Kim, C., and Hu, Y., *Acta Mater.* 54 (2006) 4489.
- Ranganathan, S., *Acta Crystallogr.* 21 (1966) 197.
- Rauch, E.F. and Duft, A., *Mater. Sci. Forum* 495–497 (2005) 197.
- Rauch, E.F. and Dupuy, L., *Arch. Metall. Mater.* 50 (2005) 87.
- Ray, R.K., Jonas, J.J., and Hook, R.E., *Int. Mater. Rev.* 39 (1994) 129.
- Reed, B.W. and Kumar, M., *Scr. Mater.* 54 (2006) 1029.
- Reeves, A., Le Gouic, F., Pannetier, J., Anne, M., Bordet, P., and Hodeau, J.L., *Mater. Sci. Forum* 217–222 (1996) 595.
- Reimer, L., *Transmission Electron Microscopy: Physics of Image Formation and Microanalysis* (4th edition), Springer-Verlag, Berlin (1997).
- Reimer, L., *Scanning Electron Microscopy: Physics of Image Formation and Microanalysis* (2nd edition), Springer-Verlag, Berlin (1998).
- Rhines, F.N., Craig, K.R., and Rousse, D.A., *Metall. Trans.* 7A (1976) 1729.
- Ridha, A.A. and Hutchinson, W.B., *Acta Metall.* 30 (1982) 1929.
- Riecke, W.D., *Optik* 18 (1961) 278, 373.
- Riecke, W.D., *Optik* 19 (1962) 273.
- Rietveld, H.M., *J. Appl. Crystallogr.* 2 (1969) 65.
- Ro, Y.J., Agnew, S.R., and Gangloff, R.P., *Scr. Mater.* 52 (2005) 531.
- Rodriguez-Navarro, A.B., *J. Appl. Crystallogr.* 39 (2006) 905.
- Rodriguez-Navarro, A.B., *J. Appl. Crystallogr.* 40 (2007) 631.
- Roe, R.J., *J. Appl. Phys.* 36 (1965) 2024.

- Rohrer, G.S., Saylor, D.M., El-Dasher, B.S., Adams, B.L., Rollett, A.D., and Wynblatt, P., *Z. Metallkd.* 95 (2004) 197.
- Rollett, A.D. and Wright, S.I., in *Texture and Anisotropy, Preferred Orientations in Polycrystals and their Effect on Materials Properties* (Eds. U.F. Kocks, C.N. Tomé, and H.-R. Wenk), Cambridge University Press, Cambridge, UK (1998) 178.
- Röntgen, W.C., *Sitzungsbericht der Würzburger Physik.-Med. Ges.* (1896); English translation in *Nature* 53 (1896) 274.
- Ruer, D. and Baro, R., *Adv. X-ray Anal.* 20 (1977) 187.
- Ruer, D. and Vadon, A., in *Quantitative Texture Analysis* (Eds. H.J. Bunge and C. Esling), DGM Inf. Ges., Oberursel, Germany (1982) 343.
- Ryder, P.L. and Pitsch, W., *Phil. Mag.* 17 (1967) 437.
- Ryder, P.L. and Pitsch, W., *Phil. Mag.* 18 (1968) 807.
- Sætre, T.O., Solberg, J.K., and Ryum, M., *Metallography* 19 (1986) 197, 345.
- Samajdar, I., Verlinden, B., Van Houtte, P., and Vanderschueren, D., *Mater. Sci. Eng.* A238 (1997) 343.
- Sandim, H.R.Z., Bernardi, H.H., Verlinden, B., and Raabe, D., *Mater. Sci. Eng.* A467 (2007) 44.
- Santoro, A. and Mighell, A.D., *Acta Crystallogr.* (1973) 171.
- Sarma, G.B. and Dawson, P.R., *Acta Mater.* 44 (1996) 1937.
- Savoie, J. and Lücke, K., *Textures Microstruct.* 14–18 (1991) 897.
- Saylor, D.M., El-Dasher, B.S., Adams, B.L., and Rohrer, G.S., *Metall. Mater. Trans.* 35A (2004) 1981.
- Saylor, D.M., Morawiec, A., and Rohrer, G.S., *Acta Mater.* 51 (2003) 3663.
- Schaeben, H., *Phys. Stat. Sol. (b)* 148 (1988) 63.
- Schaeben, H., *J. Appl. Phys.* 69 (1991) 1320.
- Schaeben, H., Wenk, H.R., and Vadon, A., in *Preferred Orientation in Deformed Metals and Rocks: An Introduction to Modern Texture Analysis* (Ed. H.-R. Wenk), Academic Press, Orlando, FL (1985) 123.
- Schäfer, B. and Schwarzer, R.A., *Mater. Sci. Forum* 273–275 (1998) 223.
- Scheriau, S. and Pippan, R., *Mater. Sci. Eng.* A493 (2008) 48.
- Schmidt, N.H., Bilde-Sørensen, J.B., and Juul Jensen, D., *Scan. Electron. Microsc.* 5 (1991) 637.
- Schmidt, N.H. and Olesen, N.O., *Can. Mineral.* 27 (1989) 15.
- Schmidt, U. and Lücke, K., *Texture Cryst. Sol.* 3 (1979) 85.
- Schneider, E. and Österlein, L., *Mater. Sci. Forum* 210 (1996) 405.
- Schuh, C.A., Kumar, M., and King, W.E., *Acta Mater.* 51 (2003) 687.
- Schulz, L.G., *J. Appl. Phys.* 20 (1949a) 1030.
- Schulz, L.G., *J. Appl. Phys.* 20 (1949b) 1033.
- Schwarzer, R.A., *Beitr. elektronenmikr. Direktabb. Oberfl. (BEDO)* 16 (1983) 131.
- Schwarzer, R.A., in *Proceedings of EUREM '88*, Int. Phys. Conf. Ser. No. 93, Vol. 2, Ch. 1 (1988) 23.
- Schwarzer, R.A., *Die Bestimmung der lokalen Textur mit dem Elektronenmikroskop*, Habilitation thesis, TU Clausthal, Germany (1989).
- Schwarzer, R.A., *Textures Microstruct.* 20 (1993) 7.
- Schwarzer, R.A., *Microscopy and Analysis* 45 (1997a) 35.
- Schwarzer, R.A., *Ultramicroscopy* 67 (1997b) 19.
- Schwarzer, R.A., *Mater. Sci. Technol.* 16 (2000) 1384.
- Schwarzer, R.A., *Arch. Metall. Mater.* 53 (2008) 5.

- Schwarzer, R.A., Krieger Lassen, N.C., and Schäfer, B., in *Proceedings of ICOTOM 11* (Eds. Z. Liang, L. Zou, and Y. Chu), International Academic Publishers, Beijing (1996a) 170.
- Schwarzer, R.A., Singh, A.K., and Sukkau, J., *Mater. Sci. Technol.* 16 (2000) 1389.
- Schwarzer, R.A., Springer, F., and Zaeffferer, S., in *Proceedings of ICOTOM 11* (Eds. Z. Liang, L. Zou, and Y. Chu), International Academic Publishers, Beijing (1996b) 43.
- Schwarzer, R.A. and Sukkau, J., *Mater. Sci. Forum* 273–275 (1998) 215.
- Schwarzer, R.A. and Weiland, H., in *Proceedings of ICOTOM 7* (Eds. C.M. Brakman, P. Jongenburger, and E.J. Mittemeijer), Netherlands Society for Material Science, Zwijndrecht (1984) 839.
- Schwarzer, R.A. and Weiland, H., in *Experimental Techniques of Texture Analysis* (Ed. H.-J. Bunge), DGM Inf. Ges., Oberursel, Germany (1986) 287.
- Schwarzer, R.A. and Weiland, H., *Textures Microstruct.* 8/9 (1988) 551.
- Schwarzer, R.A. and Zaeffferer, S., *Mater. Sci. Forum* 157–162 (1994) 195.
- Schwarzer, R.A., Zaeffferer, S., and Kunze, K., *Adv. X-Ray Anal.* 38 (1995) 547.
- Seidel, L., Hölscher, M., and Lücke, K., *Textures Microstruct.* 11 (1989) 171.
- Seward, G.G.E., Celotto, S., Prior, D.J., Wheeler, J., and Pond, R.C., *Acta Mater.* 52 (2004) 821.
- Shimizu, M., Katayama, M., and Kitagawa, H., in *Experimental Techniques of Texture Analysis* (Ed. H.-J. Bunge), DGM Inf. Ges., Oberursel, Germany (1986) 107.
- Shimizu, R., Harase, J., and Dingley, D.J., *Acta Metall. Mater.* 38 (1990) 973.
- Simkin, B.A., Ng, B.C., Bieler, T.R., Crimp, M.A., and Mason, D.E., *Intermetallics* 11 (2003) 215.
- Sinclair, C.W., Embury, J.D., Weatherly, G.C., Conlon, K.T., and Engler, O., *Mater. Sci. Technol.* 19 (2003) 1321.
- Singh, A.K. and Schwarzer, R.A., *Z. Metallkd.* 91 (2000) 702.
- Skrotzki, W., Klöden, B., Tamm, R., Oertel, C.-G., Garbe, U., and Rybacki, E., *Textures Microstruct.* 35 (2003) 163.
- Slavik, D.C., Wert, J.A., and Gangloff, R.P., *J. Mater. Res.* 8 (1993) 2482.
- Slavik, D.C. and Gangloff, R.P., *Acta Mater.* 44 (1996) 3515.
- Small, J.A. and Michael, J.R., *J. Microsc.* 201 (2001) 59.
- Smith, K.L. and Ortega, R.B., *Adv. X-ray Anal.* 36 (1993) 641.
- Søfferud, M., Hjelen, J., Karlsen, M., Breivik, T., Krieger Lassen, N.C., and Schwarzer, R., in *EMC 2008 Vol. 1: Instrumentation and Methods* (Eds. M. Luysberg, K. Tillmann, and T. Weirich), Springer-Verlag, Berlin (2008) 623.
- Sous, S.A., Hildmann, B.O., and Kaysser, W.A., *Phys. Stat. Sol. (a)* 159 (1997) 343.
- Spence, J.C.H., and Zuo, J.M., *Electron Microdiffraction*, Springer-Verlag, Berlin (1992).
- Spies, M. and Salama, K., *Ultrasonics* 28 (1990) 370.
- Stadelmann, P.A., *Ultramicroscopy* 21 (1987) 131.
- Steeds, J.W., in *Introduction to Analytical Electron Microscopy* (Eds. J.J. Hren et al.), Plenum Press, New York (1979) 387.
- Steeds, J.W. and Vincent, R., *J. Appl. Crystallogr.* 16 (1983) 317.
- Stout, M.G., Kallend, J.S., Kocks, U.F., Przystupa, M.A., and Rollett, A.D., in *Proceedings of ICOTOM 8* (Eds. J.S. Kallend and G. Gottstein), TMS, Warrendale, PA (1988) 479.
- Szpunar, J., *J. Mater. Sci.* 19 (1984) 3467.
- Szpunar, J., *Textures Microstruct.* 12 (1990) 243.
- Szpunar, J.A., Ahlroos, S., and Tavernier, P., *J. Mater. Sci.* 28 (1993) 2366.

- Szpunar, J.A. and Davies, S.T., in *Proceedings of ICOTOM 7* (Eds. C.M. Brakman, P. Jongenburger, and E.J. Mittemeijer), Netherlands Society for Material Science, Zwijndrecht (1984) 845.
- Szpunar, J. and Gerward, L., *J. Mater. Sci.* 15 (1980) 469.
- Szpunar, J., Ojanen, M., and Laine, E., *Z. Metallkd.* 65 (1974) 221.
- Sztwiertnia, K., Faryna, M., and Sawina, G., *J. European Ceramic Soc.* 26 (2006) 2973.
- Tan, L., Sridharan, K., and Allen, T.R., *J. Nucl. Mater.* 371 (2007) 171.
- Tanaka, M., Sekii, H., and Nagasawa, T., *Acta Crystallogr. A*39 (1983) 825.
- Tarkowski, T., Bonarski, J., and Dąbrowski, W., *Nucl. Instrum. Methods A*551 (2005) 178.
- Tenckhoff, E., *J. Appl. Phys.* 41 (1970) 3944.
- Tenckhoff, E., *Deformation Mechanisms, Texture, and Anisotropy in Zirconium and Zircaloy*, ASTM, Philadelphia, PA (1988).
- Themelis, G., Chikwembani, S., and Weertman, J., *Mater. Char.* 24 (1990) 27.
- Thomas, G. and Gorringe, M.J., *Transmission Electron Microscopy of Materials*, Wiley, New York (1979).
- Thompson, R.B., Papadakis, E.P., Bluhm, D.D., Alers, G.A., Forouraghi, K., Skank, H.D., and Wormley, S.J., *J. Nondestructive Eval.* 12 (1993) 45.
- Thomson, C.B. and Randle, V., *Acta Mater.* 45 (1997a) 4909.
- Thomson, C.B. and Randle, V., *J. Mater. Sci.* 32 (1997b) 1909.
- Tixier, R. and Wache, C., *J. Appl. Crystallogr.* 3 (1970) 466.
- Tizliouine, A., Bessières, J., Heizmann, J.J., and Bobo, J.F., *J. Appl. Crystallogr.* 29 (1996) 531.
- Tobisch, J., Betzl, M., and Reichel, P., *Z. Exp. Techn. Phys.* 5 (1969) 391.
- Tobisch, J. and Bunge, H.-J., *Texture* 1 (1972) 125.
- Tomé, C., Pochettino, A., and Penelle, R., in *Proceedings of ICOTOM 8* (Eds. J.S. Kallend and G. Gottstein), TMS, Warrendale, PA (1988) 985.
- Trimby, P., Day, A., Mehnert, K., and Schmidt, N.H., *J. Microsc.* 205 (2002) 259.
- Troost, K.Z., van der Sluis, P., and Gravesteyn, D.J., *Appl. Phys. Lett.* 62 (1993) 1110.
- Tse, Y.Y., Liu, G.L., and Duggan, B.J., *Scr. Mater.* 42 (2000) 25.
- Tucker, G.E.G. and Murphy, P.C., *J. Inst. Met.* 81 (1952/53) 235.
- Uhbi, S. and Bowen, A., *Mater. Sci. Technol.* 12 (1996) 880.
- Ullemeyer, K., Braun, G., Dahms, M., Kruhl, J.H., Olesen, N.Ø., and Siegesmund, S., *J. Struct. Geol.* 22 (2000) 1541.
- Ullrich, H.-J., Bauch, J., Brechbühl, J., Bretschneider, I., and Lin, H., *Z. Metallkd.* 89 (1999) 106.
- Ullrich, H.-J., Friedel, F., Bauch, J., Meinl, G., Geise, G., Lengauer, W., and Ettmayer, P., *Mikrochim. Acta* 109 (1992) 233.
- Ullrich, H.-J., Schlaubitz, M., Friedel, F., Spann, T., Bauch, J., Wroblewski, T., Garbe, S., Gaul, G., Knöchel, A., Lechtenberg, F., Rossmanith, E., Kumpat, G., and Ulrich, G., *Nuclear Instrum. Methods Phys. Res. A*349 (1994) 269.
- Ullrich, H.-J. and Schulze, G.E.R., *Kristall Technik* 7 (1972) 207.
- Vadon, A. and Heizmann, J.J., *Textures Microstruct.* 14–18 (1991) 37.
- Van Acker, K., De Buyser, L., Celis, J.P., and Van Houtte, P., *J. Appl. Crystallogr.* 27 (1994) 56.
- Van Essen, C.G., in *Proceedings of the 25th Meeting of Electron Microscopy and Analysis Group, EMAG*, Institute of Physics, London (1971) 314.
- Van Essen, C.G., Schulson, E.M., and Donaghay, R.H., *Nature* 225 (1970) 847.
- Van Essen, C.G., Schulson, E.M., and Donaghay, R.H., *J. Mater. Sci.* 6 (1971) 213.
- Van Houtte, P., *Mater. Sci. Eng.* 43 (1980) 7.

- Van Houtte, P., *Textures Microstruct.* 6 (1983) 1.
- Van Houtte, P., *Textures Microstruct.* 6 (1984) 137.
- Van Houtte, P., *Textures Microstruct.* 7 (1987) 187.
- Van Houtte, P., *Textures Microstruct.* 13 (1991) 199.
- Van Houtte, P., Li, S., and Engler, O., *Aluminium* 80 (2004) 702.
- Van Oostrum, K.J., Leenhouts, A., and Jore, A., *Appl. Phys. Lett.* 23 (1973) 283.
- Vandermeer, R.A. and Ogle, J.C., *Trans. Metall. Soc. AIME* 245 (1969) 1511.
- Vandermeer, R.A. and Snyder, W.B., *Metall. Trans.* 10A (1979) 1031.
- Vatne, H.E., Furu, T., Ørsund, R., and Nes, E., *Acta Mater.* 44 (1996) 4463.
- Venables, J.A. and Bin-Jaya, R., *Phil. Mag.* 35 (1977) 1317.
- Venables, J.A. and Harland, C.J., *Phil. Mag.* 27 (1973) 1193.
- Vogel, S. and Klimanek, P., *Mater. Sci. Forum* 204–206 (1996) 451.
- Vogel, S.C., Hartig, C., Lutterotti, L., Von Dreele, R.B., Wenk, H.-R., and Williams, D.J., *Powder Diffrac.* 19 (2004) 65.
- Von Heimendahl, M., *Electron Microscopy of Materials*, Academic Press, San Diego, CA (1980).
- Von Heimendahl, M., Bell, W., and Thomas, G., *J. Appl. Phys.* 35 (1964) 3614.
- Von Dreele, R.B., *J. Appl. Crystallogr.* 30 (1997) 517.
- Von Meibom, R. and Rupp, E., *Z. Phys.* 82 (1933) 690.
- Von Schlippenbach, U., Emren, F., and Lücke, K., *Acta Metall.* 34 (1986) 1289.
- Wagner, F., Bechler-Ferry, E., Esling, C., and Baro, R., *J. Appl. Crystallogr.* 15 (1982) 122.
- Wagner, F., Bozzolo, N., Van Landuyt, O., and Grosdidier, T., *Acta Mater.* 50 (2002) 1245.
- Wagner F. and Dahms M., in *Advances and Applications of Quantitative Texture Analysis* (Eds. H.J. Bunge and C. Esling), DGM, Oberursel, Germany (1991) 101.
- Wagner, F., Humbert, M., Muller, J., and Esling, C., *Europhys. Lett.* 11 (1990) 479.
- Wagner, F., Obringer, P., Schwarzer, R.A., Goaer, G., and Sarti, D., in *Proceedings of ICOTOM 11* (Eds. Z. Liang, L. Zou, and Y. Chu), International Academic Publishers, Beijing (1996) 1376.
- Wagner, F., Wenk, H.R., Esling, C., and Bunge, H.-J., *Phys. Stat. Sol. (a)* 67 (1981) 269.
- Wagner, P., Engler, O., and Lücke, K., *Acta Metall. Mater.* 43 (1995) 3799.
- Walde, T. and Riedel, H., *Mater. Sci. Eng.* A443 (2007) 277.
- Walther, K., Heinitz, J., Ullemeyer, K., Betzl, M., and Wenk, H.-R., *J. Appl. Crystallogr.* 28 (1995) 503.
- Wang, F., Xu, J.Z., and Liang, Z.D., in *Proceedings of ICOTOM 8* (Eds. J.S. Kallend and G. Gottstein), TMS, Warrendale, PA (1988) 111.
- Wang, F., Xu, J.Z., and Liang, Z.D., *Textures Microstruct.* 19 (1992) 55.
- Wang, W.H., Sun, X., Köhlhoff, G.D., and Lücke, K., *Textures Microstruct.* 24 (1995) 199.
- Wang, Y.D., Luo, L., Liang, Z.D., Laruelle, C., Vadon, A., and Heizmann, J.J., *J. Appl. Crystallogr.* 30 (1997) 433.
- Wang, Y.N., Chang, C.I., Lee, C.J., Lin, H.K., and Huang, J.C., *Scr. Mater.* 55 (2006) 637.
- Wang, Y.N. and Huang, J.C., *Mater. Chem. Phys.* 81 (2003) 11.
- Warren, J.B., in *Introduction to Analytical Electron Microscopy* (Eds. J.J. Hren et al.), Plenum Press, New York (1979) 369.
- Warrington, D.H. and Boon, M., *Acta Metall.* 23 (1975) 599.
- Wassermann, G. and Grewen, J., *Texturen Metallischer Werkstoffe*, Springer-Verlag, Berlin (1962).
- Watanabe, T., *Mater. Forum* 11 (1988) 284.
- Wcislaw, L. and Bunge, H.-J., *Textures Microstruct.* 14–18 (1991) 257.

- Wcislak, L. and Bunge, H.-J., *Texture Analysis with a Position Sensitive Detector*, Cuvillier Verlag, Göttingen, Germany (1996).
- Wcislak, L., Bunge, H.-J., and Nauer-Gerhardt, C.U., *Z. Metallkd.* 84 (1993) 479.
- Wcislak, L., Klein, H., Bunge, H.-J., Garbe, U., Tschentscher, T., and Schneider, J.R., *J. Appl. Crystallogr.* 35 (2002) 82.
- Weiland, H., and Field, D.P., in *Proceedings of the 52nd Annual Meeting of the Microscopy Society of America* (Eds. G.W. Bailey A.J. and Garratt-Reed), San Francisco Press, San Francisco, CA (1994) 900.
- Weiland, H., Liu, J., and Nes, E., *Textures Microstruct.* 14–18 (1991) 109.
- Weiland, H. and Panchanadeeswaran, S., *Textures Microstruct.* 20 (1993) 67.
- Weiss, L.E. and Wenk, H.-R., in *Preferred Orientation in Deformed Metals and Rocks: An Introduction to Modern Texture Analysis* (Ed. H.-R. Wenk), Academic Press, Orlando, FL (1985) 49.
- Welch, P.I., in *Experimental Techniques of Texture Analysis* (Ed. H.-J. Bunge), DGM Inf. Ges., Oberursel, Germany (1986) 183.
- Wenk, H.-R. (Ed.), *Electron Microscopy in Mineralogy*, Springer-Verlag, Berlin (1976).
- Wenk, H.-R., in *Preferred Orientation in Deformed Metals and Rocks: An Introduction to Modern Texture Analysis* (Ed. H.-R. Wenk), Academic Press, Orlando, FL (1985) 11.
- Wenk, H.R., in *Texture and Anisotropy, Preferred Orientations in Polycrystals and their Effect on Materials Properties* (Eds. U.F. Kocks, C.N. Tomé, and H.-R. Wenk), Cambridge University Press, Cambridge, UK (1998) 126.
- Wenk, H.-R., *J. Appl. Crystallogr.* 24 (1991) 920.
- Wenk, H.-R., *J. Appl. Crystallogr.* 25 (1992) 524.
- Wenk, H.-R., *Trans. Am. Cryst. Assoc.* 29 (1994) 95.
- Wenk, H.-R., *Rev. Mineral. Geochem.* 63 (2006) 399.
- Wenk, H.-R., Bunge, H.-J., Kallend, J.S., Lücke, K., Matthies, S., and Pospiech, J., in *Proceedings of ICOTOM 8* (Eds. J.S. Kallend and G. Gottstein), TMS, Warrendale, PA (1988a) 17.
- Wenk, H.-R., Chateigner, D., Pernet, M., Bingert, J.F., Hellstrom, E., and Ouladdiaf, B., *Physica C* 272 (1996) 1.
- Wenk, H.-R., Cont, L., Xie, Y., Lutterotti, L., Ratschbacher, L., and Richardson, J., *J. Appl. Crystallogr.* 34 (2001) 442.
- Wenk, H.-R. and Grigull, S., *J. Appl. Crystallogr.* 36 (2003) 1040.
- Wenk, H.-R., Heidelbach, F., Chateigner, D., and Zontone, F., *J. Synchr. Rad.* 4 (1997) 95.
- Wenk, H.-R. and Kocks, U.F., *Metall. Trans.* 18A (1987) 1083.
- Wenk, H.-R., Larson, A.C., Vergamini, P.J., and Schultz, A.J., *J. Appl. Phys.* 70 (1991) 2035.
- Wenk, H.-R., Lutterotti, L., and Vogel, S., *Nucl. Instrum. Methods Phys. Res.* A515 (2003) 575.
- Wenk, H.-R., Matthies, S., Donovan, J., and Chateigner, D., *J. Appl. Crystallogr.* 31 (1998) 262.
- Wenk, H.-R., Matthies, S., and Lutterotti, L., *Mater. Sci. Forum* 157–162 (1994) 473.
- Wenk, H.-R. and Pannetier, J., *J. Struct. Geol.* 12 (1990) 177.
- Wenk, H.-R. and Phillips, D.S., *Physica C* 200 (1992) 105.
- Wenk, H.-R. and Van Houtte, P., *Rep. Prog. Phys.* 67 (2004) 1367.
- Wenk, H.-R., Vergamini, P.J., and Larson, A.C., *Textures Microstruct.* 8&9 (1988b) 443.
- Wert, J.A., Liu, Q., and Hansen, N., *Acta Mater.* 43 (1995) 4153.
- West, D.A. and Adams, B.L., *Metall. Mater. Trans.* 28A (1997) 229.
- Wever, F., *Z. f. Physik* 28 (1924) 69.
- Wilkinson, A.J., *Ultramicroscopy* 62 (1996) 237.

- Wilkinson, A.J. and Dingley, D.J., *Acta Metall. Mater.* 39 (1991) 3047.
- Wilkinson, A.J. and Hirsch, P.B., *Micron* 28 (1997) 279.
- Wilkinson, A.J., Meaden, G., and Dingley, D.J., *Ultramicroscopy* 106 (2006) 307.
- Will, G., Schäfer, W., and Merz, P., *Textures Microstruct.* 10 (1989) 375.
- Williams, D.B. and Carter, C.B., *Transmission Electron Microscopy: A Textbook for Materials Science*, Plenum Press, New York (1996).
- Williams, R.O., *J. Appl. Phys.* 39 (1968) 4329.
- Wolf, D., in *Materials Interfaces: Atomic Level Structure and Properties* (Eds. D. Wolf and S. Yip), Chapman & Hall, London (1992) 1.
- Wolf, D. and Lutsko, J.F., *Z. Kristall.* 189 (1989) 239.
- Wölfel, E.R., *J. Appl. Crystallogr.* 16 (1983) 341.
- Wright, S.I. and Adams, B.L., *Textures Microstruct.* 12 (1990) 65.
- Wright, S.I. and Adams, B.L., *Metall. Trans.* 23A (1992) 759.
- Wright, S.I., Beaudoin, A.J., and Gray, G.T., *Mater. Sci. Forum* 157–162 (1994a) 1695.
- Wright, S.I. and Dingley, D., *Mater. Sci. Forum* 273–275 (1998) 209.
- Wright, S.I., Gray, G.T., and Rollett, A.D., *Metall. Mater. Trans.* 25A (1994b) 1025.
- Wright, S.I. and Larsen, R.J., *J. Microsc.* 205 (2002) 245.
- Wright, S.I., Nowell, M.M., and Bingert, J.F., *Metall. Mater. Trans.* 38A (2007) 1845.
- Wright, S.I., Zhao, J.-W., and Adams, B.L., *Textures Microstruct.* 13 (1991) 123.
- Wynick, G.L. and Boehlert, C.J., *Mater. Char.* 55 (2005) 190.
- Xu, W., Ferry, M., Mateescu, N., Cairney, J.M., and Humphreys, F.J., *Mater. Char.* 58 (2007) 961.
- Yang, P., Zhao, Z., Ren, X., and Huang, S., *J. Mater. Sci. Technol.* 21 (2005) 331.
- Yang, W., Larson, B.C., Tischler, J.Z., Ice, G.E., Budai, J.D., and Liu, W., *Micron* 35 (2004) 431.
- Yi, S.B., Davies, C.H.J., Brokmeier, H.-G., Bolmaro, R.E., Kainer, K.U., and Homeyer, J., *Acta Mater.* 54 (2006) 549.
- Young, C.T. and Lytton, J.L., *J. Appl. Phys.* 43 (1972) 1408.
- Young, C.T., Steele, J.H., and Lytton, J.L., *Metall. Trans.* 4 (1973) 2081.
- Zaafarani, N., Raabe, D., Singh, R.N., Roters, F., and Zaeferer, S., *Acta Mater.* 54 (2006) 1863.
- Zaeferer, S., *J. Appl. Crystallogr.* 33 (2000) 10.
- Zaeferer, S., *Adv. Imaging Electron Phys.* 125 (2002) 355.
- Zaeferer, S., *Ultramicroscopy* 107 (2007) 254.
- Zaeferer, S., Baudin, T., and Penelle, R., *Acta Mater.* 49 (2001) 1105.
- Zaeferer, S. and Schwarzer, R.A., *Z. Metallkd.* 85 (1994) 585.
- Zaeferer, S., Wright, S.I., and Raabe, D., *Metall. Mater. Trans.* A39 (2008) 374.
- Zaldívar-Cadena, A.A. and Flores-Valdés, A., *Mater. Char.* 58 (2007) 834.
- Zhang, M., Zhang, J., and McDowell, D.L., *Int. J. Plasticity* 23 (2007) 1328.
- Zhao, J. and Adams, B.L., *Acta Crystallogr.* 44A (1988) 326.
- Zhao, J., Adams, B.L., and Morris, P.R., *Textures Microstruct.* 8&9 (1988) 493.
- Zhu, Y., Zhang, H., Wang, H., and Suenaga, M., *J. Mater. Res.* 12 (1991) 2507.
- Zhu, K.Y., Bacoux, B., Chaveau, T., Chaubet, D., and Castelnau, O., *Mater. Sci. Forum* 550 (2007) 545.
- Zink, U., Brokmeier, H.-G., and Bunge, H.-J., *Mater. Sci. Forum* 157–162 (1994) 251.

General Bibliography

CONFERENCES

Proc. 3ème Colloque Européen sur les Textures des Métaux et leurs Applications Industrielles, Pont-à-Mousson, Ed. R. Penelle, Société Française de Métallurgie, Nancy, France (1973).

Proceedings of the 5th International Conference on Textures of Materials, Aachen (ICOTOM 5), Eds. G. Gottstein and K. Lücke, Springer-Verlag, Berlin (1978).

Proceedings of the 6th International Conference on Textures of Materials, Tokyo (ICOTOM 6), Eds. S. Nagashima, The Iron and Steel Institute of Japan, Tokyo (1981).

Proceedings of the 7th International Conference on Textures of Materials, Noordwijkerhout (ICOTOM 7), Eds. C.M. Brakman, P. Jongenburger, and E.J. Mittemeijer, Netherlands Society for Materials Science, Zwijndrecht (1984).

Proceedings of the Textures in Non-Ferrous Metals and Alloys, Detroit, Eds. H.D. Merchant and J.G. Morris, TMS, Warrendale, PA (1985).

Proceedings of the 8th International Conference on Textures of Materials, Santa Fe (ICOTOM 8), Eds. J.S. Kallend and G. Gottstein, TMS, Warrendale PA (1988).

Proceedings of the 9th International Conference on Textures of Materials, Avignon (ICOTOM 9), Ed. H.-J. Bunge, Special Issue, *Textures Microstruct.* **14–18** (1991).

Proceedings of the 10th International Conference on Textures of Materials, Clausthal (ICOTOM 10), Ed. H.-J. Bunge, *Mater. Sci. Forum* **157–162** (1994).

Proceedings of the 11th International Conference on Textures of Materials, Xi'an (ICOTOM 11), Eds. Z. Liang, L. Zou, and Y. Chu, International Academic Publishers, Beijing (1996).

Proceedings of the 12th International Conference on Textures of Materials, Montreal (ICOTOM 12), Ed. J.A. Szpunar, NRC Research Press, Canada (1999).

Proceedings of the 13th International Conference on Textures of Materials, Seoul (ICOTOM 13), Ed. D.N. Lee, *Mater. Sci. Forum* **408–412** (2002).

Proceedings of the 14th International Conference on Textures of Materials, Leuven (ICOTOM 14), Eds. P. Van Houtte and L. Kestens, *Mater. Sci. Forum* **495–497** (2005).

Proceedings of the 15th International Conference on Textures of Materials, Pittsburgh (ICOTOM 15), Ed. A.D. Rollett, *Ceramic Transactions* **201** (2008).

- Proceedings of the Symposium on Textures in Non-Metallic Materials and Microstructure and Texture Evolution During Annealing of Deformed Materials, Indianapolis*, Eds. D.B. Knorr, J. Hirsch, and H.-J. Bunge, Special Issue, *Textures Microstruct.* **13** (1991).
- Proceedings of the Symposium on Microscale Textures of Materials, Cincinnati*, Eds. B.L. Adams and H. Weiland, Special Issue, *Textures Microstruct.* **20** (1993).
- Proceedings of the Interfacial Engineering for Optimised Properties*, Proc. No. 458, *Materials Research Society Fall Meeting*, Eds. C.L. Briant et al., Material Research Society, Pittsburgh, PA (1996).
- Proceedings of the Texture on a Microscale, London*, Eds. H.S. Uhbi and A.W. Bowen, Special Issue, *Mater. Sci. Technol.* **12** (1996).
- Proceedings of the International Conference on Texture and Anisotropy of Polycrystals, Clausthal (ITAP 1)*, Ed. R.A. Schwarzer, *Mater. Sci. Forum* **273–275** (1998).
- Proceedings of the International Conference on Texture and Anisotropy of Polycrystals II, Metz (ITAP 2)*, Eds. C. Esling et al., *Solid State Phenom.* **105** (2005).
- Quantitative Analysis of Texture, Cracow*, Eds. J. Karp et al., The Society of Polish Metallurgical Engineers, Cracow, Poland (1971).
- Texture and the Properties of Materials, Proceedings of the 4th International Conference on Texture, Cambridge*, Eds. G.J. Davies et al., The Metals Society, London (1976).
- Textures in Research and Practice, Clausthal*, Eds. J. Grewen and G. Wassermann, Springer-Verlag, Berlin (1969).

BOOKS

- Bacon, G.E., *Neutron Diffraction* (3rd edition), Clarendon Press, Oxford (1975).
- Barrett, C.S. and Massalski T.B., *Structure of Metals: Crystallographic Methods, Principles and Data*, McGraw-Hill, New York (1980).
- Bunge, H.-J., *Texture Analysis in Materials Science: Mathematical Methods*, Butterworths, London (1982).
- Bunge, H.-J. (Ed.), *Experimental Techniques of Texture Analysis*, DGM Inf. Ges., Oberursel, Germany (1986).
- Bunge, H.-J. (Ed.), *Theoretical Methods of Texture Analysis*, DGM Inf. Ges., Oberursel, Germany (1987).
- Bunge, H.-J. (Ed.), *Directional Properties of Materials*, DGM Inf. Ges., Oberursel, Germany (1988).
- Bunge, H.-J. (Ed.), *Advances and Applications of Quantitative Texture Analysis*, DGM Inf. Ges., Oberursel, Germany (1989).
- Bunge, H.-J. and Esling, C. (Eds.), *Quantitative Texture Analysis*, DGM Inf. Ges., Oberursel, Germany (1982).
- Bunge, H.-J., Siegesmund, S., Skrotzki, W., and Weber, K. (Eds.), *Textures in Geological Materials*, DGM Inf. Ges., Oberursel, Germany (1994).

- Cullity, B.D., *Elements of X-ray Diffraction* (2nd edition), Addison-Wesley, Reading, MA (1978).
- Dingley, D.J., Baba-Kishi, K., and Randle, V., *An Atlas of Backscatter Kikuchi Diffraction Patterns*, Institute of Physics Publishing, Bristol (1994).
- Edington, J.W., *Electron Diffraction in the Electron Microscope*, MacMillan, London (1975).
- Edington, J.W., *Practical Electron Microscopy in Materials Science*, Van Nostrand Reinhold, New York (1976).
- Goodhew, P.J., Humphreys F.J., and Beanland R., *Electron Microscopy and Analysis* (3rd edition), Taylor and Francis, London (2001).
- Hatherly, M. and Hutchinson, W.B., *An Introduction to Textures in Metals*, Monograph no. 5, The Institute of Metals, London (1979).
- Hirsch, P.B., Howie, A., Nicholson, R.B., Pashley, D.W., and Whelan, M.J., *Electron Microscopy of Thin Crystals*, Krieger Publishing, Malabar, FL (1977).
- Johari, O. and Thomas, G., *The Stereographic Projection and Its Applications*, Vol. IIA of *Techniques of Metal Research*, Ed. R.F. Bunshah, Interscience, New York (1969).
- Kocks, U.F., Tomé, C.N., and Wenk, H.-R. (Eds.), *Texture and Anisotropy, Preferred Orientations in Polycrystals and Their Effect on Materials Properties*, Cambridge University Press, Cambridge, UK (1998).
- Loretto, M.H., *Electron Beam Analysis of Materials* (2nd edition), Chapman & Hall, London (1994).
- McKie, C. and McKie, D., *Crystalline Solids*, Nelson, London (1974).
- Phillips, F.C., *An Introduction to Crystallography* (4th edition), Longman Group, London (1971).
- Randle, V., *Grain Boundary Geometry in Polycrystals*, Institute of Physics Publishing, Bristol (1993).
- Randle, V., *The Role of the Coincidence Site Lattice in Grain Boundary Engineering*, Institute of Materials, London (1996).
- Randle, V., *Microtexture Determination and Its Applications* (2nd edition), Institute of Materials, London (2003).
- Reimer, L., *Transmission Electron Microscopy: Physics of Image Formation and Microanalysis* (4th edition), Springer-Verlag, Berlin (1997).
- Reimer, L., *Scanning Electron Microscopy: Physics of Image Formation and Microanalysis* (2nd edition), Springer-Verlag, Berlin (1998).
- Schwartz, A.J., Kumar, M., and Adams, B.L. (Eds.), *Electron Backscatter Diffraction in Materials Science*, Kluwer Academic/Plenum Publishers, New York (2000).
- Smallman, R.E. and Bishop, R.J., *Modern Physical Metallurgy and Materials Engineering* (6th edition), Butterworth-Heinemann, Oxford (1999).
- Snyder, R.L., Fiala, J., and Bunge, H.-J. (Eds.), *Defect and Microstructure Analysis by Diffraction*, Inter. Union Cryst., Oxford University Press, USA (1999).

- Spieß, L., Teichert, G., Behnken, H., and Schwarzer, R.A., *Moderne Röntgenbeugung—Röntgendiffraktometrie für Materialwissenschaftler*, Reihe Teubner-Lehrbücher, B.G. Teubner-Verlag, Stuttgart-Leipzig-Wiesbaden, Germany (2005).
- Wassermann, G. and Grewen, J., *Texturen metallischer Werkstoffe*, Springer-Verlag, Berlin (1962).
- Wenk, H.-R. (Ed.), *Preferred Orientation in Deformed Metals and Rocks: An Introduction to Modern Texture Analysis*, Academic Press, Orlando, FL (1985).
- Williams, D.B. and Carter, C.B., *Transmission Electron Microscopy: A Textbook for Materials Science*, Plenum Press, New York (1996).

Index

A

- Absorption
diffraction analysis and, 64–66
pole figure data correction,
macrotexture analysis, 104–105
- Absorption edges, x-ray diffraction, 67
macrotexture analysis, 82–86
- Addition rule, microtexture analysis,
angle/axis descriptor,
misorientation data, 284–285
- Aluminum alloys
classical texture analysis, 5–6
electron backscatter diffraction,
specimen preparation, 216
- face-centered crystal structure
deformation texture, 148–153
- recrystallization texture, 162–166
- face-centered cubic structure,
deformation texture, 151–153
- Kikuchi diffraction pattern, 180
- macrotexture analysis, sample
preparation, 118–121
- microtexture analysis, Rodrigues
space representation, 276–280
- Angle/axis of rotation
coincidence site lattice, grain
boundaries, 324–326
- cylindrical angle/axis space, 43–45
- misorientation and, 42–43
microtexture analysis, 281–285
- orientation and, 40–42
- Rodrigues vector/Rodrigues space,
46–47, 49–50
- Angular resolution/accuracy, electron
backscatter diffraction, 224–229
- Annealing, body-centered cubic
(bcc) crystal structure,
recrystallization texture, 169
- Antiphase reflection, body-centered
crystal, 57–58
- Arbitrary defined cells (ADC) method,
orientation distribution
function, 139–140

- Area detector, low-symmetry materials,
peak separation, 114–115
- Asymmetrical tilt grain boundary
(ATGB), interface-plane
scheme, 327–328
- Atomic motif, crystal structure, 17–20
- Automated evaluation, Kikuchi
diffraction pattern
electron backscatter diffraction, 191–195
- pattern indexing/orientation, 188–191
- selected area channeling patterns, 198
- transmission electron microscopy,
195–198

B

- Background correction routine, electron
backscatter diffraction,
diffraction pattern
enhancement, 229–231
- Background error, pole figure data,
macrotexture analysis, 101–105
- Backscatter Kikuchi diffraction (BKD),
microtexture analysis, 12
- Barker etch, optical texture analysis,
364–367
- Beam control, sampling point location,
orientation microscopy,
305–306
- Beam normal direction, Kikuchi
diffraction pattern, orientation
determination, 185–188
- Berkeley texture package (BEARTEX),
orientation distribution
function, 138–140
- Body-centered cubic (bcc) crystal structure
Bragg's law of reflection, 58
- deformation texture, 153–157
- diffraction spectrum, 56–58
- Kikuchi mapping, 399–401
- orientation relationships, 347–350
- recrystallization texture, 166–169
- structure factor F , 59–61

- Boundary plane
 coincidence site lattice, grain boundaries, 324–326
 “five-parameter” analysis, 334–340
- Bragg angle
 Kikuchi diffraction pattern, formation mechanisms, 176–179
 pole figure measurement, 76–79
 selected area diffraction, 247–250
 synchrotron radiation, Debye-Scherrer patterns, 358–361
 x-ray diffraction, 66–67
 macrotexture analysis, 85–86
- Bragg-Brentano focusing condition
 macrotexture analysis, neutron diffraction, 109
 position-sensitive detector, 94–98
 reflection geometry, pole figure measurement, 87–90
- Bragg’s law
 electromagnetic radiation, 55–58
 energy-dispersive diffractometry, 98–99
 Laue and Debye-Scherrer techniques, 62–64
 micro-Kossel technique, scanning electron microscopy, 204–205
 selected area diffraction, 246–247
- Brandon criterion, coincidence site lattice, grain boundaries, 325–326
- Brass alloys, face-centered cubic structure
 deformation texture, 151–153
 recrystallization texture, 162–166
- Brass recrystallization texture
 component, face-centered crystal metals, 164–166
- Bravais lattices. *See also* Miller indices
 crystal structure, 17–20
- Bremsstrahlung, x-ray diffraction, macrotexture analysis, 80–86
- Bright and dark lines, Kikuchi diffraction pattern, transmission electron microscopy evaluation, 197
- Bs orientation
 face-centered crystal metals, deformation texture, 151–153
 truncation error, 133–137
- Bunge-Roe equation, Euler angles, 34–36
- Burgers phase relationship, crystallographic analysis, 347–350
- Burgers vector, coincidence site lattice, grain boundaries, 325–326
- Burns algorithm, Kikuchi diffraction pattern, electron backscatter diffraction evaluation, 191–195
- Butterfly filter, Kikuchi diffraction pattern, electron backscatter diffraction evaluation, 193–195
- C**
- Cadmium, hexagonal structure, deformation texture, 160–161
- Calibration techniques
 electron backscatter diffraction, 231–238
 iterative pattern fitting, 237–238
 known crystal orientation, 234–236
 pattern magnification, 236–237
 shadow casting, 233–234
 surface crystallographic analysis, serial sectioning, 331–332
- Camera constant, transmission electron microscopy, selected area diffraction, 244–247
- c/a ratio, hexagonal metals, deformation texture, 158–161
- Ceramics, macrotexture analysis, sample preparation, 119
- Characteristic lines, x-ray diffraction, macrotexture analysis, 81–86
- Charge-coupled device (CCD) camera differential-aperture x-ray microscopy, 355
 electron backscatter diffraction, 217–220
 data collection efficiency, 220–221
 synchrotron radiation
 Debye-Scherrer patterns, 357–361
 Laue technique, 353–355
 transmission electron microscopy, 255
 x-ray diffraction analysis, 96–98
- Chromium and chromium alloys, body-centered cubic structure, deformation texture, 156–157

- Clarity, electron backscatter diffraction, 228–229
- Cobalt, hexagonal structure, deformation texture, 158–161
- Coincidence site lattice (CSL) disorientation axis distribution, 282 grain boundaries, crystallographic analysis, 324–326 interface-plane scheme, 326–328 misorientations, 280 interfaces and, 314 Rodrigues space, 289, 291–292 orientation connectivity, 345–347 Zener drag, bcc metal recrystallization texture, 168
- Color output, spatial distribution, microtexture components, 309–313
- Complete pole figures, macrotexture analysis, 89–90
- Component method, orientation distribution function, 140
- Connectivity crystallographic analysis, 344–347 spatial distribution, microtexture components, orientation mapping, 309–313
- Continuous orientation distribution, microtexture analysis, Euler space representations, 266–270
- Continuous scanning, pole figure measurement, macrotexture analysis, 91–92
- Convergent beam electron diffraction (CBED), 255, 370
- Coordinate systems crystallographically related solutions, 25–27 Miller/Miller-Bravais indices, 377–379 Rodrigues vector/Rodrigues space, 46–47 rotation matrix, 20–24
- Copper materials face-centered crystals deformation texture, 148–153 recrystallization texture, 162–166 Kikuchi diffraction pattern, 179–180
- macrotexture analysis, sample preparation, 118–121 optical texture analysis, 366–367
- Correction function, pole figure data correction, macrotexture analysis, 102–105
- Counting statistics, macrotexture analysis neutron diffraction, 109 pole figure data correction, 104–105
- Crystal coordinate system, rotation matrix, 21–24
- Crystalline structure, atomic rearrangement, 53–55
- Crystallographically related operations, 381–382
- Crystallographic analysis grain boundaries, 324–328 coincidence site lattice, 324–326 interface-plane scheme, 326–328 tilt boundaries, 327–328 twist boundaries, 328
- orientation classical texture analysis, 3 connectivity and spatial distribution, 344–347 defined, 15 inter-phase relationships, 347–350
- related solutions, coordination systems, 25–27
- surfaces, 328–344 calibrated serial sectioning, 331–332 “five-parameter” and stereological techniques, 334–340 photogrammetric techniques, 333–334 sectioning techniques, 329–333 three-dimensional EBSD, 340–344 transmission electron microscopy, thin section analysis, 332–333 two-surface sectioning, 331
- Crystal orientation distribution, Euler space properties, 144–147
- Crystal structures and symmetries, 16–20
- Cube band formation, face-centered crystal metals, recrystallization texture, 163–166

- Cubic crystal structure
 angle/axis of rotation, 40–42
 crystal structures, 18–20
 diffraction spectrum, 56–58
 Euler space, 38–39
 fundamental zone, Rodrigues vector/
 Rodrigues space, 48–49
 Kikuchi diffraction pattern, 182
 macrotexture analysis, orientation
 distribution functions,
 128–129
 microtexture analysis, misorientation
 representation in Rodrigues
 space, 290–292
 Miller indices, 29–30
 orientation distribution function, series
 expansion method, 132–137
 symmetry operations, 381–382
 three-dimensional orientation
 distribution functions, Euler
 space, 141–147
- Current transmission, superconductors,
 6–7
- Cylindrical angle/axis space
 macrotexture analysis, 123–124
 misorientation representation,
 microtexture analysis, 289–290
 orientation and, 43–45
- D**
- Data collection efficiency
 electron backscatter diffraction,
 220–221
 orientation microscopy/orientation
 mapping, 307–308
- De Broglie relation
 electromagnetic radiation, 52
 electron diffraction, 70–71
- Debye-Scherrer patterns
 diffraction analysis, 61–64
 macrotexture analysis, 75
 position-sensitive detector, 97–98
 selected area diffraction, 247–250
 synchrotron radiation techniques,
 356–361
- Defocusing error
 pole figure data correction,
 macrotexture analysis, 102–105
- reflection geometry, pole figure
 measurement, 87–90
 selected area diffraction, 246–247
- Deformation texture
 body-centered cubic metals, 153–157
 face-centered crystal metals, 147–153
 hexagonal metals, 157–161
- Density distribution, microtexture
 analysis, pole figure and
 inverse pole figure, 262–265
- Design parameters, electron backscatter
 diffraction, 222–223
- Diamond polishing, electron backscatter
 diffraction, specimen
 preparation, 214–216
- Differential-aperture x-ray microscopy
 (DAXM), synchrotron
 radiation, 355
- Diffraction pattern center, Kikuchi
 diffraction pattern, 181–182
- Diffraction pattern enhancement, electron
 backscatter diffraction,
 229–231
- Diffraction techniques, texture analysis
 absorption and penetration depth,
 64–66
 categorization of techniques, 71–72
 electromagnetic radiation, Bragg's
 law, 52–58
 electrons, 69–71
 Kikuchi diffraction pattern
 basic principles, 175–176
 comparison of techniques, 180
 electron diffraction, 71
 face-centered crystals, recrystallization
 texture, 162–166
 formation mechanisms, 176–179
 projection, 181–182
 qualitative evaluation, 182
 pattern quality, 198–201
 quantitative evaluation, 183–198
 electron backscatter diffraction
 automated evaluation, 191–195
 indexing and orientation
 automation, 188–191
 orientation determination,
 185–188
 selected area channeling pattern,
 198

- transmission electron microscopy,
195–198
bright and dark lines, 197
dynamic range, 196–197
unambiguous indexing,
197–198
- Laue and Debye-Scherrer methods,
61–64
neutrons, 68–69
research background, 51
structure factor, 59–61
x-rays, 66–67
- Diffuse scattering, transmission electron microscopy, 251–255
- Direct methods
microtexture analysis, Euler space continuous distribution,
266–270
orientation distribution function,
137–140, 172
series expansion method *vs.*, 140–141
- Disorientation, microtexture analysis,
angle/axis descriptor,
281–285
- Ductility, classical texture analysis, 3–4
- Dynamic range, Kikuchi diffraction pattern, transmission electron microscopy evaluation, 195–198
- E**
- Earing behavior
classical texture analysis, 5–6
face-centered crystal metals,
deformation texture, 152–153
- Elastic modulus, classical texture analysis, 3–4
- Elastic scattering, neutron diffraction, 68–69
- Electrical conductivity, classical texture analysis, 4
- Electromagnetic acoustic transducers (EMAT), texture analysis, 362–363
- Electromagnetic radiation, Bragg's law and, 52–58
- Electron backscatter diffraction (EBSD) assessment, 371–374
- diffraction techniques, 72
interfacial analysis, research background, 323–324
- inter-phase orientation, 347–350
- Kikuchi diffraction pattern
automated evaluation, 191–195
fcc, bcc, and hexagonal crystals,
399–401
formation mechanisms, 178–180
orientation direction, 185–188
pattern indexing/orientation automation, 188–191
projection techniques, 181–182
transmission electron microscopy evaluation, 195–198
- low-symmetry materials, 112–115
- microtexture analysis, 11–12
Euler space representations, 268–270
intergrain misorientations, 285–286
orientation microscopy/mapping,
12–13
single-grain orientation measurements, 270–275
- orientation microscopy/orientation mapping
grain statistics, 314–315
pattern quality, 315–317
sampling point location, 306
sampling schedule, 306–307
- scanning electron microscopy
accelerating voltage, 226–227
calibration, 231–238
data collection efficiency, 220–221
evolution, 208–213
experiment design philosophy,
221–223
future research issues, 240
hardware requirements, 217–220
iterative pattern fitting, 237–238
know crystal orientation, 234–236
material requirements, 225
microscope parameters, 225
pattern clarity, 228–229
pattern magnification, 236–237
phase identification, 223–224
probe current, 227–228
resolution and operational parameters, 224–225
shadow casting, 233–234

- Electron backscatter diffraction (EBSD) (*continued*)
 specimen/microscope geometry, 225–226
 specimen preparation, 213–216
 system operation and data output, 238–239
 surface crystallographic analysis, 329–331
 calibrated serial sectioning, 331–332
 “five-parameter” analysis, 334–340
 photogrammetric techniques and, 334
 sectioning techniques, 330–333
 stereological techniques, 338–340
 system operation and data output, 238–240
- Electron channeling patterns (ECP), scanning electron microscopy, 205–207
- Electron diffraction
 atomic scattering, 53–54
 characteristics, 69–71
 mass absorption coefficients, 65–66
- Energy-dispersive diffractometry
 inverse pole figure measurement, 106–107
 low-symmetry materials, peak separation, 114–115
 x-ray diffraction analysis, 98–101
- Energy-dispersive spectroscopy (EDS), electron backscatter diffraction, 223–224
- Equal area projection, 389–390
 pole figure measurement, macrotexture analysis, 91–92
 reference sphere, 33
- Etchant materials
 macrotexture analysis, sample preparation, 119–121
 optical texture analysis, 364–367
- Euler angle
 electron backscatter diffraction, 239
 face-centered crystal metals
 deformation texture, 149–153
 recrystallization texture, 163–166
- microtexture analysis
 intergrain misorientations, 286
 three-dimensional misorientation representations, 286–289
- orientation, 33–36
 spatial distribution, microtexture components, 309–313
- three-dimensional orientation distribution functions, 141–147
- Eulerian cradle, position-sensitive detector, 95–98
- Euler space
 body-centered cubic (bcc) crystal structure, deformation texture, 153–157
- microtexture analysis, 265–275
 continuous distributions, 266–270
 individual orientations, 266
 misorientation representation, 286–289
 single-grain orientation measurements, 270–272
- orientation connectivity, 346–347
- orientation matrix, 36–39
- texture representation and display in, 141–147
- three-dimensional orientation distribution functions, 172
- macrotexture analysis, 123–124
- Even-order series expansion coefficients, orientation distribution function, ghost errors, 134–137
- Ewald space, selected area diffraction, 246–247
- Extended recovery, body-centered cubic (bcc) crystal structure, recrystallization texture, 169
- F**
- Face-centered crystal structure
 Bragg’s law of reflection, 58
 Kikuchi mapping, 399–401
 metal textures
 deformation texture, 147–153
 recrystallization, 161–166
- orientation relationships, 347–350
- structure factor F , 60–61

- Facet planes, surface crystallographic analysis, photogrammetric techniques, 334
- Fast Fourier transform (FFT), Kikuchi diffraction pattern, quality evaluation, 199–201
- Ferritic steels
- body-centered cubic (bcc) crystal structure
 - deformation texture, 155–157
 - recrystallization texture, 167–169
- macrotexture analysis, sample preparation, 119–121
- Field emission gun scanning electron microscopy (FEGSEM)
- electron backscatter diffraction, 217–220
 - operational and resolution parameters, 224–229
 - probe current, 227–228
- orientation microscopy/orientation mapping, sampling schedule, 306–307
- First-order Laue zone (FOLZ) lines, 255
- “Five-parameter” analysis, surface crystallographic analysis, 334–340
- Fixed sample geometry, inverse pole figure measurement, 106–107
- Fluorescence, x-ray diffraction, 67
- Focused aperture microdiffraction, 252–255
- Focused ion beam (FIB) tomography, surface crystallographic analysis, 341–344
- Forward-mounted backscatter detector (FMBSD), electron backscatter diffraction, 211–213, 219–220
- Frame averaging, electron backscatter diffraction, diffraction pattern enhancement, 230–231
- Friedel’s law, pole figure measurement, 79
- Fully automated evaluation, Kikuchi diffraction pattern, 183–184
- Fundamental zone, Rodrigues vector/Rodrigues space, 47–49
- G**
- Gallium, crystal structure and symmetry, 16–17
- Geiger counters, x-ray diffraction, 393–395
- macrotexture analysis, 92–93
- General area detector diffraction system (GADDS), x-ray diffraction analysis, 96–98
- General axis distribution function, macrotexture analysis, series expansion method, 132–137
- Generalized Gauss components, orientation distribution function, 140
- Geodesic lines, Rodrigues vector/Rodrigues space, 50
- Geological materials
- electron backscatter diffraction, specimen preparation, 216
 - macrotexture analysis, sample preparation, 119
- Geometry, electron backscatter diffraction, 225–226
- Ghost error, orientation distribution function, 134–137
- “Ghost error,” pole figure measurement, 79
- Gnomonic projection, 390
- Kikuchi diffraction pattern, 182
 - synchrotron radiation, Laue technique, 353–355
- Goniometry instrumentation
- diffraction techniques, 72
 - pole figure measurement, 76–79
 - x-ray diffraction, 79–80
 - pole figure diffractometry, 86–90
 - x-ray detectors, 92–98
- Goss orientation
- face-centered crystal metals
 - deformation texture, 149–153
 - recrystallization texture, 163–166
 - optical texture analysis, 364–367
 - pole figure measurement, 76–79
 - silicon iron, 4–5
- Grain boundary engineering (GBE)
- bcc metal recrystallization texture, 167–168

- Grain boundary engineering (GBE) (*continued*)
 crystallographic analysis, 324–328
 coincidence site lattice, 324–326
 “five-parameter” analysis, 334–340
 interface-plane scheme, 326–328
 tilt boundaries, 327–328
 twist boundaries, 328
- microtexture analysis, misorientation distribution function, 296–298
- orientation connectivity, junction analysis, 345–347
- orientation mapping, misorientation data, 313–314
- research background, 324–325
- G**
- Grain curling, body-centered cubic structure, deformation texture, 156–157
- Grain orientation, classical texture analysis, 3
- Grain-oriented silicon iron, classical texture analysis, 4–5
- Grain/phase boundaries, Kikuchi diffraction pattern, 182
- Grain statistics
 macrotexture analysis
 orientation distribution functions, 127–129
 sample preparation, 119–121
 orientation mapping, 314–315
- Growth selection hypothesis, face-centered crystals, recrystallization texture, 162–166
- H**
- Hardware requirements, electron backscatter diffraction, 217–220
- Harmonic method, orientation distribution functions data, 129–137, 171–172
- Hermann-Maugin notation, Laue classes/groups, 20–21
- Hexagonal metals
 crystal structures, 18–20
 Kikuchi mapping, 399–401
 recrystallization textures, 170–171
- rotation matrix, 23–24
 symmetry operations, 382
- High-order Laue zone (HOLZ) lines, transmission electron microscopy, 255
- High-pressure preferred orientation (HIPPO), time-of-flight measurements, 111–112
- High-resolution electron microscopy (HREM), microtexture analysis, 242–243
- “Hit-orientation distribution function,” microtexture analysis, single-grain orientation, 273–275
- Homochoric space, Rodrigues vector / Rodrigues space, 50
- Hough transform
 electron backscatter diffraction, data collection efficiency, 221
 Kikuchi diffraction pattern, electron backscatter diffraction evaluation, 191–195
 synchrotron radiation, Laue technique, 353–355
- Huygens-Fresnel principle, x-ray diffraction, 53–55
- Huygens spherical wave formation, planar wave front, 52–53
- I**
- Ideal orientation, electron backscatter diffraction, 239
- Image plates, position-sensitive detector, 96–98
- Incomplete pole figures, macrotexture analysis, orientation distribution functions, 127–129
- Indexing techniques
 Kikuchi patterns
 automation, 188–191
 orientation direction, 185–188
 unambiguous indexing, 197–198
 pole figure indexing, 391–392
- Indirect methods, microtexture analysis, Euler space representations, 268–270
- Individual orientations, microtexture analysis

- Euler space representations, 266
pole figure and inverse pole figure, 262–265
- In situ* investigations, macrotexture analysis, neutron diffraction, 109
- Intense Pulsed Neutron Source (IPNS), pole figure measurements, 111–112
- Interactive, semiautomated evaluation, Kikuchi diffraction pattern, 183
- Intercrystalline structure distribution function (ISDF), orientation connectivity, 346–347
- Interface damage function (IDF), orientation connectivity, 346–347
- Interface-plane scheme, grain boundary analysis, 326–328
- Interfacial parameters and properties microtexture analysis, 10
orientation mapping, misorientation data, 313–314
- Intergrain misorientations, microtexture analysis, 285–286
- Intermetallic phases, structure factor F , 60–61
- Inverse pole figure
basic principles, 33
electron backscatter diffraction, 239
face-centered crystal structure, deformation texture, 151–153
macrotexture analysis, 105–107
orientation representation in, 126
microtexture analysis, orientation representation, 260–265
- Iron and iron alloys, body-centered cubic structure, deformation texture, 155–157
- Iterative pattern fitting, electron backscatter diffraction, 237–238
- K**
- K-absorption
pole figure data correction, macrotexture analysis, 101–105
- x-ray diffraction, 67
macrotexture analysis, 82–86
- Kikuchi diffraction pattern
assessment, 370–371
basic principles, 175–176
body-centered crystals, 399–401
comparison of techniques, 180
electron backscatter diffraction
data collection efficiency, 221
pattern clarity, 228–229
scanning electron microscopy, 208–213
- electron diffraction, 71
- face-centered crystals, 399–401
recrystallization texture, 162–166
- formation mechanisms, 176–179
- Miller/Miller-Bravais indices, 378–379
- projection, 181–182
- qualitative evaluation, 182
pattern quality, 198–201
- quantitative evaluation, 183–198
electron backscatter diffraction
automated evaluation, 191–195
indexing and orientation automation, 188–191
orientation determination, 185–188
selected area channeling pattern, 198
- transmission electron microscopy, 195–198
bright and dark lines, 197
dynamic range, 196–197
unambiguous indexing, 197–198
- transmission electron microscopy, 251–255
- Kikuchi diffraction patterns, hexagonal crystals, 399–401
- Known crystal orientation, electron backscatter diffraction calibration, 234–236
- Kossel diffraction
electron diffraction, 71
Kikuchi diffraction pattern formation, 176–179
- Kurdjumov-Sachs orientation
relationship, crystallographic analysis, 347–350

L

- L-absorption, x-ray diffraction, 67
 Lambert projection, reference sphere, 33
 Laser ultrasonic (LUS), texture analysis, 362–363
 Lattice strain, Kikuchi diffraction pattern, 182
 Lattice structure
 basic properties, 16–20
 diffraction, Bragg's law, 55–58
 Laue and Debye-Scherrer analysis, 62–64
 macrotexture analysis, orientation distribution functions, 128–129
 Miller/Miller-Bravais indices, 377–379
 neutron diffraction methods, macrotexture analysis, 108–109
 pole figure measurement, 76–79
 selected area diffraction, 244–247
 structure factor F , 60–61
 Laue technique
 crystal structures, 19–21
 diffraction analysis, 61–64
 noncentro-symmetric subgroups, 20–21
 synchrotron radiation, 352–355
 Linear absorption coefficient, diffraction analysis and, 65–66
 Line-rich diffraction spectra, low-symmetry materials, 113–115
 Lithium alloys, microtexture analysis, Rodrigues space representation, 276–280
 Local orientation techniques, assessment of, 369–370
 Local property effects, microtexture analysis, 9–10
 Low-carbon steel, body-centered cubic structure, deformation texture, 154–157
 Low-symmetry materials, macrotexture analysis, 112–115
 peak separation, 113–115

M

- Mackenzie cell, microtexture analysis
 misorientation representation in Rodrigues space, 290–292
 orientation distribution normalization and evaluation, 296–298
 Macrotexture analysis
 assessment of, 368–369
 bcc metals
 deformation textures, 153–157
 recrystallization textures, 166–169
 data evaluation and representation
 bcc metals deformation, 153–157
 direct calculation methods, 137–140
 Euler space display, 141–147
 fcc metals deformation, 147–153
 hexagonal metals deformation, 157–161
 orientation distribution function, 126–129
 research background, 123–124
 series expansion method, 129–137
 series expansion vs. direct calculation, 140–141
 fcc metals
 deformation textures, 147–153
 recrystallization textures, 161–166
 future research and applications, 121
 hexagonal metals, deformation textures, 157–161
 inverse pole figure
 orientation representation, 126
 x-ray diffraction, 105–107
 low-symmetry and multiphase materials, 112–117
 multiphase materials, 115–117
 peak separation, 113–115
 neutron diffraction methods, 107–112
 pole figure measurement, 107–109
 time-of-flight measurements, 109–112
 orientation distribution function
 data evaluation and representation, 126–129
 direct calculation methods, 137–140
 Euler space display, 141–147
 series expansion method, 129–137
 pole figure measurement, 75–79

- normalization and contouring, 124–126
orientation distribution function, 126–129
series expansion method, 129–137
research background, 75
sample preparation, 117–121
x-ray diffraction methods, 79–107
energy-dispersive refractometry, 98–101
inverse pole figures, 105–107
pole figure data correction and normalization, 101–105
pole figure diffractometry, 86–90
pole figure scanning principles, 90–92
x-ray detectors, 92–98
x-ray generation, 80–86
- Magnesium and magnesium alloys, hexagonal structure, deformation texture, 158–161
- Magnetic permeability, classical texture analysis, 4
- Magnetic scattering, neutron diffraction, 69
- Manual, nonautomated evaluation, Kikuchi diffraction pattern, 183
- Mass absorption coefficient
diffraction analysis and, 65–66
x-ray diffraction, macrotexture analysis, 85–86
- Material properties, electron backscatter diffraction, 225
- Maximum entropy, orientation distribution function, 137
- Maxwell velocity distribution, neutron diffraction methods, macrotexture analysis, 107–109
- Mesotexture, microtexture analysis, 10
- Metals
electron backscatter diffraction, specimen preparation, 214–216
- texture analysis in bcc metals
deformation textures, 153–157
recrystallization texture, 166–169
- fcc metals
deformation textures, 147–153
recrystallization texture, 161–166
- hexagonal metals
deformation textures, 157–161
recrystallization texture, 170–171
- Mexican hat pattern, Kikuchi diffraction pattern, automated evaluation, 191–195
- Microbeam spot diffraction, 250
- Microdiffraction, transmission electron microscopy, 252–255
- Micro-Kossel technique, scanning electron microscopy, 203–205
- Microscope parameters, electron backscatter diffraction, 225
- Microtexture analysis, 7–13
applications, 8–11
assessment of, 369–370
coincidence site lattice, grain boundaries, 324–326
density distributions, 262–265
electron backscatter diffraction, 11–12
Euler space orientation representation, 265–275
continuous distributions, 266–270
individual orientations, 266
misorientation representation, 286–289
single-grain measurements, 270–275
- high-resolution electron microscopy, 242–243
- individual orientations, 262
- Kikuchi diffraction, microdiffraction and convergent beam electron diffraction, 251–255
- misorientation data, 280–286
angle/axis descriptor, 281–285
cylindrical angle/axis space, 289–290
distribution function normalization and evaluation, 292–298
- intergrain misorientations, 285–286
Rodrigues space, 290–292
three-dimensional spaces, 286–292
- orientation microscopy and mapping, 12–13
- orientation/misorientation data analysis, 259–260

- Microtexture analysis (*continued*)
- pole figure/inverse pole figure orientations, 260–261
 - quantified data extraction, 298–300
 - research background, 257–258
 - Rodrigues space orientations, 275–280
 - selected area diffraction, 243–250
 - pattern characteristics, 243–247
 - pole figures, 247–250
 - small convergence beam electron diffraction, 250
 - spatial distribution, orientation mapping, 309–313
 - statistical distribution, orientation/misorientation data, 258–259
 - transmission electron microscopy, techniques overview, 241–242
- Miller/Miller-Bravais indices
- coincidence site lattice grain boundaries, 328
 - derivation and characteristics, 377–379
 - face-centered crystal metals
 - deformation texture, 149–153
 - recrystallization texture, 163–166
 - macrotexture analysis, orientation distribution functions, 128–129
 - microtexture analysis, Rodrigues space representation, 276–280
 - orientation denotation, 27–30
 - pole figure indexing, 391–392
- Misorientation data
- angle/axis of rotation, 42–43
 - coincidence site lattice, grain boundaries, 324–326
 - cylindrical angle/axis space, 43–45
 - electron backscatter diffraction, 239
 - Euler space, 39
 - grain boundaries, research background, 324–325
 - microtexture analysis, 10
 - angle/axis descriptor, 281–285
 - basic principles, 280
 - intergrain misorientations, 285–286
- orientation difference distribution function, 294–298
- statistical distribution, 258–259
- three-dimensional spaces, 286–292
- orientation mapping, 313–314
- Misorientation distribution functions (MODFs), 45
- normalization and evaluation, 292–298
 - orientation connectivity, 346–347
 - orientation relationships, 348–350
- Modified crystal deformation, Kikuchi diffraction pattern evaluation, 201
- Molybdenum, body-centered cubic structure, deformation texture, 156–157
- Monochromatic radiation
- Debye-Scherrer method, 63–64
 - pole figure data correction, macrotexture analysis, 101–105
 - pole figure measurement, 76–79
 - selected area diffraction, transmission electron microscopy, 244–247
 - x-ray diffraction, 53–55
 - macrotexture analysis, 82–86
- Monoclinic systems
- crystal structures, 18–20
 - Euler space, 37–39
 - fundamental zone, Rodrigues vector/Rodrigues space, 48–49
- Morphological/geometrical grain parameters
- microtexture analysis, 10
 - orientation mapping/orientation microscopy, 321–322
- Multichannel analyzer (MCA), x-ray diffraction, macrotexture analysis, 93–98
- energy-dispersive diffractometry, 99–101
- Multiphase materials
- electron backscatter diffraction, 223–224
 - macrotexture analysis, 115–117
 - orientation mapping, phase mapping, 317–318

Multiples of random distribution (MRD), crystallographic analysis, “five-parameter” analysis, 337–340

N

Neutron diffraction
assessment of, 368–369
characteristics of, 68–69
macrotexture analysis, 107–112
 low-symmetry materials, 112–115
 multiphase materials, 115–117
 pole figure measurement, 107–109
 sample preparation, 117–121
 time-of-flight measurements,
 109–112
 mass absorption coefficients, 65–66

Nickel and nickel alloys
 face-centered crystal structure,
 recrystallization texture,
 162–166
 orientation relationships, 348–350

Niobium and niobium alloys
 body-centered cubic structure,
 deformation texture, 153–157
 orientation relationships, 348–350

Nishiyama-Wassermann orientation
 relationship, crystallographic analysis, 347–350

Noncentro-symmetric subgroups,
 Hermann-Maugin notation,
 20–21

Nondiffraction texture analysis,
 361–367
 optical methods, 363–367
 ultrasonic velocity, 362–363

Normal direction
 coordinate systems rotation matrix,
 21–24
 Euler angles, 34–36
 inverse pole figure measurement,
 106–107
 Kikuchi diffraction pattern, 186–188
 pole figure indexing, 391–392
 pole figures, 31–33
 three-dimensional orientation
 distribution function, Euler space properties, 144–147

Normalization factor, pole figure data correction, macrotexture analysis, 105

O

Oblique σ sections, three-dimensional orientation distribution function, Euler space properties, 145–147

Odd-order series expansion coefficients, orientation distribution function, ghost errors, 134–137

[111]-etching technique, optical texture analysis, 366–367

Operational parameters, electron backscatter diffraction, 224–229

Optical methods, texture analysis, 363–367

Ordered structures, structure factor F , 60–61

Orientation connectivity, crystallographic analysis, 344–347

Orientation correlation function (OCF), microtexture analysis, 294–298

Orientation data
 angle/axis of rotation, 39–43
 coordinate systems, 20–24
 crystallographically related solutions,
 25–27
 cylindrical angle/axis space, 43–45
 descriptors
 crystal structures and symmetries,
 16–20
 research background, 15
 diffraction analysis, 62–64
 Euler angles, 33–36
 Euler space, 36–39
 inverse pole figure, 33
 Kikuchi diffraction pattern, 185–188
 microtexture analysis
 Euler space representation, 265–275
 pole figure/inverse pole figure data, 260–265
 Rodrigues space representation,
 275–280
 statistical distribution, 258–259
 Miller/Miller-Bravais indices
 notation, 27–30

- Orientation data (*continued*)
 - pole figure, 30–33
 - reference sphere, 30
 - Rodrigues vector/Rodrigues space, 46–47
 - rotation matrix, 24–25
- Orientation difference distribution function (ODDF), normalization and evaluation, 293–298
- Orientation direction
 - Kikuchi diffraction pattern, 185–188
 - automation, 188–191
 - microtexture analysis, 10–11
- Orientation distribution functions (ODFs)
 - classic texture analysis, superconductors, 7
 - Euler space texture representation and display, 141–147
 - hexagonal metals, 159–161
 - inverse pole figure measurement, 107
 - macrotexture analysis
 - direct methods, 137–140
 - Euler space properties, 141–147
 - inverse pole figure representation, 126
 - pole figure data representation, 126–129
 - pole figure normalization and contouring, 124–125
 - series expansion method, 129–137
 - microtexture analysis, 11
 - Euler space representations, 268–270
 - single-grain orientation measurements, 271–275
 - selected area diffraction, 248–250
- Orientation matrix
 - basic properties, 24–25
 - electron backscatter diffraction, system operation and data output, 239
 - Miller indices, 27–30
- Orientation microscopy/mapping
 - applications, 308–318
 - grain size/shape distribution, 314–315
 - microtexture analysis, spatial distribution, 309–313
- misorientations and interfaces, 313–314
- pattern quality maps, 315–317
- phase maps, 317–318
- data storage and output, 307–308
- electron backscatter diffraction
 - data collection efficiency, 220–221
 - scanning electron microscopy, 210–213
- Kikuchi diffraction pattern, 184
- microtexture analysis, 8–9, 12–13
- research background, 303–305
- sampling point location, 305–306
- sampling schedule, 306–307
- transmission electron microscopy, 318–321
- Orientation relationships, crystallographic analysis, 347–350
- Orientation topography, historical background, 304
- Orientation tube, face-centered crystal metals, deformation texture, 149–153
- Oriented growth hypothesis, face-centered crystals, recrystallization texture, 162–166
- Oriented nucleation hypothesis, face-centered crystals, recrystallization texture, 162–166
- Orthonormal sample symmetry, Euler space, 37–39
- Orthorhombic systems
 - crystal structures, 18–20
 - symmetry operations, 382
- P**
- Parallel electron beam, transmission electron microscopy, selected area diffraction, 243–247
- Particle stimulated nucleation (PSN), face-centered crystal metals, recrystallization texture, 166
- Pattern clarity, electron backscatter diffraction, 228–229

- Pattern indexing, Kikuchi diffraction pattern
automation, 188–191
orientation direction, 185–188
- Pattern magnification, electron
backscatter diffraction
calibration, 236–237
- Pattern quality mapping, orientation
microscopy/orientation
mapping, 315–317
- Pattern source point (SP), electron
backscatter diffraction,
calibration techniques, 232–238
- Peak intensity, pole figure data
correction, macrotexture
analysis, 102–105
- Peak profiles, x-ray diffraction,
macrotexture analysis, 93–98,
121
energy-dispersive diffractometry,
100–101
- Peak separation, low-symmetry
materials, 113–115
- Penetration depth
diffraction analysis and, 64–66
macrotexture analysis, sample
preparation, 118–121
x-ray diffraction, macrotexture
analysis, 85–86
- Phase identification analysis (PIA),
electron backscatter
diffraction, 223–224
- Phase mapping, microtexture analysis,
317–318
- Phase relationship, microtexture
analysis, 11
- Phase transformation, crystallographic
analysis, orientation
relationships, 347–350
- Photogrammetric techniques, surface
crystallographic analysis,
333–334
- Photographic film, position-sensitive
detector, 96–98
- Pitsch orientation relationship,
crystallographic analysis,
347–350
- Planar wave front, Huygens spherical
wave formation, 52–53
- Planck's constant, electron diffraction,
70–71
- Point groups, crystal structure, 17–20
- Poisson's ratio, classical texture analysis,
3–4
- Pole figure inversion
inverse pole figure *vs.*, 106–107
macrotexture analysis, orientation
distribution functions, 128–129
three-dimensional orientation
distribution functions, 171–172
- Pole figure measurement
basic principles, 30–33
classic texture analysis,
superconductors, 7
electron backscatter diffraction,
system operation and data
output, 239
indexing techniques, 391–392
macrotexture analysis, 75–79
data correction and normalization,
101–105
data evaluation and representation,
123–124
direct methods, 137–140
neutron diffraction methods, 107–109
normalization and contouring,
124–125
orientation distribution function,
126–129
sample preparation, 118–121
scanning principles, 90–92
series expansion method, 129–137
x-ray diffractometry, 86–90
- microtexture analysis
orientation representation, 260–265
quantified data extraction,
298–300
position-sensitive detector, 97–98
selected area diffraction, 247–250
stereographic projection, 385–389
- Pole figure window, macrotexture
analysis, 91–92
- Polycrystalline structures
Debye-Scherrer diffraction, 62–64
pole figure measurement, 76–79
synchrotron radiation techniques,
Debye-Scherrer diagrams,
356–361

- Polysilicon materials, electron backscatter diffraction, specimen preparation, 216
- Position-sensitive detector (PSD)
low-symmetry materials, peak separation, 114–115
x-ray diffraction, macrotexture analysis, 93–98, 121
- Positivity method, orientation distribution function, 136–137
- Potential scattering, neutron diffraction, 69
- Preferred orientation, classical texture analysis, 3
- Probe current, electron backscatter diffraction, 227–228
- Projection techniques
equal-area projection, 389–390
gnomonic projection, 390
Kikuchi diffraction pattern, 181–182
spherical projection, 385
stereographic projection, 385–389
- Proportional counters, x-ray diffraction, 395
- Pseudonormalization, pole figure data correction, macrotexture analysis, 105
- Pulsed neutron sources, neutron diffraction methods, macrotexture analysis, 107–109
- Pulse height analyzers, x-ray diffraction, 396–397
- Pulse-height analyzers
angular-dispersive analysis, 98
Geiger counters, x-ray diffraction, 93
pole figure data correction, macrotexture analysis, 102–105
- Pure-metal rolling texture, face-centered crystal metals, 148–153
- Q**
- Quadratic method, orientation distribution function, 135–137
- Qualitative evaluation, Kikuchi diffraction pattern, 182
pattern quality, 198–201

- Quantified data extraction
microtexture analysis, 298–300
orientation mapping/orientation microscopy, 321–322
- Quantitative analysis
cluster analysis, orientation connectivity, 344–347
Debye-Scherrer diffraction, 63–64
- Quantitative evaluation, Kikuchi diffraction pattern, 183–198
electron backscatter diffraction
automated evaluation, 191–195
indexing and orientation automation, 188–191
orientation determination, 185–188
selected area channeling pattern, 198
transmission electron microscopy, 195–198
bright and dark lines, 197
dynamic range, 196–197
unambiguous indexing, 197–198

R

- Radiation, diffraction and Bragg's law, 52–58
- Radon transform, Kikuchi diffraction pattern, electron backscatter diffraction evaluation, 192–195
- Read-Shockley relationship, coincidence site lattice, grain boundaries, 325–326
- Reciprocal lattice structure, selected area diffraction, 246–247
- Recrystallization texture
body-centered cubic (bcc) crystal structure, 166–169
face-centered metals, 161–166
hexagonal metals, 170–171
- Rectilinear geometry, Rodrigues vector/Rodrigues space, 49–50
- Reference axes, angle/axis of rotation, 42–43
- Reference sphere, basic principles, 30
- Reflecting planes, lattice structure, Bragg's law and, 56–58
- Reflection geometry
Laue and Debye-Scherrer analysis, 63–64

- macrotexture analysis, sample preparation, 118–121
pole figure measurement, 76–79
 macrotexture analysis, 86–90
position-sensitive detector, 95–98
of radiation, 54–55
Reflection sphere, selected area diffraction, 246–247
Resolution parameters, electron backscatter diffraction, 224–229
Resonance scattering, neutron diffraction, 69
Rhombohedral (trigonal) systems, crystal structures, 18–20
Ridging (roping) surface phenomenon,
 body-centered cubic (bcc) crystal structure,
 recrystallization texture, 168–169
Rietveld texture analysis, low-symmetry materials, peak separation, 115
Rocking beam microdiffraction, 252–255
Rodrigues vector/Rodrigues space
 coincidence site lattice, grain boundaries, 324–326
 electron backscatter diffraction, 239
 fundamental zone, 47–49
 macrotexture analysis, 123–124
 microtexture analysis
 intergrain misorientations, 286
 misorientation representation, 290–292
 orientation representation, 275–280
 orientation, 46–47
 spatial distribution, microtexture components, 309–313
 properties, 49–50
Rolling texture
 body-centered cubic (bcc) crystal structure
 deformation texture, 153–157
 recrystallization texture, 167–169
 coordinate systems rotation matrix, 21–24
 Euler angles, 34–36
 face-centered crystal metals
deformation texture, 147–153
recrystallization textures, 161–166
hexagonal metals, deformation texture, 158–161
macrotexture analysis, multiphase materials, 115–117
microtexture analysis, Rodrigues space representation, 275–280
orientation distribution function, 134–137
pole figure, 31–33
pole figure indexing, 391–392
three-dimensional orientation
 distribution function, Euler space properties, 145–147
Rotation matrix
 coordinate systems, 20–24
 crystallographically related solutions, 25–27
 crystal orientation, 20–27
 Euler angles, 34–36
 orientation descriptors, 24–25
 selected area diffraction, 246–247
Rules of extinction, structure factor F , 59–61
- S**
- Sample orientation distribution (SOD), Euler space properties, 144–147
Sample preparation, macrotexture analysis, 117–121
Sample rotation, pole figure measurement, 76–79
Sample/specimen coordinate system, rotation matrix, 21–24
Sample symmetries, Euler space, 37–39
Sampling point locations, orientation microscopy, 305–306
Sampling schedule, orientation microscopy/orientation mapping, 306–307
Scale of measurements, orientation mapping/orientation microscopy, 321–322
Scanning electron microscopy (SEM)
 assessment, 371
 diffraction pattern enhancement, 229–231

- Scanning electron microscopy (SEM) (*continued*)
electron backscatter diffraction
accelerating voltage, 226–227
calibration, 231–238
data collection efficiency, 220–221
evolution, 208–213
experiment design philosophy, 221–223
future research issues, 240
hardware requirements, 217–220
iterative pattern fitting, 237–238
know crystal orientation, 234–236
material requirements, 225
microscope parameters, 225
pattern clarity, 228–229
pattern magnification, 236–237
phase identification, 223–224
probe current, 227–228
resolution and operational parameters, 224–225
shadow casting, 233–234
specimen/microscope geometry, 225–226
specimen preparation, 213–216
system operation and data output, 238–239
electron channeling diffraction/selected-area channeling, 205–207
electron diffraction, 69–71
Kikuchi diffraction pattern, formation mechanisms, 176–179
Kikuchi diffraction pattern formation, 178–179
micro-Kossel technique, 203–205
microtexture analysis, 8
electron backscatter diffraction, 12
orientation microscopy/orientation mapping, sampling schedule, 306–307
surface crystallographic analysis, 329–331
focused ion beam tomography with, 341–344
photogrammetric techniques, 333–334
techniques overview, 203
- Scanning grids, macrotexture analysis
neutron diffraction, 109
pole figure measurement, 90–92
sample preparation, 119–121
Scanning-transmission electron microscopy (STEM), 252–255
Scattering amplitude
neutron diffraction, 68–69
structure factor F , 59–61
x-ray diffraction, 53–54
Schmidt net, equal area projection, 389–390
Scintillation counters, x-ray diffraction, 395
Second-order reflection, Bragg's law, 57–58
Sectioning techniques, surface
crystallographic analysis, 329–333
Selected area channeling (SAC)
Kikuchi diffraction pattern, 176
automated evaluation, 198
orientation determination, 185–188
scanning electron microscopy, 205–207
Selected area diffraction (SAD)
assessment of, 370–371
electron diffraction, 70–71
Kikuchi diffraction pattern, transmission electron microscopy, 195–198, 251–255
microtexture analysis, 243–250
overview of applications, 241–242
pattern characteristics, 243–247
pole figures, 247–250
small convergence beam electron diffraction, 250
orientation mapping/orientation microscopy, 319–321
Selected area electron channeling diffraction (SAECD), scanning electron microscopy, 206–207
Selective particle drag, bcc metal recrystallization texture, 168
Semiconductor detectors, x-ray diffraction, 396
Serial sectioning, calibrated techniques
crystallographic analysis, "five-parameter" analysis, 337–340

- surface crystallographic analysis, 331–332
- Series expansion method, orientation distribution functions data, 129–137
direct methods *vs.*, 140–141
- Shadow casting, electron backscatter diffraction calibration, 233–234
- Silicon intensified target (SIT) camera, electron backscatter diffraction, 211–213
- Silicon iron, crystallographic orientation, 4–5
- Single-crystal monochromators, x-ray diffraction, macrotexture analysis, 83–86
- Single-crystal silicon, electron backscatter diffraction calibration, known crystal orientation, 236
- Single-crystal volumes, selected area diffraction, 243–247
- Single-grain orientation methods
low-symmetry materials, 112–115
microtexture analysis, Euler space representations, 268, 270–272
- Skeleton line, face-centered crystals, deformation texture, 151–153
- Slip traces, surface crystallographic analysis, calibrated serial sectioning, 332
- Slow-scan charge-coupled device (SSCCD), electron backscatter diffraction, 217–220
- Small convergence beam electron diffraction (SCBED), 250
orientation mapping/orientation microscopy, 318–321
- S orientation
crystallographically related solutions, texture variants, 383
face-centered cubic metals, 149–153
truncation error, 133–137
- Space groups, crystal structure, 17–20
- Spallation, neutron diffraction methods, macrotexture analysis, 108–109
- Spatial distribution, microtexture components
crystallographic analysis, 344–347
orientation mapping, 309–313
- Spatial location, microtexture analysis, 8
- Specimen/microscope geometry, electron backscatter diffraction, 225–226
calibration techniques, 231–238
- Specimen preparation, electron backscatter diffraction, scanning electron microscopy, 213–216
- Spherical harmonic function, series expansion method, orientation distribution functions data, 129–137
- Spherical projection, 385
- Stacking fault energy (SFE),
face-centered crystal metals
deformation texture, 148–153
recrystallization texture, 163–166
- Stage control, sampling point location, orientation microscopy, 305–306
- Statistical assessment, microtexture analysis
orientation/misorientation data, 258–259
single-grain orientation measurements, 270–275
- Steel materials
body-centered cubic (bcc) crystal structure
deformation texture, 153–157
recrystallization texture, 167–169
electron backscatter diffraction, specimen preparation, 216
- Step scanning, pole figure measurement, macrotexture analysis, 91–92
- Stereographic projection, 385–389
orientation and misorientation, angle/
axis of rotation, 43–45
reference sphere and, 33
- Stereological techniques, surface crystallographic analysis, 334–340, 338–340
- Stereophotogrammetry, surface crystallographic analysis, 333–334

- Straight-line geometry, Rodrigues vector/Rodrigues space, 49–50
- Strength, classical texture analysis, 3–4
- Strip metal products, classical texture analysis, 5–6
- Structure factor F
diffraction of radiation, 59–61
geometrical rules, 58
- Superconductors
classical texture analysis, 6–7
 x -ray diffraction, macrotexture analysis, 83–86
- Superlattice peaks, structure factor F , 60–61
- Surfaces, crystallographic analysis, 328–344
calibrated serial sectioning, 331–332
“five-parameter” and stereological techniques, 334–340
photogrammetric techniques, 333–334
sectioning techniques, 329–333
three-dimensional EBSD, 340–344
transmission electron microscopy, thin section analysis, 332–333
two-surface sectioning, 331
- “Sweeping” technique, synchrotron radiation, Debye-Scherrer patterns, 358–361
- Symmetrical tilt grain boundary (STGB), interface-plane scheme, 327–328
- Synchrotron radiation
assessment of, 368–369
texture analysis, 352–361
Debye-Scherrer patterns, polycrystalline regions, 356–361
Laue pattern orientation, 353–355
- T**
- Tantalum
body-centered cubic structure, deformation texture, 156–157
diffraction spectrum, Bragg angles, 56–58
macrotexture analysis, sample preparation, 119–121
- Tetragonal systems, crystal structures, 18–20
- Texture analysis
classical approach to, 3–7
grain-oriented silicon iron, 4–5
strip metal products, 5–6
superconductors, 6–7
experimental methods, comparison and assessment, 368–374
microtexture, 7–13
applications, 8–11
electron backscatter diffraction, 11–12
orientation microscopy and mapping, 12–13
nondiffraction techniques, overview, 351
- Thermal expansion, classical texture analysis, 4
- Three-dimensional electron backscatter diffraction (3D-EBSD), surface crystallographic analysis, 340–344
- Three-dimensional orientation distribution functions
direct method, 138–140
energy-dispersive diffractometry, 100–101
- Euler space properties, 141–147
texture representation and display, 143–147
inverse pole figure, 105–107
macrotexture analysis, 123–124
pole figure inversion, 171–172
series expansion method, 129–137
 x -ray diffraction, 66–67
- Three-dimensional space, misorientation data representation, microtexture analysis, 286–292
- Three-dimensional x -ray diffraction (3-D XRD), synchrotron radiation, 360–361
- Tilt boundaries, interface-plane scheme, 327–328
- Time-of-flight measurements, macrotexture analysis, neutron diffraction, 109–112

- Titanium and titanium alloys
body-centered cubic structure,
deformation texture, 153–157
electron backscatter diffraction,
specimen preparation, 216
hexagonal structure
deformation texture, 159–161
recrystallization texture, 170–171
Kikuchi diffraction pattern, 180
- Toughness, classical texture analysis, 4
- Transmission electron microscopy (TEM)
assessment of, 370–371
Debye-Scherrer method, 62–64
electron diffraction, 69–71
high-resolution electron microscopy, 242–243
- Kikuchi diffraction pattern
automated evaluation, 195–198
formation mechanisms, 176–180
microdiffraction and convergent beam electron diffraction, 251–255
orientation determination, 185–188
- microtexture analysis, 8
electron backscatter diffraction, 12
- orientation mapping/orientation microscopy, 318–321
- selected area diffraction, 243–250
pattern characteristics, 243–247
pole figures, 247–250
small convergence beam electron diffraction, 250
- surface crystallographic analysis, 329–331
sectioning techniques, 330–333
thin sections, 332–333
- techniques overview, 241–242
- Transmission geometry
Kikuchi diffraction pattern formation, 176–179
- Laue and Debye-Scherrer analysis, 63–64
- neutron diffraction methods,
macrotexture analysis, 108–109
- pole figure measurement, 76–79
macrotexture analysis, 88–90
- position-sensitive detector, 95–98
- Transverse direction (TD)
coordinate systems rotation matrix, 21–24
Euler angles, 34–36
Kikuchi diffraction pattern, 186–188
pole figure, 31–33
three-dimensional orientation
distribution function, Euler space, 142–147
- Triclinic crystal structures
basic properties, 18–20
Euler space, 37–39
fundamental zone, Rodrigues vector/Rodrigues space, 48–49
orientation distribution function, series expansion method, 131–137
- Triple junction boundaries
orientation connectivity, 345–347
surface crystallographic analysis, “five-parameter” analysis, 336–340
- Truncation error, orientation distribution function, series expansion method, 132–137
- Tungsten and tungsten alloys,
orientation relationships, 349–350
- Twinning, surface crystallographic analysis, “five-parameter” analysis, 335–340
- Twist grain boundary (TWGB),
interface-plane scheme, 327–328
- Two-surface sectioning, surface crystallographic analysis, 331
- U**
- Ultrasonic velocity, texture analysis, 362–363
- Unambiguous indexing, Kikuchi diffraction pattern, transmission electron microscopy evaluation, 197–198
- Uniaxial deformation
body-centered cubic (bcc) crystal structure, 156–157
- face-centered crystal metals, 153

V

- Vector method, orientation distribution function, 140
 Voltage acceleration, electron backscatter diffraction, 226–227
 Volume-based texture analysis, pole figure and inverse pole figure, 263–265
 Volume effect, pole figure data correction, macrotexture analysis, 104–105

W

- Wavelength characteristics, x-ray diffraction, 53–55
 macrotexture analysis, 81–86
 White radiation, x-ray diffraction, macrotexture analysis, 80–86
 WIMV method, orientation distribution function, 138–140
 Wulff net, stereographic projection, 387–389

X

- X-radiation, Debye-Scherrer technique, 62–64
 X-ray detectors, macrotexture analysis, 92–98
 X-ray diffraction
 assessment of, 368–369
 atomic scattering, 52–54
 characteristics of, 66–67
 classical texture analysis,
 superconductors, 6–7
 counters for, 393–397
 Geiger counters, 393–395
 proportional counters, 395
 pulse height analyzers, 396–397
 scintillation counters, 395
 semiconductor detectors, 396

- macrotexture analysis, 79–107
 energy-dispersive refractometry, 98–101
 inverse pole figures, 105–107
 low-symmetry materials, 112–115
 multiphase materials, 115–117
 pole figure data correction and normalization, 101–105
 pole figure diffractometry, 86–90
 pole figure scanning principles, 90–92
 sample preparation, 117–121
 x-ray detectors, 92–98
 x-ray generation, 80–86
 mass absorption coefficients, 65–66
 X-ray tubes, x-ray diffraction, macrotexture analysis, 80–86

Y

- Young's modulus, classical texture analysis, 3–4

Z

- Zener drag, bcc metal recrystallization texture, 168
 Zero-order Laue zone (ZOLZ) lines, 255
 Zero-range method, orientation distribution function, 135–137
 Zinc
 face-centered crystal metals,
 recrystallization texture, 163–166
 face-centered cubic structure,
 deformation texture, 150–153
 hexagonal structure, deformation texture, 160–161
 Zirconium, hexagonal structure
 deformation texture, 159–161
 recrystallization texture, 170–171

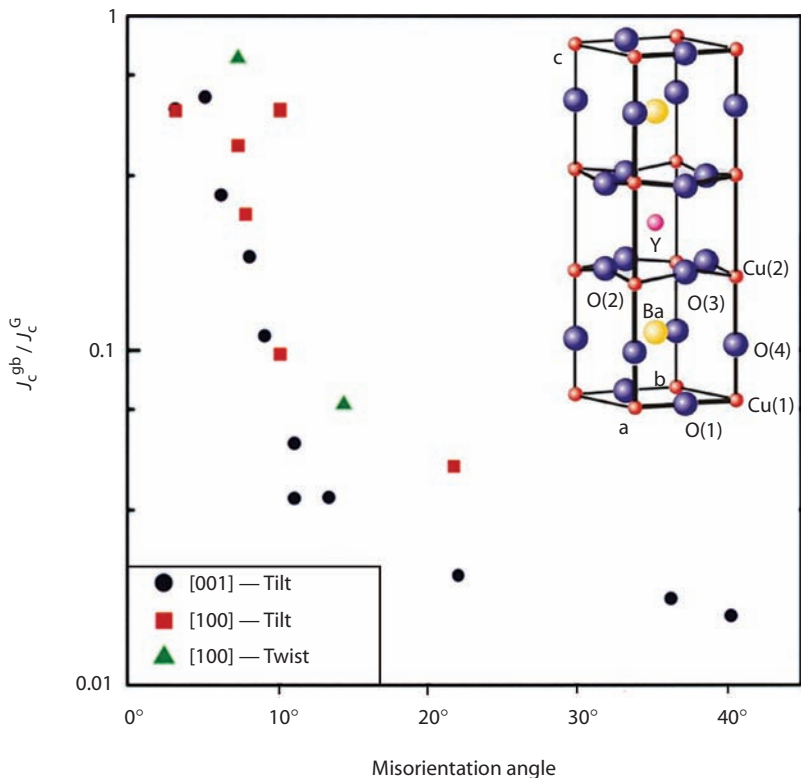


FIGURE 1.4

Current transmission, that is, the ratio of intergrain (gb) and intragrain (G) critical current densities J_c across grain boundaries in YBCO superconductors as a function of misorientation angle (at 5 K). High superconducting current transmission requires maximum fraction of low-angle grain boundaries, that is, a very sharp texture. (Courtesy of B. Obst.)

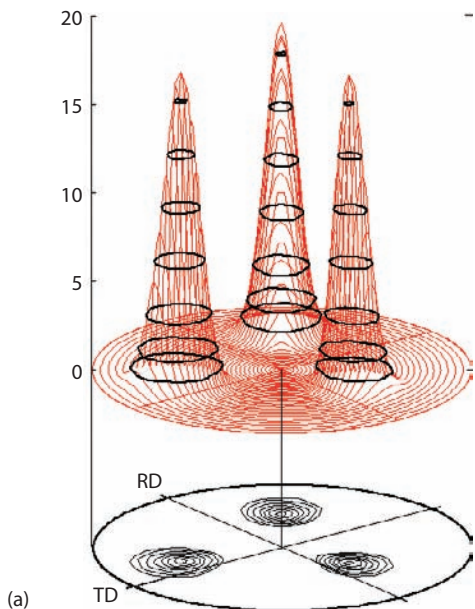


FIGURE 5.1a

Contouring of a 3-D pole density distribution to derive the standard 2-D pole figure presentation ($\{200\}$ pole figure, stereographic projection).

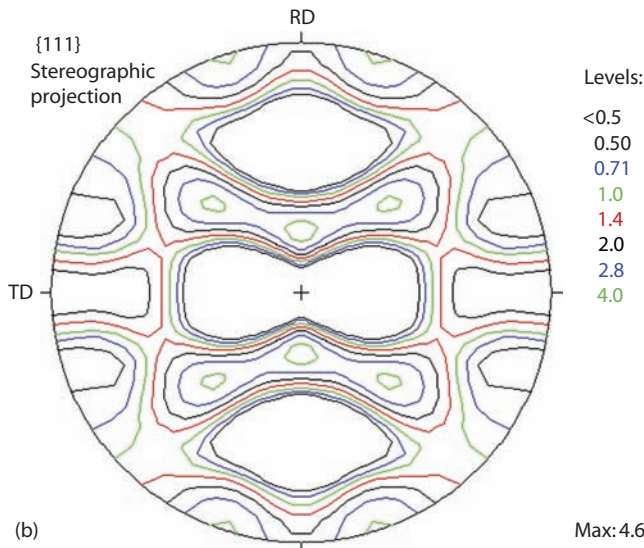


FIGURE 5.2b

{111} Pole figure plotted with contour lines (logarithmic progression; regions with intensity lower than 0.5 are dotted); (b) same pole figure as in (a) plotted with colored contour lines.

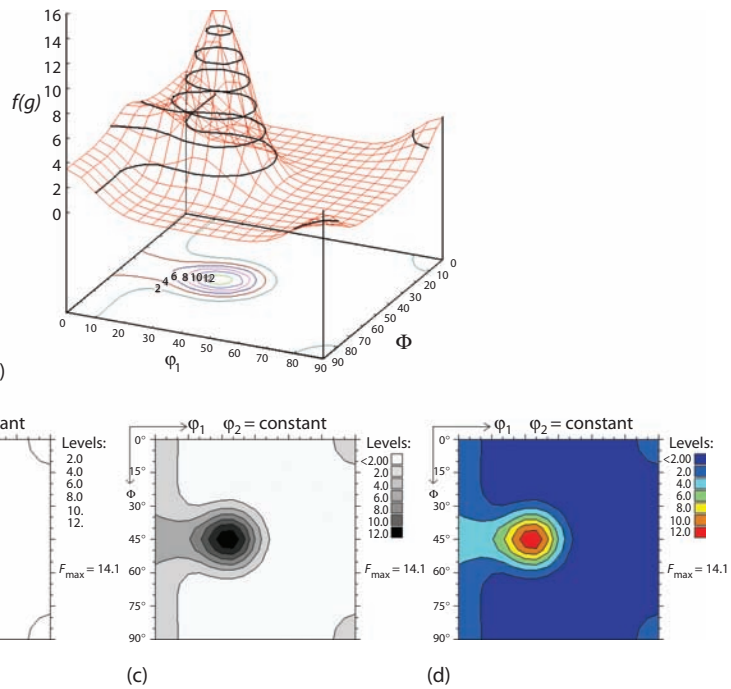


FIGURE 5.12

(a) Contouring of a 3-D orientation distribution to derive the standard 2-D presentation of ODF sections; (b) orientation distribution of (a), plotted with iso-intensity lines; (c) orientation distribution of (a), plotted with gray shades; (d) orientation distribution of (a), plotted with colors (ODF $\phi_2 = 0^\circ$ section).

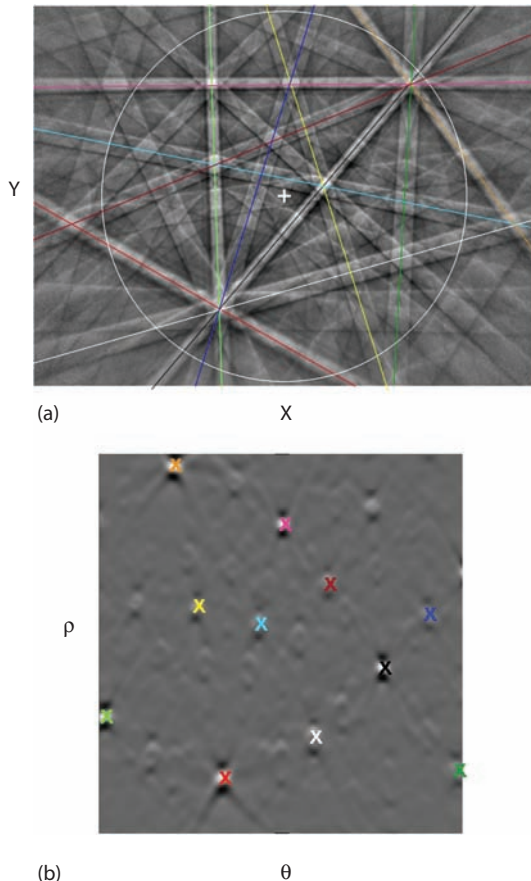


FIGURE 6.9

Gray-tone weighted Hough transform, or Radon transform, of an EBSD pattern of aluminum with overlaid bands. (a) Original EBSD pattern; (b) pattern after the Radon transform. (Courtesy of A. Gholinia.)

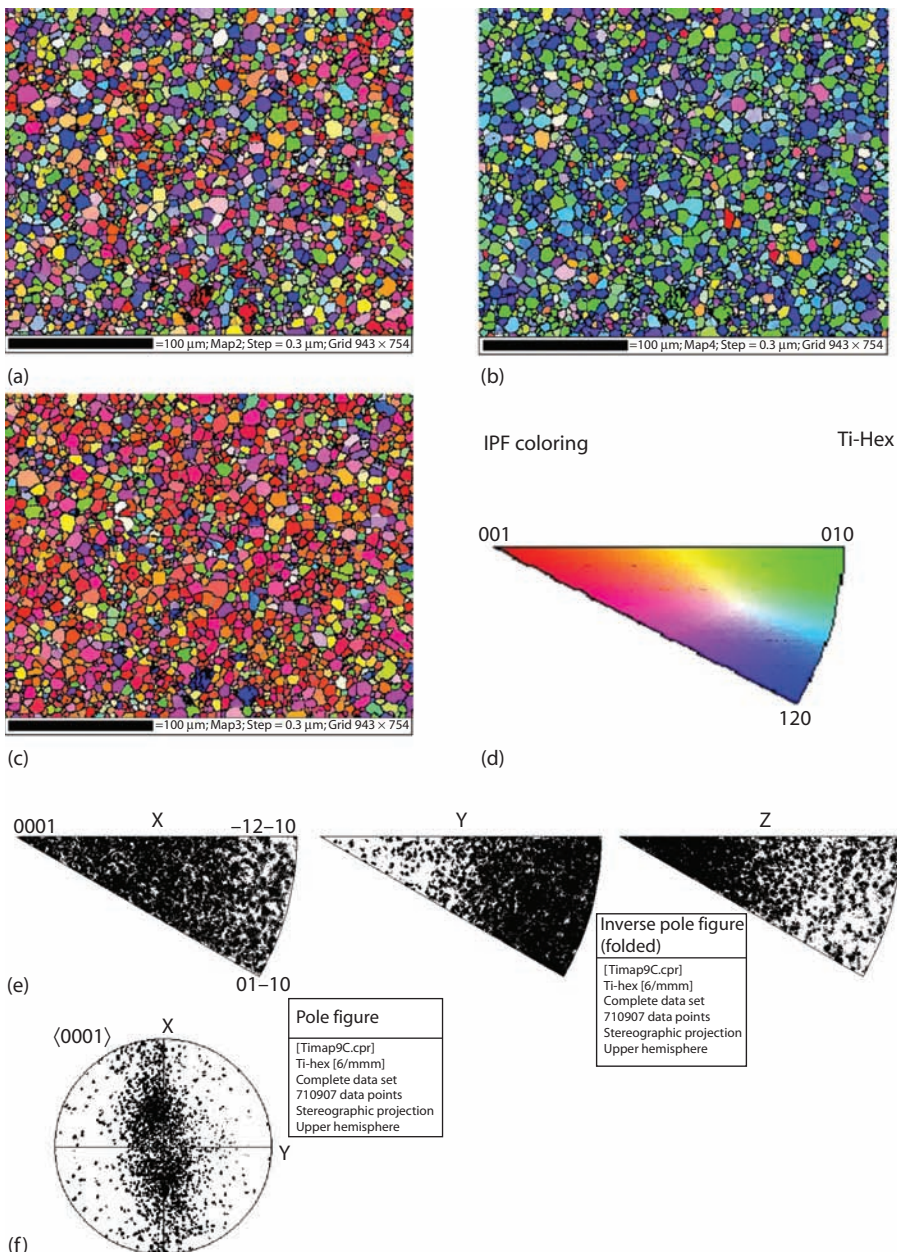


FIGURE 10.3

Orientation map from commercially pure titanium in (a) the specimen X, (b) the specimen Y, and (c) the specimen Z directions. (d) Color key for the maps; (e) inverse pole figures from the X, Y, and Z directions; (f) $\langle 0001 \rangle$ pole figure.

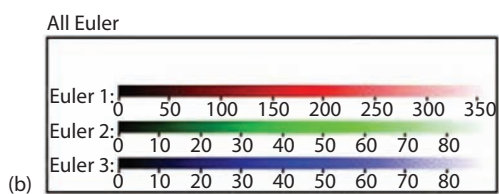
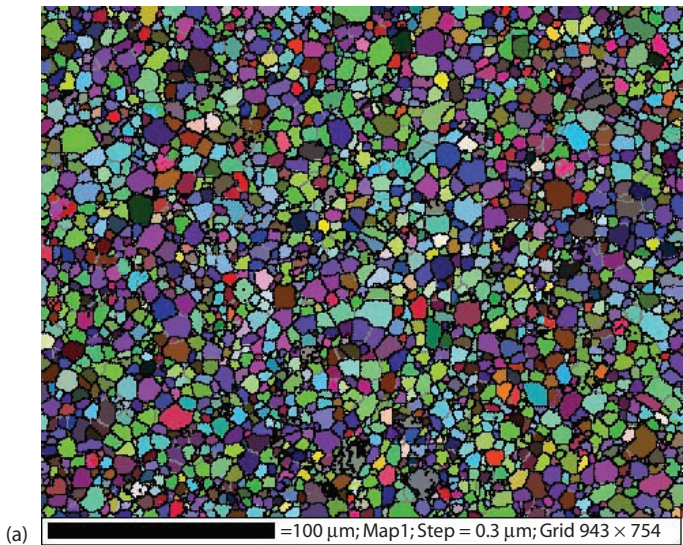


FIGURE 10.4

(a) Euler angle orientation map from commercially pure titanium. (b) Euler angle color key.

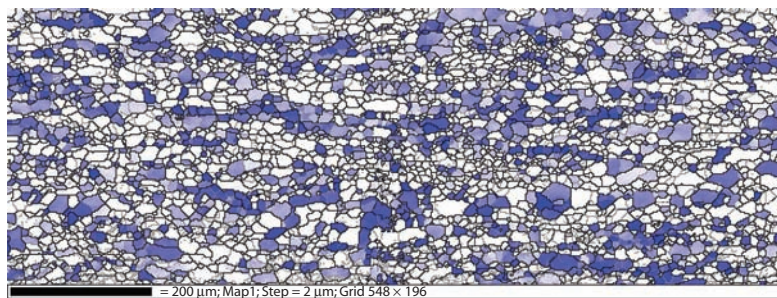


FIGURE 10.5a

(a) Orientation map from silicon iron showing grains colored in blue if the specimen Z (normal) direction is $<20^\circ$ from $\langle 111 \rangle$. The depth of color diminishes with increasing deviation from exact $\langle 111 \rangle$. High-angle grain boundaries are depicted by black lines and low-angle grain boundaries by gray lines.

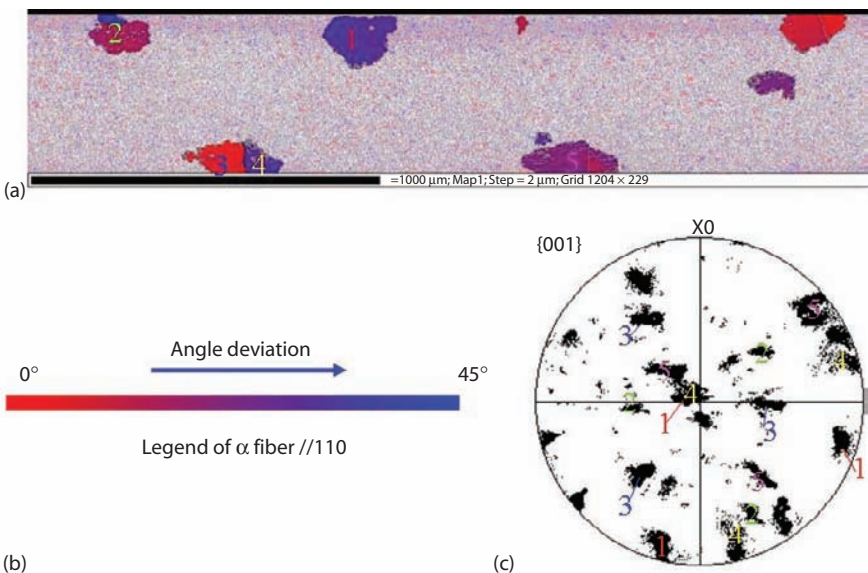


FIGURE 10.6

(a) Orientation map from silicon iron showing large grains (numbered) arising from abnormal grain growth. (b) User-defined color key for the map in (a); grains are colored according to proximity to the “ α fiber,” that is, $\langle 110 \rangle$ parallel to the rolling direction. Red depicts the exact α fiber, changing to blue for orientations having the maximum deviation from the α fiber (45°). (c) $\{001\}$ Pole figure showing the orientations of the large grains, numbered accordingly, in (a). The rolling direction is horizontal (parallel to the specimen X direction).

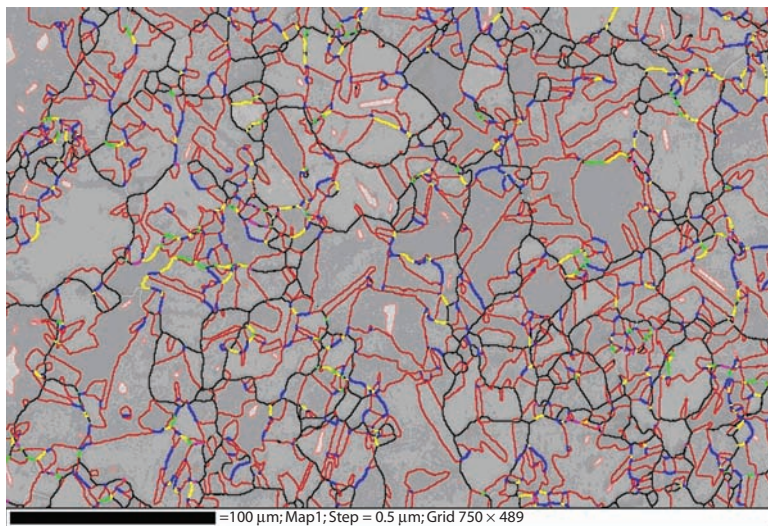


FIGURE 10.7

Orientation map made from an austenitic steel showing various grain boundary misorientation types. High-angle grain boundaries are depicted by black lines and low-angle grain boundaries by gray lines. Σ_3 , Σ_9 , and Σ_{27} boundaries (in CSL notation) are colored red, blue, and yellow, respectively. The background to the map is shaded gray according to a diffraction pattern quality parameter.

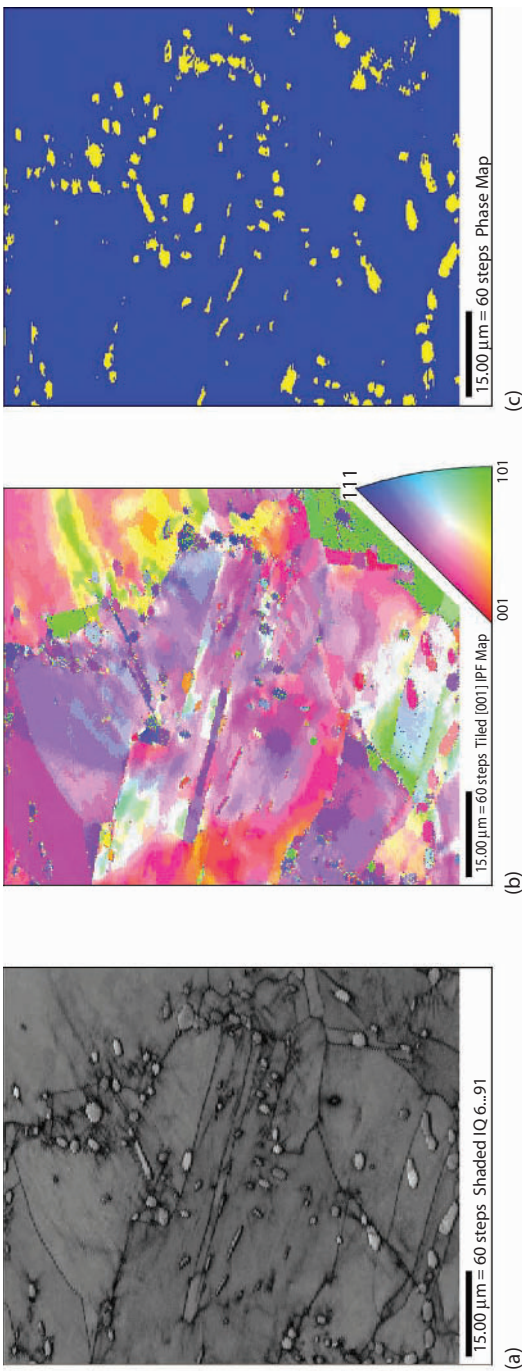


FIGURE 10.8
EBSD analysis of a mildly deformed two-phase nickel–tungsten specimen. (a) Image quality map (darker shading corresponds to poorer image quality). Note that grain and phase boundaries are not specially marked, but show up due to their low image quality; (b) orientation map; (c) phase map (blue—nickel; yellow—tungsten). (Data taken from Sinclair, C.W. et al., *Mater. Sci. Technol.*, 19, 1321, 2003.)

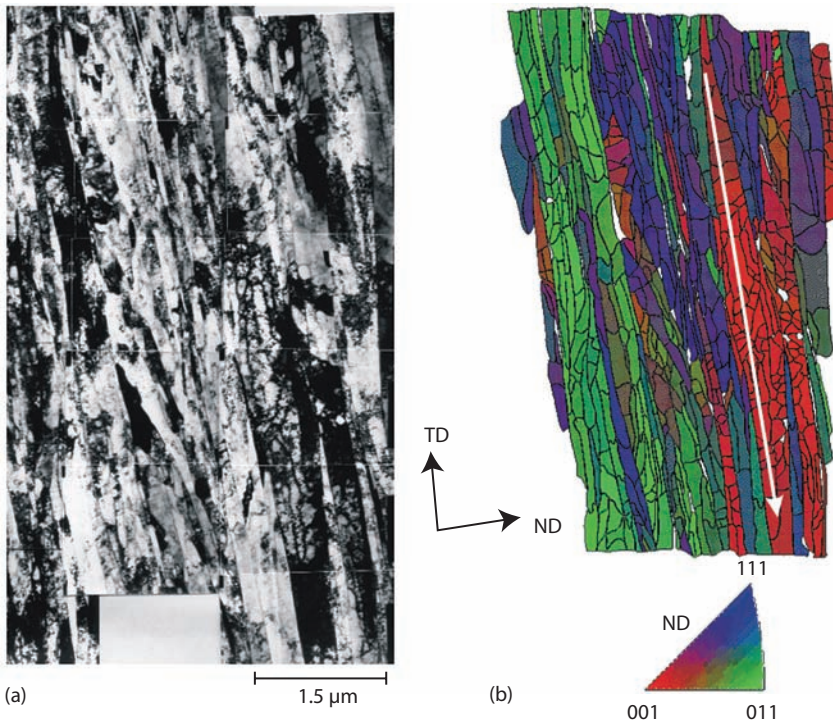


FIGURE 10.9

Example of orientation microscopy in the TEM. (a) TEM micrograph of Fe–36% Ni deformed 94% by cold rolling (longitudinal section, i.e., ND–TD plane); (b) orientation map of (a). The colors correspond to crystal directions parallel to the normal direction (ND) of the sheet. (From Zaefferer, S., Baudin, T., and Penelle, R., *Acta Mater.*, 49, 1105, 2001. With permission.)

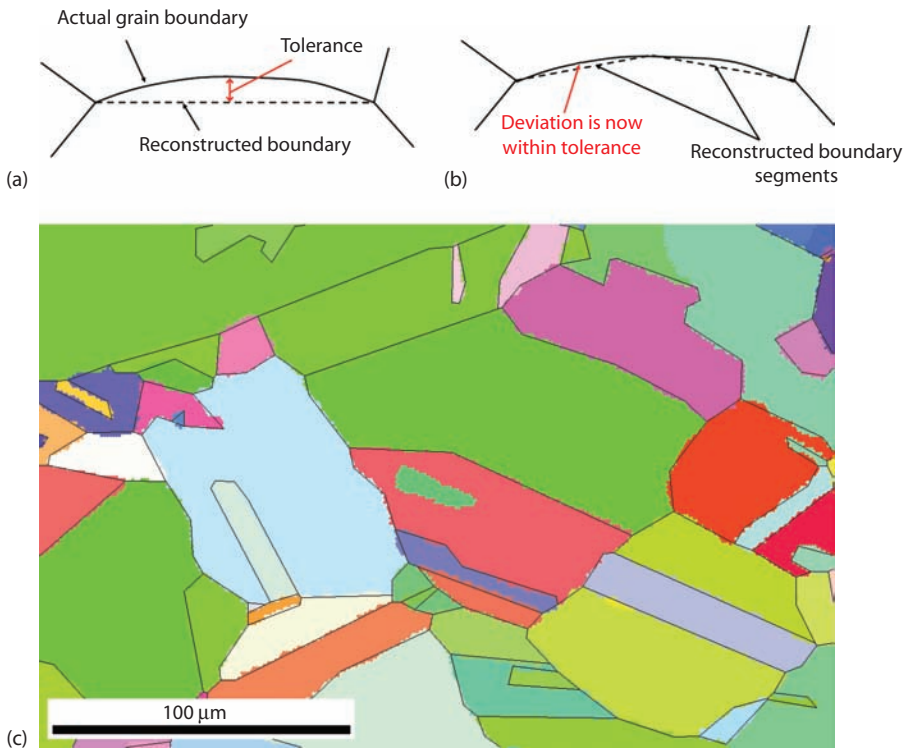


FIGURE 11.5

Illustration of the boundary trace reconstruction routine. (a) First reconstruction attempt by joining adjacent triple junctions. (b) Segmentation of the reconstructed trace. (c) Small map wherein reconstructed boundaries are superimposed on true boundaries. Grains are colored randomly.

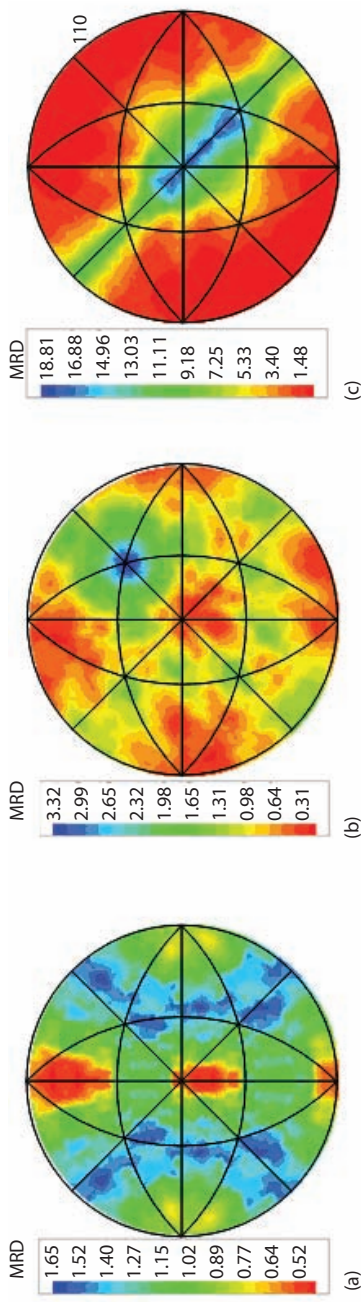
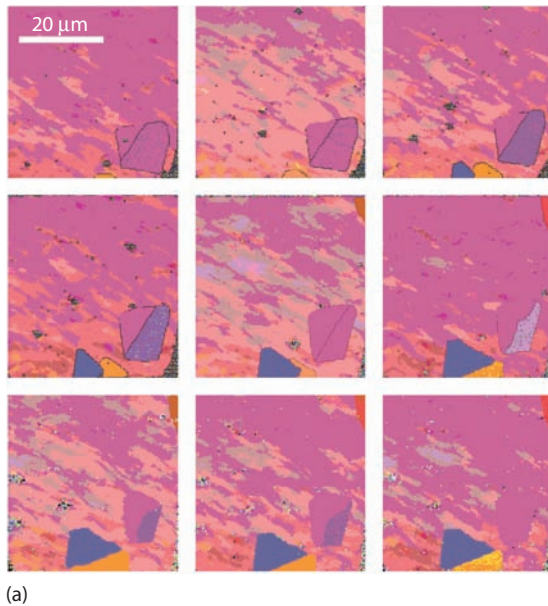
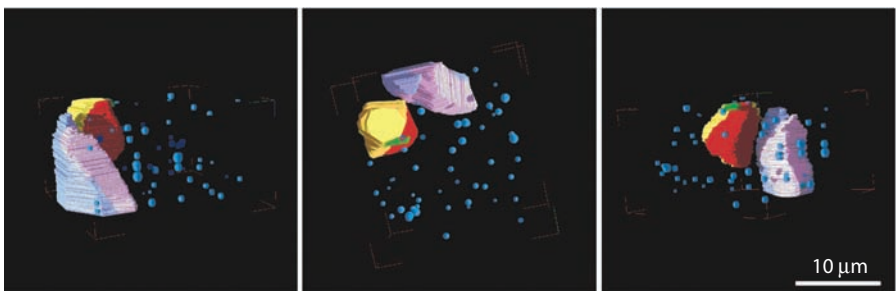


FIGURE 11.7
Distribution of boundary planes for selected misorientations in a brass specimen expressed as multiples of a random distribution (MRD) and shown in standard stereographic projection. (a) 30°/[100] misorientation; (b) 30°/[111] misorientation; (c) 30°/[110] misorientation. The [110] misorientation axis is marked in (c).



(a)



(b)

FIGURE 11.9

(a) EBSD maps of consecutive FIB sections through part-recrystallized Ni-0.3wt% Si. The slices represent section depths of $0.2 \mu\text{m} \pm 0.05 \mu\text{m}$. SiO_2 particles and recrystallized grains containing annealing twins are seen in the deformed matrix. (b) 3-D rendering of (a). (Courtesy of M. Ferry.)

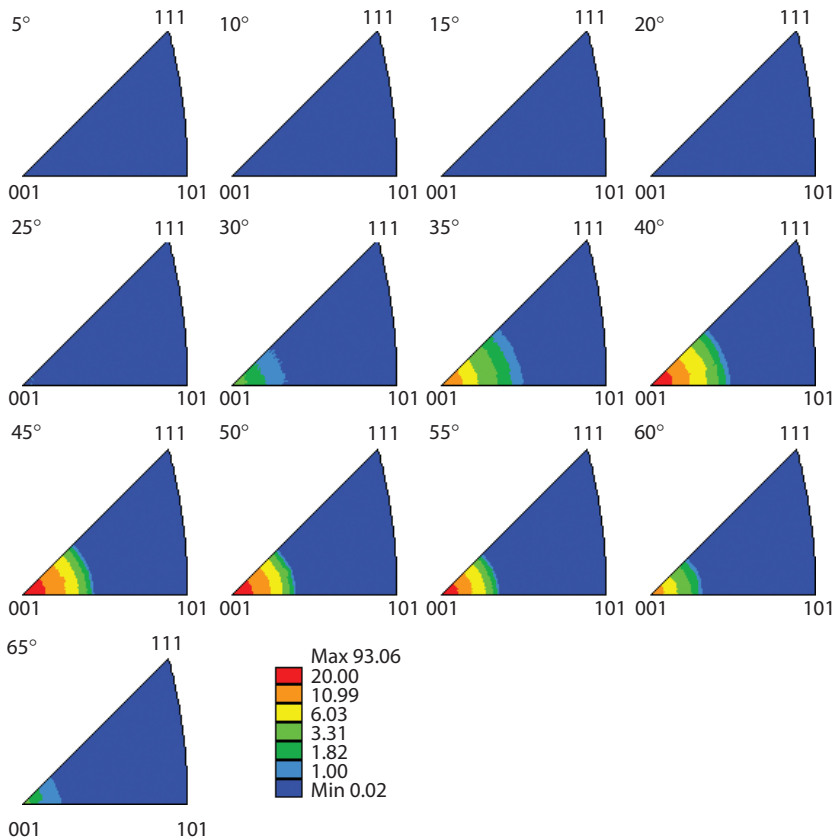


FIGURE 11.11

MODF between two different phases in a nickel/tungsten composite. The MODF was computed from the misorientations between adjacent grains of fcc nickel and bcc tungsten, which were obtained by EBSD (see also Figure 10.8).

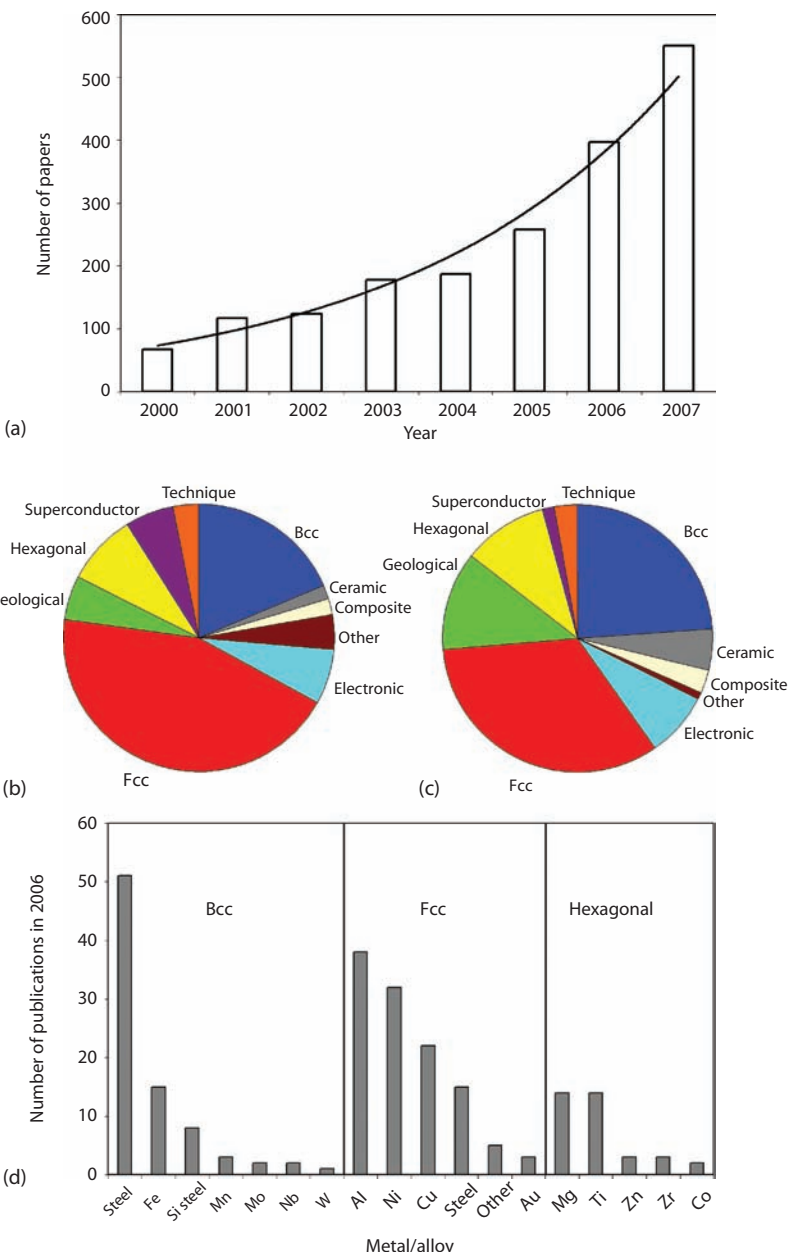


FIGURE 12.10

(a) Numbers of papers published in the period 2000–2007, which report EBSD, showing an approximately exponential increase. (From ScienceDirect.com.) (b) Breakdown of EBSD application according to material type based on publications in 2003. (c) Breakdown of EBSD application according to material type based on publications in 2006. (d) Breakdown of EBSD applications according to metals (or alloys based on that metal) in 2006.

SECOND EDITION

Introduction to TEXTURE ANALYSIS

Macrotexture, Microtexture,
and Orientation Mapping

The first edition of **Introduction to Texture Analysis: Macrotexture, Microtexture, and Orientation Mapping** broke new ground by collating seventy years worth of texture research in a convenient single-source format. Reflecting emerging methods and the evolution of the field, the second edition continues to provide comprehensive coverage of the concepts, practices, and applications of techniques used to determine and characterize texture.

Useful to experts and nonspecialists alike, **Introduction to Texture Analysis: Macrotexture, Microtexture, and Orientation Mapping, Second Edition** keeps mathematics to a minimum, enabling a clearer focus on scientific principles. It combines coverage of traditional macrotexture analysis and newer electron microscopy-based microtexture analysis, which reflects the modern approach to the field. Organized into three sections—**Fundamental Issues, Macrotexture Analysis, and Microtexture Analysis**—the book integrates the two techniques and addresses the subsequent need for a more detailed explanation of philosophy, practice, and interpretation associated with texture analysis.

COMPLETELY REVISED AND UPDATED, THIS SECOND EDITION
OF A BESTSELLER COVERS

- Relevant terminology
- Essential information on diffraction of radiation
- Data acquisition and representation of macrotexture analysis
- Experimental details of transmission- or scanning electron microscope-based techniques
- Methods of data evaluation and representation
- Innovative topics of orientation microscopy and mapping
- Advanced issues concerning crystallographic aspects of interfaces and connectivity

This is a rare introductory-level guide to texture analysis which illustrates approaches to orientation measurement and interpretation and elucidates the fundamental principles on which measurements are based. This book is an ideal tool to help you develop a working understanding of the practice and applications of texture.



CRC Press
Taylor & Francis Group
an informa business

6000 Broken Sound Parkway, NW
Suite 300, Boca Raton, FL 33487
270 Madison Avenue
New York, NY 10016
2 Park Square, Milton Park
Abingdon, Oxon OX14 4RN, UK

63650

ISBN: 978-1-4200-6365-3

90000



9 781420 063653

www.crcpress.com